Series Editor D. M. P. Mingos

Volume Editor T. Schönherr

Optical Spectra and Chemical Bonding in Transition Metal Complexes

Special Volume II

dedicated to Professor Jørgensen

107
Structure and Bonding

Managing Editor:
D.M.P. Mingos

Springer

Berlin
Heidelberg
New York
Hong Kong
London
Milan
Paris
Tokyo

Optical Spectra and Chemical Bonding in Transition Metal Complexes

**Special Volume II
dedicated to Professor Jørgensen**

**Volume Editor:
T. Schönherr**

With contributions by
C. Anthon · M. Atanasov · R. Beaulac · J. Bendix
A.-M. Boulanger · G. Boulon · S. Buddhudu
S.I. Gorelsky · P. Gütlich · P.J. van Koningsbruggen
A.B.P. Lever · M. Morita · S. Murakami · M.-C. Nolet
D. Rau · C. Reber · D. Reinen · F. Renz · H. Riesen
C.E. Schäffer

Springer

The series *Structure and Bonding* publishes critical reviews on topics of research concerned with chemical structure and bonding. The scope of the series spans the entire Periodic Table. It focuses attention on new and developing areas of modern structural and theoretical chemistry such as nanostructures, molecular electronics, designed molecular solids, surfaces, metal clusters and supramolecular structures. Physical and spectroscopic techniques used to determine, examine and model structures fall within the purview of Structure and Bonding to the extent that the focus is on the scientific results obtained and not on specialist information concerning the techniques themselves. Issues associated with the development of bonding models and generalizations that illuminate the reactivity pathways and rates of chemical processes are also relevant.

As a rule, contributions are specially commissioned. The editors and publishers will, however, always be pleased to receive suggestions and supplementary information. Papers are accepted for *Structure and Bonding* in English.

In references *Structure and Bonding* is abbreviated *Struct Bond*
and is cited as a journal.

Structure and Bonding
is also Available Electronically

For all customers who have a standing order to Structure and Bonding, we offer the electronic version via SpringerLink free of charge. Please contact your librarian who can receive a password for free access to the full articles by registration at:

http://www.springerlink.com

If you do not have a subscription, you can still view the tables of contents of the volumes and the abstracts of each article by going to the SpringerLink Homepage, clicking on "Browse by Online Libraries", then "Chemical Sciences", and finally choose Structure and Bonding.

You will find information about the

– Editorial Board
– Aims and Scope
– Instructions for Authors
– Sample Contribution

at http://www.springeronline.com using the search function.

Foreword

Axel Christian Klixbüll Jørgensen was a "Polyhistor", one of the very few in the highly specialized science of our time. His interests and contributions in chemistry covered the whole Periodic Table. This statement demonstrates the breadth of his interests, however, it also sheds light on the constraints of chemistry which deals with a large, yet limited number of elements. It is not surprising that Jørgensen went beyond these limits, exploring the probable or plausible chemistry of yet unknown elements and elementary particles such as quarks. Even chemistry itself did not place rigid limits on his mind, he was able to transfer his chemical concepts to scientific problems far beyond the normal such as in astrophysics.

"Structure and Bonding" is intimately associated with the name C.K. Jørgensen both as initiator and author over several decades. The appearance of a special edition in memory of this great scientist is a self-evident prolongation of his many contributions to the success of this series.

We owe a debt of thanks to Dr. Thomas Schönherr for his efforts in setting up this special edition. The scientific contributions reflect some of the outstanding impact on the understanding of chemistry stimulated by Jørgensen's thoughts as well as by his opening of new research areas. As an innovation in "Structure and Bonding", a number of personal notes have been added in order to give some impression of the method of thinking and communicating that was so characteristic of Jørgensen. These notes will be a reminder to all those who knew him and they will convey to those who never met him what was so special about this great man.

Stuttgart, September 2003   Arndt Simon
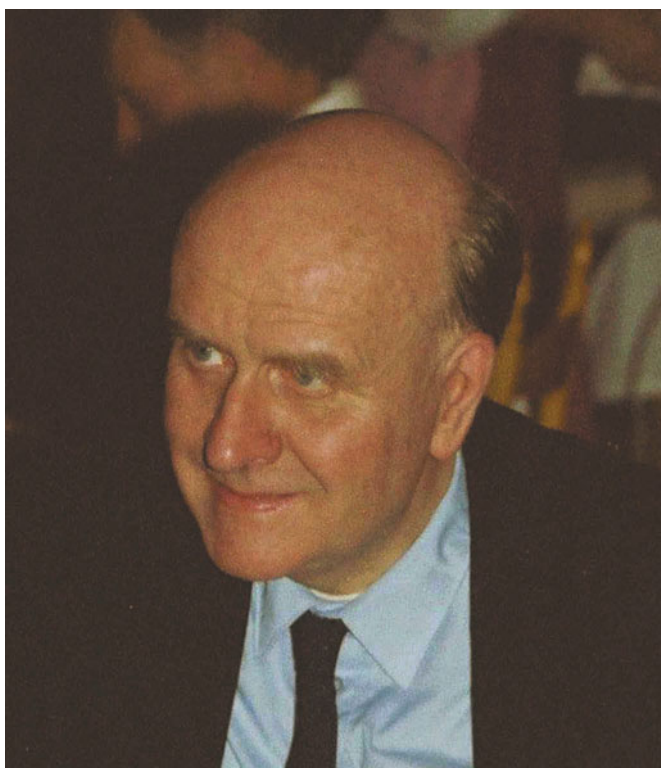
Axel Christian Klixbüll Jørgensen (1931–2001)

Axel Christian Klixbüll Jørgensen

1931 Born in Aalborg, Denmark, 18th April

1950 Graduation from high school (Abitur). Beginning of studies at the University of Copenhagen. The aim was a candidatus magisterii (cand. mag.), which would qualify him as a Danish high school teacher

1953 Teaching assistant at the Technical University of Denmark, Copenhagen

1954 Cand. mag. in chemistry, mathematics, astronomy and physics with chemistry as the main subject, University of Copenhagen

1957 Doctor philosophiae, University of Copenhagen, thesis: *Energy Levels of Complexes and Gaseous Ions, Gjellerup, Copenhagen, Denmark*

1957 Marriage to Micheline Prouvez

1959 Head of Office for Fundamental Research, Division of the Scientific Businesses, NATO, Paris

1961 Director of the Group of Theoretical Inorganic Chemistry, Cyanamid European Research Institute, Cologny, Geneva (until 1968)

1962 Books: *Absorption Spectra and Chemical Bonding in Complexes, Pergamon, Oxford, England. Orbitals in Atoms and Molecules, Academic Press, London, England*

1963 Book: *Inorganic Complexes, Academic Press, London, England*

1965 Member of the Royal Danish Academy of Sciences and Letters

1966 Editor of *Structure and Bonding* (until 1989)

1968 Invited to be Professor at the University of Geneva

1969 Book: *Oxidation Numbers and Oxidation States, Springer-Verlag, Berlin*

1970 Chair of Physical Chemistry at the University of Geneva

1971 Book: *Modern Aspects of Ligand-Field Theory, Amsterdam, North-Holland*

1974 Chair of Inorganic and Analytical Chemistry at the University of Geneva

1977 Book: *Lasers and Excited States of Rare Earth (with Renata Reisfeld), Springer-Verlag, Berlin*

1978 Death of his wife Micheline

1983 Doctor *honoris causa* from the Philosophical Faculty of the University of Zürich

1997 Professor Emeritus at the University of Geneva

2001 His death on 9th of January

Preface

The present volume of Structure and Bonding is the second one dedicated to the memory of C. K. Jørgensen by providing accounts of the present stage of development of a number of the most important areas of chemical spectroscopy to which he made influential contributions.

While Volume 106 included personal recollections of Jørgensen by his friends and colleagues, the present Volume 107 is restricted to original work.

Chemical spectroscopy signifies the conceptual area where chemistry and spectroscopy meet. In the early days of ligand-field theory, where a fusion with the molecular orbital theory of inorganic complexes happened, synergy helped our striving for understanding structure, bonding and spectroscopy. While structure and bonding are mostly conceived as static properties, spectroscopy is a collective word describing the many associated dynamic properties. The synergy arises when these dynamic properties are projected onto parameter spaces covering the semi-empirical parameters whose values are obtained by holding together the spectroscopic results and the expressions of theoretical modeling. The fact that regular and chemically transparent behavior was almost invariably found in these parameter values not only placed chemical spectroscopy in the front line of chemical science for more than a decade, but also allowed it to stay alive for at least 50 years.

The subfields of chemical spectroscopy to which Jørgensen made pioneering contributions are well represented in the present volume of Structure and Bonding. One only need to cast a brief look at the titles of the works to be reminded of the width of Jørgensen's writing.

Boulon gives us the opportunity to look back at CKJ's first series of papers: "Studies of Absorption Spectra" from 1955–56 where he pioneered the idea that $3d$ and $4f$ ions ought to be looked at in a similar way. CKJ was one of the few scientists who remained faithful to this idea in a productive way. Most other people remained attached either to the d or the f camp. CKJ was also the first to suggest (1963) that the ligand-field part of the structure of the f-f spectra of rare earth complexes was due to covalency in spite of the fact that it was smaller than the fine structure due to spin orbit coupling. In this context he saw that the σ. Part of the molecular orbital model that Yamatera had developed for the ligand field of orthoaxial $3d$ complexes could be applied easily to high-symmetry rare earth systems. This vision of his led to the Angular Overlap Model (AOM, 1965).

Gütlich, van Koningsbruggen and Renz bring us up to date with the ramifications of the spin cross-over phenomenon, which has its origin in the early recog-

nition of complexes of the same metal ion in the same oxidation state but with different total spins. This recognition could be qualitatively explained by the Pauling hybridization theory of *d*-period complexes, the theory that had been governing this part of chemistry for two decades at the time when ligand fields entered the chemical scene (around 1950). The ligand-field plus interelectronic repulsion model, which is the essence of ligand-field theory for *d*-electron complexes, was able to quantify the occurrence of the different total spins parametrically, and for cubic complexes the transition from the low spin to the high spin situation would depend on the internal field strength, which could be defined as the ratio between the cubic ligand-field parameter Δ and Jørgensen's spin pairing energy parameter *D*. CKJ was the first to see the potential of the ligand-field theory compared with that of hybridization, and he was the only chemist who had the courage to criticize Pauling's work. The rate at which the development took place can be interestingly illustrated by the fact that approximately at the time when CKJ wrote his last solo-authored book about chemical spectroscopy (1971), Pauling's latest edition of "The Nature of the Chemical Bond" hardly, if at all, mentioned the revolution that this part of science had undergone over the last 20 years.

Lever and Gorelsky remind us about three other facets of Jørgensen's initiatives. They discuss spectra of ruthenium complexes making us recall that CKJ was the first to demonstrate (1956) that the ligand-field model, which at that time was thought of mostly as a purely electrostatic model, could be used to interpret also the *d-d* spectra of 4*d* and 5*d* complexes, which at that time were thought of as being definitely much more covalent than those of the 3*d* series. Moreover, these authors concentrate on non-innocent ligands, a concept coined by Jørgensen to cover the ligands whose complexes cannot be characterized by a preponderant d^q configuration. Finally, their focus is charge transfer spectra, an area of spectra which CKJ insisted upon calling electron transfer spectra when he made his early (1959) and remarkably detailed contributions to their interpretation on the basis of the d^q configuration concept. Clearly, the Lever-Gorelsky spectra are not "innocent" enough to adhere to Jørgensen's vocabulary [1].

Morita, Buddhudu, Rau, and Murakami's work on energy transfers in rare earth nanoporous xerogels and sol-gel SiO_2 glasses illuminates the last two decades of Jørgensen's active life. During this time he was given an extraordinary opportunity to unite his legendary overview of rare earth chemistry and spectra and his practical theoretical skill in his close collaboration with Professor Renata Reisfeld, an expert on solar-energy, whose sol-gel glasses made up their favorite subject material.

Nolet, Beaulac, Boulanger, and Reber write about intensity borrowing in *d-d* spectra including the spin-forbidden transitions, subjects to which CKJ made pioneer contributions in 1956. In this context, one cannot help mentioning again Jørgensen's spin pairing energy parameter, which was not only useful in making his electron transfer transitions in complexes of different central ions commensurable, but also in general for parameterizing the electron repulsion part of the ligand-field model.

---

[1] see Vol. 106, p. 13 – 14

Reinen and Atanasov use DFT to combine the Angular Overlap Model with vibronic coupling in addressing the subjects of *s-d* and *s-p* mixing. The relevance of these orbital interactions had been foreseen by CKJ as early as 1955 and 1971, respectively. The intermixing of *s* and *d* was unfortunately introduced in an incorrect context, but this is the exception that proves the rule that he made remarkably few mistakes. However, the case illustrates the symbiosis of Jørgensen's life and writing which could have been a disaster but actually became an enrichment of our subject and of our community: when Jørgensen had an idea, he was not himself if events that were not under his control prevented him from writing about it before sunset. In his book referred to above, CKJ discussed *s-p* mixing in the context of main group stereochemistries.

Riesen treats hole-burning spectroscopy of complexes and thereby opens up for the future of Jørgensen's science. Finally, Anthon, Bendix and Schäffer exemplify how the values of the semi-empirical parameters of ligand-field theory can be obtained by computation using the commercially available Kohn-Sham DFT program package in a constrained way. At least one of these authors feels sad that he cannot enjoy Jørgensen's skeptical remarks about the almost mysterious fact that the procedure described here works so well.

CKJ interrelated concepts as well as phenomena. He saw analogies and connections. He always did things differently. He was altogether different and, therefore, controversial. He was inspiring, but with his unimaginable ability to read fast, he was also inspired by the whole chemical community, and again here, he was special because he could be inspired even by thoughts which he did not fully understand. He certainly had his own intuitive approach.

Copenhagen, March 2004 C. E. Schäffer

Contents

Contents of Volume 106

Optical Spectra and Chemical Bonding in Inorganic Compounds

Special Volume I dedicated to Professor Jørgensen

Volume Editor: Thomas Schönherr
ISBN 3-540-00853-5

Optical Transitions of Trivalent Neodymium and Chromium Centres in LiNbO$_3$ Crystal Host Material

Georges Boulon

Physical Chemistry of Luminescent Materials, Claude Bernard/Lyon 1 University,
UMR 5620 CNRS, 10 rue Ampère, 69622 Villeurbanne, France
E-mail: georges.boulon@pcml.univ-lyon1.fr

Abstract LiNbO$_3$ (LN) is a crystal which combines excellent non-linear optical properties with the possibility of trivalent optical ion doping as rare earth ions or transition metal ions. A key problem in these trivalent optical ions-doped LN has been to determine the lattice location of the activator. This is of importance because some of their attractive features depend on the crystal field surrounding the active ion. Laser spectroscopy (LS) and channelled Rutherford backscattering (RBS) spectrometry have been applied to investigate trivalent rare earth ions as active ions, whereas Cr^{3+} ions can only be studied by LS. As an example, we shall focus our attention more precisely on Nd^{3+} centres in LiNbO$_3$:Nd^{3+} and LiNbO$_3$:MgO:Nd^{3+}. The Nd^{3+} ions are in Li$^+$ octahedral sites, off-centred by three different amounts along the c-axis, giving place to three non-equivalent optical centres. Co-doping with MgO produces an additional optical centre (Nd–Mg), in which Nd^{3+} ions are not located in octahedral lattice sites. Measurements performed on Cr^{3+}-doped LN single crystals with composition varying between congruent and close to stoichiometry enabled new features to be revealed which lead us to re-interpret the optical spectra in the same way as rare earth dopants: three chromium centres (γ, α, β) are sufficient to explain the main optical features. The main centre γ occupies the Li$^+$ regular octahedral site whereas the centres α and β are shown to be strongly connected to the presence in their surrounding of intrinsic defects related to the crystal non-stoichiometry. Stoichiometry effects on the centre distribution and possible models to explain the origin of the different centres is discussed. In addition, a nephelauxetic broadening of the ^{2}E→^{4}A$_2$ transition in Cr^{3+} caused by disorder which originates from a variation in the values of the electron-electron Racah parameters. This article has been devised as the actual state of the art of the trivalent rare earth ions and the Cr^{3+} transition metal ion used as probe dopants in the LiNbO$_3$ crystal host.

Keywords LiNbO$_3$ · Luminescence · Trivalent rare earth dopant · Cr^{3+} dopant · Location of dopants

List of Abbreviations

BEB   Broad emission band
EPR   Electron paramagnetic resonance
GGG   Gadolinium gallium garnet
LN   Lithium niobate
LS   Laser spectroscopy
RBS   Rutherford backscattering
RE   Rare earth
YAG   Yttrium alumina garnet

1
Introduction

Lithium niobate (LN) is a widespread optical material used in electro-optical, photorefractive and laser applications [1–3]. Optical devices are generally built using LN crystals grown with the congruent composition which corresponds to the same composition in the melt and the crystal Xm=Xc=[Li]/([Li]+[Nb])= 48.6%. However the low optical damage threshold of the congruent crystal is a serious limitation for technological applications [4]. Considering the phase diagram of the oxides Li_2O and Nb_2O_5 as a function of the composition and the temperature, $LiNbO_3$ crystals can be grown from Xc=46% up to the nearly stoichiometric composition where Xc is almost 50%. This last composition could be of particular interest due to an expected increase of the optical damage resistance [5]. As LN melts at about 1250 °C for the congruent composition (48.6%), the Czochralski method is commonly used as crystal growth technique for LN [6]. Crystal growth now enables us to provide LN crystals with compositions varying from the congruence up to the stoichiometry by using three main techniques:

1. Vapour transport equilibration treatment of initially congruent crystals in Li excess powder of LN [7]
2. The double crucible method in which crystals are pulled from the melt with fixed Li concentration [8]
3. Crystal growth from the melt, to which K_2O has been added [6, 9]

As a consequence, a renewed interest is devoted to the characterization of the physical properties of LN as a function of crystal composition. Thus the effect of non-stoichiometry related intrinsic defects on the optical properties [10] and lattice dynamics [11] has been studied.

LiNbO$_3$ is an electro-optic and acousto-optic non-linear crystal with numerous applications in bulk and wave-guide devices. Doping LiNbO$_3$:MgO with Nd^{3+} ions has permitted the development of self-frequency-doubled [12], self-Q-switched [12] and self-mode-locked lasers [13], taking advantage of the combination of the Nd^{3+} gain with the above-mentioned properties of LiNbO$_3$. The co-doping with MgO is necessary to reduce the laser damage due to the photorefractive effect [14]. Thus LiNbO$_3$:MgO:Nd^{3+} appears as a very interesting system in integrated optics [15]. The determination of the symmetry and local environment for the Nd^{3+} ions is essential to be able to account for the gain properties of the Nd^{3+} laser active centres. In that respect it becomes necessary to know the lattice site occupied by the Nd^{3+} ions. This is also necessary to predict the changes between the bulk and wave-guide devices as well as to understand the effect of adding MgO. At present it is known [16–18] that the Nd^{3+} ions occupy several non-equivalent sites (different local environment), thus giving place to different Nd^{3+} optical centres. However the structure of these Nd^{3+} centres as well as their correlation with defined lattice positions is still an open question and a subject of controversy. By using spectroscopic techniques it is possible to determine the non-equivalent Nd^{3+} centres that is to say the non-equivalent environments as well to obtain information about the crystalline field acting on the neodymium ions. On the other hand, ion beam/channelling techniques provide information about their site location in the LiNbO$_3$ lattice [19]. In this work Laser Spectroscopy (LS) and Rutherford Backscattering Spectrometry (RBS) channelling techniques have been applied in parallel to investigate the Nd^{3+} centres and their lattice location in LiNbO$_3$:Nd^{3+} and LiNbO$_3$:MgO:Nd^{3+} crystals. It is important to remark that the LS and RBS experiments have been performed in parallel on the same samples. This has allowed us to give a direct relation between the results obtained by using both techniques, discarding possible variations due to differences in stoichiometry, active ion concentration or growing conditions. The experimental results provided a reasonable experimental basis to correlate the Nd^{3+} centres with specific lattice positions for the Nd^{3+} ions in the lattice, thus accounting for the different crystalline field related to each centre.

Doping by Cr^{3+} cation in LN crystal only enables experiments such as optical spectroscopy, especially LS. For instance, Qiu [20] proposed Cr^{3+}-doped LN crystal as a candidate for tunable solid state laser at room temperature owing to its strong broad band luminescence spanning the 770–1170 nm range. It is interesting to induce the blue wavelength necessary in the hologram recording found within this wavelength range by second harmonic generation. Cr^{3+}-doped LN crystals are still the object of many investigations using different techniques. The assignment of Cr^{3+} site in the LN matrix is still debatable [21–29]. It is stated that Cr^{3+} impurities lie in an octahedral anionic surrounding. Three Cr^{3+} occupation sites are available: Li, Nb and an empty site. Experiments undertaken on crystals with various Cr^{3+} contents have quoted that the repartition of Cr^{3+} centres is strongly dependent on total Cr^{3+} concentration in the crystal. Nevertheless, these

investigations were unable to distinguish between the effect of intrinsic defects associated with the Li deficit and the effect of extrinsic defects related to chromium insertion in the crystal. The aim of our recent study was to investigate the respective effects of intrinsic and extrinsic defects in the Cr^{3+} location in the LN lattice by using complementary spectroscopic techniques [30]. Therefore new optical spectroscopy measurements were undertaken in crystals with various samples between congruent and nearly stoichiometric compositions and different Cr^{3+} concentrations. Particular attention was paid to a nearly stoichiometric crystal Xc=49.5% and a chromium concentration $[Cr^{3+}]$=0.76 at. % for which complete studies were performed. This crystal was chosen because, in comparison to a congruent one, the optical spectra are very well resolved and some new peaks appear in the emission spectrum [31]. Series of experiments including absorption, emission, excitation and fluorescence decay recording were carried out with varying temperature. The characterization of the main Cr^{3+} centre in LN:Cr^{3+} was thus achieved and yields a critical analysis of the optical studies of LN:Cr crystals reported in the past in the literature. Satellite Cr^{3+} centres were analysed in the same way as the principal chromium centre and models are discussed to explain their behaviour as a function of the chromium content in a congruent crystal. Compared with the congruent crystal, new peaks are displayed in the off-congruent crystals and are characterized in the same way as the other peaks. This extensive work was able to distinguish the different chromium centres and their signatures in the luminescence experiments as well as their respective dependence in function of the Li content or the chromium concentration.

In addition of the detailed analysis of the location of trivalent optical ions in LN, a nephelauxetic broadening of the $^2E \rightarrow {}^4A_2$ transition in Cr^{3+} caused by disorder which results in a distribution in the values of the electron-electron Racah parameters [32] will be related as another new feature from the nephelauxetic effect as discussed by Jørgensen [33–36].

2
Experimental

2.1
Nd³⁺ Doped Crystals

Congruent $LiNbO_3$:MgO:Nd^{3+} and $LiNbO_3$:Nd^{3+} crystals were grown either at the Universidad Autonoma de Madrid (UAM) by the Czochralski technique or by the Laser Heated Pedestal Growth technique at the University Claude Bernard Lyon1 (LPCML). Excitation, emission and fluorescence decay measurements were taken both at UAM and at LPCML using a Spectra Physics 3900. Ti-Sapphire laser (resolution=1.3 cm⁻¹) as excitation source and a 30 cm focal-length monochromator followed by a Si photodiode for analysing the emissions.

RBS/channelling experiments with He⁺ ions were carried out in the 2 MV Van de Graaff accelerator of the Institut de Physique Nucléaire at LPCML. The He⁺ beam current was in the order of 4 nA with a typical energy of 1.6 MeV. The same samples were used in the RBS and LS experiments. These samples were prepared in the form of plates cut and mechanically polished perpendicular to the c-axis.

2.2
Cr^{3+} Doped Crystals

The crystals used in our measurements were grown by Dr. E. Kokanyan [6] with the Czochralski method and several samples were prepared with various compositions and different amounts of Cr^{3+} doping in the melt. The composition can be evaluated by various optical techniques [10]. Among them, we have chosen the measurement of the width of a well-resolved and intense Raman line, which varies linearly with the ratio Xc=[Li]/([Li]+[Nb]) in the crystal [10, 11].

Experiments such as excitation, absorption, emission and fluorescence decays were recorded at the LPCML. The excitation beam in the experiments was provided by an Exciton dye laser (Oxazine 725) pumped by the second harmonic of a pulsed Nd:YAG laser at 532 nm and was equal to 709.3 nm in the case of the fluorescence decay measurements and emission experiments. Experiments were carried out using a monochromator Jobin Yvon HRS1 with a 1200 grooves/mm grating blazed at 500 nm with either a visible grating coupled to a Hamamatsu photomultiplier, or an infrared grating coupled to a Ge cell detector. A cryo-refrigerator was used to cool the crystal down to 15 K. Moreover, a Lecroy oscilloscope and a Boxcar were added to the experimental devices in the case of the fluorescence decays and for the excitation spectra respectively.

3
Optical Results on Nd^{3+}-Doped LiNbO$_3$

Figure 1a shows the 1 (^{4}I$_{9/2}$)→R$_2$ (^{4}F$_{3/2}$) excitation (absorption) spectrum of Nd^{3+} in LiNbO$_3$ and LiNbO$_3$:MgO. This transition is very sensitive to the crystal environment of the Nd^{3+} ions and involves well-isolated Stark energy levels. Consequently this excitation (absorption) line is particularly useful for detecting non-equivalent Nd^{3+} centres. The triple structure observed in the LiNbO$_3$:Nd $^{3+}$ crystals is due to the presence of three main Nd^{3+} centres, as previously reported [18]. These centres can be labelled as Nd-1 (11,400 cm^{-1}), Nd-2 (11,422 cm^{-1}) and Nd-3 (11,440 cm^{-1}), in order of increasing 1→R$_2$ transition energy. It is important to note that these three same Nd^{3+} centres are present in the MgO co-doped crystals, although with a slightly different relative concentration. In addition, a new Nd^{3+} centre, denoted as Nd-Mg, appears in the doubly doped samples, but in a concentration (<10%) much lower than the other Nd-1, -2, -3 centres. Therefore four main non-equivalent kinds of Nd^{3+} ions (related to the Nd-1, Nd-2, Nd-3 and Nd-Mg centres) are present in the doubly doped crystal [45]. Excitation with the adequate laser photon energy allows us to obtain the emission spectrum of each Nd^{3+} centre. The obtained spectra are the same as those previously reported [17, 18] and are omitted here for the sake of brevity. From these spectra the ^{4}I$_{9/2}$, ^{4}I$_{11/2}$, ^{4}F$_{3/2}$ multiplets can be determined for each site.

We focus our attention into the relevant ^{4}F$_{3/2}$ multiplet. This state only splits by non-cubic distortions, so that the amount of splitting gives the trigonal (C$_3$) distortion around Nd^{3+} ions. Figure 1b shows the amount of splitting and the barycentre position of the ^{4}F$_{3/2}$ state for the different Nd^{3+} centres appearing in LiNbO$_3$:MgO:Nd^{3+} and also in LiNbO$_3$:Nd^{3+}. An inspection of this figure shows
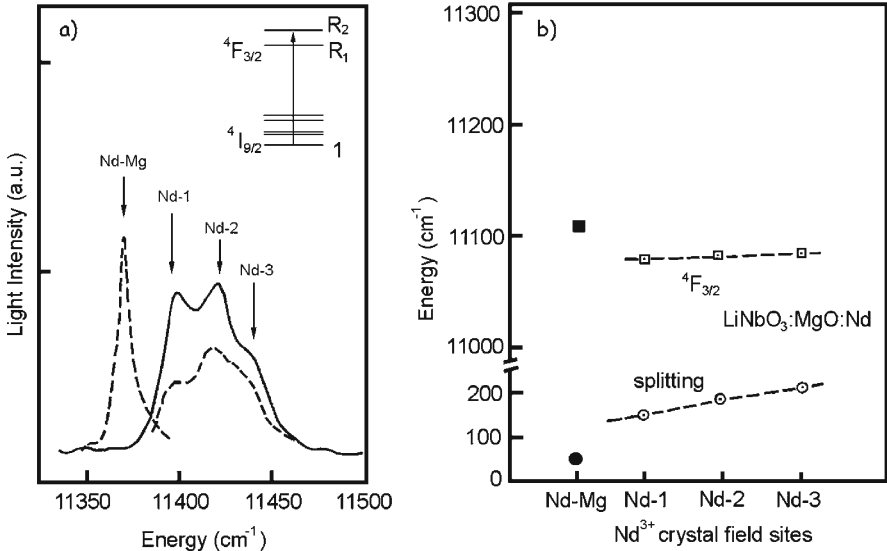
Fig. 1 **a** 10 K excitation spectra of LiNbO$_3$:Nd^{3+} (*full line*) and LiNbO$_3$:MgO:Nd^{3+} (*dotted lines*). The monochromator slit was =15 nm so that the excitation is equivalent to absorption but with a better resolution due to the Ti-sapphire laser (λ_{em}=*1096 nm* for Nd-1, -2, -3 sites and λ_{em}=1079 nm for the Nd-Mg site). **b** Splitting and barycentre of the ^{4}F$_{3/2}$ term for the non-equivalent Nd^{3+} centres. Site labels appear on the bottom

that the ^{4}F$_{3/2}$ barycentre is practically the same for the Nd-1, Nd-2 and Nd-3 centres and that it is different from the barycentre of the Nd-Mg centres, which appear only in the doubly doped crystal. However, the trigonal distortion is different from one Nd^{3+} centre to another. This behaviour strongly suggests that in the Nd-1, -2, -3 centres Nd^{3+} ions are replacing the same lattice ions, but that they are subject to three different trigonal distortions. On the other hand, the Nd-Mg centres (black symbols in Fig. 1b) are quite different from the spectroscopic point of view and must be correlated with lattice positions other than those of the Nd-1, -2, -3 centres. In any case it is important to remark that the Nd-Mg centres involve only a small fraction (less than 10%) of the total amount of neodymium into the crystal.

Self-frequency-doubling has also been demonstrated [12] at a non critical phasematching temperature of about 50 °C in a: LiNbO$_3$:0.5%Sc$_2$O$_3$:1%Nd single crystal. This is lower than in LiNbO$_3$:MgO:Nd systems [13]; moreover it is argued that LiNbO$_3$:1.5 mol%:Sc$_2$O$_3$ is easier to grow and has a photorefractive damage level comparable to that of LiNbO$_3$:5 mol%:MgO. So, in order to have more information about that question and to make a more complete comparison with LiNbO$_3$:MgO:Nd, we have studied the luminescence properties of LiNbO$_3$:1% or 1.5% Sc$_2$O$_3$:1% Nd crystal fibres [38] grown by using the Laser Heated Pedestal Growth (L.H.P.G.) technique [39]. Site selective spectroscopy has been made at 12 K with the 1% Sc$_2$O$_3$ doped sample. Figure 2 shows the excitation spectrum of the ^{4}F$_{3/2}$ level without site selection. Three sites can be clearly identified especially
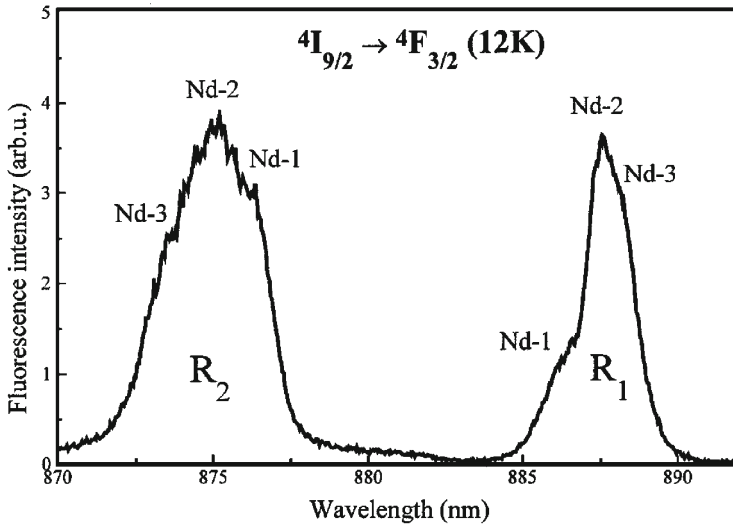
Fig. 2 Excitation spectra of a LiNbO₃:1%Sc₂O₃:1%Nd crystal fibre at 12 K by monitoring the total fluorescence intensity from the $^4F_{3/2}$ excited state

for the R Stark level. This has been confirmed by the site selective emission spectra for the transitions $^4F_{3/2} \rightarrow ^4I_{9/2}$ and $^4F_{3/2} \rightarrow ^4I_{11/2}$. Incorporation of Sc₂O₃ does not lead to the appearance of supplementary Nd³⁺ sites which is not the case of MgO doping [14], probably due to different types of charge compensation for both Sc³⁺ and Mg²⁺ cations in the vicinity of Nd³⁺ ions.

Figure 3 shows the absorption transition $^4I_{9/2} \rightarrow ^4F_{3/2} + ^2H_{9/2}$ interesting for diode pumping. The lines are broad which permits relaxed diode wavelength control. The maximum is at 813.6 nm in π-polarization and at 808.4 nm in σ-polarization. The cross sections are respectively 4 and 5.5×10⁻²⁰ cm². Infrared emission spectra of the metastable level $^4F_{3/2}$ have been recorded from 850 to 1450 nm after excitation in each of the above mentioned absorption lines.

The room temperature emission spectra corresponding to the $^4F_{3/2} \rightarrow ^4I_{11/2}$ transition are shown in Fig. 4 for 808.4 nm excitation in σ-polarization. The emission cross sections have been derived by using the JuddOfelt formalism. The JuddOfelt parameters are Ω_2=2.1×10⁻²⁰, Ω_4=6.8×10⁻²⁰ and Ω_6=3.8×10⁻²⁰ cm². The branching ratio for this transition is β=0.42 and the radiative lifetime for $^4F_{3/2}$ is τ_R=96 μs. The emission around 1084 nm is just as intense in σ as in π polarization and the σ relative intensity increases with the Sc₂O₃ concentration depending on the polarization and the wavelength of excitation. Moreover in σ-polarization, the emission lines around 1084 and 1093 nm have about the same intensities which differs with what is found in LiNbO₃:MgO:Nd [15]. This is very interesting for self-frequency-doubling in a negative crystal such as LiNbO₃: the fundamental wave must be σ-polarized for efficient doubling.

Once the presence of four non-equivalent Nd³⁺ ions has been established in LiNbO₃:MgO:Nd as well as the presence of three non-equivalent Nd³⁺ ions in LiNbO₃:Sc₂O₃:Nd, the next step is to search for their lattice location into the
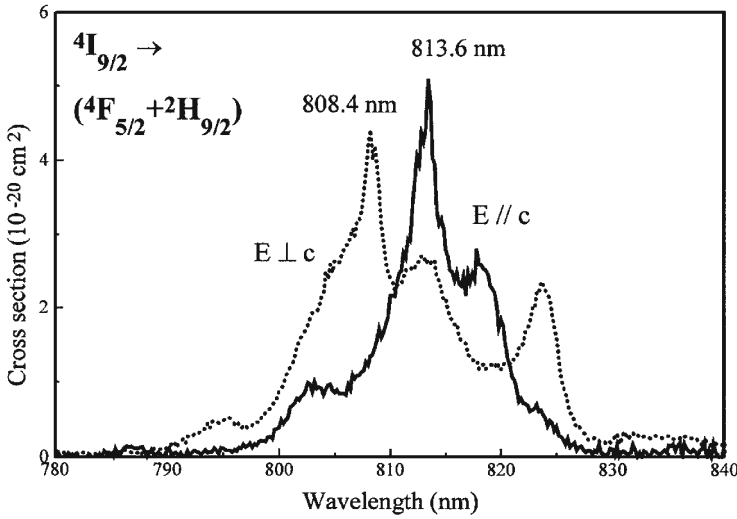
Fig. 3 Room temperature polarized absorption spectra of a LiNbO$_3$:1%Sc$_2$O$_3$:1%Nd crystal fibre
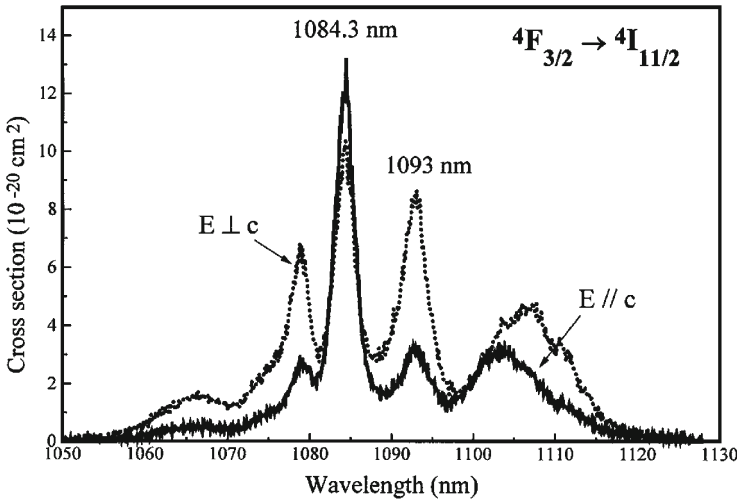
Fig. 4 Room temperature polarized emission spectra after pumping at 808.4 nm in σ-polarization

LiNbO$_3$ crystal. Assuming the expected trigonal symmetry (C$_3$) and the octahedral occupation, three substitution sites are the principal candidates to be occupied by the Nd^{3+} ions: the Li$^+$ site, the Nb^{5+} site and the intrinsic free octahedron. These three possible octahedral locations are displayed in Fig. 5, where the disposition of the constituent ions of LiNbO$_3$ along the c-axis is illustrated. RBS/channelling experiments can now provide information about which of these sites are replaced by the Nd^{3+} ions.
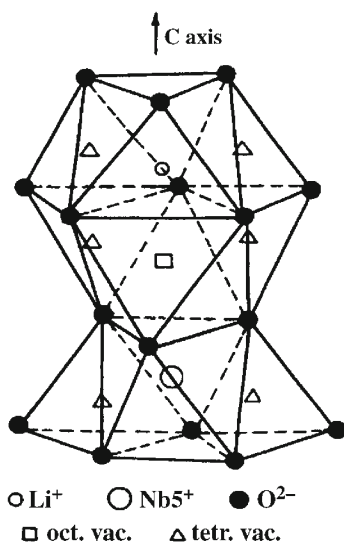
Fig. 5 Schematic representation of the unit cell of LiNbO$_3$ showing the four available sites for impurity ions: Li$^+$, Nb^{5+} and vacancy of octahedral symmetry and tetrahedral vacancy

4
RBS/Channelling Results on Trivalent RE Ions

In the RBS spectra (yield vs energy) of our crystals the trivalent RE (RE^{3+}) yield is clearly resolved from that of LiNbO$_3$ (basically due to the Nb sub-lattice). By RBS/channelling experiments the angular scans of RE^{3+} and Nb^{5+} ions are compared along relevant directions or channels, so that information about the site location for the RE^{3+} ions can be obtained. However, the RBS technique is not sensitive for detecting light ions, so that Mg^{2+} ions could not be detected. As an example the RBS spectra of Pr^{3+}-doped LiNbO$_3$ is shown in Fig. 6 [40].

4.1
LiNbO$_3$:Nd^{3+} Crystal

The very similar angular scans of Nb and Nd along the (0001) channel confirm that all the Nd^{3+} ions lie in octahedral positions: Nb, Li or free octahedron (see Fig. 2). These two latter positions appear screened by the Nb ions in Fig. 3b. Consequently, tetrahedral (between oxygen ions) positions must be rejected. In addition, the angular scan along the (0445) channel also excludes the free octahedral site for the Nd^{3+} ions. In fact, this Nd^{3+} location should give place to an ion current peak (flux peak) for the Nd^{3+} yield because of the blocking effect of the channel by the free octahedron (see Fig. 3b). On the other hand, the Nb and Nd angular scans along the (0221) channel display marked differences between them. This result excludes the possibility of having all the Nd^{3+} ions located in Nb^{5+} sites. According to the spectroscopic results (see previous section) the
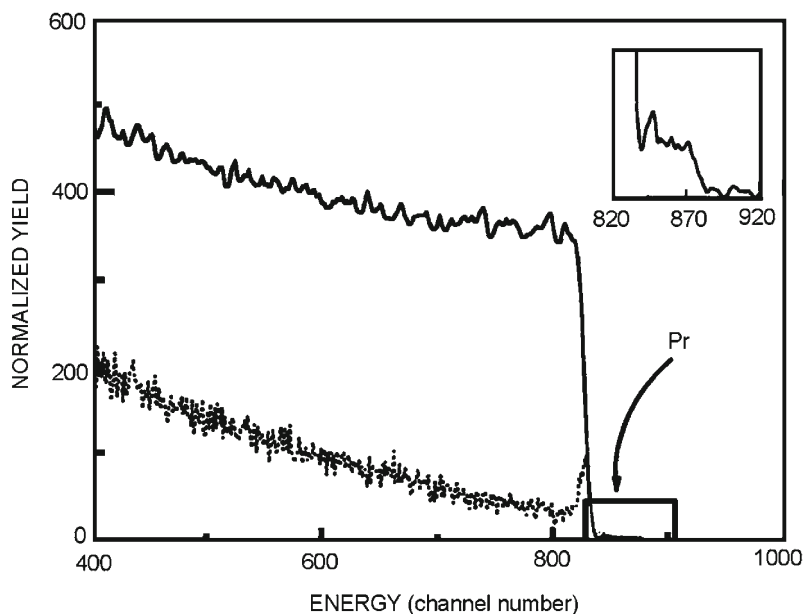
Fig. 6 RBS spectra of Pr^{3+}-doped $LiNbO_3$ for a random orientation of the crystal (*solid line*) and for the crystal oriented along the (0110) axis (*dotted line*)

double occupancy (Li^+ and Nb^{5+}) has also to be disregarded. Therefore the Nd^{3+} ions forming the Nd-1, -2, -3 centres have to be located in Li octahedrons. Thus, the (0221) channel is blocked, as observed in the corresponding angular scan. However, the complicated shape of this angular scan does not match with the angular scan reported for the Li^+ sub-lattice in $LiNbO_3$, obtained by nuclear-reaction methods [40]. The anomalous shapes of angular scans for impurity ions in $LiNbO_3$ have been recently investigated by computer simulation methods [19]. These angular scans were explained by supposing that the impurity ions are shifted by a certain amount from the regular Li^+ site along the c-axis (see Fig. 2). Under this scheme the Nd-1, -2, -3 centres would be consistent with three different displacements for the Nd^{3+} ions. Then the resulting angular scan should be the convolution of those related to the Nd-1, Nd-2 and Nd-3 centres.

4.2
$LiNbO_3$:MgO:Nd^{3+} Crystal

Now the effect of co-doping with MgO can be analysed by RBS/channelling. The angular scans in the doubly doped system (see Fig. 3a) are essentially similar to those obtained for the singly doped (without MgO) crystals, in good agreement with the spectroscopic results. However, the appearance of small differences is still appreciated. The angular scan along the (0001) channel shows as a small flux peak in the dip of the Nd^{3+} yield. This fact indicates that a fraction of Nd^{3+} (less

than=10%) is not aligned along the c-axis connecting the octahedral sites. As for the singly doped system, the angular scan along the (0445) axis reveals that the free octahedron site is not significantly occupied by the Nd^{3+} ions, at variance with results reported elsewhere [41]. The scan along the (0221) axis is again rather complex.

The spectroscopic results reported in this work clearly show the presence of four non-equivalent Nd^{3+} ions in the LiNbO$_3$:MgO:Nd laser crystals. These ions are related to the Nd-1, Nd-2, Nd-3 and Nd-Mg centres. The latter centres appear only in the MgO-codoped crystals. The Nd-1, -2, -3 centres are closely related to the same octahedron, but having a different trigonal crystalline field. RBS/ channelling experiments indicate that in the crystals without MgO the Nd^{3+} ions lie in the Li octahedron but shifted from the regular Li$^+$ site (which is off-centred in the octahedron, see Fig. 2) along the c-axis. Therefore we can infer that, in the Nd-1, -2, -3 centres, the Nd^{3+} ions are in Li octahedrons but off-centred by three different amounts. This explains the complicated shape of the (0221) angular scan for the Nd^{3+} ions and the different trigonal crystalline field ($^4F_{3/2}$ splitting) measured for the Nd-1, -2, -3 centres. Under this model the higher the trigonal crystalline field the more off-centre position. Therefore the Nd-3 centre would be consistent with the highest off-centre displacement for the Nd^{3+} ions, while in the Nd-1 centre the Nd^{3+} ions would be more centred.

The appearance of these three non-equivalent centres must be due to the presence of different types of charge-compensating defects associated to the non-stoichiometry of LiNbO$_3$ [42]. However, these defects, 6% of anti-sites (Nb^{5+} ions in Li$^+$ sites) and the corresponding number of Nb^{5+} vacancies, do not provide simple charge compensating models for the Nd^{3+} ions. Thus, the complete structure of the Nd^{3+} centres cannot be easily inferred.

Let us now discuss the results in the MgO-codoped crystal. The RBS results (see Fig. 3a), show similar angular scans to those of the singly doped crystal. This fact is in good agreement with the spectroscopic results; the Nd-1, -2, -3 centres are still dominant in the doubly doped crystal. However, the effect of MgO co-doping is clearly manifested in the angular scan along the (0001) direction. The small flux peak over the dip in the signal of Nd^{3+} indicates that a small fraction (<10%) of Nd^{3+} ions is blocking the (0001) channel. This fraction is obviously related to the Nd-Mg centres, which present an optical behaviour quite different to that of the Nd-1, -2, -3 centres. Although it is difficult to give a definitive structure for these centres, some important details can be advanced. In these centres the Nd^{3+} ions do not enter octahedral sites because they should produce the same (0001) angular scan as Nb. Thus, the fraction of Nd^{3+} ions occupying the Nd-Mg centres could be in tetrahedral sites (between the oxygen ions) or in interstitial positions. In principle tetrahedral sites should not produce a defined flux peak in the middle of the (0001) channel [19], so that the second possibility seems to be more probable. In any case the non-octahedral location explains the well-isolated positions of the optical bands associated to the Nd-Mg centres as well as the small differences between the angular scans of the singly and doubly doped systems.

4.3
RE-Doped LiNbO₃ Crystals

At this point it is important to mention that similar results of the angular dependence of the backscattering yield along some selected channels as in Fig. 7 have been obtained for other trivalent RE ions. It has been demonstrated that RE ions occupy Li^+ octahedral sites [43]. However, the shape of the angular scan depicted by the Nd^{3+} ions along the $\langle 0221 \rangle$ is different to the one expected for a location in regular Li^+ sites represented by dotted lines in Fig. 7 that have been obtained by nuclear reaction methods [12]. Anomalous angular scans displayed by RE ions along certain directions of LiNbO₃ have been systematically investigated by Monte Carlo computer simulation methods [8]. They were unambiguously identified with off-centre displacements of the RE ions, relative to the regular position of Li^+ lattice sites, along the c-axis towards the nearest oxygen triangle in the down direction in Fig. 5. As can be seen in Fig. 8, different behaviours for Pr^{3+}, Ho^{3+} and Yb^{3+} ions along the planar direction (0001), which is very sensitive channel to Li^+ site displacements, indicate different off-centred shifts for each type of RE ion. Using the simulated angular scans reported for these channels, an average displacement can be estimated for each ion relative to the regular Li^+ position. The amount of the displacement has been plotted in Fig. 9 as a function of the ionic radius of the RE ion: linear dependence is observed. The bigger the ion size, the larger is the off-centre displacement. The larger RE ions are then forced to move towards the bigger oxygen triangle. The linear dependence can be used to predict the location of other RE ions [44].
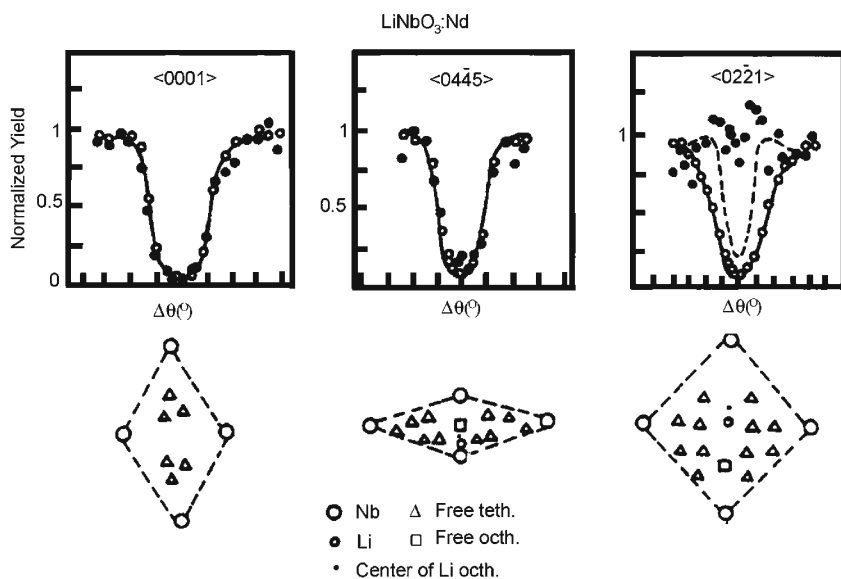
Fig. 7 Angular dependence of the backscattering yield for Nb (*open circles*) and Nd (*full circles*) along three channels. The projections of the lattice sites on planes perpendicular to each channel are also displayed [45]
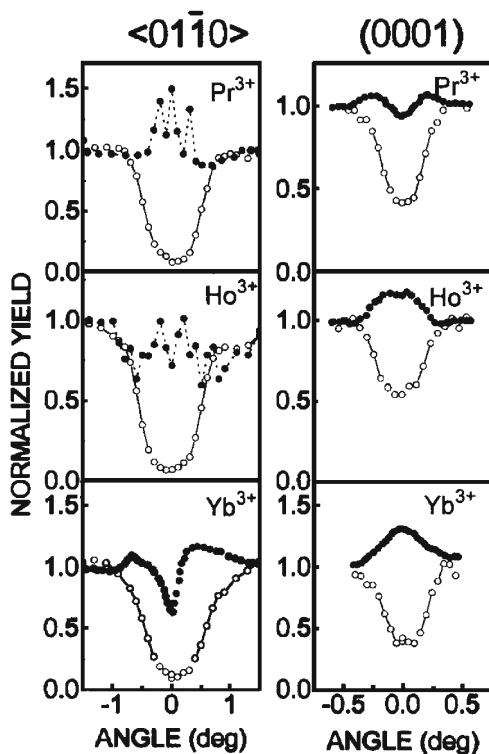
Fig. 8 RBS angular scans along one axis (*left*) and one plan (*right*) for rare earth ions in LiNbO₃ [16]
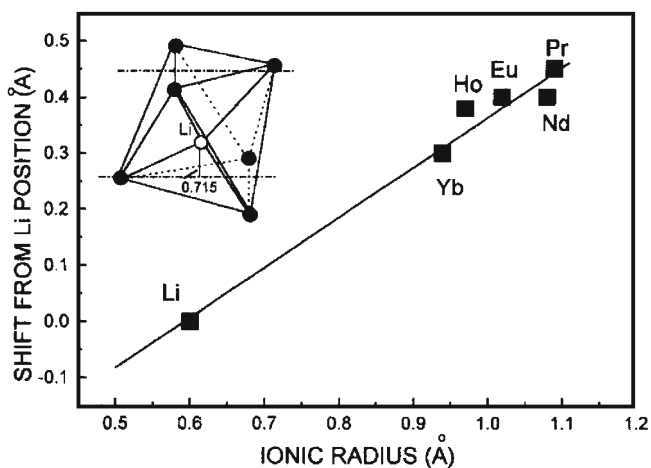
Fig. 9 Shift from the Li position as a function of the ionic radius of the incorporated trivalent rare earth ion [16]
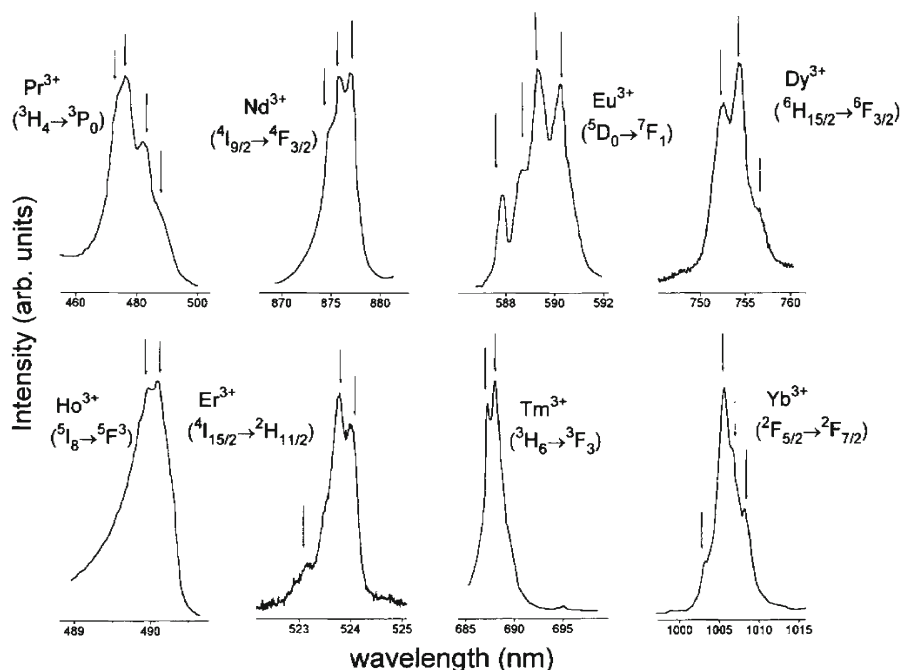
Fig. 10 Low temperature (10–20 K, depending on each case) optical spectra corresponding to single inter-stark transitions of rare earth ions in LiNbO$_3$. *Arrows* indicate the peaks related to non-equivalent centres [17]

The observation of non-equivalent centres, that is to say of RE ions in specific local environments, is also a general phenomenon. In Fig. 10, low temperature optical spectra corresponding to specifically selected inter-Stark transitions have been shown for a variety of RE ions from absorption, excitation or emission [45, 46].

5
Spectroscopic Results on Cr^{3+} Trivalent Transition Metal Ions

5.1
Energy Levels of Cr^{3+} Ion

The familiar luminescence features of a particular Cr^{3+} system are discussed in terms of the $^4T_2$, ^2E and $^4A_2$ levels. $^4A_2$ state arising from the strong field electronic configuration t_2^3 is the ground state level. The trigonal field affects the $^4A_2$ state and lifts the spin degeneracy to give a doublet term, $^4A_2(\bar{E})$ and $^4A_2(2\bar{A})$ separated with 2D which is the zero-field splitting. ^2E springs from the same strong field configuration as $^4A_2$. A slight energy difference between these two states occurs when the crystal field strength increases. The intra-configuration transition $^2E \rightarrow {}^4A_2$, which is a spin forbidden transition ($\Delta S \neq 0$) in an octahedral field, can

only be driven by the combined effect of spin-orbit coupling and trigonal field which enable the lift of degeneracy into two sublevels $^2E(2\bar{A})$ and $^2E(\bar{E})$. This transition generally gives rise to narrow lines which are called R-lines. $^4T_2$ state arises from the $t_2^2 e$ strong field configuration and displays a linear energy difference with the $^4A_2$ level with increasing crystal field strength. As the inter-configuration transition $^4T_2 \leftrightarrow ^4A_2$ involves a change in the coupling of the Cr^{3+} with its ionic surroundings, it gives rise to a spin-allowed broad multi-phonon band ($\Delta S=0$). Regarding the variation of the electronic crystal field states of Cr^{3+} with an octahedral crystal field, we can define the low-field case when the $^4T_2$ state is energetically lower than the ^2E state, and the high-field case when the $^4T_2$ state is energetically higher than the ^2E state.

5.2
Absorption and Emission Spectra: Main Features

The literature contains a lot of controversy on the interpretation of Cr^{3+}-doped LiNbO$_3$ absorption and emission spectra. We have shown that the optical properties needed to be revisited by means of different high resolution laser spectroscopy techniques in crystalline samples with both various extrinsic (Cr^{3+} doping) and intrinsic (compositions from congruent to nearly stoichiometric samples) defect concentrations.

Figure 11 displays the absorption and emission spectra recorded in the wavenumber 7000–27,000 cm^{-1} for the crystal with Xc=49.5% and [Cr^{3+}]=0.76 at.%. We observe in the absorption spectrum (see Fig. 2a) two broad bands with maximum intensity at about 15,350 and 20,650 cm^{-1}. The lowest energy band is assigned to a transition $^4A_2 \rightarrow ^4T_2$ and is consequently broad. The second broad absorption band corresponds to the $^4A_2 \rightarrow ^4T_1$ transition of the cation Cr^{3+}. In addition to the broad bands, the absorption spectrum (Fig. 11a) exhibits at high wavenumber the tail of the very intense absorption band lying around 28,000 cm^{-1} which corresponds to the ultraviolet absorption of the 2p orbitals of oxygen in LiNbO$_3$ crystals. Some less intense peaks can be observed at 13,773 (L_a) and 13,810 cm^{-1} (L_b) on the low energy side (see the inset of Fig. 11). The emission spectrum reported in Fig. 2b displays a large and broad band peaking at 10,690 cm^{-1}, which is denoted hereafter as the BEB (broad emission band), together with less intense peaks on the high energy side (see the inset of Fig. 11b). The narrow and well resolved lines L_1 and L_2 are lying about 13,680 and 13,603 cm^{-1} respectively whereas the more intense L_3 and L_4 lines peaking around 13,540 and 13,415 cm^{-1} are broader and partly hidden by the BEB peak. The characteristics and assignment of every emission line have been made in details as well as their link to chromium centres.

5.3
Origin of the Lines L_1, L_2, L_3 and L_4

Whereas the assignment of the main emission band (BEB) and the lines L_1 and L_2 have been associated with the Cr^{3+} centres γ, β and α respectively, the emission lines L_3 and L_4 lying at low energy in the inset of Fig. 11b were not so far attributed.
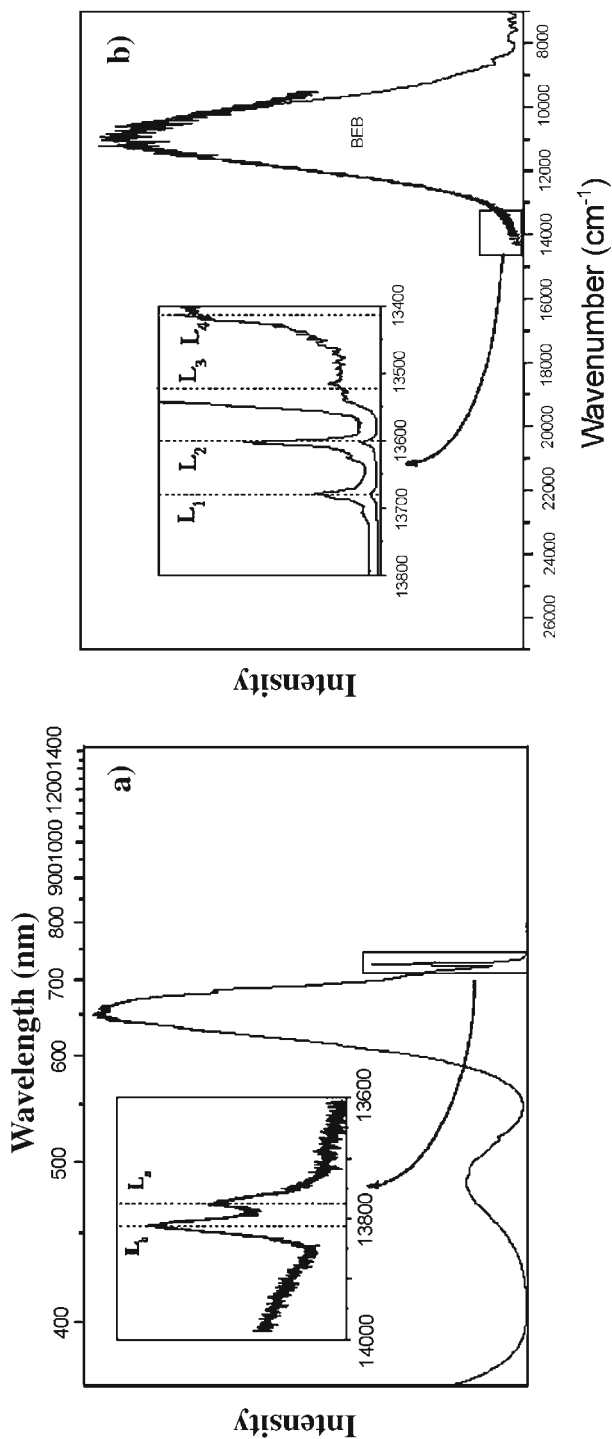
Fig. 11 **a** Absorption spectra recorded at 15 K in the crystal Xc=49.5% and [Cr³⁺]=0.76 at. %. *Inset:* zoom of the absorption spectrum in the wavenumber range 13,600–14,000 cm⁻¹. **b** Low temperature emission spectrum recorded at 15 K with either a visible grating and a Hamamatsu photomultiplier (high energy side) or an infrared grating and a Ge cell detector (low energy side) after excitation at 14,085 cm⁻¹. *Inset:* zoom of the emission in the wavenumber range 13,400–13,800 cm⁻¹
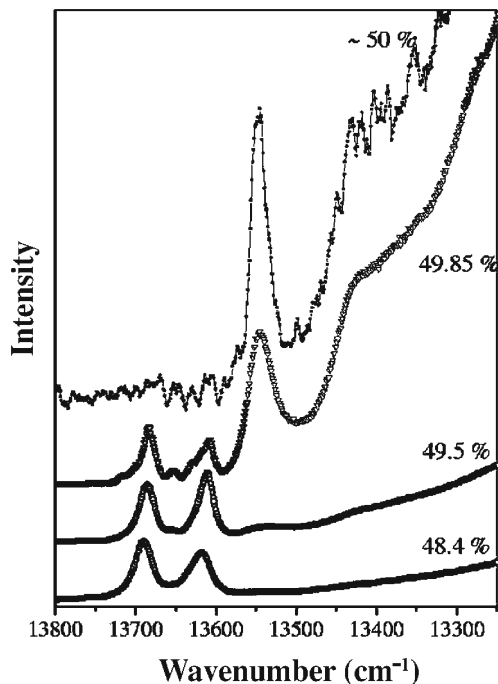
Fig. 12 Low temperature emission spectra after excitation at 19,436 cm^{-1} of slightly Cr-doped LN crystals with different compositions (Xc=48.4–50%)

In fact, the occurrence of these lines was previously proved to be largely dependent on the composition [31]. Therefore this part is devoted to the influence of crystal composition on optical spectra. Figure 12 displays the emission spectra for the LN crystals doped with a small amount of Cr^{3+} but with different compositions. The spectrum exhibits four main peaks as in the inset of Fig. 11b: the R-lines L$_1$ and L$_2$ and two peaks occurring at lower energy L$_3$ and L$_4$. For the lines L$_1$ and L$_2$, the maximum position moves towards lower wavenumber whereas the width and the intensity decrease with increasing Xc. The lines L$_3$ and L$_4$ occur only in the emission spectra for crystal with Xc close to the stoichiometric composition so that they are the sole lines present in the spectrum of the stoichiometric crystal. This shows that the origins of the lines L$_1$ and L$_2$ from one side, and the peaks L$_3$ and L$_4$ from the other side, are completely different. In other terms this means that the opposite behaviours of L$_1$-L$_2$ and L$_3$-L$_4$ can be directly related to the intrinsic defect structure of LN.

   Data reveal that the lines L$_1$ and L$_2$, which are linked to Cr^{3+} centres β and α, seems to be governed by the amount of the intrinsic defects. They tend to decrease when the Li content in the crystal is increased up to the stoichiometric composition for which they totally vanish. Thus it appears so reasonable to assume that these two centres are directly related to intrinsic defects as stated in the model used above to describe the effect of chromium concentration in congruent LN:Cr^{3+}.
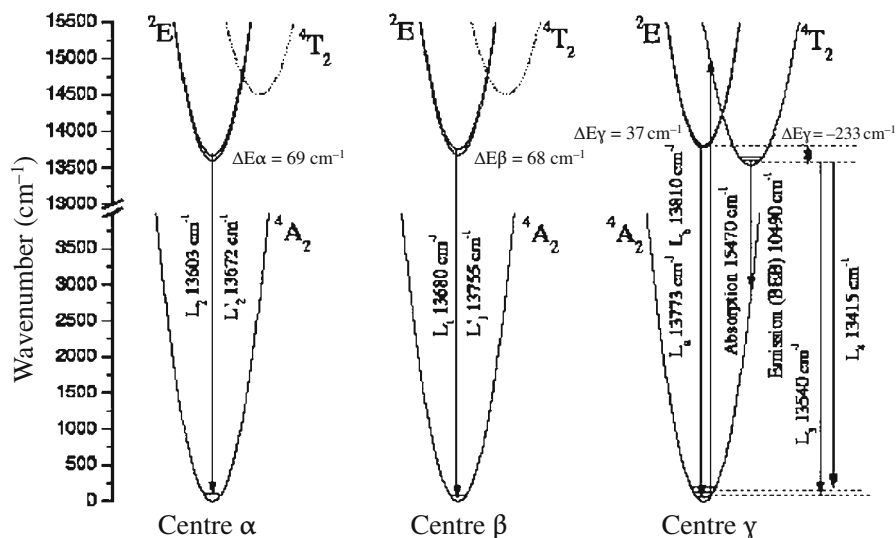
Fig. 13 Representation of the energy levels and transitions of the three characterized Cr^{3+} centres

Since L_3 and L_4 are clearly not linked to the centres α and β, they could be attributed to the main centre γ, like the BEB band.

Our results lead to distinguish only three Cr^{3+} centres in substitution of Li^+ sites as indicated in Fig. 13. The main centre γ corresponds to a rather low crystal field scheme, for which relaxed $^4T_2$ is the first excited level and just above ^2E excited level is located at around 233 cm^{-1}. $^4T_2 \rightarrow {}^4A_2$ is responsible for the main broad band in emission and $^4A_2 \rightarrow {}^4T_2$ for the absorption spectra. The lines L_3 and L_4 were found to be vibronic peaks of the $^4T_2 \rightarrow {}^4A_2$ transition. This γ centre is interpreted as a Cr^{3+} ion substituting for Li octahedral site consisting of C_3 point group symmetry which is not distorted by the first Nb^{5+} and Li^+ neighbouring shells. The L_3 line is interpreted as the $^4T_2 \leftrightarrow {}^4A_2$ 0-phonon line whereas the L_4 line is due to one-phonon line. The other Cr^{3+} centres α and β give rise respectively to L_2 and L_1 emission lines which have been demonstrated to belong to $^2\bar{E}{}^4A_2$ transitions of these centres due to transitions from ^2E levels lower than $^4T_2$ levels. The centres α and β correspond to rather high crystal field scheme sites. These centres are linked to Cr^{3+} ion substituting Li octahedral sites distorted by intrinsic defects in their neighbourhood shell as seen by the higher ^2E splitting.

6
Assignment of RE and Cr^{3+} Multi-Centres

Up to this point we have established that trivalent RE ions replace Li^+ ions in $LiNbO_3$. RBS/channelling has demonstrated that they are shifted towards the free octahedron and then retaining the local C_3 symmetry of the Li^+ site. Evidence

of their structure has been also gained by RBS in the particular case of Pr^{3+} ions [44]. The Pr^{3+} centres correspond to different c-axis positions of the c-axis of the Pr^{3+} ions around the average position measure by RBS (0.42 Å displaced from the Li^+ site). Therefore, in the most general case, non-equivalent centres in LiNbO₃ have to be visualized as due to different displacements of the RE ions along the c-axis inside the Li^+ octahedral site.

The next step is to explain the origin of these non-equivalent centres, i.e. to think about possible local surrounding configurations producing different c-axial displacements. As the relative concentration of each centre can be handled to some extent by stoichiometry changes, the origin of the non-equivalent centres has to be connected with the defects associated to the non-stoichiometry of LiNbO₃, which may be creating different local surroundings for the active ions. The same type of interpretation has already advanced in RE-doped garnets as YAG or GGG, in which a fraction of Al^{3+} or Ga^{3+} sites can be also occupied by Y^{3+} or Gd^{3+} ions that in the ideal garnet structure are located in the dodecahedral sites. It is known that in the case of YAG crystals the Y^{3+} ions occupy about 1.5–2% of the octahedral sites. Owing to the large difference between the octahedral radii of Y^{3+} and Al^{3+}, this substitution produces large local distortions of the crystalline lattice that can perturb the ideal symmetry of the neighbouring cationic sites at quite large distances leading to satellite lines close to the main line [47]. The same argument based on the disordered structure of the activator ion location has been used in both Cr^{3+}-doped GGG and Nd^{3+}-doped GGG garnet to explain the broad emission spectra of active ions [48]. Then, we can propose by analogy, in LiNbO₃, that the Li-deficiency is compensated by a certain amount of Nb^{5+} ions located in Li^+ sites, which are called anti-sites creating multi-centres for the activator ions. The controversy emerges in LiNbO₃ with the defects that are created to compensate the excess of charge introduced by the Nb^{5+} ions in anti-sites [49]. Among a lot of intrinsic defects which has been considered [50], we think that the most logical interpretation seems be due to the simultaneous presence of anti-sites and Nb^{5+} vacancies which are naturally connected according the charge compensated complex:

1. 5 Nb_{Li}^{5+}(anti-site)+4 V_{Nb} (Nb vacancy)
   instead of:
2. Nb_{Li}^{5+}(anti-site)+4 V_{Li} (Li vacancy) complex which needs creation of supplementary Li vacancies

Now, when Li^+ is substituted by RE^{3+} or even trivalent transition metal ions like Cr^{3+}, the positive charge excess can be compensated in the nearest shells by both:

1. Two Li vacancies (connected with so-called Li-vacancy model)
   or
2. Every 5 RE^{3+} located in Li^+ ions by 2 Nb^{5+} vacancies (connected with so-called Nb-vacancy model)

Our preference for the second hypothesis to understand RE^{3+} multi-centres structures is based on the following considerations:

- Again, the presence of Nb^{5+} vacancies which are naturally connected with anti-sites in the $LiNbO_3$ lattice.
- Since Li vacancy has only one negative charge relative to the ideal lattice, it produces a 4–5 times weaker perturbation of the crystal field than either anti-sites or Nb vacancies.
- Such compensation model means that RE^{3+} ions are forming aggregates in the $LiNbO_3$ lattice: pairing or clustering in RE^{3+}-doped $LiNbO_3$ has been recently demonstrated by using Yb^{3+} ion co-operative emission as a probe [51, 52]. The co-operative emission usually rather difficult to observe in RE^{3+}-doped crystals, could be originated by two Yb^{3+} ions both located either in neighbouring Li^+ sites of $LiNbO_3$ (without MgO) since the separation between them is a specially very short one (3.76 Å) or even in neighbouring Li^+ and Nb^{5+} sites of $LiNbO_3$ (with MgO) in which the separation is shorter (3.01 Å).
- In addition, it can be seen that the association of RE^{3+} in Li^+ site together with Nb^{5+} vacancy either in the nearest Nb shell at 3.01 Å or in the fourth Nb shell at 3.92 Å leads both to axial centres (C_3 point group symmetry) [50]. The same kind of axial centre is also expected for anti-site around Li^+ (anti-site) in the fifth shell at 6.93 Å. The other Nb shells around Li and Li shells around Li respectively are characterized by C_1 lower point group symmetry [50]. Then, it is possible to find at least three axial centres in the nearest neighbourhood of one Li centre substituted by RE^{3+} which could be in agreement with the model of the RE^{3+} shifts in RE^{3+}-doped $LiNbO_3$ along the c-axis given by RBS/channelling observations and also by laser spectroscopy results.
- With the help of EPR, experimental evidence has been found that one of the main non-stoichiometric defects in Cr^{3+}-doped $LiNbO_3$ is related to Nb vacancy. Anti-site is also detected by EPR [50]. Such research works are very useful to understand the main features of trivalent active ions, the approach being the same as well with RE ions as transition metal ions.

The comparison between experimental results on the emission spectra relative intensities and the first calculations from the statistical probability of having 0, 1, 2, ... non-stoichiometric defects in the surroundings of the active ion estimated according to the Poissonian distribution seen in Fig. 14 do not coincide with accuracy. Whereas centres 1, which represent unperturbed centres, are dominant in the calculations, as we found it in Cr^{3+}-doped YAG [47] and Cr^{3+}-doped GGG [48], the emission spectra of Fig. 2 (three multi-centres) and those shown both in [37] (also three multi-centres) and in [49] (six multi-centres) show closer populations of each types of centres for at least three of them. We can only say that the relative concentrations are closer in the Nb vacancy model than in the Li vacancy model. This is the trend we have shown in this study.

Thus, a statistical model leads to assign the centre β to a Cr^{3+} in a Li^+ site perturbed by niobium anti-site in the first cation shells whereas the centre α seems to be due to a Cr^{3+} in a Li^+ site perturbed by niobium vacancy in the first cation shells. Among a lot of intrinsic defects which have already been considered, we think that the most logical interpretation of the compensation process would
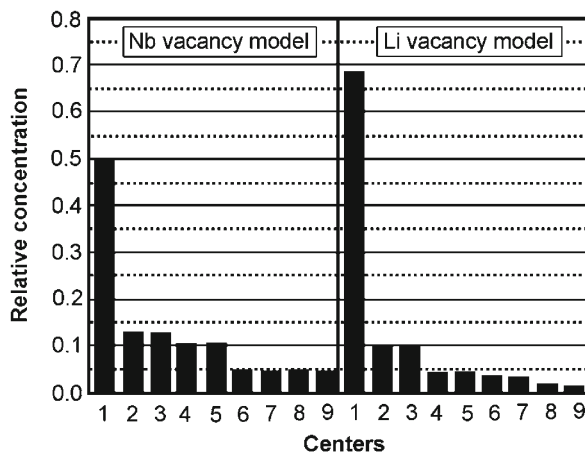
Fig. 14 Relative concentration (normalized to one) of centres created by statistical disorder according to a Poissonian distribution for the two models used to account for the charge compensation [20]. (1): no defects in the nearest environment; (2) and (3): one anti-site (Nb vacancy model) or Li vacancy (Li vacancy model); (4) and (5): one Nb vacancy (Nb vacancy model) or one anti-site (Li vacancy model); (6) and (7): one anti-site along the c-axis (Nb vacancy model) or one Li vacancy along the c-axis (Li vacancy model); (8) and (9): one vacancy of Nb along the c-axis (Nb vacancy model) or one anti-site along the c-axis (Li vacancy model)

be due to the simultaneous presence of anti-sites and Nb^{5+} vacancies which are naturally connected in the LiNbO$_3$ lattice. When Li$^+$ is substituted by trivalent Cr^{3+} ions, the positive charge excess can be compensated in the nearest shells by the following charge compensated complex: every five Cr^{3+} located in Li$^+$ sites by two Nb^{5+} vacancies. The difference in crystal field strengths acting on the three main Cr^{3+} centres can be observed by the trigonal perturbation estimated from the ^{2}E splitting: 38 cm^{-1} in the γ centre, 69 cm^{-1} in the α centre and 68 cm^{-1} in the β centre in keeping with expected symmetry perturbations on each type of site. The same value of the ^{2}E trigonal splitting (68–69 cm^{-1}) for the two perturbed sites which has been characterized by two different ^{2}E absolute energy positions (L$_2$=13,603 cm^{-1} for α centre and L$_1$=13680 cm^{-1} for β centre) reflected roughly the same type of perturbation from either Nb^{5+} anti-site or Nb^{5+} vacancy in the first shells around the Li$^+$ site occupied by the Cr^{3+} ion. Such observation might be related to the interpretation we gave above, consisting of C$_1$ point group symmetry Cr^{3+} in Li$^+$ sites perturbed, either by one Nb $^{5+}$ vacancy in the first Nb^{5+} shells around Li$^+$ located at 3.01, 3.05 or 3.38 Å, or by one anti-site Nb$^{5+}_{Li+}$ in the first Li$^+$ shell located at 3.76 Å around Li$^+$ site (see Table 1 in [50]).

We would like to emphasize the very important role played by stoichiometry dependence since all lines associated with perturbed centres in Fig. 12 disappear near the stoichiometric composition and only the main centre γ remains in excellent keeping with our structural interpretations.

7
Nephelauxetic Effect

Another interesting feature merits attention in the optical spectra of Cr^{3+}-doped $LiNbO_3$. Macfarlane et al. have shown that the inhomogeneous broadening of the transitions is dominated by variation in the centre energy of the split ^2E state which is determined by the Racah parameters B and C and the octahedral crystal field strength that is characterized by the $^4A_2 \rightarrow ^4T_2$ splitting, 10 Dq. The Racah parameters quantify the Coulomb inter-electron interaction energy for the ranges 1.5<Dq/B<3.5 and 3<C/B<6, the energy of the ^2E level is approximately given by [44]

$$E(2E) = 3.05C + 7.9B - 18B^2/10\ Dq$$

A simple diabatic model of the mixing of the electronic and vibrational wavefunctions of the ^2E and $^4T_2$ states suggests that the approximation in Eq. (1) may not be valid when the energy separation between the states is small. This model predicts increased inhomogeneous broadening of the R-line fluorescence, as increase in the phonon side band and a reduction in the fluorescence lifetime. However, a fuller adiabatic model [54] shows that the result of this mixing is indeed to vary the relative intensity of the R-line and its phonon side band and to influence the fluorescence lifetime of the state but that the energy of the approximate ^2E state remains almost unaltered. We have demonstrated this feature in (Ca, Zr)-substituted GGG as a host for Cr^{3+} ions [54]. Normally, the Racah parameters are assumed constant for any given optical centre and the energy of the ^2E state varies due to changes in 10 Dq that result from small differences in the size of oxygen octahedra. If large variations in 10 Dq exist with in the material, then the R-line fluorescence peak will vary as a function of excitation energy when exciting the $^4A_2 \rightarrow ^4T_2$ as different sets of sites are preferentially excited. Such measurements for Cr^{3+}-doped $LiNbO_3$ reveal no such change in fluorescence peak energy. It has been concluded therefore, that there can only be a small variation in 10 Dq and that the broadening is caused by variation of the Racah parameters. The Racah parameters of Cr^{3+} in crystals are reduced from their free ion values by covalency between the 3d ligand electrons, a phenomenon known as the nephelauxetic effect which has largely been pointed out by Jørgensen [33–36]. Processes which alter the overlap between ligand and the *3d* electrons on the Cr^{3+} ion will change the Racah parameters and hence the energy of the R-line. For example, the R-line energy in ruby is reduced by an applied hydrostatic pressure because the Racah B parameter reduces as the oxygen ions are forced closer to the Cr^{3+} ions [55]. In Cr^{3+}-doped $LiNbO_3$, the site-to-site variation in the magnitude of the Racah parameters causes the inhomogeneous broadening of the R-lines, a radically different process from those discussed previously [54]. The probable origin of this nephelauxetic effect is the strong covalent contribution to bonding in $LiNbO_3$ [53].

8
Conclusion

In summary, it is concluded that the Nd^{3+} ions occupy at least three off-centred Li$^+$ octahedral sites in LiNbO$_3$, giving place to three non-equivalent optical centres. These centres still remain in the MgO-codoped crystal, where a small percentage (<10%) of Nd^{3+} ions lie in non-Li octahedral position, giving place to a new optical centre, as in the case of Cr^{3+} dopant, may be located in the Nb^{5+} octahedral site or even in the tetrahedral site as suggested by some essays of RBS. More generally, it has been shown in LiNbO$_3$ lattice that RE ions occupy Li$^+$ octahedral sites but placed in different off-centred positions along the c-axis depending on their cationic sizes. The need of use both Laser Spectroscopy and Rutherford Back Scattering techniques to understand the multi-centre phenomena in RE-doped LiNbO$_3$ is evidenced in this work.

The literature contains a lot of controversy on the interpretation of Cr^{3+}-doped LiNbO$_3$ absorption and emission spectra. We have shown that the optical properties needed to be revisited by means of different high resolution laser spectroscopy techniques in crystalline samples with both various extrinsic (Cr^{3+} doping) and intrinsic (compositions from congruent to nearly stoichiometric samples) defect concentrations Our results lead to distinguish only three Cr^{3+} centres in substitution of Li$^+$ sites in LiNbO$_3$ without MgO. The main centre γ corresponds to undistorted Li octahedral site exhibiting a rather low crystal field. The two other Cr^{3+} centres α and β, on the other hand, correspond to rather high crystal field scheme sites which are linked to Cr^{3+} ion substituting Li octahedral sites distorted by intrinsic defects in their neighbourhood shell. A statistical model leads to assign the centre β to a Cr^{3+} in a Li$^+$ site perturbed by niobium anti-site in the first cation shell, whereas the centre α could be due to a Cr^{3+} in a Li$^+$ site perturbed by niobium vacancy in the first cation shell.

Among a lot of intrinsic defects which have already been considered, we think that the most logical interpretation of the compensation process both in RE and transition metal ions would be due to the simultaneous presence of anti-sites and Nb^{5+} vacancies which are naturally connected in the LiNbO$_3$ lattice.

In contrast to the broadening of Cr^{3+}-doped glasses and disordered garnet oxides where distributions in the crystal field terms are dominant, nephelauxetic broadening was involved. This means a reduction in the Racah parameters of transition metal ions in crystals from their free ion values by covalency between the 3d ligand electrons. The probable origin of this nephelauxetic effect is the strong covalent contribution to bonding in LiNbO$_3$.

9
References

1. Armenise MN, Canali C, De Sario M, Zanoni E (1993) Mater Chem Phys 9:267
2. Krätzig E, Schirmer O (1988) Photorefractive materials and their applications I. Springer, Berlin Heidelberg New York
3. He Q, De Micheli M, Ostrowsky D, Lallier E, Pocholle JP, Papuchon M, Armani F, Delecourt D, Grezes-Besset G, Pelletier E, (1992) Optics Commun 89:54
4. Guo Zhong G, Jian J, Kang Wu Z (1980) IEEE Cat No 80 1561–0:631
5. Jermann F, Simon M, Krätzig E (1995) J Opt Soc Am 12:7273
6. Malovichko GI, Grachev VG, Yurchenko LP, Proshko VY, Kokanyan EP, Gabrielyan VT (1992) Phys Status Solidi A 133:K29; Malovichko G, Grachev V, Kokanyan EP, Schirmer OF, Betzler K, Gather B, Jermann F, Klauer S, Schlarb U, Wöhlecke M (1993) Appl Phys A Solids Surf A56:103
7. Bordui PF, Norwood RG, Bird CD, Calvert GD (1991) J Cryst Growth 113:61
8. Kitamura K, Furukawa Y, Iyi N (1997) Ferroelectrics 202:21
9. Polgar K, Peter A, Kovacs L, Corradi G, Szaller Z (1997) J Cryst Growth 177:211
10. Wöhlecke M, Corradi G, Betzler K (1996) Appl Phys B 5
11. Ridah A, Bourson P, Fontana M, Malovichko G (1996) J Phys Condens Matter 9:9687
12. Fan TY, Cordova-Plaza A, Gigonnet M, Shaw HJ (1986) Opt Soc Am B 4:140
13. Lallier E, Pocholle JP, Papuchon M, He O, De Micheli M, Ostrowgsky DB, Grezes-Bresset C, Pelletier E (1991) Electron Lett 27:936
14. Bryan DA, Gerson R, Tomaschek HE (1984) Appl Phys Lett 44:847
15. Lallier E (1992) Appl Opt 31:5276
16. Lifante G, Cusso F, Jaque F, Sanz-Garcia JA, Monteil A, Varrel B, Boulon G, Garcia Solé J (1991) Chem Phys Lett 176:482
17. Tocho JO, Sanz-Garcia JA, Jaque F, Garcia Solé J (1991) J Appl Phys 70:5582
18. Tocho JO, Camarillo E, Cusso F, Jaque F, Garcia Solé J (1991) Solid State Commun 80:575
19. Rebouta L, Smulders PJ, Boerma DO, Aguillo-Lopez F, Da Silva MF, Soares JC (1993) Phys Rev B 48:3600
20. Qiu Y (1993) J Phys Condens Matter 5:2041
21. Dierolf V, Koerdt M (2000) Phys Rev B 61:8043
22. Dierolf V, Sandmann C, Kutsenko AB, Tröster T (2001) Radiat Eff Defects Solids 154:253
23. Salley GM, Basun SA, Imbusch GF, Kaplyanskii AA, Kapphan S, Meltzer RS, Happek U (1999) J Lumin 83/84:423
24. Salley GM, Basun SA, Kaplyanskii AA, Meltzer RS, Polgar K, Happek U (2000) J Lumin 87/89:1133
25. Basun SA, Salley GM, Kalyanskii AA, Gallagher HG, Polgar K, Lu L, Happek U (1999) J Lumin 83/84:435
26. Dierolf V, Kaplyanskii AA, Kapphan S, Kutsenko AB (2001) Radiat Eff Defects Solids 1544:241
27. Basun SA, Kaplyanskii AA, Kutsenko AB, Kapphan SE, Dierolf V, Troester T, Polgar K (2001) Appl Phys B 73:453
28. Kaminska A, Suchocki A, Arizmendi L, Callejo, Jaque D, Grinberg M (2000) Phys Rev B 62:10802
29. Grachev V, Malovichko G (2000) Phys Rev B 62:7779
30. Lhommé F, Bourson P, Boulon G, Guyot Y, Fontana M (2002) Eur Phys J AP 20:29
31. Lhommé F, Bourson P, Fontana MD, Malovichko G, Aillerie M, Kokanyan E (1998) J Phys Condens Matter 10:1137
32. Macfarlane P, Holliday K, Henderson B (1996) Chem Phys Lett 252:311
33. Schäffer CE, Jørgensen CK (1958) J Inorg Nucl Chem 8:143
34. Jørgensen CK (1962) Absorption spectra and chemical bonding in complexes. Pergamon Press, Oxford
35. Jørgensen CK (1962) Prog Inorg Chem 4:73

36. Reisfeld R, Jørgensen CK (1977) Lasers and excited states of rare earths, Springer, Berlin Heidelberg New York
37. Garcia Solé J, Petit T, Jaffrezic H, Boulon G (1993) Europhys Lett 24:719
38. Burlot R, Moncorgé R, Boulon G (1997) J Lumin 72/74:812
39. Foulon G, Ferriol M, Brenier A, Cohen-Adad MT, Boulon G (1995) Chem Phys Lett 245:555
40. Rebouta L, Soares JC, Da Silva MF, Sanz-Garcia JA, Dieguez E, Aguillo-Lopez F (1992) Mat Res 7:130
41. Kovacs L, Rebouta L, Soares JC, Da Silva MF, Rage-Ali M, Stouqert JP, Siffert P, Sanz-Garcia JA, Corradi G, Szaller Z, Polgar K (1993) J Phys Condens Matter 5:781
42. Schimer OF, Thiemann O, Wohlecke M (1991) J Phys Chem Solids 52:185
43. Lorenzo A, Jaffrezic H, Roux B, Boulon G, Bausa LE, Garcia-Solé J (1995) Phys Rev B 52:6278
44. Lorenzo A, Loro, Munoz Santiuste J, Terile M, Boulon G, Bausa L, GarciaSolé J (1997) Opt Mater 8:55
45. Garcia-Solé J (1994) Phys Scr T 55:30
46. Sugano S, Tanabe Y, Kamimura H (1970) Multiplets of transition ions in crystals. Academic Press, New York London
47. Lupei V, Lou L, Boulon G, Lupei A (1993) J Phys Condens Matter 5:L35
48. Brenier A, Boulon G, Pedrini C, Madej C (1992) J Appl Phys 71:6062
49. Garcia Solé J, Bausa L, Jaque D, Montoya E, Murrieta H, Jaque F (1998) Spectrochim Acta 54:1571
50. Malovichko G, Grachev V, Kokanyan E, Schirmer O (1999) Phys Rev B 59:9113
51. Montoya E, Espeso O, Bausa L (2000) J Lumin 87/89:1036
52. Montoya E, Bausa L, Schaudel B, Goldner P (2001) J Chem Phys 114:3200
53. Henderson B, Imbusch GF (1990) Optical spectroscopy of inorganic solids. Oxford University Press, Oxford
54. Grinberg M, Brenier A, Boulon G, Pedrini C, Madej C (1993) J Lumin 55:303
55. Sharma S, Gupta Y (1989) Phys Rev B 40:3329

CHAPTER 1

Recent Advances of Spin Crossover Research

Philipp Gütlich[1] · Petra J. van Koningsbruggen[2] · Franz Renz[1]

[1] Institut für Anorganische Chemie und Analytische Chemie, Johannes Gutenberg-Universität,
Staudinger-Weg 9, 55099 Mainz, Germany
E-mail: guetlich@uni-mainz.de
E-mail: franz.renz@uni-mainz.de

[2] Stratingh Institute for Chemistry and Chemical Engineering, University of Groningen,
Nijenborgh 4, 9747 AG Groningen, The Netherlands
E-mail: P.van.Koningsbruggen@chem.rug.nl

Abstract Thermal spin transition (spin crossover), one of the most fascinating dynamic electronic structure phenomena occurring in coordination compounds of third row transition metal ions, mostly of iron(II), iron(III) and cobalt(II) with critical ligand field strengths competing with the spin pairing energy, has attracted increasing attention by many research groups. One of the reasons is the promising potential for practical applications. In this chapter we intend to cover essential recent work, primarily accomplished within the European research network on "Thermal and Optical Switching of Molecular Spin States (TOSS)". New spin crossover compounds and their thermal spin transition behaviour, also under applied pressure, novel effects observed by irradiation and magnetic field, will be discussed. Progress in theoretical treatments of spin crossover phenomena, particularly cooperativity, will be briefly outlined. The chapter concludes with a summary of research highlights published by the partner laboratories of the TMR network TOSS.

Keywords Spin crossover · Physical properties · Cooperativity · Pressure · Light effects

List of Abbreviations and Symbols

EPR   Electron paramagnetic resonance
HS   High spin
LD-LISC   Ligand-driven light-induced spin change
LIESST   Light induced excited spin state trapping
LIOH   Light induced optical hysteresis
LiPOH   Light-perturbed optical hysteresis
LiPTH   Light perturbed thermal hysteresis
LITH   Light induced thermal hysteresis
LS   Low spin
NIESST   Nuclear decay induced excited spin state trapping
SCO   Spin crossover
ST   Spin transition
$T_{1/2}$ Spin transition temperature (temperature of 50% conversion
          of all "SCO-active" metal centres)
γ_{HS} High spin molar fraction

1
Introduction

The phenomenon of thermal spin crossover (SCO), though already well known in inorganic chemistry for more than seven decades, has developed in recent years to one of the most actively studied subjects in coordination chemistry [1–5]. Not only has the fundamental interest regarding "why" and "how" thermal spin transition particularly in the solid state takes place stimulated many re-

search groups, with primary interest in the design and synthesis of new compounds as well as those equipped for and experienced in the physical characterization, to become active in this field. It has likewise been the hope that SCO compounds with suitable bistability properties for switching under the action of temperature variation, application of light or pressure, may eventually become good candidates for practical application in devices (sensors, displays, storage).

A research network comprising altogether ten European groups (P. Gütlich, H. Spiering/Mainz, W. Linert/Vienna, F. Varret/Versailles, O. Kahn, J.F. Létard/ Bordeaux, J. Haasnoot/Leiden, J.A. Real/Valencia, J. McGarvey/Belfast, A.X. Trautwein/Lübeck, H. Toftlund/Odense, A. Hauser/Geneva), financially supported by the European Community and administered by the University of Mainz, was installed in 1998 (Contract No. ERB-FMRX-CT98-0199) in order to strengthen the research activities on "Thermal and Optical Switching of Molecular Spin States (TOSS)". This network has focused on the fascinating class of transition metal compounds that has the ability to change their spin states and thereby their magnetic and optical properties by varying the temperature.

Specifically, many iron(II) complexes with FeN_6 core have been reported, where the strongly paramagnetic high spin (HS, S=2) state changes to the (nearly) diamagnetic low spin state (LS, S=0) upon cooling; raising the temperature brings about a reversal of this transition, mostly with a drastic change of colour, and often with hysteresis. This holds promise to be the basis for thermal display. SCO research has recently received a considerable boost with the recognition that such materials can also be switched optically between the two spin states with light of different wave lengths, leading eventually to applications in optical devices. Moreover, the large volume change accompanying the spin state transition makes such materials sensitive to pressure and eventually suited for application in pressure sensors. The switching properties, as is well known, can be varied over a wide range by chemical modification and physical influences.

The "key scientific objectives" of this network TOSS have been:

– To synthesize new SCO compounds with hysteresis near to room temperature
– To explore the physics, especially the interaction mechanism, of SCO compounds with one-, two- and three-dimensional networks, and in thin films
– To search for SCO compounds with long-lived light-induced spin states
– To understand in detail the intersystem crossing dynamics of thermal and light-induced transitions, the cooperative interactions, and the intrinsic driving forces
– To develop concepts for optical devices, thermal and pressure sensors

In the following we shall summarize the most prominent results of a four-year collaboration of chemists, physicists and theoreticians within this research network. In many instances, whenever appropriate and indicated, we shall refer to earlier work in this field, in order to emphasize how progress has developed in a particular context. We shall subdivide our chapter into the following sections.

The first one gives an overview of new SCO materials that have been synthesized and, wherever possible, structurally characterized. The second part deals with physical studies such as special structural investigations, intersystem crossing dynamics under various conditions, new light effects, influence of pressure

and magnetic field. The third part describes briefly the progress made in developing theoretical models. The chapter concludes with a summary of research highlights accomplished by the partner laboratories of the TMR network TOSS.

2
Selected Examples of Novel Mononuclear and Polynuclear Fe(II) Spin Crossover Compounds

2.1
Mononuclear Fe(II) Spin Crossover Compounds

2.1.1
Fe(II)hexakis(azole) Compounds

Mononuclear compounds containing $[Fe(II)(ligand)_6]^{2+}$ spin crossover chromophores consisting of six chemically identical ligands have already been known for decades. However, the examples had been limited to the well-studied hexakis(1-alkyl-tetrazole)iron(II) compounds of various monovalent anions [1, 2, 5–21]. Among these, the extensively studied $[Fe(1\text{-propyl-tetrazole})_6](BF_4)_2$ [1, 5–10, 22] shows very abrupt spin transitions, a feature which may very well be described by the model of elastic interactions [23–25], and even thermal hysteresis, followed by a first order crystallographic phase transition [26]. The analysis of the Fe(II) spin crossover properties in relation to the variation of the alkyl substituent at the N1 position of the tetrazole does not reveal a clear picture. In fact, upon varying the N1 alkyl substituent, as well as on selecting other non-coordinating anionic groups, the crystallographic features of the material change in such a way that the Fe(II) spin transition behaviour is dramatically and unpredictably changed throughout the series. Interestingly, almost all types of Fe(II) spin crossover behaviour, i.e. involving abrupt or rather gradual transitions, complete or only involving a part of the Fe(II) ions, have been observed within this family, and could be interpreted in view of the crystal structure features.

Recent advances in this field include the use of tetrazole ligands with halogen containing substituents. $[Fe(1\text{-}(2\text{-chloroethyl})tetrazole)_6](BF_4)_2$ [27] has been reported to exhibit an Fe(II) spin crossover behaviour involving two transitions taking place in a 1:1 ratio at 190 K and 107.5 K. The origin for this magnetic behaviour could not yet be clarified, since the structure determination has only been carried out at room temperature revealing symmetry-equivalent Fe(II) ions in the high-spin state.

These mononuclear materials of tetrazole derivatives show some structural similarity with the hexakis Fe(II) isoxazole compounds, of which the first examples have already been known since 1977 [28]. Only recently, could this be confirmed by the crystal structure determination of the Fe(II) high-spin modification of $[Fe(isoxazole)_6](BF_4)_2$ carried out at 230 K (see Fig. 1) [29]. $[Fe(isoxazole)_6](BF_4)_2$ crystallises in the space group $P\text{-}3$ with $Z=3$.

There are two crystallographically independent Fe(II) ions. The asymmetric unit consists of Fe1 together with one ligand, Fe2 with two ligands, and one tetrafluoroborate anion. Fe1 lies on the inversion centre and the $[Fe1(isoxazole)_6]^{2+}$
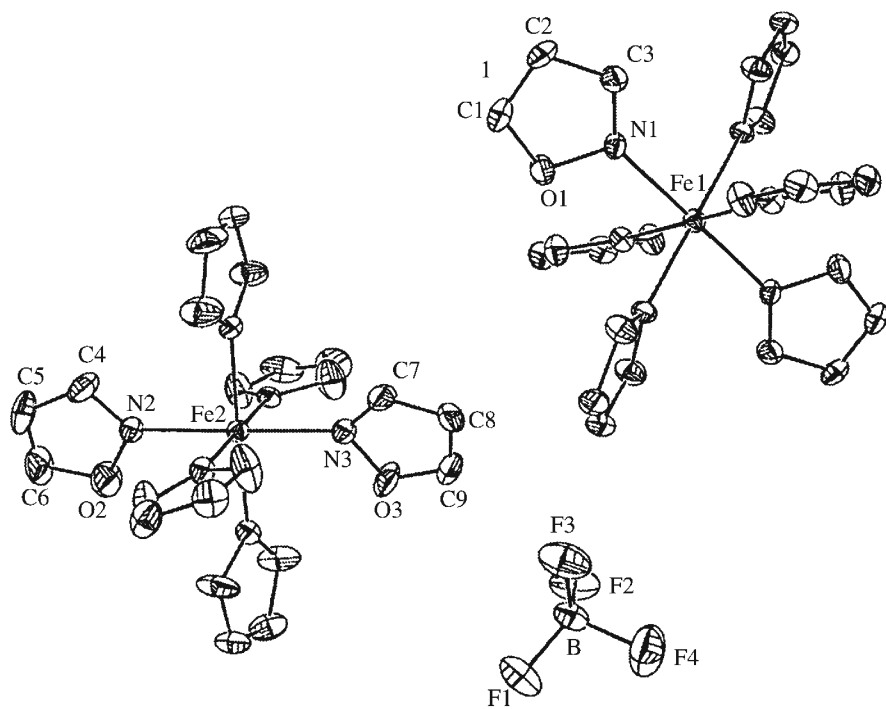
Fig. 1 Projection showing the structure of [Fe(isoxazole)$_6$](BF$_4$)$_2$ ([29] – reproduced by permission of the Royal Society of Chemistry)

unit is generated by the crystallographic symmetry. On the other hand, Fe2 lies on the threefold axis, and generates its crystallographic counterpart using the inversion centre located on Fe1. Therefore, the ratio Fe1:Fe2 units is 1:2. This crystallographic study also allowed to relate the two-step Fe(II) spin crossover features to the presence of two crystallographically independent [Fe(isoxazole)$_6$]$^{2+}$ sites. The magnetic data could be analysed by attributing the transition occurring at 91 K to Fe2, whereas Fe1 is undergoing its spin transition at 192 K. The individual spin crossover behaviour of each Fe(II) site has its origin in the unequality of the Fe1 and Fe2 high-spin chromophores, such as the slight differences in bond lengths and bond angles, as well as in the geometrical disposition of the isoxazole ligands.

Bis[hydrotris(1,2,4-triazol-1-yl)borate]iron(II) [30–34] represents the only mononuclear Fe(II) spin transition compound containing an Fe(II) octahedron consisting of six N1-donating 1,2,4-triazole ligands. [Fe{HB(C$_2$H$_2$N$_3$)$_3$}$_2$] has been reported to exhibit a very abrupt spin transition between 334 and 345 K via variable temperature UV-VIS and ^{57}Fe Mössbauer spectroscopy studies [32]. After the publication of a preliminary magnetic study in 1994 [32], a more detailed report appeared in 1998 [33], the results of which corresponded with measurements carried out independently at about the same time [34]. The magnetic data for [Fe{HB(C$_2$H$_2$N$_3$)$_3$}$_2$] show a very abrupt spin crossover. At 300 K, the χT value of

0.15 cm^3 K mol^{-1} is consistent with a singlet spin state, whereas at 350 K, the χT value of 2.90 cm^3 K mol^{-1} corresponds to the Fe(II) high-spin state. The transition temperature, $T_{1/2}$, where equivalent amounts of spin switching Fe(II) ions in low-spin and high-spin forms are present, is 331 K. Thermal hysteresis of ~1.5 K is observed using a 70 mK min^{-1} sweep rate.

2.1.2
Fe(II) Compounds Containing Bidentate Chelating 1,2,4-Triazole Ligands

Although 3-(pyridin-2-yl)-1,2,4-triazole derivatives, as well as 4-amino-3,5-bis(pyridin-2-yl)-1,2,4-triazole, act as bidentate chelating 1,2,4-triazole-based ligands, their coordination mode towards Fe(II) ions is different. Both ligands appear in Fe(II) spin crossover compounds in their neutral form and use the N of one pyridyl ring for coordination; however, 3-(pyridin-2-yl)-1,2,4-triazole further coordinates to Fe(II) by the N4 of the 1,2,4-triazole moiety [20], whereas 4-amino-3,5-bis(pyridin-2-yl)-1,2,4-triazole only has the N1 of the 1,2,4-triazole ring available for coordination [35–38].

The physical properties of mononuclear Fe(II) spin crossover compounds of 3-(pyridin-2-yl)-1,2,4-triazole derivatives have been studied since 1986 [39–41]; however, the first crystallographic data of a member of this family have only recently become available [20]. The crystal structure of [Fe(3-(pyridin-2-yl)-1,2,4-triazole)$_3$](BF$_4$)$_2$·2H$_2$O has been solved at 95 and 250 K in the space group *P*bam with *Z*=8 [20]. The asymmetric unit contains one [Fe(Hpt)$_3$]$^{2+}$ dication in a *mer* configuration. The Fe(II) ion is octahedrally surrounded by three crystallographically independent bidentate Hpt ligands coordinating through the N2 of the pyridine ring and the N4 of the 1,2,4-triazole moiety. The average Fe–N bond length diminishes by about 0.15 Å upon cooling down to 95 K. [Fe(Hpt)$_3$](BF$_4$)$_2$·2H$_2$O displays a gradually proceeding incomplete Fe(II) spin crossover behaviour with $T_{1/2}$=135 K [20]. The spin transition appears to be complete at higher temperatures, whereas at 75 K, about 30% of the Fe(II) ions are still in the high-spin state.

On the other hand, Fe(II) ions surrounded by three didentate coordinating 4-amino-3,5-bis(pyridin-2-yl)-1,2,4-triazole ligands do not show any spin crossover behaviour [42]. Still, the formation of mononuclear Fe(II) spin transition compounds with 4-amino-3,5-bis(pyridin-2-yl)-1,2,4-triazole (abbreviated as abpt) appeared to be possible; this required the incorporation of additional N-donating co-ligands in *trans* positions. The first representative of this family is [Fe(abpt)$_2$(TCNQ)$_2$] (TCNQ=7,7′,8,8′-tetracyanoquinodimethane), the first Fe(II) complex containing coordinated radical anions, which undergoes a thermally induced Fe(II) spin crossover with $T_{1/2}$=280 K [35]. The structure of [Fe(abpt)$_2$(TCNQ)$_2$] could be solved in the triclinic space group *P*-1 at 298 and 100 K (see Fig. 2).

The unit-cell contains one [Fe(abpt)$_2$(TCNQ)$_2$] unit with the Fe(II) ion at the inversion centre. The equatorial coordination sphere is formed by two bidentate chelating abpt ligands coordinating via N(pyridyl) and N1(1,2,4-triazole). The Fe(II) spin crossover can be monitored by the evolution in Fe–N bond lengths upon going from 298 to 100 K. The Fe–N(pyridyl) bond shortens from 2.12(1) Å
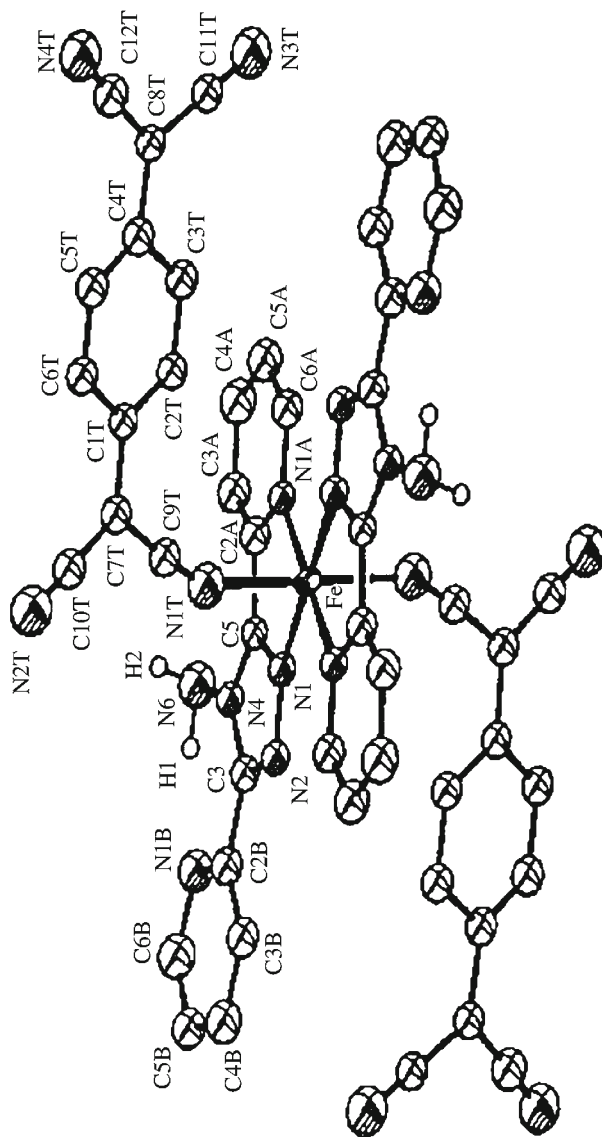
Fig. 2 Projection showing the structure of [Fe(abpt)$_2$(TCNQ)$_2$] at T=298 K (Reprinted with permission from [35] – copyright (1996) American Chemical Society)

to 2.02(1) Å, whereas the Fe–N1(1,2,4-triazole) bond length diminishes from 2.08(1) Å to 2.00(2) Å, respectively. The TCNQ radical anions occupy the axial positions. The tremendous shortening of the Fe–N(TCNQ) bond lengths upon cooling is worth noting. This change by 0.23 Å, i.e. from 2.16(1) Å at 298 K to 1.93(1) Å at 100 K, is among the largest changes in bond lengths that have been observed for Fe(II) spin crossover compounds. It can probably be related to the extended π-system of TCNQ, which favours increased backbonding when Fe(II) is in the low-spin state. The [Fe(abpt)$_2$(TCNQ)$_2$] entities are packed in such a way that the

TCNQ molecules form dimers in the usually found eclipsed conformation, like the one existing in the $(TCNQ)_2^{2-}$ diads [43–48]. This feature is essential for explaining the magnetic data. The antiferromagnetic coupling within such a stacked entity is so strong that these form diamagnetic units over the whole temperature range studied in the magnetic measurements; therefore, the magnetic data only reflect the magnetic behaviour of the Fe(II) ions. The variable temperature magnetic susceptibility data for $[Fe(abpt)_2(TCNQ)_2]$ show a complete and gradually proceeding Fe(II) spin crossover behaviour. The χT value of 3.70 $cm^3 mol^{-1}$ K at 450 K is consistent with all Fe(II) ions being in the high-spin state. At 7 K, the χT value has decreased to 0.25 $cm^3 mol^{-1}$ K, which is very close to the value expected for all Fe(II) ions being in the low-spin state. The residual paramagnetism at these lower temperatures may be caused by the presence of small TCNQ$^{•-}$ radical anion impurities, which have indeed been observed by EPR spectroscopy. On the other hand, the presence of high-spin Fe(II) species could be ruled out based on the ^{57}Fe Mössbauer spectra.

Later on, it was demonstrated that instead of TCNQ$^{•-}$, NCS$^-$ or NCSe$^-$ [36, 37, 49] can also occupy the *trans*-located axial positions, resulting in Fe(II) spin crossover compounds with structures comparable to those of $[Fe(abpt)_2(TCNQ)_2]$ [35]. The Fe(II) spin transition also proceeds rather gradually for these derivatives, however with considerably lower transition temperatures: 224 K for the NCSe$^-$ derivative and 180 K for the NCS$^-$ analogue.

Recently, the magnetic susceptibility data for $[Fe(abpt)_2\{N(CN)_2\}]$ revealed a significantly different Fe(II) spin crossover behaviour characterized by an incomplete high-spin to low-spin transition with a transition temperature of only 86 K [36]. The apparent two steps observed during the Fe(II) spin crossover could not be explained on the basis of the crystallographic data recorded at 298 K, which showed a structure related to those of the other members of this family. Also $[Fe(abpt)_2\{N(CN)_2\}]$ has been found to crystallise in the triclinic space group *P*-1 and contains one centrosymmetric mononuclear Fe(II) unit per unit cell. Below 60 K, around 37% of the Fe(II) ions are still in the high-spin state.

2.2
Dinuclear Fe(II) Compounds with Interplay Between AF Coupling and Thermal SCO

Coordination compounds with multiple nuclearity may combine different electronic properties like magnetic exchange and spin transition in the same molecule. Indeed, a first step in this line aimed to achieve such a multiproperty material began with 2,2′-bipyrimidine (bpym)-bridged iron(II) dinuclear compounds [50].

The series of compounds $\{[Fe(L)(NCX)_2]_2(bpym)\}$, where L is bpym or bt and X is S or Se, comprises four complexes, two of which, (**bpym, S**) and (**bt, S**), have been characterised by X-ray single crystal diffraction. The centrosymmetric dinuclear units $\{[Fe(L)(NCS)_2]_2(bpym)\}$, where L=bpym [50] or bt [51], are shown in Fig. 3. Each iron(II) atom is surrounded by two NCS$^-$ anions in *cis* positions, two nitrogen atoms of the bridging bpym ligand and the remaining positions are occupied by the peripheral bpym or bt ligands. The $[FeN_6]$ chromophore is rather distorted with Fe–N bond distances characteristic for an iron(II) ion in the HS state.
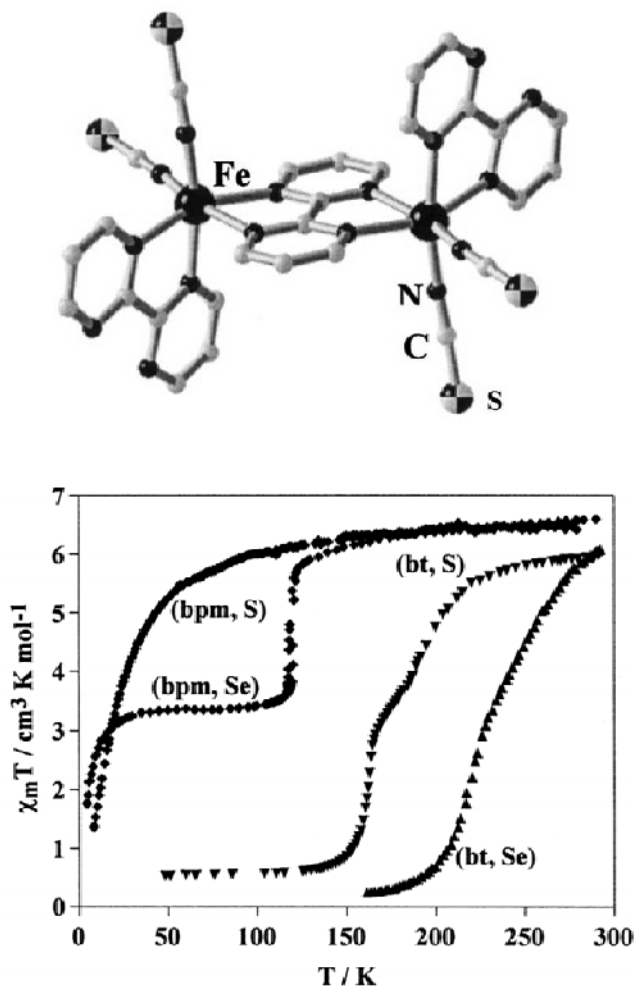
Fig. 3 Molecular structure of {[Fe(bpym)(NCS)$_2$]$_2$(bpym)} (bpym=2,2′-bipyrimidine) (*left*) and magnetic behaviour of the family {[Fe(L)(NCX)$_2$]$_2$(bpym)} (L=bpym, 2,2′-bithiazoline (bt) and X=S and Se) (*right*) [51, 125, 146]

The magnetic behaviour in Fig. 3 shows no thermal spin transition for the iron(II) complex denoted as (**bpym, S**) in the whole range of temperature, but is indicative of antiferromagnetic coupling between two iron(II) high-spin (S=2) centres. In contrast, the iron (II) complexes denoted as (**bt, S**), (**bpym, Se**) and (**bt, Se**) undergo spin transition, caused by a slightly higher ligand field strength most probably due to the bigger Se atoms. In all four compounds, spin crossover can be influenced under pressure.

2.3
Polynuclear Fe(II) Spin Crossover Compounds

An approach directed towards the obtaining of cooperative Fe(II) spin cross-over behaviour is based on polynuclear compounds. This method makes use of ligands capable of linking the active spin switching metal centres, and has been motivated by the fact that an efficient propagation of the molecular distortions originating from the Fe(II) spin transition through the crystal lattice is enhanced by the direct covalent intramolecular bonds. During the past years, much progress has been made in this research field yielding materials with such favourable Fe(II) spin crossover characteristics that these may be considered for various technical applications.

2.3.1
One-Dimensional Compounds

In the last few years, considerable progress has been made in the field of the synthesis, characterization and the tuning of the Fe(II) spin crossover properties of linear chain Fe(II) materials. The well-known polymeric compounds [Fe(4-R-1,2,4-triazole)$_3$](anion)$_2$ (R=amino, alkyl, hydroxyalkyl) have been extensively studied, because of their spin crossover characteristics involving pronounced thermochromism, transition temperatures near room temperature and large thermal hysteresis [52–55]. This makes these the compounds of choice for various applications in molecular electronics [3, 52–54] or as temperature sensors [53, 56]. Furthermore, a new class of one-dimensional Fe(II) spin crossover materials has been obtained using α,β- and α,ω-bis(tetrazol-1-yl)alkane type ligands [57, 58].

Fe(II) compounds of 4-R-1,2,4-triazole appear as fine microcrystalline powders. Fortunately, the EXAFS technique provided not only evidence for the local structure about the Fe(II) ion, but could also confirm that [Fe(Htrz)$_2$(trz)](BF$_4$) and [Fe(Htrz)$_3$](BF$_4$)$_2$·H$_2$O (Htrz=4H-1,2,4-triazole; trz=1,2,4-triazolato) consist of linear chains with typical Fe–Fe separations of 3.65 Å in the low-spin state [59, 60]. Later on, the EXAFS data of these Fe(II) derivatives could be compared with those of the structurally characterised Cu(II) derivative [Cu(hyetrz)$_3$](ClO$_4$)$_2$·3H$_2$O (hyetrz=4-(2′-hydroxy-ethyl)-1,2,4-triazole), pointing out that both metal ions form one-dimensional compounds [61]. The structure of [Cu(hyetrz)$_3$](ClO$_4$)$_2$·3H$_2$O determined at 298 K shows Cu(II) ions linked by triple N1,N2 1,2,4-triazole bridges yielding a slightly alternating chain with Cu1–Cu2 and Cu2–Cu3 distances of 3.853(2) Å and 3.829(2) Å, respectively.

For the corresponding Fe(II) compounds, the spin crossover characteristics may be tuned by the systematic variation of the substituent situated at N4 of the 1,2,4-triazole ligand, as well as by changing the non-coordinated anionic groups. In this way, thermochromic Fe(II) spin crossover materials showing a spin transition in close vicinity of room temperature and accompanied by hysteresis have been obtained. As an example, the optical measurements recorded for [Fe(4-amino-1,2,4-triazole)$_3$](2-naphthalene sulfonate)$_2$·xH$_2$O will be discussed [62]. Since this compound is highly thermochromic, the Fe(II) spin transition has

been studied optically. This technique provides an accurate determination of the transition temperatures; however it does not give an accurate information on the percentage of Fe(II) ions involved in the spin transition. Since the possible use of the material in molecular electronics requires stability of the physical behaviour (i.e. retaining of the hysteresis loop) the spin crossover behaviour has been investigated during at least three thermal cycles. The temperature has firstly been raised to 400 K followed by additional cooling and heating experiments. At room temperature, the thermodynamical stable state for the dihydrated [Fe(4-amino-1,2,4-triazole)$_3$](2-naphthalene sulfonate)$_2\cdot$2H$_2$O is in the low-spin state. This stabilization of the low-spin state by interactions with lattice water molecules has frequently been observed for mononuclear Fe(II) spin crossover compounds [63–66]. Upon heating, the compound starts to loose its lattice water molecules, and consequently, the stabilization of the low-spin state ceases, and an abrupt transition to the Fe(II) high-spin state occurs at 340 K. The now dehydrated material is cooled down, and subsequently, a rather abrupt high-spin to low-spin transition occurs at $T_{1/2}\downarrow$=283 K. Heating up the compound once more reveals another abrupt low-spin to high-spin transition, now situated at 297 K. Additional heating and cooling experiments show that this hysteresis of 14 K centred in the close vicinity of room temperature (290 K) remains stable. Therefore, the non-solvated [Fe(4-amino-1,2,4-triazole)$_3$](2-naphthalene sulfonate)$_2$ [62] represents one of the very few Fe(II) spin crossover materials showing a spin transition with hysteresis and an associated thermochromic effect in close vicinity of room temperature. Up to now, such Fe(II) spin crossover characteristics have also been observed for several related Fe(II) linear chain materials of various 4-substituted 1,2,4-triazole ligands [67–71].

Recently, it has been demonstrated that the use of α,β- and α,ω-bis(tetrazol-1-yl)alkane type ligands allowed a novel strategy towards the obtaining of polynuclear Fe(II) spin crossover materials. [Fe(btzp)$_3$](ClO$_4$)$_2$ (btzp=1,2-bis(tetrazol-1-yl)propane) [58] and [Fe(btze)$_3$](BF$_4$)$_2$ (btze=1,2-bis(tetrazol-1-yl)ethane) (see Fig. 4) [57] represent the first structurally characterised Fe(II) linear chain compounds exhibiting thermal spin crossover.

[Fe(btzp)$_3$](ClO$_4$)$_2$ [58] shows gradual spin crossover behaviour with a transition temperature $T_{1/2}$ of 148 K, as determined from variable temperature magnetic susceptibility measurements and ^{57}Fe Mössbauer spectroscopy. The magnetic behaviour of [Fe(btzp)$_3$](ClO$_4$)$_2$ shows that at higher temperatures, the spin crossover is fairly complete yielding 100% of high-spin Fe(II) ions, whereas at 60 K a mixture of low-spin and high-spin Fe(II) ions, with the molar fractions 0.80 and 0.20, respectively, could be detected. The presence of Fe(III) could be ruled out based on the ^{57}Fe Mössbauer spectroscopy data. [Fe(btze)$_3$](BF$_4$)$_2$ [57] exhibits a somewhat more abrupt spin transition centred at 140 K. The variable temperature magnetic susceptibility measurements, as well as the ^{57}Fe Mössbauer spectroscopy study gave evidence for an Fe(II) spin crossover behaviour that is complete at higher temperatures, however with a residual Fe(II) high-spin fraction of about 9.3% at lower temperatures. Superimposed on this spin crossover behaviour of the Fe(II) ions, the ^{57}Fe Mössbauer spectra recorded over the whole temperature range also revealed the presence of a small fraction (7%) of high-spin Fe(III) ions. Both compounds crystallise in the trigonal space group $P\bar{3}$c1,
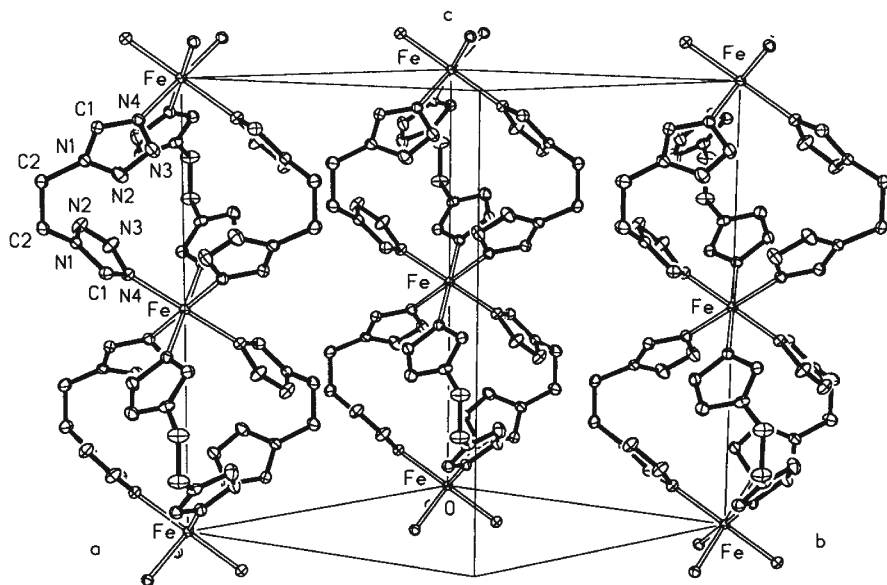
Fig. 4 Projection showing the unit cell of $[Fe(btze)_3](BF_4)_2$. Alternative orientation of the chains is omitted for clarity ([57] – reproduced by permission of Elsevier)

and this crystallographic symmetry is retained upon the Fe(II) spin crossover. The structure of $[Fe(btzp)_3](ClO_4)_2$ [58] has been solved at 200 K and 100 K, whereas the structure of $[Fe(btze)_3](BF_4)_2$ [57] has been determined at 296, 200, 150 and 100 K. The asymmetric unit consists of an iron(II) ion, one half of the bis(tetrazole)alkane ligand and an anion. Because of symmetry considerations, in both compounds the Fe(II) ion lies on the threefold axis and has an inversion centre. It is in an octahedral environment formed by six crystallographically related N4 coordinating 1-tetrazole moieties. The almost perfect O_h symmetry for the FeN_6 core is therefore present in the high-spin and low-spin state. The Fe–N bond lengths are markedly temperature dependent: the Fe–N4 distance of 2.164(4) Å at 200 K for $[Fe(btzp)_3](ClO_4)_2$ [58] is typical for an Fe(II) ion in the high-spin state, whereas the Fe–N4 distance of 2.038(4) Å at 100 K corresponds to an Fe(II) ion in the low-spin state. The Fe–N4 distances for $[Fe(btze)_3](BF_4)_2$ [57] show similar features: At room temperature the Fe–N bond length of 2.182(1) Å corresponds to a typical Fe(II) ion in high-spin state. After a small contraction to 2.160(1) Å at 200 K, there is a significant decrease to 2.095(2) Å at 150 K and to 2.004(1) Å at 100 K. This is accompanied by a concomitant change in the colour of the crystal from colourless (296 and 200 K) to an intense pink (150 K and 100 K). The short Fe–N distance at 100 K is consistent with the transition to the low-spin state. Three bis(tetrazole)alkane ligands link the Fe(II) centres to form regular cationic chains running parallel to the crystallographic c-axis. The Fe(II) spin crossover can also be monitored by the temperature dependence of the Fe–Fe separations over the bis(tetrazole)alkane ligands in bent *syn* conformation. The Fe–Fe separation over the btzp ligand is 7.422(1) Å at

200 K and 7.273(1) Å at 100 K, whereas these are 7.477, 7.461, 7.376 and 7.293 Å at 296, 200, 150 and 100 K, severally, for the btze analogue. In the *ab* plane the linear chains are arranged in a hexagonal close-packed fashion, creating channel-like hexagonal cavities between them, in which the non-coordinated anionic groups reside. Evidently, although both classes of materials have linear chain structures, the Fe(II) spin crossover characteristics are fairly different. It has been generally accepted that the cooperative nature of the spin transition encountered for the series of linear chain compounds of formula $[Fe(4-R-trz)_3](anion)_2 \cdot xH_2O$ (4-R-trz=4-substituted-1,2,4-triazole) [3, 52–66, 68–71] is directly related to the tight linkage of the active Fe(II) spin-switching centres by the extremely stiff and rigid triple N1,N2 1,2,4-triazole bridges. When the ligand spacer linking the Fe(II) ions becomes more flexible, as is the case for $[Fe(1,2-bis(tetrazol-1-yl)propane)_3(ClO_4)_2$ [58] and $[Fe(1,2-bis(tetrazol-1-yl)ethane)_3](ClO_4)_2$ [57], the spin crossover behaviour becomes more gradual. This is the signature for the slightness of the elastic interactions, which is most probably due to the 1,2-propane or 1,2-ethylene unit acting as some kind of shock absorber of the elastic interactions.

2.3.2
Two-Dimensional Compounds

The first reported two-dimensional Fe(II) spin crossover materials are represented by $[Fe(4,4'-bis-1,2,4-triazole)_2(NCX)_2]$ (X=S [72, 73], or Se [74]) (see Fig. 5). These compounds consist of layers of six-coordinated Fe(II) ions linked in the equatorial plane by single bridges of the 4,4'-bis-1,2,4-triazole ligand via the N1 atoms. The NCX$^-$ anions are coordinated in *trans* positions.

Two novel 2-D materials have been synthesised during the last few years. These compounds have a related layer-type architecture. However, the ligands used contain longer spacers between the N-coordinating heterocyclic moieties, which allowed the interpenetration of these layers. $[Fe(tvp)_2(NCS)_2] \cdot CH_3OH$ (tvp= 1,2-di-(4-pyridyl)-ethylene) is the first supramolecular 2-D catenane exhibiting thermal spin crossover behaviour [75]. Its structure has been elucidated at room temperature and consists of two interpenetrating two-dimensional $[Fe(tvp)_2(NCS)_2]^{2+}$ sheets. The octahedrally coordinated Fe(II) ion contains two thiocyanate anions in *trans* positions, whereas the four surrounding bidentate N-coordinating tvp ligands link the Fe(II) ions into 2-D layers. The Fe...Fe separation through the tvp ligand is 13.66 Å. The Fe...Fe separations involving metal ions originating from interpenetrating layers are 22.59 and 15.36 Å. Upon using 1,4-bis(4-pyridyl)-butadiyne (abbreviated as bpb) having a more extended and less flexible spacer, the threefold interlocked 2-D catenane system $[Fe(bpb)_2(NCS)_2] \cdot 0.5CH_3OH$ could be obtained [76]. The structure consists of 2-D $[FeL_2(NCS)_2]$ sheets comparable to the ones found in the former materials. The crystal structure involves two symmetry independent networks leading to Fe...Fe separations over the direct bpb linkage of 16.628 Å and 16.393 Å, respectively.

Both $[Fe(tvp)_2(NCS)_2] \cdot CH_3OH$ [75] and $[Fe(bpb)_2(NCS)_2] \cdot 0.5CH_3OH$ [76] exhibit very gradually proceeding and incomplete spin transitions. Although the
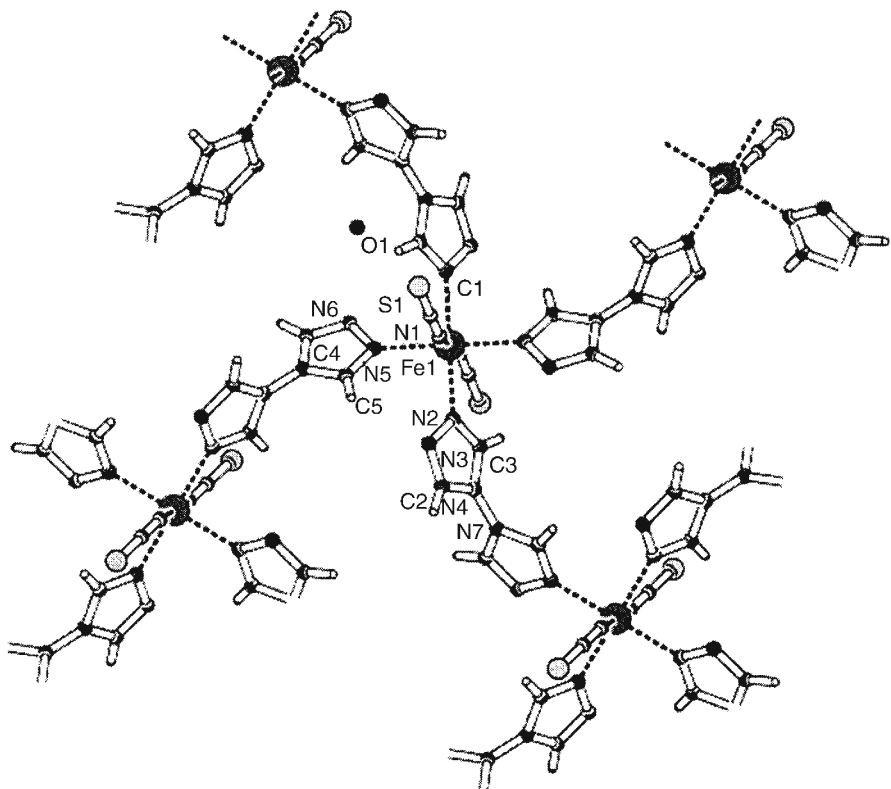
Fig. 5 Projection showing the structure of [Fe(4,4′-bis-1,2,4-triazole)$_2$(NCS)$_2$] (from [73])

1,2-di-(4-pyridyl)-ethylene and 1,4-bis(4-pyridyl)-butadiyne ligands themselves may a priori not be considered as flexible, it seems that the negligible magnitude of the elastic interactions is brought about by the flexibility of the 2-D network itself. This is illustrated by the absence of significant intra- and intermolecular interactions, which leads to the formation of large channels between the inter-locked lattices.

2.3.3
Three-Dimensional Compounds

[Fe(btr)$_3$](ClO$_4$)$_2$ (btr=4,4′-bis-1,2,4-triazole) [77] may be regarded as the 3-D analogue of the 2-D spin crossover materials [Fe(btr)$_2$(NCX)$_2$] (btr=4,4′-bis-1,2,4-triazole; X=S [72, 73], or Se [74]). The latter systems were first reported 15 years ago, and solely by incorporating the non-coordinating anion perchlorate for the N-coordinating thiocyanate anion, the 3-D Fe(II) spin transition com-pound has been obtained. The structure of [Fe(btr)$_3$](ClO$_4$)$_2$ [77] has been solved at 150, 190 and 260 K and comprises a 3-D network in which the crystallograph-ically inequivalent Fe1 and Fe2 ions are connected by single μ-*N*1,*N*1′-4,4′-bis-

1,2,4-triazole bridges. Each Fe site displays its own magnetic behaviour leading to a two-step spin conversion with 50% of the Fe(II) ions (site Fe1) undergoing a very abrupt spin transition with a small hysteresis of 3 K centred at 184 K, whereas the other 50% of Fe(II) ions (site Fe2) display rather gradual spin crossover behaviour with $T_{1/2}$=222 K. The Fe(II) spin transitions may also be monitored by the shortening of the metal-metal separations over the bridging btr ligands upon cooling, ranging from Fe1...Fe2 (both in the HS form)=8.67 Å at 260 K to Fe1 (HS)...Fe2 (LS)=8.55 Å at 190 K, and decreasing to Fe1...Fe2 (both in the LS form)=8.42 Å at 150 K.

[Fe(btzb)$_3$](ClO$_4$)$_2$ (btzb=1,4-bis(tetrazol-1-yl)butane) is the first highly thermochromic Fe(II) spin crossover material with a supramolecular catenane structure consisting of three interlocked 3-D networks [78, 79]. Unfortunately, only a tentative model of the 3-D structure of [Fe(btzb)$_3$](ClO$_4$)$_2$ could be determined based on the X-ray data collected at 150 K [80]. Since each of the btzb ligands is located on an inversion centre, all central C–C linkages are in the *anti* conformation. Of the six independent N–C–C–C torsions in the ligands, four are also in the *anti* conformation, but two fit the electron density best when brought into a *gauche* conformation. A detailed reanalysis of the crystallographic data has been carried out recently [81]. This revealed a model showing three symmetry related, interpenetrating, 3-D Fe-btzb networks. The shortest Fe–Fe separations of 8.3 and 9.1 Å occur between Fe(II) ions of two non-connected networks. The crystal structure of the Cu(II) analogue confirmed this threefold interpenetrating 3-D catenane structure [82]. Interestingly, the crystal structure determination did not reveal any well-defined type of intra- or intermolecular interaction, which could be responsible for the stabilization of this unusual supramolecular structure.

The results of the variable temperature optical measurements show that, upon cooling, a very abrupt high-spin to low-spin transition takes place at 155 K. Subsequent heating shows the low-spin to high-spin transition at 180 K, yielding a stable and reproducible thermal hysteresis loop of 25 K width. Surprisingly, the magnetic susceptibility measurements revealed that only ca. 16% of the Fe(II) ions participate in the spin transition, characterised by $T_{1/2}\downarrow$=150 K and $T_{1/2}\uparrow$= 170 K. This hysteresis of 20 K has been reproduced along several thermal cycles.

It is worth noting that this is the largest thermal hysteresis observed up to now for iron(II) tetrazole derivatives. Apparently, the rigidity originating from the interweaving within this threefold 3-D interlocked supramolecular lattice, is responsible for the efficient propagation of the elastic interactions leading to this type of cooperative spin crossover behaviour. However, the same factors may also be invoked for explaining the small fraction of Fe(II) ions undergoing the spin transition. Most probably, the structural changes accompanying the Fe(II) spin transition modify the structure in such a way that the further spin crossover of the high-spin Fe(II) ions upon cooling is severely hampered.

The first two-dimensional heterobimetallic Fe(II) spin transition materials have been reported in 1996 [83], and are based on the well-studied Hofmann clathrates. [Fe(pyridine)$_2$Ni(CN)$_4$] comprises a 2-D layer of alternating square planar diamagnetic tetracyanonickel(II) entities and octahedral spin-switching *trans*-bis(pyridin)tetracyanoiron(II) fragments bridged by cyano linkages [83].
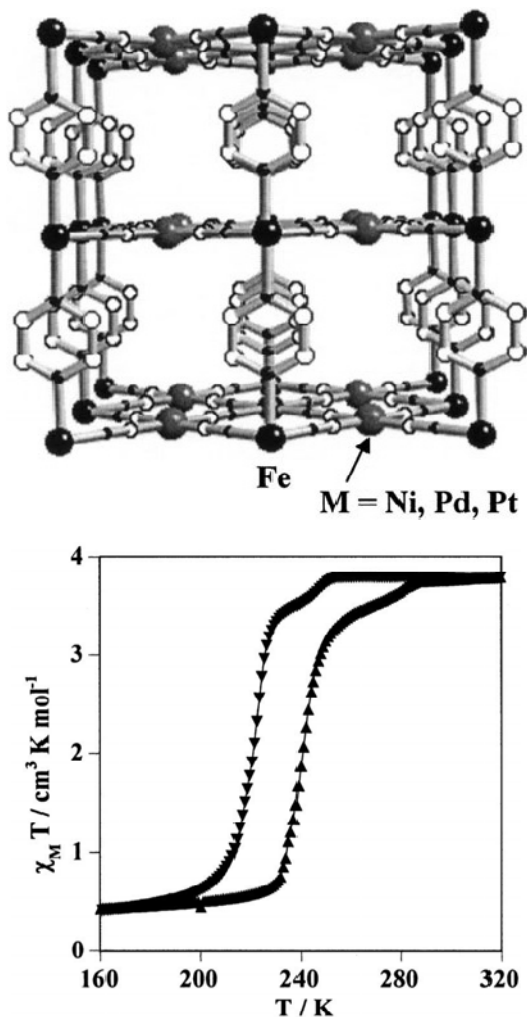
Fig. 6 Perspective view of the {Fe(pyrazine)[M(CN)$_4$]}·2H$_2$O (M=Ni, Pd, Pt) (*right*) and magnetic properties of the Pt derivative showing the strong cooperative behaviour characteristic of these 3-D frameworks (from [84])

Recently, the isostructural two-dimensional compounds [Fe(pyridine)$_2$M-(CN)$_4$] (M(II)=Pd, Pt) have been prepared and these materials have also been successfully modified with the objective to increase the dimensionality [84]. The monodentate coordinating pyridine has been replaced by bidentate bridging pyrazine ligands now yielding three-dimensional compounds of formula [Fe(pyrazine)M(CN)$_4$]·xH$_2$O (M(II)=Ni (x=2), Pd (x=2.5), Pt (x=2) [84]. The structure of these polycrystalline materials could only be determined using X-ray powder diffraction data confirming that the pyrazine ligand indeed connects the layers together yielding a three-dimensional network.
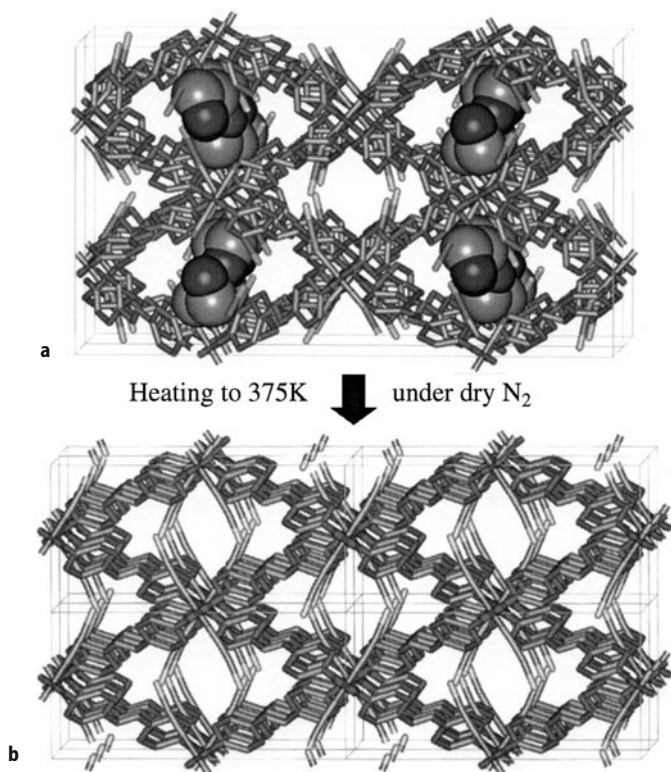
Fig. 7a,b The structure of: **a** $Fe_2(4,4'\text{-azpy})_4(NCS)_4 \cdot (EtOH)$; **b** $Fe(4,4'\text{-azpy})_2(NCS)_2$, viewed approximately down the 1-D channels. Framework atoms are represented as sticks and atoms of the ethanol guests as spheres. In $Fe_2(4,4'\text{-azpy})_4(NCS)_4 \cdot (EtOH)$ the ethanol guests occupy every second 1-D channel in a 'chess board' arrangement. Removal of the ethanol by heating gives single crystals of $Fe(4,4'\text{-azpy})_2(NCS)_2$, which has empty equivalent 1-D channels [85]. (Reprinted with permission from copyright (2002) American Association for the Advancement of Science)

The Fe(II) ion shows cooperative spin crossover behaviour for all derivatives. The comparison between the related two- and three-dimensional materials reveal that all higher dimensional pyrazine compounds show higher transition temperatures and considerably larger thermal hysteresis loops than the corresponding lower dimensional pyridine compounds. On the other hand, no direct relation between the size of M (M(II)=Ni, Pd, Pt), which evidently co-determines the dimensions of the three-dimensional network, and the Fe(II) spin crossover features could be established. The transition temperatures for the two-dimensional compounds range from $T_{1/2}\downarrow=186$ K and $T_{1/2}\uparrow=195$ K for Ni to $T_{1/2}\downarrow=208$ K and $T_{1/2}\uparrow=213$ K for Pd to $T_{1/2}\downarrow=208$ K and $T_{1/2}\uparrow=216$ K for Pt, whereas the three-dimensional materials show the following pattern $T_{1/2}\downarrow=280$ K and $T_{1/2}\uparrow=305$ K for Ni, $T_{1/2}\downarrow=233$ K and $T_{1/2}\uparrow=266$ K for Pd and $T_{1/2}\downarrow=220$ K and $T_{1/2}\uparrow=240$ K for Pt (see Fig. 6), respectively.

Halder et al. [85] described a nanoporous metal-organic framework $Fe_2(azpy)_4(NCS)_4 \cdot$(guest) (azpy is *trans*-4,4′-azopyridine) and studied the reversible uptake and release of guest molecules by X-ray structure analysis (see Fig. 7). The iron(II) centres show a thermally induced spin crossover sensitive to the nature of the adsorbed guests, the adsorbed phases undergoing "half-spin" crossovers, and the desorbed phase showing no switching property.

3
Physical Characterisation and Novel Effects

Beside the design and synthesis of new SCO compounds, the physical characterisation employing a variety of techniques has become the most important activity in SCO research [1, 2, 5, 86]. In studies of thermal, pressure- and light-induced spin transitions it is the temperature dependence of the molar fractions of HS molecules, $\gamma_{HS}(T)$, that is followed as a function of the external perturbations. Due to the presence of more or less strong cooperative interactions in solids, the spin transition functions $\gamma_{HS}(T)$ may be gradual or abrupt (classified as continuous transitions), with hysteresis (discontinuous transitions) or may take place in steps [2]. Physical studies are conducted to unravel such features, which tell us much about the nature of the cooperative interactions and finally about the possibilities of applying SCO materials in devices.

3.1
Structural Investigations

It is well established, by crystal structure determination, that spin transitions are always accompanied by structural changes, not necessarily by changes of the space group, but always by changes of the metal ligand bond lengths due to the different electron populations of the antibonding e_g^* orbitals and the essentially non-bonding t_{2g} orbitals in the HS and LS states [87]. Structural investigations have become very important in SCO research, particularly in view of the nature of cooperative interactions, which are known to arise from or to be altered by chemical modification of the SCO material such as metal dilution, ligand substitution, change of the non-coordinating anion or crystal solvent, creation of hydrogen bonding and π-stacking effects. All these influences are considered more or less responsible for an interplay of short and long range elastic interactions [23–25]. Much progress in temperature dependent crystal structure investigations was made in recent years, mainly due to significant improvements in instrumentation (cryogenics, CCD detector, X-ray focusing devices). Some remarkable results are described in the following.

The "classical" iron(II) SCO compound $[Fe(phen)_2(NCS)_2]$ was studied by single crystal X-ray diffraction above and below the transition temperature ($T_{1/2} \approx 175$ K) [88], and it was found that the space group does not change upon the spin transition, despite the fact that a small hysteresis was observed in the spin transition function of this system [89]. The first such observation, i.e. no change of space group in a SCO compound with hysteresis in the spin transition functions $\gamma_{HS}(T)$, was reported for $[Fe(2-pic)_3]Br_2 \cdot EtOH$ (2-pic=2-aminomethyl-
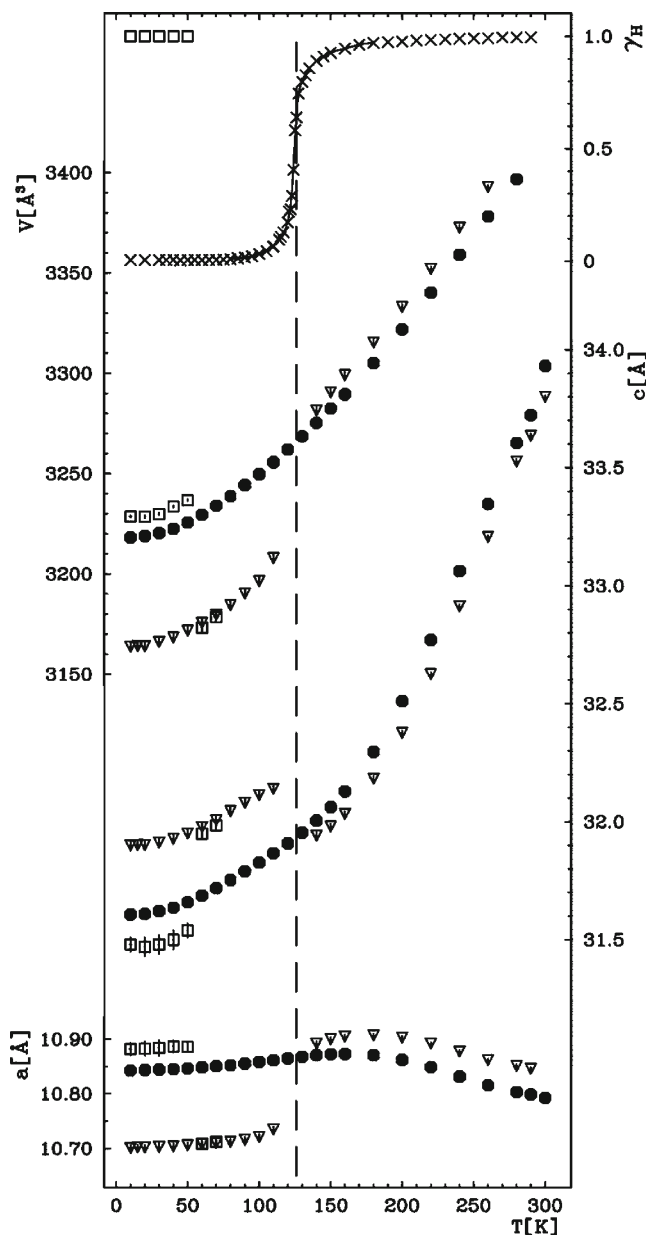
Fig. 8   The lattice parameters *a*, *c* and the unit-cell volume *V* of $[Fe(ptz)_6](BF_4)_2$ (*inverted filled triangles*) and the isomorphous zinc compound (*filled circles*) vs temperature. At high temperature and low super-cooled phase the space group is R3i. The (*open squares*) symbols indicate the measurements of the Fe crystal in the metastable HS state after LIESST. The fraction of molecules in the HS state $\gamma_{HS}(T)$ measured by optical spectroscopy is shown on top of the figure (symbol x). The *vertical dashed line* marks the spin transition temperature at $T_{1/2}=126$ K upon warming the super-cooled crystal in the R3i phase (from [92])

pyridine=2-picolylamine) [90]. A more recent example with a similar behaviour is [Fe(pmbia)$_2$(NCS)$_2$] with pmbia=N-(2-pyridylmethylene)aminobiphenyl [91]. It is evident that the observed hysteresis in these cases is only due to cooperative interactions accompanying the spin transition, as it is well known that a first order phase transition is generally accompanied by a hysteresis loop.

The [Fe(ptz)$_6$](BF$_4$)$_2$ SCO system (ptz=1-propyltetrazole) was subject to structural investigations by several research groups. L. Wiehl communicated results from structure determinations above and below the spin transition temperature of ca. 135 K [8] and assigned the space group R3i above T$_{1/2}$ and the space group P/1 below T$_{1/2}$, which seemed to be in line with the observed hysteresis of ca. 7 K width in this system [7]. In a more recent crystal structure determination, however, it has been found that the Bragg reflections began to broaden and split into two signals upon spin transition near T$_{1/2}$=135 K, which means that the structure is disordered and a space group cannot be assigned [92]. [Fe(ptz)$_6$](BF$_4$)$_2$ is the SCO system where the LIESST phenomenon (Light-Induced Excited Spin State Trapping) was first observed [93]. As the long-lived metastable HS state created by irradiation with green light at low temperatures may be sufficiently long for X-ray diffraction studies, this system was structurally investigated as a function of temperature before and after LIESST [92]. The lattice parameters of a single crystal of [Fe(ptz)$_6$](BF$_4$)$_2$ were measured between 300 and 10 K, while the crystal changed abruptly from the HS state (white) to the LS state (red) near 135 K (see Fig. 8). Using the green light (514 nm) of an argon-ion laser, the LS state was quantitatively converted to the metastable LIESST state at 10 K. Its lattice parameters were measured up to 50 K, where the LIESST state begins to decay on a minute timescale. The change of the lattice parameters can be interpreted by a superposition of a normal temperature dependence, for which the isostructural zinc compound served as a reference, and an almost temperature-independent part which is proportional to the fraction of molecules in the HS state.

Structural investigations were also helpful in exploring the nature and strength of cooperative investigations in the [Fe(ptz)$_6$](BF$_4$)$_2$ system. It was found in studies on mixed crystals of the [Fe(2-pic)$_3$]Cl$_2$·EtOH SCO system [94] that the spin transition behaviour can be strongly influenced by isomorphous metal dilution, which changes massively the cooperative interactions. This effect was later convincingly interpreted as arising from elastic interactions accompanying the spin transition in crystals [2]. The metal dilution effect was also studied in the isomorphous mixed crystals series [Fe$_x$Zn$_{1-x}$(ptz)$_6$](BF$_4$)$_2$ [26]. From powder X-ray measurements the lattice deformation (tensor ε) accompanying the spin transition was determined. For diluted mixed crystals with x<0.44 the lattice deformation was found to be directly related to the spin transition, whereas in concentrated mixed crystals with x>0.44 the above-mentioned first-order crystallographic phase transition (R3i→disordered) sets in on cooling, which is triggered by the spin transition and can be suppressed by rapid cooling. The thermal spin transition was followed with UV/VIS absorption spectroscopy on a supercooled mixed single crystal in the R3i structure. This experiment has proven that the spin transition phenomenon in the ptz complex is independent of the structural phase change, and that the latter is rather a consequence of the spin transition.

The crystal structure of the SCO complex $[Fe(mtz)_6]X_2$ (mtz=methyltetrazole; $X=BF_4^-$, ClO_4^-) was also determined by L. Wiehl [8], the space group being $P2_1/n$. It was confirmed that the iron(II) ions occupy two inequivalent lattice sites, where only one of them (site A) undergoes thermal spin transition while the other one (site B) remains in the HS state at all temperatures, as was found earlier by Mössbauer spectroscopy [13]. In a more recent structural study [95] the lattice parameters of a single crystal of $[Fe(mtz)_6](BF_4)_2$ were determined between 300 and 10 K. With green light of an argon ion laser (514 nm) the LS state in site A was quantitatively converted to the HS state, and with red light of a laser diode (820 nm) the HS state in site B was almost completely converted to the LS state. This is the first example where the thermodynamically stable HS state was converted by light to a metastable long-lived LS state (LIESST with HS→LS conversion) [13]. The lattice parameters of both metastable states were measured up to 50 K, where decay sets in on a minute timescale. The volume change of the crystal per complex molecule accompanying the spin transition is ca. 32 Å^3 at site A and, most surprisingly, nearly zero at site B. A full data set for evaluation of the crystal structure was recorded at 10 K [95].

Guionneau et al. [96] have characterized the crystal structure of the LIESST state in the classical SCO complex $[Fe(phen)_2(NCS)_2]$. The same group has structurally characterized four SCO complexes of the type $[Fe(PM-L)_2(NCS)_2]$, where PM is N-2′-pyridylmethylene and the aromatic substituent L is 4-aminophenyl, 4-(phenylazo)aniline, 4-aminobiphenyl, 4-(phenylethynyl)aniline [97]. The four chemically related complexes show quite different spin transition properties, which apparently can be rationalised on the grounds of structural differences in the combination of intrasheet and intersheet contacts in the two-dimensional lattice. One of these complexes represents another example for the rather rare observation that the spin transition takes place with a hysteresis of ca. 5 K in the $\gamma_{HS}(T)$ curve, but without change of the space group. Remarkable progress in X-ray diffraction studies under applied pressure was recently reported by Guionneau et al. [98]. Modern equipment is now available which enables one to investigate the structural changes of SCO systems as a function of temperature, pressure, and light irradiation, i.e. all applied perturbations in one experiment.

Dinuclear, trinuclear, tetranuclear and pentanuclear iron(II) SCO complexes have been synthesized (see above) and structurally characterized. In the case of polymeric SCO systems, however, it has hardly been successful to grow single crystals of sufficient quality for X-ray diffraction. In such cases EXAFS measurements have helped to unravel important structural features of the local environment [58–61, 99–101]. The polymeric chain SCO compounds with triply bridged 1,2,4-triazole ligands through the nitrogen atoms in 1,2-position and H or various alkyl, aryl or other substituents in the 4-position mostly show spin transition in the room temperature region, often with hysteresis, and are therefore potential candidates for applications. The anions and the solvent molecules, if present, are located between the chains as has been evidenced by X-ray diffraction on the related Cu(II) system [61]. It is worth mentioning that EXAFS studies have recently been performed on short-lived photo-induced states (after LIESST) in some iron(II) complexes [102, 103].

The first structures of a polymeric 3-D SCO Fe(II) triazole complex and its Cu(II) analogue were solved, $[M(4L)_3](ClO_4)_2$ (M=Fe(II), Cu(II), 4L=1,4-bis (tetrazol-1-yl)butane; nL=tz-$(CH_2)_n$-tz; several n=1–12 were studied) with a supramolecular catenane structure consisting of three interlocked 3-D networks [78,79].

3.2
Investigations Under Applied Pressure

Investigations of the influence of applied pressure on the spin transition behaviour in solid SCO compounds were carried out in the early stage of SCO research, mostly using a diamond anvil cell for (axial) pressures up to 100 kbar and employing vibrational, electronic or Mössbauer spectroscopy, often only in the room temperature region [104–108]. Kambara has interpreted the pressure influence on the grounds of ligand field theory considering a coupling of the molecular deformation of the SCO molecules with lattice strain [109]. A major breakthrough came with the work of Meissner et al. [110], who first succeeded to measure the temperature dependent Mössbauer spectra of the SCO picolylamine system under hydrostatic pressure; the results were interpreted satisfactorily in the frame of the model of elastic interactions. König et al. studied the effect of pressure on the first-order spin transition in $[Fe(phy)_2]X_2$ (phy=1,10-phenanthroline-2-carbaldehyde phenylhydrazone; X=BF_4^-, ClO_4^-) [111]. They explained the observed linear dependence of the hysteresis width on pressure on the basis of the Landau theory, and assigned the increase of the residual HS fraction to a decreasing size of the cooperative region with pressure. Adler et al. [112] studied the thermodynamics and spin state conversion processes in several SCO complexes by pressure dependent Mössbauer spectroscopy. The rate constants for the HS→LS intersystem crossing processes were determined by line shape analysis of the Mössbauer spectra. Interaction parameters and pressure-induced volume changes for systems with gradual and abrupt transitions were evaluated within the lattice expansion model of Spiering et al. [113]. The pressure-influenced spin transition was also studied in FeP_4X_2 core complexes such as the $[Fe(dppen)_2X_2]$ (X=Cl^-, Br^-; dppen=cis-1,2-bis(diphenylphosphino)ethylene) with a diamond anvil cell (axial pressure up to >100 kbar) and Mössbauer spectroscopy [114]. The difference in transition pressures is interpreted in terms of lattice cooperativity, in addition to ligand field and polarizability effects induced with increasing pressure.

In order to arrive at a deeper insight into the complex behaviour of the two-step spin transition, which was first observed in $[Fe(2-pic)_3]Cl_2 \cdot EtOH$ [115], susceptibility and Mössbauer measurements on mixed-metal complexes and under hydrostatic pressure helped decisively to explain on thermodynamical grounds within mean field theory that the two-step transition is probably due to specific short-range interactions [116]. This explanation found strong support later by heat capacity measurements [117] and Monte-Carlo calculations [118].[1]

---

[1] Very recently, Bürgi et al. (Angew. Chem. Int. Ed. 42 (2003) 3825) have reported on structural reinvestigations of this SCO system and point out that the steps is most probably due to the formation of an intermediate phase with two kinds of iron(II) lattice positions exhibiting slightly different SCO behaviour.
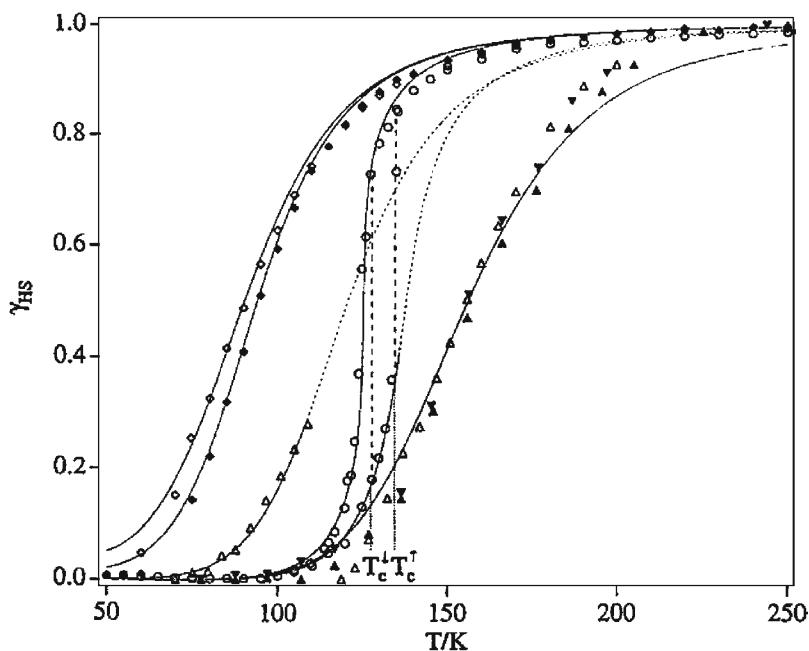
Fig. 9 Transition curves for $[Zn_{1-x}Fe_x(ptz)_6](BF_4)_2$ at 1 bar for (*open diamonds*) x=0.005 and (*filled diamonds*) x=0.1, as well as at 1 kbar for x=0.1 in the metastable high-spin-phase below 120 K (*open triangles*) and the low-spin-phase (*filled triangles – upright and inverted*). Transition curve for $[Fe(ptz)_6](BF_4)_2$ at 1 bar in the supercooled high-spin-phase as well in the low-spin-phase (*open circles*) (from [120])

The HS→LS relaxation kinetics in the highly metal-diluted system $[Fe_{0.1} Zn_{0.9} (ptz)_6](BF_4)_2$ was investigated under hydrostatic pressure and found to accelerate by one order of magnitude per kbar due to the large volume difference of 26 Å^3/molecule between the HS and LS states (see Fig. 9) [119]. The relative vertical and horizontal shifts of the potential wells of the two spin states as a function of pressure are estimated to be 130 cm^{-1}/kbar and 10^{-3} Å^3/kbar, respectively. Pressures above 250 bar were observed to induce a crystallographic phase transition even in the diluted system, resulting in a discontinuous spin transition [120]. Similar pressure effect studies were carried out with the neat $[Fe(ptz)_6](PF_6)_2$ compound, where the thermal spin transition is extremely steep because of cooperative effects of elastic origin [19]. External pressure of 1 kbar shifts the transition temperature from 74 K to 102 K. The volume difference $V_{HS} - V_{LS}$ was evaluated to be 24 Å^3/molecule, and the interaction parameter Γ, a measure of the cooperative elastic interactions [2] to be ca. 100 cm^{-1}. Surprisingly, this complex with PF_6^- anion was found to exhibit no hysteresis in contrast to the related compound with BF_4^- anion.

The pressure-induced spin state conversion was followed by near-edge X-ray absorption (XANES) spectroscopy at room temperature in a number of iron(II) SCO complexes [121, 122]. A plot of the LS fraction as a function of pressure,
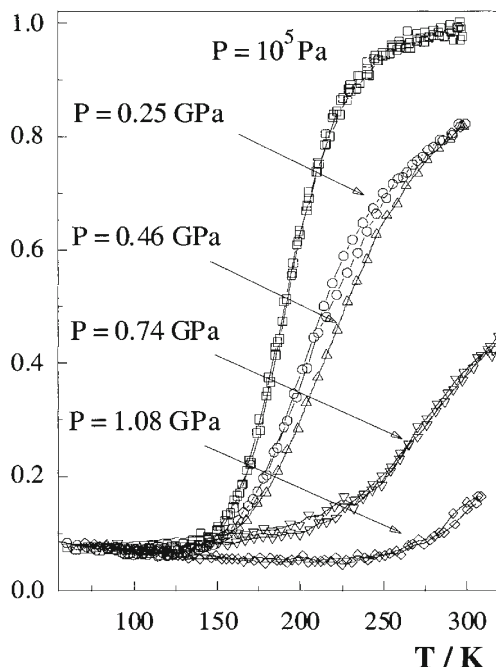
Fig. 10 Thermal spin transition in the mononuclear [Fe(PM-Aza)$_2$(NCS)$_2$] at different pressures [124]

$\gamma_{LS}(p)$ yielded characteristic critical transition pressures p_c, which were analysed with respect to spin transition temperature, entropy change, crystal structures, crystal volume change, and compressibility coefficient.

A newly developed pressure cell [123] for magnetic susceptibility measurements in vibrating sample and SQUID magnetometers down to ca. 2 K and under hydrostatic pressure up to ca. 12 kbar have enormously stimulated the investigation of SCO behaviour under pressure. It has been used, e.g. to control the pressure-induced spin state conversion in mononuclear SCO systems of iron(II) with large aromatic ligands based on 2′-pyridylmethylene-4-anilino units [124] (see Fig. 10), in antiferromagnetically coupled Fe(II) dinuclear complexes [125] (see Fig. 11), in tetranuclear grid-like complexes [126], in novel cyanide-bridged Fe(II)-Ag(I) bimetallic compounds (Hofmann type) with three dimensional interpenetrating double structure [127], and in polynuclear SCO compounds with substituted tetrazole and triazole ligands. Applying pressure to the chain compound [Fe(hyetrz)$_3$](3-nitrophenylsulfonate)$_2$ provokes a parallel shift of the spin transition curve $\gamma_{HS}(T)$ from 100 K at ambient pressure upwards near to room temperature [70], while the steep $\gamma_{HS}(T)$ curve and the hysteresis width remain unaffected (see Fig. 12). This lends support to the conclusion that the cooperative interactions in this system are confined within the iron(II) triazole chains. A similar pressure effect was observed on another SCO chain compound with a pressure-induced shift of $\gamma_{HS}(T)$ to well above room temperature
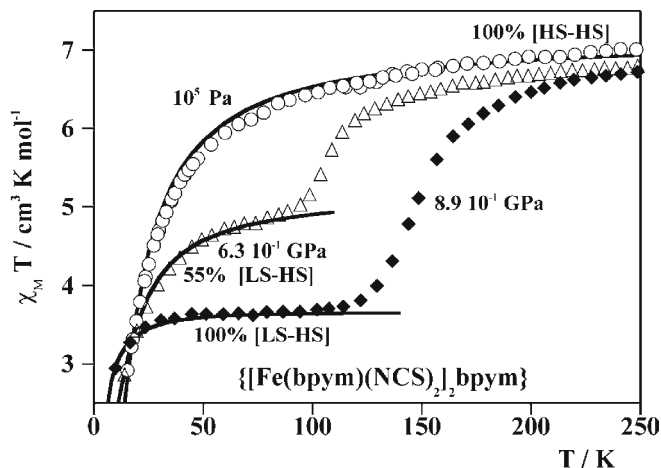
Fig. 11 Temperature dependence of $\chi_M T$ for $\{[Fe(bpym)(NCS)_2]_2(bpym)\}$ at different pressures. The *solid lines*, together with estimated concentrations of [HS-LS] and [HS-HS] species correspond to calculations using the appropriate Hamiltonian. The magnetic behaviour of $\{[Fe(bt)(NCS)_2]_2(bpym)\}$ at ambient pressure (10^5 Pa) has also been included for comparison [125]
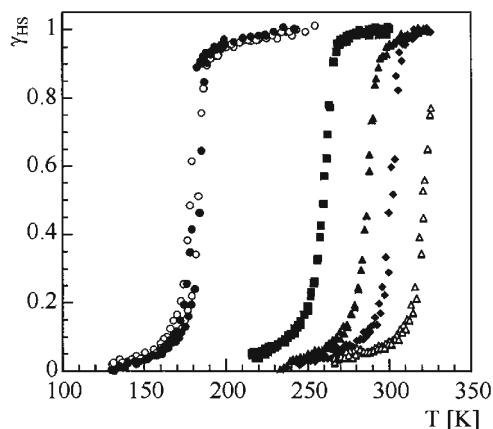
Fig. 12 γ_{HS} vs T plot for $[Fe(hyptrz)_3](4\text{-chlorophenylsulfonate})_2 \cdot H_2O$ at different pressures. (*filled circles*, P=1 bar; *filled squares*, P=4.1 kbar; *filled triangles*, P=5 kbar; *filled diamonds*, P=5.3 kbar; *open triangles*, P=5,9 kbar; *open circles*, P=1 bar after releasing the pressure) (from Garcia et al. [70])

[128]. Interestingly, the hysteresis width of this compound disappears and then reappears under pressure. A very steep HS→LS transition is observed at room temperature around ca. 6 kbar accompanied by a colour change from white to purple. Theoretical models have been developed to rationalize these pressure effects observed on SCO chain compounds [129–131].

A layered SCO compound has also recently been studied under pressure [132, 133]. Application of hydrostatic pressure up to 10 kbar on $[Fe(btr)_2(NCS)_2] \cdot H_2O$ (btr=4,4′-bis-triazole), which is known to show discontinuous ST at ca. 132 K [73], results in an unexpected stabilization of the HS state. This is surprising, as pressure normally stabilizes the LS state due to its smaller molecular volume. A pressure-induced structural phase transition is believed to cause this result. Hysteresis loops of $[Fe(btr)_2(NCS)_2] \cdot H_2O$ pure or diluted in a Ni-homologue were recorded by optical reflectivity as a function of temperature and pressure and the phase diagram in p,T-axes plotted [133]. Pressure hysteresis loops were recorded at constant temperature. The findings support the above mentioned pressure-induced structure change in the neat compound.

Far-infrared spectroscopy was employed to follow the changes of the metal-ligand vibrational modes upon pressure-induced spin transition in iron(II) tri-azole complexes [134]. Grey and Butler review the effects of high external pressures (diamond anvil cell) on the electronic spectra of coordination compounds, among them SCO systems [135].

Pressure-induced SCO was also observed in a novel mononuclear iron(III) SCO complex [136] and in a binuclear iron(III) SCO complex [137].

3.3
Magnetic Field Effects

The influence of a magnetic field on the spin transition behaviour was first reported by Qi et al. [138]. It was found that the very steep transition curve $\gamma_{HS}(T)$ in $[Fe(phen)_2(NCS)_2]$ at $T_{1/2}$=178 K (with hysteresis width of <0.5 K) is shifted by only –0.10(4) K in a magnetic field of 5.5 T, well in accordance with theory. Bousseksou et al. [139] recently repeated the experiment in a large pulsed magnetic field of 32 T, corresponding to an expected temperature shift of 2.0 K at $T_{1/2}$. The HS fraction was determined by optical reflectivity (see Fig. 13). The hysteresis shows a complex response of the HS fraction with time (rise time of the field was 75 ms, the decay time 0.5 s). An increase of the HS fraction is observed with an irreversible (reversible) character in the ascending (descending) branch of the hysteresis loop. The time dependence of the HS fraction provides information on the kinetics of the SCO process. Similar experiments accompanying the magnetic field effect on other SCO complexes of iron(II) have been reported [140].

Bousseksou et al. [141] have also studied the influence of a pulsed intense magnetic field (32 T) on a Co(II) SCO system. At a certain position of the ascending branch of the thermal hysteresis loop, a magnetic field pulse of 32 T induces an irreversible and nearly complete jump from S=1/2 (LS) to S=3/2 (HS). $T_{1/2}$ was shifted downwards by 4.9 K. This field-induced SCO was explained with an Ising-like two-level model. A most recent study deals with the magnetic field effect on the cooperative photo-induced spin state conversion (LIESST) process [142, 143]. The thermal spin transition was shifted downwards by only 0.2 K upon increasing the field to 7 T in agreement with the above described findings. The photo-conversion efficiency from LS to HS state, however, increased by a factor of 7.1, and the relaxation time of the LIESST state decay increased by a factor of 1.5. The
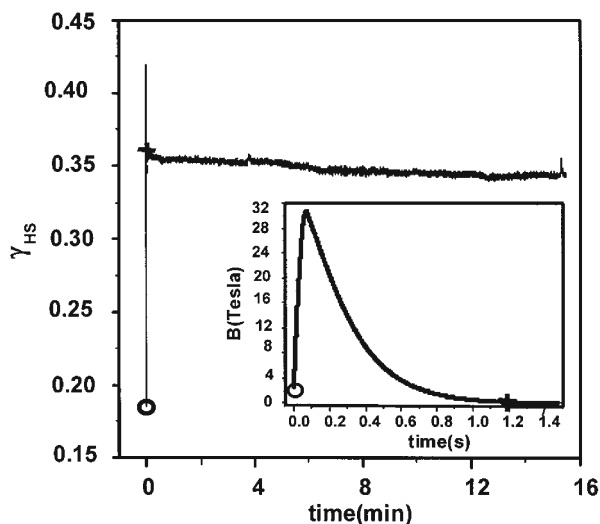
Fig. 13 A typical pulsed field experiment, showing the irreversible jump of the HS fraction (*top curve*) of [Fe(phen)$_2$(NCS)$_2$]. An *open circle* and a *cross* show the initial and the final states, respectively (from Bousseksou et al. [141])

results were interpreted in terms of a tunnelling relaxation model which includes the effect of correlations and the magnetic field influence.

The influence of an external magnetic field has also been studied on SCO complexes of Co(III) [144] and Mn(III) [145].

An elegant method has been developed for direct monitoring the spin state in dinuclear iron(II) complexes by Mössbauer spectroscopy in applied magnetic field [146]. The method enables one to distinguish between HS-HS, HS-LS and LS-LS dinuclear iron(II) pairs, which is not possible with susceptibility measurements or any other technique employed in SCO research (see Fig. 14).

3.4
Spectroscopy with Synchrotron Radiation

It has already been pointed out above that the use of synchrotron radiation has proven to be very helpful to detect local structural changes, particularly changes of metal-ligand bond lengths, in SCO systems where single crystals for X-ray diffraction are not available. EXAFS and XANES are well established techniques; many examples of their successful application in SCO research and relevant references are given above (sect. 3.1).

New possibilities of application of synchrotron radiation have been opened with the development of the techniques of nuclear resonant scattering of synchrotron radiation (NRS). The nuclear forward scattering (NFS) technique has proven to be a powerful tool to probe hyperfine interactions; it complements conventional Mössbauer spectroscopy where the latter reaches its limits (very small samples with very small content of resonating nuclei). NFS measurements have
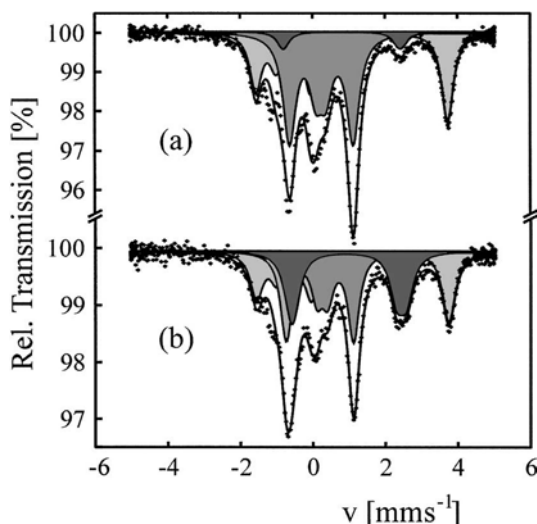
Fig. 14 ^{57}Fe Mössbauer spectra of {[Fe(bpym)(NCS)$_2$]$_2$bpym} recorded at 4.2 K in a magnetic field of 50 kOe: **a** before, **b** after light irradiation. LS in HS-LS and LS-LS pairs (*grey*), HS in HS-LS pairs (*light grey*), HS in HS-HS pairs (*dark grey*) (from [146])

been carried out on iron(II) SCO complexes with remarkable success [147]. The so-called quantum beat structures are entirely different in the HS and LS states due to the different quadrupolar interactions, and this enables one to analyse the SCO behaviour as a function of various perturbations. Another advantage of NFS over conventional Mössbauer spectroscopy is that the so-called Lamb-Mössbauer factor, whose knowledge is necessary for accurate determination of the molar fractions of the HS and LS species, can be evaluated with higher precision. Another method based on NRS is "nuclear inelastic scattering" of synchrotron radiation (NIS). This technique has developed to an astonishingly powerful method for probing the local vibrational properties and their changes, e.g. upon spin transition [148]. In combination with density-functional calculations (B3LYP), individual molecular vibrational modes could be identified unambiguously in an iron(II) SCO complex and in a nitroprusside complex [149]. For the first time the angular-resolved iron partial density of states (PDOS) was extracted from NIS spectra (see Fig. 15) [150].

The PDOS corroborates a vibrational entropy difference as the driving force of the spin transition. In a recent characterisation of an iron(II) SCO complex employing EXAFS, NFS, NIS, Mössbauer and SQUID measurements and DFT methods, Paulsen et al. [151] have demonstrated the strength of a combined application of these modern techniques in SCO research.

X-Ray emission spectroscopy (XES) with synchrotron radiation has proven to be suited to distinguish between LS and HS states in SCO compounds of Fe^{3+}, Fe^{2+} and Co^{2+} [152]. XES is based on K_α and K_β (3p to 1 s transition) X-ray emission after 1 s core ionisation of the metal ions. The K_β spectra, which reflect the variation of the spin states of different transition metal ions of well-defined *3d* con-
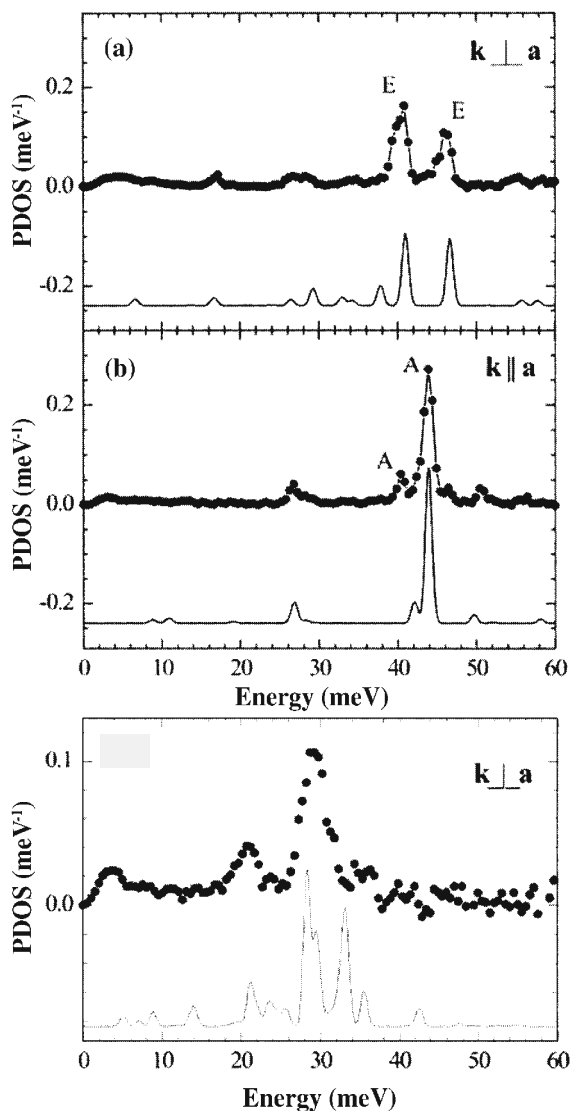
Fig. 15a,b Experimental (*filled circles*) partial density of vibrational states (PDOS) of a single crystalline spin crossover compound (upper) at *T*=30 K for: **a** *k*⊥*a*; **b** *k*||*a* and (*lower*) at room temperature. The wavevector of the photons that excite the molecular vibrations is denoted by *k* whereas *a* denotes the crystallographic axis that coincides with the threefold symmetry axis of the complexes. For better comparison the PDOS calculated with a density functional method (*solid lines*) is shifted and reduced in height by a factor of 2 (from Paulsen et al. [150])

figurations, with preserved chemical environment and valence state, can be regarded as benchmark measurements in studying magnetism with XES. The emitted X-rays can also be used to measure the X-ray absorption spectra in the fluorescence mode. However, a higher resolution can be achieved if a single feature of the emission spectrum is used for the detection. This technique, called partial fluorescence yield XANES spectroscopy (PFY-XANES), were also applied to follow the spin transition phenomenon [152]. The detection of the K_α, K_β and valence emission features were compared and surprisingly, besides the higher count rate, the first gave the better energy resolution. XES and PFY-XANES are new techniques which bear the potential to stimulate further research in the field of molecular magnetism.

3.5
Metal-Centred Light Effects

3.5.1
LIESST and Reverse LIESST

The phenomena of LIESST (Light-Induced Excited Spin State Trapping) and reverse LIESST are well reviewed in the literature [2, 5, 86]. The occurrence of LIESST in the SCO compound [Fe(pic)(3)]Cl·2.EtOH (pic=2-picolylamine) was reported long ago [153]. Quite recently, the question regarding the quantum efficiency of this photoconversion process and its possible dependence on irradiation intensity [154, 155] gave rise to some controversy [156]. New experimental results demonstrate convincingly that the quantum efficiency of the photoconversion at 11 K is on the order of unity, with no noticeable dependence on irradiation intensity. It does, however, depend to some extent on the fraction of complexes already converted to the high-spin state [156].

An interesting interplay between the thermal spin crossover phenomenon and antiferromagnetic coupling found in dinuclear iron(II) complexes with bipyrimidine bridges [50, 51] has been explored in more detail by Mössbauer spectroscopy in applied magnetic field and making use of the LIESST effect. If the ligand field strength is relatively weak, both iron(II) centres may be in the HS state and antiferromagnetic coupling through the bpym bridge is present down to very low temperatures. At sufficiently strong ligand field strength one or even both iron centres may undergo spin crossover and reach a singlet-singlet (SS) ground state at low temperature. The total spin for the molecule then is S=0. The LIESST effect generated the metastable excited quintet-quintet (QQ) state. Because the iron atoms in the high-spin state are again antiferromagnetically coupled, this QQ excited state yields another S=0 singlet spin state quite different in nature [157]. At high temperature the system relaxes back first to a plateau with a finite HS fraction of QS dimers and at higher temperatures to the SS ground state. Using Mössbauer spectroscopy with the sample in applied magnetic field together with LIESST excitation a detailed picture about the coexistence of all types of dimer pairs SS, SQ, QQ have been evaluated [146]. A theoretical model was proposed which describes the synergistic effect of intramolecular interactions favouring the formation of SQ states [51].

LIESST experiments have almost routinely been performed with many newly synthesized SCO compounds, with special emphasis mainly on the LIESST state relaxation kinetics. One primary objective is to increase the LIESST decay temperature, and the hope is to observe LIESST or related phenomena in the room temperature region for special applications in optical devices. Another objective is the study of the relaxation behaviour; more or less strong deviation from single-experimental behaviour of the decay curves $\gamma_{HS}(T,t)$ reflects the importance of cooperative interactions [2, 86]. A brief survey of remarkable LIESST experiments is as follows. The occurrence of LIESST is not restricted to neat solid SCO compounds. It was reported to take place in polymer matrices like polyvinyl alcohol [158, 159], polyvinyl acetate [159], embedded in a Nafion foil [159, 160] and in pellets of KBr [158, 161], CsI and TlBr [161]. Létard et al. have reported on the observation of LIESST in a Langmuir-Blodgett film [162]. While in most LIESST experiments with iron(II) SCO compounds the LS ground state is excited with green light to a metastable long-lived HS state, like in the first observation of this phenomenon by Decurtins et al. [93], examples of LIESST with red light converting a HS ground state to a metastable LS state were also reported [13, 14, 16]; it occurs, e.g. in the iron(II) tetrazole complexes $[Fe(mtz)_6](BF_4)_2$ and $[Fe(etz)_6]$ $(BF_4)_2$ (mtz=1N-methyl-tetrazole, etz=1N-ethyl-tetrazole) with inequivalent lattice sites A and B for iron(II), where Fe(II) ions in sites A undergo spin transition, but in sites B the Fe(II) ions remain in the HS state even at low temperatures. LIESST (LS→HS)$_A$ with green light is observed in A sites, LIESST (HS→LS)$_B$ with red light in B sites. The latter process was also observed on mixed-crystals of $[Fe_xZn_{1-x}(mtz)_6](ClO_4)_2$ [17]. In another mixed-crystal system with mtz ligands $[Fe_{0.35}Ni_{0.65}(mtz)_6](ClO_4)_2$ unusually slow LIESST state relaxation HS→LS was measured even above liquid nitrogen temperatures, which was ascribed to structural changes induced by irradiation [18]. Thermal hysteresis in the LIESST regime was observed on the SCO system $[Fe(etz)_6](BF_4)_2$ [16] and interpreted in terms of strong cooperative effects of elastic origin which cause characteristic deviations of the relaxation from first-order kinetics (self-acceleration) on B site ions.

Measurements of the HS→LS relaxation in $[Fe(ptz)_6](BF_4)_2$ under external pressure have shown that pressure of 1 kbar accelerates the HS→LS relaxation by one order of magnitude [19]. Cooperative phenomena and light-induced bistability in iron(II) SCO compounds is very well reviewed by Hauser et al. [163]. LIESST state relaxation has been compared with HS→LS relaxation after thermal spin state trapping by rapidly cooling the sample. In the system $[Fe(bpp)_2](BF_4)_2$ (bpp=2,6-bis(pyrazol-3'-yl)pyridine) strong deviations from first-order kinetics were monitored for the HS→LS relaxation, regardless of the origin of the metastable HS states. This system was the first SCO complex in which long-lived metastable HS states could be generated by LIESST at temperatures well above that of liquid nitrogen [164]. Changing the anion from BF_4^- to $CF_3SO_3^-$ in this system leads to differences in the mechanism which were ascribed to the different dynamics of a phase transition compared to the decay kinetics of the LIESST state [165]. Létard et al. have proposed a method of characterizing SCO compounds exhibiting LIESST by a critical LIESST temperature, T_c(LIESST), the temperature for which the light-induced HS state signal disappears in the SQUID

cavity, and correlated this temperature with the thermal spin transition temperature $T_{1/2}$ [166, 167]. An unusually high T_c(LIESST) above 130 K was reported by Hayami et al. [168].

Sophisticated equipment for single crystal diffraction experiments which is now available has enabled to carry out structural studies at temperatures close to that of liquid helium before and after LIESST [92, 95, 169].

Although by far most of the known "LIESST"-active SCO compounds have an $Fe^{II}N_6$ core, the phenomenon has also been communicated for SCO complexes of Fe(II) with phosphine ligands, viz [Fe(dppen)$_2$X$_2$]·2S, where dppen=cis-1,2-bis(diphenylphosphino)ethylene and X=Cl$^-$, Br$^-$ and S=CHCl$_3$, CH$_2$Cl$_2$ [170]. Interestingly, the HS→LS relaxation after LIESST is relatively slow, compared to $Fe^{II}N_6$ complexes under similar conditions, which has been ascribed to the relatively large change in Fe–P bond lengths accompanying the HS→LS transition.

It has been explained by Hauser [171] that the best candidates for LIESST are SCO compounds of iron(II). The reason is that the change in metal-donor atom distance between the HS and LS states, Δr(Fe-L), which is the most important factor determining the lifetime of the metastable LIESST state, is highest in the case of iron(II) SCO compounds, due to the fact that two electrons move from the antibonding e_g^* orbitals in the HS state to the weakly bonding t_{2g} orbitals in the LS state. This rearrangement of the electronic structure causes changes of metal-donor atom distances of ca. 10% in Fe(II) SCO compounds, but smaller changes in the iron(III) and even smaller ones in cobalt(II) SCO complexes. And yet, Juhasz et al. [172] have reported that LIESST is possible in iron(III) SCO complexes.

3.5.2
Strong-Field LIESST (SF-LIESST)

Octahedral strong-field complexes of iron(II) are in the LS state at all temperatures. They usually relax very fast after light excitation, with rates of the order of nanoseconds, from the excited HS state back to the LS state as expected within the frame of the inverse energy gap law [2]. A typical example is [Fe(tpy)$_2$]$^{2+}$ (tpy=2,2′:6′,2″-terpyridine). This LS compound decays at a rate of 4.59×10^{-7} s^{-1} as was recently found in MeOH at 295 K [173]. Mössbauer spectroscopy of the solid compound after green light irradiation at 10 K yields only Fe(II) in the LS ground state, as expected according to the inverse energy gap law. The mixed crystal system [Fe$_x$Mn$_{1-x}$(tpy)$_2$]$^{2+}$ (x<0.1), however, converts under irradiation with green light (514 nm, argon-ion laser) to a metastable HS state with a lifetime of more than several days below 20 K, which is more than ten orders of magnitude longer than predicted within the frame of the inverse energy gap law. This observation is not in agreement with LIESST effect studies; we have denoted it as *strong-field light-induced excited spin state trapping (SF-LIESST)* [174]. The reason for the unusually long lifetime of the metastable HS state in this strong field system is not known. A plausible explanation could be that the immediate environment of the iron(II) ions is somewhat altered by light irradiation leading to a weaker ligand field strength, the lifetime of which determines the relaxation rate of the light-induced HS state.

3.5.3
Light-Induced Thermal and Optical Hysteresis (LITH/LIOH)

A new effect was discovered by permanently irradiating a spin crossover compound in the LS state [91, 175]. The effect was called LITH (Light-Induced Thermal Hysteresis). The compounds show bistability. At constant intensity a hysteresis vs temperature (LITH) and at constant temperature a hysteresis vs intensity of the radiation, called LIOH (Light-Induced Optical Hysteresis), is observed. Both effects have been evidenced by magnetic and reflectivity measurements. The experimental data can be interpreted in mean approximation with a master equation including a non-linear relaxation term [175].

3.5.4
Light-Perturbed Thermal and Optical Hysteresis (LiPTH, LiPOH)

Another unusual effect was observed for the Fe(II) compound $[Fe(phy)_2](BF_4)_2$ (phy=1,10-phenanthroline-2-carbaldehyde phenylhydrazone) which shows spin crossover behaviour with a thermal hysteresis between 270 K and 280 K. Continuous irradiation with green light shifts the hysteresis curves to lower temperatures. Red light shifts towards higher temperatures, but less significantly [176]. The thermal hysteresis with and without light irradiation was observed by Mössbauer spectroscopy. The mechanism of the green and red light shifts can be understood on the basis of LIESST and reverse LIESST mechanisms [2] with the master equation extended by a term accounting for the thermal activation probability. The effect has been named Light-Perturbed Thermal Hysteresis (LiPTH) and reverse LiPTH. At constant temperature a hysteresis versus intensity of the radiation called LiPOH (Light-Perturbed Optical Hysteresis) and reverse LiPOH is observed [177]. However, the nature of the excited state is not yet clear as its lifetime is much longer than observed at temperatures well below the transition region. For the molecular LIESST effect the lifetime at this temperature of the hysteresis transition is expected to be much shorter than milliseconds evaluated from the LiPTH effect. While the LIESST and LITH effects are observed at lower temperatures, the LiPTH effect may occur below and above room temperature. This eventually may lead to optical switching around room temperature.

3.5.5
Nuclear Decay Induced Excited Spin State Trapping (NIESST)

The nuclear decay of radioactive atoms embedded in a compound is known to lead to various chemical and physical "after effects" such as redox processes, bond rupture, formation of metastable states and others. One of the most elegant ways of investigating such after effects in solid compounds exploits the Mössbauer effect and has been termed "Mössbauer Emission Spectroscopy" (MES) or Mössbauer source experiments. For instance, the electron capture (EC) decay of ^{57}Co into ^{57}Fe, denoted $^{57}Co(EC)^{57}Fe$, in cobalt or iron compounds has been widely explored. Usually the ^{57}Co labelled compound is used as the Mössbauer source vs a single-line absorber material such as $K_4[Fe(CN)_6]$. The recorded spectrum yields information on the chemical state of the nucleogenic ^{57}Fe at ca. 10^{-7} s,

which is approximately the lifetime of the 14.4 keV level of ^{57}Fe, after nuclear decay of ^{57}Co.

Using this technique the temperature dependent Mössbauer emission spectra of ^{57}Co labelled cobalt(II) and iron(II) coordination compounds with strong, intermediate, and weak ligand fields have been examined. Among the most interesting results are the formation of metastable HS states of ^{57}Fe(II) in strong and intermediate ligand fields. Many examples are described in a recent review article [178]. The essential information from these Mössbauer source experiments is that, at a given temperature, the probability of "trapping" the HS state of the nucleogenic ^{57}Fe(II) within the ^{57}Fe Mössbauer time window is significantly greater in a SCO compound with intermediate field strength than in strong field compounds. The discovery of the LIESST phenomenon (generating and trapping of metastable HS states by irradiation with an external light source) has enabled us to understand the mechanism of the "Nuclear Decay Induced Excited Spin State Trapping (NIESST)", where the nuclear decay process ^{57}Co(EC)^{57}Fe may be regarded as an "internal" molecular excitation source.

3.6
Ligand-Centred Light Effects

3.6.1
Ligand-Driven Light-Induced Spin Change (LD-LISC)

Roux et al. [179] have reported a new method to obtain ligand-driven light-induced spin changes (LD-LISC) in transition metal compounds. This method is based on the utilization of photo-sensitive ligands, such as *cis-trans* photo-isomerizable ligands. The ligand photo-isomerization can spontaneously alter the ligand field strength and induce a spin state conversion at the metal centre. The system where this LD-LISC effect was first observed is [Fe^{II}L$_4$(NCS)$_2$] with L=*cis, trans* 4-styrylpyridine (see Fig. 16) [179]. The method has been explored further by Boillot et al. on similar complexes embedded in a cellulose acetate matrix [180] and more recently on a photo-isomerisable system which exhibits the LD-LISC effect even at room temperature [181]. LD-LISC has not yet been
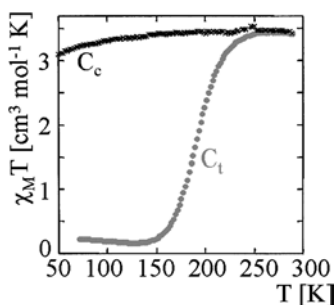
Fig. 16 Temperature dependence of $\chi_M T$ for the *trans* C$_t$ and the *cis* C$_c$ forms of [Fe(stpy)$_4$(NCBPh$_3$)$_2$] (from [180])

observed in crystalline compounds because of the unfavourable mechanical strain going along with the *cis/trans*-isomerisation.

However, with the amphiphilic complexes [FeL$_2$(NCS)$_2$] (L=2,2′-bipyridine substituted in positions 4 and 4′ by a *cis/trans* photo-isomerisable group and a long aliphatic chain) [182] thermal spin crossover [182] as well as the LD-LISC process [183] have been demonstrated to occur in a Langmuir-Blodgett film.

3.6.2
Ring Open/Close Switching

Photochromic and electrochemical changes may be effected by photo-induced interconversion between bond-open and -closed forms in extended dithienylethene compounds [184], sexithiophenes [185], as well as in thiophene oligomers [186]. Incorporation of a photochromic moiety in a mixed-valent complex allows switching "On" and "Off" an intervalence electron transfer [187].

Irie et al. have reported on the reversible photo-switching of the intra-molecular magnetism of the two nitronyl nitroxides placed at the extremities of a photochromic diarylethene molecule [188, 189]. Such spin couplers could be replaced by SCO molecules yielding the possibilities to observe light-induced switching of spin states similar to the LD-LISC phenomenon [190].

4
Theoretical Treatment of Spin Transition Phenomena

4.1
General Remarks

The experimentally determined spin transition curves, usually the fraction of HS molecules as a function of temperature, $\gamma_{HS}(T)$, may have different shapes in solid state, whereas in solutions it always follows a gradual Boltzmann distribution function. Thermal populations of all electronic levels of the HS and LS state are also considered for solids, but there must be extra features playing a decisive role in the spin transition mechanism which are responsible for the occurrence of different types of $\gamma_{HS}(T)$ curves, e.g. gradual, abrupt, with hysteresis, stepwise, incomplete [2, 5]. To understand the nature of such extra features and to incorporate their importance in physically meaningful theoretical approaches has been one of the main goals since the very beginning of SCO research.

The importance of differences in the molecular vibrational frequencies of the HS and LS states has been recognized already by Ewald et al. [191] and König et al. [192, 193]. These authors have also pointed out that differences in the molecular volumes of the HS and LS states are expected to play an important role in the spin transition mechanism.

Considering such "local properties" only, which in fact makes no distinction in the treatment of spin transition in solution and in a solid, respectively, led to no satisfactory agreement between measured and calculated magnetic moments as a function of temperature. A significant breakthrough, however, came with the recognition that the SCO complex molecules may "communicate" with each other

during the spin transition in the solid state by virtue of the above-mentioned molecular properties, thereby setting up cooperative interactions, which are not present in solutions.

Various models have been developed to describe spin transition phenomena in solid compounds, e.g. the models of Chesnut [194], Wajnflasz [195], Drickamer and Slichter [196], Bari and Sivardiere [197], Zimmermann and König [198], Sorai and Seki [199], Kambara [200], and the "Mainz model" of lattice expansion and elastic interactions developed by Spiering [23–25]. Most of these models are discussed in recent reviews [5, 201]. It is by now commonly agreed upon that any attempt to treat solid state spin transition phenomena theoretically, particularly those with significant deviations from Boltzmann like transition curves, must include short- and long-range cooperative interactions.

4.2
Mainz Model of Cooperative Elastic Interactions

The model which, at the present stage of SCO research, perhaps describes best the mechanical cooperative interactions during the spin transition in solids is the one developed by Spiering. The basic feature of this model is that the essential contribution to the interaction between the spin changing molecules is of elastic origin. The change of size and shape accompanying the spin transition causes strain in the crystal resulting in elastic energy which contributes to the interaction energy. This mechanism was worked out in the approximation of a homogeneous elastic medium for the crystal and point defects describing the misfit of the SCO molecules to the lattice. Taking the data of the lattice deformation due to the LS–HS transition from X-ray diffraction and the elastic constants from Brillouin scattering data an interaction constant could be calculated in mean field theory, which is in satisfactory agreement with the interaction constant derived from experimental spin transition curves [26, 202]. As elastic interaction is of long range nature, mean field theory can be considered a good approximation. From the range of elastic constants typical for the material of spin crossover compounds and the deformations observed in X-ray crystallography an expected range of interaction constants can be estimated and in turn a range of transition temperatures and hysteresis widths to be met in spin crossover compounds [26, 203]. One of the new one-dimensional compounds, $[Fe(Htrz)_2(trz)](BF_4)_2$, however, showed a hysteresis of 50 K still at a very high temperature of T_t=370 K, which is much too large to be interpreted by long range elastic interactions. The one-dimensional structure with strong bonding between the molecules inside the chains and weak bonding between chains requires a different interaction scheme. Fortunately, the scheme of long range interaction treated by the mean field approximation and strong nearest neighbour interaction has an analytical solution, so that chain compounds are good candidates for the study of the interplay of short range and long range interactions between the spin changing molecules [130]. The width, shape, and position of the hysteresis loop depend on the balance between long and short range interactions. An interesting result is that the hysteresis width reaches a maximum determined by long range interactions only when short range interaction energies are much larger than thermal
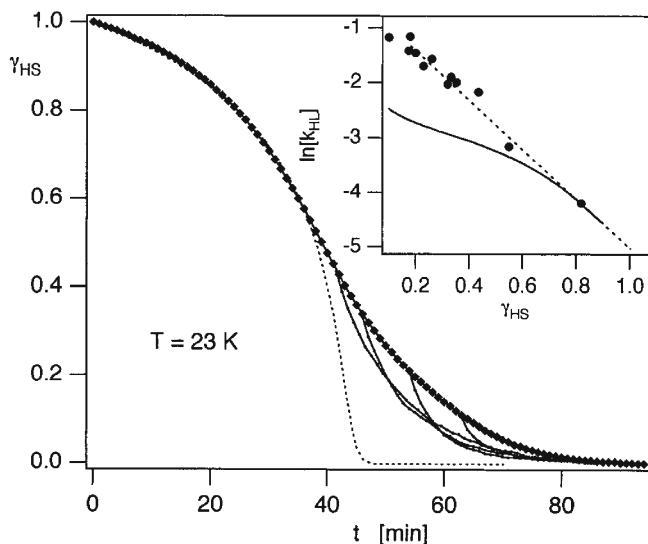
Fig. 17 The high-spin→low-spin relaxation in [Fe(pic)$_3$]Cl$_2$·EtOH at T=23 K: full relaxation curve following a quantitative light-induced conversion to the high-spin state, (*filled diamonds*) experimental, (*dashed line*) mean-field prediction (*filled circles*) relaxation curves following partial conversion. *Insert*: $ln[k_{HL}]$ (k$_{HL}$ in min^{-1}) plotted as a function of the low-spin fraction: (*continuous line*) from the full relaxation curve, (*dashed line*) mean field prediction, (*filled circle*) from the initial rate constants following partial conversion (from [207])

energy at temperatures above T$_{1/2}$. This situation is met for the compound [Fe(Htrz)$_2$(trz)](BF$_4$)$_2$ [204].

After the discovery of the so-called two-step transitions it became obvious that short range interactions and therefore correlations are not negligible [2]. The first anomalous transition of this kind was observed on [Fe(2-pic)$_3$]Cl$_2$·EtOH (2-pic=2-picolylamine) [115], where the transition curve γ$_{HS}$(T) exhibits a plateau near the transition temperature T$_{1/2}$. For systems with equivalent lattice sites of the SCO molecules like in this compound it is not possible to reproduce the plateau in mean field theory. Short range interactions must be taken into account explicitly in addition to long range interactions. The transition behaviour of the neat iron compound and the influences of the metal dilution with the corresponding Zn compound and of application of pressure have been studied in great detail; the γ$_{HS}$(T) curves have been well reproduced with the Monte Carlo method with an Ising-like Hamiltonian considering specifically infinite range and short range interactions [118, 205]. A similar treatment was employed to interpret the dynamical behaviour of SCO systems and the relaxation kinetics after LIESST in the low temperature tunnelling regime [204, 206]. The existence and importance of correlations has been demonstrated by Hauser et al. [207] in a most remarkable HS→LS relaxation study where the behaviour of time-shifted relaxation curves in the picolylamine complex was investigated (see Fig. 17). The results show that the relaxation rate depends on the LS fraction in the crystal which is unambiguous evidence for the formation of correlations. The role of

long-range interactions in photo-induced spin state transitions has been treated theoretically by Koshino and Ogawa [208].

4.3
On the Importance of Molecular Vibrations

It is well known that the driving force of the spin transition is the entropy gain on going from the LS state to the HS state [2]. The observed increase evaluated
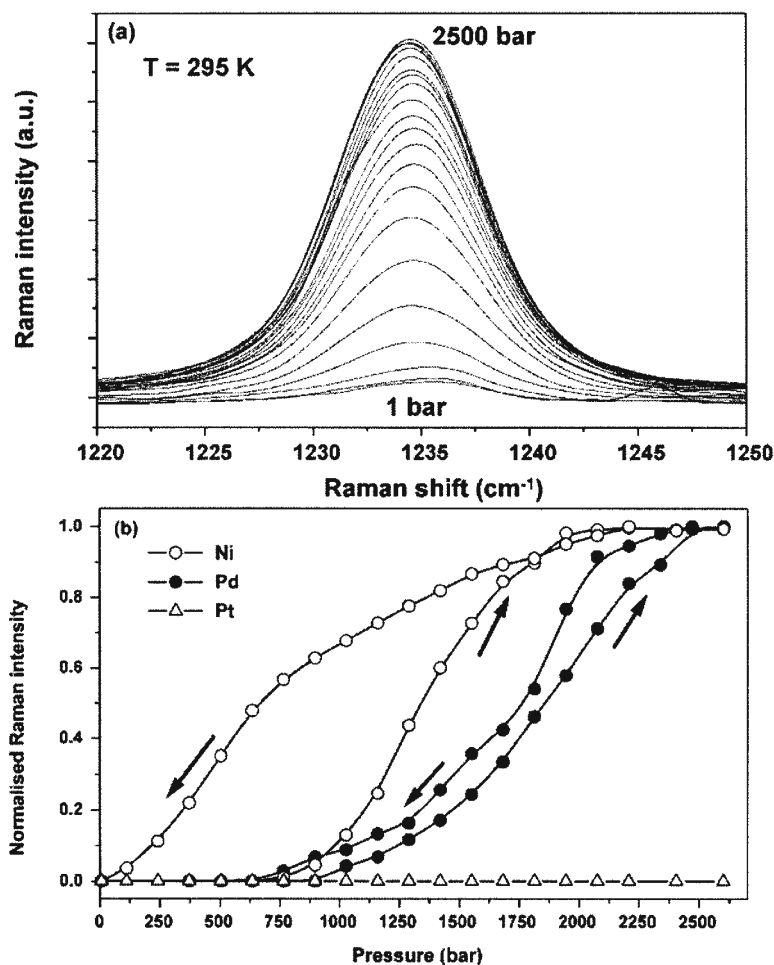
Fig. 18 Influence of pressure on the Raman spectra of SCO coordination polymers, Fe(pyrazine)[M(CN)$_4$]·2H$_2$O (M=Ni, Pd, Pt) [210]: pressure dependence over the range 1–2500 bar of the LS pyrazine mode at 1235 cm^{-1} for the polymer with M=Ni; intensity of the 675 cm^{-1} LS marker band as a function of pressure for the polymers with M=Ni, Pd, Pt. *Arrows* indicate increase and subsequent decrease of pressure. *Lines* connecting the data points are a guide to the eye (from [210])

from thermodynamic data, however, turned out to be much larger than expected from the change of spin multiplicity [199, 209]. The main contribution was recognized to be caused by the difference of vibrational energies of the molecules in different spin states. Simple considerations of the entropy change of a six-fold coordinated iron atom, however, required unreasonable differences in frequencies as compared to LS and HS compounds which do not change spin.

This gap of understanding could be closed by experimental data from infrared spectroscopy [199], classical Raman (see Fig. 18) [210] and resonance Raman spectroscopy [211–213] and especially nuclear inelastic scattering (NIS) of synchrotron radiation [148–151]. Nuclear inelastic scattering at the iron centres has the advantage of being sensitive specifically to local vibrations of the iron site. One obtains a so-called partial density of phonon states (PDOS). When comparing the data with the results from density functional theory (DFT), the Fe-N stretching vibrations of both low spin and high spin phases could be unambiguously identified. Taking into account all frequencies of the molecules from DFT calculations, the obtained differences in entropy between HS and LS molecular states agree well with those determined from thermodynamical data [151].

Bousseksou et al. [214] have reported a simple Ising-like model for spin transitions including molecular vibrations. The same research group has communicated examples where spin transition appears to be monitored by molecular vibrations [215, 216]. Klokishner et al. [217] have presented a model of non-radiative relaxation in spin crossover molecules with particular emphasis on electron-vibrational interaction. Analytical expressions are derived for the multi-phonon decay rate. The vibrational frequency effects is shown to arise from the quadratic term of this interaction. The role of molecular vibrations have also been considered in the thermodynamical treatment of SCO in both liquid and solid state by Koudriavtsev and Linert [218–220]. Boca et al. have recently published a theoretical analysis of a series of SCO complexes of iron(II), where they have used a model with an explicit vibrational partition function to describe the experimental heat capacity data [221].

5
Conclusion

Research on spin crossover phenomena has intensified enormously during the past decade, and the publication rate has increased exponentially. Undoubtedly, the most efficient boost commenced in 1998 with the installation of the European TMR network on "Thermal and Optical Switching of Molecular Spin States (TOSS)" financed by the European Community. Most of the objectives set out in the four-year TOSS program have been reached. More than 100 new spin crossover compounds have been synthesized and in many cases structurally characterized, they may be categorized in the following way:

– Chains of 4-substituted 1,2,4-triazole bridged iron(II) complexes showing SCO in the room temperature region. Nearly all show hysteresis, whose width and position on the temperature scale depend on the ligand substituent and the nature of the non-coordinating anion and solvent molecules. The length of the

4-substituents controls the spin transition behaviour, e.g. the hysteresis width decreases and becomes less steep with increasing alkyl substituent. Moreover, weakening of the cooperativity mainly arises from a diminution of the length of the polymeric chains with increasing alkyl substituent on the triazole. These SCO materials seem to be very suitable for optical devices and temperature threshold indicators [55, 62, 222, 223].

– 2-D and 3-D SCO complexes with bridging triazoles exhibiting hysteresis and two-step-transition due to lattice site inequivalency [77].

– Mononuclear *N*-alkyl tetrazole complexes with different iron(II) lattice positions exhibiting different SCO behaviour and photophysical properties. LIESST [11] and reverse-LIESST can be achieved individually in the different lattice positions [95].

– Polynuclear α,β- and α,ω-tetrazol-1-yl-alkane complexes: formation of 1-D chain-type and threefold interpenetrating 3-D coordination polymers [57, 58, 78–80].

– Supramolecular grid- and catenane-like SCO systems, e.g. tetranuclear iron(II) grids with ligands derived from terpyridine show successive thermal, light- and pressure-induced spin transition, a potential candidate for multiple switching devices [126].

– Dinuclear iron(II) complexes with bipyrimidine bridges featuring a fascinating interplay between antiferromagnetic coupling and thermal SCO. Chemical modification as well as external pressure alters the local ligand field strength and controls this interplay [50, 51, 125, 146, 224].

– Cyanide-bridged "Hofmann" type complexes of iron(II) with 3-D structure showing thermal SCO, which seem to be particularly suited for the study of co-operative interactions in 3-D systems, as the bridging hetero transition metal ion can be exchanged in a broad range, thereby affecting the cooperative interactions in the layered iron(II) ions [83, 84, 127].

– Polypyridyl SCO complexes of iron(II) synthesized from building blocks containing SCO centres. The SCO relaxation kinetics, the slowest one observed so far in solution, depends on a geometrical rearrangement of the pendant pyridyl arms.

– New photo-switchable "Irie" type complexes of iron(II) featuring a thermal open/close bond switching behaviour [188, 189].

– Iron(II) complexes with stilbenoid ligands sensitive to light-induced *cis/trans* isomerization. Such complexes show the LD-LISC effect (Ligand-Driven Light-Induced Spin Change) even at room temperature, but only in solution due to unfavourable mechanical strain in solids [179, 181].

– Iron(II) SCO complexes with large aromatic ligands based on 2′-pyridyl-methylene-4-anilino units with strong π-π stacking connections. The SCO behaviour is very sensitive to pressure, which makes the material suitable for pressure sensors [124].

– Substituted phenanthroline with long alkyl substituents proved to be appropriate as ligands for iron(II) SCO complexes embedded in LB films [162, 183].

The physical properties of known and newly prepared SCO materials have been investigated in great detail. Remarkable highlights are:

– The cell parameters and full structures of SCO compounds above and below the spin transition temperature and after LIESST, i.e. in the metastable state, have been determined [92, 95].
– Structure determination under pressure and at variable low temperatures is now possible. This is particularly important in SCO research, where pendant questions and problems about cooperative interactions can be solved by direct methods [98].
– Temperature dependent Brillouin spectroscopy has enabled one to distinguish between crystallographic phase transition and spin transition in a single crystal, where it was observed earlier by optical spectroscopy that the spin transition takes place independently of the crystallographic phase transition [26, 202, 203].
– Time-resolved resonance Raman spectroscopy has been developed further for thermal and light-induced SCO studies in solution [213].
– The first structure of a polymeric 3-D SCO triazole complex has been solved [77].
– A pressure cell for magnetic susceptibility measurements under hydrostatic pressure up to 12 kbar and down to ca. 2 K has been constructed for Foner type vibrating sample and SQUID magnetometers [123].
– A pressure cell has also been constructed for optical reflectivity measurements under hydrostatic pressure up to 2 kbar and successfully employed for studies of cooperative interactions [225].
– New photophysical phenomena have been observed such as light-induced thermal hysteresis (LITH) [91, 175], which occurs in a SCO complex under constant light irradiation while cycling the temperature, light-induced optical hysteresis (LIOH) [175] by isothermal light irradiation at variable intensities, light-perturbed thermal hysteresis (LiPTH) [177] in a SCO complex, where the hysteresis is shifted to lower temperatures with green light and upwards with red light.
– Ligand-Driven Light-Induced Spin Change (LD-LISC) has been observed with iron(II) complexes in the room temperature region [181], and also with an iron(III) SCO complex [226].
– Cobalt(II) ions incorporated in a chromium(III) tris-oxalato lattice are forced to undergo thermal spin transition due to the chemical pressure acting in the cavities [227].
– A method (Mössbauer spectroscopy in applied magnetic field) has been developed to monitor the spin state of iron(II) in HS-HS, HS-LS, and LS-LS pairs in dinuclear complexes exhibiting magnetic interaction and thermal SCO [146].
– Pressure-induced spin transition properties have been explored extensively in SCO complexes suitable for application in pressure sensors [128].
– The use of synchrotron radiation has successfully been employed for structural studies of polymeric SCO complexes above and below spin transition with EXAFS [58], to determine hyperfine interactions (Nuclear Forward

Scattering) and to measure phonon spectra and lattice dynamics properties (Nuclear Inelastic Scattering) [147–151, 228].

– The effect of a high pulsed magnetic field on the SCO behaviour was investigated. The results show that SCO can be triggered by a high magnetic field [139, 141].
– Temperature dependent positron lifetime spectroscopy [229–231] and solid state NMR [74, 126, 232] have been shown to be suitable techniques to monitor phase transitions and molecular motion in a SCO crystal.
– The first µSR experiments on SCO compounds have been carried out successfully (at ISIS/England) [233].
– EPR, although known to be inappropriate to study SCO systems of iron(II), has been demonstrated to be very useful when probing incorporated Mn^{2+} ions regarding local structure changes [74].

Much progress has also been made in the theoretical treatment of cooperativity in spin transition phenomena. It is by now commonly accepted that any attempt to reproduce deviations from simple Boltzmann like spin transition curves must include extra terms for short range and long range interactions between the spin state changing molecules. Mean field theory is a good approximation to treat long range elastic interactions and yields reliable data for interaction constants, spin transition temperatures and hysteresis widths. Short range interactions leading to characteristic correlations like HS-LS pair formation have been recognized to be responsible for special features like stepwise spin transitions. In polymeric chain SCO compounds with strong bonding inside the chains and weak bonding between the chains, the width, shape and position of the hysteresis depends on the balance between short and long range interactions. An analytical solution has been worked out. For mononuclear SCO compounds interaction constants have been calculated using lattice deformation data from X-ray diffraction and elasticity constants from Brillouin scattering, agreement with experimental results from spin transition curves is remarkably good.

DFT calculations of vibrational frequencies of HS and LS states and of thermodynamic parameters have reached good agreement with experimental data. The theoretical basis for HS-LS relaxation bridging quantum mechanical tunnelling and thermal activation has been worked out and successfully employed in many LIESST studies. A master equation for interpretation of LITH, LIOH, LiPTH has been worked out.

SCO triazole complexes of iron(II) with hysteresis near room temperature are potential candidates for practical applications in thermal sensors and displays. Pressure sensitive SCO complexes of iron(II) are likewise ready for application in pressure sensors, particularly in remote positions. SCO complexes of iron(II) exhibiting drastic spin state changes upon release of crystal solvent molecules have been suggested to be used in "smart cards".

Electronic spin crossover in transition metal compounds induced by various external perturbations like change of temperature, irradiation with light, application of pressure or a magnetic field is one of the most fascinating dynamic electronic structure phenomena, which has attracted the attention of many research groups worldwide. The first comprehensive book in this fields, entitled

"Spin Crossover in Transition Metal Compounds" (edited by P. Gütlich and H.A. Goodwin) containing 30 review articles in three volumes is scheduled to appear in 2004 in the Springer series Topics in Current Chemistry.

6
References

1. Gütlich P (1981) Struct Bond 44:83
2. Gütlich P, Hauser A, Spiering H (1994) Angew Chem Int Ed 33:2024
3. Kahn O (1993) Molecular Magnetism. VCH, New York
4. Gütlich P, Garcia Y, Goodwin HA (2000) Chem Soc Rev 29:419
5. Gütlich P, Garcia Y, Spiering H (2002) In: Miller JS, Drillon M (eds) Magnetism: Molecules to Materials IV. Wiley-VCH, Weinheim, p 271
6. Franke PL, Haasnoot JG, Zuur AP (1982) Inorg Chim Acta 59:5
7. Müller EW, Ensling J, Spiering H, Gütlich P (1983) Inorg Chem 22:2074
8. Wiehl L (1993) Acta Crystallogr Sect B Struct Commun 49:289
9. Gütlich P, Hauser A (1990) Coord Chem Rev 97:1
10. Gütlich P, Jung J, Goodwin HA (1996) NATO ASI Series. Kluwer Academic, Dordrecht, p 327
11. Poganiuch P, Gütlich P (1988) Hyperfine Interact 40:331
12. Adler P, Poganiuch P, Spiering H (1989) Hyperfine Interact 52:47
13. Poganiuch P, Decurtins S, Gütlich P (1990) J Am Chem Soc 112:3270
14. Gütlich P, Poganiuch P (1991) Angew Chem Int Ed 30:975
15. Buchen T, Gütlich P (1994) Chem Phys Lett 220:262
16. Hinek R, Spiering H, Gütlich P, Hauser A (1996) Chem Eur J 2:1435
17. Buchen T, Poganiuch P, Gütlich P (1994) J Chem Soc-Dalton Trans:2285
18. Buchen T, Schollmeyer D, Gütlich P (1996) Inorg Chem 35:155
19. Jeftic J, Hinek R, Capelli SC, Hauser A (1997) Inorg Chem 36:3080
20. Stassen AF, de Vos M, van Koningsbruggen PJ, Renz F, Ensling J, Kooijman H, Spek AL, Haasnoot JG, Gütlich P, Reedijk J (2000) Eur J Inorg Chem:2231
21. Roubeau O, Stassen AF, Gramage IF, Codjovi E, Linares J, Varret F, Haasnoot JG, Reedijk J (2001) Polyhedron 20:1709
22. Gütlich P, Goodwin HA, Hendrickson DN (1994) Angew Chem Int Ed 33:425
23. Sanner I, Meissner E, Köppen H, Spiering H, Gütlich P (1984) Chem Phys 86:227
24. Spiering H, Willenbacher N (1989) J Phys Condens Matter 1:10089
25. Willenbacher N, Spiering H (1989) J Phys C Solid State Phys 21:1423
26. Jung J, Schmitt G, Wiehl L, Hauser A, Knorr K, Spiering H, Gütlich P (1996) Z Phys B Condens Matter 100:523
27. Dova E, Stassen AF, Driessen RAJ, Sonneveld E, Goubitz K, Peschar R, Haasnoot JG, Reedijk J, Schenk H (2001) Acta Crystallogr Sect B Struct Sci 57:531
28. Driessen WL, Van der Voort PH (1977) Inorg Chim Acta 21:217
29. Hibbs W, Arif A, van Koningsbruggen P, Miller J (1999) Cryst Eng Comm 4
30. Janiak C (1994) J Chem Soc-Chem Commun 545
31. Janiak C (1994) Chem Ber 127:1379

32. Janiak C, Scharmann TG, Green JC, Parkin RPG, Kolm MJ, Riedel E, Mickler W, Elguero J, Claramunt RM, Sanz D (1996) Chem Eur J 2:992

33. Janiak C, Scharmann TG, Brauniger T, Holubova J, Nadvornik M (1998) Z Anorg Allg Chem 624:769

34. van Koningsbruggen P, Miller J (2003) Unpublished results

35. Kunkeler PJ, van Koningsbruggen PJ, Cornelissen JP, van der Horst AN, van der Kraan AM, Spek AL, Haasnoot JG, Reedijk J (1996) J Am Chem Soc 118:2190

36. Moliner N, Munoz MC, Letard S, Letard JF, Solans X, Burriel R, Castro M, Kahn O, Real JA (1999) Inorg Chim Acta 291:279

37. Moliner N, Munoz MC, van Koningsbruggen PJ, Real JA (1998) Inorg Chim Acta 274:1

38. Moliner N, Gaspar AB, Munoz MC, Niel V, Cano J, Real JA (2001) Inorg Chem 40:3986

39. Stupik P, Reiff WM, Hage R, Jacobs J, Haasnoot JG, Reedijk J (1988) Hyperfine Interact 40:343

40. Stupik P, Zhang JH, Kwiecien M, Reiff WM, Haasnoot JG, Hage R, Reedijk J (1986) Hyperfine Interact 28:725

41. Sugiyarto KH, Craig DC, Rae AD, Goodwin HA (1995) Aust J Chem 48:35

42. Haasnoot JG (2003) Private communication

43. Cornelissen JP, Van Diemen JH, Groeneveld LR, Haasnoot JG, Spek AL, Reedijk J (1992) Inorg Chem 31:198

44. Lacroix P, Kahn O, Gleizes A, Valade L, Cassoux P (1984) New J Chem 8:643

45. Miller JS, Zhang JH, Reiff WM, Dixon DA, Preston LD, Reis AHJ, Gebert E, Extine M, Troup J et al. (1987) J Phys Chem 91:4344

46. Humphrey D, Fallon G, Murray K (1988) J Chem Soc-Chem Commun 1356

47. Lau C-P, Singh P, Cline S, Seiders R, Brookhart M, Marsh W, Hodgson D, Hatfield W (1982) Inorg Chem 21:208

48. Kaim W, Moscherosch M (1994) Coord Chem Rev 129:157

49. Maeda Y, Manago T, Komatsu H, Hayami S (1996) Mol Cryst Liq Cryst Sci Technol Sect A Mol Cryst Liq Cryst 285:393

50. Real A, Zarembowitch J, Kahn O, Solans X (1987) Inorg Chem 26:2939

51. Real JA, Bolvin H, Bousseksou A, Dworkin A, Kahn O, Varret F, Zarembowitch J (1992) J Am Chem Soc 114:4650

52. Jay C, Groliere F, Kahn O, Kröber J (1993) Mol Cryst Liq Cryst Sci Technol Sect A Mol Cryst Liq Cryst 234:255

53. Kahn O, Martinez CJ (1998) Science 279:44

54. Kahn O, Kröber J, Jay C (1992) Adv Mater 4:718

55. Kahn O, Codjovi E, Garcia Y, van Koningsbruggen PJ, Lapouyade R, Sommier L (1996) Molecule-Based Magnetic Materials (ACS Symposium Series), vol 644. American Chemical Society, Washington, p 298

56. Garcia Y, van Koningsbruggen PJ, Codjovi E, Lapouyade R, Kahn O, Rabardel L (1997) J Mater Chem 7:857

57. Schweifer J, Weinberger P, Mereiter K, Boca M, Reichl C, Wiesinger G, Hilscher G, van Koningsbruggen PJ, Kooijinan H, Grunert M, Linert W (2002) Inorg Chim Acta 339:297

58. van Koningsbruggen PJ, Garcia Y, Kahn O, Fournes L, Kooijman H, Spek AL, Haasnoot JG, Moscovici J, Provost K, Michalowicz A, Renz F, Gütlich P (2000) Inorg Chem 39:1891

59. Michalowicz A, Moscovici J, Ducourant B, Cracco D, Kahn O (1995) Chem Mater 7:1833

60. Michalowicz A, Moscovici J, Kahn O (1997) J Phys IV 7:633

61. Garcia Y, van Koningsbruggen PJ, Bravic G, Guionneau P, Chasseau D, Cascarano GL, Moscovici J, Lambert K, Michalowicz A, Kahn O (1997) Inorg Chem 36:6357

62. van Koningsbruggen PJ, Garcia Y, Codjovi E, Lapouyade R, Kahn O, Fournes L, Rabardel L (1997) J Mater Chem 7:2069

63. Sugiyarto KH, Goodwin HA (1988) Aust J Chem 41:1645

64. Sugiyarto KH, Craig DC, Rae AD, Goodwin HA (1994) Aust J Chem 47:869

65. Sugiyarto KH, Craig DC, Goodwin HA (1996) Aust J Chem 49:497

66. Sorai M, Ensling J, Hasselbach KM, Gütlich P (1977) Chem Phys 20:197

67. Baran M, Dyakonov V, Gladczuk L, Levchenko G, Piechota S, Szymczak H (1995) J Magn Magn Mater 140:1327
68. Bronisz R, Drabent K, Polomka P, Rudolf MF (1996) Conference Proceedings ICAME95 50:11
69. Codjovi E, Sommier L, Kahn O, Jay C (1996) New J Chem 20:503
70. Garcia Y, van Koningsbruggen PJ, Lapouyade R, Fournes L, Rabardel L, Kahn O, Ksenofontov V, Levchenko G, Gütlich P (1998) Chem Mater 10:2426
71. Kröber J, Codjovi E, Kahn O, Groliere F, Jay C (1993) J Am Chem Soc 115:9810
72. Vreugdenhil W, Haasnoot JG, Kahn O, Thuery P, Reedijk J (1987) J Am Chem Soc 109:5272
73. Vreugdenhil W, van Diemen JH, De Graaff RAG, Haasnoot JG, Reedijk J, van der Kraan AM, Kahn O, Zarembowitch J (1990) Polyhedron 9:2971
74. Ozarowski A, Shunzhong Y, McGarvey BR, Mislankar A, Drake JE (1991) Inorg Chem 30:3167
75. Real JA, Andres E, Munoz MC, Julve M, Granier T, Bousseksou A, Varret F (1995) Science 268:265
76. Moliner N, Munoz C, Letard S, Solans X, Menendez N, Goujon A, Varret F, Real JA (2000) Inorg Chem 39:5390
77. Garcia Y, Kahn O, Rabardel L, Chansou B, Salmon L, Tuchagues JP (1999) Inorg Chem 38:4663
78. Rudolf MF (1998) Third Spin Crossover Family Meeting TMR-TOSS Kick-Off Meeting. University Mainz, Seeheim, Germany
79. Bronisz R (1999) On spin crossover phenomena in supramolecular Fe(II)-polytetrazole systems. Ph. D. thesis University Wroclaw, Wroclaw
80. van Koningsbruggen PJ, Garcia Y, Kooijman H, Spek AL, Haasnoot JG, Kahn O, Linares J, Codjovi E, Varret F (2001) J Chem Soc-Dalton Trans:466
81. Mereiter K, Kooijman H, van Koningsbruggen PJ, Grunert M, Weinberger P, Linert W (2002) Unpublished results
82. van Koningsbruggen PJ, Bravic G, Chasseau D, Mereiter K, Grunert M, Weinberger P, Linert W (2004) In preparation
83. Kitazawa T, Gomi Y, Takahashi M, Takeda M, Enomoto M, Miyazaki A, Enoki T (1996) J Mater Chem 6:119
84. Niel V, Martinez-Agudo JM, Muñoz MC, Gaspar AB, Real JA (2001) Inorg Chem 40:3838
85. Halder GJ, Kepert CJ, Moubaraki B, Murray KS, Cashion JD (2002) Science 298:1762
86. Gütlich P, Hauser A, Spiering H (1999) In: Solomon EI, Lever ABP (eds) Inorganic electronic structure and spectroscopy, vol 2. Wiley, New York Weinheim, p 575
87. König E (1987) Prog Inorg Chem 35:527
88. Gallois B, Real JA, Hauw C, Zarembowitch J (1990) Inorg Chem 29:1152
89. Müller EW, Spiering H, Gütlich P (1982) Chem Phys Lett 93:567
90. Wiehl L, Kiel G, Köhler CP, Spiering H, Gütlich P (1986) Inorg Chem 25:1565
91. Létard JF, Guionneau P, Rabardel L, Howard JAK, Goeta AE, Chasseau D, Kahn O (1998) Inorg Chem 37:4432
92. Kusz J, Spiering H, Gütlich P (2000) J Appl Cryst 33:201
93. Decurtins S, Gütlich P, Köhler CP, Spiering H, Hauser A (1984) Chem Phys Lett 105:1
94. Sorai M, Ensling J, Gütlich P (1976) Chem Phys 18:199
95. Kusz J, Spiering H, Gütlich P (2001) J Appl Cryst 34:229
96. Marchivie M, Guionneau P, Howard JAK, Chastanet G, Létard JF, Goeta AE, Chasseau D (2002) J Am Chem Soc 124:194
97. Guionneau P, Letard JF, Yufit DS, Chasseau D, Bravic G, Goeta AE, Howard JAK, Kahn O (1999) J Mater Chem 9:985
98. Guionneau P, Brigouleix C, Barrans Y, Goeta AE, Létard JF, Howard JAK, Gaultier J, Chasseau D (2001) C R Acad Sci Ser II C 4:161
99. Bausk NV, Erenburg SB, Mazalov LN, Lavrenova LG, Ikorskii VN (1994) J Struct Chem 35:509
100. Erenburg SB, Bausk NV, Lavrenova LG, Varnek VA, Mazalov LN (1997) Solid State Ion 101:571

101. Erenburg SB, Bausk NV, Lavrenova LG, Mazalov LN (2001) J Magn Magn Mater 226:1967
102. Erenburg SB, Bausk NV, Lavrenova LG, Mazalov LN (1999) J Synchr Rad 6:576
103. Lee JJ, Sheu HS, Lee CR, Chen JM, Lee JF, Wang CC, Huang CH, Wang Y (2000) J Am Chem Soc 122:5742
104. Ewald AH, Martin RL, Sinn E, White AH (1969) Inorg Chem 8:1837
105. Sacconi L, Ferraro JR (1974) Inorg Chim Acta 9:49
106. Butcher RJ, Ferraro JR, Sinn E (1976) Inorg Chem 15:2077
107. Long GJ, Becker LW, Hutchinson BB (1981) Adv Chem Ser 194:453
108. Fisher DC, Drickamer HG (1971) J Chem Phys 54:4825
109. Kambara T (1981) J Phys Soc Jpn 50:2257
110. Meissner E, Köppen H, Spiering H, Gütlich P (1983) Chem Phys Lett 95:163
111. König E, Ritter G, Waigel J, Goodwin HA (1985) J Chem Phys 83:3055
112. Adler P, Spiering H, Gütlich P (1989) J Phys Chem Solids 50:587
113. Spiering H, Meissner E, Köppen H, Müller EW, Gütlich P (1982) Chem Phys 68:65
114. McCusker JK, Zvagulis M, Drickamer HG, Hendrickson DN (1989) Inorg Chem 28:1380
115. Köppen H, Müller EW, Köhler CP, Spiering H, Meissner E, Gütlich P (1982) Chem Phys Lett 91:348
116. Köhler CP, Jakobi R, Meissner E, Wiehl L, Spiering H, Gütlich P (1990) J Phys Chem Solids 51:239
117. Jakobi R, Spiering H, Gütlich P (1992) J Phys Chem Solids 53:267
118. Kohlhaas T, Spiering H, Gütlich P (1997) Z Phys B Condens Mat 102:455
119. Jeftic J, Hauser A (1996) Chem Phys Lett 248:458
120. Jeftic J, Romstedt H, Hauser A (1996) J Phys Chem Solids 57:1743
121. Boillot ML, Zarembowitch J, Itie JP, Polian A, Bourdet E, Haasnoot JG (2002) New J Chem 26:313
122. Roux C, Zarembowitch J, Itie JP, Polian A, Verdaguer M (1996) Inorg Chem 35:574
123. Baran M, Dyakonov V, Gladczuk L, Levchenko G, Piechota S, Szymczak H (1995) Physica C 241:383
124. Ksenofontov V, Levchenko G, Spiering H, Gütlich P, Letard JF, Bouhedja Y, Kahn O (1998) Chem Phys Lett 294:545
125. Ksenofontov V, Gaspar AB, Real JA, Gütlich P (2001) J Phys Chem B 105:12266
126. Breuning E, Ruben M, Lehn JM, Renz F, Garcia Y, Ksenofontov V, Gütlich P, Wegelius E, Rissanen K (2000) Angew Chem Int Ed 39:2504
127. Niel V, Munoz MC, Gaspar AB, Galet A, Levchenko G, Real JA (2002) Chem Eur J 8:2446
128. Garcia Y, Ksenofontov V, Levchenko G, Gütlich P (2000) J Mater Chem 10:2274
129. Camp PJ, Patey GN (1998) J Phys Condens Matter 10:10909
130. Linares J, Spiering H, Varret F (1999) Eur Phys J B 10:271
131. Klokishner S, Linares J, Varret F (2000) Chem Phys 255:317
132. Garcia Y, Ksenofontov V, Levchenko G, Schmitt G, Gütlich P (2000) J Phys Chem B 104:5045
133. Codjovi E, Menendez N, Jeftic J, Varret F (2001) C R Acad Sci Ser II C 4:181
134. Smit E, de Waal D, Heyns AM (2000) Mater Res Bull 35:1697
135. Grey JK, Butler IS (2001) Coord Chem Rev 219:713
136. Sunatsuki Y, Sakata M, Matsuzaki S, Matsumoto N, Kojima M (2001) Chem Lett 12:1254
137. Hayami S, Hosokoshi Y, Inoue K, Einaga Y, Sato O, Maeda Y (2001) Bull Chem Soc Jpn 74:2361
138. Qi Y, Müller EW, Spiering H, Gütlich P (1983) Chem Phys Lett 101:503
139. Bousseksou A, Negre N, Goiran M, Salmon L, Tuchagues JP, Boillot ML, Boukheddaden K, Varret F (2000) Eur Phys J B 13:451
140. Negre N, Consejo C, Goiran M, Bousseksou A, Varret F, Tuchagues JP, Barbaste R, Askenazy S, Haasnoot JG (2001) Physica B 294:91
141. Bousseksou A, Boukheddaden K, Goiran M, Consejo C, Boillot ML, Tuchagues JP (2002) Phys Rev B 65:172412
142. Ogawa Y, Ishikawa T, Koshihara S, Boukheddaden K, Varret F (2002) Phys Rev B 66:073104
143. Ogawa Y, Koshihara SY, Takesada M, Ishikawa T (2002) Mol Cryst Liq Cryst 379:357
144. Lejay J, Jansen AGM, Wyder P, Bronger W, Kläui W (1991) Phys Rev B 43:8196

145. Garcia Y, Kahn O, Ader JP, Buzdin A, Meurdesoif Y, Guillot M (2000) Phys Lett A 271:145
146. Ksenofontov V, Spiering H, Reiman S, Garcia Y, Gaspar AB, Moliner N, Real JA, Gütlich P (2001) Chem Phys Lett 348:381
147. Grünsteudel H, Paulsen H, Meyer-Klaucke W, Winkler H, Trautwein AX, Grünsteudel HF, Baron AQR, Chumakov AI, Rüffer R, Toftlund H (1998) Hyperfine Interact 113:311
148. Grünsteudel H, Paulsen H, Winkler H, Trautwein AX, Toftlund H (1999) Hyperfine Interact 123:841
149. Paulsen H, Winkler H, Trautwein AX, Grünsteudel H, Rusanov V, Toftlund H (1999) Phys Rev B 59:975
150. Paulsen H, Benda R, Herta C, Schünemann V, Chumakov AI, Duelund L, Winkler H, Toftlund H, Trautwein AX (2001) Phys Rev Lett 86:1351
151. Paulsen H, Grünsteudel H, Meyer-Klaucke W, Gerdan M, Grünsteudel HF, Chumakov AI, Rüffer R, Winkler H, Toftlund H, Trautwein AX (2001) Eur Phys J B 23:463
152. György V, Neisius T, Renz F, Kárpáti S, Shukla A, Mirone A, de Groot F (2002) Highlights ESRF 59
153. Decurtins S, Gütlich P, Köhler CP, Spiering H (1985) J Chem Soc Chem Commun 430
154. Ogawa Y, Koshihara S, Koshino K, Ogawa T, Urano C, Takagi H (2000) Phys Rev Lett 84:3181
155. Ogawa Y, Oiwa A, Koshihara SY, Munekata HO (2001) Phase Transit 74:35
156. Enachescu C, Oetliker U, Hauser A (2002) J Phys Chem B 106:9540
157. Létard JF, Real JA, Moliner N, Gaspar AB, Capes L, Cador O, Kahn O (1999) J Am Chem Soc 121:10630
158. Baldenius KU, Campen AK, Hoehnk HD (1987) J Mol Struct 157:295
159. Hauser A, Adler P, Gütlich P (1988) Chem Phys Lett 152:468
160. Nakamoto A, Ono Y, Kojima N, Matsumura D, Yokoyama T, Liu X, Moritomo Y (2003) Synth Met 137:1219
161. Herber R, Casson LM (1986) Inorg Chem 25:847
162. Létard JF, Nguyen O, Soyer H, Mingotaud C, Delhaes P, Kahn O (1999) Inorg Chem 38:3020
163. Hauser A, Jeftic J, Romstedt H, Hinek R, Spiering H (1999) Coord Chem Rev 192:471
164. Buchen T, Gütlich P, Goodwin HA (1994) Inorg Chem 33:4573
165. Buchen T, Gütlich P, Sugiyarto KH, Goodwin HA (1996) Chem Eur J 2:1134
166. Létard JF, Capes L, Chastanet G, Moliner N, Letard S, Real JA, Kahn O (1999) Chem Phys Lett 313:115
167. Marcen S, Lecren L, Capes L, Goodwin HA, Létard JF (2002) Chem Phys Lett 358:87
168. Hayami S, Gu Z, Einaga Y, Kobayashi Y, Ishikawa Y, Yamada Y, Fujishima A, Sato O (2001) Inorg Chem 40:3240
169. Money VA, Evans IR, Halcrow MA, Goeta AE, Howard JAK (2003) Chem Commun 158
170. Wu CC, Jung J, Gantzel PK, Gütlich P, Hendrickson DN (1997) Inorg Chem 36:5339
171. Hauser A (1991) Coord Chem Rev 111:275
172. Juhasz G, Hayami S, Sato O, Maeda Y (2002) Chem Phys Lett 364:164
173. McCusker JK, Rheingold AL, Hendrickson DN (1996) Inorg Chem 35:2100
174. Renz F, Oshio H, Ksenofontov V, Waldeck M, Spiering H, Gütlich P (2000) Angew Chem Int Ed 39:3699
175. Desaix A, Roubeau O, Jeftic J, Haasnoot JG, Boukheddaden K, Codjovi E, Linares J, Nogues M, Varret F (1998) Eur Phys J B 6:183
176. Renz F, Spiering H, Goodwin HA, Gütlich P (2000) Hyperfine Interact 126:155
177. Renz F, Spiering H, Gütlich P, Sugiyarto KH, Goodwin H (2002) TOSS-Meeting, Seeheim, Germany
178. Gütlich P (2004) In: Gütlich P, Goodwin H (eds) Spin crossover in transition metal compounds (Topics in Current Chemistry, Vol. 234). Springer, Berlin Heidelberg New York
179. Roux C, Zarembowitch J, Gallois B, Granier T, Claude R (1994) Inorg Chem 33:2273
180. Boillot ML, Roux C, Audiere JP, Dausse A, Zarembowitch J (1996) Inorg Chem 35:3975
181. Boillot ML, Chantraine S, Zarembowitch J, Lallemand JY, Prunet J (1999) New J Chem 23:179
182. Boillot ML, Sour A, Delhaes P, Mingotaud C, Soyer H (1999) Coord Chem Rev 192:47

183. Soyer H, Mingotaud C, Boillot ML, Delhaes P (1998) Langmuir 14:5890
184. Tsivgoulis GM, Lehn JM (1996) Chem Eur J 2:1399
185. Tsivgoulis GM, Lehn JM (1997) Adv Mater 9:39
186. Saika T, Irie M, Shimidzu T (1994) J Chem Soc Chem Commun 2123
187. Launay JP, Fraysse S, Coudret C (2000) Mol Cryst Liq Cryst 344:125
188. Matsuda K, Irie M (2000) J Am Chem Soc 122:7195
189. Matsuda K, Irie M (2000) J Am Chem Soc 122:8309
190. Garcia Y, Ksenofontov V, Lapouyade R, Gütlich P (2001) German Patent 10039903.7
191. Ewald AH, Martin RL, Ross GI, White AH (1964) Proc R Soc A 28:235
192. König E, Madeja K (1966) Chem Commun 3:61
193. König E, Madeja K (1967) Inorg Chem 6:48
194. Chesnut DB (1964) J Chem Phys 40:405
195. Wajnflasz J (1970) Phys Stat Sol 40:537
196. Drickamer HG, Slichter CP (1972) J Chem Phys 56:2142
197. Bari RA, Sivardiere J (1972) Phys Rev B 5:4466
198. Zimmermann R, König E (1977) J Phys Chem Solids 38:779
199. Sorai M, Seki S (1974) J Phys Chem Solids 35:555
200. Kambara T (1979) J Chem Phys 70:4199
201. Spiering H (2004) In: Gütlich P, Goodwin H (eds) Spin crossover in transition metal compounds (Topics in Current Chemistry, Vol. 235). Springer, Berlin Heidelberg New York
202. Jung J, Bruchhäuser F, Feile R, Spiering H, Gütlich P (1996) Z Phys B Condens Mat 100:517
203. Jeftic J, Hauser A, Varret F, Ecolivet C (2000) High Pressure Res 18:195
204. Boukheddaden K, Linares J, Spiering H, Varret F (2000) Eur Phys J B 15:317
205. Spiering H, Kohlhaas T, Romstedt N, Hauser A, Bruns-Yilmaz C, Kusz J, Gütlich P (1999) Coord Chem Rev 192:629
206. Boukheddaden K, Shteto I, Hoo B, Varret F (2000) Phys Rev B 62:14796
207. Romstedt H, Hauser A, Spiering H (1998) J Phys Chem Sol 59:265
208. Koshino K, Ogawa T (1999) J Phys Soc Jpn 68:2164
209. Sorai M, Seki S (1972) J Phys Soc Jpn 33:575
210. Molnar G, Niel V, Real JA, Dubrovinsky L, Bousseksou A, McGarvey JJ (2003) J Phys Chem B 107:3149
211. Bousseksou A, McGarvey JJ, Varret F, Real JA, Tuchagues JP, Dennis AC, Boillot ML (2000) Chem Phys Lett 318:409
212. Molnar G, Niel V, Gaspar AB, Real JA, Zwick A, Bousseksou A, McGarvey JJ (2002) J Phys Chem B 106:9701
213. Coates CG, Olofsson J, Coletti M, McGarvey JJ, Onfelt B, Lincoln P, Norden B, Tuite E, Matousek P, Parker AW (2001) J Phys Chem B 105:12653
214. Bousseksou A, Constant-Machado H, Varret F (1995) J Phys I 5:747
215. Bousseksou A, Verelst M, Constant-Machado H, Lemercier G, Tuchagues JP, Varret F (1996) Inorg Chem 35:110
216. Bousseksou A, Salmon L, Varret F, Tuchagues JP (1998) Chem Phys Lett 282:209
217. Klokishner S, Linares J, Varret F (2001) J Phys Condens Matter 13:595
218. Koudriavtsev AB (1999) Chem Phys 241:109
219. Linert W, Koudriavtsev AB (1999) Coord Chem Rev 192:405
220. Koudriavtsev AB, Linert W (2001) Monatshefte Chemie 132:235
221. Papankova B, Simon P, Boca R (2003) Solid State Chem 90/91:177
222. Garcia Y, Ksenofontov V, Gütlich P (2001) C R Acad Sci Ser II C 4:227
223. Garcia Y, Moscovici J, Michalowicz A, Ksenofontov V, Levchenko G, Bravic G, Chasseau D, Gütlich P (2002) Chem Eur J 8:4992
224. Real JA, Castro I, Bousseksou A, Verdaguer M, Burriel R, Castro M, Linares J, Varret F (1997) Inorg Chem 36:455
225. Jeftic J, Menendez N, Wack A, Codjovi E, Linares J, Goujon A, Hamel G, Klotz S, Syfosse G, Varret F (1999) Meas Sci Technol 10:1059
226. Hirose S, Hayami S, Maeda Y (2000) Bull Chem Soc Jpn 73:2059

227. Sieber R, Decurtins S, Stoeckli-Evans H, Wilson C, Yufit D, Howard JAK, Capelli SC, Hauser A (2000) Chem Eur J 6:361
228. Grünsteudel H, Haas M, Leupold O, Mandon D, Matzanke BF, Meyer-Klaucke W, Paulsen H, Realo E, Ruter HD, Trautwein AX, Weiss R, Winkler H (1998) Inorg Chim Acta 276:334
229. Vertes A, Suvegh K, Hinek R, Gütlich P (1994) J Phys Chem Solids 55:1269
230. Vertes A, Suvegh K, Hinek R, Gütlich P (1994) Hyperfine Interact 84:483
231. Vertes A, Suvegh K, Bokor M, Domjan A, Marek T, Klapper M, Chisholm CU, El-Sharif M, Tompa K, Nemes-Vetessy Z, Burger K (1999) J Radioanal Nucl Chem 239:29
232. Bokor M, Marek T, Suvegh K, Tompa K, Vertes A, Nemes-Vetessy Z, Burger K (1996) J Radioanal Nucl Chem 211:247
233. a) Campbell SJ, Ksenofontov V, Garcia Y, Lord JS, Boland Y, Gütlich P (2003) J Phys Chem B 107:14289; b) Campbell SJ, Ksenofontov V, Garcia Y, Lord JS, Reiman S, Gütlich P (2002) Hyperfine Interact C5:363

CHAPTER 1

Ruthenium Complexes of Non-Innocent Ligands: Aspects of Charge Transfer Spectroscopy

A. B. P. Lever[1] · S. I. Gorelsky[2]

[1] Department of Chemistry, York University, 4700 Keele St., Toronto, Ontario, Canada M3J1P3
   E-mail: blever@yorku.ca
[2] Department of Chemistry, Stanford University, 333 Campus Dr., Stanford, California 94305, USA
   E-mail: gorelsky@stanford.edu

Abstract The chapter presents in some detail how the electronic structure of a series of ruthenium complexes of non-innocent, i.e. redox active, ligands can be assessed through a combination of optical spectroscopy and INDO/S computation. Complexes of the type $[Ru(NH_3)_4(LL)]^{n+}$ and $[Ru(bpy)_2(LL)]^{n+}$ are analyzed where LL is *o*-phenylenediamine or its series of congeners where the nitrogen atom is replaced by oxygen or sulfur. The complexes obtained by one- or two-electron oxidation of these species to their semiquinone and quinone oxidation state analogs, are discussed in detail in a comparative and pedagogical fashion. The consequences of the very strong covalent interaction which occurs between ruthenium and most of these ligands are probed in depth and the methodology for dealing with such systems is presented.

Keywords Ruthenium · Non-innocent ligand · Redox active ligand · Quinone · DFT · INDO/S

Dedicated to the memory of Christian Klixbüll Jørgensen, a valued friend and distinguished scientist

List of Abbreviations

AO   Atomic Orbital
CT   Charge Transfer
CTTS   Charge Transfer To Solvent
DFT   Density Functional Theory
FMO   Frontier Molecular Orbital
HOMO   Highest Occupied Molecular Orbital
INDO/S   Intermediate Neglect of Differential Overlap/Spectroscopy
LCAO   Linear Combination of Atomic Orbitals
L′LCT   Ligand to Ligand Charge Transfer
LMCT   Ligand to Metal Charge Transfer
LUMO   Lowest Unoccupied Molecular Orbital
MLCT   Metal to Ligand Charge Transfer
M′MCT   Metal to Metal Charge Transfer
MO   Molecular Orbital

MPA   Mulliken Population Analysis
NIR   Near Infrared
OSCT   Outer Sphere Charge Transfer
TD-DFT   Time-Dependent DFT
ZINDO   Zerner's INDO method

1
Introduction

In the middle of the last century, with his series of books and review articles and a deluge of research publications, written in a style that was pure Jørgensen, Christian introduced us to the theory and practice of the electronic spectra of inorganic complex molecules. While there were certainly other outstanding contributors to the field at the time, Jørgensen was the major force by virtue of his incisive understanding of the field, and by the sheer magnitude of his output.

At that time, the emphasis of most workers lay in reporting d-d spectra but Christian showed us how to understand and predict charge transfer spectra, on the basis of the d^n configuration and using, for example, the concept of 'optical electronegativity' [2, 5–10].

Jørgensen developed the basic tenets of charge transfer (CT) spectroscopy by observing the systematic behavior of the CT spectra of hexahalometallates as a function of their d^n configuration, so called 'ligand to metal charge transfer' (LMCT) spectra. In those early years, rather little attention was placed on 'metal to ligand charge transfer' (MLCT) transitions but Jørgensen provided the framework for the subsequent development of the theory. Intensive research into complexes of easily reducible polyatomic unsaturated ligands with low lying π^* levels then led to a surge in publications involving MLCT spectra. Indeed since then the field has been dominated by studies of MLCT spectra with relatively much less development of LMCT spectra.

'Ligand to ligand charge transfer' (L'LCT) spectra [11–13], 'metal to metal charge transfer' (M'MCT) spectra [14–16], 'outer sphere charge transfer' (OSCT), and 'charge transfer to solvent' (CTTS) etc. are also now recognized.

A reason for the considerable focus on charge transfer bands is that when one combines an easily oxidizable metal ion with an easily reducible ligand (or vice versa) then the resulting charge transfer bands will generally lie in the visible or near infrared (NIR) region and will be significantly more intense than most d-d bands. Hence they are usually far removed energetically from internal ligand π-π^* bands and are very easy to study.

Two major aspects, which have developed intensively during the past few decades, have been the relationships between the energies of charge transfer transitions and electrochemical redox potentials, and the role the solvent plays in tuning charge transfer spectra. It has been recognized for a long time that, since an MLCT band, for example, involves formally the oxidation of the metal and the reduction of the ligand, its energy must be related to the formal potentials for these processes [9, 15, 20–32]. Charge transfer excited states tend to be polar because of the charge separation that is induced. As a consequence such

transitions usually have energies which can be quite solvent dependent (solvato-chromism) [28, 33–47]. Conversely if there is extensive delocalization of electron density from the central metal ion into the ligand of concern, i.e. extensive co-valency and π-mixing, then the extent of electron transfer from metal to ligand can be significantly reduced. This is generally interpreted in terms of a greatly reduced electron transfer 'distance' being smaller than the geometric distance for electron transfer [14, 48–51]. This delocalization has an effect on the energy, the intensity and the bandwidths of the CT transitions which can therefore be used as a means to probe delocalization [29, 37, 52–57].

Since Christian and the current authors share a love of the pedagogy of electronic spectroscopy, and especially of charge transfer spectroscopy, this chapter will be written in a pedagogical vein as an aid to young and new researchers in the field. We assume that the reader will be conversant with the basics of charge transfer spectroscopy as outlined in the various books referenced above. Here we will be concerned primarily with how delocalization and molecular symmetry affect the observed charge transfer transitions and we will focus exclusively on the MLCT spectra of a group of ruthenium complexes of non-innocent, i.e. redox active, ligands.

2
Necessary Background Theory

2.1
Electrochemical Considerations

This has been dealt with in considerable detail and therefore only a broad outline is presented here. Considering an MLCT transition in an $M^{II}L$ species, where L is one (reducible) ligand in, for example, an octahedral complex, an $[M^{III}L^-]$ excited state is generated. This can be written:

$$M^{II}L + h\nu \rightarrow [M^{III}L^-]^\star \qquad h\nu(MLCT)^\star \qquad (1)$$

where the asterisk indicates a Franck-Condon excited state (see below). Clearly, the metal is being oxidized and the ligand reduced. These processes can be written as half-cells, with potentials as noted:

$$M^{II}L \rightarrow M^{III}L + e^- \qquad -E_{1/2}[M^{III/II}(L)] \qquad (2)$$

$$M^{III}L + e^- \rightarrow M^{III}L^- \qquad E_{1/2}[L^{0/-}(M^{III})] \qquad (3)$$
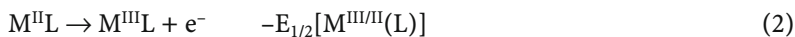
By summing Eqs. (2) and (3) and changing the sign of the right part of the equation (to allow for the uphill nature of an electronic transition), we obtain

$$h\nu(MLCT) = E_{1/2}[M^{III/II}(L)] - E_{1/2}[L^{0/-}(M^{III})] \qquad (4)$$

However half-cell potentials Eqs. (2) and (3) are equilibrium processes while the excited state generated in Eq. (1) is a Franck-Condon excited state which has not thermally equilibrated to the equilibrium excited state. It will have the geometry of the ground state instead of the excited state; these differ in energy by an amount, χ_i, the so-called *inner reorganization energy*. Further, the solvent

environment will be that appropriate to the ground state not the excited state, and these differ in energy by an amount χ_o, or *outer reorganization energy.* This situation arises because the electronic excitation takes place in femtoseconds, far more rapidly than the nuclei of the molecule can adopt the equilibrium geometry of the excited state, and far more rapidly than the solvent can re-equilibrate. These energies must be accommodated in the expression (units of eV):

$$h\nu(MLCT)^\star = E_{1/2}[M^{III/II}(L)] - E_{1/2}[L^{0/-}(M^{III})] + \chi_i + \chi_o \qquad (5)$$

Note that the half-cell potentials in Eq. (5) define, first the ligand reduction potential when it is bonded to M^{III}, and the M^{II} oxidation potential when it is bonded to L (in its initial oxidation state). The charge transfer energy is an enthalpy whereas the redox potentials are Gibbs free energies; thus there is an implicit assumption that there is no significant entropy difference between the ground and excited state species. With that caveat, Eq. (5) is exact but recall that we set up the general case for a species $M^{II}L$ and experimentally we should be able to measure $E_{1/2}[L^{0/-}(M^{II})]$ rather than the desired reduction of L attached to M^{III}. There are means to estimate the value of $E_{1/2}[L^{0/-}(M^{III})]$ knowing the value of $E_{1/2}[L^{0/-}(M^{II})]$ but, in general, Eq. (5) is not so useful. Rather, we need the corresponding expression which utilizes the measured experimental redox potentials, which, in this general case are $E_{1/2}[L^{0/-}(M^{II})]$ and $E_{1/2}[M^{III/II}(L)]$. The difference between these two potentials which is usually simply the gap between oxidation and reduction of the bulk solution species is called $\Delta E(Redox)$:

$$\Delta E(Redox) = E_{1/2}[M^{III/II}(L)] - E_{1/2}[L^{0/-}(M^{II})] \qquad (6)$$

While in Eq. (5) the solvation energies of the equilibrated redox states are contained within the potentials and do not explicitly appear, they must do so if $\Delta E(Redox)$ is employed. Their total sum is frequently quite small so that $\Delta E(Redox)$ provides an estimate usually to within a few tenths of an eV to the corresponding optical MLCT transition. As we demonstrate below, it transpires that this estimate is better if the extent of mixing between the metal and ligand orbitals is small, but agreement between calculated and observed energies can be relatively poor (differ by as much as 1 eV) if mixing is important.

The explicit relationship connecting $\Delta E(Redox)$ with $h\nu(MLCT)$ is given by Eq. (7) [29, 41]:

$$h\nu(MLCT)^\star = [\Delta E(Redox) + \chi_i + \Delta\Delta G_s + Q] + \chi_o + \Delta_{sol} \qquad (7)$$

where Q is discussed below, Δ_{sol} is the difference in solvation free energy between the relaxed excited state and the ground state, and $\Delta\Delta G_s = 2\Delta G_s^{o-} - \Delta G_s^{o+} - D\Delta G_s^{o-}$ (difference between twice the ground state and oxidized and reduced species free energies of solvation). The term in square brackets (in Eq. 7) is solvent independent because of cancellation within $\Delta E(Redox)$. Equation (7) supposes a transition to the spin-singlet state, and assumes the same orbitals, presumably HOMO and LUMO of the complex, are involved in both the optical transition and the redox process.

Equation (7) can be also written in a simplified form:

$$h\nu(CT) = \Delta E(Redox) + C \tag{8}$$

This is a very commonly used expression, almost invariably relating the lowest energy *intense* visible region charge transfer transition to the difference in the first oxidation and first reduction potential of a complex. C usually, at least in heavy transition metal chemistry, e.g. ruthenium, osmium and rhenium chemistry, has the magnitude of 0.2–0.4 eV [23, 29]. It can be the case that the HOMO-1 or HOMO-2, rather than HOMO, is involved in the optical transition but since the energy difference between these orbitals and the HOMO is usually very small, C, in Eq. (8), is still small.

The parameter Q is an electronic term which is defined as the energy of the process: (using our example):

$$[M^{II}L]^- + [M^{III}L]^+ \rightarrow M^{II}L + [M^{III}L^-] \tag{9}$$
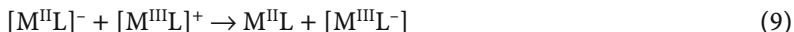
which actually involves the gas phase transfer of an electron from the reduced ground state species to the oxidized ground state species, to generate, on the right, the ground state and the thermally equilibrated excited state. It can be written in the form

$$Q = 2\,K(d,L) - J(d,L) + \Sigma\varepsilon \tag{10}$$

where $K(d,L)$ and $J(d,L)$ are the exchange and Coulomb integrals for a pair of orbitals involved in the MLCT excitation and $\Sigma\varepsilon$ is net change in energies of all the orbitals between the ground and excited state. We return to this discussion later. With this brief introduction, we can now move to some examples of its application.

2.2
Computation

In our recent work we have employed the INDO/S semi-empirical model as developed by Michael Zerner, so-called ZINDO, the modern Density Functional Theory (DFT) [62–64] and time-dependent DFT [63, 64]. We have compared these two methods by analyzing the same set of complexes with both INDO/S and DFT [45, 52, 65, 66]. At least with the ruthenium complexes of non-innocent ligands which we have studied, the two theories give very similar results in terms both of predicted electronic spectra and molecular orbital compositions. Since INDO/S is computationally much less demanding, we mostly restrict ourselves here to the use of that model. However, semi-empirical methods for geometry optimization, such as INDO/1, generally are not as reliable as INDO/S for electronic spectra. Thus all the optimized geometries were obtained using Gaussian 98 [67] and employing spin-restricted (for closed shell species) and spin-unrestricted (for open shell species) DFT using the hybrid B3LYP exchange-correlation functional [68, 69] and LanL2DZ basis set [70–72]. Since this is a mainly pedagogical contribution we do not provide details of the geometries used. It is possible that using a different exchange-correlation functional and a better basis set would

provide 'better' geometries. Thus the spectroscopic and molecular orbital (MO) data presented herein are not necessarily the best data that can be obtained (also see later).

It is not our intention in this article to compare *comprehensively* experimental with calculated absorption spectra, but we do wish to make the point that the agreement between the experimental and calculated spectra and between INDO/S and TD-DFT results is generally good to excellent lending credence to the analyses presented here.

2.3
Molecular Orbital Compositions

Within the MO-LCAO approximation, the wave function for the i-th eigenstate of the molecule/ion can be written as

$$\phi_i^\alpha = \sum_\mu c_{\mu i}^\alpha \chi_\mu \tag{11}$$

for an atom localized basis set (χ_μ).

If overlap between any two different basis functions, $S_{\mu\nu} = \langle \chi_\mu | \chi_\nu \rangle$, is neglected, the contribution of the μ-th atomic orbital (AO) to the i-th molecular orbital (MO) is simply equal to the square of the corresponding MO-LCAO coefficient, $(c_{\mu i}^\alpha)^2$ for α spin and $(c_{\mu i}^\beta)^2$ for β spin. This is not true when the overlap between atomic orbitals is non-zero. It is then necessary to include the overlap population in the MO decomposition analysis. Several ways have been proposed in the literature to deal with overlap populations, the most commonly used being the Mulliken population analysis (MPA) [73–76]. In MPA the overlap population is split equally between two atoms, so the contribution of the μ-th AO to the i-th MO is equal to

$$(c_{\mu i}^\alpha)^2 + \sum_{\nu \neq \mu} c_{\mu i}^\alpha c_{\nu i}^\alpha S_{\mu\nu} \tag{12}$$

and

$$(c_{\mu i}^\beta)^2 + \sum_{\nu \neq \mu} c_{\mu i}^\beta c_{\nu i}^\beta S_{\mu\nu} \tag{13}$$

for α and β spin orbitals respectively.

By means of the program AOM$_{IX}$ [77] the compositions of the MOs were evaluated using Eqs. (12) and (13). They are tabulated in Tables 1 and 2 and graphically presented in Figs. 2 and 8.

2.4
Charge Transfer Character of Electronic Transitions

Typically, one interprets features in the electronic spectra of transition metal complexes as d-d, MLCT, LMCT, L'LCT transitions, etc. However, such descriptions are only appropriate in the weak metal-ligand coupling limit, where "pure" CT excited states are most rigorously defined. When the metal-ligand coupling is high, the MOs are of mixed metal-ligand character, and descriptions of electronic transitions such as *pure* d-d, MLCT or LMCT become approximate.

For characterization of the electronic transitions as partial CT transitions the following definition of the CT character can be used:

$$CT_I(\%) = 100\,(P_g(Ru) - P_I(Ru)), \tag{14}$$

where $P_g(Ru)$ and $P_I(Ru)$ are electronic populations on the metal in the electronic ground and excited states, respectively. Positive CT values correspond to MLCT transitions, negative CT values to LMCT transitions. This definition can be easily expressed using the AO contributions to MOs. The CT character for the HOMO–x $\rightarrow$ LUMO+y excitation is [45]

$$CT(\%) = \%\,(Ru)_{HOMO-x} - \%\,(Ru)_{LUMO+y} \tag{15}$$

If the excited state is formed by more than one single-electron excitation, then the CT character of this excited state is expressed as a sum of CT characters of each participating excitation, $\phi_i \rightarrow \phi_a$:

$$CT_I(\%) = \sum_{i,a} [C_I(\phi_i \rightarrow \phi_a)]^2\,(\%\,(Ru)_i - \%(Ru)_a) \tag{16}$$

where $C_I(\phi_i \rightarrow \phi_a)$ are the corresponding coefficients of the I-th eigenvector of the configuration interaction matrix of single electron excitations (CIS). So, one can use the AO contributions to MOs to probe the nature of electronic transitions.

2.5
Convolution of Absorbance Spectra

An absorption profile for a transition metal complex can be calculated as a sum of Gaussian-shaped bands using the formula [45, 77]

$$\varepsilon(\omega) = 2.174{*}10^8 \sum_I \frac{f_I}{\Delta_{1/2,I}} \exp\left(-2.773\frac{(\omega-\omega_I)^2}{\Delta_{1/2,I}^2}\right), \tag{17}$$

where molar absorptivity, ε, is given in units of $mol^{-1}\,L\,cm^{-1}$. The sum in Eq. (17) includes all transitions with energies, ω_I (expressed in cm^{-1}), and oscillator strengths, f_I. The total integrated intensity under an absorption profile obtained from Eq. (17) is equal to a sum of the oscillator strengths:

$$4.319\times10^{-9} \int \varepsilon(\omega)d\omega = \sum_I f_I. \tag{18}$$

The Gaussian band shape can be chosen because low-resolution spectroscopic bands follow this shape closely. The half-bandwidths of transitions, $\Delta_{1/2,I}$, were assumed to be equal to 3000 cm^{-1} (a typical value for the MLCT bands of complexes under consideration). This assumption is justified because the absorption bands in the electronic spectra of $[Ru(NH_3)_4(LL)]^{n+}$ and $[Ru(bpy)_2(LL)]^{n+}$ mostly belong to the same type. The oscillator strengths calculated using the dipole length approximation at the CIS level are usually overestimated by a factor of 2–3 [45, 58, 65, 78, 79]. Thus intensities of electronic transitions from INDO/S calculations were scaled by a factor of 1/2.

3
o-Benzoquinonediimine(Tetraammine)Ruthenium and Related Complexes

o-Benzoquinonediimine, termed (q.NH.NH) or bqdi, and its analogs are very interesting ligands because they couple strongly to ruthenium and osmium and more specifically because they are so-called *non-innocent* ligands which can exist in several oxidation states. The fully reduced species is *o*-phenylenediamine, termed (cat.NH$_2$.NH$_2$), which can coordinate both in its neutral form or as its deprotonated dianion, *o*-phenylenediamide (2-), termed (cat.NH.NH). One-electron oxidation of (cat.NH.NH) (or of (cat.NH$_2$.NH$_2$) with deprotonation) leads to the *o*-benzosemiquinonediiminato (1-) ligand, termed (sq.NH.NH). Further one-electron oxidation yields the neutral (q.NH.NH). In principle, these species may bind either ruthenium(II) or ruthenium(III).

We discuss here the optical, electrochemical and computational approaches that can be used to explore how the bonding of these ligands to ruthenium varies with the net oxidation level. In the following sections, we exclude any discussion of d-d transitions, which, of course, can give rise to weak absorption in the visible, near infrared (NIR) or ultra violet (UV) regions.

We present, in some detail, the data for the [Ru(NH$_3$)$_4$(LL)]$^{n+}$ species (n=0–3) and then discuss, in rather less detail, how our understanding of these compounds is used to analyze the [Ru(bpy)$_2$(LL)]$^{n+}$ series.

3.1
Frontier Orbitals of (q.NH.NH) and their Possible Coupling to d Orbitals of the Central Metal Atom

The frontier molecular orbitals (FMOs) of the (q.NH.NH) ligand (C$_{2v}$ symmetry) are shown in Fig. 1. We suppose a coordinate axis centered at the metal with the z axis lying along the molecular C$_2$ axis, and with the (q.NH.NH) plane defined
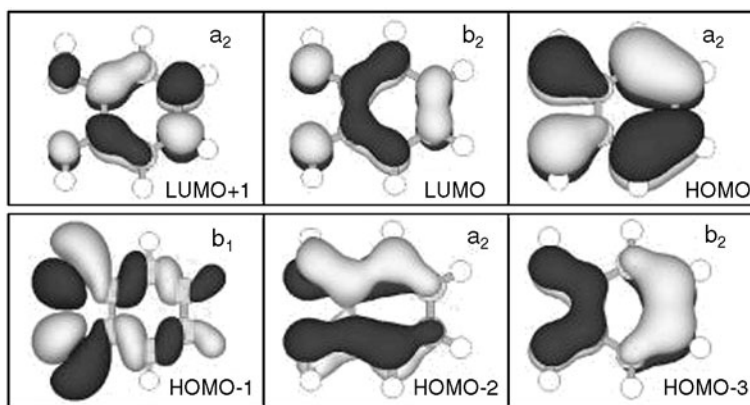
Fig. 1 Frontier molecular orbitals of (q.NH.NH)

as xz. The central metal d_{yz} orbital (b_2 in C_{2v}) is then appropriately directed towards the π-framework of the ligand. The phases of the π* LUMO (b_2) map properly onto d_{yz} and thus this orbital provides a π-pathway to mix electron density on the metal with the (q.NH.NH) ligand. The HOMO-3 (b_2) has similar phases and can also mix with d_{yz} of the metal atom while the HOMO and HOMO-2 (a_2) orbitals have the correct symmetry to couple with d_{xy} (a_2) in a δ-interaction.

The other d(t_{2g}) component is the d_{x2-z2} orbital, which, lying in the molecular plane, has σ-symmetry with respect to the ligand.

3.2
Ru^{II}(NH$_3$)$_4$(cat.NH.NH)

Geometry optimization (using B3LYP/LanL2DZ) led to a structure with C_2 symmetry, in which the N-H bonds are canted slightly above and below the plane xz of the (cat.NH.NH) ring. There is considerable mixing between metal d and ligand orbitals (Table 1, Fig. 2). The MO pattern is really quite similar to those seen in the ensuing sq.NH.NH and q.NH.NH species. Indeed it will become evident that the electronic structures of the cat.NH.NH, sq.NH.NH and q.NH.NH species (this and the following three sections) are very similar, differing primarily in the electron occupation of FMOs (see Fig. 2).

The LUMO, LUMO+1 and LUMO+2 (#41–43) are anti-bonding metal-ligand (dσ*, dσ* and sσ* respectively) orbitals while LUMO+3 (#44) is the lowest π* of the ligand. The HOMO is mostly π-ligand and this is followed by the d_{xy} (δ), d_{x2-z2} (σ) and d_{yz} (π) orbitals. With the exception of d_{x2-z2} which is almost a pure d orbital, the other d orbitals are heavily mixed with ligand orbitals of appropriate symmetry. The π-interaction is expressed through the πL-dπ antibonding HOMO and the bonding dπ+Lπ orbital #37. Orbitals #36 and #39 are the corresponding bonding and antibonding MOs constructed with the δ-interaction of d_{xy} with the ligand HOMO (Fig. 1).

The ruthenium(II) tetraammine fragment has no low energy charge transfer absorption and the Ru(cat.NH.NH) fragment should also lack absorption in the visible region. The ruthenium is connected to the phenyl ring via a Ru-NH-C link. However the (cat.NH.NH) ligand is a very strong base and the interaction with Ru is highly covalent. Extensive Ru-L coupling is observed in many FMOs (Fig. 2).

Metcalfe et al. reduced [Ru(NH$_3$)$_4$(q.NH.NH)]$^{2+}$ in aqueous H$_3$PO$_4$ and thereby prepared [Ru(NH$_3$)$_4$(cat.NH$_2$.NH$_2$)]$^{2+}$ and so the experimental spectrum of [Ru(NH$_3$)$_4$(cat.NH.NH)] is not yet available. The predicted spectrum (not shown) consists of a moderate intensity band near 31,000 cm^{-1} and a much more intense band near 40,000 cm^{-1}. Both these transitions are predominantly π-π* but with appreciable MLCT character because of the mixing of d–πL content. There are a number of predicted d-d transitions in the visible to near-UV region with somewhat greater intensities than usual because of the d–πL mixing.

Table 1 Orbital symmetries, energies and compositions[a] of the frontier molecular orbitals of $[Ru(NH_3)_4(LL)]^{n+}$ (INDO/S calculations were performed on DFT optimized structures)

MO	ε (eV)	Γ	Ru (%)	LL (%)	NH$_3$ (%)
$[Ru(NH_3)_4(cat.NH.NH)]$					
44	2.1	b	10	84	7
43	2.0	a	48	4	48
42	1.9	b	43	35	22
41 LUMO	1.7	a	58	10	32
40 HOMO	−5.4	b, yz, π	19	79	2
39	−6.3	a, xy, δ	57	42	1
38	−6.8	a, x^2-z^2, σ	95	4	1
37	−7.1	b, yz, π	73	25	2
36	−7.4	a, xy, δ	32	67	1
35	−9.4	A	8	89	3
$[Ru(NH_3)_4(sq.NH.NH)]^+$					
44	−1.7	a″	0	100	0
43	−1.7	a″	0	100	0
42	−1.7	a′	55	24	21
41 LUMO	−2.1	a′	70/61	0/7	30/32
40 SOMO	−9.8	a″, b_2	24/13	74/87	2/1
39	−10.2	a″, a_2	57/54	41/45	2/1
38	−10.8	a′, a_1	94/95	4/4	2/1
37	−10.9	a″, b_2	66/72	32/26	2/2
36	−11.4	a″, a_2	33/32	66/67	1/1
35	−13.5	a″	7/11	90/84	3/5
34	−13.9	a″	6/11	93/88	1/1
$[Ru(NH_3)_4(q.NH.NH)]^{2+}$					
42	−5.8	a_2	1/0	99/100	0/0
41	−6.1	a_1	67/62	7/7	26/31
40 LUMO	−8.7	b_2	21/15	78/84	1/1
39 HOMO	−14.3	a_2	57/55	41/44	2/1
38	−14.7	b_2	67/68	31/30	2/2
37	−14.8	a_1	93/94	5/4	2/2
36	−15.4	a_2	33/34	66/65	1/1
35	−17.6	b_2	8/11	89/86	3/3
34	−18.4	a_2	6/8	93/90	1/2
$[Ru(NH_3)_4(q.NH.NH)]^{3+}$					
42	−10.0	$b_1\sigma$	54	30	16
41	−10.6	a_1	59	8	33
40 LUMO	−12.6	b_2	6	93	1
39 SOMO	−20.2	a_2	85	13	2
38	−18.9	a_2	6	94	0
37	−19.3	b_2	60	38	2
36	−19.7	a_1	92	5	3
35	−21.4	b_2	26	70	4

[a] When two numbers are reported, they correspond to compositions of MOs according to B3LYP/LanL2DZ (MPA) [45] and INDO/S calculations respectively.
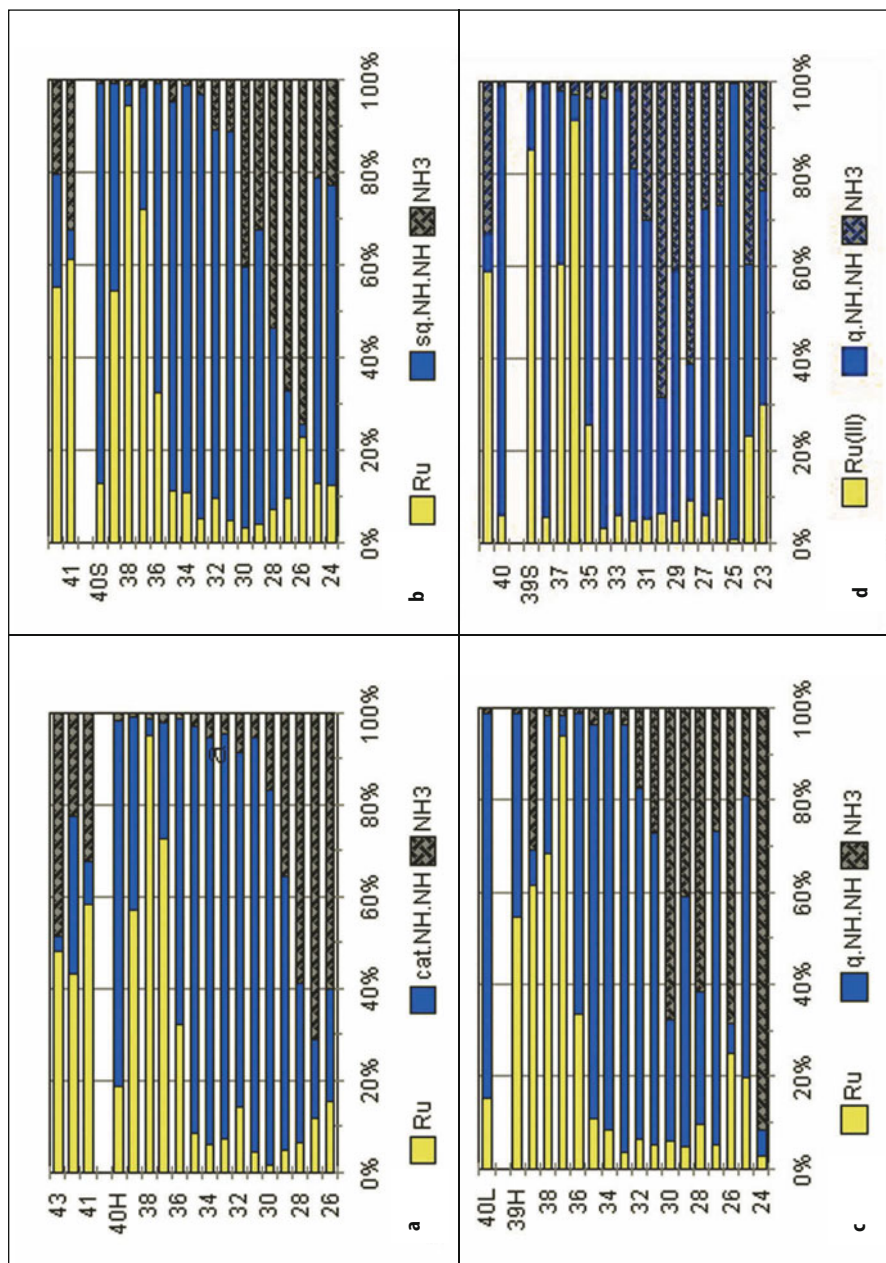
Fig. 2a–d Percentage contributions of ruthenium (Ru), quinonoid ligand (as defined) and ammonia to the FMOs of: **a** $[Ru(NH_3)_4(cat.NH.NH)]^{2+}$; **b** $[Ru(NH_3)_4(sq.NH.NH)]^+$; **c** $[Ru(NH_3)_4(q.NH.NH)]^{2+}$; **d** $[Ru^{III}(NH_3)_4(q.NH.NH)]^{3+}$. The *gap* near the top of each diagram delineates the HOMO-LUMO or SOMO-LUMO gap

3.3
[Ru(NH$_3$)$_4$(sq.NH.NH)]$^+$

Oxidation of the (cat.NH.NH) ligand lowers the energy of the first π^* and creates a hole in it so that low energy MLCT transitions should now appear. This particular species is, as yet, unknown, since oxidation of [Ru(NH$_3$)$_4$(cat.NH$_2$.NH$_2$)]$^{2+}$ led directly to [Ru(NH$_3$)$_4$(q.NH.NH)]$^{2+}$.

Geometry optimization led to a structure with C$_s$ symmetry, but it deviated only slightly from C$_{2v}$. For ease of discussion of the orbitals, we will use C$_{2v}$ symmetry representations.

Bonding in complexes of C$_{2v}$ symmetry was initially discussed by Magnuson and Taube (MT) who noted that the interaction of d$_{yz}$ (b$_2$) with ligand π^* (b$_2$) will yield a pair of bonding and anti-bonding orbitals, while d$_{xy}$ (δ,a$_2$) and d$_{x2-z2}$ (σ,a$_1$) were considered to be non-bonding. In fact there will be interactions between these latter two orbitals and ligand orbitals of a$_2$ and a$_1$ symmetry respectively, and in the case of the δ-type a$_2$ bonding interaction it can be significant (Table 1). Further, the MT model would predict that the b$_2$ orbital would lie below the other two components of the d(t$_{2g}$ in O$_h$) subset. This is true for this complex but is often not the case because interactions with other orbitals of a$_2$ or b$_2$ symmetry can be important [43].

This species is anticipated to be a free radical with a formal valence bond description of Ru^{II}sq and indeed the SOMO (#40) is 87% localized on the (sq.NH.NH) ligand. However there is appreciable Ru character in this orbital (13%). The highest filled component of the d(t$_{2g}$) set is d$_{xy}$ (a$_2$) (HOMO, #39) which (Fig. 2b) is obviously highly mixed with a ligand a$_2$ orbital. Next follows d$_{x2-z2}$ (a$_1$) (#38) which has σ-symmetry and, as such, is almost pure d, i.e. very little mixing. Then follows the d$_{yz}$ (b$_2$) orbital (#37), also highly mixed with ligand b$_2$ but to a lesser degree than is the a$_2$ orbital mixed with ligand. However, the most conspicuous feature of the mixing is that one cannot readily identify a group of three d(t$_{2g}$) orbitals, separate from other MOs. It is clear from Table 1 and Fig. 2 that, while orbitals #37–#39 may be identifiable as d(t$_{2g}$), there is d character into all orbitals from #34 to #40.

3.3.1
Electronic Spectrum of [Ru(NH$_3$)$_4$(sq.NH.NH)]$^+$

The predicted electronic spectrum of this species is shown in Fig. 3.

The low-energy, broad and weak, absorption is typical of many semiquinone derivatives and is an internal π-π transition of the semiquinone; however it evidently has significant MLCT character in view of the d$_{xy}$ content of orbital #39. The first, and most intense, charge transfer transition near 19,000 cm^{-1} is #37→#40 (SOMO), the b$_2$→b$_2^*$ transition where the same d$_{yz}$ (dπ) orbital is coupled into both #37 and #40. *It is a common theme in this entire series of complexes that this transition will give rise to the most intense charge transfer band because of the extensive overlap between the ground and excited state.*

To higher energy are a series of π-π^* transitions as identified, but most have significant MLCT character, especially #39→#44.
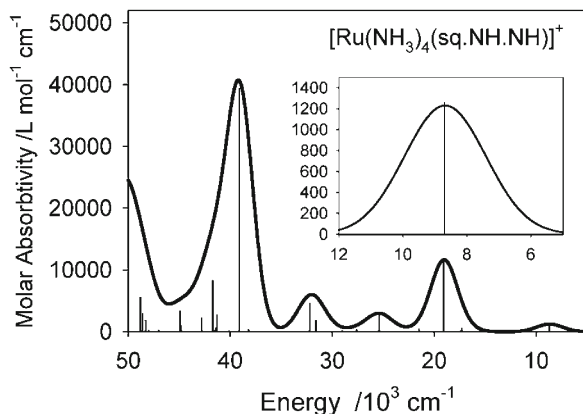
Fig. 3 The predicted electronic spectrum and assignments for $[Ru(NH_3)_4(sq.NH.NH)]^+$. The *vertical bars* in this, and subsequent figures, indicate MLCT transitions scaled, according to their relative oscillator strengths, to the molar absorptivity

3.4
$[Ru(NH_3)_4(q.NH.NH)]^{2+}$

This system has been explored in some considerable depth. We present it in some detail here, to use as a model for the other species under consideration later in the chapter. The *o*-benzoquinonediimine ligand and its relatives are known to be excellent π-accepting ligands [17, 45, 80, 84], i.e. there is extensive coupling between metal d and ligand π-orbitals. On the basis of DFT geometry optimization, the complex has C_{2v} symmetry and therefore it is the d_{yz} (b_2) orbital which couples to the LUMO (π*) b_2 (Fig. 4).

The orbital mixing information is also displayed graphically in Fig. 2. The LUMO is fairly well separated, energetically, from the next set of unoccupied orbitals so that transitions to this level alone dominate the visible spectrum (see the next section). The LUMO (b_2) has substantial Ru(4d) character. It is pertinent that one does not see an obvious t_{2g} set, i.e. three frontier orbitals with a large Ru(4d) component. Rather, the t_{2g} mixing with ligand π- and π*-orbitals is so
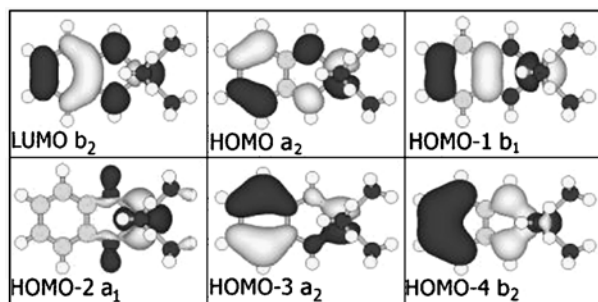
Fig. 4 FMOs of the $[Ru(NH_3)_4(q.NH.NH)]^{2+}$ species (INDO/S calculations)

Fig. 5 Comparison of the experimental spectrum (*solid line*) of $[Ru(NH_3)_4(q.NH.NH)]^{2+}$ (recorded in 0.1 mol/l H_3PO_4 aqueous solution) with the INDO/S calculated spectrum (*hatched line*)

extensive that the orbitals #34–#39 (HOMO) all have quite substantial 4d character (Table 1, Fig. 5). The purest (>90%) is #37, HOMO-2 (a_1) which has σ-symmetry with respect to the (q.NH.NH) ligand plane and so is only very weakly mixed. The d_{yz} (b_2) orbital density is spread significantly over three MOs, the LUMO, HOMO-1 and HOMO-4 (Table 1, Fig. 2) highlighting not only the extensive mixing, but also the over-simplification of the MT model. Mixing with the $d_{xy}(a_2)$ orbital is also seen to be extensive and spread between HOMO, HOMO-3 and HOMO-5.

3.4.1
Electronic Spectrum of [Ru(NH₃)₄(q.NH.NH)]²⁺

The visible absorption of this species arises from a series of excited states which are generated by excitation of electrons from the highest occupied orbitals to the LUMO. The most intense MLCT transition, near 20,000 cm⁻¹, is expected to arise from excitation of an electron in the d_{yz} ($d\pi$, b_2) to the LUMO ($^1A_1\leftarrow^1A_1$). Because of the extensive mixing between these orbitals (Table 1) which means that the ground and excited states will overlap appreciably, an intense transition can be expected. This can be described as MLCT with significant π-π* character. Comparison of the experimental spectrum with that calculated using INDO/S is shown in Fig. 5. Agreement is excellent.

The transition from the HOMO to the LUMO ($^1B_1\leftarrow^1A_1$) gives rise to a very weak long-wavelength absorption near 10,000 cm⁻¹ (shown in Fig. 5). The transition from HOMO-2 is overlap forbidden and has vanishingly small intensity. The HOMO-3 to LUMO transition ($^1B_1\leftarrow^1A_1$) is calculated to appear at 23,000 cm⁻¹; its intensity is ~10% of the principal MLCT band at 22,000 cm⁻¹ and apparently this transition is obscured by the principal band. The shoulder observed near 33,300 cm⁻¹ may be d-d in origin. The intense UV feature near

38,500 cm^{-1} is HOMO→LUMO+2 ($^1A_1$←$^1A_1$) and is primarily a π-π* (q.NH.NH) transition. For a detailed and tabulated comparison of experimental vs calculated spectra, see [45, 80].

3.5
[Ru(NH$_3$)$_4$(q.NH.NH)]$^{3+}$

Oxidation of [Ru(NH$_3$)$_4$(q.NH.NH)]$^{2+}$ leads to a species, [Ru(NH$_3$)$_4$(q.NH.NH)]$^{3+}$ formally containing Ru^{III}, the only example of Ru^{III} bonded to (q.NH.NH). Its electronic structure and spectrum are therefore of especial interest. The optimized structure of the complex has C$_{2v}$ symmetry with frontier orbital descriptions and mixing shown in Table 1. The SOMO is mainly on the metal and the LUMO, a π*(q.NH.NH) orbital has only 6% Ru content much less than in the species of lower oxidation state noted above. This is, of course, consistent with the higher positive charge on the Ru center. Unlike the previous cases, one can easily identify the set of three d(t$_{2g}$) orbitals in this species as MOs #39, #37 and #36, being much less mixed with ligand orbitals (Fig. 2). Thus this species is best described as Ru^{III}(q.NH.NH).

However, one can still recognize features which are similar to those seen in the Ru^{II} species. Thus the in and out of phase coupled a$_2$(δ) orbitals appear at #38 and #39 but the coupling is weak with #38 being almost pure ligand π and #39 being almost pure metal d. The somewhat greater π(b$_2$) coupling results in an appreciable re-distribution of the d$_{yz}$ orbital over MOs #35, #37 and #40.

3.5.1
Electronic Spectrum of [Ru(NH$_3$)$_4$(q.NH.NH)]$^{3+}$

The experimental and predicted (INDO/S) spectra of this species are shown in Fig. 6. The overall agreement is very satisfactory. Aside from variations in the degree of mixing, all the species have rather similar electronic descriptions so that the major visible region band near 26,300 cm^{-1} is still the b$_2$→b$_2$ MLCT transition (#37→#40 LUMO) even though the species contains Ru^{III}. The intense UV band near 45,500 cm^{-1} is another b$_2$→b$_2$ transition (#35→#40 LUMO) which is π→π* (q.NH.NH) with appreciable MLCT character. The weaker band lying between these two transitions (ca. 31,300 cm^{-1}) has very mixed provenance and cannot be assigned to just one transition. It is natural to wonder whether we should not see an LMCT transition to the SOMO. Indeed this (e.g. #35→#39) is one of the contributors to the ca. 31,300 cm^{-1} absorption. The very weak predicted absorption near 17,200 cm^{-1} (which probably corresponds with the low energy shoulder seen in the experimental spectrum) is actually a composite of at least three weak transitions comprising both MLCT from the d(a$_2$)→b$_2$ LUMO, and another component of the b$_2$→b$_2$ (LUMO) MLCT transition but also an LMCT transition #38→#39. We see no strong LMCT band likely because the SOMO is the dδ orbital of a$_2$ symmetry and its overlap with ligand orbitals, especially in the Ru^{III} oxidation state, is minimal.

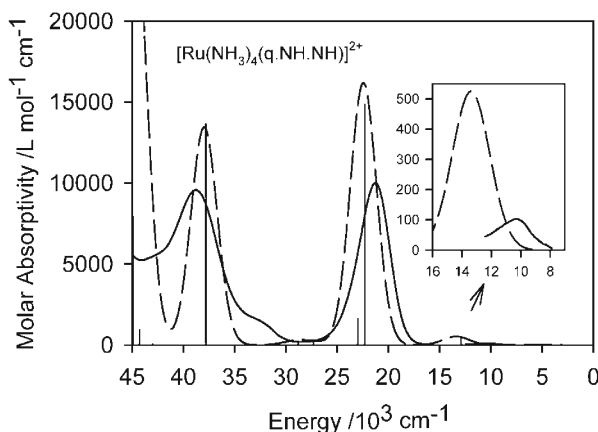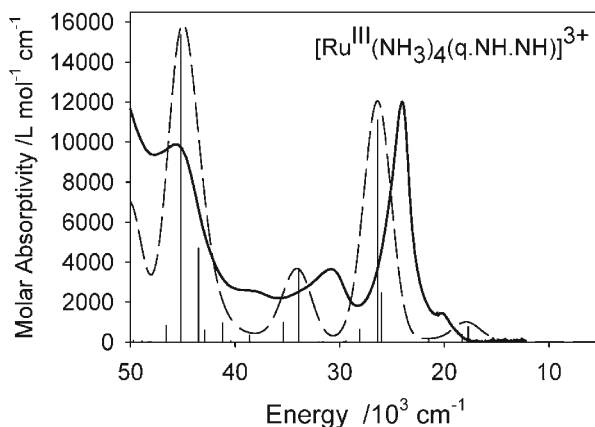**Fig. 6** Comparison of the experimental spectrum (*solid line*) of $[Ru(NH_3)_4(q.NH.NH)]^{3+}$ (recorded in 0.1 mol/l H_3PO_4 aqueous solution) with the INDO/S calculated spectrum (*hatched line*)

4
Bis(2,2′-bipyridine)ruthenium Complexes, $[Ru(bpy)_2(X.Y)]^{n+}$ (X,Y=O, NH, S)

This group of complexes will be discussed in groups defined by net oxidation state and symmetry and in somewhat less detail than the tetraammine systems above. For greater detail see [52, 65]. The basic principles laid out above still apply but with some modifications imposed by the lower symmetry. If X=Y then the highest symmetry is C_2. The principle axis is still the z axis bisecting the (X.X) ligand. In descending from C_{2v} to C_2, the d_{x2-z2} (a_1) and d_{xy} (a_2) orbitals now transform as (a) and can, in principle mix, while the d_{yz} (b_2) transforms as (b) and so is less affected by the descent in symmetry. There remains the possibility for strong coupling between the metal $d\pi$ and (X.X) ligand $\pi^\star$ orbitals. The spectroscopic features observed with the tetraammine complexes are basically repeated here but with the added complication of the presence of MLCT transitions to the bipyridine ligands, and the possibility of L′LCT transitions from an electron rich (X.Y) ligand to bpy.

4.1
$[Ru(bpy)_2(cat.NH_2.NH_2)]^{2+}$

The (cat.NH_2.NH_2) ligand is innocuous, similar to ethylenediamine, and will give rise to no low energy MLCT absorption. The ruthenium atom is separated from the unsaturated ring by two single bonds. Thus the frontier molecular orbitals and visible and near-UV spectra of this species depend primarily on the bipyridine ligands as can be clearly seen from the density-of-states plot of $[Ru(bpy)_2(cat.NH_2.NH_2)]^{2+}$ (Fig. 8). It is therefore a useful species to introduce the anticipated behavior of a bis(bipyridine) ruthenium fragment.

   Recognize that the bipyridine unit is asymmetrically bound; call them bpy1 and bpy2. Then one pyridine ring of bpy1 is *trans* to a pyridine ring of bpy2, and
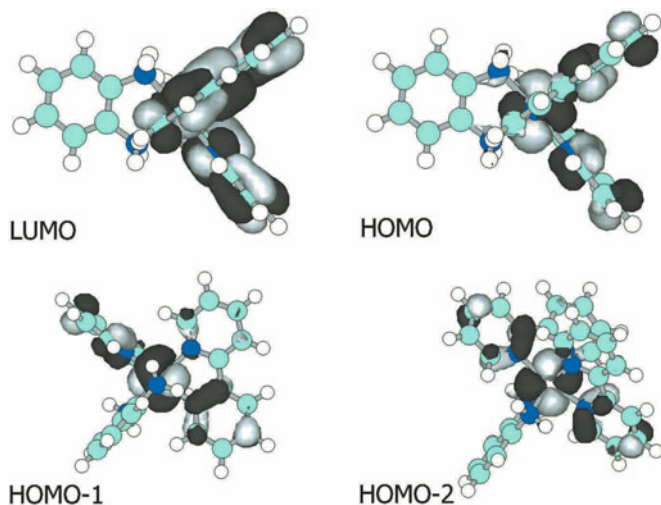
Fig. 7a–d   Frontier molecular orbitals of $[Ru(bpy)_2(cat.NH_2.NH_2)]^{2+}$

the other pyridine ring of bpy1 is *cis* to a pyridine ring on bpy2. The pair of *trans* pyridine rings have their molecular planes orthogonal to one another, while the planes of the *cis* pyridine rings are aligned with one another but at an angle of approximately 90°. This difference in orientation becomes crucial when one questions how the Ru(d) orbitals will interact with the bpy ligands.

The HOMO (Fig. 7) is the dσ (in the plane of the cat.NH$_2$.NH$_2$) orbital and this is nicely organized to couple the pair of *cis* pyridine rings. There is relatively little contribution to this MO from the uncoupled pyridine rings. The HOMO-1 is the dδ orbital and HOMO-2 is the dπ orbital, both of which are aligned appropriately to couple the pair of *trans* pyridine rings (Fig. 7). However, as shown in Table 2, these ruthenium d orbitals are much purer and more readily recognized as the d(t_{2g}) set with 20% or less contribution of the ligands. There is about 5% Ru(d) mixed into the LUMO+1 which is typical for ruthenium bipyridine species. Nevertheless the coupling is strong enough that these orbitals tend to localize on one pyridine ring rather than (equally) over both pyridine rings.

Figure 8 is a 'density-of-states' (DOS) plot which is a pictorial representation of the energy and compositions of the FMOs. Since energy levels are quantized in molecular solids, it should not be confused with more conventional DOS plots used in solid state quantum mechanical studies.

The LUMO (π_1^*), LUMO+1 (π_2^*) and LUMO+2 (π_3^*) of the free 2,2′- bipyridine ligand are shown in Fig. 9. These are anti-symmetric (LUMO, LUMO+2) and symmetric (LUMO+1) with respect to the twofold axis as was initially pointed out by Orgel. In this bipyridine series, the first six bpy-based unoccupied orbitals will be the in- and out-of-phase combinations of these three π* bpy orbitals.

However, because π_1^* and π_3^* have the same symmetry, they will couple together and so the situation is a little more complex than one might initially realize. π_1^*, π_2^* and π_3^* describe the first three unoccupied orbitals of the free bipyridine
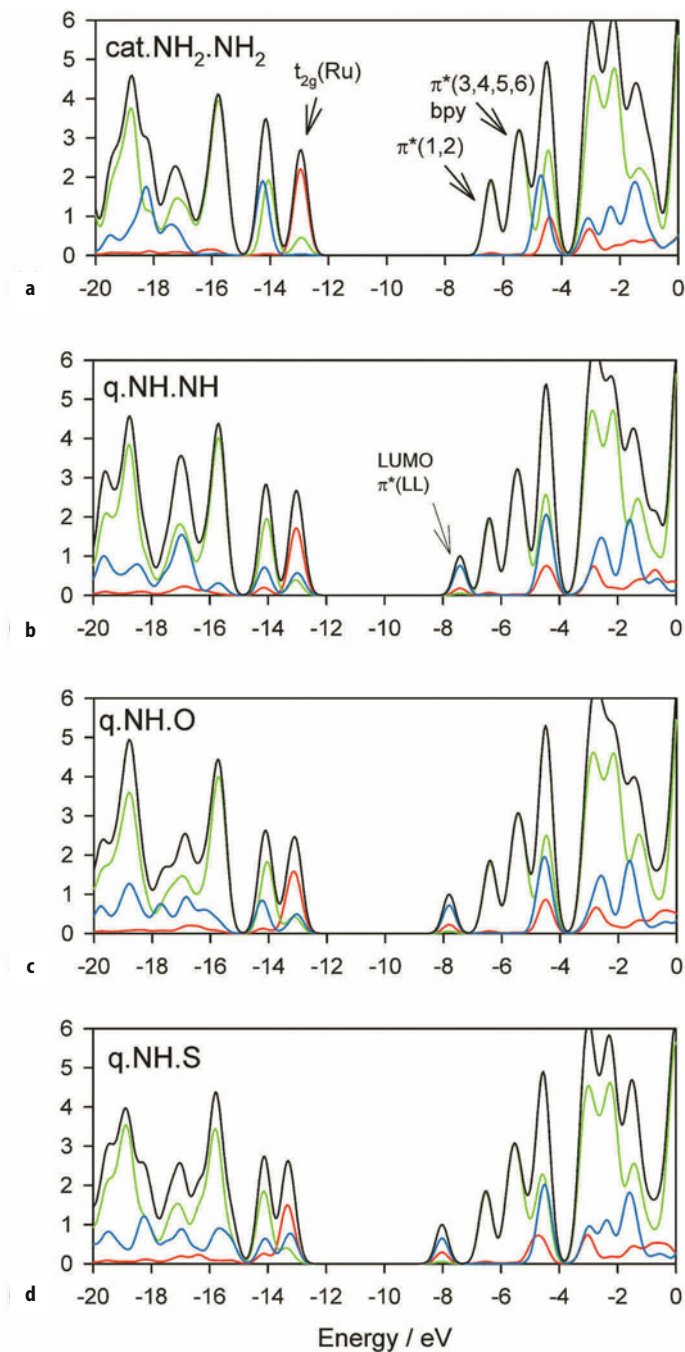
Fig. 8a–d Density-of-states plots for: **a** $[Ru(bpy)_2(cat.NH_2.NH_2)]^{2+}$; **b** $[Ru(bpy)_2(q.NH.NH)]^{2+}$; **c** $[Ru(bpy)_2(q.NH.O)]^{2+}$; **d** $[Ru(bpy)_2(q.NH.S)]^{2+}$. The contributions are ruthenium (*red*), bipyridine (*green*) and LL ligand (*blue*). The total DOS is a *black line*

Table 2 Orbital symmetries, energies and compositions of the frontier molecular orbitals of a selection of $[Ru(bpy)_2(LL)]^{n+}$ (INDO/S calculations were performed on DFT optimized structures)[a]

#MO	ε (eV)	Γ	Ru (%)	LL (%)	bpy (%)
$[Ru(bpy)_2(cat.NH_2.NH_2)]^{2+}$					
86	−5.6	$\pi^\star(4)$	1	0	99
85	−5.6	$\pi^\star(3)$	0	0	100
84	−6.4	$\pi^\star(2), d\sigma$	5	0	95
83 LUMO	−6.5	$\pi^\star(1), d\pi$	2	0	98
82 HOMO	−12.8	$d\sigma$	77	2	21
81	−13.0	$d\delta$	83	1	16
80	−13.1	$d\pi$	85	1	14
$Ru(bpy)_2(cat.O.O)$					
86	−0.1	$a, \pi^\star(4)$	5	0	95
85	−0.3	$b, \pi^\star(3)$	1	0	99
84	−0.8	$a, \pi^\star(2), d\sigma$	10	1	89
83 LUMO	−1.0	$b, \pi^\star(1), d\pi$	7	0	93
82 HOMO	−6.0	$b, d\pi$	24	67	9
81	−6.4	$a, d\sigma$	61	10	29
80	−6.6	$a, d\delta$	73	17	10
79	−6.9	$b, d\pi$	48	37	15
78	−7.4	$a, d\delta$	10	87	3
$[Ru(bpy)_2(cat.NH.O)]^+$					
84	−0.9	$\pi^\star(2), d\sigma$	10	1	89
83 LUMO	−1.1	$\pi^\star(1)$	9	2	89
82 HOMO	−5.3	$d\pi(NH)$	18	72	10
81	−6.5	$d\pi'(O)$	55	29	16
80	−6.6	$d\sigma$	66	14	20
79	−6.9	$d\pi$	55	28	17
78	−7.4	$\pi, d\delta$	20	75	5
$[Ru(bpy)_2(cat.NH_2.O)]^{2+}$					
84	−3.6	$\pi^\star(2)$	6	0	94
83 LUMO	−3.8	$\pi^\star(1)$	5	0	95
82 HOMO	−9.5	$d\pi(O)$	56	32	12
81	−9.6	$d\sigma$	74	6	20
80	−9.9	$d\pi(NH_2)$	82	1	17
79	−10.2	$\pi, d\pi(O)$	24	70	6
78	−10.9	π	0	99	1
$[Ru(bpy)_2(sq.O.O)]^+$					
86	−2.7	$a, \pi^\star(4)$	3	0	97
85	−2.8	$b, \pi^\star(3)$	1	0	99
84	−3.5	$a, \pi^\star(2)$	7	0	93
83 LUMO	−3.6	$b, \pi^\star(1)$	3	0	97
82 SOMO	−10.1	$b, d\pi$	9	90	1
81	−9.4	$a, d\sigma$	70	6	24
80	−9.6	$a, d\delta$	81	6	13
79	−9.8	$b, \pi, d\pi$	70	14	16

Table 2 (continued)

#MO	ε (eV)	Γ	Ru (%)	LL (%)	bpy (%)
$[Ru(bpy)_2(sq.NH.O)]^+$					
84	−3.6	$\pi^\star(2)$	6	0	94
83 LUMO	−3.7	$\pi^\star(1)$	4	0	96
82 SOMO	−10.4	π	14	84	2
81	−9.6	$d\sigma$	71	6	23
80	−9.7		66	25	9
79	−10.0		63	23	14
78	−10.7		13	83	4
$[Ru(bpy)_2(q.NH.NH)]^{2+}$					
83	−6.4	$b, \pi^\star(1)$	3	2	95
82 LUMO	−7.4	$b, d\pi$	18	76	6
81 HOMO	−12.9	$a, d\delta$	62	30	8
80	−13.1	$a, d\sigma$	74	4	22
79	−13.1	$b, d\pi$	56	32	12
78	−14.0	b, π	1	1	98
77	−14.0	a, π	4	27	69
76	−14.2	$a, d\delta$	15	48	37
$[Ru(bpy)_2(q.NH.O)]^{2+}$					
83	−6.5	$\pi^\star(1)$	4	1	95
82 LUMO	−7.8	$\pi^\star, d\pi(NH)$	22	72	6
81 HOMO	−13.0	$d\pi(NH)$	50	40	10
80	−13.1	$d\sigma$	70	6	24
79	−13.3	$d\pi(O)$	72	12	16
78	−14.0	π	3	3	94
77	−14.1	π	1	9	90
76	−14.2	$\pi, d\delta$	10	76	14

[a] Some small variation between the data in this Table and that previously published by us is due to some small changes in the semi-empirical INDO/S parameters we subsequently used to be consistent with another research group

ligand. For clarity we define $\pi^\star(1)$ to $\pi^\star(6)$ as the first six unoccupied molecular orbitals belong to both bipyridine ligands in the bis(bipyridine) complexes. Close examination of the *individual* bipyridine MOs in $\pi^\star(1)$ reveals that this individual component on one bipyridine ligand can be written as an in-phase, roughly equal, mixture of $\pi_1^\star$ and $\pi_3^\star$, let us call that $\pi_{1m}^\star$. Then $\pi^\star(1)$ and $\pi^\star(2)$ are out- and in-phase combinations of $\pi_{1m}^\star$ on each bipyridine unit. Note then that $\pi^\star(3)$ and $\pi^\star(4)$ are in- and out-of-phase combinations of free ligand bipyridine $\pi_2^\star$. Finally close examination of $\pi^\star(5)$ shows that it is composed, on each bipyridine ring as the $\pi_3^\star$ - $\pi_1^\star$ mixture and in and out of phase combinations of this lead to $\pi^\star(5)$ and $\pi^\star(6)$.

Given that there are three filled d orbitals, up to six transitions are feasible to each pair of $\pi^\star$ (1), $\pi^\star(2)$, and $\pi^\star(3)$, $\pi^\star(4)$ and $\pi^\star(5)$, $\pi^\star(6)$ bipyridine orbitals and indeed many of them have non-zero intensity in the lower symmetry species (see Fig. 10). As discussed below, they mostly group together in three energy regions and can be simply described as d→$\pi^\star(1,2)$, d→$\pi^\star(3,4)$ and d→$\pi^\star(5,6)$
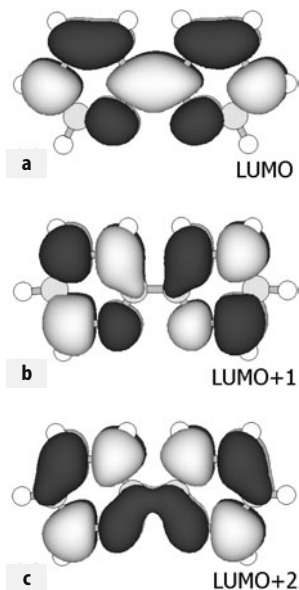
Fig. 9 **a** LUMO (π_1^*) of 2,2′-bipyridine. **b** LUMO+1 (π_2^*) of 2,2′-bipyridine. **c** LUMO+2 (π_3^*) of 2,2′-bipyridine

4.1.1
Electronic Spectrum of [Ru(bpy)$_2$(cat.NH$_2$.NH$_2$)]$^{2+}$

Figure 10 shows the predicted electronic spectrum of this species. The overall features agree with the experimental data. This is the archetype for this group of complexes, so it will be discussed in some depth. Generally speaking, the first visible region transition in [Ru(bpy)$_2$X$_2$] complexes, usually observed near 25,000 cm^{-1}, is assigned as d→π^*(1,2) MLCT (bpy) and a peak or shoulder usually observed about 8000 cm^{-1} to higher energy is assigned as d→π^*(3,4) MLCT. More intense absorption following this band is usually treated as π-π^* internal to bipyridine.

The intense visible band in this cat.NH$_2$.NH$_2$ species is assigned, according to the INDO/S calculation, as HOMO-1 #81→LUMO #83.

However, as shown in Fig. 10, there are four MLCT transitions to π^*(1,2) of some intensity under the visible band envelope (plus a very weak transition to a higher π^* level). In fact, in this low symmetry, five transitions do have significant intensity but only four are noted above because two overlap. The most intense corresponds to the HOMO-1→LUMO excitation with 75% MLCT character.

The next band near 32,000 cm^{-1} is seen to comprise all six possible transitions to the two π^*(3,4) acceptor orbitals, while to higher energy are a series of MLCT to higher π^* acceptor levels. Note three of the weak features in the 30–35,000 cm^{-1} range are transitions to π^*(5,6). In fact most of the absorption is due to MLCT. There is a small π-π^* contribution in the near UV but the MLCT transitions apparently dominate.
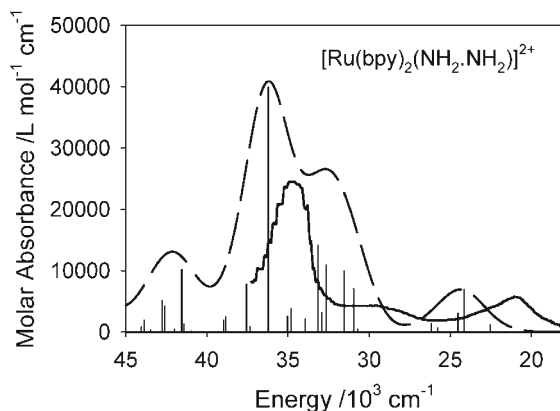
Fig. 10 Comparison of the experimental spectrum (solid line) of $[Ru(bpy)_2(cat.NH_2.NH_2)]^{2+}$ with the INDO/S calculated spectrum (hatched line). (The structure on the expt.data is an artifact)

4.2
$[Ru(bpy)_2(cat.X.X)]$ Complexes

We discuss here the reduced but not protonated $[Ru(bpy)_2(cat.O.O)]$ complex. This neutral species displays significant metal-ligand mixing with major Ru d contributions to five occupied frontier orbitals and several unoccupied π^* orbitals (Table 2). For example, MOs #80–82 are metal-cat ligand anti-bonding with symmetry as shown in Table 2, while #78 and #79 are bonding. The catecholate (cat.O.O) ligand is very electron rich and confers significant covalency on the Ru-ligand bonds.

The electronic spectrum of the catecholate species was recorded by Haga et al. The spectroscopic characteristics of the Ru-bpy fragment can be expected to parallel largely those of the previous, fully protonated, species, but shifted to lower energies because the dianionic (cat.O.O) ligand will render the ruthenium center a better electron donor. However the HOMO is now a π-orbital localized on the (cat.O.O) ligand. It is the orbital which will be the LUMO π^* in the quinonoid species. Just as in that species (see below) there is extensive mixing with the metal $d\pi$ orbital (Table 3). Transitions from this orbital to the series of π^* bpy levels will contribute in a major way to the observed electronic spectrum, so-called ligand to ligand or L′LCT transitions. The lowest energy L′LCT bands in the $Ru(bpy)_2(cat.O.O)$ species are predicted to lie at 14,600–14,900 cm^{-1} (mostly #82 (HOMO)→#83,84) agreeing well with a broad weak band seen experimentally at 13,700 cm^{-1}. Because of the extensive mixing of metal d into orbital #82, these transitions can also be said to have MLCT character.

The first strong d→π^*(1,2) band is predicted to lie at 16,700 cm^{-1}, and is experimentally seen at 16,200 cm^{-1}. A series of L′LCT and MLCT bands span the region 22,000–27,000 cm^{-1} and also agree reasonably with experiment. Ligand-ligand mixing, i.e. molecular orbitals containing major contributions from both bpy and catecholate ligand, is much more prevalent in these low symmetry

Table 3 Energy and composition[a] of the redox active molecular orbital (#82)[b] of the [Ru(bpy)$_2$(LL)]$^{n+}$ complexes

LL	cat.X.Y		sq.X.Y		q.X.Y	
	ε (eV)	%[a]	ε (eV)	%[a]	ε (eV)	%[a]
O.O	−6.0	24, 67, 9	−10.1	8, 90, 1	−8.4	22, 73, 5
NH.NH	−5.0	12, 73, 15	−9.0	12, 86, 2	−7.4	18, 76, 6
NH.O	−5.3	18, 72, 10	−10.4	14, 84, 2	−7.8	22, 72, 6
NH.S	−5.5	21, 70, 9	−10.6	20, 78, 2	−8.0	29, 65, 6
NH$_2$.O	−9.5	56, 32, 12	–	–	–	–
NH$_2$.S	−9.6	58, 30, 12	–	–	–	–

[a] Ru(%), LL(%), bpy(%) respectively.
[b] #82 is the HOMO in the cat, the SOMO in the sq and the LUMO in the q complexes.

species. This should be recognized when resonance Raman studies are used to probe the provenance of transitions, i.e. for example, d→π* (bpy) transitions may show X.Y ligand resonance enhancement because of such mixing.

The [Ru(bpy)$_2$(cat.NH.NH)] species has never been reported. It contains the extremely electron rich (cat.NH.NH)ligand and should give rise to quite low energy L′LCT transitions The lowest energy optimized structure is predicted to exist in a spin triplet rather than a spin singlet configuration and so we exclude it from this discussion until such a time as it is experimentally available.

4.3
[Ru(bpy)$_2$(cat.NH.X)] Complexes

The asymmetry in this species does not have a major effect on the predicted electronic structure or spectrum when compared with the symmetric cat.X.X^{2-} species. Neither species, X=O or S, has yet been isolated. However, it is worth exploring in some detail how their electronic characteristics would appear. Rather than dπ and dδ orbitals as aligned along the z axis in the cat.X.X species, there are now two π-type orbitals which are aligned along the Ru-NH (dπ(NH)) and Ru-X (dπ(X)) bond vectors. For example for the cat.NH.O species MOs, #82 (HOMO) and #83 (LUMO) are π-anti-bonding along the Ru-NH vector while #79 and #78 are dπ and dδ bonding respectively and interact more symmetrically with the (cat.NH.O)$^{2-}$ ligand. There is significant Ru d electron density spread over five d orbitals plus additional coupling to the π* (bpy) (see Table 2, Fig. 11). The cat.NH.S complex has similar MOs. The lowest energy L′LCT is predicted at 9600–10,700 cm^{-1} in both the NH.O and NH.S species. An unusual feature is that some components of the d→π*(3,4) transitions appear as low in energy as the d→π*(1,2) as also commented on above. One might conclude that electronic coupling occurs primarily through the NH donor being the more basic of the two. These neutral species reveal a great deal more metal-ligand (and ligand-ligand) coupling than the cationic, fully reduced, species (below).
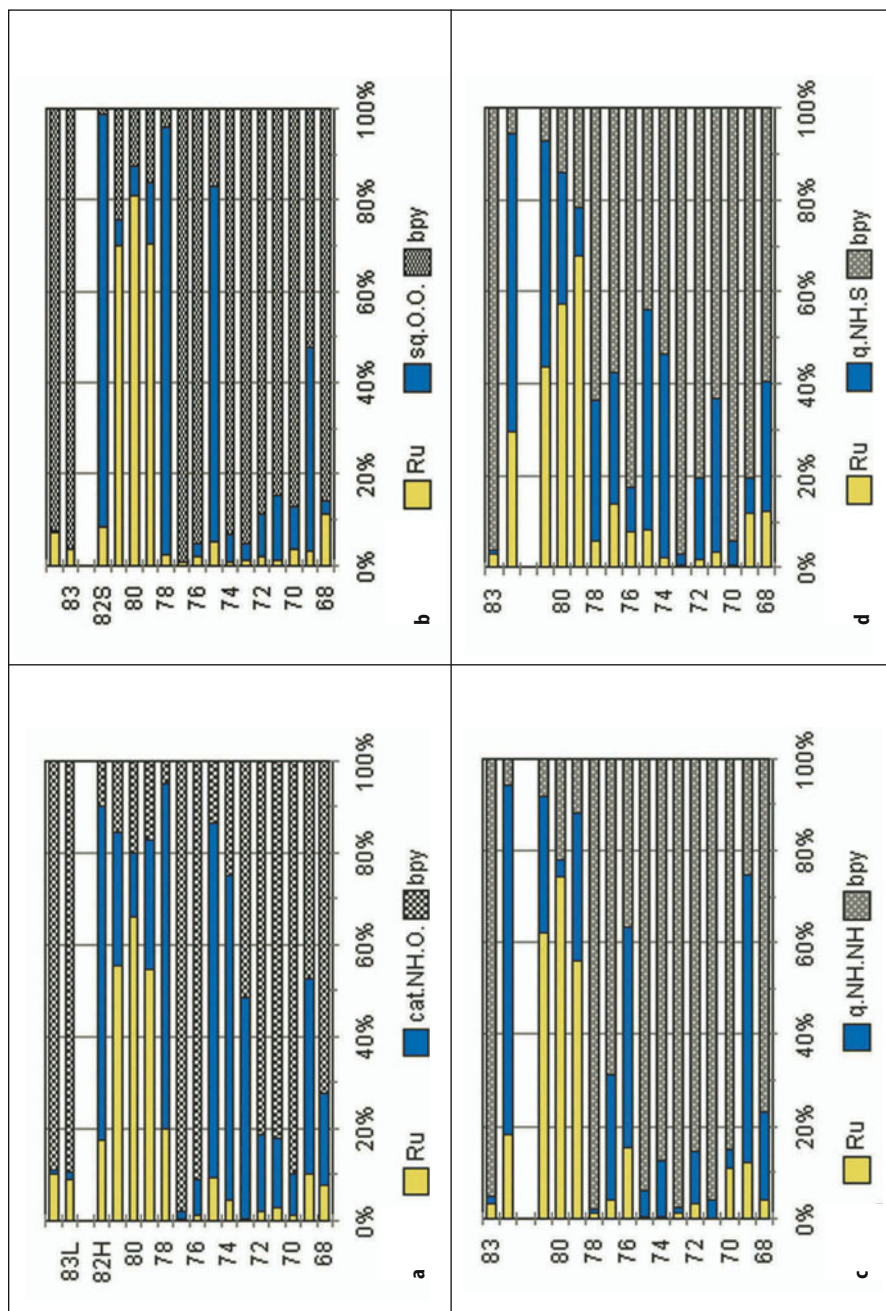
Fig. 11a–d Percentage contributions of ruthenium (Ru), quinonoid ligand (as defined) and 2,2′-bipyridine to the FMOs of: **a** [Ru(bpy)$_2$(cat.NH.O)]$^{2+}$; **b** [Ru(bpy)$_2$(sq.O.O)]$^+$; **c** [Ru(bpy)$_2$(q.NH.NH)]$^{2+}$; **d** [Ru(bpy)$_2$(q.NH.S)]$^{2+}$. The *gap* near the top of each diagram delineates the HOMO-LUMO or SOMO-LUMO gap
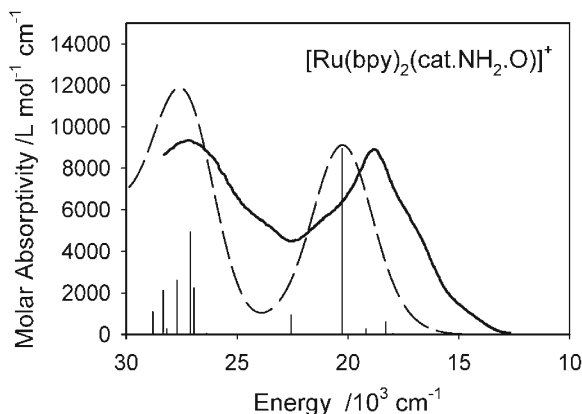
Fig. 12 Experimental (*solid line*) and INDO/S predicted (*hatched line*) spectra of [Ru(bpy)$_2$(cat.NH$_2$.O)]$^+$ [87]

All of these species containing the very electron rich dianionic (cat.X.X or cat.X.Y) ligand show ruthenium mixing of the order of 10% to the π*(1,2) bipyridine MOs (Fig. 12), substantially larger than the 5% commonly observed in most other Ru(bpy)$_2$(LL) species.

4.4
[Ru(bpy)$_2$(cat.NH$_2$.X)]$^+$ Complexes (X=O, S)

The protonated reduced species, the (cat.NH$_2$.X) ligands, are much poorer donors than the dianionic species discussed above. A consequence is rather less metal-ligand mixing but the d electron density is still distributed over four filled frontier orbitals (Table 2). The X atom is now the more strongly donor ligating atom and the dπ orbital in the HOMO (#82) is oriented anti-bonding with respect to that atom. MO #79 is the corresponding bonding interaction. The other two d orbitals are relatively pure (Table 2). Thus it is the interaction with the electron rich O- or S-donor atom which is the main source of coupling with the (cat.NH$_2$.X) ligand.

4.4.1
Electronic Spectrum of [Ru(bpy)$_2$(cat.NH$_2$.O)]$^+$

We can anticipate that the spectrum of this species, containing the (cat.NH$_2$.O)$^-$ ligand, will be similar to that of *Ru(bpy)$_2$(cat.NH.O)* but with both the L'LCT (cat→π* (bpy)) and d→π* (bpy) shifted to higher energies. The shift would be greatest for the L'LCT bands and this is seen to be the case.

The first two predicted L'LCT bands occur at 18,000 and 22,500 cm^{-1} but are rather weak. They probably contribute to the low energy shoulder seen in the experimental data (Fig. 12). The very strong band near 20,000 cm^{-1} is an excitation combining both MLCT to π*(1,2) and L'LCT to π*(1,2), the former being

rather more important. Other components under that first band involve other d→π*(1,2) transitions, all with some reasonable intensity in this very low symmetry species. Another intense L'LCT, to π*(3,4), is predicted at 27,100 cm⁻¹ and contributes in a major way, along with the MLCT to π*(3,4), to the band above 25,000 cm⁻¹ in Fig. 11.

4.5
[Ru(bpy)₂(sq.X.X)]⁺ Complexes–C₂ Symmetry

In these complexes, the SOMO is mainly on the semiquinone ligand and there is moderate coupling to the metal dπ orbital (Tables 2 and 3). The three d(t₂g) orbitals remain moderately pure. Above the SOMO and these d orbitals lie the two pairs of π*(1,2) and π*(3,4) orbitals. The presence of the hole on the semiquinone ligand, as the SOMO, should lead to properties similar to those discussed above with the superimposition of the Ru-bpy components. L'LCT transitions from semiquinone to π* (bpy) can be anticipated. Since we are one oxidation state higher than the cat.X.X series species, we can expect them at higher energies since the ligand must be more difficult than the former to oxidize. They now fall in the visible, rather than NIR, region and are generally very weak and obscured by the d→π* (bpy or sq) MLCT transitions. Thus in [Ru(bpy)₂(sq.O.O)]⁺ the lowest such transition is predicted near 21,000 cm⁻¹, while in the more electron rich [Ru(bpy)₂(sq.NH.NH)]⁺ it falls near 14,000 cm⁻¹. The sq/cat oxidation of the latter is 0.76 V (ca. 6100 cm⁻¹) more negative than the former, comparable to the 7000 cm⁻¹ optical bandshift [23, 42].

4.5.1
[Ru(bpy)₂(sq.O.O)]⁺ (SOMO is #82)

The major bands in [Ru(bpy)₂(sq.O.O)]⁺ occur experimentally at 11,250, 20,300 and 29,050 cm⁻¹. The predicted data are in excellent agreement with experiment, as follows. A moderately strong band is predicted at 11,100 cm⁻¹ assigned to #79, dπ→SOMO (MLCT) corresponding with a transition which might be written (bpy)₂Ru^II.sq→(bpy)₂Ru^III.cat. Weaker components to lower energy (8400 and 9100 cm⁻¹) are MLCT from the other two d orbitals. A strong d→π*(1,2) bpy MLCT component is predicted at 21,300 cm⁻¹ with some weaker components to slightly lower energy. This is followed by three roughly equal intensity transitions from the three d orbitals to π*(3,4) components at 27,700, 28,500 and 29,000 cm⁻¹ clearly accounting for the experimental band at 29,050 cm⁻¹.

4.5.2
[Ru(bpy)₂(sq.NH.NH)]⁺ (SOMO is #82)

The situation in this complex is essentially the same as that for the sq.O.O species above and the agreement between experimental and predicted spectra is good though not as good as for the former species. The major difference is that the lowest energy intense #79, dπ→SOMO transition shifts from around 11,000 cm⁻¹ in the sq.O.O species to 16,000 cm⁻¹ (expt.) (predicted 19,100 cm⁻¹) in this species.

This is clearly due to the fact that the (sq.NH.NH) ligand is much more electron rich than the (sq.O.O)⁻ ligand and more difficult to reduce formally to the cat oxidation level. Indeed one may compare the observed sq/cat reduction potentials for these two species (–1.13 V and –0.57 V vs SCE) hence differing by ca. 4500 cm⁻¹ while the observed MLCT transitions differ by ca. 4900 cm⁻¹. Although we do not discuss such optical-electrochemical relationships in depth here, they do play an important role in understanding optical, charge transfer, spectra [29, 32].

4.6
[Ru(bpy)$_2$(sq.X.Y)]$^+$

There is a noticeably increased degree of mixing between the d and ligand orbitals in these lower symmetry species relative to the X.X series; five filled frontier MO have appreciable metal character (Table 2). The overall spectroscopic features are the same as for the symmetric species but the asymmetry does lead to greater mixing between the d and ligand orbitals.

4.6.1
Electronic Spectra of [Ru(bpy)$_2$(sq.NH.O)]$^+$

The first major absorption (14,700 cm⁻¹ expt.) is mostly #79→#82 SOMO (MLCT to the semiquinone) but there are quite a few other contributing excitations. A number of weaker bands involving MLCT and inter-ligand L'LCT etc. lie to lower energy contributing to the experimentally observed shoulder at 12,200 cm⁻¹. A structured band with at last two components observed experimentally near 20,000 cm⁻¹ contains several d→π*(1,2) (bpy) MLCT. This is followed at higher energy by the expected d→π*(3,4) (bpy) transitions. The lowest energy L'LCT transition is predicted as a very weak band at 20,400 cm⁻¹ where is it obscured by other more intense transitions.

4.6.2
Electronic Spectra of [Ru(bpy)$_2$(sq.NH.S)]$^+$

The experimental data [88, 89], calculated spectrum and individual transitions are shown in Fig. 13.

The intense band near 15,000 cm⁻¹ (Fig. 13) is again MLCT to the semiquinone, #79→#82 (SOMO) with the lower energy component ascribed to another MLCT to semiquinone, #81→#82. The broad and structured band between 20,000 and 25,000 cm⁻¹ encompasses several transitions which are partially resolved in the experimental spectrum but generate a single band in the predicted spectrum. They are all d→π*(1,2) (bpy) and include #79,80,81→#83 and the strongest component, #80→#84. Rising absorption near 30,000 cm⁻¹ is, of course, due to d→π*(3,4) (bpy) MLCT. L'LCT bands are not resolved experimentally but are predicted at 17,200 and 19,200 cm⁻¹.
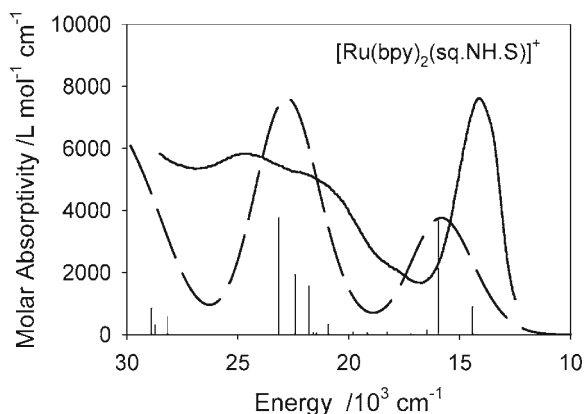
Fig. 13 Experimental (*solid line*) and INDO/S predicted (*hatched line*) spectra of [Ru(bpy)₂(sq.NH.S)]⁺ [88, 89]

4.7
[Ru(bpy)₂(q.X.X)]²⁺ Complexes-C₂ Symmetry

Historically the q.O.O species was the first quinone oxidation level species we had made and which sparked our interest in this type of complex. Usually, MLCT bands shift to lower energy as the ligand becomes a better acceptor, other ligands being constant, but in this series the d→π* q MLCT band was of higher energy than the d→π* sq MLCT transition. Reproduced also in the q.NH.NH species, this is a curious observation to which we return below.

Orbital #82 is now the LUMO and the ligand is the neutral quinone or quinonediimine, presumably the best π-acceptor of the series. The three d(t$_{2g}$) orbitals are again fairly well defined and the interaction with the quinone ligand is so strong that the molecular orbitals appear as if they belong to the point group C$_2$ rather than C$_2$. The dδ- and dσ-orbitals (HOMO and HOMO-1 respectively) are moderately pure (Table 2, q.NH.NH) while the dπ orbital distributes itself mostly between HOMO-2 and the LUMO. While the three filled d orbitals are present mostly in three frontier filled orbitals rather than spread over four or five as noted above for the sq.X.Y and cat.X.Y species, there are d orbital contributions to each of many deeper lying molecular orbitals. For example, HOMO-5 of q.NH.NH at –14.2 eV is a dδ bonding orbital being 15% Ru dδ and 48% π-ligand (q.NH.NH) while HOMO-12 at –16.7 eV is a dπ bonding orbital being 12% Ru dπ and 62% π-ligand (q.NH.NH).

4.7.1
Electronic Spectrum of [Ru(bpy)₂(q.NH.NH)]²⁺

The first major band is the dπ→π* (q.NH.NH) (HOMO-2→LUMO) band as we would expect, and can be described as MLCT (38%) with appreciable π-π* (q.NH.NH) character (44%). The other two d→LUMO transitions are very weak and were observed as a weak feature to the red of the main band (Fig. 14).
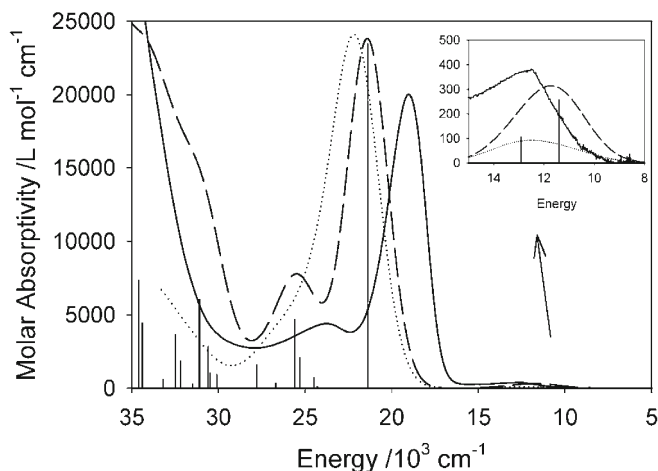
Fig. 14 Experimental (*solid line*), in acetonitrile, and INDO/S (*hatched line*) and TD DFRT (*dotted line*) predicted spectra of [Ru(bpy)$_2$(q.NH.NH)]$^{2+}$ [17, 65, 87]

The next band near 25,000 cm^{-1} primarily involves components of d→π*(1,2) (bpy) but there is also a significant contribution from HOMO-5→LUMO which is π-π* (q.NH.NH) with a substantial L'LCT component (see Table 2 and Fig. 13).

The collection of bands at 30–35,000 cm^{-1} are d→π*(3,4) (bpy) and π–π* (bpy). There follow (Fig. 14) a large number of transitions, such as MLCT to higher π* levels of bpy and π-π*. The most intense of these, near 37,000 cm^{-1}, is MLCT d→π*(5,6) (bpy).

4.8
[Ru(bpy)$_2$(q.X.Y)]$^{2+}$ Complexes

In parallel with the cat and sq asymmetric systems, the lack of symmetry causes a greater degree of mixing and in particular more scrambling of d orbital density into many MOs (Fig. 13), and will result in reduced CT character (Eq. 14) of the MLCT transitions. Indeed, if in the q.NH.NH species the principal excitation for the dπ→π* band has 38% of MLCT character (Table 3), in the q.NH.O and q.NH.S species the corresponding values are 28% and 14%. The asymmetry also causes two, rather than one, d→π* (q.NH.X) transitions in the visible region to be moderately intense. They are well resolved experimentally in the q.NH.O species (Fig. 15) though not in the q.NH.S analog.

The intense visible region MLCT transition is HOMO→LUMO; both of these MOs involve coupling between the dπ orbital aligned along the Ru-NH coordinate (dπ(NH)) and the q.NH.O π-orbitals. Transitions from the other two d orbitals (HOMO-1, HOMO-2) to LUMO provide the very weak transitions near 10,000 cm^{-1} in parallel with the other q-level complexes. The second fairly strong MLCT band, seen in these asymmetric species, is HOMO-5→LUMO predicted at ca. 23,000 cm^{-1}; this probably gives rise to the experimentally observed shoulder near 20,000 cm^{-1} (Fig. 15). This transition was noted for the C$_2$ q.NH.NH species
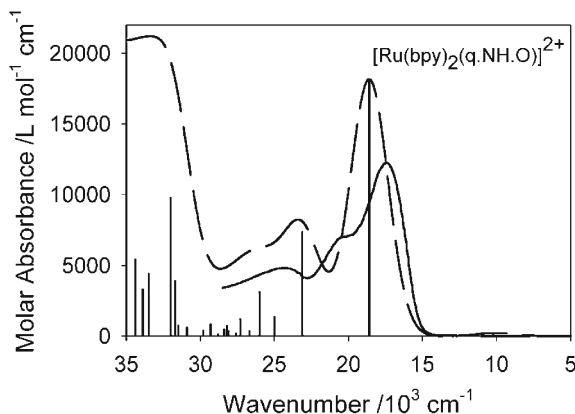
Fig. 15 Experimental (*solid line*), in acetonitrile, and INDO/S predicted (*hatched line*) spectra of $[Ru(bpy)_2(q.NH.O)]^{2+}$ [52, 87]

above but it is calculated therein to have a substantially smaller oscillator strength than in the less symmetric q.NH.X species.

5
Electronic Mixing

5.1
Wavefunction Contributions

It has been shown that substantial mixing occurs between the d shell and many filled π-orbitals as well as with the virtual π* orbitals, and between ligand orbitals, as presented in some detail in Tables 1 and 2 and Figs. 2, 8 and 12. Data just for the key redox active molecular orbital (#82) are summarized in Table 3. There is a clear trend for all the series that mixing is a maximum for the q complex, decreases for sq and then increases again for cat. A similar trend is seen for orbital #40 in the $[Ru(NH_3)_4(LL)]$ series (Table 1). In the q complexes the mixing is a consequence of the good π-acceptor character of the ligands and a synergism whereby electron density transferred from d to π* makes the ligand a better donor. In the sq series the extra negative charge tends to inhibit the back donation. While the cat series has two negative charges, the dosicity is very high and the orbital energies of frontier π-orbitals on the cat ligand are an excellent match for the frontier d orbitals, maximizing their interaction.

It is also apparent that, of the species studied here, the NH.S series are the most heavily mixed, i.e. most covalent, perhaps not surprising, given the nature of the coordinating sulfur atom. The S.S series, e.g. based on $[Ru(bpy)_2(q.S.S)]^{2+}$ would surely be even more delocalized but no members of this series are yet known.

5.2
Exchange Energy Contributions and Net Charge Transfer

The relative magnitude of the exchange integrals $K(i,a)$, is a measure of delocalization [45, 52, 53, 65, 94, 95]. The magnitude of $K(i,a)$ can be obtained from the CIS matrix [45, 77]. Thus $K(i,a)$ can be evaluated for MLCT, d-d, or π-π* transitions etc. It is now well known that in an excitation such as Ru^{II} d→L leading to the excited state $[Ru^{III}L^-]$ the time-average distance of the electron from the central metal could, in principle, approximate to the geometric distance if the electron is entirely localized on the ligand. However if, for a $\phi_i \rightarrow \phi_a$ excitation, the occupied and unoccupied molecular orbitals are strongly coupled together, as is the case for the intense dπ→L transitions discussed herein, the net electron transfer distance can be much smaller than the geometric distance estimated from the electron localized model. This has been discussed in depth by several authors [48–50, 95]. In such a situation, the corresponding exchange integral $K(i,a)$ can be quite large [17, 94] and will have the effect of increasing the transition energy (via Eq. 19) and also increasing the value of Q in Eqs. (7) and (10):

$$h\nu(\phi_i \rightarrow \phi_a) = \varepsilon_a - \varepsilon_i - J(i, a) + 2 K(i, a), \tag{19}$$

where ε_i and ε_a are the MO energies of molecular orbitals ϕ_i and ϕ_a, J is the Coulomb integral, and K is the exchange integral between these MOs.

Charge transfer transitions between states involving MO pairs which involve large values of the exchange integral can also be expected to be relatively intense because of good overlap between ground and excited state wavefunctions (which gives rise to the large value of K(i,a)). Thus, if we evaluate *exchange integrals* for electron excitations from metal d orbitals to a specific π*(L), we have a measure of the extent to which the d electrons are delocalized into that orbital [17, 45, 94].

The magnitude of K for excitations involving molecular orbitals, which are localized on two different molecular fragments, is usually less than 2000 cm^{-1}. We can expect, for example, that a dσ→π* (L) transition will have a small value of K because overlap, nominally, is zero and so the net charge transfer for this transition should be large. Thus if we compare the K values for the MLCT excitations in $[Ru(NH_3)_4(q.NH.NH)]^{2+}$ and $[Ru(bpy)_2(q.NH.NH)]^{2+}$ we deduce the data shown in Table 4 [77, 94].

Table 4 The exchange integrals $K(i,a)$ for $[Ru(NH_3)_4(q.NH.NH)]^{2+}$ and $[Ru(bpy)_2(q.NH.NH)]^{2+}$ (INDO/S calculations, all quantities are in 10^3 cm^{-1})

Complex	$K(i,a)$; a=LUMO, π*(q.NH.NH)			$K(i,a)$; a=π*(bpy)
	i=(dσ)[a]	i=(dπ)	i=(dδ)	
$[Ru(NH_3)_4(q.NH.NH)]^{2+}$	0.7	7.5	3.6	
$[Ru(bpy)_2(q.NH.NH)]^{2+}$	0.7	7.3	2.8	0.8[b]

[a] Symmetry of the MO with respect to the ligand LL.
[b] dσ→π* (bpy) (#81→#83) (dσ is with respect to q not bpy; see Fig. 9, HOMO).

We find generally that for all the q.X.X and q.X.Y species, the intense dπ→π*(q) transitions have K values of about 7000 cm^{-1} which is much higher than the K values noted for most other excitations and is fully consistent with the view that the dπ and π*(q) orbitals are significantly coupled.

As another example, consider data for the electron rich (cat.NH.NH)ligand in [Ru(bpy)$_2$(cat.NH.NH)]. The L′LCT transitions #82 (HOMO)→#83,84 have K=2250 and 1160 cm^{-1} which are surprisingly large. Recall that #83 and #84 are almost pure π* (bpy) and #82, while mostly π-cat, does have 15% π-bpy component. The d→π*(1,2) (bpy) transitions in this species (#80→#83,84) have K=1650 and 3070 cm^{-1} respectively. This is much larger than for [Ru(bpy)$_2$(q.NH.NH)]$^{2+}$ noted above and is consistent with the greater d-π*(bpy) mixing in the latter complex.

Pure π-π* transitions, i.e. transitions between molecular orbitals which are wholly localized on the ligand, can have K values in the 8000–11,000 cm^{-1} range because of the obvious extensive overlap. Interestingly, when the π or π* orbital is heavily mixed with a metal d orbital, it will be delocalized away from the ligand and will exhibit much smaller K values. This will result in smaller intensities and somewhat lower energies, for these mixed-character transitions.

Note that the energies of transitions with a high CT character are expected to be quite dependent upon the polarity of the solvent, i.e. to be solvatochromic, while those which, because of delocalization involve little net charge transfer, should not be solvatochromic [7, 9, 45, 96, 97].

5.3
Delocalization and ∆E(Redox)

Equation (8) is commonly used to confirm specific assignments of MLCT transitions by demonstrating that the optical energy is approximately equal to, usually slightly larger than, the experimental ∆E(Redox), the difference between the first oxidation potential of M and the first reduction potential of bound L [17, 23, 27, 30, 43, 84, 87, 98, 99]. Thus C in Eq. (8) is usually small, ca. 0.2 eV (for Ru^{II}, Os^{II} systems etc.). However the remarkable success of this approach relies on two fortuitous events: a) it is almost invariably the lowest energy *intense* MLCT transition which is studied and not any lower energy weaker, MLCT transitions, and b) most complexes studied have not involved highly delocalized species. As noted in Eqs. (7) and (8), C is actually a composite of several terms some of which may be quite large. The fact that C is relatively small for most systems studied in the literature may reflect an accidental choice of systems where K lies within a fairly narrow range, neither very small nor very large.

When one moves to large values of K, as in the delocalized systems under study here, C, via Q (Eq. 10) becomes very much larger, viz: using electrochemical data from and the most intense d→π* (q) transition energy:

q.NH.NH	$C = 0.59$ V	(ΔE(Redox) $= 1.82$ V)
q.NH.O	$C = 0.67$	(ΔE(Redox) $= 1.50$ V)
q.NH.S	$C = 1.24$	(ΔE(Redox) $= 1.16$ V)

The very large C value for the q.NH.S complex is consistent with the view noted above that it is the most highly delocalized of all the species studied here.

Conversely, if one considers the lowest energy weak MLCT transition for $[Ru(bpy)_2(q.NH.NH)]^{2+}$ shown in Fig. 14 (Expt. value 13,300 cm^{-1}, i.e. 1.65 eV) then, for this transition, $C=-0.17$ V.

We can now understand in detail, the reason for the unusual observation we first made in 1986 that the intense visible region MLCT band for the q.NH.NH and q.O.O species lay at higher energy than the corresponding intense transitions in the poorer π-acceptor semiquinone analogs. The answer lies, of course, in the substantially larger value of K which contributes to the off-diagonal element increasing the energy separation of the bonding and anti-bonding components of the dπ–$\pi^\star$ interaction (c.f. the MT model above). Indeed, we had, in 1986, supposed that this must be the explanation!

6
Summary

Complexes of fairly readily oxidizable metal ions with redox active ligands generally give rise to very rich optical spectra. This contribution, restricted to complexes containing one such ligand, has shown how their optical spectra, coupled with fairly straightforward computational techniques, can be used to extract detailed information about the nature of the metal-ligand interaction.

Complexes involving second or third row transition elements, especially ruthenium, osmium, rhenium etc., are usually quite covalently bound with strong interactions between metal d and ligand π and $\pi^\star$ orbitals. Such interactions greatly influence the resulting optical properties. Thus strongly coupled systems give rise to intense MLCT absorption in the visible and occasionally in the near infrared region. These complexes with C_{2v} or close to C_{2v} symmetry can formally give rise to, at least, three low energy transitions which may be written as dπ, dδ and d$\sigma\rightarrow\pi^\star(1)$ MLCT (plus, of course higher energy transitions to $\pi^\star(2)$ etc.). The most intense transition is always d$\pi\rightarrow\pi^\star(1)$ and the weakest, d$\sigma\rightarrow\pi^\star(1)$. The high intensity of the former arises because of the extensive mixing between dπ and $\pi^\star$ orbitals, while the latter is the weakest because dσ does not mix at all with $\pi^\star$ due to overlap restrictions. The intensity of the d$\delta\rightarrow\pi^\star(1)$ varies depending on the extent of mixing of this orbital with ligand orbitals of appropriate symmetry.

However we have observed that the three d(t_{2g}) orbitals can be mixed with ligand π orbitals, and/or higher energy $\pi^\star$ orbitals, leading to the distribution of significant d electron density over four or five molecular orbitals. Transitions from these orbitals have MLCT character and can be of significant intensity (e.g. #36$\rightarrow$#40 in $[Ru(NH_3)_4(q.NH.NH)]^{2+}$). Several intense MLCT transitions may develop when the symmetry is below C_{2v}, e.g. in the q.NH.X species (X=O,S).

The energy separation between the various MLCT transitions is, inter alia, related to the extent of orbital mixing through the magnitude of the exchange integrals $K(i,a)$. Electronic transitions between orbitals which are extensively mixed with each other involve a relatively small net electron transfer leading to large values of $K(i,a)$ and higher excitation energy (via Eq. 19); such transitions will

also not be especially solvatochromic. On the other hand, transitions such as dσ→π* MLCT will involve substantial electron transfer, be solvatochromic, have smaller values of $K(i,a)$ and hence lower excitation energies. The extraction of the values of $K(i,a)$ through INDO/S calculations provides a simple method to identify the extent of mixing between the metal and ligand orbitals in the complex.

The previous literature has been dominated by discussion of the intense MLCT features and largely omits discussion of the weak MLCT bands, which occur at lower energy and are often not reported. Such transitions do convey important information about the electronic structure.

It has long been recognized that the energy of 'the' intense MLCT transition is related to ΔE(Redox) (Eqs. 7 to 10) which usually underestimates its energy by the quantity C (Eq. 8). The magnitude of C is dependent, in part, on $K(i,a)$ (Eq. 10). While C is often small, ca 0.2 eV for many ruthenium(II) complexes [23] it can exceed 1 eV when extensive coupling is involved. It can also be negative when the corresponding exchange integral is very small as in the very weak 'forbidden' MLCT transitions.

The validity of the computational analysis is assessed through the agreement between observed and calculated optical spectrum. Further confidence is provided by the similarity in the description of the electronic coupling in these molecules using two very different methodologies, INDO/S and Density Functional Theory.

7
INDO/S Computational Details

Spin-restricted closed shell INDO/S calculations employed Hyperchem 6.0 (Hypercube, Inc.; Florida). The atomic INDO/S parameters were the same as those employed by Reimers and Hush [100] using the overlap weighting factors, $f_{p,\sigma}$=1.267 and $f_{p,\pi}$=0.585. The SCF convergence limit was 0.1 cal/mol and the CIS calculations included 20 highest occupied and 20 lowest unoccupied molecular orbitals. Restricted open-shell calculations employed INDO/S code written by Reimers [100] and the same atomic parameters as for closed shell species.

Some preliminary computational studies of these species, from a research perspective, appeared in reference [88].

8
References

1. Jørgensen CK (1962) In: Absorption spectra and chemical bonding in complexes. Pergamon Press, Oxford
2. Jørgensen CK (1962) In: Orbitals in atoms and molecules. Academic Press, London
3. Jørgensen CK (1969) In: Oxidation numbers and oxidation states. Springer, Berlin Heidelberg New York

 4. Jørgensen CK (1971) Modern aspects of ligand-field theory. North-Holland, Amsterdam
 5. Jørgensen CK (1970) Progr Inorg Chem 12:101
 6. Byers W, FaChun Chou F, Lever ABP, Parish RV (1969) J Am Chem Soc 91:1329
 7. Dodsworth ES, Lever ABP (1990) Coord Chem Rev 97:271
 8. Lever ABP (1968) Inorganic electronic spectroscopy, 1st edn. Elsevier Science, Amsterdam
 9. Lever ABP (1984) Inorganic electronic spectroscopy, 2nd edn. Elsevier Science, Amsterdam
10. Lever ABP (1974) J Chem Ed 51:612
11. Vogler A, Kunkely H (1990) Comments Inorg Chem 9:201
12. Kunkely H, Vogler, A (1998) Eur J Inorg Chem1863
13. Acosta A, Zink JI, Cheon J (2000) Inorg Chem 39:427
14. Bublitz GU, Laidlaw WM, Denning RG, Boxer SG (1998) J Am Chem Soc 120:6068
15. Glöckle M, Katz NE, Ketterle M, Kaim W (2002) Inorg Chim Acta 336:55–60
16. Kunkely H, Vogler A (1997) Inorg Chim Acta 254:195–198
17. Gorelsky SI, Dodsworth ES, Lever ABP, Vlcek AA (1998) Coord Chem Rev 174:469
18. Kunkely H, Vogler A (2000) Inorg Chim Acta 310:279
19. Vogler A, Kunkely H (2002) Coord Chem Rev 229:147
20. Shriver DF, Posner J (1966) J Am Chem Soc 88:1672
21. Vlcek AA (1968) Rev Chim Minerale 5:299
22. Vlcek AA (1958) Discuss Faraday Soc 26:164
23. a) Haga M, Dodsworth ES, Lever ABP (1986) Inorg Chem 25:474; b) Dodsworth ES, Lever ABP (1986) Chem Phys Lett 124:152
24. Rillema DP, Allen G, Meyer TJ, Conrad D (1983) Inorg Chem 22:1617
25. Timpson CJ, Bignozzi CA, Sullivan BP, Kober EM, Meyer TJ (1996) J Phys Chem 100: 2915
26. Ohsawa Y, Hanck KW, DeArmond MK (1984) J Electroanal Chem 175:229.
27. Kvam, PI, Puzyk MV, Cotlyr VS, Songstad J, Balashev KP (1996) Acta Chem Scand 50:6
28. Mayer U, Kotocova A, Gutmann V, Gerger W (1979) J Electroanal Chem 100:875
29. Lever ABP, Dodsworth ES (1999) In: Solomon EI, Lever ABP (eds) Inorganic electronic structure and spectroscopy, vol 2. Wiley, New York, pp 227–287
30. Lever ABP, Licoccia K, Magnell K, Minor PC, Ramaswamy BS (1982) In: Kadish K (ed) Electrochemical and spectrochemical studies of biological redox components, vol 201. Advances in Chemistry Series, ACS, p 237
31. Lever ABP, Licoccia S, Minor P, Ramaswamy BS, Pickens SR (1981) J Am Chem Soc 103:6800
32. Lever ABP (2004) In: Lever ABP (ed) Comprehensive coordination chemistry, II, vol II, p 251. Elsevier Amsterdam
33. Curtis JC, Sullivan BP, Meyer TJ (1983) Inorg Chem 22:224
34. Gritzner G, Danksagmuller K, Gutmann V (1976) J Electroanal Chem 72:177
35. Chang YP, Fung EY, Curtis JC (1986) Inorg Chem 25:4233
36. Kadish KM, Das K, Schaeper D, Merrill C, Welch BR, Wilson LJ (1980) Inorg Chem 19:2816
37. Watzky MA, Macatangay AV, Vancamp RA, Mazzetto SE, Song XQ, Endicott JF, Buranda T (1997) J Phys Chem A 101:8441
38. Coe BJ, Chamberlain MC, Essexlopresti JP, Gaines S, Jeffery JC, Houbrechts S, Persoons A (1997) Inorg Chem 36:3284
39. Tom Dieck H, Renk IW (1970) Angew Chem Int Ed Engl 9:793
40. Hupp JT, Meyer TJ (1987) Inorg Chem 26:2332
41. Dodsworth ES, Lever ABP (1984) Chem Phys Lett 112:567
42. Masui H, Lever ABP, Dodsworth ES (1993) Inorg Chem 32:258
43. Dei A (1993) Inorg Chem 32:5730
44. Dodsworth ES, Linert W, Hasegawa M (2004) In: Comprehensive coordination chemistry, II, vol II, p 351. Elsevier
45. Gorelsky SI, Lever ABP (2003) Can J Appl Spectrosc 48:93
46. Demadis KD, Hartshorn CM, Meyer TJ (2001) Chem Rev 101:2655
47. Connick WB, Gray HB (1997) J Am Chem Soc 119:11620
48. Oh DH, Sano M, Boxer SG (1991) J Am Chem Soc 113:6880

49. Walters K (2004) In: Lever ABP (ed) Comprehensive coordination chemistry, II, vol II, p 303. Elsevier
50. Lockhart DJ, Goldstein RF, Boxer SG (1988) J Chem Phys 89:1408
51. Brunschwig BS, Creutz C, Sutin N (1998) Coord Chem Rev 177:61
52. Gorelsky SI, Lever ABP, Ebadi M (2002) Coord Chem Rev 230:97
53. Endicott JF, Schlegel HB, Uddin MJ, Seniveratne DS (2002) Coord Chem Rev 229:95
54. Endicott JF, Uddin MJ (2001) Coord Chem Rev 219:687
55. Hartl F, Vlcek A (1996) Inorg Chem 35:1257
56. Salaymeh F, Berhane S, Yusof R, Delarosa R, Fung EY, Matamoros R, Lau KW, Zheng Q, Kober EM, Curtis JC (1993) Inorg Chem 32:3895
57. Anderson PA, Deacon GB, Haarmann KH, Keene FR, Meyer TJ, Reitsma DA, Skelton BW, Strouse GF, Thomas NC, Treadway JA, White AH (1995) Inorg Chem 34:6145
58. Ridley J, Zerner MC (1973) Theor Chim Acta 32:111
59. Ridley J, Zerner MC (1976) Theor Chim Acta 42:223
60. Zerner MC (1996) In: Russo N, Salahub DR (eds) Metal-ligand interactions. Kluwer Academic, p 493
61. Martin C, Zerner MC (1999) In: Solomon EI, Lever ABP (eds) Inorganic electronic structure and spectroscopy, vol 1. Wiley, p 555
62. Li J, Noodleman L, Case DA (1999) In: Solomon EI, Lever ABP (eds) Inorganic electronic structure and spectroscopy, vol 1. Wiley, New York, p 661
63. Kosh W, Holthausen MC (2001) A chemist's guide to density functional theory, 2nd edn. Wiley-VCH Weinheim
64. Autschbach J, Ziegler T (2003) Coord Chem Rev 238:83
65. Gorelsky SI, Lever ABP (2001) J Organomet Chem 635:187; 659:202
66. Gorelsky SI (2004) In: Lever ABP (ed) Comprehensive coordination chemistry, II, vol II, p 651. Elsevier
67. Frisch MJ, Trucks GW, Schlegel HB, Scuseria GE, Robb MA, Cheeseman JR, Zakrzewski VG, Montgomery JA Jr, Stratmann RE, Burant JC, Dapprich S, Millam JM, Daniels AD, Kudin KN, Strain MC, Farkas O, Tomasi J, Barone V, Cossi M, Cammi R, Mennucci B, Pomelli C, Adamo C, Clifford S, Ochterski J, Petersson GA, Ayala PY, Cui Q, Morokuma K, Malick DK, Rabuck AD, Raghavachari K, Foresman JB, Cioslowski JOJV, Stefanov BB, Liu G, Liashenko A, Piskorz P, Komaromi I, Gomperts R, Martin RL, Fox DJ, Keith T, Al-Laham MA, Peng CY, Nanayakkara A, Gonzalez C, Challacombe M, Gill PMW, Johnson B, Chen W, Wong MW, Andres JL, Gonzalez C, Head-Gordon M, Replogle ES, Pople JA (1998) Gaussian 98 Revision A.11. Gaussian Inc., Pittsburgh
68. Becke AD (1993) J Chem Phys 98:5648
69. Lee C, Yang W, Parr RG (1988) Phys Rev 37B:785
70. Dunning TH Jr, Hay PJ (1976) In: Schaefer HF III (ed) Modern theoretical chemistry, vol 3. Plenum Press, New York, p 1
71. Hay PJ, Wadt WR (1985) J Chem Phys 82:270
72. Hay PJ, Wadt WR (1985) J Chem Phys 82:299
73. Mulliken RS (1955) J Chem Phys 23:1833
74. Mulliken RS (1955) J Chem Phys 23:1841
75. Mulliken RS (1955) J Chem Phys 23:2338
76. Mulliken RS (1962) J Chem Phys 36:3428
77. Gorelsky SI (2003) http://www.obbligato.com/software/
78. Zerner MC (1991) In: Reviews In computational chemistry, vol. 2. VCH Publishers, New York, p 313
79. Baker JD, Zerner MC (1991) J Phys Chem 95:8614
80. Metcalfe RA, Lever ABP (1997) Inorg Chem 36:4762
81. Note: Ligand abbreviations are in round brackets, e.g q.NH.NH). In the absence of the round bracket, q.NH.NH will refer to 'the' complex containing this ligand, e.g. [Ru(bpy)$_2$(q.NH.NH)]$^{2+}$. This abbreviation is only used when the context makes it clear to which complex it refers.
82. Magnuson RH, Taube H (1975) J Am Chem Soc 97:5129

83. Since this contribution is intended to be mainly a pedagogical view of these complexes, we do not present a detailed assessment of the spectra of this entire series, but rather present cogent examples. More detail can be found in our recent publications. Also see reference [88]

84. da Cunha CJ, Fielder SS, Stynes DV, Masui H, Auburn PR, Lever ABP (1996) Inorg Chim Acta 242:293

85. Orgel LE (1961) J Chem Soc 3683

86. Juris A, Balzani V, Barigelletti F, Campagna S, Belser P, Zelewsky AV (1988) Coord Chem Rev 84:85

87. Masui H, Auburn PR, Lever ABP (1991) Inorg Chem 30:2402

88. Ebadi M (1997) M. Sc. thesis Ruthenium complexes of quinone-related ligands; study of the redox states of the 2-aminothiophenol. York University Toronto

89. Ebadi M, Lever ABP (2004) To be submitted

90. Rusanov E, Lever ABP (2003) Work in progress

91. Parr RG (1963) Quantum theory of molecular electronic structure. W.A. Benjamin, New York

92. Szabo A, Ostlund NS (1982) Modern quantum chemistry. Macmillan, New York

93. Lever ABP, Solomon EI (1999) In: Solomon EI, Lever ABP (eds) Electronic structure and spectroscopy, vol 1. New York

94. Lever ABP, Gorelsky SI (2000) Coord Chem Rev 208:153

95. Shin Y, Brunsschwig BS, Creutz C, Newton MD, Sutin N (1996) J Phys Chem 100:1104

96. Dodsworth ES, Lever ABP (1990) Inorg Chem 29:499

97. Metcalfe RA, Dodsworth ES, Fielder SS, Stufkens DJ, Lever ABP, Pietro WJ (1996) Inorg Chem 35:7741

98. Matsubara T, Ford PC (1976) Inorg Chem 15:1107

99. Vlcek AA, Dodsworth ES, Pietro WJ, Lever ABP (1995) Inorg Chem 34:1906

100. Zeng J, Hush NS, Reimers JR (1996) J Phys Chem 100: 19292

Photoluminescence and Excitation Energy Transfer of Rare Earth Ions in Nanoporous Xerogel and Sol-Gel SiO$_2$ Glasses

M. Morita[1] · S. Buddhudu[1,2] · D. Rau[1] · S. Murakami[1,3]

[1] Department of Applied Chemistry, Faculty of Engineering, Seikei University, Kitamachi 3, Kichijoji, Musashino-Shi, Tokyo 180-8633, Japan
 E-mail: morita@ch.seikei.ac.jp
[2] SriVenkastewara University, Tirupati 517058, India
[3] Shimadzu Co. Ltd., Kyoto, Japan

Abstract Luminescence and excitation energy migration processes in the nanoporous hosts are investigated of Eu^{3+} and codoped lanthanide ($Ln^{3+}=La^{3+}, Pr^{3+}, Nd^{3+}, Sm^{3+}, Gd^{3+}, Tb^{3+}, Dy^{3+}, Er^{3+}, Yb^{3+}$) ions dispersed in xerogel and annealed sol-gel silica glasses by the measurements of spectral characteristics and decay profiles as a function of temperatures between 300 K and 10 K. The observed non-single exponential decay curves are approximated by the sum of two exponential functions. The energy transfer parameters are discussed by two models: (1) Huber-Krol-Boulon model of multi-step energy transfer and (2) Dexer-Inokuchi-Hirayama model of single step energy transfer. The critical distance of energy transfer R_0 is found to be 0.9 nm (±10%) on the average, irrespective of models, temperatures and matrices. The experimental results give evidence of the fact that the trapping-limited energy transfer mechanism is dominant in the disordered nanomatrices.

Keywords Luminescence · Energy transfer · Rare earth · Sol-gel silica · Xerogel

List of Abbreviations

CPL   Circularly Polarized Luminescence
CYCLEN 1,4,7,10-Tetraazacyclododecane
DEDMS   Diethoxydimethylsilane
EXAFS   Extended X-ray Absorption Fine Structure
FLN   Fluorescence Line Narrowing
LMCT   Ligand-to-Metal Charge Transfer
NC   Nanocrystal
PLZT $(Pb,La)(Zr,Ti)O_3$
RE   Rare Earth
TEM   Transmittance Electron Microscope
TEOS   Tetraethylorthosilicate
TRFLN   Time-resolved Fluorescence Line Narrowing
XRD   X-Ray Diffraction

1
Introduction

1.1
Luminescence of Transition Metal Ions and Complexes in Xerogel and Sol-Gel SiO$_2$ Glasses

Sol-gel derived SiO$_2$ glasses and xerogels are very strategic amorphous materials of nanometer size porous structures. The glasses of desired optical and electric properties are easily available by designing doping colorants or luminescence species in glasses and preparation conditions, e.g., redox reactions and thermal annealing processes, which can be controlled by analysis of TEM and XRD spectral patterns [1–3]. Sol-gel glasses are simply prepared from a water-ethanol mixed solution of silicon alkoxide and dopants at room temperature. After a few months xerogel is gradually grown as a wet solid in a glass container. Sol-gel silica glasses in the form of thin films, bricks or fibers are prepared by annealing xerogel in an electric furnace at about 500 °C for one day. Such sol-gel glasses are optically homogeneous and transparent having mesoporous structures with pore-sizes of about 5–10 nm. There are a variety of applications for coating films, photochromic films, chemical sensors, nonlinear-electro-optical devices, and compact lasers in electronic circuits. Conventional rigid glasses are prepared at temperatures above 1000 °C. In comparison, the "low temperature" sol-gel glasses have a mesoporous structure in which small metal ion particles substitute the

Si site or the porous centers. Luminescence from doped sol-gel silica is very sensitive to the surface condition due to the presence of size-confinement effects and dangling bonds. In the following, we outline the background of our research object briefly [4].

Transition metal ions and complexes embedded in xerogel and sol-gel silica glasses show a strong luminescence band in the visible spectral region [5–8]. We have been interested in luminescence of metal ions doped in sol-gel derived SiO_2 glasses [9]. Bright and red emission was observed from SiO_2:Cr^{6+} at room temperature [10, 11]. Recently, we investigated luminescence of sol-gel silica glasses doped with various transition metal ions of 3d, 4d and 5d groups (M=Ti^{4+}, V^{5+}, Cr^{6+}, Zr^{4+}, Nb^{5+}, Mo^{6+}, Hf^{4+}, Ta^{5+}, W^{6+}) [8]. These glasses show strong emission bands at around 18,000 cm^{-1} under a N_2-laser excitation at room temperature. Such luminescence is due to the ^{3}LMCT transition of ions with closed-shell electronic structures in tetrahedral molecular complex centers [MO_4]. These ions reveal vibronic luminescence which is sensitive to the surface conditions. The presence of oxygen-coordinated octahedral [MO_6] centers must be also considered to understand the higher energy band in Ti, Nb, Ta, and W doped glasses. Luminescence, time-resolved luminescence, decay times, excitation and absorption spectra were measured at temperatures between 300 and 10 K to investigate the electronic states of metal ions in mesoporous matrices. We prepared sol-gel silica glasses and xerogel doped with open shell transition metal complexes: (a) Cr(III)(AA)$_3$ (AA=acetylacetonato), (b) tris-nuclear basic acetate (Cr(III)-trimer), (c) V(III)(AA)$_3$, and (d) V(IV)O(AA)$_2$ [7, 8]. Using glasses annealed at temperatures below 150 °C, sharp emission lines are observed at 13,000 cm^{-1} which are due to (a) single Cr(III) ions and (b) exchange-coupled Cr(III) pairs. In the glasses annealed at temperatures above 500 °C, a broad band with vibronic structures was found. This is due to the Ligand-to-Metal Charge Transfer (^{3}LMCT) transition of either [Cr(VI)O$_4$]$^{2-}$ or [V(V)O$_4$]$^{3-}$ complex ion center if the following thermo-chemical reaction proceeds with increase of annealing temperatures: (c) [V(III)(AA)$_3$]→ (d)V(IV)O(AA)$_2$]→[V(V)O$_4$]$^{3-}$. Moreover, the luminescence spectra due to Cr(III) and Cr(VI) ions were detected simultaneously in some glasses prepared under mild chemical conditions.

Sol-gel glasses doped with such metal ions or complexes are promising new materials for display phosphors.

1.2
Luminescence of Rare Earth Ions and Complexes in Xerogel and Sol-Gel SiO_2 Glasses

Luminescence of rare-earth (RE) ions and complexes doped in sol-gel glasses is very important to investigate fundamental transitions related to up-conversion, hole-burning, and energy transfer etc. [12, 13]. Doping of rare earth complexes in various sol-gel glass and ceramic hosts makes it possible to develop new organic/inorganic composites [9, 14]. Photoluminescence behavior of various Eu complexes with carboxylate [15], cryptate [16, 17] and β-diketonato [18] as ligands is examined in xerogel for improvement of spectral properties and increase of quantum yields. For example, Eu (III) β-diketonates supported on sol-gel silica are good red phosphors. The bi-exponential decay curve indicates

the presence of Eu^{3+} site on the surface of the SiO_2 [19]. Electron-hole carrier emission at 530 nm and Eu^{2+} band at 410 nm are observed in the Eu^{3+}-doped silica xerogel [20]. In addition, there are miscellaneous spectral changes of rare earth ions in xerogels. Structural changes along the sol-gel-xerogel transition in silica are probed by emission of pyrene in xerogel [21]. White light emission and EXAFS of Eu^{3+}-based organic/inorganic xerogels are measured [22]. Optical properties of doped RE ions are unique in the hybrid organic-inorganic materials of siloxane-zirconia [23]. Strongly enhanced Tb luminescence from titania xerogel solids is mesoscopically confined in porous anodic aluminum [24].

Energy up-conversion is demonstrated in a sol-gel processed silica glass codoped with Eu^{3+}-Yb^{3+} ions [25, 26]. Similarly, luminescence of Er^{3+}-Yb^{3+} doped SnO_2 xerogel was found to be due to centers at a substitutional Sn site and to the site at the particle surface [27]. Upconversion luminescent emission from Y_2O_3:Eu^{3+} is found under 632.8 nm light excitation [28]. Infrared-to-visible upconversion from an Yb^{3+} ion pair in a sol-gel multi-component silica glass gives rise to yellow-orange emission [29]. Crystal field calculation of Eu^{3+} ions is carried out in various matrices. The trivalent europium ion doped in sodium disilicate glass is in accord with calculations of crystal field splitting of Eu^{3+} ions by point charge crystal field potential model [30, 31]. Emission spectra were investigated of Eu^{3+} ions of C_2 site symmetry in In_2O_3 oxide and the crystal field calculation was performed using 14 crystal field parameters [32]. Eu (III) emission in oxide glasses is dependent on the glass composition [19]. Judd-Ofelt parameters and long/short range order interactions in emission are discussed in glasses [33, 34]. Rare-earth clustering in sol-gel silica has been investigated by fluorescence line-narrowing (FLN) techniques. Clustered and isolated Eu^{3+} ions are separated in silica by the lack of a line-narrowing effect in the former, present in samples with Eu^{3+} concentrations as low as 0.5 wt% [35].

Energy transfer between adjacent Eu (III) ions was proposed by lack of a FLN effect [35]. The zero-phonon transition of Eu^{3+} in sol-gel silica glass was found to be non-resonant because a redistribution of the excitation energy occurs among the different environments by a phonon-assisted energy transfer mechanism [36]. This was experimentally confirmed by temperature dependence of decays and time-resolved luminescence studies [37]. Time-resolved FLN was used again to analyze energy transfer between Eu^{3+} ions in sol-gel derived silica glasses due to the multipolar interaction of resonant energy transfer. These resonant/non-resonant energy transfer mechanisms are not readily acceptable in our experiments on glassy matrices as we will see later in discussions. We have to consider a competitive mechanism due to trapping-limited energy transfer processes. In comparison with RE ions in bulk hosts, we expect to find some new aspects in mesoporous matrices [32, 33, 38].

1.3
Quantum Confinement Effects in Luminescence of Nanoporous Sol-Gel Glasses

Quantum confinement effects in mesoporous matrices are very important objects in luminescence of metal ions, metal complexes and semiconductor nanocrystals doped in sol-gel derived silica glasses or xerogel. In semiconductor nanocrystals

(NCs), quantum confinements effects have been found as a blue shift of the emission and absorption bands with decrease of the particle sizes from bulk (10 μm) to NCs (nm range) [39]. Similar optical and luminescent processes can be observed in sol-gel ceramics and glasses. The optical properties of nanometer sized semiconductor particles in glasses prepared by the sol-gel method are very interesting for electro-optical applications [40]. New spectroscopic bands are found in various nanoparticles. For example, Yang and his group have reported luminescence properties of Ti_2S_3 nanoparticles embedded in sol-gel derived silica xerogel which show red emission of NCs in xerogel at 600 nm under 550 nm excitation [41]. Strong visible-light emission of ZnS nanocrystals is observed from ZnS NCs in Na^+ doped silica xerogels which is 300 times as strong as pure NCs [42]. Luminescence of CaS and MnS nanocrystallites is also reported from coactivated sol-gel derived silica xerogel at 440 nm and 580 nm, respectively [43]. Photoluminescence characteristics of NiS nanocrystallites give new emission at 610 nm (λ_{exc}=490 nm) due to NiS NCs embedded in sol-gel silica xerogel [44].

Synthesis and luminescence properties of CdS:Mn NCs are studied in transparent xerogel matrices [45]. High quantum yield up to 70% is realized by efficient energy transfer from trap carrier on the surface to Mn^{2+}. Semiconducting quantum-sized cadmium sulfide particles doped with RE^{3+} (=Eu^{3+}, Tb^{3+}) ions in amorphous sol-gel films, ZrO_2:CdS (Eu^{3+}, Tb^{3+}), show strong luminescence [46, 47]. We have prepared thin zirconia films doped with semiconductor nanocrystals x$ZrO_2\cdot$(100−x)CdS:Mn^{2+} and Eu^{3+} (X=0, 20, 50, 80, 100) by sol-gel method to clarify emission centers of nano-particles [33, 48]. The broad emission band over the 24–13×10^3 cm^{-1} is found to be composed of four spectral components due to band-edge emission (CdS), LMCT transition (ZrO_2), surface-bound deep centers, and lattice-bound d-d (Mn^{2+}) or f-f (Eu^{3+}) transitions. Luminescence of Mn^{2+} and Eu^{3+} showed composition-dependent spectral profiles and shortening of lifetimes to 5–50 μs at 10 K. Ultra fast decay components of 0.5–1.5 ns were also detected in thin films at room temperature. Luminescence properties of doped-CdS nanocrystals are dependent on annealing temperatures. Luminescence is characterized by very fast decay times and low thermal activation energy of 1300 cm^{-1} in comparison with that of bulk crystals.

Circularly polarized luminescence (CPL) and decay profiles are measured of chiral complexes in sol-gel glasses [14]. We have doped Ln(III)(15-crownether-5) (Ln=Ce, Sm, Eu, Tb) and optical active Tb(III) complexes of 1,4,7,10 tetraazacyclododecane (abbreviated as cyclen) derivative ligand into xerogel and sol-gel silica glasses. We measured their optical properties to characterize the electronic structure in the excited states. The crystal field parameter values $B_0^{(2)}$, $B_2^{(2)}$ were obtained from the analysis of the $^5D_0\rightarrow^7F_1$ transition. Since the axial crystal field term is present in luminescence of xerogel and sol-gel glasses prepared at temperatures below 100 °C, the pentagonal and planar structure of Eu(III) (15-crownether-5) is kept stable in the sample. As the annealing temperature is elevated from 80 °C to 750 °C, the Eu(III) complexes in sol-gel glasses are found to decompose to isolated Eu^{3+} ions. The Tb(III)-(S)-and Tb(III)-(R)-cyclen derivative complexes in xerogel at room temperature and 10 K present sharp circularly polarized luminescence (CPL) spectra with luminescence dissymmetry factors g_{lum}=−0.1 and 0.1 for (S) and (R), respectively [49].

1.4
Energy Transfer Processes in Nanoporous Sol-gel Glasses

Energy transfer processes of RE ions in mesoporous matrices are the most important object of research in sol-gel materials. Luminescence measurements of rare earth ions in sol-gel glasses are quite important to clarify dynamical aspects of energy transfer processes associated with very fast (10 ns order) nonradiative process in nanoporous systems. Excitation energy transfer processes of rare earth ions in ordered and disordered systems have been well understood in the past decades [50, 51]. However, in the case of disordered sol-gel glasses, the presence of residual impurities as traps and killers makes the energy transfer process more complex and in the extreme case trapping-limited energy migration processes become dominant [52].

Luminescence of Eu^{3+} and Tb^{3+} ions in the microporous structure of xerogel and mesoporous anodic aluminum oxide is enhanced by TiO_2 and Al_2O_3 doped xerogel thin films [53]. Intermolecular energy transfer from coumarin-120 to rare earth ions (Eu^{3+}, Tb^{3+}) is also observed in silica xerogels [54]. Similarly, energy transfer was found between Eu^{3+} ions and CdS quantum dots in sol-gel derived $SiO_2/CdS:Eu^{3+}$ gel [55]. There are a lot of reports on lanthanide complexes in xerogel matrices associated with energy transfer processes [14, 56–58]. SiO_2-M_xO_y composites doped with the europium(III)di(1,10-phenanthroline) complex present energy transfer between the neighboring Eu^{3+} ions in xerogel matrices [59]. Energy transfer from Tb to Eu ions is observed in luminescence behavior of the $Eu(TTFA)_3$ and TbSSA co-doped xerogel [60]. Picolinic acid:Eu^{3+} complex in SiO_2 xerogels reveals energy transfer from picolinic acid to Eu^{3+} [61].

We have reported luminescence properties and excitation energy transfer of Eu^{3+} and rare earth ions in amorphous $(Pb,La)(Zr,Ti) O_3$ (PLZT) ceramics [34, 62–65]. Luminescence and decay times of sol-gel PLZT (9/65/35) ceramics doped with Eu^{3+}, Nd^{3+} and chromium ions were investigated to elucidate site occupancy and energy transfer processes at low temperatures down to 10 K. Luminescence and excitation energy transfer in the sol-gel PLZT: Eu^{3+}, Nd^{3+} are discussed with regard to trapping-limited energy transfer processes with critical distances of about 0.5 nm. Alumina is similarly a good ceramic host material. Luminescence properties of Tb^{3+} and Eu^{3+}-doped alumina films are prepared by sol-gel method under various conditions. In sensitized luminescence, the energy transfer from Tb^{3+} to Eu^{3+} was found to enhance Eu^{3+} emission with quadratic dependence on acceptor concentration. This is explained by fast radiationless energy transfer rates to OH groups [66]. Energy transfer among Eu^{3+} ions in sol-gel derived silica glasses was studied using TR-FLN (time-resolved fluorescence line narrowing) spectroscopy in the $^5D_0 \rightarrow {}^7F_0$ transition of Eu^{3+} (2.5 mol%) in sol-gel derived silica glasses. The resonant energy transfer processes of multipole character were found to be dependent on annealing conditions of the samples [67]. Site distribution and thermalization effects in europium-doped silica glasses are found in the $^5D_0 \rightarrow {}^7F_0$ transition of Eu^{3+} in sol-gel derived glass. The mechanism of redistribution of the excitation energy is interpreted as being due to phonon-assisted energy transfer processes from temperature dependence of decays and time resolved emission measurements [68].

We have demonstrated various interesting aspects of luminescence study of RE ions doped in sol-gel materials. We have measured luminescence and decay times of Eu^{3+} ions codoped with other rare-earth ions (Nd^{3+}, Sm^{3+}, Dy^{3+}, Er^{3+} and Yb^{3+}) at temperatures between 10 and 300 K using nanostructured xerogel and annealed sol-gel silica glasses as hosts [69, 70]. The critical distances (R_0) of energy transfer obtained by Dexter model are almost the same for five activators. The energy transfer mechanisms are affected by confined nano-structured networks in the sol-gel SiO_2 glasses. In this chapter, we extend our previous study on luminescence and decay profiles of Eu^{3+} and rare earth ions in xerogel and sol-gel silica glasses in several ways. Further experiments are added using materials with different ions, concentration dependence on donor-acceptor pairs and their temperature dependence. They afford us sufficient information on energy transfer processes in the temperature range between 10 and 300 K.

Luminescence spectral shapes, relative intensities, efficiencies and decay-times of lanthanides ions are compared in xerogel and sol-gel silica glasses. The energy transfer processes in sol-gel glasses are examined, using (1) a multi-step energy transfer model in disordered systems and (2) a conventional single-step energy transfer model. From analysis of the decay curve, the energy transfer rates and critical distances of energy transfer are calculated to be nearly constant irrespective of activators. Since the overlap integrals are different in a pair of codopants, a competitive trapping-limited energy transfer mechanism is found to be dominant in the disordered networks of xerogel and sol-gel SiO_2 glasses.

2
Theoretical Considerations

2.1
Luminescence Decay Profiles in Disordered Systems

In this section, we overview the conventional theoretical arguments on excitation energy transfer in disordered systems. Using simple energy transfer schemes, we analyze the observed decay profiles and deduce the excitation energy transfer rate and the critical distance of energy transfer for rare earth ions in sol-gel silica glasses. First of all, we need to accept complicated luminescence decay profiles of rare earth ions in disordered systems which cannot be expressed by a single-exponential decay function as in the case of rare earth ions in PLZT ceramics [63, 65]. Luminescence processes in amorphous solids are complicated, because there are miscellaneous optical channels in the presence of intrinsic and perturbed centers, activators, impurities, defects and traps. Therefore, the luminescence decay curve may be approximated as the sum of two exponential functions by

$$I(t) = A_1 \exp(-m_1 t) + A_2 \exp(-m_2 t) \qquad (1)$$

where $I(t)$ is the luminescence intensity of a sensitizer, A_1 and A_2 fractional intensities, m_1 and m_2 the inverse of short and long decay times of τ_1 ($=1/m_1$) and τ_2 ($=1/m_2$) with $m_1 > m_2 > 0$, respectively. In order to analyze the energy migration processes, we introduce new parameters $m(D)$, $m(D+A)$, $m^\star(D)$ and $m^\star(D+A)$ defined as follows:

$$m(D) = m_1(D) + m_2(D) \tag{2a}$$

$$m(D+A) = m_1(D+A) + m_2(D+A) \tag{2b}$$

$$m^*(D) = m_1(D) - m_2(D) \tag{3a}$$

$$m^*(D+A) = m_1(D+A) - m_2(D+A) \tag{3b}$$

where notations of (D) and (D+A) refer to the rate constant terms of a donor in the absence and the presence of an acceptor, respectively.

2.2
Multi-Step Energy Transfer Model in Insulating Solids

Energy transfer in insulating substances is classified to two types: (1) multi-step energy transfer which assumes the energy migration from an intrinsic center to activators, traps and killers and (2) microscopic single-step energy transfer from a sensitizer (donor) to an activator (acceptor) [71]. We shall first consider the energy migration processes based on model (1), because sol-gel glasses should have miscellaneous traps and killers in the porous structure by which the luminescence quenching process becomes more pronounced at low temperatures. This model (1) must be compared carefully with the Dexter model (2), because the latter is widely applied to almost all insulating materials.

Huber has given a general theory of excitation energy transfer of ions in disordered systems by assuming a lack of translational symmetry and the presence of traps [52, 71, 72]. This general theory of trapping-limited energy transfer can be solved for two extreme cases in the limit of the case (a) of donor-donor energy transfer faster than donor-trap transfer and (b) in the absence of donor-donor energy transfer [52]. The former case (a) can be found in some insulating oxides at higher temperature and this results in a single exponential decay rate. This is proven by other models of hopping and diffusion kinetics. The latter case (b) occurs in our system, because we deal with the non-exponential decay profile and the energy transfer of much diluted rare earth ions (0.1–1.0 mol%) in porous glasses. In the (b) limit, we obtain the general expression for the donor fluorescence decay function $I(t)$:

$$I(t) = I_0 \exp(-\gamma_R t) \, \Pi_l \, \{1 - c_A + c_A \exp(-t/\tau(0 \to l))\} \tag{4}$$

where γ_R is the intrinsic radiative transition probability of the donor, c_A the acceptor concentration, and $\tau(0 \to l)$ the lifetime of the transfer from the donor to the acceptor at a site l. In the case of a single site ($l=1$), the complex equation gives a simple sum of two single exponential functions. In practice, the site in sol-gel glasses is occupied by many traps, and we require many parameters to reproduce complex decay curves.

Krol [73] and Boulon [74, 75] have independently proposed an energy transfer scheme for ions and traps in insulating solids. We shortly outline their models which are based on a general model by Huber. Krol proposed a two-level scheme to explain luminescence and decay profiles associated with the diffusion-limited energy transfer of uranyl ions in $Cs_2UO_2Br_4$ crystals [73]. Using this model, we have discussed the energy transfer processes and determined the kinetic param-

eters in $[N(CH_3)_4]_2UO_2Cl_4$ [76] and RE ion doped PLZT ceramics [63]. According to the energy band scheme by the Krol model, we consider the presence of intrinsic and perturbed centers, a shallow trap, an acceptor and a killer. The luminescence spectra and the bi-exponential decay curves give information on the populations of the donor (N_2) and the shallow trap (N_1). By introducing an acceptor in the rate equations, we get the following expressions of m_1 and m_2:

$$m_{1,2} = \frac{1}{2} (n_{tr}w_{tr} + n_q w_q + W + w'_{tr} + p_r + p'_r)$$

$$\pm \left\{ \begin{array}{l} \frac{1}{4} (n_{tr}w_{tr} + n_q w_q + W + w'_{tr} + p_r + p'_r)^2 \\ -(n_{tr}w_{tr} + n_q w_q + W + p_r)(w'_{tr} + p'_r) \\ + n_{tr}w_{tr}w'_{tr} \end{array} \right\}^{1/2} \qquad (5)$$

with $w'_{tr} = w_{tr} \exp(-\Delta/kT)$

where m_1 and m_2 refer to the positive and the negative signs of the second term, respectively. n_{tr} is the population of the trap, w_{tr} the transfer rate from the donor to the trap, w_{tr} the back transfer rate from the trap to the donor, n_q the population of the quencher, w_q the transfer rate to the quencher, W the energy transfer rate to the acceptor, Δ the trap depth, p_r the radiative transition probability of the intrinsic donor, p'_r the radiative transition probability of the perturbed donor. In this equation, a Boltzmann distribution is assumed between the donor and the shallow trap. The temperature dependence of the intrinsic emission intensity relative to the trap emission is explained very well by this expression.

On the other hand, Boulon considered the energy transfer in a three-level scheme assuming the presence of the shallow and the deep traps. This model has been well applied to understand the energy transfer process in oxides and glasses doped with alkali-earth and rare earth ions [71]. We get the following m_1 and m_2 parameters by considering the populations of the donor (N_2), the shallow trap (N_1) and the deep trap (N_0) in the presence of an acceptor:

$$m_1 = w_r + w_{21} + w_{12} + w_{20} + w_q + W \qquad (6a)$$

$$m_2 = w_r + \frac{w_{12}(w_q + W + w_{20}) - w_r^2}{m_1 + w_r} \qquad (6b)$$

where w_r is the radiative transition probability of both the intrinsic and the perturbed donors, w_{21} the transfer rate from the donor to the shallow trap, w_{12} the back transfer from the shallow trap to the donor, w_{20} the transfer rate from the donor to the deep trap (with neglect of back transfer w_{02}), w_q the transfer rate to the quencher, and W the transfer rate to the acceptor. In these models, different notations are cited from the original papers, but they are equivalent as follows: $n_{tr}w_{tr}=w_{21}$, $n_q w_q=w_q$, $w_{tr}'=w_{12}$, $p_r=w_r$. The rate equation involving multiple origin of centers p_{ri} can be solved in more than four-level scheme. Although the relation at Eq. (2) can be solved for $l>2$, increase of additional parameters is not

practical for us. Instead, we can extend the solution for many centers. In the frame work of two- and three-level schemes, we introduce the two different donor-acceptor transfer rates

$$W_I = m(D + A) - m(D) \tag{7a}$$

$$W_{II} = m^*(D + A) - m^*(D) \tag{7b}$$

The validity of the relations at Eqs. (5) and (6) is proven in the practical models. In Krol model, the following expression is satisfied:

$$W = W_I \approx W_{II}. \tag{8a}$$

Similarly, Boulon model results in the following expression:

$$W \approx W_I \approx W_{II} \tag{8a}$$

In this way, the excitation energy transfer rate W_I is exactly the same as that in the Krol model. The other transfer rate W_{II} is approximately equivalent to W in the two different models.

2.3
Single-Step Energy Transfer Model in Insulating Solids

The Dexter model of resonant energy transfer has been widely accepted for RE ions in glasses and solids [77]. In the following we shall compare it with the Huber-Krol-Boulon models. For electric dipole-dipole interactions, luminescence decay curve of a donor is

$$I(t) = I_0 \exp\left(-\gamma_R t - \sqrt{\pi} \left(\frac{R_0}{R}\right)^6 \sqrt{\gamma_R t}\right) \tag{9}$$

where R is the distance between donor and acceptor, R_0 the critical distance at which γ_R coincides with W. Fujii et al. [78] has discussed the excitation energy transfer of dye molecules dispersed in sol-gel glasses in terms of the luminescence intensity $I(t)$, the weight-averaged decay time $\langle \tau_3 \rangle$ and the rate parameter $\langle m_3 \rangle$ as

$$I(t) = I_0 \exp(-\langle m_3 \rangle t) \tag{10}$$

$$\langle m_3 \rangle = \frac{A_1 \tau_1 + A_2 \tau_2}{A_1 \tau_1^2 + A_2 \tau_2^2} = \frac{1}{\langle \tau_3 \rangle} \tag{11}$$

where $I(t)$ is approximated by the single exponential decay function. The energy transfer rate W_3 in Dexter model is given by

$$W_3 = \langle m_3(D + A) \rangle - \langle m_3(D) \rangle \tag{12}$$

where notations in the relation (2) are referred and $\langle m_3(D) \rangle$ is approximately equal to γ_R.

2.4
Energy Transfer Rate and Critical Distance in Four Different Models

In this way, we have considered three kinetic models in order to estimate the excitation energy transfer rates W. Luminescence decay curves of the donor are analyzed using rate constants m_1, m_2 (in the bi exponential curve fitting) and m_3 (single exponential). In these models, we have assumed that the difference of decay profiles of the donor in the (D+A) and (D) matrices should be attributed to the presence of the acceptor. The energy transfer rates in such three models are summarized below.

Model I is based on Huber-Krol-Boulon theory for insulating and disordered matrices and it gives

$$\text{Model I:} \quad W_1 = m(D + A) - m(D)$$
$$= m_1(D + A) + m_2(D + A) - m_1(D) - m_2(D) \tag{13}$$

Model II is based on the same model using a different approximation:

$$\text{Model II:} \quad W_2 = m^\star(D + A) - m^\star(D)$$
$$= m_1(D + A) - m_2(D + A) - m_1(D) + m_2(D) \tag{14}$$

Model III is based on the resonant energy transfer theory developed by Dexter-Inokuchi-Hirayama which gives approximately

$$\text{Model III:} \quad W_3 = \langle m_3(D + A)\rangle - \gamma_R \tag{15}$$

Our next approach is to estimate energy transfer processes in sol-gel glasses and to derive critical distances of energy transfer R_0 from the transfer rate W_i (i=1,2,3) defined in Eqs. (13), (14), and (15). According to conventional methods, we have

$$R_0 = (W\gamma_R)^{\frac{1}{6}}R = \left(\frac{W\gamma_R}{16\pi^2 c_A^2}\right)^{\frac{1}{6}} \tag{16}$$

where R_0 is the critical distance of energy transfer for the transfer rate W in three models. Since W is proportional to an overlap integral between donor and acceptor, R_0 is varying according to the combination of RE ion donor-acceptors. We then define energy transfer efficiency η using biexponential decay functions as follows:

$$\eta = W_3/\langle m_3(D)\rangle \tag{17}$$

where $\langle m_3(D)\rangle$ is the weight-averaged rate constant. According to Dexter's theory the concentration of the acceptor c_A is correlated to the transfer rate W_3 as

$$W_3 = \langle \tau_3(D + A)\rangle \gamma_R(c_A/c_0)^2 \tag{18}$$

in which c_0 is the critical concentration of the acceptor. The transfer rate W_3 is proportional to c_A^2 in the resonant energy transfer treatments.

In addition to the models described above we have considered a further model, *Model IV*, which deals with the trapping-limited energy transfer in porous

solids in which the energy transfer rates to traps and acceptors are of competitive order of magnitudes. If we assume the presence of a single trapping site in Eq. (4), the energy transfer rate W_4 is

$$\text{Model IV:} \quad W_4 = [m(D + A) - m(D)]/2 \tag{19}$$

This result is different from Eq. (13) only by factor 0.5. Therefore we cannot discriminate the two processes: (i) the resonant energy transfer, and (ii) the trapping-limited energy transfer mechanism. However, if the energy transfer rate or the critical distance of energy transfer are nearly the same for all lanthanides ions, the trapping-limited mechanism is dominant as we will see later.

3
Experimental Procedures

We have prepared xerogel and annealed sol-gel SiO_2 glasses singly-doped with Eu^{3+} (0.01–10.0 mol%) and those materials co-doped with Eu^{3+} (1 mol%) and Ln^{3+} (nominally 1 mol%, Ln=La, Pr, Nd, Sm, Gd, Tb, Dy, Er, Yb). In the case of experiments on concentration dependence of Nd^{3+}, 0.1–2.0 mol% activator was put into the host [69]. From a solution of tetraethylortho-silicate (TEOS), diethoxydimethyl-silane (DEDMS), water, ethanol, and RE nitrates in suitable proportions, xerogel was obtained in one to three months. We gradually heated it up to 600 °C with a temperature gradient of 50 °C/h and kept at 600 °C for 24 h. The obtained sol-gel glasses are transparent and homogeneous solids. The glass sample was attached to a cold finger inside the cryogenic system using a silver paste. Luminescence and decay times were measured at temperatures between 10 and 300 K under a N_2-laser (337.1 nm) excitation using a computer controlled spectroscopic system based on a Spex 1401 double monochromator, SR400 photon counter, and DG420 digital oscilloscope, developed in our laboratory [14, 65].

4
Luminescence and Energy Transfer of RE Ions in Xerogel and Sol-Gel SiO$_2$ Glasses

4.1
Luminescence Spectra, Selection Rules and Decay Curves

Figure 1 shows the luminescence of Eu^{3+} (1 mol%) in xerogel and sol-gel glasses at 300 K. The central peak at 16,300 cm^{-1} is due to the ${}^5D_0 \rightarrow {}^7F_2$ transition. The intensity in annealed silica glass is about three times as large as that in xerogel. Furthermore, the line width observed in sol-gel glass is broader than that in xerogel. This is because of strong inhomogeneous broadening of Eu^{3+} emission in sol-gel glasses.

Luminescence of Eu^{3+} ions in xerogel and sol-gel silica glasses was investigated as a function of concentration in the wide range (0.01–10.0 mol%). Figure 2 shows luminescence spectra of xerogel doped with 0.01 (solid line) and 1.00 (broken line) mol% of Eu^{3+} at 300 K. A line with an asterisk is a plasma line of a
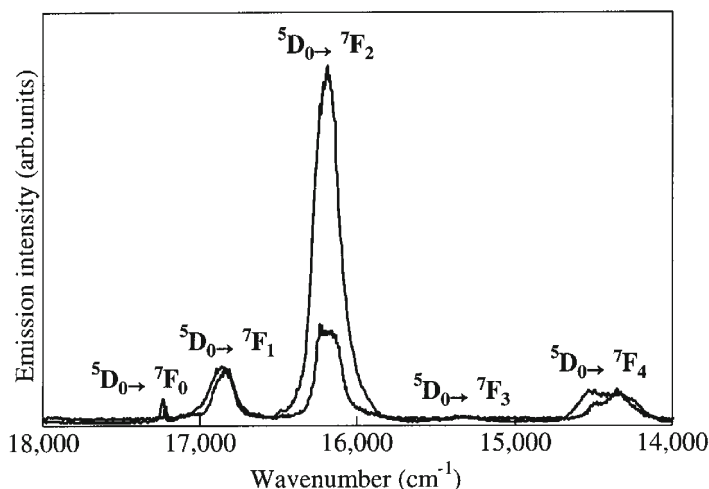
Fig. 1 Luminescence spectra of Eu^{3+} in xerogel (*lower line*) and annealed sol-gel (*upper line*) silica glass measured at $T=300$ K under a N_2-Laser excitation. Unless otherwise stated, the concentration of RE ions is set to be 1 mol% in the following figures
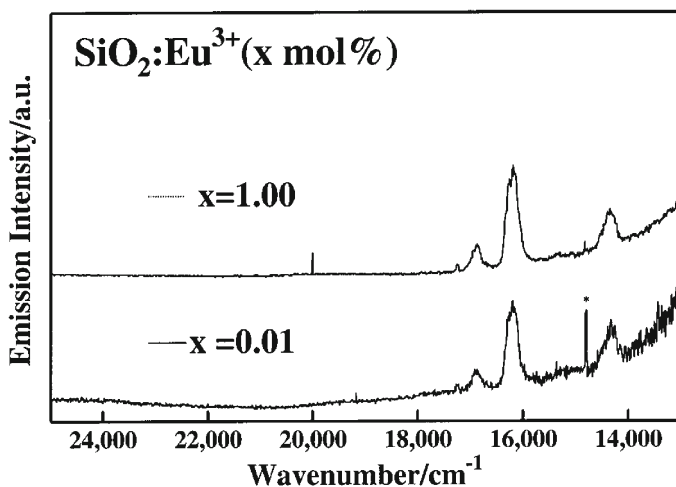
Fig. 2 Luminescence spectra of xerogel doped with 0.01 (*solid line*) and 1.00 (*broken line*) mol% of Eu^{3+}, measured at 300 K under a N_2-Laser excitation. The spectra are corrected for optical gain in the detection system

N_2-laser for reference. The sharp f-f lines are seen over a broad band tail extending to 12,000 cm^{-1}. The emission band in the lower energy is apparently enhanced in intensity by computer calibration of photomultiplier (PMT) gain. This is comparable to raw spectra in Fig. 1. Even if the concentration is increased from 0.01 to 10 mol%, we do not see any spectral changes in luminescence.
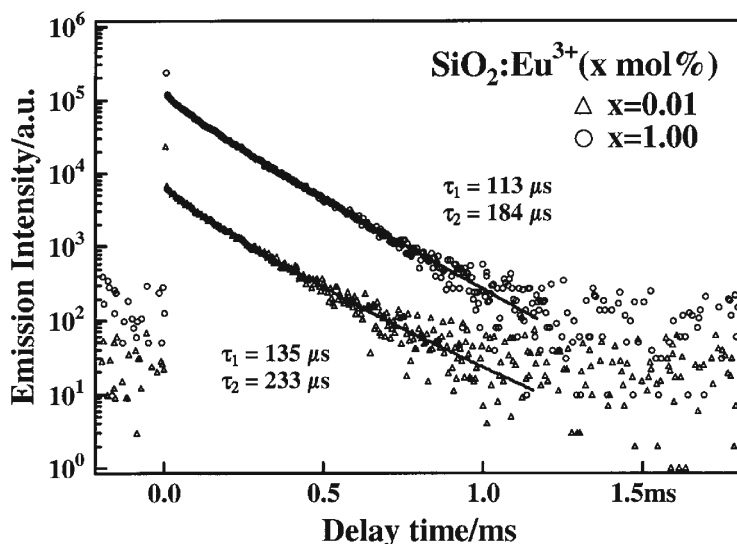
Fig. 3 Luminescence decay profiles of 16,300 cm^{-1} peak in xerogel doped with 0.01 (*triangle*) and 1.00 (*open circle*) mol% of Eu^{3+}, measured at 300 K under a N$_2$-Laser excitation. The short and long lifetimes are calculated by assuming the biexponential decay curves

Figure 3 presents luminescence decay profiles of the 16,300 cm^{-1} peaks of Eu^{3+}-doped xerogel at 300 K. The dopant concentrations are 0.01 (triangle) and 1.00 (open circle) mol%. The two decay curves obey approximately to the biexponential decay function. Table 1 summarizes calculated short lifetimes τ_1 ($=1/m_1$) and long lifetimes τ_2 ($=1/m_2$) of various samples in units of ms.

With increase of the concentration of dopants, short and long lifetime components are found to become smaller by concentration quenching. If we assume the diffusion-limited donor-donor energy transfer among Eu^{3+} ions, the decay function can be expressed by a single exponential function at long time limit [72, 78]. The inverse of the lifetime is a sum of the intrinsic decay rate and the diffusion-constant-dependent energy migration rate. If a decay time of 0.233 ms, taken from the most diluted xerogel sample, is considered to be the intrinsic decay component, the energy migration in porous xerogel occurs within 0.9±0.1 ms when concentration is less than 1 mol%. From these experiments, the concentration of

Table 1 Concentration dependence of short, long and average life times (in units of ms) of Eu^{3+} emission at 16,200 cm^{-1} measured from Eu(III)-doped xerogel at room temperature. See text for details

Eu^{3+}(mol%) in xerogel	0.01	0.1	0.5	1.0	5.0	10.0
Short lifetime: τ_1 (ms)	0.135	0.139	0.115	0.113	0.142	0.064
Long lifetime: τ_2 (ms)	0.233	0.198	0.195	0.184	0.177	0.176
Average lifetime (ms)	0.166	0.155	0.196	0.183	0.163	0.178
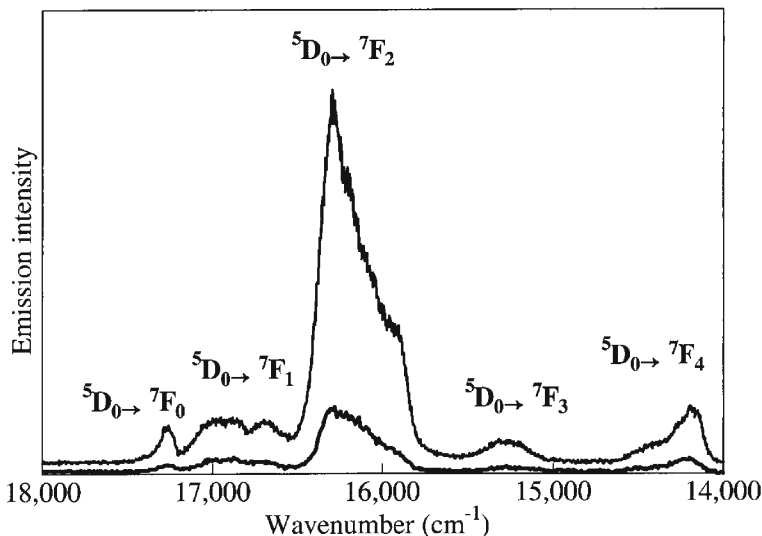
Fig. 4 Luminescence spectra of Eu^{3+} in xerogel (*lower line*) and annealed sol-gel (*upper line*) silica glass with codopant Yb^{3+}, measured at T=300 K under a N_2-Laser excitation

dopant is set to be 1 mol% in which enough gains are obtainable while concentration quenching is avoided.

Figure 4 shows luminescence of Eu^{3+} in the presence of Yb^{3+}. The prominent peak in the center has a dissymmetric spectral shape with a large linewidth broadening. Since this spectral change can only be seen in the presence of La, Pr, and Yb, it should be due to the nephelauxetic effects of the respective codopants. Explicitly, it is induced by cloud expansion or a loosening of the 4f cloud by weak covalent bonding in the hypersensitive transition [77].

Decay profiles of Eu^{3+} at 16,300 cm^{-1} were measured at 10 and 300 K, as shown in Fig. 5, in sol-gel silica glasses doped with Eu^{3+} and Er^{3+}. Luminescence decay times at 300 K are shorter than those at 10 K because of thermal quenching. As shown in this figure, the decay curve of Eu^{3+} in the glass becomes faster by energy migration from Eu^{3+} to Er^{3+} ions. A shortening of the lifetime by codopants is generally observed in the decay profiles for most of the Ln^{3+} ions, but annealed glasses doped with Eu^{3+} and Tb^{3+} are more complex because of spectral overlaps. Decay times in xerogel are also in general shorter than those in sol-gel glasses. This is because nonradiative processes are enhanced in xerogel by OH^- (hydroxy) ions. We further notice in Fig. 5 that the decay curves are not reproducible by a single exponential function. This observation is an important point of discussion on excitation energy transfer processes in this paper. We assume the presence of various centers (intrinsic and perturbed ones, defects, killers, traps etc.) in a model scheme which should give rise to the complex decay profiles in the glasses.

Luminescence spectra of annealed sol-gel SiO_2:Eu^{3+} and SiO_2:Eu^{3+}, Dy^{3+} at 10 K and room temperature are shown in Fig. 6. The corresponding thermal
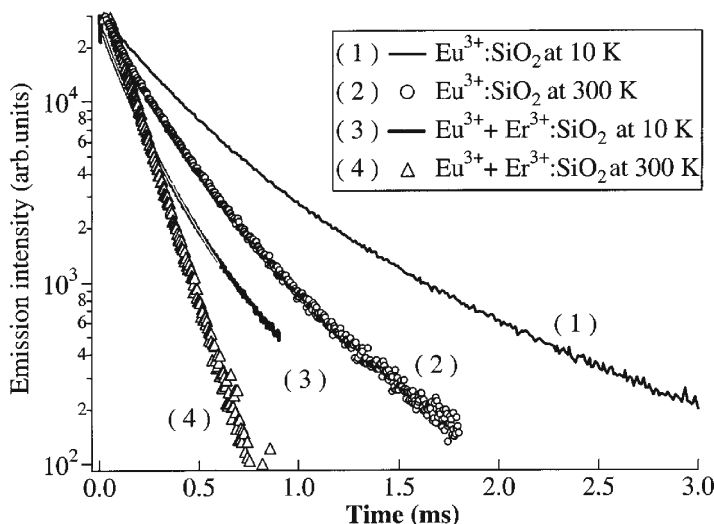
Fig. 5 Luminescence decay profiles in the $^5D_0 \rightarrow {}^7F_2$ transition of Eu^{3+} ion at 16,300 cm^{-1} in annealed sol-gel silica glasses doped with Eu^{3+} at T=10 K (*graph 1*) and 300 K (*graph 2*). Decay curves for similar glasses doped with Eu^{3+} and Er^{3+} at T=10 K (*graph 3*) and 300 K (*graph 4*) are also shown for comparison

quenching of the luminescence decay is seen in Fig. 5. Three peaks are assigned to the $^5D_0 \rightarrow {}^7F_1$ (16,900 cm^{-1}), $^7F_2$ (16,300 cm^{-1}), and $^7F_4$ (15,500 cm^{-1}) transitions of Eu^{3+}. New and relatively weak peaks appearing at around 17,400 cm^{-1} are due to the $^4F_{9/2} \rightarrow {}^6H_{13/2}$ transition of Dy^{3+} ions. The relative intensities of the three prominent peaks are changing by the addition of Dy^{3+}. In order to understand the interaction between Eu^{3+} and the codopant, the relative emission intensities for the $^7F_1$, $^7F_2$ and $^7F_4$ terminal levels were measured at 10 and 300 K for a combination of various RE ions doped in SiO_2 glasses, as shown in Table 2.

The transition mechanisms of three transitions of Eu^{3+} are ascribed either to the magnetic-dipole allowed transition ($^5D_0 \rightarrow {}^7F_1$) or to the forced electric-dipole transitions ($^5D_0 \rightarrow {}^7F_2$, $^7F_4$). All these fluorescent transitions do not show changes in spectral shapes at temperatures between 10 K and 300 K. It is noticed that the relative emission intensities of these peaks show strong dependence on codopants. We want to consider the selection rules for the transition by symmetry. In amorphous sol-gel silica glasses water molecules may be octahedrally co-ordinated to the dopant. The Eu^{3+} ion usually substitutes the Si site of tetrahedral symmetry (without inversion symmetry), but it takes also the interstitial site of pseudo-octahedral symmetry (close to inversion symmetry). If the Eu^{3+} ion occupies an interstitial site with inversion symmetry, electric-dipole transitions are strictly forbidden by the parity selection rule [51]. On the other hand, magnetic-dipole and vibronically induced (vibronic) electric-dipole transitions may be allowed in the case of no inversion center. If a site with inversion symmetry is occupied by Eu^{3+} ions, the $^5D_0 \rightarrow {}^7F_1$ emission transition is dominant. If on the
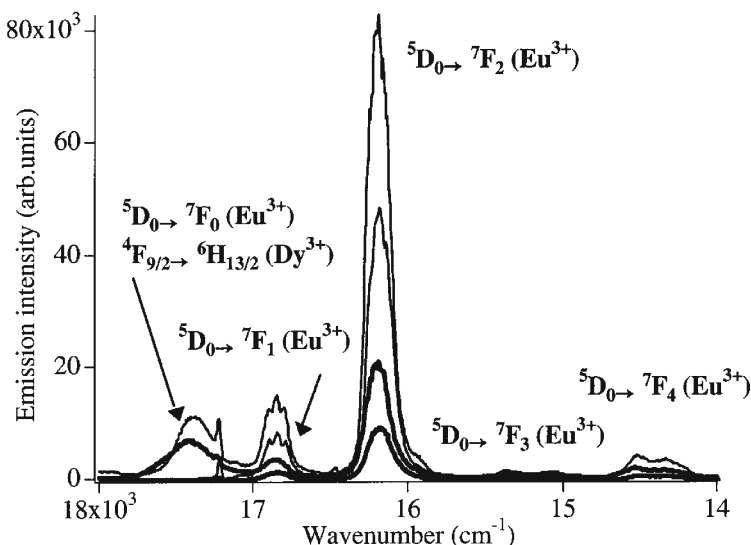
Fig. 6 Luminescence spectra of annealed sol-gel silica glasses doped with Eu^{3+} and those with Eu^{3+} and Dy^{3+}, measured at $T=10$ and 300 K under a N_2-Laser excitation. *From top to bottom*, the spectra of (1) Eu^{3+} at $T=10$ K, (2) Eu^{3+} at $T=300$ K, (3) $Eu^{3+}+Dy^{3+}$ at $T=10$ K and (4) $Eu^{3+}+Dy^{3+}$ at $T=300$ K are displayed in relative intensity units

Table 2 Relative emission intensities of the $^5D_0 \rightarrow ^7F_J$ (J=1, 2, 4) transition of Eu^{3+} with other RE ions co-doped in SiO_2 xerogel and sol-gel glasses at 10 and 300 K[a]

RE(III) ion dopant	$I(^7F_2/^7F_1)$			$I(^7F_2/^7F_4)$		
	Glass		Xerogel	Glass		Xerogel
	10 K	300 K		10 K	300 K	
Eu, La	4.0	4.5	2.1	3.7	3.7	5.0
Eu, Pr	10.3	12.2	N.A.	7.7	9.1	N.A.
Eu, Nd	6.1	9.8	11.3	11.0	11.0	8.5
Eu, Sm	7.0	5.7	2.8	9.2	9.2	5.7
Eu	5.6	6.2	1.9	11.7	10.8	3.1
Eu, Gd	3.0	3.2	1.7	6.9	5.5	3.4
Eu, Dy	7.3	6.1	N.A.	13.0	10.6	N.A.
Eu, Er	5.4	5.7	5.1	10.9	9.7	13.7
Eu, Yb	6.2	7.5	7.0	6.0	6.3	5.3

[a] $I(^7F_2/^7F_1)$ and $I(^7F_2/^7F_4)$ stand for the relative emission intensity of $I(^5D_0 \rightarrow ^7F_2)/I(^5D_0 \rightarrow ^7F_1)$ and $I(^5D_0 \rightarrow ^7F_2)/I(^5D_0 \rightarrow ^7F_4)$, respectively.

other hand there occurs a small deviation from inversion symmetry, the $^5D_0{\rightarrow}^7F_2$ transition becomes allowed by forced electric-dipole mechanism. This principal line is hypersensitive to the appearance of inversion symmetry or to the different coordination geometry (chemical environment) of the Eu^{3+} ion. The increase of the intensity ratio of $I(^5D_0{\rightarrow}^7F_2)/I(^5D_0{\rightarrow}^7F_1)$ is now considered to be due to the lack of inversion symmetry by addition of Ln. The intensity ratio of $I(^5D_0{\rightarrow}^7F_2)/I(^5D_0{\rightarrow}^7F_4)$ should remain constant irrespective of chemical properties of codopants, because both transitions are due to the forced electric-dipole mechanism. The observed changes of intensity ratios, especially in the co-presence of La^{3+}, Pr^{3+} and Yb^{3+} are due to hypersensitivity or to the expansion of interatomic electronic clouds by the nephelauxetic effect mentioned above.

4.2
Concentration Dependence of Energy Transfer Rate

To verify the usefulness of *Model I*, we measured concentration dependence of the energy transfer rate W_1 using Eu^{3+} and Nd^{3+} co-doped sol-gel silica glasses prepared by different conditions. Figure 7 shows changes of W_1 (s^{-1}) from Eu^{3+} ion (1 wt%) to Nd^{3+} ion as a function of Nd^{3+} concentration (0.1–2.0 wt%).

A linear correlation is clearly observed between m and the square of Nd concentration according to Eq. (18). Measurements were done at 10, 80, 200, and 300 K and the following critical distances were obtained using *Model I* for glasses
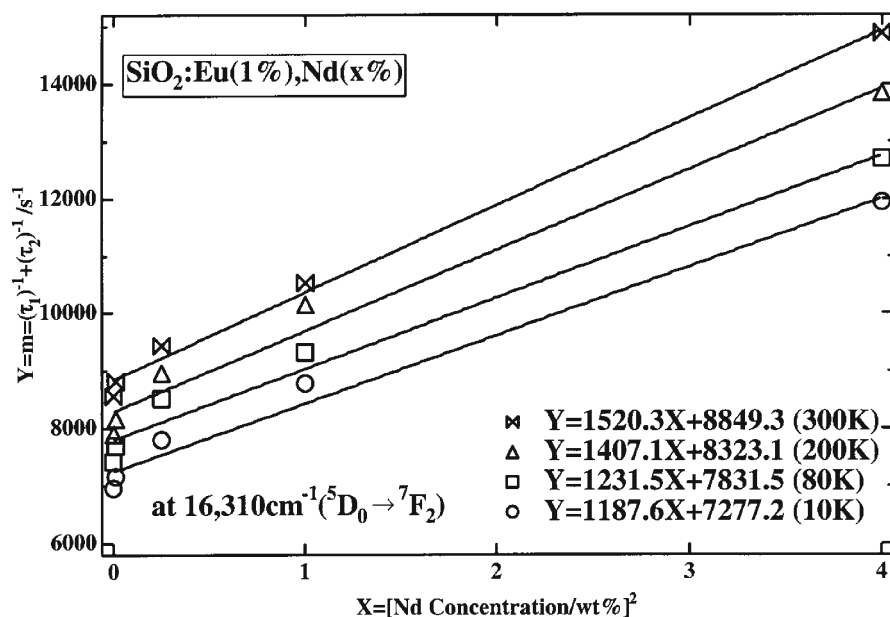
Fig. 7 Energy transfer rate constant m (s^{-1}) as a function of Nd^{3+} concentration in Eu^{3+} and Nd^{3+} co-doped sol-gel silica glasses at T=10, 80, 200, and 300 K

Table 3 Critical distance of energy transfer R_0 (in nm) based on *Models I* and *III* of Eu^{3+} in the presence of rare earth (RE=La^{3+}, Pr^{3+}, Nd^{3+}, Sm^{3+}, Gd^{3+}, Dy^{3+}, Er^{3+}, Yb^{3+}) co-dopants in xerogel and sol-gel SiO_2 glasses at T=10 and 300 K[a]

Dopant[a]	Model III[b]			Model I[b]			Ref.
	Sol-gel SiO_2		Xerogel	Sol-gel SiO_2		Xerogel	Glass[c]
	10 K	300 K		10 K	300 K		300 K
Eu, La	0.94	0.80	0.97	1.05	1.01	1.31	N.A.
Eu, Pr	0.98	0.96	N.A.	1.07	1.04	N.A.	0.80
Eu, Nd	0.93	0.90	1.03	1.04	1.02	1.20	1.05
Eu, Sm	0.80	0.79	0.70	0.97	0.99	1.37	0.37[d]
Eu, Gd	0.95	0.87	0.96	1.00	1.03	1.24	N.A.
Eu, Dy	0.96	0.95	1.04	0.99	1.00	1.19	0.71
Eu, Er	0.93	0.86	0.88	0.88	0.90	1.18	0.81
Eu, Yb	1.00	0.89	0.98	1.09	1.07	1.35	0.51
Average	0.94	0.88	0.94	1.02	1.01	1.26	0.71
Deviation[e]	10	10	17	10	10	8	48

[a] Values are given for xerogel and sol-gel glass samples by two models.
[b] *Models III* and *I* stand for Dexter-Inokuchi-Hirayama and Huber-Krol-Boulon models, respectively.
[c] R_0 values determined by decay times in $Ca(PO_3)_2$ glass [79].
[d] R_0 value determined by change of emission intensity [79].
[e] Deviation from the average (in %).

annealed at 500 °C (and 200 °C): 0.66 (0.58), 0.64 (0.58), 0.63 (0.59), and 0.62 (0.59) in units of nm at 10 K, 80 K, 200 K and 300 K, respectively. The average R_0 values are 0.64 nm and 0.59 nm for glasses annealed at 500 and 200 °C, respectively. In this derivation, the transfer rate in the $^5D_0 \rightarrow {}^7F_2$ transition was calculated. The short and long lifetimes of SiO_2:Eu^{3+} (1 mol%) at 10 K are 0.213 and 0.444 ms, respectively. Since the calculation is not based on the total transfer rate (see below), the R_0 values are about half of those shown in Table 3. We shall then see the usefulness of *Model I* to describe the energy transfer scheme in sol-gel glasses.

4.3
Excitation Energy Transfer Processes of Rare Earth Ions

In this section we shall analyze the energy transfer processes in amorphous glasses using models to explain experiments on luminescence and decay curves. We introduce weight-averaged decay times and the energy transfer schemes. The total energy transfer rate (W_t) and the critical distance of the energy transfer (R_o) are calculated in the following way. First, it should be noticed that parameters in the $^5D_0 \rightarrow {}^7F_2$ transition are not sufficient to estimate the exact energy transfer rates and efficiency. In the calculation, we consider a total sum of the emission lifetimes from the $^5D_0$ to the three terminal levels, namely $^7F_1$, $^7F_2$ and $^7F_4$. This is because the emission probabilities were found to be dependent on the
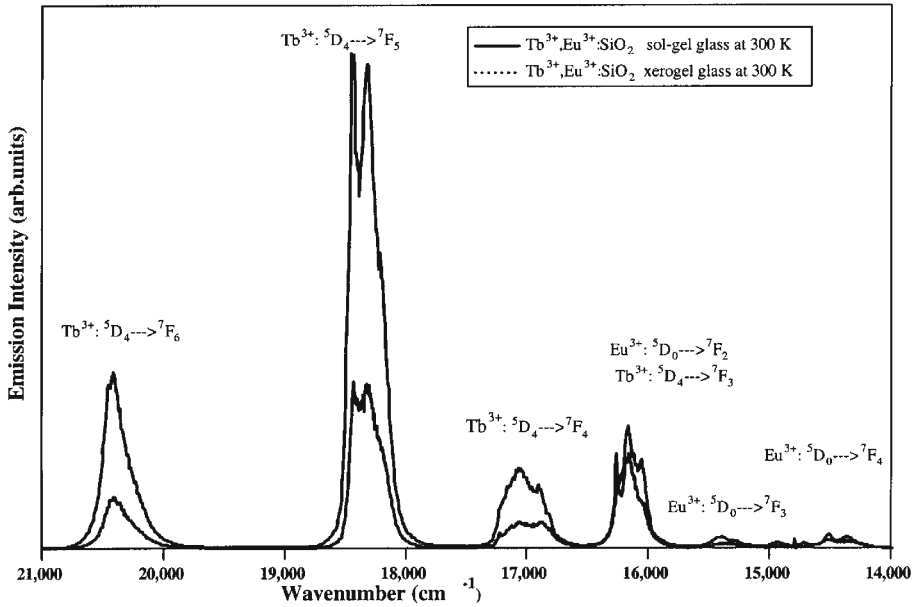
Fig. 8 Luminescence spectra of xerogel (*lower line*) and annealed sol-gel silica glass (*upper line*) doped with Eu^{3+} and Tb^{3+}, measured at 300 K under a N_2-Laser excitation

terminal levels, as shown in Table 2. The total transfer rate W_t is defined in our experiments as

$$W_t = W(^5D_0 \rightarrow {}^7F_1) + W(^5D_0 \rightarrow {}^7F_2) + W(^5D_0 \rightarrow {}^7F_4) \quad\quad (20)$$

Second, we use the following rate constants of $m(D+A)$, $m(D)$, $m^\star(D+A)$, $m^\star(D)$, $\langle m_3(D+A) \rangle$, $\langle m_3(D) \rangle$ obtained from decay profiles. The rate constants of SiO_2:Eu,Tb xerogel and sol-gel glasses are not included in this paper, because the luminescence spectra are accidentally overlapping at 16,300 cm^{-1} as shown in Fig. 8.

The critical distances for the energy transfer from Eu^{3+} to Ln^{3+} in SiO_2 xerogel and annealed sol-gel SiO_2 glasses are calculated at 10 and 300 K and they are presented in Table 2 for the cases of *Model I* (Huber-Krol-Boulon model) and *Model III* (Dexter-Inokuchi-Hirayama model).

Figure 9 illustrates the comparative critical distances of energy transfer from Eu^{3+} to Ln^{3+} ions in xerogel and sol-gel SiO_2 glasses. We employed *Models I* and *III* for the analysis of decay profiles measured at 300 and 10 K. The distances are displayed for the Ln^{3+} ions in the order of increasing atomic numbers. Calculation by *Model II* is not given in this chapter, because *Model II* requires approximations of higher order in a three-level scheme, as shown in the relation at Eq. (6). For comparison, reported data due to Eq. (9) and *Model III* are given for $Ca(PO_3)_2$ glasses prepared at high temperatures above 1000 °C [79]. Critical distances obtained by *Model I* give larger values than by *Model III*. R_0 values in xerogel glasses are larger than those found for annealed SiO_2 glasses. No appre-
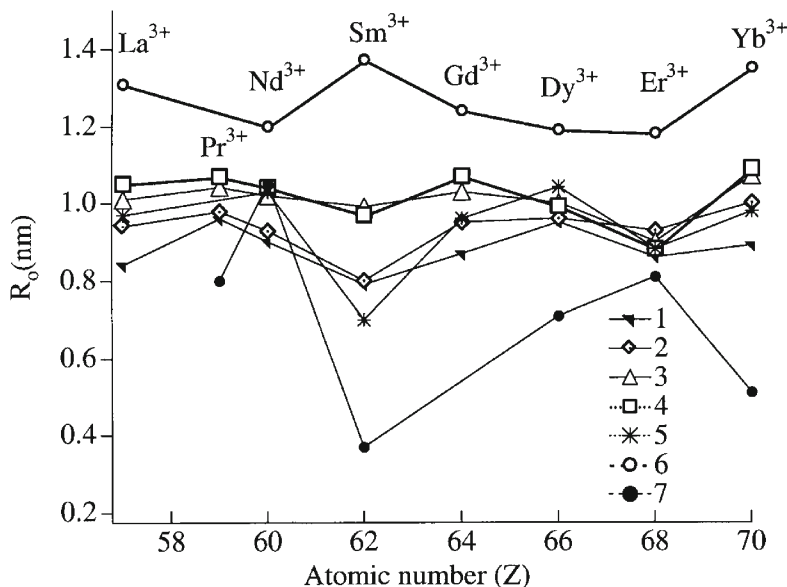
Fig. 9 Comparison of R_0 (nm) values of SiO_2:Eu^{3+}, RE^{3+} xerogel and annealed sol-gel glasses in two models at $T=300$ K and 10 K. For comparison, reported values in $Ca(PO_3)_2$ glasses prepared at high temperatures are displayed. Calculation is done for different models and sample conditions, as shown from *top to bottom*: (1) *Model III*, glass at $T=300$ K; (2) *Model III*, glass at $T=10$ K; (3) *Model I*, glass at $T=300$ K; (4) *Model I*, glass at $T=10$ K; (5) *Model III*, xerogel at $T=300$ K; (6) *Model I*, xerogel at $T=300$ K; and (7) reference data: *Model III*, $Ca(PO_3)_2$ glass at $T=300$ K. See text for models and calculations

ciable changes of R_0 values are found by change of temperatures and calculation methods as shown in Fig. 9. Using Dexter's model, the obtained R_0 values at room temperature, for example, are in the range of 0.88–0.07 nm for annealed glasses and 0.93–0.11 nm for xerogel glasses. Similarly the deviation is very small for R_0 values observed at 10 K. Namely, R_0 values were found in xerogel and sol-gel glasses to be with a deviation less than 10% from its average. On the contrary, in normal high-temperature $Ca(PO_3)_2$ glasses, they range over 0.71–0.36 nm with deviation of 48% at room temperature.

Dexter theory of resonant energy transfer indicates that the critical distance is a function of the overlap integral, that is to say, the overlap of the absorption spectrum of Eu^{3+} and the luminescence spectrum of the acceptor Ln^{3+}. Therefore, the critical distance should be different for a combination of lanthanides ions. However, on the average, the critical distance is about 1 nm in almost all xerogel and sol-gel glasses. Deviation from the average is about 10% in those sol-gel glasses, but it is about 48% in the reported normal glasses. These experimental findings are explained as follows. We reconsider the numerical values of a two-level scheme in Eq. (5). If the transfer rate to traps $n_{tr}w_{tr}$ is the fastest process among all the transition processes or as much fast as the intrinsic transition, the rate constant m is mostly determined by the transfer rate to traps. As we have seen in Fig. 5, m in SiO_2:Eu^{3+}+Nd^{3+} is 7.2×10^3 s^{-1} at 10 K in the absence of Nd^{3+}.

This factor increases to about 8.2×10^3 (s^{-1}) by addition of 1 mol% of Nd ion. By putting $p_r = 5 \times 10^3$ (s^{-1}) (200 µs at 10 K) and $W_I = 1000$ (s^{-1}) into Eq. (3) and Eq. (7), the transfer rate to traps is estimated to be 2.2×10^3 s^{-1} with neglect of terms due to the back-transfer w'_{tr}, the quenching process $n_q w_q$ and the perturbed rate p'_r. Furthermore, from temperature dependence of m, the activation energy of 66 cm^{-1} is obtained. Therefore, the transfer rate to traps is twice as fast as the energy transfer rate to the acceptor. The results give evidence of the fact that the energy transfer in sol-gel glasses is due to trapping-limited energy transfer mechanisms. The sol-gel glass is based on homogeneously broadened nm-size glassy network, and it is this material where size-limited energy transfer phenomena are clearly shown by luminescence spectroscopy.

4.4
Temperature Dependence of Luminescence and Decay Curves

Temperature dependence of luminescence spectra of Eu^{3+} ions doped in annealed sol-gel SiO$_2$ glass is shown in Fig. 10. With increase of the temperature from 10 to 300 K, the central peak due to the $^5D_0 \rightarrow ^7F_2$ transition as well as other peaks decrease in intensity together and show a spectral broadening of the sharp lines. Figure 11 shows similar luminescence spectra of annealed SiO$_2$:Eu^{3+}, La^{3+} glasses as a function of temperatures between 10 and 300 K. By comparing Figs. 10 and 11, remarkable spectral changes of structures are noticed after the addition of La^{3+} ion. The vibronically broadened structures with stark splittings are also found in other sol-gel glasses co-doped with Pr^{3+} and Yb^{3+}.
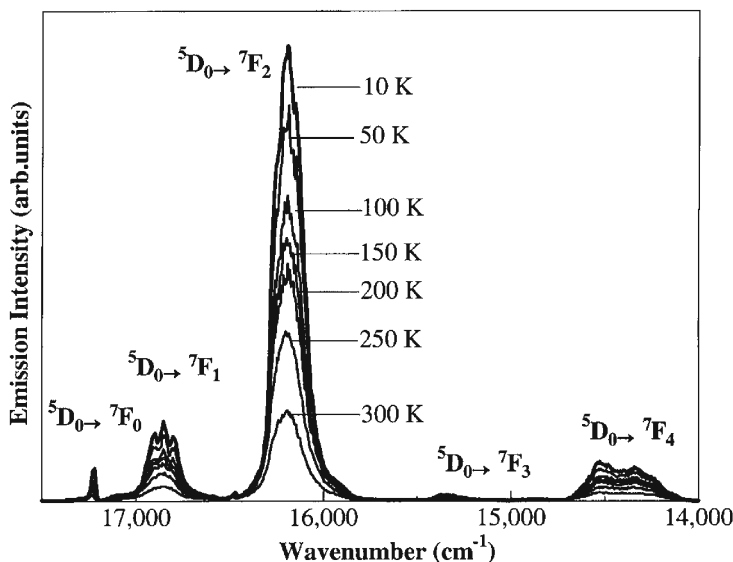
Fig. 10 Luminescence spectra of annealed sol-gel SiO$_2$:Eu^{3+} glass as a function of temperature between T=10 and 300 K
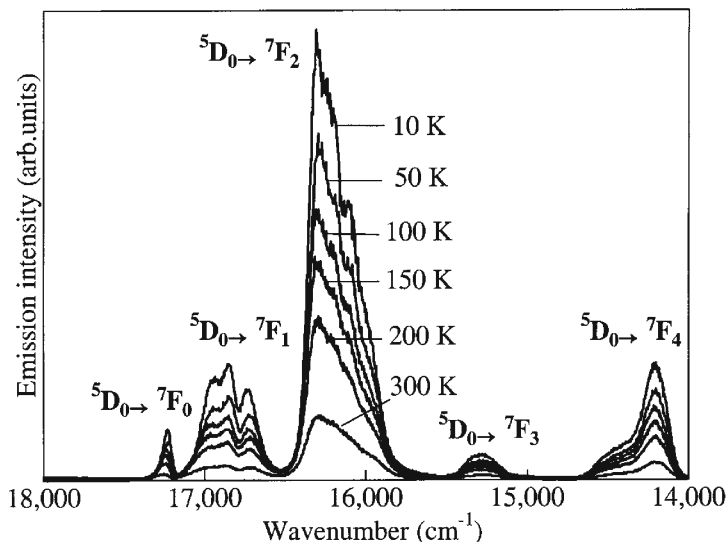
Fig. 11 Luminescence spectra of annealed sol-gel SiO_2:Eu^{3+}, La^{3+} glass as a function of temperature between $T=10$ and 300 K
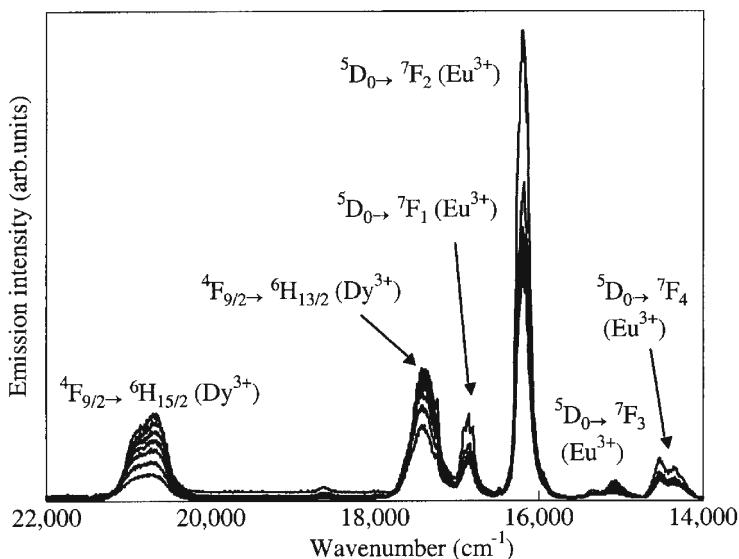
Fig. 12 Luminescence spectra of annealed sol-gel SiO_2:Eu^{3+}, Dy^{3+} glass as a function temperature, measured from *top to bottom* at $T=10, 50, 100, 150, 200, 250,$ and 300 K

Figure 12 shows luminescence spectra of annealed SiO_2:Eu^{3+}, Dy^{3+} as a function of temperatures between 10 and 300 K. By comparison of Figs. 6 and 12, the appearance of the same peaks is due to Dy^{3+} origins. In Fig. 12 thermal quenching of Dy^{3+} emission (at about 20,700 cm^{-1}) is seen to be stronger than that of Eu^{3+} (at about 16,300 cm^{-1}).

Smooth and continuous decrease in emission intensity was observed with increasing temperatures from 10 to 300 K as shown in Figs. 10–12. Figure 13 shows a variation of weight averaged lifetimes of the emission transition $^5D_0 \rightarrow ^7F_2$ of Eu^{3+} of annealed sol-gel glasses: SiO_2:Eu^{3+} and SiO_2:Eu, RE^{3+} (RE=Nd, Er, Yb). This result manifests the absence of the phase transitions in sol-gel glasses at low temperatures. Thermal quenching of emission intensities gave the following deactivation energy or trap depths (in cm^{-1}) in annealed and doped sol-gel glasses: 104 (Eu, Yb), 115 (Eu), and 124 (Eu, Pr). In the previous section we deduced a trap depth of 66 (Eu, Nd) cm^{-1}. Therefore, we have to assume the presence of a trap level or perturbed state at about 100 cm^{-1} below the intrinsic or perturbed Eu^{3+} ion level. Because of the absence of phase transitions in these glasses, it should be said that this sol-gel glass is an ideal host material for investigations of multi phonon relaxation processes in the confined amorphous structures.

Energy transfer between Eu^{3+} and other RE ions has been studied in $Ca(PO_3)_2$ glass [79] and other insulating solids [37, 50]. However, there are not sufficient data on the temperature dependence of energy transfer rate in sol-gel glasses. Figure 14 shows the energy transfer rate for *Model III* of annealed sol-gel SiO_2:
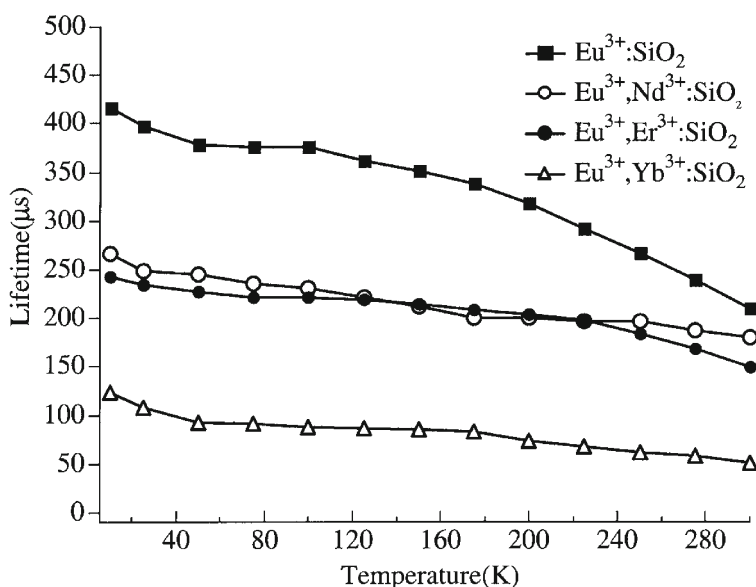
Fig. 13 Comparison of weight averaged lifetimes $\langle\tau_3\rangle$ of the emission transition $^5D_0 \rightarrow ^7F_2$ of Eu^{3+} of annealed sol-gel SiO_2:Eu^{3+} and SiO_2:Eu^{3+}, RE^{3+} (RE=Nd, Er, Yb) glasses at different temperatures. See text for definition of lifetimes
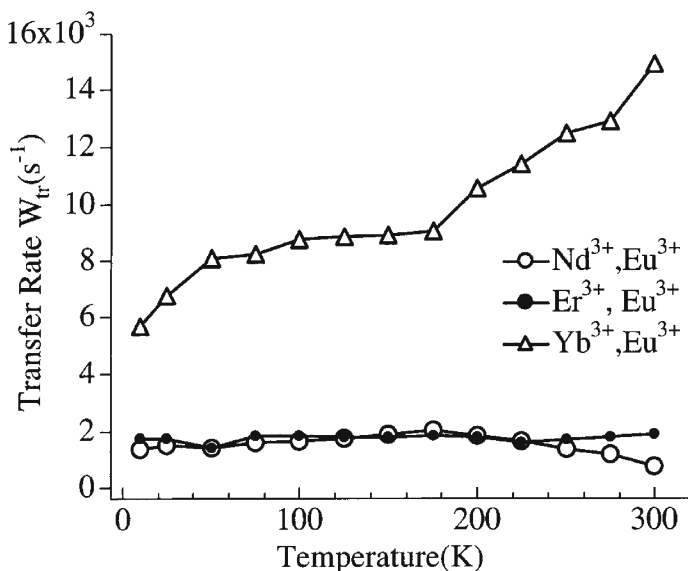
Fig. 14 Energy transfer rates W_I of annealed sol-gel SiO_2:Eu^{3+}, RE^{3+} (RE=Nd, Er, Yb) glasses as a function of temperature. The remarkable temperature dependence is due to the phonon assisted energy transfer mechanism. See text for details

Eu^{3+}, RE^{3+} (RE=Nd, Er, Yb) glasses as a function of temperatures. Temperature dependence of the energy transfer rates is not found in (Eu, Nd) and (Eu, Er) glasses. In the case of (Eu,Yb) glass, however, temperature dependent transfer rates are found because of the phonon-assisted energy transfer mechanism. From temperature dependence of the curve we estimate that the phonon-assisted energy transfer process involves four phonons of 2500 cm^{-1} [80].

The luminescence efficiency is expressed in terms of lifetimes by Eq. (17). In order to examine the temperature dependence of luminescence efficiency, we introduce a new luminescence population parameter $f(T)$ which is

$$f(T) = \frac{I(T) \langle \tau(0) \rangle}{I(0) \langle \tau(T) \rangle} = \frac{N(T)}{N(0)} \tag{21}$$

where $I(T)$ and $I(0)$ are luminescence intensities at temperatures T and $T=10$ K, respectively, $\langle \tau(T) \rangle$ and $\langle \tau(0)Y \rangle$ are corresponding weight-averaged lifetimes defined in Eq. (10). $N(T)$ and $N(0)$ are number of electrons in the lowest excited state at T and $T=0$ when the single exponential decay function holds in the whole temperature range. Figure 15 illustrates the temperature dependence of a parameter f in luminescence of sol-gel SiO_2:Eu^{3+}, Nd^{3+} glasses. With increase of temperatures from 10 to 300 K, the f value decreases to 0.12 gradually by thermal quenching of the population of the $^5D_0$ state. No discontinuous points are seen at all temperatures. This also verifies the absence of the structural changes at low temperatures. The problems of complex decay profiles in other Eu-Tb systems will be discussed separately.
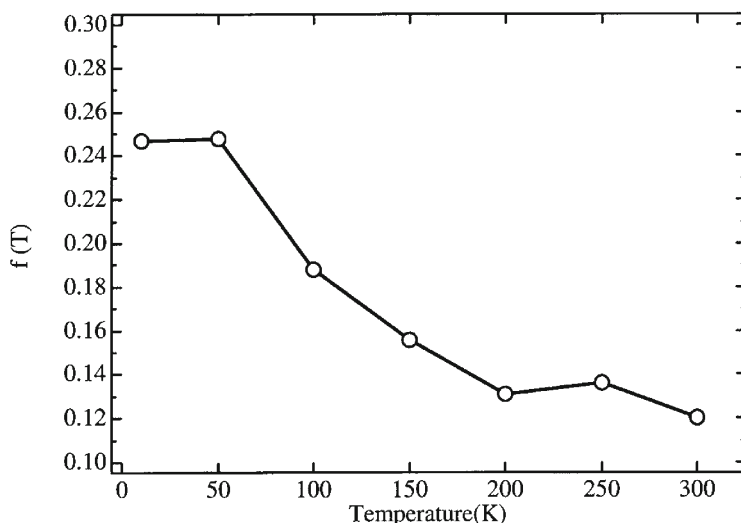
Fig. 15 Temperature dependence of a luminescence efficiency parameter f of sol-gel SiO_2: Eu^{3+}, Nd^{3+} glasses. For definitions, see text

5
Summary

We have investigated luminescence, decay times and energy transfer processes in xerogel and sol-gel SiO_2 glasses doped with Eu^{3+} and codopants (Ln=La, Pr, Nd, Sm, Gd, Dy, Er, Yb) as a function of temperatures in the temperature range between 10 and 300 K. We have not observed any unusual spectroscopic behavior below 300 K. Therefore, sol-gel glasses are good host materials to investigate spectral dynamics in nanometer size media. Furthermore the decay profiles may be approximated by bi-exponential functions. Luminescence and energy transfer processes from Eu^{3+} (sensitizer) to Ln^{3+} (activator), traps and other centers are discussed in terms of different model schemes: (i) *Model I* and *II* based on Huber-Krol-Boulon theory of multi-step energy transfer due to trapping-limited energy transfer processes, and (ii) *Model III* based on Dexter-Inokuchi-Hirayama theory, i.e. a single-step energy transfer due to a resonant energy transfer mechanism. Assuming *Models I* and *III*, we investigated energy transfer processes in nanoporous xerogel and sol-gel glasses. The average critical distance of energy transfer R_0 is 0.9 nm (±10%) in the porous hosts, irrespective of temperatures and a pair of Ln elements and choice of the matrix of xerogel or sol-gel glasses. In the sol-gel glass SiO_2:Eu^{3+}, Nd^{3+}, the transfer rate to traps was found to be twice as much fast as the donor-acceptor transfer rate. From these results we conclude that trapping-limited energy transfer mechanism is dominant in porous xerogel and sol-gel silica glasses in the wide temperature range.

Although quantum confinement effects were not observed in the nanoporous insulating solids, surface-enhancement effects and the presence of ultrafast decay times of less than 10 ns were observed as size effects in nanoporous matrices [2,

3, 7, 11, 33, 48]. We have newly prepared nanocrystals of ZnS: Cu, Al in nanoporous xerogel and sol-gel silica glasses. Their luminescence, time-resolved luminescence (TRS) and lifetimes were measured in the temperature range 10–300 K [81]. At room temperature, the doped xerogel represents a green band due to D(donor)-A(acceptor) pairs at 19,000 cm^{-1}. Under the excitation of a picosecond UV-laser (300 nm), a combination of blue and green bands is observed after a delay time of 2 ns. The luminescence spectral features are associated with D-A pairs and self-activated (SA) centers in the presence of surface-modified defect centers. We hope to prepare various new nano-phosphors due to complex ion centers in the advancement of sol-gel technology [9, 56].

6
References

  1. Reisfeld R, Jørgensen CK (1992) Struct Bond 77:207
  2. Reisfeld R (1996) Struct Bond 85:215
  3. Sakka S (1996) Struct Bond 85:1
  4. Morita M, Herren M (1997) J Sci Inform Display 5:127
  5. Herren M, Yamanaka K, Miyazaki N, Morita M (1997) J Lumin 72/74:417
  6. Morita M, Miyazaki N, Murakami S, Herren M, Rau D (1998) J Lumin 76/77:238
  7. Morita M, Kajiyama S, Kai T, Rau D, Sakurai T (2001) J Lumin 94/95:91
  8. Morita M, Kajiyama S, Rau D, Sakurai T, Iwamura M (2002) J Lumin 102/103:608
  9. Morita M, Kajiyama S, Rau D, Sakurai T, Baba M, Iwamura M (2004) Mater Sci Poland 22:5
 10. Herren M, Nishiuchi H, Morita M (1994) J Chem Phys 101:4461
 11. Herren M, Yamanaka K, Morita M (1995) Technical Report Seikei Univ 32:61
 12. Xu W, Dai S, Toth LM, Del G, Cul D, Peterson JR (1995) J Phys Chem 99:4447
 13. Gudong Q, Minquan W, Mang W, Xianping F, Zhanglian H (1997) J Lumin 75:63
 14. Morita M, Rau D, Kai T (2002) J Lumin 100:97
 15. Zhang Y, Wang M, Wu D (1998) J Phys Chem Solid 59:1053
 16. Hnatejko Z, Klonkowski A, Lis S, Czarnobaj K, Pietraszkiewicz M, Elbanowski M (2000) Mol Cryst Liq Cryst 354:795
 17. Klonkowski AM, Lis S, Hnatejko Z, Czarnobaj K, Pietraszkiewicz M, Elbanowski M (2000) J Alloy Compd 300/301:55
 18. Matthews LR, Knobbe ET (1998) Sol-gel Process Adv Mater 247:1
 19. Nassar EJ, Serra OA, Calefi PS, Manso CMPC, Neri CR (2001) Mater Res 4:18
 20. Zaitoun MA, Kim T, Lin CT (1998) J Phys Chem B 102:1122
 21. Kaufmann VR, Avnir D (1986) Langmuir 2:717
 22. Carlos LD, Sa Ferreira RA, De Zea Bermudez V, Molina C, Bueno LA, Ribeiro SJL (1999) Phys Rev B 60:10042
 23. Cordoncillo E, Escribano P, Guaita FJ, Philippe C, Viana B, Sanchez C (2002) J Sol Gel Sci Tech 24:155
 24. Gaponenko NV, Davidson JA, Hamilton B, Skeldon P, Thompson GE, Zhou X (2000) Appl Phys Lett 76:1006
 25. Maciel GS, Biswas A, Prasad PN (2000) Opt Commun 178:2
 26. Andrews DL, Jenkins RD (2001) J Chem Phys 114:1089

27. Maciel GS, Biswas A, Prasad PN (2000) Opt Comm 178:65
28. Morais EA, Ribeiro SJL, Scalvi LVA, Santilli CV, Ruggiero LO, Pulcinelli SH, Messaddeq Y (2002) J Alloy Compd 344:217
29. Silver J, Martinez-Rubio MI, Ireland TJ, Fern GR, Withnall R (2001) J Phys Chem B 105:9107
30. Schweizer T, Samson BN, Hector JR, Brocklesby WS, Hewak DW, Payne DN (1999) J Opt Soc Am B 16:308
31. Cormier G, Capobianco JA, Morrison CA, Monteil A (1993) Phys Rev B 48:16290
32. Antic-Fidancev E, Lemaitre-Blaise M, Porcher P, Taibi M, Aride J (1992) J Alloy Compd 188:242
33. Morita M, Fujii H, Minami Y, Rau D, Baba M, Yoshita M, Akiyama H (2000) J Lumin 87/89:478
34. Murakami S, Herren M, Rau D, Sakurai T, Morita M (1999) J Lumin 83/84:215
35. Lochhead MJ, Bray KL (1995) Chem Mater 7:572
36. Sellars MJ, Fraval E, Longdell JJ (2004) J Lumin 107:150
37. Bouajaji A, Monteil A, Bovier C, Ferrari M, Piazza A (1944) J Phys (Paris) C4:579
38. Brecher C, Bertram RH, Lempicki A (2004) J Lumin 106:159
39. Bhargava RN, Gallaghu D, Hong X, Nurmikko (1994) Phys Rev Lett 72:416
40. Reisfeld R (2002) J Alloys Compds 341:56
41. Yang P, Lue M, Song C, Liu S, Ai ZP, Xu D, Yuan D, Cheng X (2003) Opt Mater 23:513
42. Yang P, Lue M, Song C, Ai ZP, Xu D, Yuan D, Cheng X (2003) Mater Sci Eng B 97:149
43. Yang P, Lue M, Song C, Gu F, Liu S, Xu D, Yuan D, Cheng X (2002) J Non-Cryst Solid 311:99
44. Yang P, Lue M, Song C, Xu D, Yuan D, Zhou G (2002) J Phys Chem Solids 63:2047
45. Counio G, Esnouf S, Gacoin T, Boilot JP(1996) J Phys Chem 100:20021
46. Reisfeld R, Zelner M, Saraidarov T, Minti H (2001) Adv Energy Transfer Processes 341:03
47. Reisfeld R, Gaft M, Saraidarov T, Panczer G, Zelner M (2000) Mater Lett 45:154
48. Morita M, Baba M, Fujii H, Rau D, Yoshita M, Akiyama H, Herren M (2001) J Lumin 94/95:191
49. Rau D, Morita M (2001) J Lumin 94/95:283
50. Yen WM (1989) In: Kaplyanskii AA, Macfarlane RM (eds) Spectroscopy of solids containing rare earth ions. North-Holland, New York, p 185
51. Blasse G, Grabmaier GB (1994) Luminescent materials. Springer, Berlin Heidelberg New York, p 43
52. Huber DL (1987) In: Excited-states spectroscopy in solids. North Holland, NY, p 272
53. Gaponenko NV, Molchan IS, Gaponenko SV, Lyu Tich AA, Mudry AV, Misiewich J, Kudrawiec R (2003) J Appl Spectrosc 70:59
54. Wang M, Qian G, Lu S (1998) Mater Sci Eng B55:119
55. Hayakawa T, Selvan ST, Nogami M (2000) J Sol Gel Sci Technol 19:779
56. Morita M (1998) In: Shionoya S, Yen WM (eds) Phosphor handbook. CRC Press, NY, chap 3.4
57. Zheng Y, Wang M, Zhang C (1996) Mater Sci Eng B40:171
58. Jiang XC, Sun LD, Yan CH (2004) J Phys Chem 108.3287
59. Li H, Ueda D, Inoue S, Machida K, Adachi G (2002) Bull Chem Soc Jpn 75:161
60. Fan X, Wang Z, Wang M (2002) J Lumin 99:247
61. Zhang Y, Wang M, Xu J (1997) Mater Sci Eng B 47:23
62. Murakami S, Herren M, Morita M (1996) J Lumin 60/61:170
63. Murakami S, Herren M, Morita M (1998) J Lumin 76/77:460
64. Murakami S, Morita M, Herren M, Sakurai S, Rau D (2000) J Lumin 87/89:694
65. Murakami S, Herren M, Rau D, Morita M (2000) Inorg Chim Acta 300:1014
66. Ishizaka T, Nozaki R, Kurokawa Y (2002) J Phys Chem Solids 63:613
67. Martin IR, Mendez-Ramos J, Delgado F, Lavin V, Rodriguez-Mendoza UR, Yanes AC (2001) J Alloy Compd 323:773
68. Wang RY (2004) J Lumin 106:211
69. Buddhudu S, Morita M, Murakami S, Rau D (1999) J Lumin 83/84:199
70. Buddhudu S, Morita M, Zhang HX, Kam CH, Lam Y-L et al. (1999) Proc SPIE 3896:459

71. Blasse G (1983) In: DiBartolo B (ed) Energy transfer processes in condensed matter. Plenum Press, New York, p 251
72. Huber DL, Hamilton DS, Barnett S (1997) Phys Rev B 16:4642
73. Krol DM, Roos A (1981) Phys Rev 23:2135
74. Joubert MF, Jacquier B, Moncorge R, Boulon G (1982) J Phys 43:1267
75. Boulon G (1983) In: DiBartolo B (ed) Energy transfer processes in condensed matter. Plenum Press, New York, p 603
76. Morita M, Shoki T (1988) J Lumin 40/41:678
77. Reisfeld R, Jørgensen CK (1977) Lasers and excited states of rare earth. Springer, Berlin Heidelberg New York, p 157
78. Fujii T, Kodaira K, Kawauchi S, Tanaka N, Yamashita H, Anpo M (1997) J Phys Chem 101:10631
79. Nakazawa E, Shionoya S (1967) J Chem Phys 47:3211
80. Yamada N, Shionoya S, Kushida T (1972) J Phys Soc Jpn 32:1577
81. Morita M, Baba M, Rau D, Koike M, Takada K, Ishii T, Yoshita M, Akiyama (2002) Nonlinear Opt 29:367

Allowed and Forbidden d-d Bands in Octahedral Coordination Compounds: Intensity Borrowing and Interference Dips in Absorption Spectra

Marie-Christine Nolet · Rémi Beaulac · Anne-Marie Boulanger · Christian Reber

Département de chimie, Université de Montréal, Montréal QC H3C 3J7, Canada
E-mail: reber@chimie.umontreal.ca

Abstract Absorption spectra with weak spin-forbidden and more intense spin-allowed bands are observed for many different octahedral transition metal complexes. The simplest electron configurations showing these two different types of transitions are d^2 and d^8 with singlet and triplet electronic states. Spectra of vanadium(III) and nickel(II) complexes show effects of interactions between singlet and triplet excited states, leading to intensity borrowing and interference dips. These effects are quantitatively analyzed with modern theoretical models based on coupled potential energy surfaces. Both effects can be rationalized in terms of quantum interference processes.

Keywords Absorption spectroscopy · Nickel(II) complexes · Vanadium(III) complexes · Intensity borrowing · Interference dips

1
Introduction

One of C.K. Jørgensen's seminal research contributions is the analysis of absorption spectra with spin-allowed and spin-forbidden d-d bands in transition metal complexes and the characterization of spectroscopic effects arising from the interaction between excited electronic states of different spin multiplicity [1–3]. His work in this area is based on ligand field theory, now a routine tool used both in its traditional (crystal-field) and modern (angular overlap) formalisms to analyze the electronic transitions observed in absorption spectra of transition metal complexes [3, 4]. This approach does not, however, lead to precise predictions of band shapes in experimental spectra, where particular features

occur for compounds with states of different multiplicity that are coupled by spin-orbit coupling and are close in energy. Modern theoretical work has led to methods for calculating the electronic spectra corresponding to this situation [5–9].

In this chapter we review two of these intriguing spectroscopic effects: intensity borrowing of a spin-forbidden transition and interference dips in broad absorption bands. Many measurements of such phenomena for a range of compounds have been reported [6, 7, 10–28], but their quantitative analysis has long been neglected. We use a recently developed theoretical model [5] to calculate absorption band shapes and to obtain meaningful molecular parameters for excited electronic states from the fit of the theoretical spectrum to the experimental data. These spectroscopic phenomena are examples of quantum interference processes, effects that occur in many areas of chemistry and physics [9]. We use room-temperature absorption spectra of classical octahedral Werner complexes for our discussion, experiments that are often sufficient to analyze intensity borrowing and interference dips. We refer, where appropriate, to more resolved low-temperature single-crystal spectra in the literature.

The simplest electron configurations leading to electronic states with different spin multiplicities for transition metal complexes are d^2 and d^8. The singlet and triplet electronic states that arise from these configurations are related by the electron-hole analogy, as shown in the combined Tanabe-Sugano diagram for O_h point group symmetry given in Fig. 1a. The areas of interest are the lowest-energy intersections between singlet and triplet states, highlighted by circles in Fig. 1a. For nickel(II) complexes (d^8 configuration), they are the crossings of the ^1E_g and $^3T_{1g}$ or $^3T_{2g}$ states on the left-hand side of the figure. The $^3T_{2g}$ state is split by spin-orbit coupling into different levels: A_{2g}, E_g, T_{1g} and T_{2g}. The coupling occurs between the $E_g(^1E_g)$ state and the E_g spin-orbit component of the $^3T_{2g}$ state. The $^3T_{1g}$ state is split by spin-orbit coupling into A_{1g}, E_g, T_{1g} and T_{2g} levels. Again, the coupling occurs between the $E_g(^1E_g)$ state and the E_g component of the $^3T_{1g}$ state. For vanadium(III) complexes (d^2 configuration), the intersection of interest involves the $^1T_{2g}$ and $^3T_{2g}$ states, as shown on the right-hand side of Fig. 1a. The coupling occurs between the $T_{2g}(^1T_{2g})$ state and the T_{2g} component of the $^3T_{2g}$ state split by spin-orbit coupling. In order to obtain a quantitative comparison between electronic states and absorption spectra, Fig. 1a is not sufficient, and a model based on potential energy surfaces for both the singlet and triplet states has to be used [5–7, 29]. The simplest case of such a model, based on one-dimensional potential energy surfaces, is shown in Fig. 1b. The singlet excited state has its potential energy minimum at the same position as the ground state along all normal coordinates, since the two states arise from the same strong-field electron configuration. The triplet excited state has its potential energy surface offset, typically along the totally symmetric metal-ligand stretching coordinate, but possibly also along Jahn-Teller coordinates. In the following the model in Fig. 1b will be applied quantitatively to analyze absorption spectra with transitions to both singlet and triplet excited states.
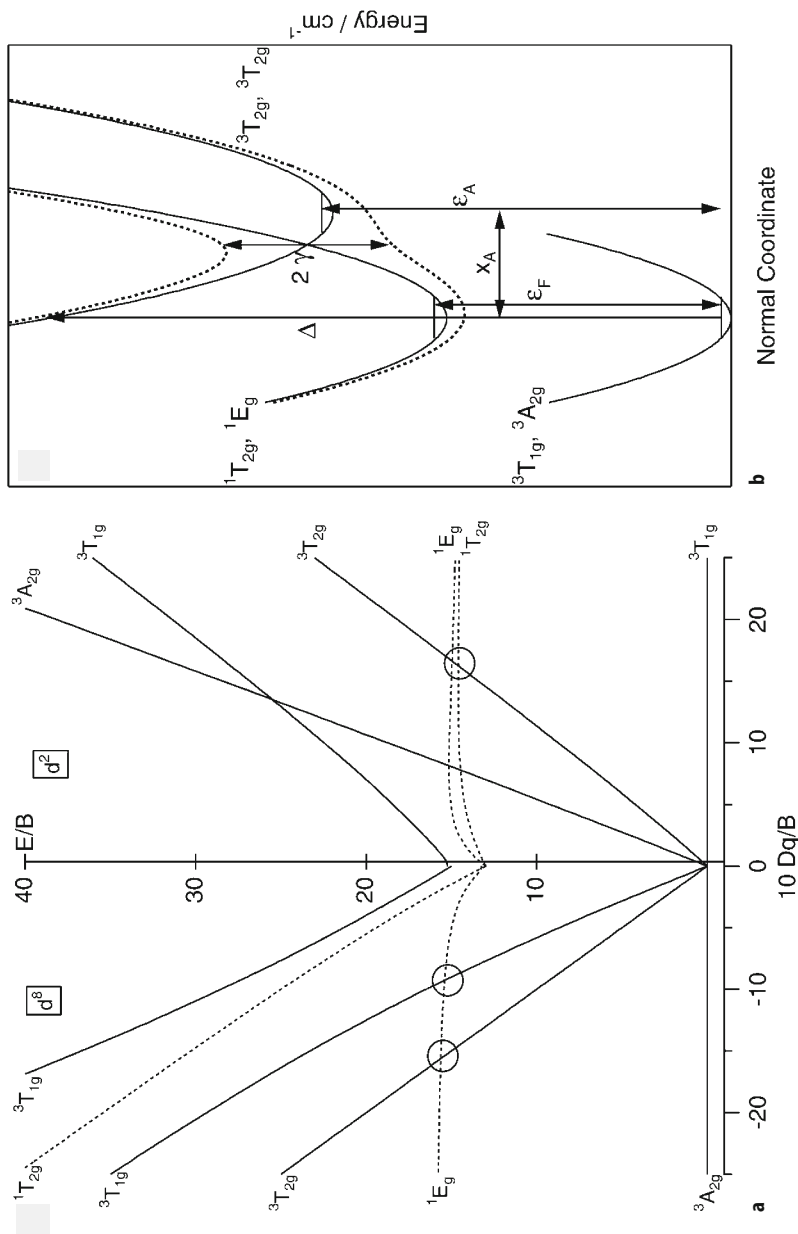
Fig. 1 **a** Tanabe-Sugano diagrams defining all triplet and the two lowest-energy singlet ligand-field electronic states for the d^2 and d^8 configurations (C/B=4). **b** Potential energy curves (*solid lines*: diabatic; *dotted lines*: adiabatic) for singlet and triplet excited states coupled by spin-orbit coupling along a single normal coordinate, illustrating the parameters used for the calculations

2
Analytical Model Equation

Recent theoretical work by Neuhauser, Zink and coworkers [5] has led to an analytical equation for the spectrum resulting from transitions to coupled excited states described by the Hamiltonian in Eq. (1), defined using the same symbols as in the original theoretical work [5]:

$$H = \frac{p^2}{2M} \begin{bmatrix} 1 & 0 \\ 0 & 1 \end{bmatrix} + \begin{bmatrix} \frac{1}{2} M\omega_F^2 x^2 + \varepsilon_F & \gamma \\ \gamma & \frac{1}{2} M\omega_0^2 (x - x_A)^2 + \varepsilon_A \end{bmatrix} \quad (1)$$

This equation describes the excited states shown in Fig. 1b, with the diagonal elements shown as harmonic (diabatic) potential energy curves, and the "coupled" potentials with the avoided crossing between spin-orbit levels of identical symmetry corresponding to the adiabatic potential energy surfaces. The entire set of curves must be used to calculate a spectrum, limitations to either the diabatic or adiabatic curves are inadequate. The vibrational frequencies ω_F and ω_0 describe the harmonic potential energy surface for the "forbidden" and "allowed" excited states, respectively. They are set to identical values in the following and only ω_0 is listed in Table 1. The potential energy minima are at ε_F and ε_A and the coupling constant is γ. M is the mass of the harmonic oscillator. In addition, the final state of the formally allowed transition is offset by x_A along the normal coordinate, as shown in Fig. 1b.

The absorbance $\sigma(\omega)$ (in arbitrary units) as a function of the wavenumber ω is given by [5]

$$\sigma(\omega) = \frac{1}{2\pi} \int_{-\infty}^{\infty} \langle \Psi_0 | e^{-i(H - \omega)t - \Gamma|t|} | \Psi_0 \rangle \, dt \quad (2)$$

$$= \frac{1}{\pi} \operatorname{Im} \langle \Psi_0 | H - \omega - i\Gamma)^{-1} | \Psi_0 \rangle.$$

Table 1 Values for the molecular parameters obtained from the fits of Eq. (3) to the absorption spectra of nickel(II) and vanadium(III) complexes

Parameter	V(urea)$_6^{3+,a}$	Ni(ethylene-diamine)$_3^{2+,b}$	Ni(o-phenan-throline)$_3^{2+,c}$	Ni(dimethyl-sulfoxide)$_6^{2+,d}$
ω_0, cm^{-1}	465	446	450	390
λ, cm^{-1}	11,500 (3760)	5206	3022	6770
Γ, cm^{-1}	366 (175)	900	796	556
γ, cm^{-1}	405	530	545	425
ε_F, cm^{-1}	9966 (9898)	12,326	12,006	14,027
Δ, cm^{-1}	16,091	11,552	12,276	13,138

[a] Fig. 2a; values in parentheses are used in Fig. 3.
[b] Fig. 5a; [c] Fig. 6a; [d] Fig. 7a.

If a Lorentzian shape is assumed for the broad, allowed transition in the absence of coupling between states, i.e. for $\gamma=0$, the equation simplifies to

$$\sigma(\omega) = -\frac{1}{\pi} \, \text{Im} \left(\frac{\beta}{1 - \gamma^2 \alpha \beta} \right) \quad (3)$$

with α and β defined as

$$\alpha = \frac{1}{\omega - \varepsilon_F + i\Gamma}$$

$$\beta = \frac{1}{\omega - \Delta + i\sqrt{\omega_0 \lambda}} \quad , \quad (4)$$

where Γ denotes a phenomenological damping factor expected to be similar in magnitude to the vibrational frequency ω_0 in order to lead to the unresolved spectra discussed here and the product $\sqrt{(\omega_0 \lambda)}$ defines the width of the spin-allowed transition [5]. Equation (2) can be solved numerically for a bandshape resulting from a displaced harmonic oscillator potential, as demonstrated and discussed in detail elsewhere [5, 29].

   Numerical models based on the time-dependent theory of electronic spectroscopy have been applied to a variety of spectra arising from transitions to coupled final states [6–8, 30–32]. This approach is exact, within the numerical limits of the wavepacket propagation method used [6], but is more difficult to apply than the analytical equation presented above. In the following, we use the analytical Eq. (3) to obtain fits to experimental spectra, a procedure that has been compared in detail to the numerical methods [29].

3
Intensity Borrowing: The Absorption Spectrum of V(urea)$_6^{3+}$

Intensity borrowing by the lowest-energy spin-forbidden transition from the lowest-energy spin-allowed band in a typical d^2 complex is illustrated by the absorption spectrum of solid V(urea)$_6$(ClO$_4$)$_3$ shown in Fig. 2a. The broad band in this figure corresponds to the spin-allowed transition from the $^3T_{1g}$ ground state to the $^3T_{2g}$ excited state. The weak, sharp peak at 9900 cm^{-1} is the lowest-energy spin-forbidden transition to the $^1T_{2g}$ state; the shoulder at 12,500 cm^{-1} is most likely the transition to the ^1E_g state. The $^1T_{2g}$ excited state is lower in energy than the $^3T_{2g}$ excited state. This is confirmed by the comparison of luminescence and absorption spectra in Fig. 2b. The luminescence spectrum is in agreement with data reported previously in the literature [33]. According to Kasha's rule, the luminescence transition identifies the lowest-energy excited state and the observation of the narrow band at identical energy in absorption and luminescence spectra is therefore clear evidence for an electronic origin of the lowest-energy transition. The narrow overall width indicates that the emitting-state potential energy minimum is at the same position in normal coordinate space as the ground-state minimum, indicative of the spin-flip transition between the $^3T_{1g}$ ground state and the $^1T_{2g}$ excited state. The oscillator strength of this spin for-
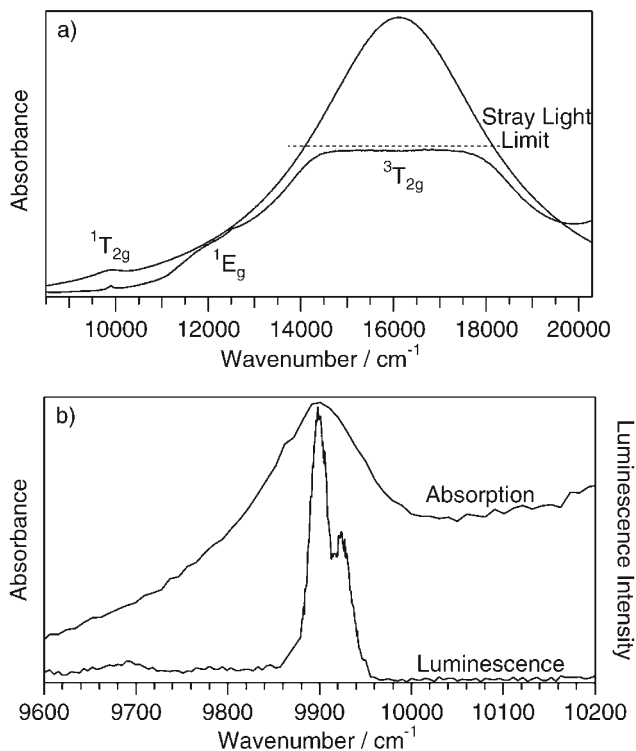
Fig. 2 **a** Room-temperature absorption spectrum of $V(urea)_6(ClO_4)_3$ compared to a calculated spectrum obtained with Eq. (3). The parameters used for the calculation are given in Table 1. **b** Room-temperature absorption and 10 K luminescence spectra of $V(urea)_6(ClO_4)_3$ in the region of the lowest-energy electronic transition to the $^1T_{2g}$ excited state

bidden band is enhanced by intensity borrowing from the nearby triplet excited state, the final state of the spin-allowed transition in the absorption spectrum. Jørgensen has rationalized this effect with perturbation theory [2]. The case of $V(urea)_6^{3+}$ corresponds to the right-hand circle in Fig. 1a. The two excited states in this circle are close in energy for many vanadium(III) compounds [34, 35].

Figure 2a contains a calculated absorption spectrum using Eq. (3) in comparison with the experimental data. The parameters given in Table 1 were obtained by a least-squares fit of Eq. (3) to the spectrum, excluding from the fit the region limited by stray light. The overall intensity ratio of the allowed and

Fig. 3 **a** Calculated absorption spectra for different values of the coupling constant γ, increasing from 0 cm⁻¹ to 900 cm⁻¹ in intervals of 50 cm⁻¹. All other parameters are given in Table 1. The allowed and forbidden bands are indicated by the solid square and circle, respectively. **b** Intensity of the forbidden band as a function of γ. **c** Energies of the band maxima for the two bands as a function of γ. *Squares and circles* are used to denote the bands as in the calculated spectra in a and a damping factor Γ of 10 cm⁻¹ was used to obtain the precision needed to determine the maxima of the spin-forbidden band
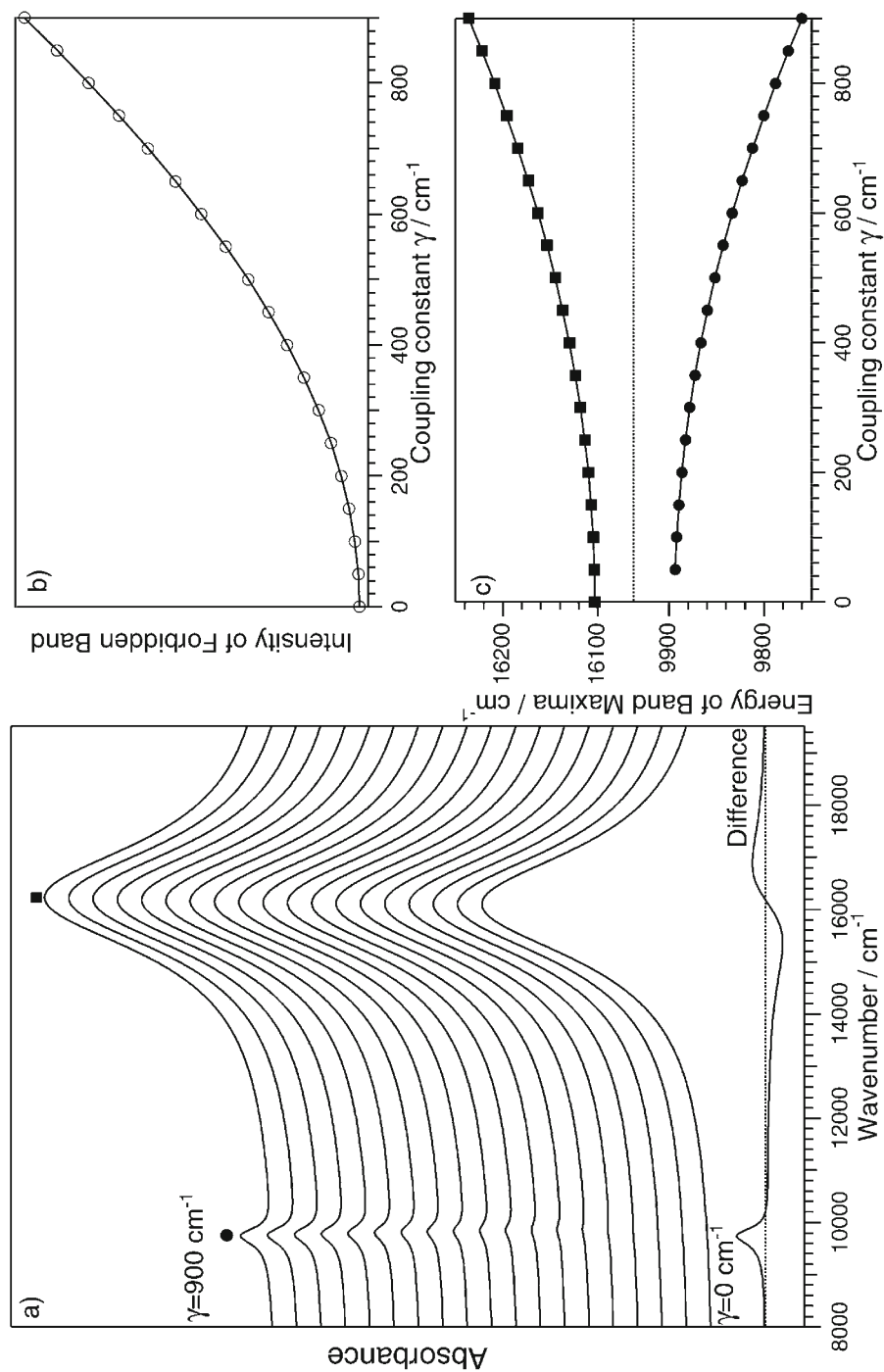
forbidden transitions and the overall band shapes are well reproduced. The main simplification of this approach is to include the entire broad triplet band, instead of only the component with the same symmetry as the singlet state in idealized O_h symmetry. The broad band includes all spin-orbit split levels and low-symmetry split components of the $^3T_{2g}$ state. These energy differences have been analyzed for the ground state of this complex and are found to be on the order of 1500 cm^{-1} [36], clearly showing the approximate nature of the calculated spectrum in Fig. 2a, where no such energy separation of the $^3T_{2g}$ state is included. Nevertheless, the model provides a very efficient way to analyze spectra involving coupled excited states and all parameter values are within a reasonable numerical range.

Figure 3 shows calculated spectra similar to the fit in Fig. 2a, but for coupling strengths γ varying from 0 cm^{-1} to 900 cm^{-1}. It is obvious that the forbidden transition, denoted by the circle in Fig. 3a, gains intensity through coupling with the broad, allowed transition to the triplet state, denoted by a square in Fig. 3a. The intensity increases with the square of the coupling constant γ and with the inverse of the square of the energy difference between the two states, as derived by Jørgensen [2]. The total intensity of the forbidden transition is therefore expected to increase proportionally to $γ^2$, confirmed by the model defined by Eq. (3) which leads to the calculated integrated intensities shown as open circles in Fig. 3b.

The positions of the band maxima in the calculated spectra with increasing coupling constant γ are shown in Fig. 3c. This aspect of the spectra is not obtained from the traditional perturbation theory based on purely electronic states. The avoided crossing in Fig. 1b leads to an energy separation between the band maxima that increases with γ. The effect is not exactly symmetric, it depends on the vibrational frequencies and on the positions of the potential minima in Fig. 1b along the normal coordinate and energy axes. The variations of the band maxima in Fig. 3c show clearly that it is important to treat the full problem, even in cases where the allowed and forbidden bands appear to be well separated in energy.

The bottom trace in Fig. 3a shows the difference spectrum obtained by subtracting the spectrum for zero coupling, a Lorentzian bandshape in our model, from the spectrum with the highest coupling constant γ of 900 cm^{-1}. It is easy to rationalize qualitatively this trace: the forbidden transition gains intensity, and therefore a positive peak is observed at approximately 9800 cm^{-1}. The broad allowed band loses a little of its intensity to the forbidden transition due to intensity borrowing, and its maximum shifts to higher energy, as shown in Fig. 3c. This leads to the asymmetric down-up part of the difference trace between 14,000 cm^{-1} and 18,000 cm^{-1}. This total up-down-up trace is characteristic for molecular spectra involving two coupled final states of formally allowed and forbidden transitions. It is the characteristic quantity that is common to all spectra discussed here and a signature of the quantum interference process underlying the spectroscopic phenomena [29].

4
Interference Dips: Absorption Spectra of Ni(ethylenediamine)$_3^{2+}$, Ni(*o*-phenanthroline)$_3^{2+}$, and Ni(dimethylsulfoxide)$_6^{2+}$

In situations where the energy difference between the two excited states is smaller than in Fig. 3, the spectroscopic effects of interactions are no longer as straightforward to identify in terms of an allowed and a forbidden transition as for the case of intensity borrowing illustrated in Figs. 2 and 3. This is shown by the spectra in Fig. 4, where bands with two maxima separated by an interference dip are observed for three nickel(II) complexes. This dip occurs in different bands: $^3T_{1g}(^3F),^1E_g$ for the dimethylsulfoxide complex (top trace), corresponding to the middle circle in Fig. 1a, and the $^3T_{2g},^1E_g$ bands for the ethylenediamine and *o*-phenanthroline complexes (middle and bottom traces), corresponding to the leftmost circle in Fig. 1a. For the two complexes with nitrogen ligator atoms, the dip is observed at different sides of the overall band maximum: to the high-energy side for the ethylenediamine complex and to the low-energy side for the
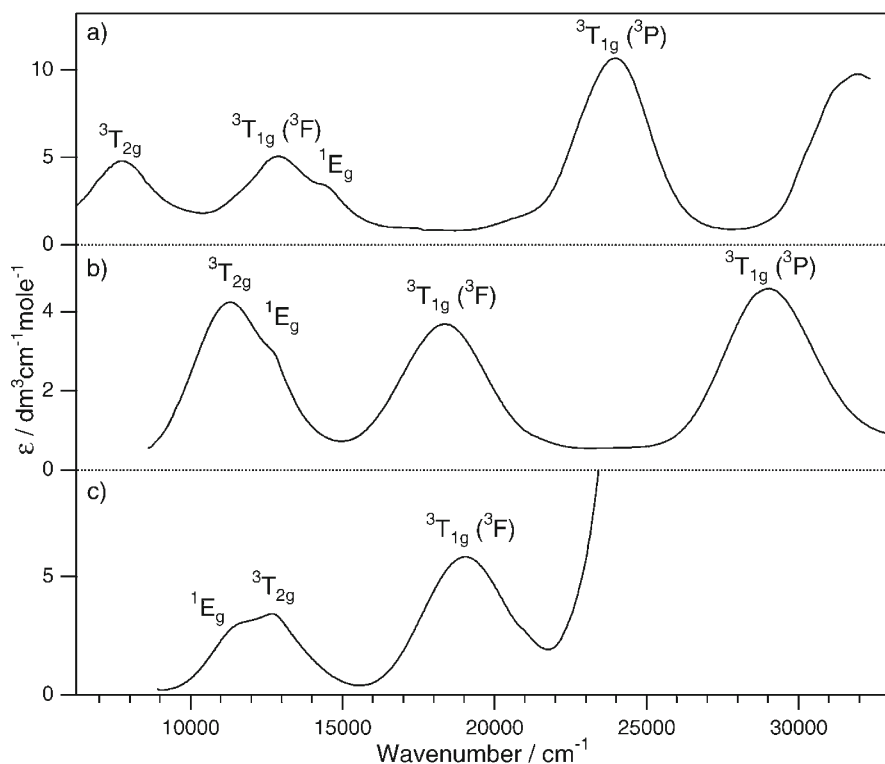
Fig. 4a–c Absorption spectra in solution at room temperature for; **a** Ni(dimethylsulfoxide)$_6^{2+}$; **b** Ni(ethylenediamine)$_3^{2+}$; **c** Ni(*o*-phenathroline)$_3^{2+}$. Interference dips involving the lowest-energy spin-forbidden and one of the spin-allowed absorption bands are observed in each spectrum

Fig. 5 **a** Absorption spectrum of Ni(ethylenediamine)$_3^{2+}$ (*dotted line*) with a calculated spectrum (*solid line*) obtained from the fit of Eq. (3). All parameters are given in Table 1. **b** Calculated spectra for coupling constants γ of 0 cm^{-1}, 250 cm^{-1}, 530 cm^{-1} (corresponding to the *solid line* in a), 750 cm^{-1} and 1000 cm^{-1}. Traces are offset along the ordinate for clarity. The *dotted line* denotes the difference between the spectra calculated with γ values of 0 cm^{-1} and 530 cm^{-1}

o-phenanthroline complex. The key difference to the intensity borrowing discussed in the preceding section is that the intensities of the two transitions are very obviously no longer a simple sum of a weak, narrow forbidden band and a more intense, large allowed transition. The analytical equation developed by Neuhauser, Zink and coworkers [5] provides therefore an essential and easy-to-use tool to fit the entire bandshape of such spectra and to obtain values of the molecular parameters illustrated in Fig. 1b.

Figure 5a shows the experimental and calculated spectra for the Ni(ethylenediamine)$_3^{2+}$ complex. The agreement between the fit and the experimental spec-
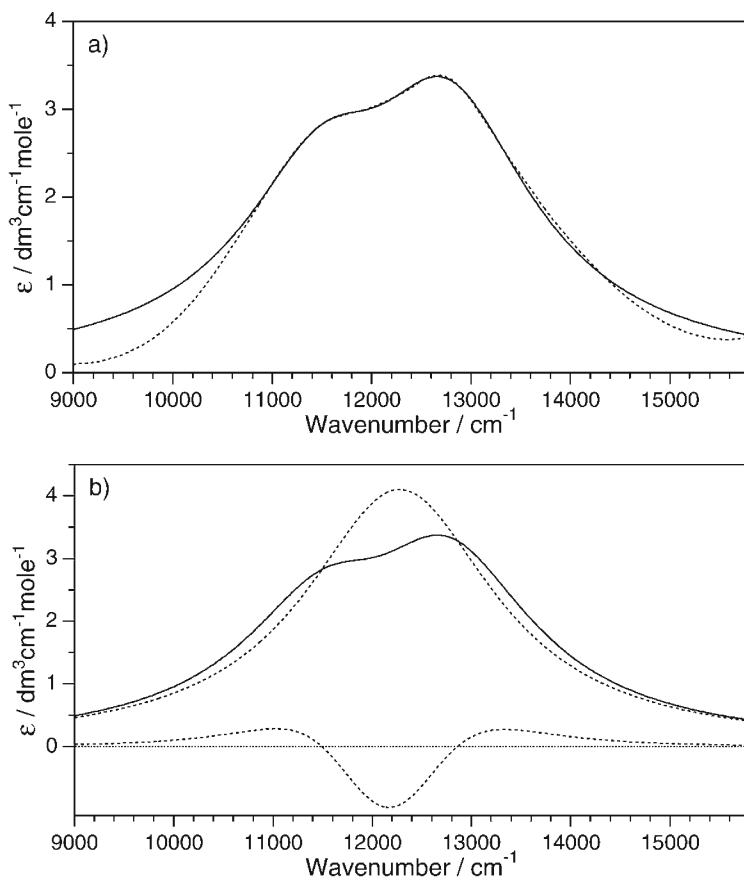
Fig. 6 a Absorption spectrum of Ni(*o*-phenanthroline)$_3^{2+}$ (*dotted line*) with a calculated spectrum (*solid line*) obtained from the fit of Eq. (3). All parameters are given in Table 1. **b** Calculated spectra for coupling constants γ of 0 cm^{-1}, *dotted line*, and 545 cm^{-1}, *solid line* identical to the *solid line* in a. The *dotted trace* at the bottom of the figure denotes the difference between the two calculated spectra

trum is very good, except for the wings of the absorption spectrum, where the limitations of the Lorentzian bandshape lead to calculated absorbance values higher than observed in the experimental spectrum. The vibrational frequency in Table 1 is within the expected range for the totally symmetric stretching mode of this complex. The difference spectrum analogous to the lowest trace in Fig. 3a is easily calculated and shown in Fig. 5b, together with calculated spectra obtained for five different values of the coupling constant γ. It is obvious from these calculated spectra that the interference dip becomes more prominent with increasing γ. Again, a difference spectrum with an up-down-up shape as for Fig. 3a is obtained, but for this compound the "components" of the difference trace are overlapping. The energy ε_F for the lowest level of the singlet excited state

in the absence of coupling, as defined in Fig. 1b and Eq. (3), is 12,326 cm^{-1}, approximately corresponding to the energy of the minimum of the dip. It is therefore not correct to obtain the energies of the ^1E_g and $^3T_{2g}$ states by fitting a sum of Gaussians to a spectrum [37] and then simply assigning their maxima as the energies of the ligand field excited states. The ^1E_g energy obtained from this approach is too high for the spectrum in Fig. 5.

Figure 6a shows the spectrum of Ni(o-phenanthroline)$_3^{2+}$ compared to the fitted spectrum obtained with Eq. (3). The fit reproduces the experimental result very well, again with the exception of the low-intensity wings of the band system. Figure 6b shows the difference trace with its up-down-up characteristic. The difference spectra in Figs. 5b and 6b are very similar, and it is obviously no longer possible to assign easily their features to allowed or forbidden transitions, as was the case for the difference trace in Fig. 3a. In addition, the comparison in Fig. 6b shows that the spectrum for $\gamma=0$, given as a dotted line with a single maximum differs over the entire wavelength range relevant to the experiment from the spectrum obtained as a fit in Fig. 6a. It is therefore not possible to reliably obtain a "background spectrum for zero coupling" from the wings at high and low energy of a measured band system in order to fit afterwards a theoretical expression for a difference trace, as has often been done with equations based on Fano's pioneering work on quantum interferences in atomic spectroscopy [38, 39]. These difficulties have been discussed in detail [29]. Again, ε_F is located near the minimum of the dip. If the approach based on fitting a sum of Gaussians is applied here, an energy that is too low is obtained for the ^1E_g state. Figures 5 and 6 illustrate the significant systematic errors that such fits can create. The total spectrum has to be fitted with a model based on meaningful physical parameters, such as the analytical Eq. (3) or more general numerical approaches [5, 6, 29].

Figure 7 shows that the analytical equation can also be applied to crossings of the lowest-energy singlet excited state and the $^3T_{1g}(^3F)$ state. The best studied case of the interaction between these two states is the spectrum of Ni(H$_2$O)$_6^{2+}$ [1, 2, 10, 32, 40–43], another complex where Jørgensen contributed pioneering spectroscopic work. The Ni(dimethylsulfoxide)$_6^{2+}$ complex has band maxima at energies similar to Ni(H$_2$O)$_6^{2+}$, as expected from the identical ligator atoms. A good fit is obtained with Eq. (3), showing again the typical up-down-up difference trace, as given in Fig. 7b, and values of the fit parameters close to those obtained for Ni(H$_2$O)$_6^{2+}$ determined before both from solution spectra and from better resolved single-crystal spectra [29, 32].

The energies ε_F given in Table 1 as obtained from the fits to experimental spectra of three nickel(II) complexes follow the qualitative trend of Jørgensen's nephelauxetic series [3] with a different quantitative variation than the nephelauxetic effects defined via the Racah parameter B calculated from the maxima of the spin-allowed absorption bands. The calculations in Figs. 2, 5, 6 and 7 show that the model defined by Eq. (3) works well for unresolved spectra of different transition metal complexes. For more highly resolved spectra, multi-dimensional potentials may be needed [17]. The analytical equation can easily be generalized to multiple dimensions and to situations with multiple formally forbidden transitions [29]. The spectra analyzed here also illustrate that a straight-
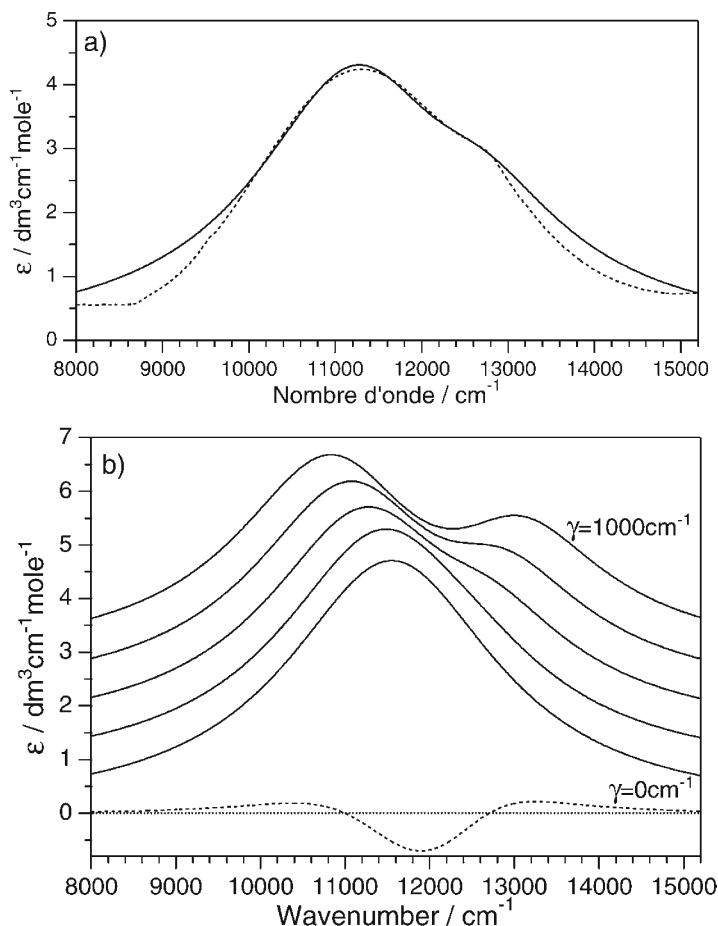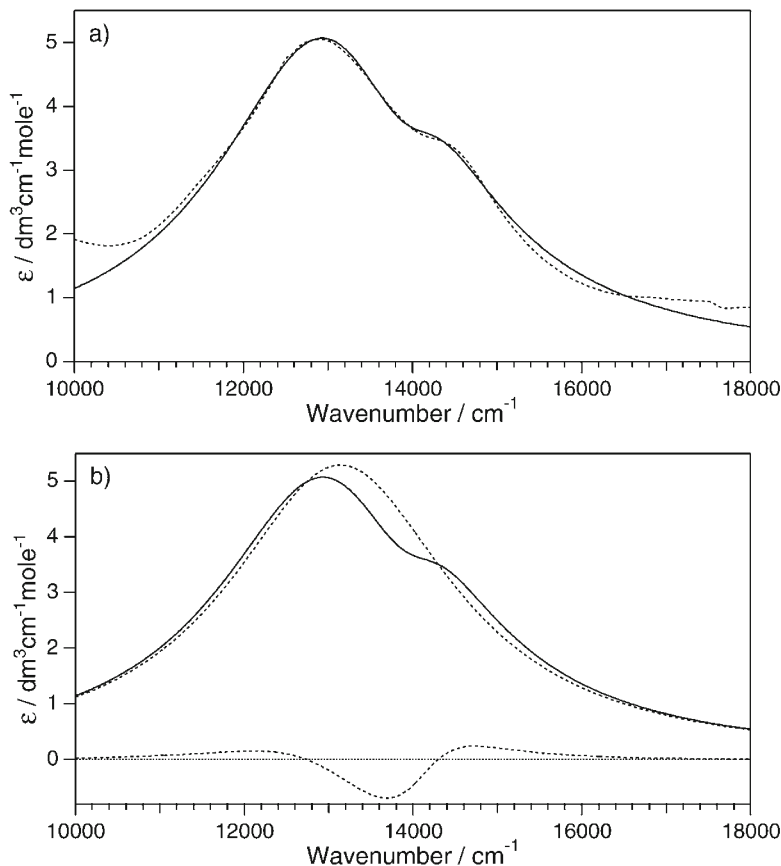
Fig. 7 **a** Absorption spectrum of Ni(dimethylsulfoxide)$_6^{2+}$ (*dotted line*) with a calculated spectrum (*solid line*) obtained from the fit of Eq. (3). All parameters are given in Table 1. **b** Calculated spectra for coupling constants γ of 0 cm^{-1}, *dotted line*, and 425 cm^{-1}, *solid line* identical to the *solid line* in a. The *dotted trace* at the bottom of the figure denotes the difference between the two calculated spectra

forward assignment of maxima and shoulders to individual ligand-field excited states can not be made from absorption spectra such as those in Fig. 4. In such situations, a coupled ensemble of states as defined by Eq. (1) must be used to correctly interpret the entire experimental bandshape.

5
References

1. Jørgensen CK (1955) Acta Chem Scand 9:405
2. Jørgensen CK (1955) Acta Chem Scand 9:1362
3. Jørgensen CK (1962) Absorption spectra and chemical bonding in complexes. Addison-Wesley, Reading Mass. Absorption spectra of nickel(II) complexes similar to those discussed here are shown in Fig. 11, p 120
4. Reisfeld R, Jørgensen CK (1988) Struct Bond 69:63
5. Neuhauser D, Park T-J, Zink JI (2000) Phys Rev Lett 85:5304
6. Reber C, Zink JI (1992) J Chem Phys 96:2681
7. Reber C, Zink JI (1992) Comments Inorg Chem 13:177
8. Zink JI (2001) Coord Chem Rev 211:69
9. Rau ARP (2004) Phys Scripta 69:C10
10. Pryce MHL, Agnetta G, Garofano T, Palma-Vittorelli MB, Palma MU (1964) Phil Mag 10:77
11. Sturge MD, Guggenheim HJ, Pryce MHL (1970) Phys Rev B 2:2459
12. Bermudez VR, McClure DS (1979) J Phys Chem Solids 40:129
13. Lempicki A, Andrews L, Nettel SJ, McCollum BC, Solomon EI (1980) Phys Rev Lett 44:1234
14. Meijerink A, Blasse G (1989) Phys Rev B 40:7288
15. Reber C, Zink JI (1992) J Phys Chem 96:571
16. Rodrìguez-Mendoza UR, Rodrìguez VD, Lavin V, Martin IR, Nuñez P (1999) Spectrochim Acta A55:1319
17. Schenker R, Triest M, Reber C, Güdel HU (2001) Inorg Chem 40:5787
18. Voda M, Garcia-Solé J, Vergara I, Kaminskii A, Mill B, Butashin A (1994) Phys Rev B 49:3755
19. McDonald RG, Stranger R, Hitchman MA, Smith PW (1991) Chem Phys 154:179
20. Illaramendi MA, Balda R, Fernández J (1993) Phys Rev B 47:8411
21. Illaramendi MA, Fernández J, Balda R, Lucas J, Adam JL (1991) J Lumin 47:207
22. Hazenkamp MF, Güdel HU, Atanasov M, Kesper U, Reinen D (1996) Phys Rev B 53:2367
23. Illaramendi MA, Fernández J, Balda R (2002) J Phys: Condens Matter 14:555
24. Buñuel MA, Alcalá R, Cases R (1998) Sol Stat Commun 107:491
25. Kück S, Hartung S, Hurling S, Petermann K, Huber G (1998) Phys Rev B 57:2203
26. Mendoza CR, Costa BJ, Messaddeq Y, Zilio SC (1997) Phys Rev B 56:2483
27. Pavlov RS, Marza VB, Carda JB (2002) J Mater Chem 12:2825
28. Noginov MA, Loutts GB, Warren M (1999) J Opt Soc Am B 16:475
29. Bussière G, Reber C, Walter DA, Neuhauser D, Zink JI (2003) J Phys Chem A 107:1258
30. Wexler D, Zink JI (1995) Inorg Chem 34:1500
31. Wexler D, Zink JI, Reber C (1992) J Phys Chem 96:8757
32. Bussière G, Reber C (1998) J Am Chem Soc 120:6306
33. Flint CD, Greenough P (1972) Chem Phys Lett 16:369
34. Reber C, Güdel HU (1988) J Lumin 42:1
35. Wenger OS, Güdel HU (2002) Chem Phys Lett 354:75
36. Beaulac R, Tremblay JC, Bussière G, Reber C (2001) Can J Anal Sci Spectros 46:152
37. Stranger R, McMahon KL, Gahan LR, Bruce JI, Hambley TW (1997) Inorg Chem 36:3466
38. Fano U (1961) Phys Rev 124:1866
39. Fano U, Cooper JW (1965) Phys Rev 137: A1364
40. Liehr AD, Ballhausen CJ (1959) Ann Phys 2:134
41. Reedijk J, Van Leeuwen PWNM, Groeneveld WL (1968) Rec Trav Chim Pays-Bas 87:129
42. Solomon EI, Ballhausen CJ (1975) Mol Phys 29:279
43. Bussière G, Beaulac R, Cardinal-David B, Reber C (2001) Coord Chem Rev 219/221:509

The Angular Overlap Model and Vibronic Coupling in Treating s-p and d-s Mixing – a DFT Study

D. Reinen[1] · M. Atanasov[1, 2]

[1] Fachbereich Chemie and Zentrum für Materialwissenschaften, Philipps-Universität,
Hans-Meerweinstrasse 1, 35043 Marburg, Germany
[2] *Extra address:* Institute of General and Inorganic Chemistry, Bulgarian Academy
of Sciences, Bl. 11, Sofia 1113, Bulgaria
E-mail: reinen@chemie.uni-marburg.de

Abstract   The steric and energetic lone pair effect induced by s-p mixing can be parameterised within the angular overlap model (AOM), as is shown for a series of halide molecules and complexes mainly of the fifth main group (oxidation state +III) with the coordination numbers 3 to 6. The derived effective AOM parameters e_{sp}^{eff}, defined for the average bond lengths of the distorted structures, decrease the softer the considered entity is, and seem to be transferable within groups of chemically related species. We base the analysis on results of DFT calculations, using specifically Kohn-Sham MO diagrams in comparison to corresponding many-electron energies. There is definite experimental evidence for s-p and for d-s mixing as well, as is demonstrated by the DFT analysis of spectral data for some model complexes. The equivalence of the vibronic coupling approach on the MO level with the AOM is emphasized; the advantage of the AOM is, however, that angular and radial (bond length) contributions can be cleanly separated.

Keywords   Lone-pair effect · s-p and d-s Mixing · Density functional theory · Angular overlap model · Electronic transition energies

1
Introduction

One of the many merits of C.K. Jørgensen's scientific oevre, which is characterized by numerous intuitive approaches and basic ideas, is his contribution in creating the angular overlap model (AOM) [1] – elaborating and generalizing an early suggestion of H. Yamatera [2]. Ever since, the AOM has become a valuable

tool to semiquantitatively describe and understand bonding properties and symmetry splittings in the optical spectra of particularly transition metal (TM) complexes [3]. The success of the model has to be mainly traced back to *the additivity of the ligand contributions to the chemical bonds within a complex*, thus meeting the chemists' understanding of binding phenomena.

s-p mixing effects in main group stereochemistry can also be treated successfully by the AOM, as first discussed by C.K. Jørgensen [4] and later more extensively by J.K. Burdett [5]. The parameterisation of such mixing is equally possible in a vibronic coupling approach, as was shown by R.G. Pearson utilizing for example the second-order or pseudo Jahn-Teller (PJT) coupling for s^2p^0 or p^2s^0 lone pair configurations [6]. We will compare the two models, considering first the series of compounds AX_3 and AH_3 with one lone pair (A^{III}=N,P,As,Sb,Bi; X^{-I}=F,Cl,Br,I), for which detailed studies of the PJT coupling, based on Density Functional Theory (DFT) have already been reported [7]. Later, we derive AOM expressions for the stabilization of the lone pair and calculate the respective energies via the Kohn-Sham MOs; they allow one to separate the radial (bond length) from the angular contributions. We explore the ability of the AOM to describe and to interpret lone-pair orbital effects adopting two limiting situations – the weak (perturbation) and strong coupling approach. Furthermore, we compare the orbital energies with the total energy changes, thus bridging the molecular orbital description, so popular among chemists, with the DFT results from a more rigorous many-electron treatment. As further representative examples we have chosen some molecules and complexes with the coordination numbers (CN) four, five and six, such as SF_4, ClF_5, PF_4^-, AsF_4^-, PF_5^{2-}, AsF_5^{2-} and AsF_6^{3-} in order to study the effect of the lone pair activity when increasing the CN and the negative charge. The universality and limitations of these approaches will be discussed.

The modelling of the d-s mixing by the AOM is shortly reviewed in the following section; here *direct* experimental evidence exists in optical and EPR spectroscopy. Spectroscopic data on lone-pair systems are numerous as well – see the reviews of G. Blasse [8] and A. Vogler and H. Nikol [9]. We will analyse some representative examples for the CN=3 ($SnCl_3^-$), CN=4 ($SbCl_4^-$) and CN=6 ($SbCl_6^{3-}$, $SeCl_6^{2-}$, $TeCl_6^{2-}$) by applying respective AOM approaches and in comparison with the results of many electron DFT calculations.

2
d-s Mixing in the AOM

The Jahn-Teller coupling of six-coordinated Cu^{2+} complexes usually leads to a considerable tetragonal elongation of the octahedral parent complex and quite often even to square planar species (Fig. 1). The optical spectra in the latter case [$Cu(NH_3)_4$]$^{2+}$ for example, with $e_\pi \approx 0$ are not in agreement with the expected energies $2e_\sigma$ and $3e_\sigma$ for the $a_{1g}^* \rightarrow b_{1g}^*$ and $e_g, b_{2g} \rightarrow b_{1g}^*$ electronic transitions however, but suggest an energy for the former electron excitation of $2e_\sigma + 4e_{ds}$. Here, e_{ds} is due to the d_{z^2}-s interaction and of considerable magnitude ($e_{sd} \approx (1/4) e_\sigma$) [3]. It contributes to stabilizing the elongated with respect to the compressed D_{4h} conformation [10], because in the former case two electrons are lowered in energy
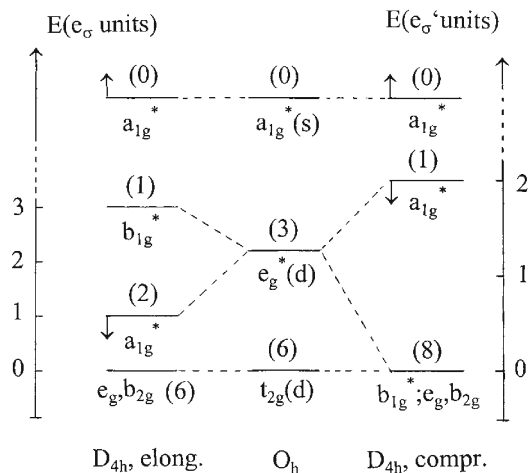
Fig. 1 Schematic orbital energy diagram for an octahedral d^9 complex under the influence of a first order Jahn-Teller interaction, leading to a D_{4h} elongation or compression. The AOM energies (assuming non-bonding t_{2g} orbitals: $e_\pi = 0$) are given for the extreme cases of an elongation (square planar; e_σ) and compression (linear; e'_σ); the d-s interaction between the two $a_{1g}^\star$ MOs from $(n+1)s$ and nd_{z2} – which leads to a preference of the tetragonal elongation by higher order coupling terms – is indicated by *arrows*; this effect may even depress the $a_{1g}^\star(d_{z2})$ MO into the non-bonding region, thus changing the occupation numbers (see text; the energy scaling is arbitrary)

instead of only one in the latter case. The e_{ds}/e_σ ratio for the planar $Cu^{II}O_4$ coordination (in Li_2CuO_2) [11] and for the planar $CuCl_4^{2-}$ complex [12] is found to be similar to the value above ($\cong 0.26$), while it is much smaller in the case of the ionic F^- ligand (≈ 0.07: $Cu^{II}F_4$ square plane in $BaCuF_4$ [13]). In the $CuCl_4^{2-}$ case it is remarkable that the AOM parameters are well transferable from the planar to the (D_{2d}-distorted) tetrahedral coordination [10].

Even more direct evidence for a d-s interaction is detected in the EPR spectra of Jahn-Teller distorted octahedra, which have been forced by ligand or host lattice strain into a tetragonally compressed conformation, with the unpaired electron in the $a_{1g}^\star(d_{z2})$ MO (see Fig. 1). The hyperfine interaction with the copper nucleus, particularly the isotropic contribution, is extremely sensitive to s-admixing – here induced by the $a_{1g}^\star(3d_{z2})$-$a_{1g}^\star(4s)$ pseudo Jahn-Teller interaction – because this implies a small unpaired electron density directly at the copper nucleus via the 1s orbital [13].

Finally, we discuss the stereochemical anomaly of some nd^{10} cations, such as Au^+, Ag^+ and also Cu^+, which tend to adopt mostly or frequently a linear coordination. One may consider this geometry as the extreme of the tetragonal compression of a parent octahedron. L. E. Orgel has invoked a pseudo-Jahn-Teller interaction between the occupied $a_{1g}^\star(nd_{z2})$ and the empty $a_{1g}^\star[(n+1)s]$ MO as the cause for the distortion – with one critical condition being an only small initial separation δ between these levels (Fig. 1) [14].

The admixing of s into d_{z2} weakens the four bonds within the x,y-plane and strengthens those along z in an D_{4h} distorted octahedral complex (active Q_θ com-

ponent of the octahedral ε vibrational mode), thus stabilizing the σ-antibonding $a_{1g}^*(d_{z2},s)$ MO considerably. The interaction matrix has the simple form

$$\frac{\begin{array}{c} a_{1g}^*(s) \\ \hline a_{1g}^*(d_{z2}) \end{array}}{} \begin{bmatrix} E_s & H_{ds} \\ H_{ds} & E_d \end{bmatrix} \tag{1}$$

The energy stabilisation of the singly (compressed octahedron of Cu^{2+}) or doubly occupied $a_{1g}^*(d_{z2})$ MO (elongated octahedron of Cu^{2+}; linear coordination of Cu^{1+}) is correspondingly – for large s-d separations $\delta \equiv E_s - E_d$ [15]:

$$-\Delta E_{ds} \approx -H_{ds}^2/\delta = -4(h_{ds}^{ax} - h_{ds}^{eq})^2/\delta = 4e_{ds}^{ax} + 4e_{ds}^{eq} - 8(e_{ds}^{ax} \cdot e_{ds}^{eq})^{1/2} \tag{2a}$$

In Eq. (2a) we have substituted H_{ds} by the difference $2(h_{ds}^{ax} - h_{ds}^{eq})$, where h_{ds}^{ax} and h_{ds}^{eq} – for the axial and equatorial ligands, respectively – represent the coupling between the s and d-orbitals via intervening ligand orbitals of σ-symmetry. Equation (2a) is based on the assumption, that the d-orbitals are largely localized, implying preferentially ionic bonds with only weak metal-ligand overlap. Each parameter e_{sd} refers to one TM-ligand bond (Eq. 2b); the total energy stabilisation for the complex ΔE_{ds} contains a non-additive contribution, reflecting the bond anisotropy with respect to the equatorial and axial bonds.

$$e_{ds} = h_{ds}^2/\delta \tag{2b}$$

It is derived from the electronic spectra of linear $CuCl_2$ and $NiCl_2$ [16] – later supported by DFT calculations [17] – that the energy of the $\sigma_g^*(d_{z2})$ MO $(=2e_\sigma' - 4e_{ds}')$ is indeed very low, even lower than the π $(d_{xz,yz})$ MOs $(2e_\pi')$ – again manifesting a considerable d-s mixing effect. The resulting $d_{xy,x2-y2} \leq d_{z2} < d_{xz,yz}$ MO sequence is consistent with a $^2\Pi$ and with a $^3\Sigma$ ground state for $CuX_2(X=F,Cl)$ and $NiCl_2$, respectively. The linear chromophores $Ni^{II}O_2^{2-}$ in K_2NiO_2 [18] and $Ni^IO_2^{3-}$ in K_3NiO_2 and KNa_2NiO_2 [19] are other key examples illustrating the role of s-d mixing. For the latter compounds a $d_{xy,x2-y2} < d_{xz,yz} < d_{z2}$ MO order is proposed, based on EPR spectra [18, 19], while later DFT calculations suggest again the sequence above [20]. Finally, DFT results for AgS_2^{3-} show that the highest occupied MO is of σ_g^* type, containing an about equal contribution of d_{z2} and s and implying a very small initial s-d separation δ and/or a matrix element H_{ds}, which exceeds by far this separation [21].

The s-p interactions in systems with one lone-pair (s^2p^0) or (p^2s^0) follow an analogous description pattern and will be treated in the following section. Polyhedra with cations possessing two or even three lone pairs – s^2p^2 and s^2p^4, respectively – undergo first order Jahn-Teller distortions and will not be considered here.

3
s-p Mixing Effects in Systems with One Lone Pair

When applying the AOM to s-p mixing effects, one has to recall that perturbation theory is not generally applicable anymore (see matrix 1 and Eq. 2a) – due to rather small initial splittings δ in comparison to frequently large non-diagonal
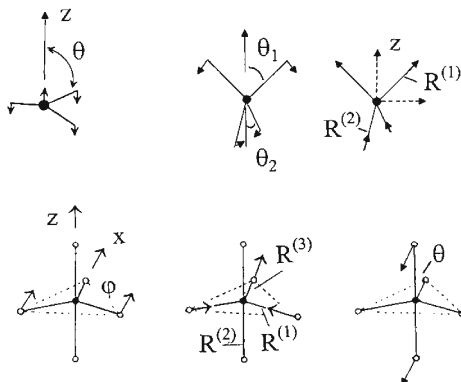
Fig. 2 Vibronically active modes for geometric lone pair activities: α_2''(CN=3, $D_{3h} \rightarrow C_{3v}$), τ_2 (CN=4, $T_d \rightarrow C_{2v}$) and ε' (CN=5, $D_{3h} \rightarrow C_{2v}(\approx C_{4v})$)

energies H_{sp} (strong PJT coupling). Nevertheless, perturbation treatments – including second and third order energy corrections – have often been uncritically applied to s-p lone pair effects in the past (see [5] for example), though one has to realize, that the energetic situation is rather different from the one treated in the preceding section.

In the following we will derive AOM expressions for the two limiting cases of very small H_{sp}/δ ratios (Eq. 2a) and of vanishing initial splittings δ and discuss these results facing the fact, that reality is somewhere between these limits – though presumably not too far from the perturbation approach, however (see below).

Molecules AX_3, where A is a fifth main group element in a (+III) oxidation state (A^{III}: N to Bi; X^{-I}: F to I and H) possess one lone pair. In the highest symmetry parent geometry D_{3h} the HOMO is either of a_1' or of a_2'' nature, corresponding to a $s(a_1')^2$ or $p_z(a_2'')^2$ lone pair, respectively [7]. In the former case the HOMO is σ-antibonding (A^{III}=P to Bi; X^{-I}: F to I), while in the latter case it is non-bonding (AH_3 with A^{III}: N to Bi) or π-antibonding (NX_3 with X^{-I}: F to Br). In an AOM description we start from a matrix analogous to that of Eq. (1) and describe the s-p mixing effect between the a_2''(or a_1') LUMO and the a_1' (or a_2'') HOMO, which distorts the planar AX_3 geometry via the vibronically active α_2'' vibration according to C_{3v} (Fig. 2), in terms of an e_{sp} parameter and a bond angle distortion, with ($-\Delta E_{sp}$) being the HOMO stabilisation energy:

$$\Delta E_{sp} \cong H_{sp}^2/\delta = 9 \cos^2\theta \; e_{sp}^p \tag{3a}$$

$$\Delta E_{sp} \cong H_{sp} = 3|\cos\theta|e_{sp}^o \tag{3b}$$

Here, Eq. (3a) is the perturbation expression – see the corresponding Eq. (2a), Eq. (2b) for the d-s mixing; upper index p – and Eq. (3b) refers to the limit δ=0 – see matrix (1); upper index o. In the following we base our analysis on the absolute energy minima of the many-electron ground state (energy stabilisation ΔE_t) as obtained by DFT for the optimised D_{3h} and C_{3v} geometries. The HOMO energies in D_{3h} and C_{3v} are taken from the Kohn-Sham orbital diagrams; though

these are not strictly MOs but represent projections of many-electron onto one-electron energies – thus not only comprising energy gains due to the formation of new covalent bonds when transforming the D_{3h} to the C_{3v} geometry, but also repulsive forces of electrostatic and exchange character – they have been shown to be chemically significant [22]. We consider the stabilisation $\Delta\varepsilon_{sp}$ of the Kohn-Sham HOMO by s-p mixing as equivalent to the sum of $(-\Delta E_{sp})$ and ΔE_r:

$$\Delta\varepsilon_{sp} \equiv \Delta E_r - \Delta E_{sp} \tag{4}$$

the latter being the energy change of the HOMO caused by the shrinking (s^2 type lone pairs) or by the expansion (p_z^2 type lone pairs) of the A-X bond lengths, which inevitably accompanies the $D_{3h} \rightarrow C_{3v}$ transitions, and is by definition, a pure bond length effect. As expected, it is positive in the former case and negative (or vanishing) in the latter. ΔE_{sp} is then the energy change of the HOMO at the bond distance in C_{3v} and equals the orbital overlap parameter e_{sp}, weighted by the angular function (Eq. 3). e_{sp} is the gain in overlap energy due to central ion s-p_z hybridisation for a reference ligand on the z-axis (Fig. 2). For a selection of molecules the so-far defined parameters are collected in Table 1 and Table 2. e_{sp}^p and e_{sp}^o as well – the latter turns out to be about 50% larger than the former – mostly follow the trend of ΔE_{sp}, because θ varies only slightly between ≈ 116–$122°$, the exceptions being the hydrides ($\theta \approx 125°$, and $\theta \cong 113°$ for NH_3) and NCl_3, NBr_3 ($\theta \cong 111°$) with $a_2''(p_z))^2$ – type lone pairs.

We focus now on the many-electron energy parameters derived from DFT when applying a vibronic coupling model. Here, the total stabilisation energy δE_t is described as being composed of two contributions, the restoring energy E_{rf}^m and the vibronic coupling energy E_{vib}^m (Eq. 5) [23]. The latter represents a pure overlap effect, but takes account of the interaction of *all* occupied a_1' (or a_2'') MOs with the a_2''(or a_1') LUMO, while ΔE_{sp}, which is an orbital overlap quantity,

$$\delta E_t = E_{rf}^m - E_{vib}^m \tag{5}$$

considers only the HOMO-LUMO interaction. Nevertheless the vibronic energy E_{vib}^m and the energies ΔE_{sp}, e_{sp} – the latter deduced from DFT by an AOM parameterisation – exhibit roughly similar dependencies on the constituting atoms:

$$F > Cl > Br > I \text{ and } N > P > As > Sb > Bi \tag{6}$$

These parallel trends of E_{vib}^m and ΔE_{sp} are obeyed better the more exactly the equality Eq. (7) is satisfied (Table 1) – implying that the essential energy

$$\delta E_t \approx 2 \Delta\varepsilon_{sp} \tag{7}$$

gain is connected with solely the stabilisation of the lone pair in the HOMO. For the molecules with an a_2'' HOMO (Table 2), however, other MOs also contribute essentially to ΔE_t – thus the one-electron approach is unsatisfactory.

The AOM parameterisation according to Eq. (3) allows the separation of the stabilisation by s-p mixing at any bond distance into a *radial* and an *angular* part. e_{sp} follows the stabilisation sequence Eq. (6) nicely in the case of a p_z admixture (Table 1); considering an s-admixture (p_z ground state), this is not true for the hydrides anymore (Table 2). We stress here again that the one-electron quantity

Table 1 Lone-pair orbital parameters ($\Delta\varepsilon_{sp}, \Delta E_r, \Delta E_{sp}$) and corresponding many-electron quantities ($\delta E_t, E_{rf}^m, E_{vib}^m$, in eV), resulting from DFT and vibronic-coupling treatments [24], respectively, for planar AX_3 molecules with a s^2 ground state; the AOM parameters e_{sp}^p and e_{sp}^o – from Eqs. (3), in eV – and the DFT optimised angles for the C_{3v} type pyramidalisation (θ in°), starting from the parent planar D_{3h} geometry ($\theta = 90°$), are also listed

Molecule	$\Delta\varepsilon_{sp}$	ΔE_r	ΔE_{sp}	e_{sp}^p	e_{sp}^o	δE_t	E_{rf}^m	E_{vib}^m	θ
PF_3	−1.34	0.88	2.22	0.99	1.48	−2.87	0.57	3.44	119.8
AsF_3	−1.16	0.71	1.87	0.81	1.23	−2.01	0.36	2.37	120.5
SbF_3	−1.08	0.46	1.54	0.64	1.00	−1.70	0.17	1.87	121.3
PCl_3	−0.78	0.79	1.57	0.85	1.15	−1.91	0.05	1.96	116.7
$SbCl_3$	−0.61	0.43	1.05	0.52	0.74	−1.33	−0.03	1.30	118.7
PBr_3	−0.66	0.53	1.19	0.68	0.90	−1.49	−0.12	1.37	115.9
$SbBr_3$	−0.49	0.33	0.82	0.43	0.60	−1.13	−0.18	0.95	117.2
PI_3	−0.58	0.40	0.98	0.61	0.77	−1.05	−0.01	1.04	114.3
SbI_3	−0.38	0.24	0.62	0.37	0.48	−0.86	−0.07	0.79	116.0

Table 2 Lone-pair orbital parameters ($\Delta\varepsilon_{sp}, \Delta E_r, \Delta E_{sp}$) and corresponding many-electron quantities ($\delta E_t, E_{rf}^m, E_{vib}^m$, in eV), resulting from DFT calculations and vibronic-coupling treatments [24], respectively, for planar AX_3 molecules with a p_z^2 ground state; the AOM parameters e_{sp}^p and e_{sp}^o – from Eqs. (3), in eV – and the DFT optimised angles for the C_{3v}-type pyramidalisation (θ in °), starting from the parent planar D_{3h} geometry ($\theta = 90°$), are also listed

Molecule	$\Delta\varepsilon_{sp}$	ΔE_r	ΔE_{sp}	e_{sp}^p	e_{sp}^o	δE_t	E_{rf}^m	E_{vib}^m	θ
NF_3	−3.89	−0.43	3.46	1.96	2.60	−3.60	0.65	4.25	116.6
NCl_3	−1.90	−0.18	1.72	1.43	1.56	−1.15	−0.11	1.04	111.6
NBr_3	−1.73	−0.13	1.60	1.41	1.50	−1.18	0.01	1.19	110.9
NH_3	−0.88	0.04	0.92	0.67	0.79	−0.23	0.63	0.86	113.0
PH_3	−1.87	0.04	1.91	0.70	1.15	−1.48	0.69	2.17	123.6
AsH_3	−2.15	0.05	2.20	0.75	1.28	−1.83	0.68	2.51	124.8
SbH_3	−1.91	0.03	1.94	0.68	1.15	−1.98	0.66	2.64	125.0
BiH_3	−2.65	0.05	2.70	0.82	1.48	−2.70	0.40	3.10	125.4

e_{sp} represents the gain of orbital overlap energy due to the HOMO-LUMO interaction at a certain stage of s-p mixing. The bond length contributions ΔE_r are always much smaller than the ΔE_{sp}, which dominate the total energies $\Delta\varepsilon_{sp}$; similarly the restoring energy E_{rf}^m in the many-electron vibronic treatment is mostly of small magnitude in respect to the vibronic coupling energy (and may be even slightly negative [24, 25]) yielding in rough approximation $|\delta E_t^m| \approx E_{vib}^m$ (Tables 1 and 2). This is not true anymore for the higher CNs (Tables 3 and 4), where contributions from displacements along stretching modes to the total energy change become increasingly important.

We now turn to the discussion of a few model examples with the coordination number (CN) four, namely SF_4, PF_4^-, AsF_4^-, SbF_4^- and $SbCl_4^-$ – the anionic species charge-compensated by a solvent continuum. The HOMO containing the s^2 lone pair in the T_d parent geometry is σ-antibonding and of a_1 symmetry. The two active modes inducing the s-p interaction between $a_1(s)$ and the $t_2(p)$ LUMO
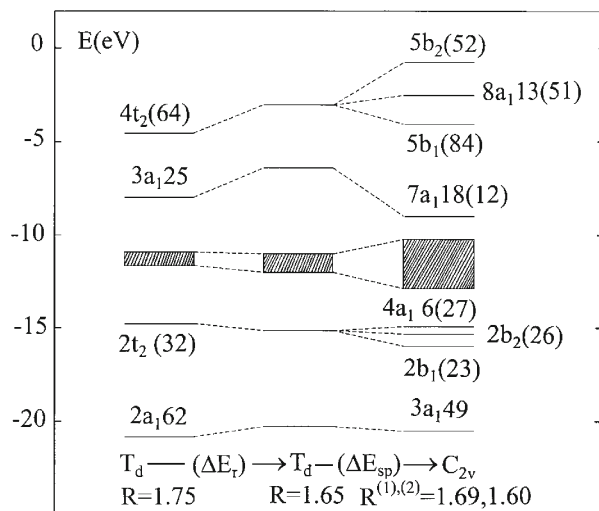
Fig. 3 Kohn-Sham MO diagram of SF_4 in the T_d parent geometry – at the corresponding S-F bond lengths of 1.75 Å and at the averaged spacing of 1.65 Å characteristic for the C_{2v} distorted tetrahedron, respectively – and in its optimised C_{2v} shape ($\theta_1=92.5°$, $\theta_2=50.2°$; see Fig. 2). The non-bonding MOs ($1e$, $1t_1$, $3t_2$ in T_d) occur in the indicated energetic range; the sulphur 3s and 3p (in parentheses) participations in the squares of the wavefunctions (in %) are listed for most MOs

possess τ_2 symmetry (Fig. 2) and lead into the C_{2v} point group. The energy stabilisation in the optimised C_{2v} geometries – using the AOM parameterisation – is

$$\Delta E_{sp} = 4 \left(\cos \theta_2 \, (e^p_{sp}(2))^{1/2} - \cos \theta_1 \, (e^p_{sp}(1))^{1/2}\right)^2 \tag{8a}$$

$$\Delta E_{sp} = 2 \left(\cos \theta_2 \, (e^o_{sp}(2)) - \cos \theta_1 \, (e^o_{sp}(1))\right) \tag{8b}$$

where the angles θ_1, θ_2 and the bond lengths $R^{(1)}$, $R^{(2)}$ are defined in Fig. 2; $e_{sp}(1)$ and $e_{sp}(2)$ (for the numerical evaluation see footnote[1]) refer to the spacings $R^{(1)}$ and $R^{(2)}$ respectively. As expected the average bond length decreases during the $T_d \rightarrow C_{2v}$ distortion process, inducing positive ΔE_r energies (see Eq. 4 and Fig. 3). Relation Eq. (7) is only valid for SF_4, where the HOMO-LUMO interaction nicely reflects the vibronic coupling between the many-electron A_1 ground and the T_2 excited state (Table 3). The Kohn-Sham MO scheme of SF_4 (Fig. 3) demonstrates, that not only the lone-pair HOMO $3a_1$ undergoes energetic changes during the $T_d \rightarrow C_{2v}$ transition, but also most of all the other occupied MOs. However, if the MO energies in the tetrahedral T_d geometry and in C_{2v} are compared at the same (average) bond distance characteristic for C_{2v}, it is striking, that indeed solely the HOMO [$3a_1(R=1.65$ Å$)\rightarrow 7a_1$] is predominantly affected. As expected according

---

[1] In evaluating $e_{sp}(1)$ and $e_{sp}(2)$ an additional DFT calculation, in which θ_1 was set equal to 90° was performed, allowing to calculate directly $e_{sp}(2)$ from $\Delta E'_{sp}=4\cos^2\theta_2 \cdot e^p_{sp}(2)$ or $\Delta E'_{sp}=2\cos\theta_2 \cdot e^o_{sp}(2)$, respectively. Adopting this value in Eq. (8) then yields the $e_{sp}(1)$ parameter. An analogous procedure (setting $\varphi=90°$ in Eq. 9a) was applied for the CN=5.

Table 3 Lone-pair orbital parameters ($\Delta\varepsilon_{sp}, \Delta E_r, \Delta E_{sp}$) and corresponding many-electron quantities ($\delta E_t, E_{rf}^m, E_{vib}^m$, in eV), resulting from DFT calculations and vibronic-coupling treatments [24], respectively, for SF_4 and some selected pseudo-tetrahedral complexes (in a charge compensating polarizable dielectric continuum for the anionic species); the AOM parameters $e_{sp}^p(1), e_{sp}^p(2)$ and $e_{sp}^o(1), e_{sp}^o(2)$ – from Eq. (8), in eV – and the DFT calculated angular (θ_1, θ_2) and bond length($R^{(1)}, R^{(2)}$) distortion parameters[a] (Fig. 2) from the parent tetrahedral T_d ($\theta_1 = \theta_2 = 54.7°$) to the C_{2v} geometry are also listed

Species	$\Delta\varepsilon_{sp}$	ΔE_r	ΔE_{sp}	$e_{sp}^p(1)$	$e_{sp}^p(2)$	$e_{sp}^o(1)$	$e_{sp}^o(2)$	δE_t	E_{rf}^m	E_{vib}^m
SF_4	−1.01	1.57	2.58	0.65	1.44	2.53	1.84	−1.93	0.81	2.74
$(PF_4^-)_{solv}$	−1.23	1.18	2.41	0.49	1.08	2.11	1.52	−1.83	0.66	2.49
$(AsF_4^-)_{solv}$	−0.55	0.92	1.47	0.44	0.75	1.58	0.99	−0.73	0.88	1.61
$(SbF_4^-)_{solv}$	−0.54	0.66	1.20	0.40	0.54	1.30	0.71	−0.54	0.63	1.17
$(SbCl_4^-)_{solv}$	−0.21	0.17	0.38	0.27	0.32	0.70	0.42	−0.04	0.74	0.78

[a] $\theta_1(\theta_2)$ angles (°): 92.5(50.2); 94.9(48.8); 95.3(48.2); 99.9(48.2); 86.5(48.6) and $R^{(1)}(R^{(2)})$ spacings (Å): 1.69(1.60); 1.80(1.66); 1.94(1.81); 2.08(1.99); 2.64(2.45) for SF_4, $(PF_4^-)_{solv}$, $(AsF_4^-)_{solv}$, $(SbF_4^-)_{solv}$, $(SbCl_4^-)_{solv}$, respectively.

to the relations in Eq. (6) the E_{vib}^m and ΔE_{sp} energies get smaller in the sequence of the negatively charged complexes from $(PF_4^-)_{solv}$ via $(AsF_4^-)_{solv}$ and $(SbF_4^-)_{solv}$ to $(SbCl_4^-)_{solv}$ – hence with decreasing chemical hardness [23].

The e_{sp} parameters in Eq. (8) represent the energetic effect of the symmetry-breaking *stretching* τ_2 mode solely, while the angular factors modify these energies according to the *bending* τ_2 vibration. It is expected that $e_{sp}(1)$ and $e_{sp}(2)$ should not differ too much ($e_{sp}(1) \lesssim e_{sp}(2)$)[2] – at least if the bond length changes in respect to the average distance are not too large (<4% for the examples in Table 3). While the perturbation approach yields rather small $e_{sp}^p(1)$ energies as compared to $e_{sp}^p(2)$, in the case of the other limit $e_{sp}^o(1)$ parameters are obtained, which are even much larger than $e_{sp}^o(2)$ and hence far from chemical and physical reality. These results indicate, that an intermediate situation has to be considered – but presumably closer to the perturbation limit. Nevertheless all e_{sp} parameters follow the trend of ΔE_{sp}, which is expected because the angular distortions from T_d don't differ much for the entities in Table 3, with the exception of $(SbCl_4^-)_{solv}$.

We now analyse four examples with the CN=5 (Table 4). The HOMO in the D_{3h} parent geometry is analogous to that for CN=3, while the LUMO is of ($\sigma+\pi$) antibonding e′ nature, originating from $p_{x,y}$ (Fig. 4). The three vibronically active ε′ modes, inducing the s-p mixture and distorting the species to a geometry of C_{2v} symmetry (which turns out to be always very close to C_{4v}), are depicted in Fig. 2. The AOM analysis yields the expressions in Eq. (9) for ΔE_{sp}:

$$\Delta E_{sp} \cong (2\cos\varphi\,(e_{sp}^p(1))^{1/2} + 2\cos\theta\,(e_{sp}^p(2))^{1/2} + (e_{sp}^p(3))^{1/2})^2 \qquad (9a)$$

$$\Delta E_{sp} \cong 2\cos\varphi\,e_{sp}^o(1) + 2\cos\theta\,e_{sp}^o(2) + e_{sp}^p(3) \qquad (9b)$$

[2] This is so, because a bond length change is energetically more pronounced if the bond becomes shorter than longer.

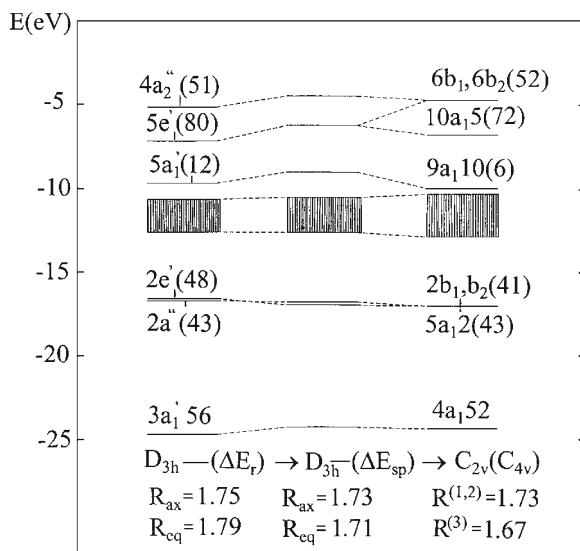**Fig. 4** Kohn-Sham MO diagram of ClF_5 in the D_{3h} parent geometry – at the corresponding Cl-F bond lengths of 1.75 Å (R_{ax}) and 1.79 Å (R_{eq}), and at the spacings of 1.73 Å (R_{ax}) and 1.71 Å (R_{eq} (averaged)) characteristic of the C_{4v} distorted trigonal bipyramid, respectively – and in its optimised tetragonal-pyramidal C_{4v} shape: $\phi=\theta=87.6°$ (see Fig. 2). The non-bonding MOs ($1a_2'$, $1e''$, $2e''$, $3a_2''$, $3e'$, $4a_1'$, $4e'$ in D_{3h}) occur in the indicated energetic range; the chlorine 3s and 3p (*in parentheses*) participations in the squares of the wavefunctions (in %) are listed for most MOs

θ and φ are specified in Fig. 2 and Table 4, and $e_{sp}(1)$, $e_{sp}(2)$ and $e_{sp}(3)$ (see first footnote) refer to the respective bond distances $R^{(1)}$, $R^{(2)}$ and $R^{(3)}$ in the final C_{2v} geometry. If the C_{2v} approximates the C_{4v} geometry ($\varphi \cong \theta$), Eqs. (9a) and (9b) simplify to

$$\Delta E_{sp} \cong (4\cos\varphi \, (e_{sp}^p(1,2))^{1/2} + (e_{sp}^p(3))^{1/2})^2 \tag{10a}$$

$$\Delta E_{sp} \cong 4\cos\varphi \, e_{sp}^o(1,2) + e_{sp}^o(3) \tag{10b}$$

The Kohn-Sham MO scheme of ClF_5 in Fig. 4 possesses analogous energetic features to that in Fig. 3. As expected for a species for which the relation in Eq. (7) is approximately valid, from all occupied MOs only the HOMO $5a_1'$ is significantly stabilized, if the molecule distorts from D_{3h} – at the same Cl-F spacings of $R_{ax}=1.73$ Å and R_{eq}(averaged)=1.71 Å as in the distorted geometry – to $C_{2v}(\approx C_{4v})$. As for the CN=4, ΔE_{sp} (or the various e_{sp} parameters) and E_{vib}^m follow approximately the same trend in the sequence of the charged complexes from P^{III} via As^{III} to Sb^{III} (Table 4). Furthermore, these energies are always smaller than those of the CN=4 (Table 3), when comparing $(A^{III}F_4^-)_{solv}$ with $(A^{III}F_5^{2-})_{solv}$ for $A^{III}=P$, As or Sb (Eq. 6). Molecules and complexes are the less susceptible to lone pair distortions, the larger the CN and the negative charge becomes [25] – in agreement with the hardness rule [23]. We note, that the AOM parameters have the same properties as observed for the CN=4, namely that in particular the $e_{sp}^o(1,2)$ ener-

Table 4 Lone-pair orbital parameters ($\Delta\varepsilon_{sp}, \Delta E_r, \Delta E_{sp}$) and corresponding many-electron quantities (δE_t, E_{rf}^m, E_{vib}^m, in eV), resulting from DFT calculations and vibronic-coupling treatments [24], respectively, for ClF_5 and some selected complexes with the CN=5 (in a charge compensating polarizable dielectric continuum for the anionic species); the AOM parameters $e_{sp}^p(1,2)$, $e_{sp}^p(3)$ and $e_{sp}^o(1,2)$, $e_{sp}^o(3)$ – from Eq. (10), in eV – and the angular (φ) and bond length ($R^{(1,2)}$, $R^{(3)}$) distortion parameters[a] (Fig. 2) from the parent D_{3h} ($\varphi=120°$, $\theta=90°$) to the $C_{2v}(\cong C_{4v})$ geometry are also given

Species	$\Delta\varepsilon_{sp}$	ΔE_r	ΔE_{sp}	$e_{sp}^p(1,2)$	$e_{sp}^p(3)$	$e_{sp}^o(1,2)$	$e_{sp}^o(3)$	δE_t	E_{rf}^m	E_{vib}^m
ClF_5	−0.30	0.65	0.95	0.49	0.74	1.29	0.74	−0.80	0.28	1.08
$(PF_5^{2-})_{solv}$	−0.23	1.28	1.50	0.45	0.92	1.46	0.92	−0.89	0.67	1.56
$(AsF_5^{2-})_{solv}$	−0.33	0.62	0.95	0.32	0.57	0.97	0.57	−0.18	0.71	0.89
$(SbF_5^{2-})_{solv}$	−0.46	0.57	1.03	0.31	0.44	0.92	0.44	−0.18	0.73	0.91

[a] φ angles (°): 87.6; 84.3; 84.4; 80.8 and $R^{(1,2)}$, $R^{(3)}$ spacings (Å): 1.73,1.67; 1.88,1.69; 2.00,1.84; 2.14,2.02 for ClF_5, $(PF_5^{2-})_{solv}$, $(AsF_5^{2-})_{solv}$ and $(SbF_5^{2-})_{solv}$, respectively.

gies are much larger than $e_{sp}^p(1,2)$ – leading to the relations: $e_{sp}^p(3)>e_{sp}^p(1,2)$ and $e_{sp}^o(3)<e_{sp}^o(1,2)$.

Equations (8) and (10) can be grossly simplified, if the angles θ_1 and φ are near to 90° in the case of the CN=4 and 5, respectively:

$$CN = 4: \quad \Delta E_{sp} \cong 4\cos^2\theta_2\, e_{sp}^p(2); \quad \Delta E_{sp} \cong 2\cos\theta_2\, e_{sp}^o(2) \tag{11a}$$

$$CN = 5: \quad \Delta E_{sp} \cong e_{sp}^p(3) \qquad ; \quad \Delta E_{sp} \cong e_{sp}^o(3) \tag{11b}$$

In the perturbation limit, the contributions from θ_1 (CN=4: Eq. 8a, Eq. 11a) and φ (CN=5: Eq. 10a, Eq. 11b) to ΔE_{sp} in the considered cases are mostly between 10 and 20%, but amount to even 40% for $(PF_5^{2-})_{solv}$ (Tables 3 and 4). Accepting Eq. (11) as fair approximations, it should be emphasized that only bonds are relevant to ΔE_{sp}, which have *large projections onto the direction, which is opposite to the lone-pair orientation*. Explicitly, these are 3cosθ (projections of the three ligands along (−z)) and 2cosθ₂ (projections of the two ligands with the short bond lengths along (−z)) for the CNs of 3 and 4, respectively – or the corresponding squares, if the perturbation treatment is chosen; in the case of the CN=5 solely the one short-bonded ligand at $R^{(3)}$ and positioned on the x axis is involved (Fig. 2). Thus the imagination behind the AOM energies e_{sp} as reflecting the changes of the orbital overlap by s-p mixing, meets the chemists' demand of pictorial concepts.

s-p mixing in octahedral lone pair complexes is expected to lead to alternatively C_{4v}, C_{3v} or C_{2v} distortions (Fig. 5) via the vibronically active τ_{1u} modes in O_h. In particular the C_{4v} case is interesting, because the ligand positioned in the (−z) direction is strongly repelled by the lone pair and usually abandons the coordination sphere completely. As has been shown elsewhere [23], in such case a small dissociation energy supports the s-p mixing effect, reducing the CN from 6 to 5. Furthermore, DFT calculations indicate that the C_{4v} pathway seems to be preferred with respect to C_{2v} and C_{3v} type distortions. Reviewing the structural data for isolated octahedral complexes however, they mostly remain in their O_h parent geometry with an s^2-type lone-pair. As interesting model examples we
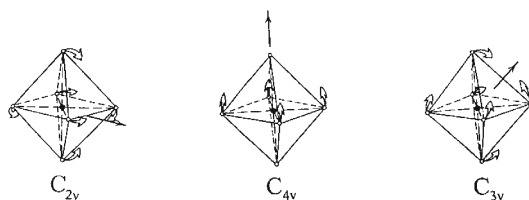
Fig. 5 The highest symmetry distortions of an octahedral complex along τ_{1u}-type pathways, the arrows indicating the (+z) directions opposite to the lone pair orientation; C_{4v} (see Eq. 12): $R^{(3)}$, $R^{(4)}$ refer to the ligands along (+z), (−z) and φ is the bond angle of the equatorial ligands (at $R^{(1,2)}$) with respect to (+z)

shortly discuss the complexes AsF_6^{3-}; SeF_6^{2-} and SbF_6^{3-}; TeF_6^{2-}. Focussing on $(AsF_6^{3-})_{solv}$ first – using water as the charge-compensating dielectric continuum in the DFT calculations – we present in Fig. 6 the bond distance dependence of the energy change along the C_{4v}, C_{2v} and C_{3v} pathways, choosing the energy of the undistorted octahedron as the reference. Here, every point corresponds to a DFT geometry optimisation, where only the longest spacings (one, two or three in C_{4v}, C_{2v} and C_{3v} respectively – see Fig. 5) are kept constant, while relaxing all other bond lengths and the bond angles. It is seen that $(AsF_6^{3-})_{solv}$ is unstable with respect to an $(AsF_5^{2-})_{solv}$ fragment of C_{4v} symmetry and an $(F^-)_{solv}$ ligand – which has left the complex completely – by an enthalpy $\Delta H_5^s = -0.07$ eV; on the other hand, the C_{2v} and C_{3v} pathways imply positive energy changes. Calculating the
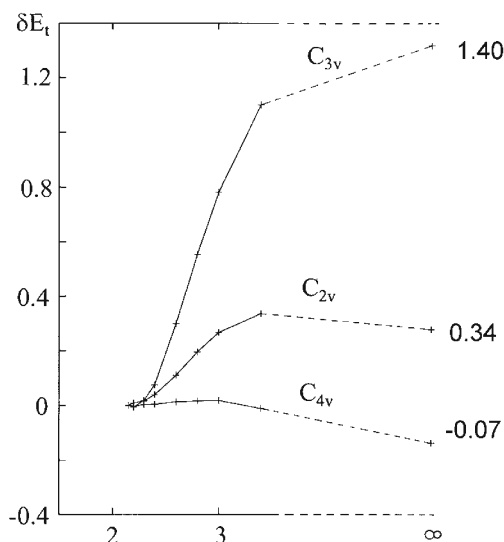
Fig. 6 Bond distance (Å) dependence of the stabilisation energy (eV) for distortions of $(AsF_6^{3-})_{solv}$ along the C_{4v}, C_{2v} and C_{3v} pathways (the respective longest bond lengths – 1 for C_{4v}, 2 for C_{2v}, 3 for C_{3v} (see Fig. 5) – are chosen as the variable; for further details see text); the energies at infinite spacings (in eV) refer to the dissociation enthalpies ΔH_{CN}^s towards the complexes with CN=5(C_{4v}), 4(C_{2v}) and 3(C_{3v})

dissociation energy for the process O_h(CN=6) to D_{3h} (CN=5), where the lone-pair effect ($D_{3h} \rightarrow C_{4v}$) is suppressed, one obtains $(\Delta H_5^s)_{D3h}$=0.53 eV. Apparently the s-p mixing effect (–0.60 eV) is large enough to overcome this rather low energy barrier. Thus, AsF_6^{3-} – and SbF_6^{3-} as well (with a vanishing ΔH_5^s enthalpy [23]) – should not be stable as octahedral complexes – in agreement with the experimental evidence.

The AOM expressions characterizing the lone pair effect for the $O_h \rightarrow C_{4v}$ distortion are (see also Fig. 5):

$$\Delta E_{sp} \cong (4\cos\varphi \, (e_{sp}^p(1,2))^{1/2} + (e_{sp}^p(3))^{1/2} - (e_{sp}^p(4))^{1/2})^2 \qquad (12a)$$

$$\Delta E_{sp} \cong 4\cos\varphi \, e_{sp}^o(1,2) + e_{sp}^o(3) + e_{sp}^o(4) \qquad (12b)$$

which – with $e_{sp}(4)$=0 – match Eq. (10). We conclude, that the driving force behind the octahedral C_{4v} distortion is the s-p mixing effect, connected with the $D_{3h} \rightarrow C_{2v}(\approx C_{4v})$ transformation of the $(AsF_5^{2-})_{solv}$ fragment after the removal of one ligand from $(AsF_6^{3-})_{solv}$. The isoelectronic $(SeF_6^{2-})_{solv}$ complex is calculated by DFT to be stable in O_h symmetry. In contrast, the recently described compound $(pip^+)_2SeF_6$ [26] possesses an approximately C_{3v}-distorted anion (spacings: $\approx$1.84(3×), $\approx$2.02 Å(3×) and bond angles 101°(3×), 85°(3×)); however, the calculated energy barrier for this deformation is low ($\cong$0.1 eV) and may be easily overcompensated by a solid state strain. Also $(TeF_6^{2-})_{solv}$ – though not yet reported – should be stable as an undistorted octahedral complex according to DFT, but as in the Se^{IV} case, with a flat potential energy surface along the vibronically active τ_{1u}-type pathways (Fig. 5).

We note here that the numerical values for E_{vib}^m and E_{rf}^m listed in Tables 1–5 differ distinctly from those reported earlier [7, 23]. They result from a vibronic coupling analysis based on Slater's transition state theory [27] and have to be considered as more reliable – for reasons thoroughly discussed elsewhere [24].

4
Spectroscopic Implications of the Lone Pair Effect

Figure 7 presents the many-electron state diagram of the $(SnCl_3^-)_{solv}$ complex in the D_{3h} parent and in the final C_{3v} geometry – as calculated by DFT optimisations. Only the vibronically interacting $A_1'(s^2)$ and $A_2''(s^1 p_z^1)$ states are depicted and the Franck-Condon (FC) transitions (δ, E_{FC}^m) indicated. If the A_1 excited state is optimised using DFT, a relaxation towards an energy minimum with planar geometry occurs ($\rightarrow A_2''(D_{3h})$), with bond lengths smaller by 0.1 Å than those in the parent D_{3h} ground state geometry. The corresponding FC transition to the ground state is observed in luminescence at 2.43 eV for $[NEt_4][SnCl_3]$ in acetonitrile solution [28], matching rather well the calculated value (δ'=2.24 eV). Equally satisfying is the agreement of the observed transitions $^1A_1 \rightarrow {}^1A_1$ and $^3A_1$ in absorption, at 4.56 and 4.25 eV respectively, with E_{FC}^m=4.57 eV. We may hence consider the DFT calculations as reliable and the results for the hypothetical D_{3h} parent geometry with the initial splitting δ (=2.44 eV) as well. As is easily deduced from the matrix in Eq. (1), it is the non-diagonal element, which is responsible for shifting the $A_1' \rightarrow A_2''$ absorption band to higher energies by
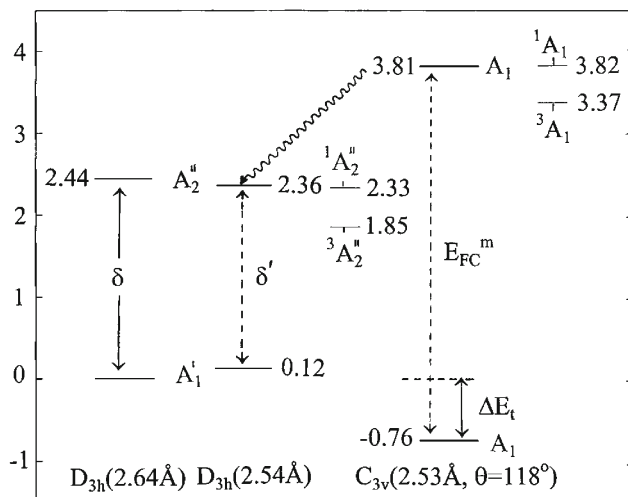
Fig. 7 Energy (eV) diagram of the charge compensated $(SnCl_3^-)_{solv}$ complex (only the interacting A_1' and A_2'' states in D_{3h}, corresponding to s^2 and $s^1p_z^1$ respectively, are depicted) in D_{3h} (*left*) and C_{3v} (*right*); the DFT optimisation for the excited state, which is of planar D_{3h} symmetry (*central part*), is also shown. The *hatched arrows* indicate spectroscopic Franck-Condon transitions in absorption (E_{FC}^m) and emission (δ'), and the *meandering arrow* the relaxation in the excited A_1 state, preceding the emission; the excited states' splittings according to different spin orientations are also indicated (absorption: $^1A_1 \rightarrow {}^1A_1(C_{3v})$; luminescence: $^3A_2'' \rightarrow {}^1A_1'(D_{3h})$)

$E_{FC}^m - \delta = 2.13$ eV. Thus here the s-p mixing energy is reflected in very good approximation by the calculated Stokes' shift $\delta E_{st} \approx \delta E_{FC}^m - \delta' = 2.33$ eV. If interelectronic interactions distinguishing between singlet and triplet spin orientations are included in the excited A_2'' and A_1 states (see Fig. 7), the agreement between the DFT and the experimental transition energies is still reasonable – though the luminescence originating from $^3A_2''$ is calculated to occur at a by about 0.5 eV lower energy now. The possible reason might well be the steric constraint of the solvation shell (solvent reorganisation energy), which is only approximately taken into account using a dielectric continuum without mass. A steric hindrance of the geometry change from C_{3v} to D_{3h} in the vibrational relaxation process should tend to avoid a completely planar structure in the emitting state.

Figure 8 sketches the MO analogue to Fig. 7, considering the HOMO-LUMO interaction as representative for the s-p interaction. When calculating the orbital FC transitions, Slater's transition state method [27] was applied, utilizing results from a DFT-SCF calculation; here, the energy of the excited state $a_1'^1 a_2''^1$ with respect to $a_1'^2$ for example is slightly modified according to the averaged $a_1'^{1.5} a_2''^{0.5}$ configuration. With such corrections, Δ_{MO}, Δ'_{MO} and Δ''_{MO} adopt slightly higher energy values (2.44, 2.23 and 4.56 eV) than those in Fig. 8 – which are practically identical with δ, δ' and E_{FC}^m in Fig. 7, respectively. Accounting for spin-orbit coupling leads to lower energy shifts of these transitions by only about 0.1 eV. Translating the Kohn-Sham MO results into the energy increments of Eq. (3) and Eq. (4) (recalling, that the bond lengths from the DFT optimisations of
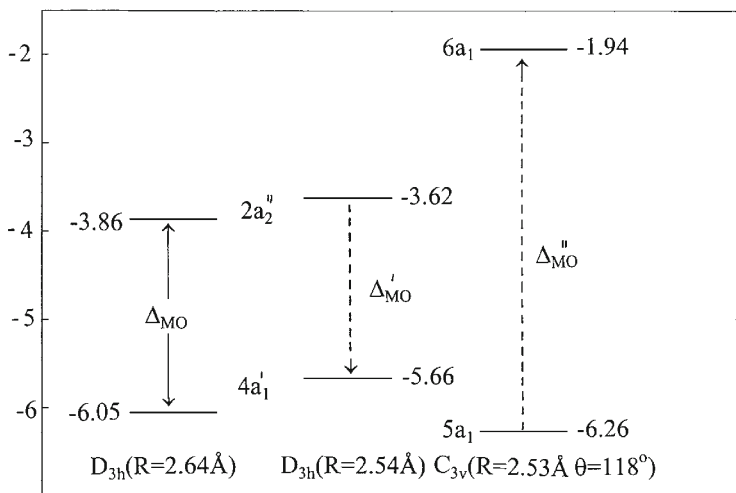
Fig. 8 Kohn-Sham MO diagram of the charge-compensated $(SnCl_3^-)_{solv}$ complex (only the HOMOs and LUMOs are depicted) in D_{3h} (*left*) and C_{3v} (*right*); the DFT optimisation for the $a_1(=a_2'')$ LUMO (*central*) is also shown (energies in eV)

the ground state $A_1(C_{3v})$ and the excited state $A_2''(D_{3h})$ are practically equal by chance), we calculate from Fig. 8: $\Delta E_r = 0.39$, $\Delta E_{sp} = 0.60$ eV and $e_{sp}^o = 0.42$; $e_{sp}^p = 0.30$ eV. The latter values are distinctly smaller in comparison to those of the isoelectronic $SbCl_3$ molecule (Table 1), suggesting weaker bonds; the obvious reason is a more pronounced soft behaviour of $(SnCl_3^-)_{solv}$ induced by the decrease of the oxidation state and by the presence of an anionic charge.

A quite different situation of the optical behaviour is met in $(SbCl_4^-)_{solv}$. The spectra of $[NEt_4][SbCl_4]$ in acetonitrile solution show an absorption in the UV region (4.38 eV) and an emission of red light (1.68 eV), corresponding again to a large Stokes shift of 2.70 eV [29]. However, its origin is more complex as compared to $(SnCl_3^-)_{solv}$, which may be deduced from the state diagram in Fig. 9. The two ground state (left and right) and the excited state (central) DFT optimisations correspond to the parent T_d symmetry, the C_{2v} geometry as the consequence of the lone-pair effect and to a near-to-planar D_{4h} coordination, respectively. The latter results from a first order Jahn-Teller effect in the excited T_2 state, induced by the ε vibrational mode ($T_2 \otimes \varepsilon$ coupling); it is also present in the C_{2v} geometry, but to a much less pronounced extent. The calculated absorption and emission band energies are about 13% smaller than the experimental values. If singlet and triplet spin orientations are included into the calculations, the disagreement between the calculated and observed luminescence energy $^3B_{2g} \rightarrow {}^1A_{1g}$ becomes even larger (see below however). Because the position of the excited A_1 state in C_{2v} with respect to the T_2 energy in T_d is not only determined by the A_1-T_2 lone pair interaction but also by the distinct Jahn-Teller splitting of T_2, a correlation of the s-p mixing effect with the Stokes' shift δE_{st} is not straightforward. However, the A_{1g}–T_{2g} (centre of gravity of B_{2g} and E_g) separation in D_{4h} is close to δ, and one may also roughly transfer one-third of the Jahn-Teller splitting in D_{4h} into
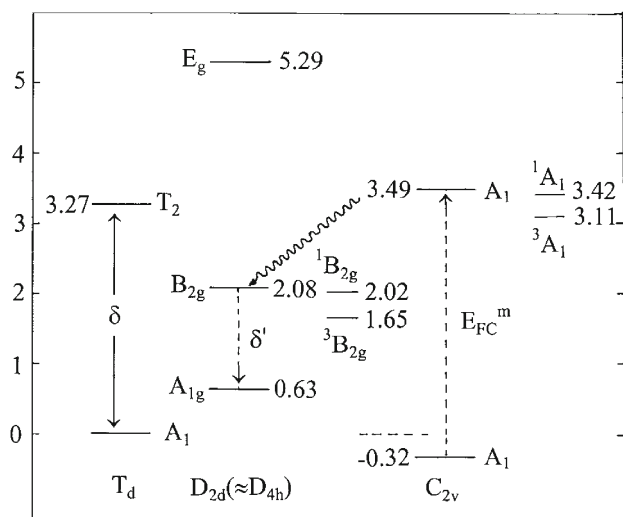
Fig. 9 State diagram of $(SbCl_4^-)_{solv}$ with ground state optimisations in T_d (R=2.58 Å) – *left* – and C_{2v} (R$^{(1)}$=2.64, R$^{(2)}$=2.45 Å; θ_1=86.6°, θ_2=48.6 °) – *right* (energies in eV); the *central part* refers to the excited state optimisation, indicating a nearly planar geometry (R=2.55 Å(4×); θ=90.0(±0.9)°(4×)). The *hatched arrows* indicate spectroscopic FC transitions in absorption (E_{FC}^m) and emission (δ'); the excited states' splittings according to different spin orientations are also indicated (absorption: $^1A_1 \rightarrow {}^1A_1(C_{2v})$; luminescence: $^3B_{2g} \rightarrow {}^1A_{1g}(D_{4h})$)

the C_{2v} geometry – estimating the ε-type distortion component in C_{2v} ($\Delta\theta\cong13°$, besides $\Delta\theta(\tau_2)\cong\pm19°$; Table 3, Fig. 2) in comparison to that in D_{4h} ($\Delta\theta$=35.3°). An s-p mixing effect of ≈1.3 eV is thus derived, which does not show up in δE_{st} (≈2.4 eV), however; the latter predominantly reflects the influence of the excited state Jahn-Teller effect in this case.

From the MO scheme of $(SbCl_4^-)_{solv}$ in Fig. 10, considering only the HOMOs and the respective LUMOs, the Slater-corrected Δ'_{MO} and Δ''_{MO} transitions are again calculated to appear at the same energies as E_{FC}^m and δ' in the state diagram (Fig. 9), namely at 3.80 and 1.45 eV, respectively. As discussed for $(SnCl_3^-)_{solv}$, a pure planar D_{4h} geometry is probably not realized in the excited B_{2g} state (see the central parts of Figs. 9 and 10) due to the rather pronounced demand of the solvent shell. Thus an emission energy lower than the calculated value is not unlikely.

The corresponding $(SbF_4^-)_{solv}$ complex, for which no spectroscopic investigation is reported, is calculated to exhibit an even larger Stokes' shift of δE_{st}=4.0 eV (absorption: 6.1 eV, emission: 2.1 eV), with otherwise stereochemical results analogous to those for the chloride species. In this case the lone pair effect is expected to shift the absorption band by ≈3.0 eV. We conclude that s-p mixing is not always quantitatively reflected by the optical data; an analysis by reliable calculations is necessary.

The electronic transition of the octahedral s^2-type $(SbCl_6^{3-})_{solv}$ complex from the $^1A_{1g}$ ground state to the $^1T_{1u}$ excited state is calculated using DFT to appear
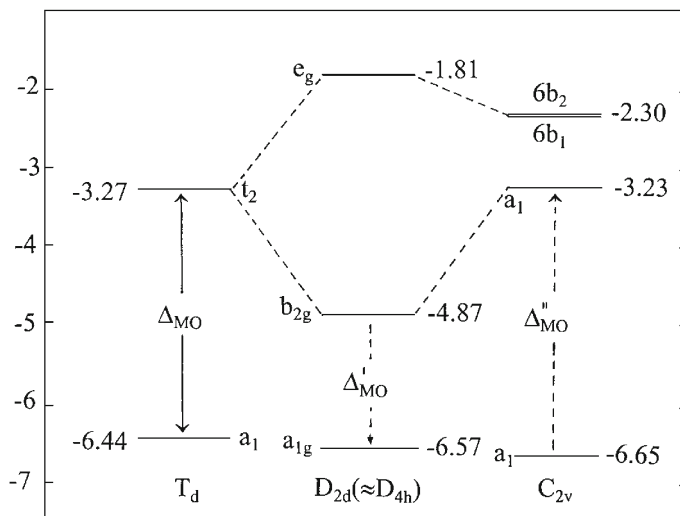
Fig. 10 The Kohn-Sham MO diagram of $(SbCl_4^-)_{solv}$ (for details see Fig. 9)

at 3.56 eV, in reasonable agreement with the solution spectrum of the anion in acetonitrile (4.05 eV) [29]. Emission is predicted to occur from a Jahn-Teller elongated octahedral geometry (D_{4h}), splitting the excited $^3T_{1u}$ state into $^3A_{2u}$ and ^3E_u; the corresponding $^3A_{2u} \to {}^1A_{1g}$ transition lies in the green spectral region at 2.38 eV [29] and is calculated at 1.53 eV. A similar emission spectrum has been observed in solid Cs_2SeCl_6 at 1.74 eV [30]; the beautifully resolved ε_g type progression is interpreted in terms of a distinct excited state Jahn-Teller coupling. A lone-pair influence is not detected in both cases. In contrast, the $^1A_{1g} \to {}^1T_{1u}$ absorption band of $[N(But)_4]$ $TeCl_6$ in the solid state is split by about 0.4 eV [31], and the symmetry effect is discussed as originating from the combined effect of spin-orbit coupling and a dynamic orthorhombic field component of C_{2v} symmetry [4(chap 32), 31]. One may suggest, that a solid state strain is present, which has distorted the flat potential curve along the C_{2v} pathway (Fig. 5), thus causing a weak lone pair effect.

5
Discussion: Trends of the AOM Parameter e_{sp}

In Table 5 we have listed effective e_{sp}^{eff} parameters for a series of molecules AF_3 and complexes $(AF_4^-)_{solv}$, $(AF_5^{2-})_{solv}$ [A^{III}:P, As, Sb]. e_{sp}^{eff} is the weighted (by the number of ligands) linear average of the various e_{sp}^P energies for the CNs=4 and 5 (Tables 3 and 4) – the corresponding A-F spacings are also linear averages (R^{eff}) – and is the bond strength of a virtual ligand opposite to the lone pair at the distance R^{eff}. *It represents an energy, which is solely due to the s-p mixing and reflects the average bond strength increase of all ligands present in the molecule or complex by the lone pair effect.* We have chosen the AOM parameters from the perturbation approach, because – as follows from the discussion for the CN=4

and 5 – they are more representative than the e_{sp}^{o} energies. One should have in mind though, that more reliable parameters are surely intermediate, but still mostly much closer to the perturbation limit. e_{sp}^{eff} decreases considerably, if one proceeds from PF_3 (or AsF_3 or SbF_3) to the respective complexes with CN=4 and CN=5, which is also the trend of increasing average R^{eff} bond lengths – with a distance dependence approximately corresponding to R^{-6}. There is no obvious correlation with the extent of s-p mixing, however; though e_{sp}^{eff} varies between 0.99 and 0.34 eV, the participation of p_z electron density, in relation to the sum of s and p_z, in the cationic part of the HOMO wavefunction ($P(p_z)$, in %) remains roughly unchanged (33±5%). It is apparently not the extent of p_z admixture, which finally determines the e_{sp}^{eff} variation with increasing CN and negative charge. This is not unexpected, because e_{sp}^{eff} reflects only the radial contribution to the s-p mixing effect. We also note, that a remarkable correlation with the vibronic energy E_{vib}^{m} exists, though this quantity contains contributions not only from stretching but also from bending nuclear motions (Fig. 2). We further mention the role of the chemical hardness η, when considering energetic and stereochemical lone pair effects in the context of a vibronic coupling approach, as discussed in detail elsewhere [23, 25]. The observable quantity η mirrors the sequences Eq. (6); the softer the considered species is, the smaller e_{sp}^{eff} and E_{vib}^{m} become. The mentioned trends only very roughly hold, when compounds and complexes with central ions from different main groups and with different oxidation states are compared. Thus $S^{IV}F_4$ possesses an e_{sp}^{eff} parameter (1.05 eV) ≈30% larger than the isoelectronic $(P^{III}F_4^-)_{solv}$ complex, while e_{sp}^{eff} is about the same for $Cl^{V}F_5$ (0.54 eV) and $(PF_5^{2-})_{solv}$ (Tables 3–5).

We summarize by stating, that the *AOM parameter* e_{sp}^{eff} – though an orbital energy reflecting only the HOMO properties and though calculated via perturbation theory, which only very approximately holds – is apparently a *useful quantity in parameterising s-p_z mixing and seems to be even semiquantitatively transferable within groups of similar species with central ions of identical oxidation states* (Table 5).

Table 5 Effective AOM parameters e_{sp}^{eff}, defined for the respective averaged bond lengths R^{eff} (Å) – see text – as well as the vibronic coupling energy E_{vib}^{m} for selected P^{III}, As^{III} and Sb^{III} molecules and complexes; additionally the relative central atom p_z density (with respect to s+p_z) in the HOMO ($P(p_z)$, in %) is given

Species	e_{sp}^{eff}	R^{eff}	$P(p_z)$	E_{vib}^{m}
PF_3	0.99	1.63	38	3.44
$(PF_4^-)_{solv}$	0.79	1.74	36	2.49
$(PF_5^{2-})_{solv}$	0.54	1.84	38	1.56
AsF_3	0.81	1.75	34	2.37
$(AsF_4^-)_{solv}$	0.60	1.87	29	1.61
$(AsF_5^{2-})_{solv}$	0.37	1.97	27	0.89
SbF_3	0.64	1.94	34	1.87
$(SbF_4^-)_{solv}$	0.47	2.02	31	1.17
$(SbF_5^{2-})_{solv}$	0.34	2.11	34	0.91

Concluding, we add that convincing spectroscopic evidence exists not only for the presence of d-s mixing, but also for s-p type vibronic coupling – with sometimes very pronounced energetic lone pair effects, as has been demonstrated for some model complexes.

6
Computational Details

The calculations have been performed using the Amsterdam Density Functional (ADF) program package, program release 2002.02 [32–36] with the choice of the functionals described in detail elsewhere [23]. We used a triple zeta basis with the option of "CORE SMALL" and scalar relativistic corrections (ZORA option). In the case of charged species AX_4^- and AX_5^{2-} we accounted for charge compensation by using a solvent according to the Conductor-like Screening Model (COSMO) [37], as implemented [38] in the ADF. Parameters in the solvent calculation were those for water [23], and we used solvent radii for P, As, Sb and F, Cl of 2.40, 2.46, 2.67 and 1.40, 1.75 Å, respectively. Geometry optimisations for the charged species have been performed using the option "ALLPOINTS" along with "INTEGRATION 5.0 5.0", where symmetry was used as much as possible; otherwise problems with convergence of geometry are frequently encountered. Single point calculations could be performed faster without using "ALLPOINTS".

7
References

1. Jørgensen CK, Pappalardo R, Schmidtke H-H (1963) J Chem Phys 39:1422; Jørgensen CK, Schmidtke H-H (1963) Z Phys Chem NF 38:118; Schmidtke H-H (1964) Z Naturforsch A 19:1502
2. Yamatera H (1958) Bull Chem Soc Jpn 31:95
3. Figgis BN, Hitchman MA (2000) Ligand field theory and its applications. Wiley-VCH, New York
4. Jørgensen CK (1971) Modern aspects of ligand field theory. North-Holland, Amsterdam
5. Burdett JK (1976) Struct Bond 31:67; Burdett JK (1980) Molecular shapes. Wiley-Interscience, New York
6. Pearson RG (1976) Symmetry rules for chemical reactions, orbital topology, and elementary processes. Wiley, New York
7. Atanasov MA, Reinen D (2001) J Phys Chem A 105:5450
8. Blasse G (1988) Progr Solid State Chem 18:79
9. Vogler A, Nikol H (1993) Comments Inorg Chem 14:245
10. Reinen D, Atanasov M (1991) Magn Res Rev 15:167
11. Reinen D, Atanasov M, Nikolov G, Steffens F (1988) Inorg Chem 27:1678
12. Hitchman MA, Cassidy PJ (1979) Inorg Chem 18:1745
13. Steffen G, Reinen D, Stratemeier H, Riley MJ, Hitchman MA, Matthies HE, Recker K, Wallrafen F, Niklas JR (1990) Inorg Chem 29:2123
14. Orgel LE (1958) J Chem Soc 4186; Dunitz JD, Orgel LE (1960) Adv Inorg Chem Radiochem 2:1.
15. Ceulemans A, Beyens D, Vanquickenborne LG (1982) Inorg Chim Acta 61:199
16. DeKock CW, Gruen DM (1966) J Chem Phys 44:4387; DeKock CW, Gruen DM (1967) J Chem Phys 46:1096
17. Bridgeman AJ (1996) J Chem Soc Dalton Trans 2601; Wang SG, Schwarz WHE (1998) J Chem Phys 109:7252

18. Hitchman MA, Stratemeier H, Hoppe R (1988) 27:2506
19. Möller A, Hitchman MA, Krausz E, Hoppe R (1995) Inorg Chem 34:2684
20. Wang SG, Schwarz WHE (1997) J Alloys Comp 246:131
21. Liao MS, Schwarz WHE (1997) J Alloys Comp 246:2
22. Stowasser R, Hoffmann R (1999) J Am Chem Soc 121:3414
23. Atanasov M, Reinen D (2002) J Am Chem Soc 124:6693
24. Atanasov MA, Reinen D (2003) Adv Quantum Chem 44:355
25. Atanasov MA, Reinen D (2004) Inorg Chem 43:1998
26. Mahjoub AR, Zhang X, Seppelt K (1995) Chem Eur J 1:261
27. Slater JC (1972) Adv Quantum Chem 6:1
28. Nikol H, Becht A, Vogler A (1992) Inorg Chem 31:3277
29. Nikol H, Vogler A (1991) J Am Chem Soc 113:8988
30. Wernicke R, Kupka H, Ensslin W, Schmidtke H-H (1980) Chem Phys 47:235
31. Couch DA, Wilkins CJ, Rossman GR, Gray HB (1970) J Am Chem Soc 92:307
32. Baerends EJ, Ellis DE, Ros P (1973) Chem Phys 2:41
33. Baerends EJ, Ros P (1973) Int J Quantum Chem 2:42
34. Baerends EJ, Ros P (1973) Int J Quantum Chem 2:51
35. Boerrigter PM, te Velde G, Baerends EJ (1988) Int J Quantum Chem 33:87
36. te Velde G, Baerends EJ (1992) J Comput Phys 99:84
37. Klamt A, Schürmann G (1993) J Chem Soc Perkin Trans 2:799
38. Pye CC, Ziegler T (1999) Theor Chem Acc 101:396

Progress in Hole-Burning Spectroscopy of Coordination Compounds

Hans Riesen

The University of New South Wales, School of Physical, Environmental and Mathematical Sciences, University College, ADFA, ACT 2600 Canberra, Australia
E-mail: h.riesen@adfa.edu.au

Abstract Electronic transitions in condensed phases are invariably broadened by the variation of local fields: consequently valuable information about the electronic structure is obscured. Several laser techniques, such as spectral hole-burning, fluorescence line narrowing and photon-echo measurements, can overcome this inhomogeneous broadening and it is often possible to increase the spectral resolution by many orders of magnitude and to approach the homogeneous (or natural) linewidth of an electronic origin. Spectral hole-burning is a highly successful laser selective technique that has been applied to a wide range of problems in chemistry, physics and biology. The present chapter reviews recent progress made by hole-burning experiments in the spectroscopy of coordination compounds, in particular chromium(III) complexes.

Keywords Hole-Burning · Linewidth · Zeeman · Deuteration · Chromium(III)

1
Introduction

Remarkable progress has been achieved in laser spectroscopy of solids since the first reports of transient and persistent spectral hole-burning in the 1970s [1–4]. Spectral hole-burning is a highly successful laser technique that can reveal the subtlest details of electronic and vibrational structures [5, 6]. Spectral hole-burning has been applied to a wide range of problems in inorganic, organic and biological chemistry [7–12]. In a recent development, differences in non-photo-chemical hole-burning of normal and carcinoma ovarian cells incubated with rhodamine 800 were investigated [13]. Spectral hole-burning has also numerous potential applications in optical data storage, quantum computing, laser stabil-ization schemes and in frequency standards [5, 14, 15]. The present chapter pre-sents an introduction to spectral hole-burning and reviews some of our work, emphasizing recent success in the application of inexpensive diode lasers in high-resolution spectroscopy of coordination compounds.

1.1
The Homogeneous Linewidth

The homogeneous (or natural) linewidth of an electronic transition of an ion, molecule or molecular ion in the solid state is governed by the excited state life-time T_1 and pure dephasing processes in the ground and excited state, charac-terized by the time T_2^* [5, 16]. Dephasing can arise through phonon-scattering processes, as well as electronic and nuclear spin fluctuations in the environment of the optical centres. Pure dephasing based on phonon scattering processes is usually strongly temperature dependent and can virtually be frozen out at 1.5 K. Dephasing based on electronic and nuclear spin fluctuations may be reduc-ed by the application of external magnetic fields and by chemical variations of the host.

In the following we consider an isolated system in the solid state consisting of an electronic ground and an electronic excited state. The excited state life-time and the pure dephasing time, T_1 and T_2^*, can be combined to an effective dephasing time, T_2, according to Eq. (1):

$$\frac{1}{T_2} = \frac{1}{2T_1} + \frac{1}{T_2^*} \tag{1}$$

The homogeneous linewidth Γ_h can then be expressed in terms of the effective dephasing time, T_2, by Eq. (2) [17]:

$$\Gamma_h = \frac{1}{\pi T_2} \sqrt{(1 + \omega_1^2 T_1 T_2)} \tag{2}$$

The second term in the square root describes the power broadening. The Rabi frequency ω_1 is proportional to the product of the electric field vector of the electromagnetic radiation and the transition dipole moment. It is a measure for

the time needed to drive an ensemble of chromophores, which is initially in the ground state, to 50% excited state population:

$$\omega_1 = \frac{\mu \cdot E}{\hbar} \qquad (3)$$

If non-radiative relaxation of the excited state can be neglected, and the pure dephasing is frozen out, the power term approaches

$$\omega_1^2 T_1 T_2 \cong 2\omega_1^2 T_1^2 \cong 4\times10^{-4}\, \lambda^3 T_1 J_{rms}\left(n\left(\frac{n^2+2}{3}\right)\right)^{-1} \qquad (4)$$

where λ is the wavelength in [nm], n the refractive index of the material and J_{rms} the irradiance in [mW/cm^2]. For example, assuming $n=1$, for a chromium(III) ^{2}E←^{4}A$_2$ transition at 690 nm with a lifetime of 1 ms, a factor of ≈36 is calculated with J_{rms}=10 mW/cm^2. This corresponds to a 6-kHz power broadening of a transition with a 160 Hz lifetime limited linewidth. If the 10-mW laser is focussed to a spot size of 10 μm diameter, a massive broadening of ≈6 MHz is calculated. The dependence of the homogeneous linewidth on the excitation power density has been reported for photon-echo experiments in the ^{5}D$_0$↔^{7}F$_0$ transition of Y$_2$SiO$_5$:Eu^{3+} [18].

If the laser power is kept minimal and all dephasing can be frozen out by lowering the temperature and/or applying a magnetic field, then the lifetime limited linewidth may be approached:

$$\Gamma_h = \frac{1}{2\pi T_1} \qquad (5)$$

If the coherence of the ensemble of excited chromophores decays by T$_1$ and T$_2^*$ processes as a single exponential, the line shape of the homogeneous transition is Lorentzian: the frequency distribution is given by the Fourier transformation of the T$_2$ decay curve. Lorentzian line-shapes are indeed often observed. For example, ^{1}π-^{1}π* transitions in organic molecules are insensitive to electronic and nuclear spin fluctuations in their environment. The pure dephasing time T$_2^*$ is thus governed by phonon scattering processes that can be frozen out at 1.5 K, and the lifetime limited linewidth may be approached [9, 19]. An excellent example is also provided by the ^{5}D$_0$↔^{7}F$_0$ transition in the Y$_2$SiO$_5$:Eu^{3+} system [18, 20]. Both the ground state ^{7}F$_0$ and the excited state ^{5}D$_0$ have no magnetic moment in first order since J=0 in both states. Consequently, they are insensitive to any electronic or nuclear spin fluctuations in the surroundings. Moreover, the Y$_2$SiO$_5$ host provides an environment of minimal nuclear magnetic moments and the measured homogeneous linewidth of Γ_h=122 Hz in this system is very close to the lifetime limit of 85 Hz at 1.4 K. This is one of the narrowest transitions reported yet in a solid.

Reported linewidths for coordination compounds are far above the lifetime limit, and electron and nuclear spin interactions limit the resolution. This is because the magnetic moment of the ground state in many transition metal complexes is rather large and thus sensitive to electronic and nuclear spin fluctuations in the environment. Typically, impurity concentrations of the order of mag-

nitude of 1% have been used in optical experiments in this class of compounds. At this concentration direct and indirect electron-spin–electron-spin interactions are dominant, leading to rapid dephasing, that is well described by a single exponential, and thus to Lorentzian line shapes with linewidths in the 10–200 MHz range. At very low concentrations, low temperatures and in high magnetic fields the effects of electron-spin–electron-spin interactions become negligible and superhyperfine limited optical dephasing may be observed. This is based on the interaction of the magnetic moment of the paramagnetic metal ion with neighbouring nuclear spins. *Non-exponential* decays of photon-echoes have been observed in this limit for ruby, $YLiF_4:Er^{3+}$ and $LaF_3:Er^{3+}$ [21, 22]. The effective dephasing time T_2 and the homogeneous linewidth are not defined anymore in this limit, and the line shape may be non-Lorentzian. The non-exponential decay of photon-echoes in the superhyperfine limit has been explained in terms of the so-called "frozen-core" effect. The neighbouring nuclear spins are significantly affected by the large magnetic moment of the chromophores. This interaction is distance dependent and thus only nuclear spins far from the optical centre will flip at early times. Eventually, the nearby spins that interact more strongly with the electronic spin will flip too. This "melting of the frozen-core" leads to nonexponential dephasing [21, 22].

1.2
Temperature Dependence of Linewidths and Shifts

As discussed above, the effective homogeneous linewidth in transition metal complexes doped into crystal lattices is often dominated by electronic and nuclear spin fluctuations in the environment of chromophores at liquid helium temperatures [23–25]. In contrast, the temperature dependence is in many cases governed by dynamic interactions with the phonons or vibrations of the host and guest.

Figure 1 depicts the four main mechanisms that are based on electron-phonon interactions, and can lead to the broadening of electronic origins [26]. The direct process (I) is particularly important in coordination compounds due to the relative high density of phonon states. If the energy gap is larger than the maximum phonon frequency a multiphonon process may take place: such a process is strongly dependent on the number of phonons that have to be created or annihilated to bridge the gap and the relative displacement of the two states along the metal-ligand normal coordinate. The contribution by a direct one-phonon process between levels a and b, separated by ΔE, to the linewidth of the electronic origins can be calculated by using Eq. (6) and Eq. (7) for the absorption and emission of one phonon, respectively:

$$\Gamma_{direct}(a) = \frac{1}{2\pi T_1(b)} \, \bar{n}(\Delta E) \tag{6}$$

$$\Gamma_{direct}(b) = \frac{1}{2\pi T_1(b)} \, (\bar{n}(\Delta E) + 1) \tag{7}$$
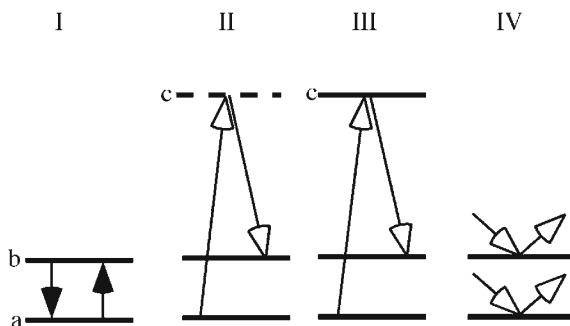
Fig. 1 The four main relaxation mechanisms leading to homogeneous line broadening. Electronic levels can be broadened by the direct process (I), two-phonon Raman scattering (II), the Orbach process (III) and quasi-elastic phonon scattering (IV)

where $\bar{n}(\Delta E)=1/[\exp(\Delta E/k_B T)-1]$, k_B is the Boltzmann constant and $[T_1(b)]^{-1}$ is the relaxation rate b→a at 0 K.

Two-phonon Raman processes (II) have often been reported to dominate the temperature dependence of electronic origins. When the quadratic electron-phonon coupling is weak, the contribution to the linewidth by this process can be described by the perturbative expression [27]

$$\Gamma_{Raman} \propto \int_0^\infty \rho(\omega)^2\, \bar{n}(\omega)[\bar{n}(\omega)+1]\, d\omega \tag{8}$$

where $\rho(\omega)$ is the weighted density of phonon states. The Raman process will broaden levels a and b by the same amount. Applying the Debye approximation for the density of phonon states in Eq. (8), the famous T^7 temperature dependence for the two-phonon Raman process results, as given in Eq. (9) [28], where T_D is the Debye temperature:

$$\Gamma_{Raman} \propto \left(\frac{T}{T_D}\right)^7 \int_0^{T_D/T} \frac{x^6 \exp(x)}{(1-\exp(x))^2}\, dx \tag{9}$$

In a crude approximation the density of phonon states can be estimated from the intensity, $I(\omega)$, of vibrational sidelines in the luminescence spectrum by using Eq. (10) [27]:

$$I(\omega) \propto \frac{\rho(\omega)}{\omega^2} \tag{10}$$

where the angular frequency ω is measured relative to the electronic origin.

In coordination compounds, vibrations which couple to the electronic states are often best described as pseudo-local. If the frequency and lifetime of the pseudo-local modes in the ground electronic state are given by ω_0^i and τ_0^i, respectively, and their product $\tau_0^i\omega_0^i \gg 1$, Eq. (8) can be approximated by [29–31]

$$\Gamma_{Raman} \approx \sum_i a_i \bar{n}(\omega_0^i)[\bar{n}(\omega_0^i)+1] \tag{11}$$

where a_i are coupling constants.

If the energy difference between levels a and b is much less than between a and c the Orbach process (III) broadens both a and b by equal amounts and the rate is proportional to $\bar{n}(\Delta E)=1/[\exp(\Delta E/k_BT)-1]$ where ΔE is the energy difference between (a,b) and c. At low temperatures $\Delta E\gg k_BT$ and thus $\bar{n}(\Delta E)\approx\exp(-\Delta E/k_BT)$.

In addition to these three mechanisms, intrinsic Raman scattering (IV) may occur: this is a pseudo-elastic scattering process that dephases the total vibronic wave function. This process has the same functional dependence as the two-phonon Raman scattering discussed above (Eqs. 8–11).

In the weak coupling limit the temperature-dependent shift of electronic origins by two-phonon Raman processes can be described by the perturbative expression [31]

$$\delta E_{Raman} \propto \int\limits_0^\infty \rho(\omega)\bar{n}(\omega)d\omega \tag{12}$$

and within the Debye approximation for the density of phonon states, the well-established T^4 temperature dependence is predicted [28]:

$$\delta E_{Raman} \propto \left(\frac{T}{T_D}\right)^4 \int\limits_0^{T_D/T} \frac{x^3}{\exp(x)-1} dx \tag{13}$$

Again, the density of phonon states in Eq. (12) can be crudely approximated by the intensity of vibrational sidelines in the luminescence spectrum.

If the model is restricted to pseudo-local modes, Eq. (12) simplifies to [29]

$$\delta E_{Raman} = \sum_i b_i \bar{n}_i(\omega) \tag{14}$$

where the sum is taken over all pseudo-local modes i.

1.3
The Inhomogeneous Linewidth

Electronic origins of ions, molecules and molecular ions in solids are inhomogeneously broadened through the variation of local fields [19]: each chromophore has a (slightly) different local environment, even in well defined single crystals, due to imperfections such as point defects, dislocations, strain, isotope distributions of ligand atoms etc [16, 25, 26]. The energy of an electronic transition depends on the local field, and thus varies over a range reflecting its distribution. This is schematically illustrated in Fig. 2 for a Gaussian distribution of transitions with a Lorentzian line shape.

In conventional spectroscopy a large number of centres are simultaneously measured, and hence the natural or homogeneous linewidth, Γ_h, is obscured by the inhomogeneous broadening. Figure 3 illustrates an inhomogeneously broadened spectrum as a function of the number of molecules in the probed volume. For the chosen ratio of the inhomogeneous/homogeneous width, $\Gamma_{inh}/\Gamma_h=50$, the transitions of individual centres are clearly visible up to 1000 molecules in the probed volume. This has been termed statistical fine structure [32, 33]. Single molecule spectroscopy has evolved out of early measurements of statistical fine
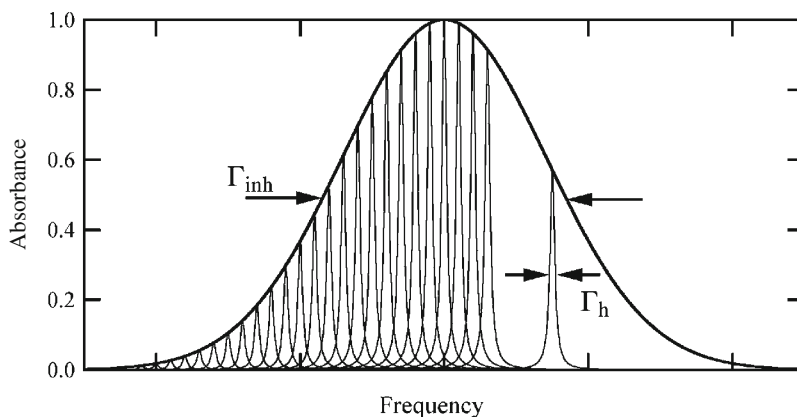
Fig. 2 Schematic illustration of the inhomogeneous broadening of an electronic transition. Individual chromophores would exhibit electronic origins with Lorentzian line shape and width Γ_h but due to variations of the local fields the transition energies of an ensemble of optical centres will show a distribution with width Γ_{inh}
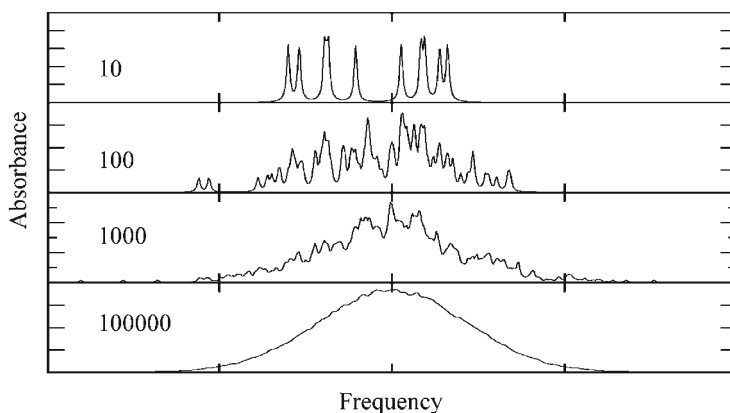
Fig. 3 Simulation of statistical fine structure with $\Gamma_{inh}/\Gamma_h=50$. A random Gaussian number generator was used to simulate the transition frequencies of 10, 100, 1000 and 100,000 optical centres

structure: for such measurements the number of molecules in the probed volume has to be very small [34].

The inhomogeneous width of an electronic origin depends on its nature. For example, a charge-transfer transition is expected to show a relatively large width due to its susceptibility to electric fields. Also, ligand-field transitions may be rather broad due to the $1/R^5$ variation of the transition energy with the metal-ligand distance R. In contrast, *f-f* transitions and pure spin-flips, such as the $^2E\leftarrow{^4A_2}$ excitation in d^3-systems, display relatively narrow inhomogeneous distributions. Table 1 summarizes typical values for inhomogeneous widths of electronic origins of coordination compounds.

Table 1. Typical inhomogeneous widths for classical transitions in coordination complexes in [cm^{-1}]

Transition	Crystalline host	Amorphous host
d-d	0.1–100	10–1000
f-f	0.01–10	1–100
^{3}MLCT, ^{3}LC	1–100	100–1000

1.4
Hole-Burning Mechanisms

There are basically three classes of Laser techniques that can overcome aspects of the inhomogeneous broadening [11]. 1. Fluorescence line narrowing [35] and spectral hole-burning are based on the selective excitation of a subset of chromophores and spectra are recorded in the *frequency domain* [16]. 2. Coherent transient effects such as photon-echoes [36], phase switched coherent transients [37] and optical free induction decays [38] are *time-domain* experiments. 3. *Double resonance* experiments facilitate sensitive optical detection of magnetic resonance: a radio-frequency field and the laser field are superimposed on the sample and changes in hole-burning, photon-echoes, etc are recorded as a function of the radio-frequency. For example, in photon-echo double resonance (PENDOR) the photon-echo amplitude is monitored as a function of the frequency of an applied radio-frequency pulse [38]. In Raman heterodyne detected NMR spectroscopy a continuous wave or pulsed radio-frequency field is applied at resonance with a sublevel splitting [39].

The present work focuses on the application of spectral hole-burning experiments. Upon selective excitation of a subset of chromophores within the inhomogeneously broadened transition by a narrow laser, there are three basic mechanisms that can lead to hole-burning:

1. Spectral holes can arise through a depletion of the ground state at the laser frequency by population storage in an excited state or in a (hyperfine) level of the ground state. This is in principle a general phenomenon but more easily measured for long lived excited states [40]. For example, the first report of transient spectral hole-burning was based on the population storage in the long-lived ^{2}E multiplet in ruby [1]. If transient spectral hole-burning is based on population storage in the excited state *stimulated emission* has to be taken into account for rationalizing hole-depths. The hole-depth is proportional to the sum of absolute population changes in the ground and excited states. Moreover, relative depths of side-holes, that are due to electronic splittings in the ground and/or excited states (Zeeman split levels, hyperfine levels etc), reflect the degree of thermalization.

   Population storage in hyperfine levels of the ground state is the most common mechanism for hole-burning in rare earth ions doped in solids, and holes based on these reservoirs last for seconds to minutes [11] (Fig. 4). The ground state levels that act as storage reservoirs have larger than equilibrium populations and thus enhanced absorptions are observed at frequencies cor-
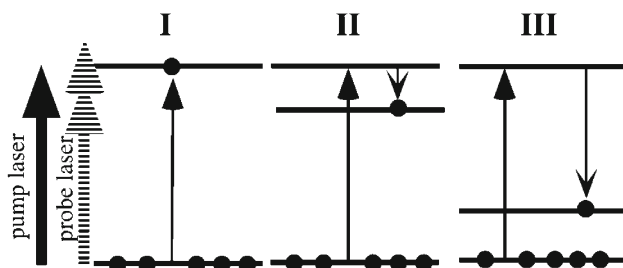
Fig. 4 Transient spectral hole-burning by population storage. The directly excited state (I), a lower-lying excited state (II) or a ground state (III) can act as the storage level
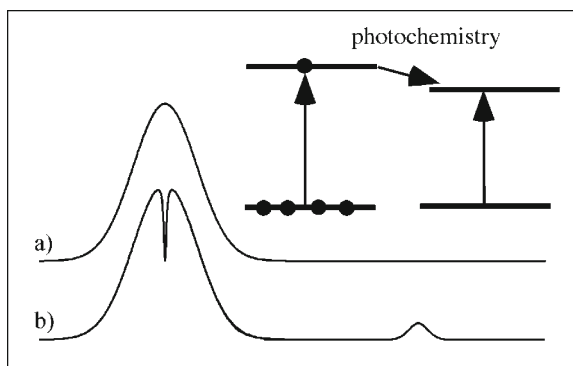

Fig. 5 Illustration of photochemical spectral hole-burning. The selectively excited subset of chromophores undergoes chemistry leading to a photoproduct with a different spectrum. a) and b) show the absorption spectrum before and after hole-burning

responding to transitions initiating from these levels. If energy levels are well correlated within the inhomogeneous distribution, the enhanced absorptions are well defined, leading to so-called anti-holes [41].

2. In photochemical spectral hole-burning (Fig. 5) the selected subset of chromophores may undergo some photochemistry, resulting in a depletion of chromophores at the laser frequency. A frequently observed photochemical spectral hole-burning mechanism is based on photo-ionisation [42, 43]. The photoproduct in photochemical hole-burning leads to (broad) absorption features outside of the inhomogeneous distribution of the original chromophore.

3. Non-photochemical spectral hole-burning (Fig. 6) is based on slight re-arrangements of host-guest interactions [44]. For example, a hydrogen bond between the chromophore and solvent or host lattice molecules may be re-arranged. Non-photochemical spectral hole-burning is a ubiquitous phenomenon in amorphous hosts, however the number of crystalline systems for which this mechanism has been reported is still limited [7, 45–47]. The so-called two-level systems (TLSs) model developed for rationalising anomalies
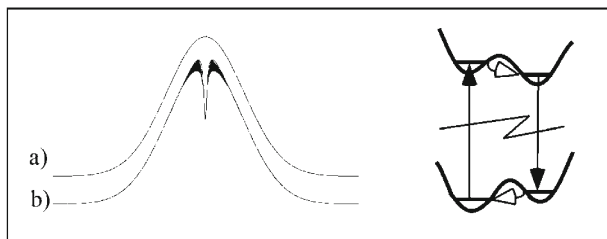
Fig. 6 Illustration of non-photochemical spectral hole-burning. Host-guest interactions are subject to variations upon excitation of a subset of chromophores. The spectrum of the "photo-product" is only slightly altered. Non-photochemical hole-burning in amorphous systems is often interpreted by the TLS model, schematically illustrated in the diagram. Relaxation between the wells in the excited state by tunnelling may be much faster than the back relaxation in the ground state. a) and b) show the absorption spectrum before and after hole-burning

in low-temperature thermal properties of amorphous systems [48, 49] is widely applied to describe and quantify the dynamics of this hole-burning mechanism [44, 50]. Although the basic version of this model provides a semi-quantitative understanding, it is far from complete and it may be necessary to differentiate between, and take into account, intrinsic and extrinsic TLSs [51]. In crystals the non-photochemical hole-burning is often based on the movements of ions or atoms. The "photoproduct" in non-photochemical hole-burning is distributed within the inhomogeneous width of the initial transition. Whereas this mechanism leads to *broad* anti-holes in *amorphous* systems, it is possible to observe narrow anti-holes in crystals if the hole-burning is based on a well defined rearrangement of atoms or groups of atoms.

The initial quantum efficiency of spectral hole-burning can be estimated by applying Eq. (15) where N_A is Avogadro's number, $c(\Gamma_h)$ is the concentration of chromophores within one homogeneous linewidth, Γ_h, in units of mol/cm^3, d is the optical path length in [cm], I is the laser irradiance in [W/cm^2] and A_0 is the initial absorbance at the laser frequency v. Equation (15) represents the ratio of chromophores that undergo hole-burning per unit time to the number of photons absorbed per unit time [52]:

$$\phi = \frac{N_A c(\Gamma_h) d \left(\dfrac{dA}{dt}\right)}{A_0 \dfrac{I}{hv} \left(1-10^{-A_0}\right)} \tag{15}$$

1.5
Spectral Diffusion

It is well documented that spectral hole-burning may not provide the homogeneous linewidth because of saturation effects [9]. Furthermore, spectral diffusion can occur on the time scale of the hole-burning experiment [53–62]. Spectral diffusion is the observation of the broadening of spectral lines with time. This

broadening can be due to the dynamics of the host matrix. For example, in amorphous systems, such as a frozen organic glass or polymer, relaxations within the TLSs of the environment of a chromophore may lead to slight shifts of the transition frequency and hence to a broadening of the hole in time. There are various models that deal with spectral diffusion based on TLSs. On the basis of the "standard TLS" model the contribution to spectral diffusion is predicted to be logarithmic in time and linear in temperature [62]:

$$\Delta\Gamma_{SD} \propto T \ln(t/t_0) \qquad (16)$$

However, the 'standard' TLS model assumes a flat distribution of relaxation rates. It is plausible that a Gaussian distribution may be more appropriate. Equation (17) has been derived for the contribution of spectral diffusion to the optical linewidth [57]:

$$\Delta\Gamma_{SD} \propto \int P(R)[1 - \exp(-Rt_w)]\, dR \qquad (17)$$

In Eq. (17), $P(R)$ is the distribution function for the TLS relaxation rate R and t_w is the waiting time which can be taken as the sum of the burn and read time in time-dependent hole-burning experiments [44]. Equation (17) has been successfully applied to describe the non-logarithmic behaviour of spectral diffusion in a number of systems by using a Gaussian distribution of the tunnelling parameter λ as given in Eq. (18):

$$P(R)dR = \frac{1}{\sigma\sqrt{2\pi}} \exp\left[-\frac{\{\ln(R/R_0)\}^2}{2\sigma^2}\right] d(\ln R) \qquad (18)$$

There is on-going theoretical and experimental work on TLS based spectral diffusion in amorphous systems [60, 63–66].

Electronic and nuclear spin flips in the surrounding of an impurity site can cause magnetic fluctuations and hence a stochastic change of the transition frequency of the chromophore. These interactions have various time scales and can lead to experimentally accessible spectral diffusion [21, 22]. Electronic and nuclear fluctuations can be suppressed and slowed down, respectively, at low temperature by the application of high magnetic fields. This can enable the measurement of spectral diffusion caused by the fluctuations of nuclear spins in the environment of a chromophore. The fluctuations can be quantified by numerical simulations. For example, semi-quantitative agreement with the time-dependent hole-shapes has been achieved by simulations of the dynamics of the ^{19}F nuclear spins in LiF$_4$:Er^{3+} [67, 68].

1.6
Hole-Burning Instrumentation

There is a wide range of tuneable lasers suitable for performing spectral hole-burning experiments [69]. The majority of hole-burning experiments to date have been performed by dye and/or Ti:sapphire lasers. More recently diode lasers have been applied [70] and it has been shown that these inexpensive devices can enable the acquisition of highest quality data [71–73]. Spectral hole-burning
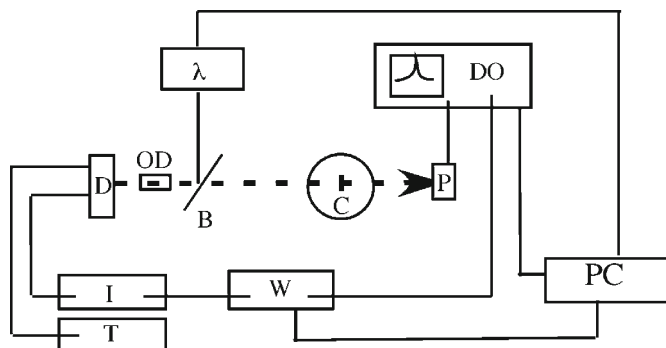
Fig. 7 Basic hole-burning instrumentation based on a temperature and current controlled diode laser for experiments in transmission. I: current controller; T: temperature controller; W: waveform generator; D: thermoelectric mount with laser diode; OD: optical isolator; B: beamsplitter; C: cryostat with sample; P: photodiode with amplifier; DO: digital storage oscilloscope; PC: personal computer; λ: wavemeter

experiments can be performed in excitation or transmission. The former is suitable for very low concentrations whereas the latter is the method of choice for samples with optical densities larger than ≈0.05. A pump and a probe laser have to be applied in transient spectral hole-burning based on population storage. If the lifetime of the probed excited state is longer than the tuning rate of the laser, the pump can also serve as the probe laser in *transmission* hole-burning experiments. A typical hole-burning apparatus, based on a diode laser, and suitable for experiments on coordination compounds, is shown in Fig. 7. The frequency of diode lasers can be rapidly modulated by a variation of the injection current. Frequency sweeps of several GHz on the microsecond timescale are readily facilitated. Of course, if the laser is very rapidly slewed, the Fourier transform limit for its linewidth has to be taken into account.

Hole-burning experiments can also be conducted with fixed single-frequency lasers by tuning the transition frequency of the sample via the application of external magnetic or electric fields.

2
Spectral Hole-Burning Studies of Coordination Compounds

2.1
Transient Spectral Hole-Burning in [Ru(bpy)$_3$]$^{2+}$

The question of localization/delocalization of the transferred electron in the lowest-excited triplet metal-to-ligand charge transfer transition (^{3}MLCT) has resulted in a vast number of studies of the spectroscopy of [Ru(bpy)$_3$]$^{2+}$ and related compounds. A wide range of experiments is in agreement with a localized description of the lowest three triplet metal-to-ligand charge transfer (^{3}MLCT) zero phonon lines of [Ru(bpy)$_3$]$^{2+}$ in crystalline [Zn(bpy)$_3$](ClO$_4$)$_2$ [74]. In particular selective deuteration experiments were very useful: individual transitions to

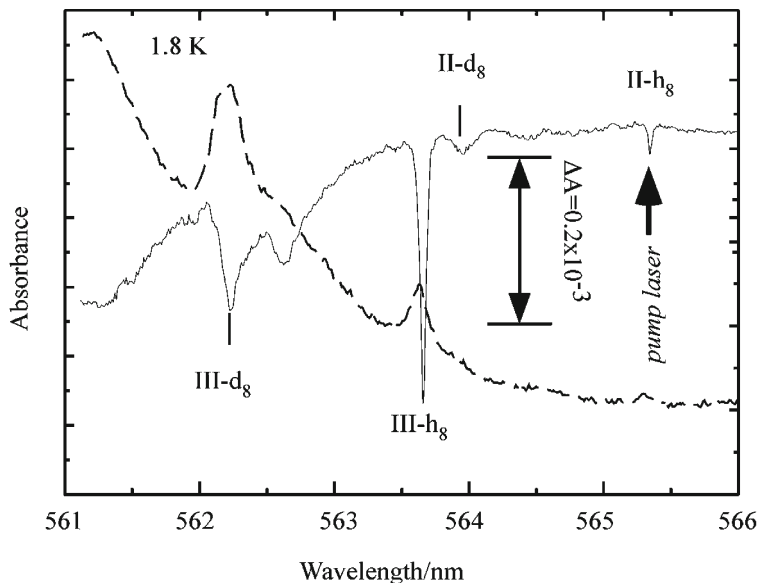**Fig. 8** Transient spectral hole-burning in $[Ru(bpy-d_8)_2(bpy-h_8)]^{2+}/[Zn(bpy)_3](ClO_4)_2$ at 1.8 K. The burn laser is chosen in the ^{3}MLCT origin II of the bpy-h_8 ligand. Side-holes are observed in the transitions involving the bpy-d_8 ligand [62]

the bpy-d_n and the bpy-d_m ligand are observed in the $[Ru(bpy-d_n)_{3-x}(bpy-d_m)_x]^{2+}$ ($x=1,2$; $n=0,2$, $m=2,8$ $n\neq m$) complexes in $[Zn(bpy)_3](ClO_4)_2$ [75]. For example, two sets of transitions are observed in $[Ru(bpy)_{3-x}(bpy-d_2)_x]^{2+}$ ($x=1,2$) with relative intensities reflecting the number of bpy and bpy-d_2 ligands. By applying transient spectral hole-burning we have established that the two sets of transitions indeed occur on a *single chromophore* and are not due to two sites. In this experiment two dye lasers were employed in a standard pump-probe configuration.

The main aim of hole-burning experiments appears to often be the measurement of minimal linewidths. However, the experiment illustrated in Fig. 8 shows that relatively low resolution hole-burning spectroscopy can be an invaluable tool for addressing chemical problems.

Racemic $[Zn(bpy)_3](ClO_4)_2$ and $[Ru(bpy)_3](ClO_4)_2$ crystallize in the C2/c space group. Bond angles and bond lengths are comparable for all three ligands. However, one ligand is crystallographically unique and has a different anion environment in comparison to the two crystallographically equivalent ligands, and its MLCT transitions are estimated to be at higher energy by $\approx$900 cm^{-1} [74]. The inequivalence of the ligands has ramifications in polarized absorption and luminescence spectroscopy and facilitates Stark-swept transient hole-burning experiments. When an electric field is applied in the metal-ligand plane perpendicular to the *b* axis, the two crystallographically equivalent ligands become Stark inequivalent, leading to a pseudo-Stark splitting of the origins [76, 77]. Due to the charge-transfer nature of the origins, the effect of an external electric field is

significant. Hence, only small voltage ramps of the order of magnitude of 10 V are required to perform Stark-swept hole-burning experiments. In these experiments, the laser is kept at constant wavelength and the read-out of the spectral hole is conducted by the application of an external voltage ramp. From these experiments it followed that the homogeneous linewidth in the electronic origin II of $[Ru(bpy)_3]^{2+}/Zn(bpy)_3(ClO_4)_2$ is $\approx$15 MHz and the *intramolecular* excitation energy transfer between the equivalent ligands occurs on a timescale of $\approx$10 ns for the lowest-excited ^{3}MLCT levels.

2.2
Temperature Dependence of the R-lines of $[Cr(oxalate)_3]^{3-}$

The spectroscopy of the R-lines ($^2E \leftarrow ^4A_2$ transitions) in chromium(III) doped $NaMgAl(oxalate)_3 \cdot 9H_2O$ has attracted the interest of several research groups over the years [78–82]. $NaMgAl(oxalate)_3 \cdot 9H_2O$ crystallizes in the P3c1 space group with six formula units per unit cell [83]. $[Cr(oxalate)_3]^{3-}$ is an archetypal complex and can be considered to be the coordination chemist's ruby. Polarized absorption spectra in the region of the R-lines of chromium(III) in $NaMgAl(oxalate)_3 \cdot 9H_2O$ are shown in Fig. 9.

The ^2E excited state and the $^4A_2$ ground state splittings of 21 cm^{-1} and 1.6 cm^{-1}, respectively, are the result of spin-orbit coupling and the trigonal and rhombic ligand field contributions. The ground state splitting is well described by the spin Hamiltonian of Eq. (19) [79]:

$$H = D \left[S_z^2 - \frac{1}{3} S (S + 1) \right] + E(S_x^2 - S_y^2) \tag{19}$$

with $|D|$=0.7786 cm^{-1} and $|E|$=0.0306 cm^{-1}. It followed from magnetic susceptibility experiments [84] that the $\pm$3/2 Kramers doublet is lowest. The inhomogeneous broadening is relatively small and the system lends itself to spectral hole-burning studies by using inexpensive diode lasers.

Diode lasers are well suited for transient spectral hole-burning (THB) experiments since they can be rapidly tuned by varying the injection current. A typical THB spectrum in the R-lines of chromium(III) doped $NaMgAl(oxalate)_3 \cdot 9H_2O$ is shown in Fig. 10 [85]. The current of the laser diode, and hence the wavelength, is kept constant during the burn period; subsequently it is scanned by varying the injection current. A current variation of $\pm$0.5 mA results in a frequency scan of approximately $\mp$1.25 GHz. The transient nature of the holes can be verified by a multiple readout of the hole as is shown in Fig. 10b. The hole depth decreases with the deactivation of the excited state by a single exponential $I=I_0 \exp(-t/T_1)$ with T_1=0.90 ms.

We have studied the temperature dependence of the linewidths in the R-lines by transient spectral hole-burning and typical data for a 4% chromium(III) doped crystal are shown in Fig. 11 [85]. The T-dependence can be well described by Eq. (20):

$$\Gamma(T) = \Gamma_0 + \Gamma_{direct} + \Gamma_{Raman} \tag{20}$$
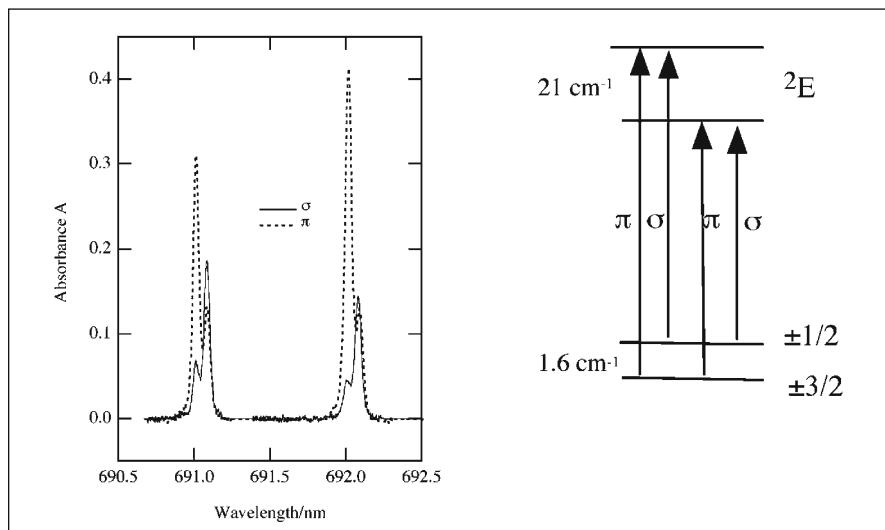
Fig. 9 Polarized absorption spectra of the R-lines ($^2E \leftarrow {}^4A_2$ transitions) in chromium(III) doped NaMgAl(oxalate)$_3$·9H$_2$O. A schematic energy diagram and the dominant polarizations of the four transitions are shown [79]
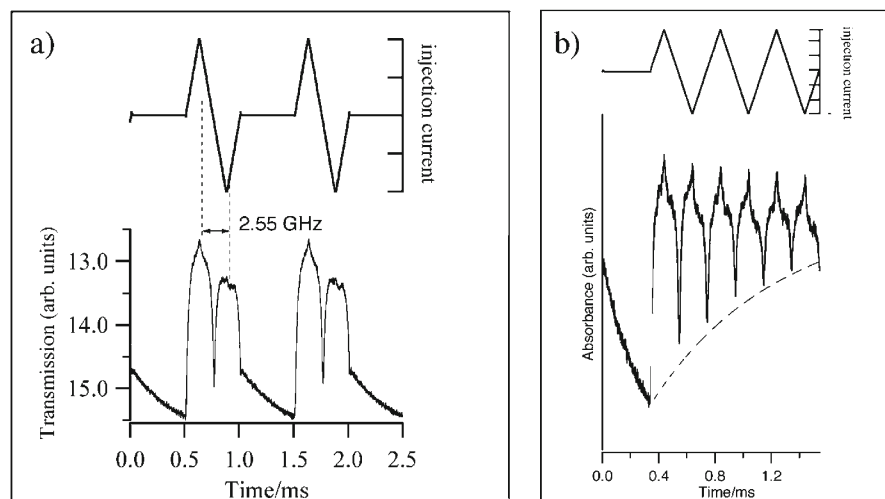
Fig. 10a,b Transient spectral hole-burning experiments in the R$_1$-line of chromium(III) doped NaMgAl(oxalate)$_3$·9H$_2$O. The frequency of a diode laser is kept constant during the burn period and subsequently tuned by varying the injection current by applying a voltage to the current controller: **a** an experiment with one readout per cycle; **b** an experiment with sequential readouts after the burn period [72]
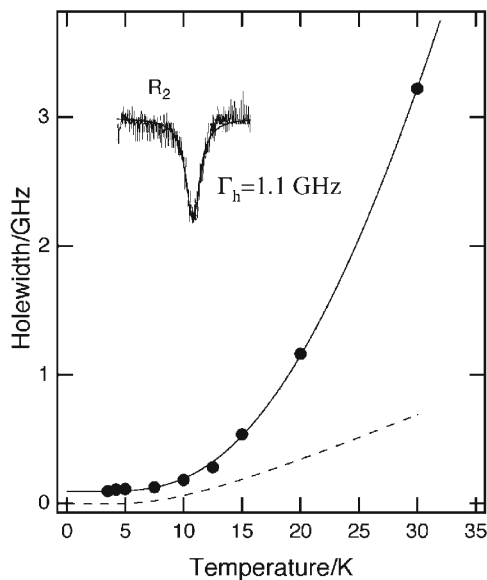
Fig. 11 Temperature dependence of the homogeneous linewidth of the R_1-line in NaMgAl(ox-alate)$_3$·9H$_2$O:Cr(III) 4%. The *dashed line* is the contribution by the direct process between the two levels of the ^{2}E multiplet. The 2.5-K transient hole in the R_2 line, shown in the *inset*, provides the parameter for the T-dependence of the direct process [72]

where Eq. (11) is employed for the Raman term with two pseudo-local phonons with experimentally determined frequencies of 33.3 and 52.3 cm^{-1}. Γ_0 is the residual hole-width for temperatures approaching 0 K; it can contain both homogeneous and heterogeneous contributions. The direct process can be quantified by the residual linewidth of 1.1 GHz of the R_2 transition at 2.5 K; pure dephasing is relatively slow at this temperature and the dominant contribution to the hole width of the R_2 line is by the direct process, reflected in $T_1(R_2)=$ $1/2\pi\Gamma_h=284$ ps. This lifetime lies between the values for ruby ($\approx$1 ns) [86] and [Rh(bpy)$_3$](PF$_6$)$_3$:Cr(III) ($\approx$3 ps) [87] in accord with expectations. The ^{2}E splitting in the three systems is comparable but the density of phonon states at 20–30 cm^{-1} increases in the order Al$_2$O$_3$:Cr(III)<NaMgAl(oxalate)$_3$·9H$_2$O:Cr(III) <[Rh(bpy)$_3$](PF$_6$)$_3$:Cr(III).

The residual linewidth Γ_0 of the R_1-line at 2.5 K is strongly dependent on the chromium(III) concentration. The 4% crystal displays a width of $\Gamma_0=90$ MHz whereas a 1% and 0.5% crystal show values of 40 MHz and 20 MHz, respectively [73]. This dependence indicates the importance of *indirect* electron-spin–electron-spin interactions [59]. An excited chromium(III) centre experiences fluctuating magnetic fields due to the presence of other chromium(III) ions in its neighbourhood. These fluctuations lead to a dephasing of the wave function and, consequently, to variations of the transition energy. Superhyperfine interactions with the ^{27}Al nuclear spin, I=5/2, of the surrounding [Al(oxalate)$_3$]$^{3-}$ complexes and the proton spin of the water molecules also contribute to the linewidth, but

only become significant for the 0.5% crystal. The direct process between the $\pm 3/2$ and $\pm 1/2$ spin components of the $^4A_2$ ground state will also add to the hole width at 2.5 K but this contribution has been estimated to be only of the order of magnitude of 0.5 MHz [85].

2.3
Determining *g*-Factors in Minute Magnetic Fields

The zero field splitting of the $^4A_2$ ground state is almost resolved in the R_1-line absorption spectrum of $NaMgAl(oxalate)_3 \cdot 9H_2O$:Cr(III) and the polarizations of the two transitions allow *selective* transient hole-burning experiments: σ-polarized light at the red edge of the R_1-line or π-polarized light at the blue edge selects the $R_1(\pm 1/2)$ or the $R_1(\pm 3/2)$ transition, respectively. This selectivity simplifies the multiple hole patterns observed in weak external magnetic fields and a four level model can be used to rationalize the data.

Transient hole-burning experiments enable the determination of *g*-factors in *minute* magnetic fields as is illustrated in Fig. 12 where a hole-burning spectrum measured in zero field and in B||c=15.3 mT is shown for red-edge excitation of the R_1-line in a $NaMgAl(oxalate)_3 \cdot 9H_2O$:Cr(III) 1% crystal [73]. The laser light was σ-polarized and hence selects the $R_1(\pm 1/2)$ transitions. The four pairs of side-holes in 15.3 mT arise from the Zeeman splittings of the ground and excited state.

The eigenvalues of the $^4A_2$ ground state in a small external magnetic field B||c are well approximated by Eq. (21) and (22) where |zfs| is $2(D^2+3E^2)^{1/2} \approx 2|D|$ and μ_B is the Bohr magneton:

$$E(\pm 1/2) \approx \pm 1/2 \mu_B B_z g_z + |zfs|/2 \qquad (21)$$

$$E(\pm 3/2) \approx \pm 3/2 \mu_B B_z g_z - |zfs|/2 \qquad (22)$$

The excited state splitting of the lower ^2E level in B||c is given by $\mu_B B_z g_z^{ex}$. Thus side-holes occur at $\pm \mu_B B_z g_z$ ($\pm$ ground state splitting, γ pair), $\pm \mu_B B_z g_z^{ex}$ ($\pm$ excited state splitting, β pair), $\mu_B B_z(g_z + g_z^{ex})$ ($\pm$ sum of ground and excited state splitting, δ pair) and at $\pm \mu_B B_z(g_z + g_z^{ex})$ ($\pm$ difference of ground and excited state splitting, α pair) [88]. The data allows the direct determination of *g*-factors of the ground and excited state. We have performed a series of experiments with B||c and B$\perp$ c in the $R_1(\pm 1/2)$ and $R_1(\pm 3/2)$ transitions, also employing a pseudo external cavity laser with an effective linewidth of ≈ 4 MHz. At this resolution *g*-factors can be determined in fields as low as 1 mT.

The *g*-factors determined from these experiments and the relative hole depths indicate a significant deviation from trigonal behaviour, in accord with the general position of the $[Cr(oxalate)_3]^{3-}$ complex in the P3c1 crystal structure.

An interesting feature arising from these experiments is the strong dependence of the observed linewidth on the external magnetic field strength: Γ(zero field) ≈ 19 MHz, Γ(7 mT) ≈ 4 MHz, and Γ(15 mT) ≈ 1 MHz. This dependence confirms the magnetic dipolar origin of the residual linewidth at 2.5 K, and in particular the importance of *indirect* electron-spin-electron-spin interactions.

From the relative hole areas of the side-holes and the resonant hole it appears that the Zeeman levels of the ground state and the excited state are thermalised
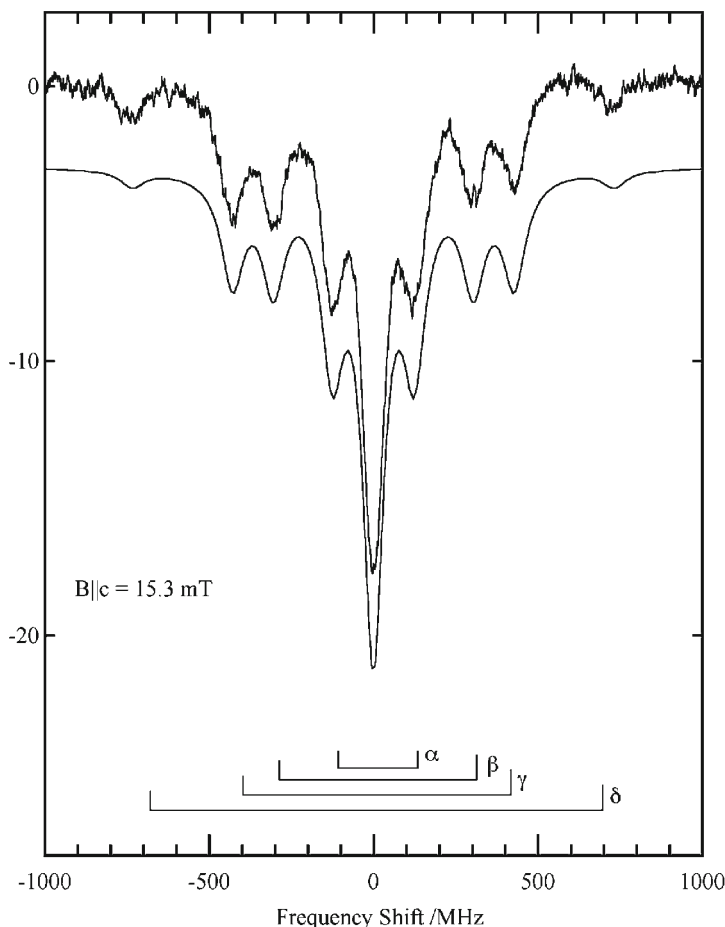
Fig. 12 Multiple hole-pattern observed in transient spectral hole-burning of the R_1-line in at 2.5 K in a magnetic field B||c=15.3 mT. The *smooth line* shows a fit to the experimental data [60]

on the timescale of the transient hole-burning experiments in NaMgAl(oxalate)$_3$·9H$_2$O:Cr(III) 1%. An example where the Zeeman levels are not equilibrated at 2.5 K on the experimental timescale is provided by pale green emerald, Be$_3$Al$_2$Si$_6$O$_{18}$:Cr(III) (0.04%) [89].

Figure 13 shows α-polarized transient hole burning spectra with B||c at 2.5 K and 8 K. A dramatic temperature dependence is observed for the relative depths of the side-holes implying that spin-lattice (and cross-relaxation) in the excited and ground state is slow at 2.5 K. The shifts of the side-holes can be rationalized in the same way as is discussed above for NaMgAl(oxalate)$_3$·9H$_2$O:Cr(III). The side-holes α and β overlap in low magnetic fields because g$_\parallel^{ex}$=1.02 and g$_\parallel^{gs}$=1.97. Assuming no thermalization in the excited state and between the ±1/2 levels of the ground state, but relatively fast −1/2↔±3/2 and +1/2↔±3/2 direct processes, a pattern of δ:γ:(β+α):resonant hole of 0:0.25:(0.15+0):1 is estimated at 2.5 K.
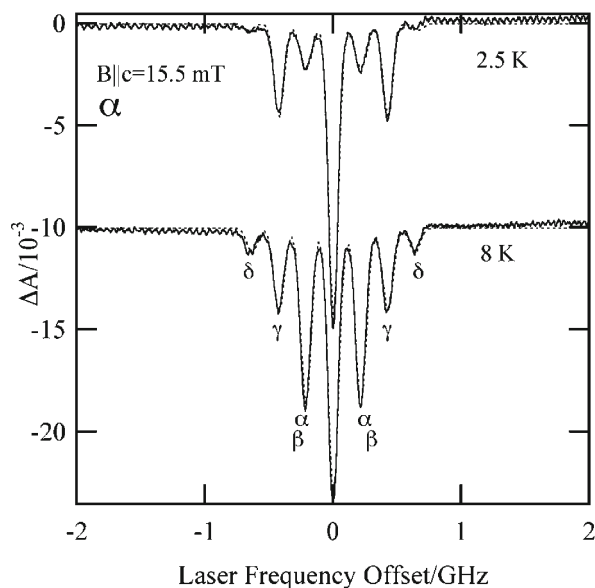
Fig. 13 Transient spectral hole-burning in α polarization of the R_1-line of Chatham created emerald (0.04% chromium(III)) at 682.25 nm with B‖c=15.5 mT at 2.5 K and 8 K

The presence of very weak δ side-holes indicates that some relaxation occurs either in the excited state or the ground state. Assuming full thermalization of the spin levels in the $2\bar{A}$ excited state at 8 K, a ratio of δ:γ:(β+α):resonant hole of 0.05:0.22:0.55:1 is predicted. If both the excited state and the ground state are fully relaxed on the experimental timescale, a ratio of 0.2:0.4:0.6:1 is calculated. The experimental ratio of 0.09:0.3:0.6:1 indicates that the excited state is close to thermalization and the relaxation in the ground state is also becoming more efficient at 8 K.

2.4
A Novel Hole-Burning Mechanism: Flips of Water Molecules

NaMgAl(oxalate)$_3$·9H$_2$O:Cr(III) is a rare crystalline system that displays non-photochemical *persistent* spectral hole-burning. Other inorganic systems that are subject to non-photochemical hole-burning include SrO:Co^{2+} [47], CaF$_2$:Pr^{3+}:D$^-$ [7], CaF$_2$:Tm^{3+}:D$^-$ [90] and Tutton salts [45]. The hole-burning mechanism has often been assigned to movements of ions along particular coordinates.

Non-photochemical spectral hole-burning in amorphous systems is often based on the rearrangement of hydrogen bonds [44]. Thus it seems plausible that the hydrogen bonds between lattice water and the oxalate ligands are responsible for the persistent spectral hole-burning in NaMgAl(oxalate)$_3$·9H$_2$O:Cr(III). All oxygen atoms of the oxalate ligands are involved in hydrogen bonding with water molecules. The six water molecules that are coordinated to magnesium(II) form one hydrogen bond each: three with an inner and three with an outer

oxygen atom of the oxalate ligands. The remaining three water molecules are hydrogen bonded to the six water ligands of the magnesium(II) and each possesses *two* hydrogen bonds to an inner and an outer oxygen atom of two oxalate ligands [83].

Experiments on deuterated samples can provide evidence for the involvement of hydrogen atoms in the hole-burning mechanism [91, 92]. In amorphous systems a decrease of the hole-burning efficiency is usually encountered upon deuteration and this has been interpreted in terms of the double well potential of the hydrogen bond. Referring to Fig. 6 for the standard TLS model, the hole-burning rate is determined by the tunnelling parameter λ in the excited state:

$$\lambda = \sqrt{2\,mV}\,\frac{d}{\hbar} \tag{23}$$

where m is the mass of the particle, V is the potential barrier, and d is the tunnelling distance [44]. Equation (23) implies an increase of the tunnelling parameter λ by approximately $\sqrt{2}$ upon deuteration. The relaxation rate between two wells is proportional to the square of the tunnelling frequency W, given in Eq. (24) and hence a massive *decrease* of the hole-burning efficiency is expected, and usually observed, upon deuteration:

$$W = \omega_0 \exp(-\lambda) \tag{24}$$

For example, aluminium phthalocyanine tetrasulfonate in hyperquenched glassy films of water shows a *reduction* of the quantum yield by a factor of >500 [92].

In contrast, crystals of NaMgAl(oxalate)$_3$·9H$_2$O:Cr(III) show a *massive increase* of the hole-burning efficiency upon partial deuteration by a factor of $\approx$1000 and a relatively high quantum efficiency of 0.1% is observed for a 50% deuterated crystal [93] (Fig. 14). On the basis of this result we have assigned the hole-burning mechanism to 180° flip motions of the lattice water molecules. The perprotonated system is nominally in an identical state after each flip. Hence hole-burning will only occur if the flip is not perfect and the system is slightly disturbed. For example, the water molecule may end up in a slightly altered position. It is also possible that in this case some of the hole-burning is based on translational tunnelling of the proton in the double well potential of the hydrogen bond. In contrast, if a DHO molecule flips, the total zero point energies of the excited and ground states of the chromophore change because the two hydrogen atoms of the water molecules are crystallographically inequivalent. The change of the zero point energy is different for the excited and ground state and hence the energy of the zero phonon line changes. Thus, each photoinduced flip of a DHO molecule is accompanied by spectral hole-burning. This interpretation is supported by following observations: the anti-holes are very sharp; the anti-holes are symmetrically arranged, indicating that the system does not equilibrate to a particular configuration at low temperature; the hole-burning efficiency is high when there is a maximum of DHO molecules in the surroundings of [Cr(oxalate)$_3$]$^{3-}$ (Fig. 15).
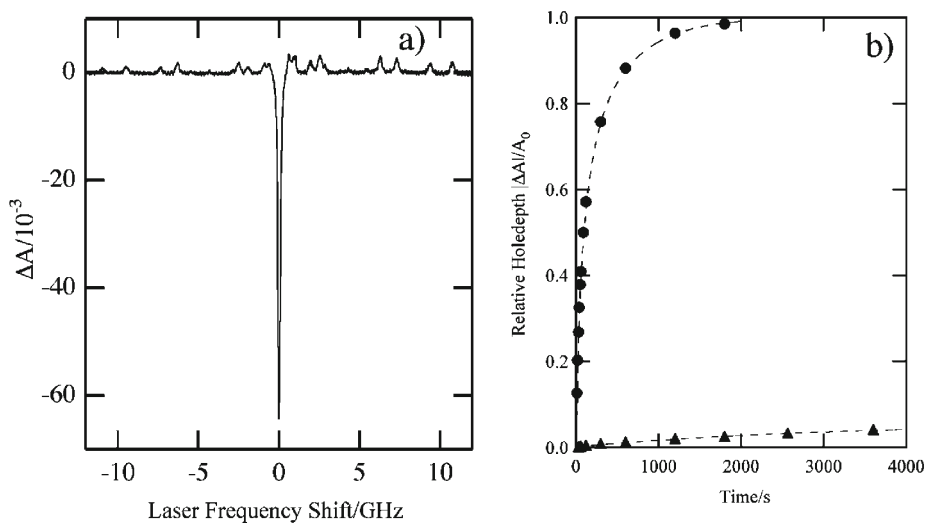
Fig. 14a,b Persistent spectral hole-burning of the R_1-line in 50% deuterated NaMgAl(oxalate)$_3\cdot$9H$_2$O:Cr(III) 0.5%: **a** sharp anti-holes appear in the ±15 GHz range; **b** comparison of the hole-burning curves of a 50% deuterated crystal (*solid circles*) and the perprotonated crystal (*solid triangles*) [79]
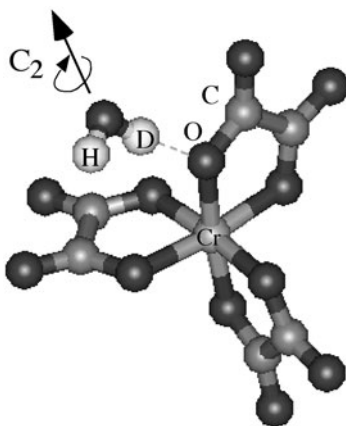
Fig. 15 A 180° flip of a HOD molecule around its pseudo-C_2 axis changes the total zero point energy of the system. This change is different for the $^4A_2$ and ^2E states leading to a shift of the electronic origin and spectral hole-burning
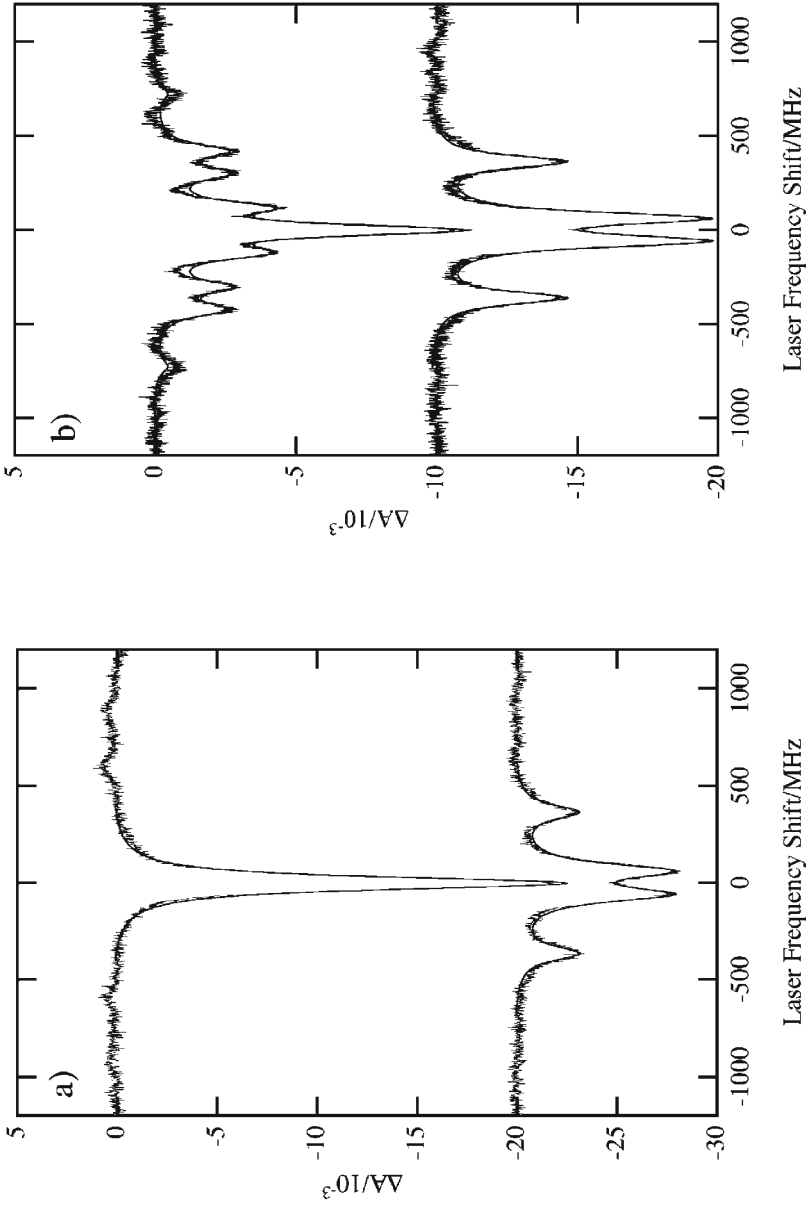
Fig. 16a,b Permanent record of the magnetic field strength in persistent spectral hole-burning; **a** the hole is burnt in zero field (*upper trace*) and then a magnetic field B||c=15.5 mT is applied; **b** the hole is burnt in a magnetic field B||c=15.5 mT (*upper trace*) and then the hole pattern is measured in zero field. Both experimental sequences lead to the same final pattern, providing a permanent record of the magnetic field [59]
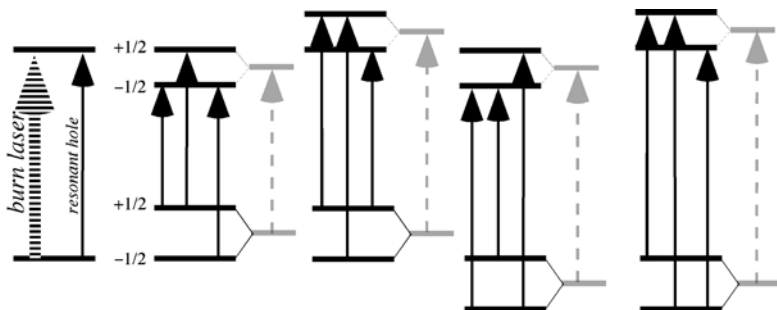
Fig. 17 Schematic diagram for the interpretation of the hole-burning patterns of Figs. 12, 13 and 16; the multiple hole pattern in a magnetic field B||c is due to side-holes at $\pm\mu_B B_z g_z$, $\pm\mu_B B_z g_z^{ex}$, $\pm\mu_B B_z(g_z + g_z^{ex})$ and at $\pm\mu_B B_z(g_z - g_z^{ex})$. If the field is removed, persistent holes may be observed at $\pm 1/2\mu_B B_z(g_z + g_z^{ex})$ and $\pm 1/2\mu_B B_z(g_z - g_z^{ex})$ [59]. The *solid arrows* indicate the side-holes in a magnetic field; the *dashed arrows* indicate the hole energies after the field is switched off

2.5
Memory of (Low) Magnetic Fields

Persistent spectral hole-burning of the R-lines of NaMgAl(oxalate)$_3$·9H$_2$O:Cr(III) in external magnetic fields provides a permanent record of the magnetic field strength [72].

This is illustrated in Fig. 16 where the effect of a magnetic field B||c=15.5 mT on a hole burnt in zero field and σ polarization is compared with the hole pattern in zero field obtained after hole-burning in a magnetic field B||c=15.5 mT.

As we discussed earlier for transient hole-burning experiments, side-holes are expected at $\pm\mu_B B_z g_z$, $\pm\mu_B B_z g_z^{ex}$, $\pm\mu_B B_z(g_z + g_z^{ex})$ and at $\pm\mu_B B_z(g_z - g_z^{ex})$ in a magnetic field for the R$_1(\pm 1/2)$-line. Upon switching off the magnetic field a persistent hole pattern results that is identical to the Zeeman spectrum of a persistent hole burnt in zero field. This can be rationalized by the schematic energy level diagram shown in Fig. 17 and provides a permanent record of (low) magnetic fields. Persistent spectral hole-burning can thus be applied to record the temporal profile of pulsed magnets or minute fluctuations of a magnetic field.

2.6
Persistent Hole-Burning in Amorphous Systems

A range of early hole-burning work on [Cr(en)$_3$]$^{3+}$, [Cr(NH$_3$)$_6$]$^{3+}$ and [Cr(NH$_3$)$_5$Cl]$^{2+}$ in frozen ethylene glycol-water glass indicated relative large R-line linewidths of the order of magnitude of 100 MHz at 1.8 K [94, 95]. It was also found that the energies of electronic levels are poorly correlated, resulting in wide distributions of zero field splittings of the ^{2}E excited state and the ^{4}A$_2$ ground state. Spontaneous hole-filling could be well described by a dispersive first-order kinetics model. This work was followed up by systematic investigations of the R-lines of [Cr(bpy)$_3$]$^{3+}$ in a range of amorphous hosts [96, 97]. Again, on the time scale of the experiments, relative broad linewidths of 80 MHz in
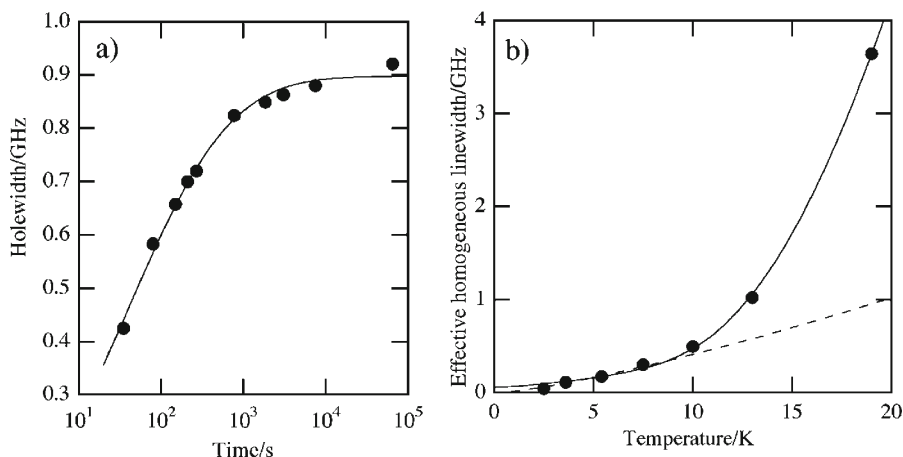
Fig. 18a,b Spectral diffusion and effective homogeneous linewidth of the R_1-line in $[Cr(NCS)_6]^{3-}$ in glycerol: **a** the time dependence of a spectral hole; **b** the temperature dependence of the effective hole width. The *dashed line* shows the $T^{1.3}$ behaviour often encountered in amorphous systems [58]

glycerol to 460 MHz in 4:1 ethanol/methanol were found at 1.5 K. Also, it was shown that the zero field splittings are not well defined within the inhomogeneous distribution. On the basis of this result it was concluded that ODMR and EPR experiments in amorphous systems have to be interpreted with care.

In these reports it was speculated that the observed linewidths are dominated by spectral diffusion. This idea has been recently addressed by an investigation of the time dependence of the spectral hole width in the R_1-line of $[Cr(NCS)_6]^{3-}$ in glycerol in the range of 10 s to 10^5 s [71]. The time dependence is non-logarithmic but can be described by Eq. (17) and Eq. (18) with λ_0=15.9 and σ=1.99 as is illustrated in Fig. 18a. It appears that hole widths in chromium(III) R-lines in amorphous systems are dominated by spectral diffusion and thus by the dynamics of the non-equilibrium host. The $[Cr(NCS)_6]^{3-}$/glycerol system deviates dramatically from a $T^{1.3}$ behaviour of the effective homogeneous linewidth for T>10 K due to the direct process between the two ^2E levels. A $T^{1.3}$-temperature dependence has been observed for $^1\pi-\pi^\star$ transitions in a range of amorphous organic systems [98]. The R-lines in $[Cr(NCS)_6]^{3-}$ are subject to a large nephelauxetic effect, a concept introduced by C.K. Jørgensen [99, 100]. It can be argued that electron delocalisation onto the ligands makes the transition energy more susceptible to dynamic host-guest interactions. However, we have reached the conclusion that this effect plays no major role in spectral diffusion properties of $[Cr(NCS)_6]^{3-}$/glycerol.

We have also studied the effects of magnetic fields on spectral holes burnt into the R_1-line of $[Cr(NCS)_6]^{3-}$ in glycerol [101]. Burning spectral holes in strong magnetic fields and subsequently varying the field strength can reveal excited state *g*-factors and their strain. Furthermore, holes can be read out by Zeeman scanning, if holes are burnt in strong magnetic fields.

3
Conclusions

Spectral hole-burning is a highly valuable laser technique that can reveal subtle details of the electronic structure of coordination compounds. For example, its high resolution facilitates the determination of *g*-factors in magnetic fields as low as 1 mT. Furthermore, both the ground state and excited state splittings are directly visible in multiple hole patterns. Also, spin-lattice relaxation times are directly measurable for the ground and excited state in time-resolved transient hole-burning. Electron-spin–electron-spin interactions are highly relevant in hole-burning spectroscopy of chromium(III) complexes doped into host lattices at concentrations of about 1%, and limit the hole-widths to the 10–100 MHz range. To approach superhyperfine limited linewidths much lower concentrations and eventually high magnetic fields will have to be applied.

Recent progress has been based on inexpensive diode lasers: these lasers are inherently stable and can be rapidly scanned, enabling elegant hole-burning experiments.

Our recent discovery of a *sensational* increase of the hole-burning efficiency upon partial deuteration of the R-lines of $NaMgAl(oxalate)_3 \cdot 9H_2O$:Cr(III) shows that there are many highly interesting phenomena to yet be discovered in inorganic molecular solids. On the basis of the increase we have assigned the hole-burning mechanism to 180° flips of lattice water molecules. This is a novel mechanism that may be observed for many other hydrates. It may also enable applications in the field of laser stabilization and in optical data storage, at least at liquid nitrogen temperatures. For example, if a dilute rare earth oxalate hydrate can be designed that shows the increase in hole-burning efficiency, it may well be possible to use the material for a practical data storage device at 77 K.

4
References

1. Szabo A (1975) Phys Rev B 11:4512
2. Kharlamov BM, Personov RI, Bykovskaya LA (1975) Izv Akad Nauk SSSR Ser Fiz 39: 1922
3. Kharlamov BM, Bykovskaya LA, Personov RI (1977) Chem Phys Lett 50:407
4. Gorokhovskii AA, Kaarli R, Rebane L (1974) Pis'ma Zh Eksp Teor Fiz 20:474
5. Moerner WE (1988) In: Moerner WE (ed) Persistent spectral hole-burning: science and applications. Top Curr Phys 44. Springer, Berlin Heidelberg New York, chap 1
6. Rebane KK (2000) J Lumin 86:167
7. Reeves RJ, Macfarlane RM (1992) J Opt Soc Am B Opt Phys 9:763
8. Reddy NRS, Small GJ, Seibert M, Picorel R (1991) Chem Phys Lett 181:391
9. Volker S (1989) Annu Rev Phys Chem 40:499
10. den Hartog FTH, van Papendrecht C, Silbey RJ, Volker S (1999) J Chem Phys 110:1010
11. Macfarlane RM, Shelby RM (1987) Coherent transient and holeburning spectroscopy of rare earths in solids. In: Kaplyanskii AA, Macfarlane RM (eds) Spectroscopy of solids containing rare earth ions. Elsevier, Amsterdam, p 51
12. Macfarlane RM, Shelby RM (1987) J Lumin 36:179
13. Walsh RJ, Reinot T, Hayes JM, Kalli KR, Hartmann LC, Small GJ (2003) Biophys J 84:1299
14. Pryde GJ, Bottger T, Cone RL, Ward RCC (2002) J Lumin 98:309
15. Bottger T, Sun Y, Pryde GJ, Reinemer G, Cone RL (2001) J Lumin 94/95:565

16. Yen WM, Selzer PM (1981) High resolution spectroscopy of ions in crystals. In: Yen WM, Selzer PM (eds) Top Appl Phys 49:141
17. Schenzle A, Brewer RG (1976) Phys Rev A 14:1756
18. Equall RW, Sun Y, Cone RL, Macfarlane RM (1994) Phys Rev Lett 72:2179
19. Friedrich J, Haarer D (1984) Ang Chemie Int Ed 23:113
20. Konz F, Sun Y, Thiel CW, Cone RL, Equall RW, Hutcheson RL, Macfarlane RM (2003) Phys Rev B 68:085109/1
21. Ganem J, Wang YP, Boye D, Meltzer RS, Yen WM, Macfarlane RM (1991) Phys Rev Lett 66:695
22. Ganem J, Wang YP, Boye D, Meltzer RS, Yen WM, Wannemacher R, Macfarlane RM (1991) Phys Rev Lett 66:1649
23. Szabo A, Muramoto T, Kaarli R (1990) Phys Rev B 42:7769
24. Szabo A, Kaarli R (1991) Phys Rev B 44:12307
25. Macfarlane RM, Cassanho A, Meltzer RS (1992) Phys Rev Lett 69:542
26. Imbusch GF, Kopelman R (1981) Optical spectroscopy of electronic centers in solids. In: Yen WM, Selzer PM (eds) Top Appl Phys 49:1
27. Imbusch GF, Yen WM, Schawlow AL, McCumber DE, Sturge MD (1964) Phys Rev 133:1029
28. McCumber DE, Sturge MD (1963) J Appl Phys 34:1682
29. Freiberg A, Rebane LA (1977) Phys Status Solidi B Basic Res 81:59
30. Glasbeek M, Smith DD, Perry JW, Lambert WR, Zewail AH (1983) J Chem Phys 79:2145
31. Hsu D, Skinner JL (1985) J Chem Phys 83:2107
32. Moerner WE, Carter TP (1987) Phys Rev Lett 59:2705
33. Carter TP, Horne DE, Moerner WE (1988) Chem Phys Lett 151:102
34. Moerner WE (2002) J Phys Chem B 106:910
35. Szabo A (1971) Phys Rev Lett 27:323
36. Kurnit NA, Abella ID, Hartmann SR (1964) Phys Rev Lett 13:567
37. Genack AZ, Weitz DA, Macfarlane RM, Shelby RM, Schenzle A (1980) Phys Rev Lett 45:438
38. Genack AZ, Macfarlane RM, Brewer RG (1976) Phys Rev Lett 37:1078
39. Mlynek J, Wong NC, DeVoe RG, Kintzer ES, Brewer RG (1983) Springer Ser Opt Sci 40:60
40. Shelby RM, Macfarlane RM (1979) Chem Phys Lett 64:545
41. Erickson LE (1977) Phys Rev B 16:4731
42. Macfarlane RM, Shelby RM (1984) Opt Lett 9:533
43. Winnacker A, Shelby RM, Macfarlane RM (1985) J Phys Colloq 543
44. Jankowiak R, Hayes JM, Small GJ (1993) Chem Rev 93:1471
45. Fei S, Strauss HL (1996) J Phys Chem 100:3414
46. Macfarlane RM, Reeves RJ, Jones GD (1987) Opt Lett 12:660
47. Riesen H, Bursian VE, Manson NB (1999) J Lumin 85:107
48. Anderson PW, Halperin BI, Varma CM (1972) Philos Mag 25:1
49. Phillips WA (1972) J Low Temp Phys 7:351
50. Hayes JM, Small GJ (1978) Chem Phys 27:151
51. Reinot T, Zazubovich V, Hayes JM, Small GJ (2001) J Phys Chem B 105:5083
52. Moerner WE, Gehrtz M, Huston AL (1984) J Phys Chem 88:6459
53. Breinl W, Friedrich J, Haarer D (1984) J Chem Phys 81:3915
54. Friedrich J, Haarer D (1985) J Phys Colloq 357
55. Al'shits EI, Kharlamov BM, Plakhotnik TV (1988) Opt Spektrosk 65:1248
56. Gorokhovskii AA, Rebane LA (1988) Proc Electrochem Soc 88:48
57. Littau KA, Bai YS, Fayer MD (1989) Chem Phys Lett 159:1
58. Jahn S, Haarer D, Kharlamov BM (1991) Chem Phys Lett 181:31
59. Szabo A, Kaarli R (1991) Phys Rev B 44:12307
60. Osad'ko IS, Yershova LB (1999) J Chem Phys 111:7652
61. Muller J, Maier H, Hannig G, Khodykin OV, Haarer D, Kharlamov BM (2000) J Chem Phys 113:876
62. Kharlamov BM (2000) J Lumin 86:225
63. Osad'ko IS, Mikhailov MA (1995) Phys Lett A 208:231
64. Khodykin OV, Muller J, Kharlamov BM, Haarer D (1998) Europhys Lett 44:68

65. Kharlamov BM, Muller J, Khodykin OV, Haarer D (2000) J Lumin 86:235
66. Koedijk JMA, Wannemacher R, Silbey RJ, Voelker S (1996) J Phys Chem 100:19945
67. Wang YP, Landau DP, Meltzer RS, Macfarlane RM (1992) J Opt Soc Am B Opt Phys 9:946
68. Meltzer RS, Ganem J, Wang YP, Boye D, Yen WM, Landau DP, Wannemacher R, Macfarlane RM (1992) J Lumin 53:1
69. Krausz E, Riesen H (1999) Laser spectroscopy. In: Solomon EI, Lever ABP (eds) Inorganic electronic structure and spectroscopy, vol 1. Wiley, New York, p 307
70. Wannemacher R, Smorenburg HE, Schmidt T, Volker S (1992) J Lumin 53:266
71. Lewis ML, Riesen H (2002) Phys Chem Chem Phys 4:4845
72. Riesen H, Hughes JL (2003) Chem Phys Lett 370:26
73. Hughes JL, Riesen H (2003) J Phys Chem A 107:35
74. Riesen H, Wallace L, Krausz E (1997) Int Rev Phys Chem 16:291
75. Riesen H, Wallace L, Krausz E (2000) Inorg Chem 39:5044
76. Riesen H, Krausz E (1993) Chem Phys Lett 212:347
77. Riesen H, Rae AD, Krausz E (1994) J Lumin 62:123
78. Piper TS, Carlin RL (1961) J Chem Phys 35:1809
79. Bernheim RA, Reichenbecher EF (1969) J Chem Phys 51:996
80. Coleman WF, Forste LS (1971) J Lumin 4:429
81. Zbieranowski WT (1975) Chem Phys Lett 36:166
82. Mortensen OS (1967) J Chem Phys 47:4215
83. Rae AD, Riesen H (to be published)
84. Lahiry S, Kakkar R (1982) Chem Phys Lett 88:499
85. Lewis ML, Riesen H (2002) J Phys Chem A 106:8039
86. Rives JE, Meltzer RS (1977) Phys Rev B 16:1808
87. Riesen H (1992) J Lumin 54:71
88. Hughes JL, Riesen H (2002) Chem Commun 1616
89. Riesen H (2003) Chem Phys Lett 382:578
90. Strickland NM, Cone RL, Macfarlane RM (1999) Phys Rev B 59:14328
91. Fearey BL, Stout RP, Hayes JM, Small GJ (1983) J Chem Phys 78:7013
92. Kim WH, Reinot T, Hayes JM, Small GJ (1996) J Chem Phys 104:6415
93. Riesen H, Hughes JL (2003) Chem Phys Lett 372:563
94. Riesen H, Manson NB (1989) Chem Phys Lett 161:131
95. Riesen H, Manson NB, Krausz E (1990) J Lumin 46:345
96. Riesen H, Krausz E (1992) J Chem Phys 97:7902
97. Riesen H, Krausz E, Dubicki L (1994) Chem Phys Lett 218:579
98. den Hartog FTH, Bakker MP, Silbey RJ, Volker S (1998) Chem Phys Lett 297:314
99. Schaffer CE, Jorgensen CK (1958) J Inorg Nucl Chem 8:143
100. Schaeffer CE, Joergensen CK (1965) Mol Phys 9:401
101. Riesen H (2000) J Phys Chem A 104:5469

Elucidation of Ligand-Field Theory. Reformulation and Revival by Density Functional Theory

Christian Anthon · Jesper Bendix · Claus E. Schäffer

Department of Chemistry, University of Copenhagen, Universitetsparken 5,
Copenhagen 2100, Denmark
E-mail: ces@kiku.dk

Abstract Constrained by the use of an "average-of-configuration" computation, Kohn-Sham-DFT allows identification of the complete set of d^q states of the ligand field plus repulsion model, LFR. A one-to-one correspondence is assumed between states defined by integer occupation numbers of real KS spin orbitals and single-determinant ligand-field states of a hierarchic cubic-tetragonal-orthorhombic strong-field approximation. The energies of these LFR states are parameterized by using mutually orthogonal parametrical operators. This orthogonality secures optimal meaningfulness of the parameters. The DFT state energies are taken as computed "data". For d^2, each parameter is defined by a 45-dimensional coefficient vector, which is orthogonal to that of all the other parameters. By forming the scalar products of the coefficient vectors and the "data" vector, the values of the parameters are determined. Identically the same parameter values may be obtained by performing the "data" reduction using a linear least squares procedure. The Amsterdam Density Functional program package (ADF) is constrained and then its shortcomings in reproducing the LFR models is quantified. Small "random errors" and "spatial errors" are identified and eliminated. Thereafter, the KS-DFT model for atomic ions is equivalent to the five-parameter Parametrical Multiplet Term model, PMT. This model is finally contracted to the three-parameter Slater-Condon-Shortley model, SCS. This "data" reduction has substantial errors. The computed sum square splitting, SSS_{ADF}, which for systems with two electrons in the partially filled shell is the sum of the squares of the 45 barycentered ADF energies, was taken as a measure of the integrated information contents of the 44 independent computed energy differences. Then, for atomic ions, by discarding 0.05% of unsystematic information a 1:1 relationship between the constrained ADF model and the PMT model was obtained. By discarding another 2% of systematic information, a 1:1 relationship with the SCS model resulted. The SCS model is parameterized in terms of Jørgensen's spin-pairing energy parameter D and the Racah parameter B. Even though KS-DFT does not lend itself to the direct determination of non-diagonal elements, the present parameterization procedure allows the full d^q spaces to be explored.

Experimental and computed parameter values have been compared satisfactorily for all the atomic d^2 and d^8 systems for which all J levels have been observed. Moreover, $V^{III}X_4^-$ and $Cr^{IV}X_4$ (X=F, Cl, Br, I) have served as molecular illustrations of the method. The spectrochemical and the nephelauxetic series of ligands as well as the large gap between F^- and the other halide ions are borne out by our computations and for VX_4^- (X=Cl and Br) the computed parameter values compare well with published semi-empirical ligand-field data. The philosophy of the cellular ligand-field model is contradicted and that of the angular overlap model supported by the computational result that the covalency of the central ion d orbitals is of dominant importance in the analysis of the frontier orbitals. The spectrochemical parameter Δ may be obtained as the appropriate KS-DFT orbital energy difference as well as from the combined KS-DFT/LFR model. The nephelauxetic ratio β may analogously be obtained in two almost independent ways, whose only common feature is the "average-of-configuration" computation. In this computation the ten spin-orbitals of the partially filled shell are equally populated, a constraint forming the basis of this whole comparative study.

Dedicated to the memory of Christian Klixbüll Jørgensen and his many original contributions to an inductive approach to inorganic chemistry, this chapter addresses particularly some of the ramifications of his pioneer parameterization of spin-pairing energy and his explanations of the nephelauxetic phenomenon.

List of Abbreviations

ADF	Amsterdam Density Functional
AOC	Average-of-configuration
AOM	Angular overlap model
CFT	Crystal-field theory
EM	Electrostatic model
HOMO	Highest occupied molecular orbital
KS-DFT	Kohn-Sham DFT
LCAO	Linear combination of atomic orbitals
LDA	Local density approximation

LFR   Ligand-field plus repulsion
LFT   Ligand-field theory
MO   Molecular orbital
PMT   Parametrical Multiplet Term model
SCF   Self consistent field
SCS   Slater-Condon-Shortley
SSS   Sum square splitting

1
Introduction

In the past this laboratory has reported on the solution of various problems on quantification of the symmetry underlying ligand-field theory (LFT) and atomic spectroscopy of d^q configurations. This work began with contributions to the invention of the nephelauxetic series [1–3] and the angular overlap model [4–12] of the ligand field, both topics to which the late C.K. Jørgensen was among the pioneer contributors. The work continued with analyses of the properties and applications of real atomic orbitals [13, 12], which were then used to establish sets of phase-fixed coupling coefficients for the point groups as well as their symmetrized forms, the so-called 3Γ symbols. The same was also done for the three-dimensional rotation group R_3 [14, 15]. An analysis of problems along these lines was also performed for all the double groups of the point groups [16]. By introducing orthonormal operators it was possible to interpret the quantitative contents of coupling coefficients and Racah lemma coefficients [17]. Thereby, these coefficients could be applied in new ways for illuminating ligand-field theory [18, 19]. Thus, examples of the transformations that take the so-called weak-field coupling schemes into their equivalent strong-field schemes were given [17, 20] as well as the relationships between the equivalent atomic and molecular parameterization schemes [11, 12, 21]. The orthogonal and orthonormal sets of operators that act on d orbital spaces and their tensor product spaces were used to quantify the relative and absolute importance of ligand-field components and to compare their influence on the d^q configurations with that of the interelectronic repulsion operators [22]. More general two-electron operators with the properties of mutual orthogonality [23, 24] were used in atomic spectroscopy to find empirical parameters that were able to account for the multiplet term energies in a more accurate way than the Slater-Condon-Shortley (SCS) model of interelectronic repulsion [25] within a genuine d^q configuration. This Parametrical Multiplet Term model (PMT) [23, 24] was supplemented by atomic spectroscopists to account better for the experimentally observed fine structure [28] than the one-electron spin-orbit coupling operator of the SCS model allowed.

Recently, we have initiated a study of time-independent Kohn-Sham DFT (KS-DFT) [29] and its possible synergy with LFT [30, 31]. Investigations of the structure, electronic structure and magnetic properties of transition metal ions and transition metal complexes [32, 33] by KS-DFT have flourished in recent years [34]. The low computational cost and high accuracy makes KS-DFT an ideal tool

for studies in inorganic chemistry [35]. The early success of KS-DFT lay mainly in structure determination of transition metal complexes. The treatment of excited states of open-shell compounds was at first limited to one-electron systems [36–38], but the extension to many-electron systems is now an ongoing effort [31, 39]. At an early stage it became clear that only energies of states corresponding to single determinants could be interpreted [40]. The use of these states to calculate the energies of excited eigenstates was also discussed and later extended in recent publications by others [39, 41–43] and by us [30, 31].

We have studied KS-DFT in the form of the commercially available program package, the Amsterdam Density Functional (ADF) [34, 44–47]. In [30], we found that there are essential symmetry reasons for using real orbitals in KS-DFT. This observation has given new actuality to our results from the past, especially regarding real linear harmonics and their products [13]. This chapter reviews and extends some of these observations.

In our work on KS-DFT in the form of the ADF, we obtained unexpected results, which we could explain as a consequence of our symmetry-based method. Thus, in spite of the fact that symmetry seems to be sometimes a problem in DFT, we found that in our constrained use of KS-DFT, the symmetry factor of the classical Coulomb interaction between the d electrons of d^q was exactly reproduced in the computations on atomic ions. Even the non-classical exchange interaction, which makes up one of the biggest problems of KS-DFT, was reproduced so well that the energies that should have come out identical for symmetry reasons alone varied only about 0.02 eV or 0.0160 μm^{-1} in the case of V^{3+}. However, especially for atomic systems, we found that in the local density approximation (LDA) the energy contributions from the exchange/correlation functional did not distinguish different orbital states having the same value of M_S. This is not a breaking of the symmetry but rather it is a lack of ability to account for the spatial splittings and thereby a failure to reproduce the empirically known values for a certain repulsion parameter (in fact the Racah parameter B). The SCS energy parameters of the Coulomb functional and the exchange/correlation functionals should for our purposes ideally have been computed to obtain equal values. However, we found that even for gradient corrected computations, the Coulomb functional gave higher and the exchange/correlation functional lower values than the empirical ones. Therefore, the Coulomb and exchange results were incommensurable. Nevertheless, when their energy contributions were added in the conventional way and averaged over the whole d^q configuration, these added energies were closer to the results from spectroscopy than those of open-shell Hartree-Fock calculations [48, 49], but the averaging was essential (see [24] for references to spectroscopic data).

We found rather large but systematic deviations of the energies of the individual, single-determinantal microstates relative to the requirements of the SCS model [30]. A description of the systematics of these deviations is an important part of this chapter. Here, the ADF has been applied to compute the repulsion splitting of all the atomic d^2 and d^8 systems for which complete data sets are available. This was done using the SCS model, and the Parametrical Multiplet Term model (PMT) was used to describe the ADF deviations from the SCS model found for the individual computed microstate energies as well as for the com-

puted values of the multiplet term energies. The PMT model [50] was found ideal as a tool for overcoming the incommensurability of the Coulomb and exchange functional of the ADF.

The repulsion parameters obtained from the ADF for atomic and corresponding molecular ions are our computed bases for calculating nephelauxetic ratios. These ratios are of special interest because the era of ligand-field theory as a forefront scientific subject left open several questions about the physical interpretation of these ratios [3, 51]. This chapter elucidates some of these questions.

A bridge from a strong-field basis, which corresponds to the KS-DFT energies, to the weak-field basis of the atomic ions, which is the eigenbasis of the effective two-electron operator, is required. Therefore, we shall go through the methods used to parameterize the atomic spectroscopical results on d^q configurations.

The VCl_4^- ion is a beautiful example of a complex that was predicted by ligand-field theory to be stable and was subsequently prepared along with VBr_4^- [52–56]. Our aim when using KS-DFT was to mimic ligand-field theory and we have obtained useful results in this direction, with atomic transition metal d^q ions and VX_4^- and CrX_4 (X=F, Cl Br, and I) as examples. We thus reported on a method for computing the empirical parameters of the SCS model for the atomic ions of the first transition series [30] and recently [31] we have shown that the ligand-field systems VX_4^- can be mimicked in a one-to-one way by a constrained application of KS-DFT. We found satisfactory values for the spectrochemical parameter Δ as well as for the interelectronic repulsion parameters of the SCS model reproducing the spectrochemical and the nephelauxetic series, respectively. Operationally, our approach differs from previous work bridging DFT and LFT primarily by attempting to extract the maximal information from the DFT calculations and model this over-complete set of data to the more restricted ligand-field plus repulsion (LFR) description. Analytically, we introduce in this chapter a number of steps that clarify the connection between constrained KS-DFT and LFR.

The eigenstates of an atomic or molecular system are in general built up out of orbitals that are different for different eigenstates. However, fixed orbitals are extremely useful conceptual as well as practical tools for our description of chemistry and spectroscopy. This is why KS-DFT is so appealing to us. Mimicking ligand-field theory requires certain constraints on KS-DFT in order to modulate it so that the concept of a d^q configuration is conserved in much the same way as chemists and atomic spectroscopists use this concept. KS-DFT is particularly adaptable to such an enforced modulation.

We talk about a characterizing or effective d^q configuration and we are only able to do this for chemical systems for which it is true that at least the ground state and the lower excited states have the symmetries predicted on the basis of an assumption about a genuine d^q configuration. Thus, for a gaseous Cr^{3+} system, all the 120 microstates with the state symmetries of a d^3 configuration have been observed. These microstates are grouped together in just the way symmetry requires and, moreover, their relative energies can on a chemical standard be well parameterized by the use of the SCS model. Similarly, the vast majority of chromium(III) complexes exhibit ligand-field spectra that can be parameterized by ligand-field theory [57, 58].

The fact that the parameters extracted from experiments follow so regular patterns as the spectrochemical and the nephelauxetic series makes the accomplishments of LFT parallel the usual results of chemical efforts, and the fact that consistent qualitative explanations can be given for the chemical variations of the parameters makes the whole effort useful in a broader chemical perspective, and that is one reason why we still meet these results in the textbooks.

By the constrained use of KS-DFT, this chapter and our previous papers [30, 31] add computational support to the most central qualitative as well as quantitative explanations of the existing ligand-field contributions to chemistry. However, our KS-DFT computational ligand-field modeling and usual semi-empirical ligand-field modeling have in common that they contradict the virial theorem by their assumption of different energy levels belonging to identically the same electronic configuration. The virial theorem requires the absolute value of the total energy of a stationary state to equal its kinetic energy [59, 60]. Since the kinetic energy operator is a one-electron operator, this means that a ligand-field system having fixed orbitals will have a fixed kinetic energy and thereby should have a fixed total energy. The two-electron contributions to the total energy, which are our main concern here, may not change this.

This situation is maybe not so worrying as it might seem at first. Two stationary atomic states of different energies, which we here classify as belonging to the same d^q configuration, will in a Hartree-Fock scheme have corresponding orbitals with radial functions that are different. The differences near the nucleus will be dominating as far as the nuclear attraction and kinetic energy – and thereby the total energy – is concerned [59–61]. On the one hand this idea is worrying. On the other hand, chemists have always been convinced that the valence shell was of dominating importance for the chemistry. The present results support this conviction by mimicking semi-empirical ligand-fields using a purely computational framework, which at least in principle is non-empirical.

In the modeling we assume that we are able to partition the energy in such a way that certain energy differences – vaguely defined, those involving the valence shell – can be parameterized. In doing this we use effective operators that are comparable with usual quantum mechanical ones except for the function spaces on which they act. The empirical parameters and in particular their regular chemical variations turn out to be computable astonishingly accurately, at least for the present ligand-field systems.

Our chapter is built up as follows: first, we describe the formalism of complete sets of mutually orthogonal operators. This formalism, which is fundamental to the chapter, allows all of LFT to be expressed in terms of a sum of products of empirical parameters and coefficient operators (2nd section), that is, including interelectronic repulsion and spin orbit coupling. The section is particularly concerned with the advantages of orthogonal operators over conventional schemes. The 3rd section deals with the empirical atomic spectroscopic basis for LFR. The section continues the discussion of the coefficient operator formalism and demonstrates the consanguinity between this formalism and that used in the least squares fitting model generally used in transforming data into model parameters. Finally, the section contains a collection of parameter values for atomic d^2 and d^8 systems including some referring to the 4d and 5d series. The

rest of the chapter treats the repulsion specifically and then combines it with the ligand field itself. The fourth section is concerned with the triplet states of these systems, and the fifth one with the singlets; the sixth section establishes the position of the parametrical multiplet term model (PMT) in LFR, and the seventh one is concerned with the strategy of our method for mimicking LFR by KS-DFT; the eighth section describes KS-DFT and LFR function bases, which bridge the two models, and the final two sections provide ADF computations for atomic and molecular systems, respectively, together with comparisons of these with those based upon spectroscopic data.

2
The Concept of the d^2 Configuration and the Coefficient Operator Formalism

2.1
Brief History and Review

Historically, ligand-field theory as well as SCS theory of interelectronic repulsion started out in the 1930s as physical theories. These were based upon the assumption of a pure d^q configuration energetically above a closed shell of electrons, which was considered to be inert, that is, independent of which energy state of d^q was under consideration. Symmetry governed the results of both theories even though this fact was not explicitly used in Condon and Shortley's book [25]. Spherical symmetry came in, however, through the LaPlace equation, which allowed all integrals to be written as a product of an angular and a radial factor. The integrals over the angular factors of the d orbitals were easy to perform (they were actually symmetry-determined). For SCS theory three explicitly expressed radial integrals, F^0, F^2, and F^4 remained, which were in principle, but not in practice computable. When the energies of the d^q states were expressed in terms of these three integrals, one of them, F^0, gave a non-observable common contribution to all the states while the other two integrals were responsible for the observable energy differences. As a consequence these two integrals were soon taken as parameters to be evaluated by comparisons between theory and experiment. Therefore, already from the beginning, the physical theory switched into a parametrical theory mainly for practical reasons and since it worked so beautifully, at first for atoms and later for molecular ligand-field systems, an almost religious belief in its physical reality became widespread. However, it soon became clear that it was symmetry that carried the success [62]. The success nevertheless remained a success for two reasons: the variations of all the parameters were systematic in that they depended satisfactorily on chemical and configurational differences including changes in oxidation states. Moreover, the dependencies could in general be given qualitative explanations that satisfied physicists as well as chemists.

This, briefly, is the historical background for the present review and, in particular, for the present section's discussion of the SCS model and its extensions.

The formalism using the concept of coefficient operators was designed for application to parametrical models of the kind just mentioned. In this connection

the concept of operator overlap is essential, and the choice of sets of mutually orthogonal and orthonormal operators became important, for practical reasons as well as for reasons of obtaining a transparent conceptual definition of the parameters as well as an analysis of their functioning. The parameters were no longer computable integrals; they were model observables whose values had to be obtained semi-empirically from observed state energies. Furthermore, new simple quantifications allowing a comparison of the contributions associated with the various parameters were found.

This section is concerned with the properties of operators of the kind just mentioned as well as various methods for generating them. Moreover, it is about an extension of the original SCS model to the most general pair-interaction model, originally used for analysis of atomic spectra. This complete set of two-electron operators (effective operators) consists of the three classical SCS operators corresponding to the three radial integrals mentioned above, plus two extension operators. Alternatively, these five operators can be linearly combined to obtain, for example, operators that refer to the five multiplet terms of d^2 (cf. Eq. 1).[1] This model is therefore called the parametrical multiplet term model, PMT.

The eigenstates of a two-electron system can be chosen as products between two-electron spin functions and two-electron orbital functions. The Pauli principle requires that the resulting product function be antisymmetric with respect to permutation of the coordinates of the two electrons:

$$d^2 : {}^1S \oplus {}^1D \oplus {}^1G \oplus {}^3\underline{P} \oplus {}^3\underline{F} \tag{1}$$

We note that the spin triplets, which comprise $M_S=1$ have symmetrical spin functions $\alpha(1)\alpha(2)=\alpha(2)\alpha(1)$. They combine with the spatially antisymmetric functions (underlined). The total number of microstates within each term is $(2S+1)(2L+1)$ so that the total number of microstates embodied in the configuration d^2 is equal to 45. This is in agreement with the binomial Pauli-principle expression ${}^{10\cdot9}/_2$ for the number of ways two electrons can be accommodated in the ten spin orbitals.

2.2
The Hamiltonian Formalism: the Concepts of Coefficient Operators and Conglomerate Operators

Our parametrical Hamiltonian is invariably written in the form of a linear combination of conglomerate operators:

$$\hat{H} = \Sigma_i P_i \hat{Q}[P_i] \tag{2}$$

where each conglomerate is a product of an energy parameter P_i and its associated coefficient operator $\hat{Q}[P_i]$. This operator factor is completely defined by its

---

[1] We mention parenthetically that the atomic spectroscopists add more effective operators, for example three-electron operators for $2<q<8$. These are all included in the general PMT model on d^q. Here we shall use the name and symbol PMT for short for the d^q model embodying only the two-electron operators.

matrix representation in some function basis covering its domain. For our present purposes this domain will be chosen as the function space d^2 or a subspace thereof. The total function space for a d^2 system is the tensor product space of two sets of ten d spin orbitals, subject to the Pauli principle. As mentioned above, this space is 45 dimensional, but in the present section this dimension will for most practical purposes be reduced to five, referring to the five multiplet terms of d^2 given in Eq. (1). This reduction will be instituted by the use of individual weight factors that are equal to the degeneracies $(2S+1)(2L+1)$ of the terms.

The simplest and almost trivial coefficient operator is that associated with the average of the energies of the domain of $\hat{H}$, that is, of the configuration d^2. This average-energy coefficient operator is *in any orthonormal function basis* represented by the 45×45 unit matrix, which may be given in the short form as the 5×5 unit matrix together with the weights 1,9,5,21,9 corresponding to $^1S, ^3P, ^1D, ^3F, ^1G$, respectively. We denote this coefficient operator by the symbol $\hat{1}$ and give its diagonal elements as a column vector in Table 1. The simplest matrix element will illustrate the formalism

$$\langle ^1S|H_{av.}\hat{Q}[H_{av.}]|^1S\rangle = H_{av.}\langle ^1S|\hat{Q}[H_{av.}]|^1S\rangle = H_{av.}\langle ^1S|\hat{1}|^1S\rangle = H_{av.} \tag{3}$$

2.3
The Number Operator and Basic Operators

For the simplest case of a non-degenerate state, the basic coefficient operator $\hat{Q}[H_S]$ is $|^1S\rangle\langle^1S|$ and the corresponding parameter H_S represents the energy of the ^1S term. This operator projects out the S term from the full configuration. Four additional operators of this kind may be defined on the five-dimensional subspace of the d^2 configuration containing each term only once regardless of degeneracy. Using the weight factors as explained above, these basic operators may be expanded to the full 45 dimensional space of d^2.

The basic spin-free operators on a d^2 configuration are similar to basic one-electron operators [17, 19] and add up to a Hamiltonian, which is diagonal in multiplet term basis and has the explicit term energy parameters as eigenvalues. This parametrical multiplet term Hamiltonian (PMT) is, expressed in conglomerate operators,

$$\hat{H}_{PMT} = H_S\hat{Q}[H_S] + H_P\hat{Q}[H_P] + H_D\hat{Q}[H_D] + H_F\hat{Q}[H_F] + H_G\hat{Q}[H_G] \tag{4}$$

whose coefficient operators are given in Table 2. Their sum is equal to $\hat{1}$ of Table 1:

$$\hat{1} = \hat{Q}[H_S] + \hat{Q}[H_P] + \hat{Q}[H_D] + \hat{Q}[H_F] + \hat{Q}[H_G] \tag{5}$$

and the following corresponding equality applies to the energy parameters:

$$45H_{av.} = H_S + 9H_P + 5H_D + 21H_F + 9H_G . \tag{6}$$

Table 1 Our standard sets of PMT and SCS coefficient operators. Array defining the Parametrical Multiplet Term model (PMT) by its coefficient operators and the Slater-Condon-Shortley model (SCS) analogously. The PMT and the SCS models represent the energy splitting of pair-interaction models within d^2 or d^8 characterizing configurations. These parameterizations require four and two parameters, respectively. However, the models have in common the average energy of the configuration $H_{av.}[d^2]$ or $H_{av.}[d^8]$. The top row contains the designations of our coefficient operators, which have their associated parameters in brackets. The five middle rows of numbers are coefficients to these parameters so that, for example, the parametrical expressions for the energy of the ^3F multiplet term are $H_F = H_{av.} - (14/21)D^S - (18/21)E^1 = H_{av.} - (14/21)D - (18/21)E$, illustrating a quantification of the stabilisation of the ground term by Hund's rules. The bottom row contains the areas of the operators over the d^2 configuration. A given operator is defined by the numbers of its column, whose squares, when weighted by the degeneracy numbers (weights) given in the second column, add up to the area of that operator. The columns are mutually orthogonal when the components of their scalar products are weighted. The third column refers to the number operator $\hat{1}$, which is the zero-electron operator counting the number of microstates by its area (and by its trace). Its associated parameter $H_{av.}$ depends upon the choice of zero point for the energies

Energies	Weights	$\hat{Q}[H_{av.}]$	$\hat{Q}[D^S]$	$\hat{Q}[E^1]$	$\hat{Q}[D^V]$	$\hat{Q}[E^0]$	$\hat{Q}[D]$	$\hat{Q}[E]$
H_S	1	1	28/21	0	84/21	0	112/21	0
H_G	9	1	28/21	0	–6/21	10/21	22/21	10/21
H_D	5	1	28/21	0	–6/21	–18/21	22/21	–18/21
H_P	9	1	–14/21	42/21	0	0	–14/21	42/21
H_F	21	1	–14/21	–18/21	0	0	–14/21	–18/21
$\langle \hat{Q} | \hat{Q} \rangle$		45	280/7	360/7	120/7	40/7	400/7	400/7

Table 2 Definition of another set of mutually orthogonal PMT coefficient operators, the basic operators. These five operators, whose parameters are by definition the multiplet term energies, are not pure two-electron operators. They contain different amounts of the number operator $\hat{1}$ (see legend to Table 1). This basic set of operators illustrates the formalism of mutually orthogonal coefficient operators by expressing trivially the energies of the multiplet terms. The energies themselves are defined up to a constant term depending on the zero point of energy

Energies	Weights	$\hat{Q}[H_S]$	$\hat{Q}[H_G]$	$\hat{Q}[H_D]$	$\hat{Q}[H_P]$	$\hat{Q}[H_F]$
H_S	1	1	0	0	0	0
H_G	9	0	1	0	0	0
H_D	5	0	0	1	0	0
H_P	9	0	0	0	1	0
H_F	21	0	0	0	0	1
$\langle \hat{Q} | \hat{Q} \rangle$		1	9	5	9	21

2.4
Consecutive Operator Generation. A: The Hund's-Rules Operators

A second method for obtaining the PMT Hamiltonian of Eq. (4), which may be called the method of consecutive (or hierarchical) generation, has the characteristics of picking out in the first place $H_{av.}\hat{1}$ as a member of the set. Each of the following operators will consecutively separate subspaces of the d^2 space from each other and do so without changing the average energy of the split entities. After the final operator has been used, each multiplet is singled out. In the present and the following sub-section we shall generate our most important set of PMT parameters $\{D^S, D^v, E^1, E^0\}$, our standard set.

The parameter $H_{av.}$ is never observable in the present ligand-field context. Moreover, it is not a neat two-electron property since it embodies one-electron energy contributions from the d orbitals. Here it becomes separable in the first place by simple subtraction after Eq. (6) has been used. The complete set of eigenstate energies thereby becomes barycentered. By this choice, only the four observable parameters remain, because the five barycentered multiplet term parameters represent only four independent energy differences.

The method of consecutive generation will now be demonstrated by the chemically most attractive example. At first we want to generate an operator mimicking Hund's first rule [63], that is, the operator that separates the total spins. The action of this operator is graphically illustrated in Fig. 1, where this operator splits the d^2 configuration as a first step.

With the spin triplets and the spin singlets comprising 30 and 15 microstates, respectively, we may choose the number –1 to represent the matrix elements of all the triplet states and the number +2 to represent the singlet states. Thereby we obtain the definition of a coefficient operator that separates the singlets from the triplets, but with no change in their average energy. This condition determines the wanted coefficient operator only up to a constant factor. In Table 1 we have chosen this factor to be $14/21=2/3$ for reasons that will be explained in connection with Eq. (21). We note that a positive value for the energy parameter D^S associated with the new spin separator $\hat{Q}[D^S]$ quantifies Hund's first rule, which states that the ground state multiplet has the maximal total spin multiplicity and therefore must be either ^3P or ^3F. One may parameterize Hund's first rule by the energy difference equation

$$H[S = 0] - H[S = 1] = 2D^S \tag{7}$$

which can be generalized to being valid for all l^q configurations and for every possible value of S, by giving it the form

$$H[S = S_0 - 1] - H[S = S_0] = 2S_0D^S . \tag{8}$$

This equation is Jørgensen's equation for the spin-pairing energy parameter D [64, 65], which he defined in the framework of the SCS model where the PMT parameter D^S becomes D.

We have now generated $D^S\hat{Q}[D^S]$, which is the only observable operator of the present set whose domain is the whole d^2 space. All the operators to follow will
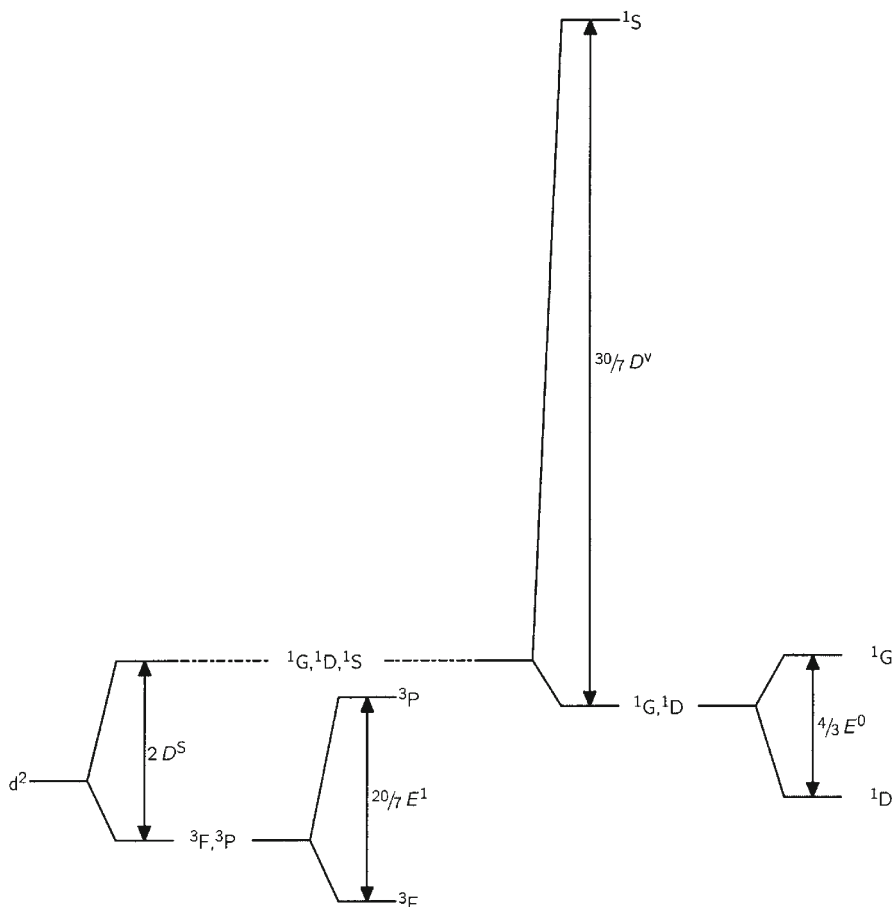
Fig. 1 The splitting of the d^2 or d^8 configurations due to the interelectronic interaction. In order to illustrate the parametrical multiplet term model (PMT), we imagine the splitting of the configuration described in terms of the parameters associated with our barycentered, orthogonal set of four coefficient operators, $\{\hat{Q}[D^S], \hat{Q}[D^v], \hat{Q}[E^1], \hat{Q}[E^0]\}$, to be taking place in four consecutive steps. The first two steps represent a quantification of Hund's first and second rule; the last two steps quantify the remaining splittings, which eventually lead to the four energy differences of the five multiplet terms making the operator set complete. The abscissa is abstract in the sense that all the four terms will always be simultaneously present

act non-trivially only on subspaces. They will be orbital in character and all included in the operators of type $\alpha\hat{L}^2$ acting on different subspaces[2]. We proceed with an operator to mimic Hund's second rule. This is the second step of Fig. 1. This operator shall separate the two spatially different terms ^3P and ^3F to give ^3F with the higher L value the lowest energy for a positive value of its parameter E^1, where the superscript refers to the total spin S=1. Since our starting point is

---

[2] This operator acting on the full d^q space was originally proposed by Trees [66] as an energy operator extending the SCS model.

a situation where the triplets are degenerate, the operator in question must not change their average energy. As in the previous example, the matrix elements required must have opposite signs and their absolute values must be inversely proportional to the degeneracy numbers of the terms that have to be separated. Hence the ratio of the matrix elements should be equal to 7/(–3). Again our choice is found in Table 1.

There is an important conclusion at this intermediate stage of the development of the complete set of PMT operators by the method of consecutive generation. We have looked at the average energy of all the d^2 states, at the average energy of all the (S=1)-states, and at the energy separation within these states. Our results may be explicitly expressed in three equations:

$$H_{av.} = \frac{1}{45} \left(H_S + 9H_P + 5H_D + 21H_F + 9H_G \right) \tag{9a}$$

$$H_{av.} [P, F] = H_{av.} - (2/3)D^S \tag{9b}$$

$$H_P - H_F = (20/7)E^1 \tag{9c}$$

The last two of these are Hund's-rules equations. These play an active role in this chapter's connection with transition metal chemistry and ligand-field theory. These equations have the same form in the SCS model. Later we present our arguments for focusing on the highest spin multiplicities, that is, on S=S$_{max}$. It will be revealed that Hund's-rules computations based upon the above three equations will suffice for most chemical purposes aiming at mimicking LFR by KS-DFT.

2.5
Consecutive Operator Generation. B: Seniority and Separation of the Spin Singlets

In the Racah description of multiplet terms, an additional symmetry determined quantum number, called seniority and denoted by v, appears as a consequence of a group-theoretical analysis based upon viewing the 1024 microstates of the d^q configurations as an entity. We do not need to worry about this analysis here but we do need to know a little about seniorities. Seniority numbers are integer quantum numbers associated with multiplet terms. They are never higher than q. For the d^0 system there is only one state, the multiplet term ^1S with seniority v=0. For the d^1 system there is also only one multiplet term, ^2D with seniority v=1. However, for d^2 the first non-trivial situation occurs. The ^1S term is now said to have the seniority zero because a ^1S term has already been met in the d^0 configuration. The other multiplet terms of Eq. (1) have not been met before, neither for d^0 nor – for reasons of spin multiplicity – for d^1. All these multiplet terms have accordingly seniorities of v=q=2. It is a general empirical result that lower seniorities have higher expectation values of the Hamiltonian, but the eigenstates have mixed seniorities for 2<q<8.

We now return to the remaining operators, which lift the degeneracy of the singlets. In order to proceed with the operator generation, we first require an operator that separates ^1S from the other singlets comprising altogether 14 micro-

states. This is the third step of Fig. 1. An operator barycentered on the singlets is obtained by choosing the ratio between the matrix elements associated with ^{1}S and the rest of the singlets equal to $(14)/(-1)$. Our choice of definition for the parameter D^v is given in Table 1.

At this stage we still have degeneracy of the two singlet terms ^{1}D and ^{1}G. Lifting this degeneracy is the final step of Fig. 1. It should no longer be a problem to write down the relative matrix elements for the remaining operator whose parameter we designate by E^0 (Table 1) and whose sign has been chosen to be positive in accordance with the experimental energy order of ^{1}D and ^{1}G.

We have now completed the alternative parameterization of the PMT Hamiltonian of Eq. (4), which reads

$$\hat{H}_{\text{PMT}} = H_{\text{av.}}\,\hat{1} + D^S \hat{Q}\,[D^S] + D^v \hat{Q}\,[D^v] + E^0 \hat{Q}\,[D^0] + E^1 \hat{Q}\,[E^1] \qquad (10)$$

The two forms of the PMT Hamiltonian of Eqs. (4) and (10) are equivalent: The five operators of Eq. (10) span the same operator space on d^2 as do the multiplet term operators of Eq. (4). Therefore, in a fitting of data to these two sets of parametrical operators, the variances and corresponding minima will be the same. This equivalence and other similar equivalences have some practical and conceptual ramifications, which will be important unifying factors of the present chapter. We shall call the parameterization of Eq. (10) our standard parameter set of the PMT, since it will turn out below and in Table 25 to have special properties in a KS-DFT context.

2.6
The Spin Separation Operator $\hat{S}^2$ and the Orbital Separation Operator $\hat{L}^2$

The two D-type operators presented in the preceding two subsections function as spin and seniority separators and when they are carried over to the domain of d^q for $2<q<8$, they still span the whole spin and seniority space. However, the two E-type operators function as orbital separators, separating multiplet terms with the same seniority and the same total spin, but with different L, and they only span a subspace of the complete set of orbital separators. In other words, the E operators are spatial operators and remain so for $2<q<8$.

In discussing the model concept of intraconfigurational energies, we shall in the rest of this chapter always give the higher priority to the spin and seniority energy separators, which we name class separators, while the spatial energy separators will be called subclass separators. We shall see eventually as an empirical as well as a computational result that the class separators alone produce a root mean square splitting of d^q which is approximately 1.5 times the one produced by the subclass operators.

The spin-separating operator acting on the full d^2 space, may be written in the form $\alpha^S \hat{S}^2$, which requires a negative value for the energy parameter α^S for Hund's first rule to be obeyed. With this definition $\alpha^S \hat{S}^2$ gives $H[S=1]=S(S+1)\alpha^S= 2\alpha^2$ and $H[S=0]=0$ and thus according to Eq. (7),

$$-\alpha^S = D^S \ (\alpha^S<0) \qquad (11)$$

The sign of α^S is defined by the choice of coefficient operator, $\hat{S}^2$, while the sign of D^s and the other PMT parameters of Eq. (10) are in Table 1 defined positive in accordance with experiment.

The remaining barycentered operators of the PMT model of Eq. (10) have no overlap with $\hat{S}^2$. Instead they have overlaps with the Trees [66] operator $\alpha_L \hat{L}^2$ and have therefore been named orbital separators.

The conglomerate operator $E^1 \hat{Q} [E^1]$ is a spatial as well as an orbital separator and can be written as $\alpha_L^1 \hat{L}^2$ giving $H_P = 2\alpha_L^1$ and $H_F = 3(3+1)\alpha_L^1 = 12\alpha_L^1$ and thus

$$-\alpha_L^1 = \frac{1}{10}(H_P - H_F) = \frac{6}{21}E^1 = \frac{3}{2}B^1 \ (\alpha_L^1 < 0) \tag{12}$$

where B^1 is the well-known Racah parameter B determined on the basis of the [S=1]-states only (cf. also Table 1).

The second spatial as well as orbital separator $E^0 \hat{Q} [E^0]$ can be written as $\alpha_L^0 \hat{L}^2$ giving $H_D = 6\alpha_L^0$ and $H_G = 20\alpha_L^0$ and thus

$$-\alpha_L^0 = \frac{1}{14}(H_G - H_D) = \frac{2}{21}E^0 = \frac{1}{2}B^0 \ (\alpha_L^0 < 0) \tag{13}$$

The seniority operator is an orbital separator, which splits one state with L=0 from two states, one with L=2 and one with L=4. A parallel definition of a seniority type Trees parameter would therefore be: $H_S = 0\alpha_L^v$ and

$$H_{av.}[D, G] = \frac{1}{14}(5 \times 6\alpha_L^v + 9 \times 20\alpha_L^v) = 15\alpha_L^v \text{ and thus according to Table 1,}$$

$$-\alpha_L^v = \frac{1}{15}(H_S - H_{av.}[D, G]) = \frac{6}{21}D^v \ (\alpha_L^v < 0) \tag{14}$$

2.7
Orthogonal Operators and the PMT Model in this Context

The two complete sets of operators giving the PMT Hamiltonian in Eqs. (4) and (10) are not chosen for their illustrative properties alone. The operators within each set also have the property of being mutually orthogonal [17].

We talk about the overlap of operators, which is an analogue to the scalar product, well known from vectors and functions. For two operators $\hat{U}$ and $\hat{V}$, acting on the same domain and expressed in the same function basis, the overlap is defined by

$$\langle \hat{U} | \hat{V} \rangle = \text{Tr}(\hat{U}^\dagger \hat{V}) = \text{Tr}(\mathbf{U}^\dagger \mathbf{V}) = \sum_{ij} \mathbf{U}_{ji}^\dagger \mathbf{V}_{ij} = \text{(for real matrices)} \sum_{ij} \mathbf{U}_{ij} \mathbf{V}_{ij} \tag{15}$$

where the bold face letters are matrix representations of the operators. The overlap of Eq. (15) is a basis-independent quantity. The overlap of operators is as useful for our applications as is the general concept of overlap between functions. The area or self-overlap of an operator is obtained from Eq. (15) by choosing $\hat{U} = \hat{V}$. The positive square root of the area is the length or norm of the operator. The length of the coefficient operator and the value of its associated parameter

are inversely proportional. The conglomerate operator carries the chemistry of the problem and is therefore invariant to these conventions.

The overlap (scalar product) also introduces the concept of angles (cf. Table 26). The angle between $\hat{U}$ and $\hat{V}$ can conventionally be derived from the expression

$$\cos(\hat{U},\hat{V}) = \frac{\langle\hat{U}|\hat{V}\rangle}{\langle\hat{U}|\hat{U}\rangle^{1/2}\langle\hat{V}|\hat{V}\rangle^{1/2}} \tag{16}$$

The operators of the PMT model, for each of the forms in Eqs. (4) and (10), all have angles of 90° between them. We say that each set consists of mutually orthogonal operators on th 45 dimensional d^2 space and, of course, on the 5-dimensional degeneracy-weighted space.

For the multiplet term parameter form of the PMT model given in Eq. (4), the orthogonalities follow directly from the fact that each operator acts nontrivially only upon its own subspace, a multiplet term. The operators of the PMT model derived by the consecutive generation method (Eq. 10) also form an orthogonal set. This is achieved by the particular procedure by which they were constructed. The orthogonalities of two operators of the set are easily checked using the coefficients and weights from Table 1, e.g., for $\hat{1}$ and $\hat{Q}[D^S]$:

$$\langle\hat{1}|\hat{Q}[D^S]\rangle = (1)\left(-\frac{2}{3}\right)\times30 + (1)\left(\frac{4}{3}\right)\times15 = 0 \tag{17}$$

Suppose one knows the conglomerate term $D^S\hat{Q}[D^S]$ of the Hamiltonian of Eq. (10), then take this term and form the scalar product with the coefficient vector $\hat{Q}[D^S]$ of Table 1 remembering the weights, and one obtains $\langle D^S\hat{Q}[D^S]|\hat{Q}[D^S]\rangle = (280/7)D^S$.

In other words: to know one *term* in an orthogonal parametrical Hamiltonian is to know the *parameter* of that term. Now, the known term $D^S\hat{Q}[D^S]$ can alternatively be written as

$$D^S\hat{Q}[D^S] = \hat{H}_{PMT} - D^v\hat{Q}[D^v] - E^1\hat{Q}[E^1] - E^0\hat{Q}[E^0] \tag{18}$$

Similarly, taking the scalar product of both sides of Eq. (18) with the coefficient operator $\hat{Q}[D^S]$ yields

$$(280/7)D^S = \langle\hat{H}_{PMT}|\hat{Q}[D^S]\rangle \tag{19}$$

where the other terms of the right hand side vanish because of the mutual orthogonality of the different coefficient operators. Equation (19) attains a more general form by writing

$$D^S = \frac{\langle\hat{H}_{PMT}|\hat{Q}[D^S]\rangle}{\langle\hat{Q}[D^S]|\hat{Q}[D^S]\rangle} = \left\langle\hat{H}_{PMT}\left|\frac{\hat{Q}[D^S]}{\langle\hat{Q}[D^S]|\hat{Q}[D^S]\rangle}\right.\right\rangle \equiv \langle\hat{H}_{PMT}|\hat{Q}[D^S_{gen}]\rangle \tag{20}$$

defining the parameter-generating coefficient operator $\hat{Q}[D^S_{gen.}]$.

Equation (20) illustrates the general fact that if the model Hamiltonian is known – and that means its matrix is known in some defined function basis –

then the parameter of any coefficient operator *of an orthogonal set* is also known in this basis. This is true for the coefficient operators of Table 1 or any linear combination of the four operators that leads to a complete orthogonal parameterization scheme for $\hat{H}_{PMT}$.

The use of mutually orthogonal operators, whenever possible, is preferable as emphasized throughout this chapter[3].

2.8
Slater-Condon-Shortley Parameters, Racah Parameters, and Parameters Based Upon Orthogonal Operators. The Concept of Sum-Square-Splitting

The classical Slater choice of parameter set $\{F^0, F^2, F^4\}$ for expressing the two-electron integrals did not take into account spin degeneracy. It was expressed in terms of integrals over products of the radial factors of the d orbitals multiplied by the interelectronic repulsion operator in its explicit form, that is, as consequences of a truly physical model. Nobody worried about operators in the abstract, but yet much more practical sense, which we use today. Nevertheless, the classical parameters can immediately be expressed as conglomerate operators and if this is done, their coefficient operators are not mutually orthogonal on d^2. However, they are in fact mutually orthogonal on the 25 dimensional spin free d^2 space, or in other words, when each multiplet term is weighted by (2L+1) rather than (2L+1)(2S+1).

The PMT model contains the entire symmetry information about the eigenstates of the d^2 configuration without the fine structure. This information results in five parameters, while the SCS model contains only three parameters. The SCS model reduces the number of parameters by two, for example by parameterizing the spin splitting and the seniority splitting using only a single parameter D and the two spatial splittings by another parameter E. The following equations:

$$D = D^S = D^v \quad \hat{Q}[D] = \hat{Q}[D^S] + \hat{Q}[D^v]$$
$$E = E^1 = E^0 \quad \hat{Q}[E] = \hat{Q}[E^1] + \hat{Q}[E^0] \tag{21}$$

then express the parameter condition for the PMT model to degenerate into the SCS model. The areas of $\hat{Q}[D]$ and $\hat{Q}[E]$ are (400/7) on d^2 and by the orthogonality of the PMT operators, the areas of $\hat{Q}[D^S]$ and $\hat{Q}[D^v]$ sum up to the area of $\hat{Q}[D]$ and the areas of $\hat{Q}[E^1]$ and $\hat{Q}[E^0]$ to that of $\hat{Q}[E]$. These area relations and the parameter relations between the two models are the reasons for choosing the proportionality factors of the individual columns (diagonal elements) of the operators of Eq. (10) the way we did in Table 1.

The parametrical expressions of Eq. (21) can be inserted in Eq. (9) associating the SCS model parameters D and E with Hund's first and second rules,

---

[3] An analogy to the d functions on which our one-electron operators operate may take us right into chemistry; one would rarely see anybody choose the d functions as the set $\{z^2–x^2, y^2–z^2, yz, zx, xy\}$, in which the first two members overlap, even though it has the convenient property of its members all having the same shape.

respectively. They can also be inserted in Eqs. (7) and (8) to obtain Jørgensen's expressions [65] for the spin-pairing energy parameter D.

We have already touched upon the analogy between operators and vectors. We can illustrate Eq. (21) geometrically by thinking about the $\hat{Q}[D^S]$ and $\hat{Q}[D^v]$ operators as orthogonal vectors (of different lengths, equal to the square root of the operators' areas; Table 1) adding up to $\hat{Q}[D]$
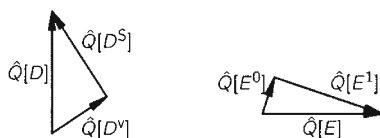
Analogous considerations apply to $\hat{Q}[E^1]$ and $\hat{Q}[E^0]$, but these are orthogonal to the $\hat{Q}[D]$ plane, and the sketch should in fact be four-dimensional.

The $D\hat{Q}[D]$ and $E\hat{Q}[E]$ conglomerate operators are connected to the Racah parameters and corresponding barycentered coefficient operators by the following equations:

$$
\hat{D} = D\hat{Q}[D] = \left(\frac{7}{6}C + \frac{35}{12}B\right)\left(\frac{6}{7}\hat{Q}[C]\right)
$$

$$
\hat{E} = E\hat{Q}[E] = \left(\frac{21}{4}\right)B\left[\left(\frac{-10}{21}\right)\hat{Q}[C] + \left(\frac{4}{21}\right)\hat{Q}[B]\right]
$$

(22)

By this construction it turns out that while the $\hat{Q}[D]$ and $\hat{Q}[E]$ coefficient operators are orthogonal and of the same length, $\hat{Q}[C]$ and $\hat{Q}[B]$ are neither:
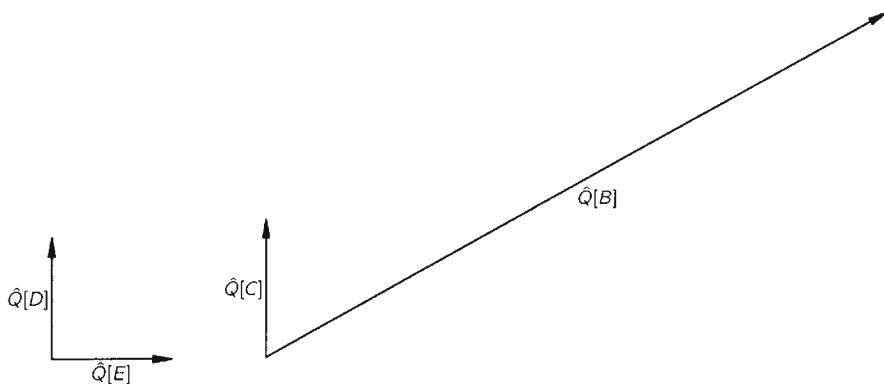
The conglomerate operators, however, still add up to the same the SCS Hamiltonian (dashed vector):
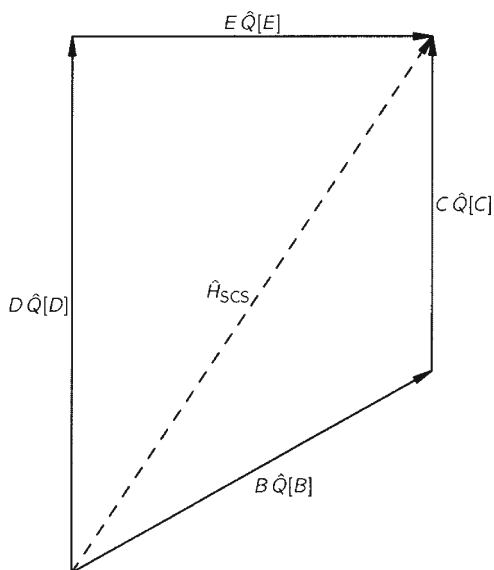
where it may be noted from Eq. (22) that $\hat{Q}[D]$ and $\hat{Q}[C]$ are proportional and therefore have been drawn as parallel vectors.

In view of the interpretation of the conglomerate operator $D\hat{Q}[D]$ as a spin and seniority operator and its associated parameter and of $E\hat{Q}[E]$ as the corresponding spatial combination, it is noteworthy that nothing like a similar interpretation can be given of Racah's parameters and their associated coefficient operators. While Racah's parameter B is proportional to the spatial parameter E and thus represents purely spatial energy differences, its coefficient operator is not interpretable in any simple way. On the other hand, the coefficient operator associated with Racah's parameter C, that is, $\hat{Q}[C]$, is proportional to $\hat{Q}[D]$ and therefore is a pure spin and seniority operator, but when $\hat{Q}[C]$ and $\hat{Q}[B]$ are used together the associated parameter contains the parameter B that represents spatial energy differences. In other words, the association between parameters and coefficient operators is much more complex in Racah's parametrical scheme even though the main idea is contained in his scheme. The combination [24] of Jørgensen's spin-pairing energy parameter D and Racah's parameter B simplifies this association and thereby provides us with the possibility of visualizing what both parameters represent in terms of eigenenergies. An even more attractive parameterization of the SCS model [24] is that using D and E whose values are directly comparable because their associated coefficient operators have the same area. Note that the vectors $\hat{Q}[D]$ and $\hat{Q}[E]$ have the same length in the sketches.

Since the area of an operator is basis invariant (cf. Eq. 15), the barycentered SCS Hamiltonian is equal to the sum of the squares of the barycentered SCS eigenenergies of all the microstates, and has therefore been called the sum square splitting (SSS, here SSS_{SCS}). The orthogonality of the coefficient operators has

conceptually simplifying ramifications for the sum square splitting, which becomes separable into parts that are associated with the individual parameters whereas using Racah parameters leads to cross product terms in the parameters

$$SSS_{SCS} = 1[^{112}/_{21}D]^2 + 9[^{22}/_{21}D + {}^{10}/_{21}E]^2 + 5[^{22}/_{21}D - {}^{18}/_{21}E]^2$$
$$+ 9[-{}^{14}/_{21}D + 2E]^2 + 21[-{}^{14}/_{21}D - {}^{18}/_{21}E]^2 \tag{23}$$
$$= {}^{400}/_7(D^2 + E^2) = {}^{400}/_7\rho^2$$

$$SSS_{SCS} = {}^{700}/_9 C^2 + {}^{3500}/_9 BC + {}^{18550}/_9 B^2 \tag{24}$$

In Eq. (23) the ratio $((400/7)(D)^2)/[SSS_{SCS}]=D^2/\rho^2$, for example, measures the fraction of the sum square splitting that is due to the spin and seniority part of $\hat{H}_{SCS}$ whereas a similar distribution upon the Racah parameters requires additional assumptions about the distribution of the overlap part. From spectroscopic data [24] the ratio $\eta=D/E$ was found to be close to 1.50 for all the atomic ions of the first transition series. This ratio corresponds to $C/B=4.25$ for which the fraction of SSS_{SCS} contained in the cross product term of Eq. (24) is as much as 0.32. Thus, Eq. (23) illustrates a new kind of individuality of the parameters, which is the consequence of the association of the parameters and their coefficient operators when these form an orthogonal set.

In conclusion, all the advantages of the Racah parameterization scheme have been conserved in the scheme described here, first of all the important conservation of a single parameter to account for the energy separation of the terms of maximum spin multiplicity. The additional advantages are that the important spin-pairing energy parameter D, which has been in the literature for more than 40 years as an extraneous quantity [67–69], has now been incorporated in its natural context. Moreover, by the use of the orthogonal coefficient operator's scheme, Racah's transparency in the definition of his parameter B has now been extended not only to the SCS model but also all the way to the PMT model (cf. Fig. 1).

2.9
Other Methods of Generating Useful Versions of the PMT Model. Relationships to the SCS Model

We saw above that the D-type and E-type operators span mutually orthogonal operator spaces, both of which are two-dimensional. Therefore, instead of letting spin/seniority separation and spatial separation represent by $\hat{Q}[D]$ and $\hat{Q}[E]$ as in the SCS model, or by $\{\hat{Q}[D^S], \hat{Q}[D^v]\}$ and $\{\hat{Q}[E^0], \hat{Q}[E^1]\}$ as in the PMT model, we can extend the operator set $\{\hat{Q}[D], \hat{Q}[E]\}$ spanning the SCS model with two new operators $\hat{Q}[D^\perp]$ and $\hat{Q}[E^\perp]$ so as to make the resulting set span the PMT model.

$\hat{Q}[D^\perp]$ completes the spin/seniority separation and $\hat{Q}[E^\perp]$ the spatial separation in orthonormal ways.

Hereby, we have obtained yet another version of the PMT model: $\hat{Q}[D^\perp]$ and $\hat{Q}[E^\perp]$ of Table 3 combined with $\hat{Q}[D]$ and $\hat{Q}[E]$ of Table 1. This version is useful because the energy parameters $D^\perp$ and $E^\perp$ are invariably numerically small since they represent corrections to the SCS model, which by itself accounts rather well for the experimental results. In this case we may write in operator form

$$\hat{H}_{PMT} = \hat{H}_{SCS} + \hat{H}_{SCS\perp}, \quad \langle \hat{H}_{SCS} | \hat{H}_{SCS\perp} \rangle = 0 \tag{25}$$

with the following inequalities applying:

$$\langle \hat{\hat{H}}_{SCS\perp} | \hat{\hat{H}}_{SCS\perp} \rangle \ll \langle \hat{\hat{H}}_{SCS} | \hat{\hat{H}}_{SCS} \rangle$$
$$0 < |D^\perp| \ll D \tag{26}$$
$$0 < |E^\perp| \ll E$$

as opposed to the equalities of Eq. (21), which make the PMT model identical to the SCS model.

The D- and E-spaces are independent of the formulation of the PMT model as illustrated in the following sketch[4]:
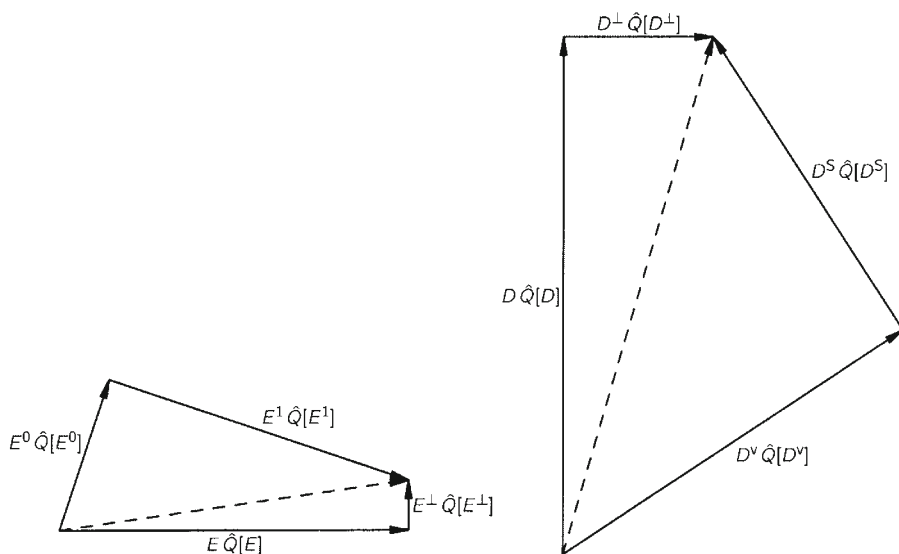
The two formulations of the PMT model, however, serve different purposes: while the one given in Table 1 provides direct information about the relative positions of the multiplet terms, this latter one provides direct information about the magnitude of the deviations from the SCS model. This is achieved by the fact that the SCS$^\perp$ parameters are an orthogonal supplement to the SCS model and that the areas of all coefficient operators involved are 400/7 (cf. Table 3).

---

[4] In the sketch, the sizes of the SCS$^\perp$ parameters are exaggerated as compared to experimental ones.

Table 3 Additional partial sets of orthogonal coefficient operators to be combined appropriately with the operators of Table 1. The two first columns of coefficients represent an alternative set of spin and seniority operators (D-type operators) of the PMT model, the second ones an alternative set of spatial operators (E-type operators). The third pair of coefficient columns contains an orthogonal supplement to the SCS model extending it to the PMT model

Energies	Weights	$\hat{Q}[D^{v'}]$	$\hat{Q}[D^{S'}]$	$\hat{Q}[E^L]$	$\hat{Q}[E^R]$	$\hat{Q}[D^\perp]$	$\hat{Q}[E^\perp]$
H_S	1	112/21	0	0	0	$-{}^{24}/_{21}\sqrt{21}$	0
H_G	9	–28/231	270/231	–10/21	20/21	${}^{6}/_{21}\sqrt{21}$	30/21
H_D	5	–28/231	270/231	18/21	–36/21	${}^{6}/_{21}\sqrt{21}$	–54/21
H_P	9	–28/231	–126/231	14/21	28/21	$-{}^{2}/_{21}\sqrt{21}$	–14/21
H_F	21	–28/231	–126/231	–6/21	–12/21	$-{}^{2}/_{21}\sqrt{21}$	6/21
$\langle\hat{Q}\|\hat{Q}\rangle$		2240/77	2160/77	80/7	320/7	400/7	400/7

The relationships between the two sets of PMT parameters are

$$D = (7/10)D^S + (3/10)D^v$$
$$E = (9/10)E^1 + (1/10)E^0$$
$$D^\perp = (\sqrt{21}/10)(D^S - D^v) \tag{27}$$
$$E^\perp = -(3/10)(E^1 - E^0)$$

These values of D and E may also be obtained by a least squares fitting of the five weighted multiplet-term-energies to the PMT model, or by projection using expressions like the one given in Eq. (20). The SCS parameters are the ones to be supplemented by the SCS$^\perp$ parameters to obtain the PMT model.

2.10
Orthogonality and Non-Orthogonality of Effective Repulsion Operators

Earlier we gave priority to spin in order to allot to the first operator $\hat{Q}[D^S]$ the quantification of Hund's first rule. We could equally well have chosen to give priority to seniority in which case the operators $\hat{Q}[D^{v'}]$ and $\hat{Q}[D^{S'}]$ would have been our alternative orthogonal choice for the two-dimensional D-type subspace (Table 3). These operators lie in the D part of the PMT operator space, but only when used together do they complete the spin and seniority space orthogonally.

Any other spin and seniority coefficient operator but $\hat{Q}[D^v]$ will supplement $\hat{Q}[D^S]$ non-orthogonally, but it will still do it in a complete way. A single example will show almost absurd consequences of these facts. If $\hat{Q}[D^S]$ and $\hat{Q}[D^{S'}]$ are chosen to span the D-type space, the fitting of data will still reach the same minimum of variance, as that of the orthogonal pair $\{\hat{Q}[D^S], \hat{Q}[D^v]\}$. However, since $\hat{Q}[D^S]$ and $\hat{Q}[D^{S'}]$ are almost parallel, the two parameters are strongly correlated. Therefore, with gaseous Ni^{2+} as an example, the parameter values will be without simple relation to the physics that they should represent. Whereas the $\{\hat{Q}[D^S], \hat{Q}[D^v]\}$-fitting gives $[D^S, D^v]=[0.822, 0.758]$, that is, both parameters obtain the
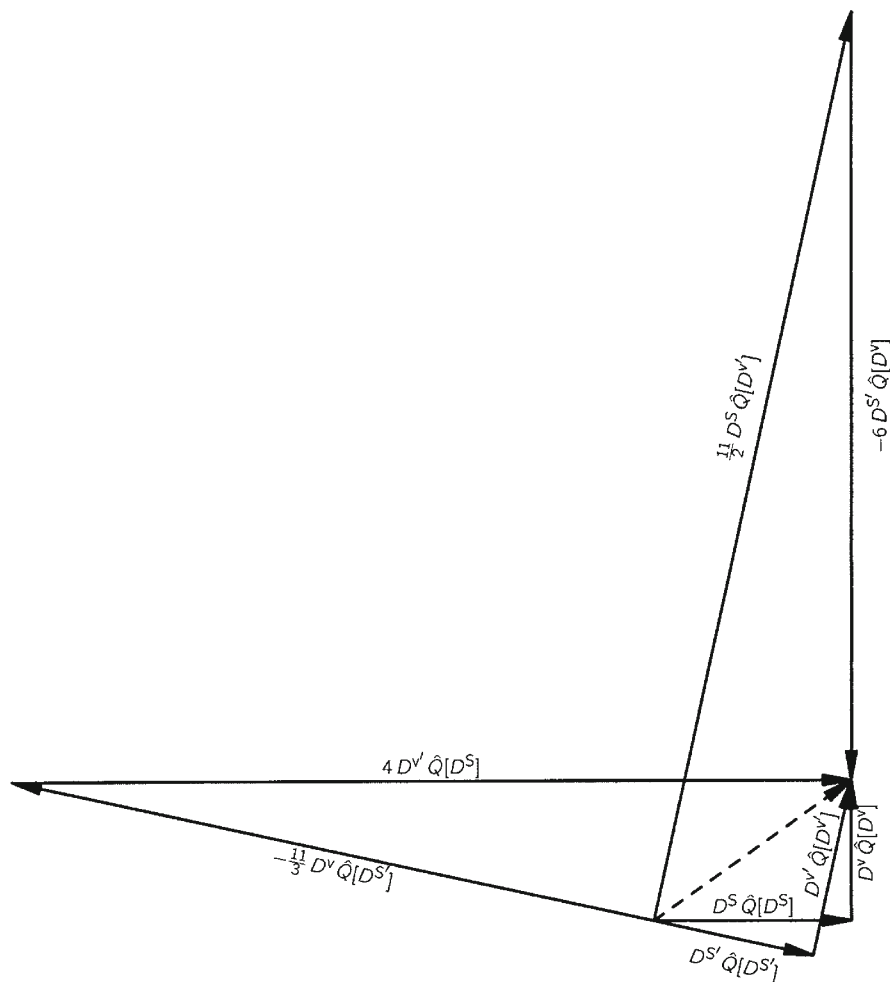
Fig. 2 The *dashed-line* vector represents the D-part of the PMT Hamiltonian. Four pairs of vectors are four different operator representations. The components within the $\{\hat{Q}[D^S], \hat{Q}[D^v]\}$ and the $\{\hat{Q}[D^{S'}], \hat{Q}[D^{v'}]\}$ sets (Tables 1 and 3) are orthogonal and the sets are related by a linear transformation, which after normalization would degenerate into an orthogonal one. The combination of two non-orthogonal components, e.g., $\{\hat{Q}[D^S], \hat{Q}[D^{S'}]\}$ results in a reproduction of the same D-part of the Hamiltonian by parameters, whose meaning is non-transparent. They are in fact proportional to $D^{v'}$ and D^v, respectively. However, the directions of $\hat{Q}[D^S]$ and $\hat{Q}[D^{S'}]$ are determined and the whole diagram can be constructed geometrically

SCS value for D with minor numerical modifications, the non-orthogonal fitting gives the strange values $[D^S, D^{S'}]=[3.096, -2.780]$. However, the two parameter-sets still result in the same Hamiltonian as illustrated in Fig. 2.

In the figure, the values of D^S and $D^{S'}$ are re-found, but not by using their corresponding coefficient operators together but rather by using the orthogonal complements $\hat{Q}[D^{v'}]$ and $\hat{Q}[D^v]$, respectively. As seen, it is not possible to construct a

model that combines parameters having non-orthogonal coefficient operators without losing either the original meaning of the parameters or the intuitive appearance of the coefficient operators. Parameter correlation is desirable only when enforced by a truly physical model giving the parametrical Hamiltonian, and only then should one accept to use mutually non-orthogonal operator sets.

2.11
Interelectronic Repulsion and Nephelauxetism. Consequences of Operator Non-Orthogonality and Associated Parametrical Correlation

Even though science is not history, it often serves a purpose in itself to go back to the roots of a matter. In this particular case of the discussion of the multiplet terms of a d^2 configuration, it is, in the formulation used here, almost obvious that the configurational splitting into multiplet terms is a two-electron operator phenomenon: for a given atomic system we have an inert core on top of which two d electrons reside; and these two electrons have an one-electron energy and a mutual repulsion, also called the interelectronic repulsion, which is a sharply defined physical phenomenon.

Here it serves a multiple purpose to go back to Slater: his model is a real physical model, where the core is a really inert central field and the d orbitals are genuine d orbitals with a radial function separable from the angular one and all the d electrons with the same radial function. The repulsion operator can then be expanded in multipole terms and the repulsion energies expressed as products of angular factors that can be calculated exactly and radial integrals that can be computed if the radial functions are known. This is of interest here because our aim is to apply Slater's atomic model on molecular systems: conventional ligand-field theory (LFR) is, though parametrical, an atomic theory as far as interelectronic repulsion is concerned. LFR differs from the parametrical atomic theory by exhibiting invariably considerably lowered repulsion parameters for chemical entities as compared with their corresponding atomic ions, that is, the d electron *cloud* in complexes exhibits an apparent *expansion* (nephelauxetism). Because of the spherical symmetry of the Hamiltonian modeling the repulsion, it was not unexpected to find discrepancies between theory and experiment when the application was extended to non-spherical molecular systems.

Such a particular discrepancy was thought to be found in the phenomenon, particularly noted by Jørgensen, that so-called ruby lines, which are spin-forbidden transitions in Cr^{III} complexes in the 1.4 μm^{-1} region, were invariably hypsochromic (shifted to higher energy) relative to their expected positions on the basis of the repulsion parameters calculated from the spin-allowed transitions of the same complex. This would seem to be a clear cut systematic discrepancy, were it not for the fact that the spin-allowed transitions only allow one of the two repulsion parameters to be determined, the Racah parameter B, whereas the spin-forbidden transitions involve the other one as well, and to a dominant extent. Therefore, in order to interpret the above-mentioned general phenomenon in the way it was done, a fixed ratio between the numerical values of the two repulsion parameters had to be assumed. For different atomic ions different ratios of F^2/F^4 might be expected because of the different radial func-

tions associated with their d orbitals, but actually this ratio, or equivalently C/B or D/E, is found empirically to be fairly invariant. This is true for the computationally determined ratios as well (Table 27), and extremely so for the atomic ions (Table 26). Jørgensen's implicit assumption at this point is therefore likely to be justified [3].

Jørgensen put forward a qualitative explanation for the ruby-line phenomenon. He said that the ruby-line transition only involved t_{2g} electrons that could not for reasons of symmetry form σ bonds and therefore should be less covalently involved than the e_g electrons, which are occupied in the excited states of the spin-allowed transitions. The ruby line is an intrasubconfigurational transition, $t_{2g}^3 \rightarrow t_{2g}^3$, and therefore, in the cubic strong-field approximation, it is independent of the orbital energy difference between the t_{2g} and e_g electrons and only dependent on the repulsion parameters describing the t_{2g} subshell. Jørgensen now associated this reasoning with the original interpretation of nephelauxetism: the less covalent, the less nephelauxetic. Thereby he arrived at the additional relation, valid for these spin-forbidden transitions: they should be blue-shifted relative to the position predicted parametrically on the basis of knowledge from the spin-allowed transitions of the same chemical species. However, because of the necessary strong-field approximation and the assumption about a constant ratio between the observable Racah parameters on going from atom to chemical species, Jørgensen was not able to express his ideas in a quantitative extension of the ligand-field model.

Ferguson did not agree with Jørgensen and claimed that the SCS model was to be taken as a genuine physical model rather than a parametrical model. On this basis it is immediately seen from the Slater expressions for the radial parameters that the two parameters have a different radial dependence. However, Ferguson made his detailed arguments based upon a fitting of data somewhat fuzzy by adding to his SCS parameters F^2 and F^4 the so-called Trees' parameter α (see above) and giving this parameter a fixed value taken empirically from atoms. This parameter is unnecessarily strongly correlated with the F^k-parameters because of the lack of mutual orthogonality of their associated coefficient operators and therefore lack of nearly vanishing diagonal orthogonality. Therefore, the Trees parameter is likely to be larger than it ought to be as a correction to the SCS model. In addition, the part of the sum square splitting lying in the overlap region of the conglomerate operators is likely to vary on going from atom to complex. Moreover, since it was not nephelauxetically reduced, Ferguson's arguments became entirely unclear as far as his experimental basis was concerned.

An important point in our criticism of Ferguson is particularly relevant in the present context because it illustrates the general consequence of non-orthogonality (actually, strictly speaking, diagonal non-orthogonality, see below) of coefficient operators, namely that the values of their associated parameters become correlated. Ferguson includes the Trees parameter α when he obtains his values of the parameters F^2 and F^4 for gaseous Cr^{3+}, which are the reference values for obtaining his nephelauxetic ratios. However, the Trees operator $\alpha\hat{L}^2$ is non-orthogonal to $F^2\hat{Q}[F^2]$ and $F^4\hat{Q}[F^4]$ with the result that all the parameters α, F^2 and F^4 become correlated. In fact, if F^2 and F^4 are determined by themselves, the values 7.15 and 4.61 μm^{-1}, respectively, are obtained. However, when α is included

in the fitting, the values are 7.22 and 4.35 μm^{-1}. Thus, the ratio F^2/F^4 changes from 1.55 to 1.66, which weakens Ferguson's arguments because this ratio is crucial for the discrimination between the nephelauxetisms of the spin-forbidden and spin-allowed transitions.

Anyway, historically, Jørgensen's qualitative explanation was accepted, but we are left with some open questions regarding the incorporation of this explanation into quantitative ligand-field theory as well as regarding the details of the explanation for nephelauxetism.

Actually, Jørgensen proposed two explanations for the nephelauxetic phenomenon, which he named central field covalency and symmetry-restricted covalency. The central field covalency was the result of a genuine nephelauxetism, that is, an expansion of the d orbitals. This covalency he believed was the dominating one, and he used it to give the parametrical d^q model the name of the expanded radial function model. The symmetry-restricted covalency resulted from a dilution of the d orbitals to make them become LCAO-MOs. In the present chapter we shall provide computational evidence that the nephelauxetic phenomenon can be almost quantitatively explained by Jørgensen's symmetry-restricted covalency rather than by his central-field covalency. Therefore the parametrical d^q model seems to be the more appropriate name.

2.12
One-Electron Operators and Full Shell Complementary Configurations.
Spin-Orbit Coupling and Hund's Third Rule. Spectrochemical Splitting

Spin orbit coupling is not the main issue of this review. However, there are several reasons for giving the subject a brief attention. First of all spin orbit coupling must be taken into account when the experimental data for the d^q configurations delivered by the atomic spectroscopists are to be parameterized. Moreover, our discussion will reveal connections and analogies with the other material of this review.

In the preceding sections we developed sets of four two-electron structure operators on d^2, which expanded the two-dimensional space of genuine interelectronic repulsion operators of the SCS model. The members of the new sets might be called effective two-electron operators because they serve to mimic the full structure of the characterizing d^2 configuration (cf. Eq. 1) by a two-electron operator formalism where they act on the complete set of d^2 functions. However, they also represent the energetic consequences of configuration interaction, e.g., those of mixing of s^2 and p^2 configurations into the d^2 configuration as an extension of its Hartree-Fock description.

The classical example of an effective operator is another symmetry-based one, namely $\lambda \, \hat{S} \cdot \hat{L}$, which describes the spin-orbit coupling splitting of an isolated multiplet term ^{2S+1}L of l^q for all q. This splitting can be parameterized by the Landé expression

$$H[J] - H[J-1] = \lambda \, (l^q, vSL) \, J \equiv \lambda J \tag{28}$$

where λ is the effective spin-orbit coupling parameter of the term $^{2S+1}_{\ \ \chi}L$ (it is instructive to compare Eq. 28) with those of the separation operators $\alpha^S \hat{S}^2$ and $\alpha_L \hat{L}^2$

dealt with earlier). For the highest spin multiplicity terms $^{2S_{max}+1}L$ and a genuine d^q ($q < 2l+1$) configuration, the simple relationship

$$\lambda = \zeta_{nd}/2S_{max.} = \zeta_{nd}/q \qquad (29)$$

exists between the one-electron spin-orbit coupling parameter ζ_{nd}, that is, the λ value of ^2D of d^1, which is always positive, and the λ value of the particular term $^{2S_{max}+1}L$ of d^q.

Earlier we discussed Hund's two first rules. However, there exists yet another general rule about p^q, d^q, and f^q configurations, which is often referred to as Hund's third rule. This rule is concerned with the relative energies of the fine-structure components $^{2S+1}L_J$ of the ground term. It says, subject to the first two of Hund's rules being obeyed: the lowest J has the lowest energy for the less than half filled l-shell and the highest J has the lowest energy for the more than half filled shell. For $S = S_{max.}$ and $q > 2l+1$, there is a change of sign of λ in Eq. (29) on going from d^q to d^{10-q} because ζ_{nd} is always positive. Equation (29) then reads as $\lambda = -\zeta_{nd}/2S_{max}$.

The PMT model was developed by theoretical atomic spectroscopists, who wanted a model for quantitatively mimicking the data assigned to belong to the classifying or effective d^2 configuration [26]. They also wanted a model involving only mutually orthogonal operators and were able to accomplish both, by using a hierarchy of Lie groups to encompass up to ten equivalent d electrons, that is, all d^q configurations containing altogether $1024 = 2^{10}$ states [27]. Their parameterization model was supposed to take into account all the various factors influencing the energy differences within the characterizing d^q configuration. The PMT model is based upon the picture of the configuration where the basis is limited by degenerate states of $^{2S+1}_v L$ type. Hansen and Judd [28] extended this model as far as to cover also the fine-structure in a complete way, giving the degenerate eigenbasis of $^{2S+1}_v L_J$ type. We introduced a compromise, the PMTζ model, which was a sum of the PMT model and well-known spin-orbit coupling as the best chemically acceptable model to define – for a given atomic system – the energies of the multiplet terms as well as of the one-electron spin orbit coupling parameter. The values of one-electron spin orbit coupling parameters ζ_{nd} based upon this model for analyzing the data provided by the atomic spectroscopists were published previously [50]. Later we shall use the same experimental data to derive the PMT parameters for the effective atomic configurations d^2 and d^8.

We need to mention some important properties regarding operator orthogonalities. All structure operators, that is, two-electron operators and ligand-field operators, are orthogonal to all fine-structure operators, which may be one-electron- or two-electron operators [28]. This is because these two classes of operators act on different spaces. Moreover, one-electron structure operators, such as ligand-field operators, are orthogonal to two-electron structure operators, such as the PMT ones [50]. The Hamiltonian of the parametrical d^q model may be written as

$$\hat{H}[d^q] = \hat{H}_{LFRSO} = \hat{H}_{LF} + \hat{H}_R + \hat{H}_{SO} \qquad (30)$$

where the ligand-field term, the repulsion term, which may be the one of the PMT model, and the spin-orbit coupling term are mutually orthogonal. In the present chapter we shall only use sub-Hamiltonians of $\hat{H}_{\text{LFRSO}}$. For the treatment of atomic spectroscopic data, we shall use $\hat{H}_{\text{PMTSO}} = \hat{H}_{\text{PMT}\zeta}$ and for the mimicking of $\hat{H}_{\text{LFR}}$ by using KS-DFT "data", we shall use $\hat{H}_{\text{LFPMT}}$ and $\hat{H}_{\text{LFSCS}}$.

2.13
Historical Remarks Regarding the Ligand Field Itself

The scientific history of a subject is often simultaneously the story about the development of the subject and about the retarding effect of the prehistory at any given time. Ligand fields illustrate this clearly.

Mainly based upon measurements of absorption spectra of pentaammine cobalt(III) complexes, the spectrochemical series of the ligands sitting in the sixth coordination position had been established before crystal-field theory (CFT) and ligand-field theory (LFT) entered chemistry. This fact has had an impeding influence upon the conceptual development of LFT.

Thus, in Ballhausen and Moffitt's early discussion [70] of the identification of the tetragonal split components of cubic complexes, the ligand-field parameter Dq of the cubic complex corresponding to a cubic coefficient operator was supplemented by the parameters Ds and Dt corresponding to superimposed operators of linear symmetry. These authors wanted to emancipate themselves from the point charge and point dipole electrostatic models, which gave additive ligand fields. They introduced a purely symmetry-based LFT, that is, a non-additive LF with respect to the individual ligand contributions. With their choice of parameters, they obtained cubic states with energies depending on Dq, whose splitting could be described by the parameters Ds and Dt. However, in addition, the cubic states suffered an energy shift that depended on Dt, but not on Ds. In other words, the Dt parameter contained a cubic contribution as well as the tetragonal one, it was designed for. The Dq parameter thus did not represent the whole cubic field. If the situation is described by the additive LF, that is, if the individual ligands give their own independent contributions to the ligand field, the energy of the transition $xy \rightarrow x^2 - y^2$ is equal to 10 Dq or Δ referring to the equatorial ligands only. Thereby, the attempted transition from the additive to the non-additive view was hampered by history, and the lack of distinction between the two views has continued to create ambiguousness.

Conversely, Yamatera, in his pioneer contributions [4, 71] to what became the angular overlap model (AOM), started out from non-additive LF views in the form of MO theory and created an additive LF model. Again with the homoleptic hexaammine cobalt(III) complex as his reference system, perturbed by the difference in bonding properties of the other substituents in the orthoaxial ligand sphere.

In connection with the use of the AOM as an additive LF model, projection of symmetry-determined, that is non-additive, parameters again became an issue [8], but it was not until later that rational methods [11, 72, 73] were gradually developed based upon orthogonal ligand-field operators [17, 19], probably introduced into chemistry by Soliverez [72].

3
Values of the Empirical Parameters Derived from Data Reduction of the d^2 and d^8 Configurational Results of Atomic Spectroscopy

3.1
The Conceptual and the Practical Background for the Analysis of the Spectroscopic Data

The splitting and mixing of the configurations by two-electron operators give the multiplet term structure $^{2S+1}$L. This structure is further split by fine-structure operators giving the levels $^{2S+1}$L$_J$. These operators further mix J levels of different multiplet terms before the eigenstates are obtained. One of these fine-structure operators, the one-electron spin orbit coupling, is the overwhelmingly dominant one.

The data provided by atomic spectroscopy are the energies of the J levels. Except for the third transition period or for very high ionic charges, the complete set of eigenenergies of the characterizing configurations d^2 and d^8 can be labeled as $(^3F)_2$, $^3F_3$, $(^3F)_4$, $(^1D)_2$, $(^3P)_0$, $^3P_1$, $(^3P)_2$, $(^1G)_4$, $(^1S)_0$ where the multiplet term symbols have been put in parentheses to indicate that they are only approximate in their meaning. These nine J-levels provide the nine pieces of data that form the empirical basis for the use of the atomic spectroscopic results in chemistry where they are modeled as if they belonged to pure configurations that are split by interelectronic repulsion and spin orbit coupling.

The conventional way of using these data in chemistry is their modeling by a fitting to a combination of the SCS model and spin orbit coupling:

$$\hat{H}_{SCS\zeta} = \hat{H}_{av.}\hat{1} + D\hat{Q}[D] + E\hat{Q}[E] + \zeta_{nd}\hat{Q}[\zeta_{nd}] \tag{31}$$

where the usual spin orbit coupling term has been added in its conglomerate operator form. This addition leads to an increase of the configurational area relative to that of $\hat{H}_{SCS}$. The additional area can be quantified by the sum square splitting obtaining the additional term $(\zeta_{nd})^2\langle\hat{Q}[\zeta_{nd}]\hat{Q}[\zeta_{nd}]\rangle = 120(\zeta_{nd})^2$, that is, the area of $\zeta_{nd}\hat{Q}[\zeta_{nd}]$ for d^2. Furthermore, inclusion of spin-orbit coupling makes the least squares fitting procedure non-linear. The Hamiltonian of Eq. (31) is adequate for chemical purposes as far as the number, kind and even values of the parameters are concerned since the SCSζ fitting accounts for most of the experimental sum square area (99.9% for gaseous Ni^{2+}, for example). Nevertheless, the large variance (0.1%) still makes it somewhat deficient because it results in a large standard deviation on the parameters. This is particularly serious for parameters that contribute only a small fraction of the configurational area (sum square splitting). Thus, the standard deviations on the values for the spin orbit coupling parameter ζ_{nd} are, in SCSζ fittings, of the same order of magnitude as the parameter values themselves [for gaseous Ni^{2+}, for example, ζ_{3d}=0.0675(0.0228) μm^{-1}].

Because of this unsatisfactory situation, we devised the PMTζ model [50] as an alternative to the SCSζ model. The PMTζ model, which for example for gaseous Ni^{2+} brought down the variance by a factor of 1160, gave satisfactorily small standard deviations on ζ_{nd} for all the d^q configurations [for Ni^{2+}, ζ_{3d}= 0.06675(0.00085) μm^{-1}] and at the same time, as a byproduct, it provided accurate values for the energies of the multiplet terms. These values are probably the best

possible representatives of what might be called empirical values for the energies of the multiplet terms. They are the parameters H_L of Eq. (4).

Once empirical values for the energies H_L are available, the finding of values for the parameters of all the parameterization schemes of the PMT model (Tables 1–3) is an easy linear problem. However, in practice we have always gone back to the level data and since the distinction between the two approaches is conceptually revealing, we briefly discuss the non-linearity problem.

3.2
The Non-Linearity of the Treatment of Level Data of the Configurations d² and d⁸. Experimental PMTζ Results

Looking at the configuration d² from the multiplet term side, one may characterize the J levels by saying that they are the result of a combined spin-orbit splitting of the multiplet terms into J components and a spin-orbit mixing of multiplet terms through levels having the same value for their J label. The splitting is linear in the one-electron parameter ζ_{nd} while the energy changes due to the mixing[5] roughly depends on $(\zeta_{nd})^2$.

The parameterization of data on d^q atomic ions takes place by using the PMTζ model. The data are interpreted as the eigenstates of this model, that is, when the splitting of d^q into multiplet terms and their levels and the mixing of these levels have taken place. The starting point is the PMTζ model in the setup Russell-Saunders basis, $^{2S+1}L_J$, and the problem is to find the PMT and ζ parameters, which result in the appropriate eigenvalues. This is a non-linear regression problem, which is the more non-linear the larger the value of ζ relative to the values of the PMT parameters, that is, chemically, the higher atomic numbers and the higher the charges of the ions.

In the context of the least squares data reduction, the non-linearity requires an iterative process where the function basis changes in each step of the process ending up with the eigenbasis, which is somewhere intermediate between the $^{2S+1}L_J$ setup basis and a jj basis. It is, however, not this eigenbasis, which is in focus. It is the set of energy parameters that leads to this eigenbasis by diagonalization of the parametrical energy matrix.

The parametrical energy matrix was set up in a ^{2S+1}L basis above. This basis was convenient for the definition of the PMT and the SCS models and it is essentially parameters that are associated with this basis, which we aim at obtaining in this chapter – either from experiment or by computation. When the 45×45 energy matrices in the ^{2S+1}L and $^{2S+1}L_J$ bases are written as parametrical sums, the terms containing the structural parameters are identical for these two bases, which are both symbols for eigenbases of the interelectronic repulsion operator or any other spherically symmetrical two-electron operator.

---

[5] We note in parentheses that for general d^q, the effective two-electron operators of the PMT model can still be grouped into D-type and E-type terms (cf. Fig. 1) but the E terms will for 2<q<8 contribute non-diagonal matrix elements connecting repeated multiplet terms of d^q with different seniorities. Thereby, these multiplet terms will be mixed by the E-type repulsion operators, which thus contribute to the non-linearity of the data reduction problem. In this review, however, we restrict ourselves to discuss data for d² and d⁸ only.

The values determined for the PMT parameters on the basis of spectroscopic data using the PMTζ model in the non-linear regression analysis are collected together in Tables 4–7.

The zero point of energy in Tables 4–7 is that chosen by the atomic spectroscopists, that is, the ground level of the d^q configuration. According to Hund's three rules, this is $(^3F)_2$ for d^2 and $(^3F)_4$ for d^8. This means that the energies of the F terms are slightly higher than $4\lambda[d^2,{}^3F]=2\zeta_{nd}$ for d^2 and $-3\lambda[d^8,{}^3F]=(3/2)\zeta_{nd}$ for d^8, these expressions being the spin-orbit stabilization of the ground term ^3F according to Landé's interval rule. The Landé parameter λ is for the highest spin multiplicity given by $\lambda=\zeta_{nd}/2S$ for d^2 and $S=1$. Since the ground levels are different, the multiplet term energies for d^2 and d^8 are not quantitatively comparable when the zero point of energy is that of Tables 4–7. However, the parameters of

Table 4 Multiplet term energies for $3d^2$ systems. Experimentally determined values for the energies in μm^{-1} of the multiplet terms. The atomic spectroscopists provide the complete set of J levels that can be labeled $(^{2S+1}L)_J$, where the parentheses indicate that the terms are impure when the configuration contains repeated J values. The J levels have been parameterized by the combination of the multiplet term parameters H_L of Table 2 and the one-electron spin orbit coupling parameter ζ_{nd}. A non-linear regression analysis has led to the tabulated values. This data treatment was designed to obtain the best available determination of the spin-orbit coupling parameters but it has served here primarily to obtain values defining the energies of the multiplet terms. These multiplet terms ^{2S+1}L are strictly speaking not observable quantities. However, they have been conceptually important in physics and inorganic chemistry for two generations. By using the data of this table together with Eq. (20), any parameter of a complete mutually orthogonal PMT set of conglomerate operators can be found as the scalar product of a column of this table and the renormalized coefficient column of Tables 1–3 associated with the parameter in question

$3d^2$	Ti	V	Cr	Mn	Fe	Co
H_P	1.065	1.333	1.582	1.827	2.073	2.325
H_F	0.024	0.043	0.067	0.098	0.137	0.186
H_S	3.247	4.245	5.113	5.923	6.702	7.416
H_D	0.848	1.099	1.325	1.545	1.766	1.992
H_G	1.440	1.839	2.201	2.550	2.891	3.233
ζ_{4d}	0.0118	0.0206	0.0319	0.0466	0.0649	0.0873

Table 5 Multiplet term energies for $3d^8$ systems. See legend of Table 4

$3d^8$	Ni	Cu	Zn
H_P	1.661	1.960	2.245
H_F	0.102	0.140	0.186
H_S	5.246	6.133	6.972
H_D	1.435	1.669	1.902
H_G	2.309	2.668	3.055
ζ_{3d}	0.0668	0.0911	0.1203

Table 6 Multiplet term energies for $4d^2$ systems. See legend of Table 4

$4d^2$	Zr	Nb	Mo	Ta	W
H_P	0.852	1.044	1.226	1.468	1.788
H_F	0.089	0.141	0.204	0.570	0.782
H_S	2.391	3.162	3.755	3.320	4.109
H_D	0.578	0.861	1.069	1.123	1.534
H_G	1.103	1.377	1.629	1.766	2.138
ζ_{nd}	0.0409	0.0646	0.0921	0.2254	0.3093

Table 7 Multiplet term energies for $4d^8$ systems. See legend of Table 4

$4d^8$	Pd	Ag	Cd
H_P	1.268	1.489	1.699
H_F	0.246	0.318	0.401
H_S	4.117	4.635	5.176
H_D	1.211	1.405	1.598
H_G	1.774	2.037	2.294
ζ_{4d}	0.1556	0.1997	0.2496

the barycentered PMT model are fully comparable because of the isomorphism of d^2 and d^8 as far as two-electron operator matrix elements are concerned.

3.3
The Consanguinity of the Orthogonal Operators Formalism and the Components of Variance of the Least Squares Machinery

When modeling of data is performed using a least squares merit function, the concept of operator orthogonality obtains particular conceptual importance. Considering that this approach aims at minimizing the selfoverlap of a matrix, namely the diagonal matrix representing the residual (difference between experiment and model), it is not surprising that the use of the orthogonal operators formalism illuminates the whole fitting process.

Once a function basis is given, it is useful to view operator overlaps and self-overlaps as consisting of a diagonal part and a non-diagonal one. For two different operators one can then talk about diagonal overlap, which determines the correlation between the associated parameters in a least squares regression analysis. The associated parameters of two operators that have zero diagonal overlap are thus completely uncorrelated.[6] Unlike the overlap between two ope-

---

[6] It is important to emphasize that this is not in general true for mutually orthogonal matrices and although the use of orthogonal parameterization schemes has been advocated on the basis that they lower parameter correlation they do not rigorously minimize parameter correlation.

rators, the diagonal part of the overlap is not invariant to changes of the function basis. If the analysis is a non-linear one and thus requires a multistep iterative procedure, the basis changes in each step and thereby the diagonal overlaps and the correlations change. The special significance of the diagonal part of the matrix representations in the fitting process follows naturally from the fact that the experiment in all model bases is represented by a diagonal matrix. The experiment being external to the model has in the fitting process no operator character and its overlap (equal to the diagonal overlap) with all coefficient matrices of the model Hamiltonian changes throughout an iterative fitting process. The driving forces (to first order) for parameter changes in an iterative fitting process are also expressible in terms of diagonal matrix overlaps, namely those of the residual matrix and the individual coefficient matrices of the Hamiltonian. Hence, in a fitting minimum, all matrix representations of the coefficient operators are diagonally orthogonal to the residual matrix, which implies orthogonal because the residual matrix is a diagonal matrix.

By dividing self-overlap into a diagonal part and a non-diagonal part, it becomes natural to introduce the degree of diagonality of an operator in a given basis as the ratio between its diagonal area and the total area of the operator. This measure is of obvious importance since the reciprocal diagonal self-overlap and the variance of the associated parameter are proportional. In the extreme case, a completely non-diagonal matrix representation prevents the associated parameter from being determined in a linear fit. Thus, when modeling interelectronic repulsion in complexes by KS-DFT, the higher complexity of the chemical system compared to atoms is not the only obstacle; the repulsion parameters become less well defined by the lower degree of diagonality of their associated coefficient operators.

Consider a set of *barycentered* experimental data, analyzed by as complete a model as desired. This leaves us with a total sum square splitting (SSS; the area of the experiment), which is the sum of the areas of the conglomerate operators of the model and the variance (the area of the residual). This simple picture follows from the diagonal orthogonality of the residual to all the involved coefficient matrices in the eigenbasis of the fit (cf. the comments above concerning driving force for parameter changes). Removing one of the conglomerate operators from the model will shift part of its area (the amount depending on parameter correlation) from the SSS_{model} to the variance. Alternatively, this picture can be viewed from the other side as a building up process: initially the complete $SSS_{experiment}$ is contained in the variance. Adding operators to the model and fitting to the experiment will shift area from the variance to the SSS_{model}. In this formulation, the construction of a model from orthogonal operators and its fitting to experimental data obeys what resembles a variational principle since $SSS_{experiment}$ represents an upper limit on SSS_{model}. In the case of a linear model this consanguinity between least squares and areas of mutually orthogonal operators becomes complete.

4

The d² Spin Triplet States. Real Orbitals and Real Slater Determinants

4.1
Background for the Discussion of (S=S_max)-states Separately

There are a number of reasons for discussing the triplet states of the d^2 and d^8 configurations (and the quartets states of the d^3 and d^7 configurations) first and separately.

– First of all, in the applications of the repulsion model in ligand-field theory, the energy difference between ^3P (^4P) and ^3F(^4F), parameterized by 15 *B*, has always been the main issue. The parameter *B* was in play in the spin-allowed transitions of all the d^3 systems and the d^8 systems of Ni^{II}, for which the Tanabe-Sugano energy diagrams are identical. These systems gave the chemically most varied contributions to our knowledge of the repulsion parameter reduction that occurred in all complexes. Moreover, octahedral complexes of the d^6 systems resemble in their observable spectroscopy corresponding d^3 systems, and they also, even though they are low-spin systems, deliver repulsion information mainly about the spatial parameter *B*.
– Second, the highest spin multiplicities are special for all configurations by embracing the ground states of their atomic ions (Hund's first rule, see Fig. 1).

The following two reasons are more special for the main issue of this chapter, namely the application of our whole conceptual framework to KS-DFT.

– Occupation numbers of spin orbitals, which make up the input for KS-DFT, may lead to situations that represent a collection of determinants corresponding to a set of simultaneous eigenstates of the spin operators $\hat{S}^2$ and $\hat{S}_z$ for highest spin multiplicity (S=1, $|M_S|$=1) whereas these inputs do not correspond to eigenfunctions of $\hat{S}^2$ in general.
– Finally, within the subspace of the spin triplets, it is unconditional and obvious that the d^2 symmetry-based treatment in the general effective-operator scheme is equivalent to the Slater-Condon-Shortley model whereas this is a more covert fact in the case of the spin singlets (see Sections 5 and 6).

4.2
Real Spherical Harmonics dλς as Basis Orbitals

The real spherical harmonics [10, 12, 13], which make up the angular factors of the usual atomic orbitals used in chemistry, are mutually orthogonal functions over the surface of the sphere. They are accordingly functions of the polar coordinates, θ and φ, and they are adapted to linear symmetry (linear harmonics). For the group C_∞ they are bases for the real symmetry species, which are mostly not irreducible representations in this case but which behave as irreducible ones for many practical problems; ligand fields, for example.

The set of real linear surface harmonics, {dσ, dπs, dπc, dδs, dδc} are more familiar when designated by there solid harmonic expressions, {d_{z^2}, d_{yz}, d_{zx}, d_{xy},

$d_{x^2-y^2}$}. They consist of a product of a function of θ alone, which has linear symmetry and depends on l and λ, and a cosine or sine function of $\lambda\varphi$. If this latter factor is a constant one speaks about a σ function, otherwise one speaks about a λ cosine (λc) function and a λ sine function (λs). The association of positive integers and Greek letters is analogous to that of orbital angular momentum in spherical symmetry:

$$\lambda: \begin{matrix} 0 & 1 & 2 & 3 & 4 \\ \sigma & \pi & \delta & \phi & \gamma \end{matrix} \tag{32}$$

However, while the number of l functions is 2l+1, the number of λ functions is one for $\lambda=0$ and two for $\lambda>0$.

We shall need the following tensor product (ordered product) expressions (cf. Eq. 1)

$$\{\lambda_1\} \otimes \{\lambda_2\} = \{\lambda_2\} \otimes \{\lambda_1\} = \{|\Lambda_1 - \Lambda_2|\} \oplus \{|\Lambda_1 + \Lambda_2|\}$$

$$\{\lambda\} \otimes \{\lambda\} = \Sigma \oplus \underline{\Sigma} \oplus \{2\Lambda\}$$

$$\{\sigma\} \otimes \{\lambda\} = \{\lambda\} \otimes \{\sigma\} = \{\Lambda\} \tag{33}$$

$$c \otimes c = s \otimes s = c$$

$$c \otimes s = s \otimes c = s$$

General expressions for the $l\lambda\varsigma$ functions (ς=cos or sin) have been given elsewhere [13].

4.3
Coupling of Two Sets of d Orbitals to Symmetry-Adapt the Individual Orbital Factors of the Spin Triplet Functions

The starting point for DFT is the electronic density distribution. This density distribution is introduced in KS-DFT by the provision of occupation numbers for the Kohn-Sham spin orbitals. When these numbers are chosen to be either zero or one, the situation corresponds to Slater determinants in the orbitals of usual quantum mechanical descriptions. We have found, however, that a real one-electron basis is a symmetry-based requirement. Thus, because the electronic density is the same for the two complex functions $|(M_L,\alpha)(M'_L,\alpha)\rangle = |(2,\alpha)(1,\alpha)\rangle$ and $|(2,\alpha)(-1,\alpha)\rangle$, KS-DFT will associate them with the same energy. However, $|(2,\alpha)(1,\alpha)\rangle$ is a neat F function whereas $|(2,\alpha)(-1,\alpha)\rangle$ consists of 60% ^{3}F and 40% ^{3}P character. This is a serious problem when the focus, as here, is on the energies of the individual multiplet terms. We therefore now aim at obtaining useful energy expressions for Slater determinants based upon the real linear-harmonics orbitals. In order to arrive at this goal, we shall use the symmetry inherent in these orbitals because they are basis functions for symmetry species of the hierarchies of groups:

$$R_{3i} \supset D_{\infty h} \supset D_{4h} \supset D_{2h}$$

$$R_{3i} \supset O_h \supset D_{4h} \supset D_{2h} \tag{34}$$

$$R_{3i} \supset T_d \supset D_{2d}$$

The eigenstates of a spin-free Hamiltonian are eigenfunctions of the operator $\hat{S}^2$ and can be chosen to be eigenfunctions also of $\hat{S}_z$. The present section will discuss the triplet functions of a d^2 configuration and one may think of the symmetrical spin functions then as being $\alpha(1)\alpha(2)=\alpha(2)\alpha(1)$ throughout this section, focusing upon the $(M_S=1)$-subspace of the $(S=1)$-space. Then, a matching orbital function must be antisymmetrical by the Pauli principle, and can therefore be written in determinantal form as for instance $|(d\sigma)(d\pi c)|$. The corresponding d^2 microstate, for instance $|(d\sigma,\alpha)(d\pi c,\alpha)|$, may or may not be an eigenstate of the Hamiltonian, i.e., a pure ^3F or ^3P function, but it is a state bridging between a KS-DFT description of a d^2 system and a conventional description.

As another example we take the tensor product function $(d\sigma)\otimes(d\delta c)$ of two specific linear-harmonics d functions. We may use Eq. (33) to see that this product constitutes a Δ function in tensor product space. Then, from Eq. (1) we may conclude that there may be only $F\Delta$ functions in the antisymmetric part and $D\Delta$ and $G\Delta$ functions in the symmetrical part of this tensor product. This means that if we, as in this section, restrict ourselves to looking at the antisymmetric part by considering the determinantal function $|(d\sigma)(d\delta c)|$, then only the F function remains and we have incidentally picked a single Slater determinant that has the proper symmetry for being an eigenfunction of an atomic d^2 system ($^3F\Delta s$).

In order to quantify the problem, we need the Wigner coefficients, that is, the coupling coefficients of R_3. In Table 17 the coefficients involving all the functions of $A(D_2)$ symmetry have been given in the form of an overlap matrix [15, 17]. The results embodied in this matrix are based upon the following formulas for the coupling coefficients

$$\langle dt_1 dt_2 | LT \rangle = (2L+1) \begin{pmatrix} d & d & L \\ t_2 & t_1 & T \end{pmatrix} = -\langle dt_2 dt_1 | LT \rangle, (L = P,F) \qquad (35)$$

valid in the antisymmetrical part of $d\otimes d$ product space. The analogous expression

$$\langle dt_1 dt_2 | LT \rangle = (2L+1) \begin{pmatrix} d & d & L \\ t_2 & t_1 & T \end{pmatrix} = +\langle dt_2 dt_1 | LT \rangle, (L = S,D,G) \qquad (36)$$

valid in the symmetrical part, is irrelevant in the present section but will be used in the next main section when the spin singlets are under discussion. The ($\blacksquare$) symbol is a 3Γ coefficient (also called a 3Γ symbol), the most important ones of which have been tabulated previously [14, 15]. Our example then runs on like this

$$\langle |(d\sigma)(d\delta c)||F\Delta s \rangle = -1 \qquad (37)$$

where the D and G functions have now vanished. The overlap matrices for the other spatial determinants of all the spin triplet states have been given in Tables 8, 9, 10, 11, which fall in blocks according to D_2 symmetry. We note that two of the determinants are pure $F\Delta$ functions.

With Tables 8–11 at hand, we proceed to set up matrices of the generalized two-electron operator $\hat{g}$, which is used in atomic spectroscopy to parameterize the experimental data on the levels of d^q configurations. This operator has spherical symmetry.

Table 8 Antisymmetrized Wigner coefficient. The number inside this table is the coupling coefficient (overlap) between the antisymmetrized orbital product function indexing the row and the resulting state function indexing the column. Small letters are used for orbitals and capital letters for state functions (cf. eq. (33)) with the exception of the sine and cosine components of the latter. The state function of this table belong to the symmetry species A(D_2) but it has the much higher symmetry FΔs referring to the standard components of the group hierarchy $R_{3i} \supset D_{\infty h}$

A(D_2)	FΔs
$|(\sigma)(\delta c)|$	−1

Table 9 Antisymmetrized Wigner coefficients. The numbers inside this table are coupling coefficients (overlaps) between antisymmetrized orbital product functions indexing the rows and the resulting state functions indexing the columns. The state functions of this table belong to the symmetry species B$_1$(D_2) but they have the much higher symmetries given in the state notation. See also legend of Table 8.

B$_1$(D_2)	PΣ	FΣ	FΔc
$|(\delta c)(\delta s)|$	$-\sqrt{4/5}$	$\sqrt{1/5}$	0
$|(\pi c)(\pi s)|$	$-\sqrt{1/5}$	$-\sqrt{4/5}$	0
$|(\sigma)(\delta s)|$	0	0	1

Table 10 Antisymmetrized Wigner coefficients. The state functions of this table belong to the symmetry species B$_2$(D_2). See also legends of Tables 8 and 9.

B$_2$(D_2)	PΠs	FΠs	FΦs
$|(\sigma)(\pi c)|$	$-\sqrt{3/5}$	$-\sqrt{2/5}$	0
$|(\pi c)(\delta c)|$	$-\sqrt{1/5}$	$\sqrt{3/10}$	$-\sqrt{1/2}$
$|(\pi s)(\delta s)|$	$-\sqrt{1/5}$	$\sqrt{3/10}$	$\sqrt{1/2}$

Table 11 Antisymmetrized Wigner coefficients. The state functions of this table belong to the symmetry species B$_3$(D_2). See also legends of Tables 8 and 9.

B$_3$(D_2)	PΠc	FΠc	FΦc
$|(\sigma)(\pi s)|$	$\sqrt{3/5}$	$\sqrt{2/5}$	0
$|(\pi c)(\delta s)|$	$\sqrt{1/5}$	$-\sqrt{3/10}$	$\sqrt{1/2}$
$|(\pi s)(\delta c)|$	$-\sqrt{1/5}$	$\sqrt{3/10}$	$\sqrt{1/2}$

4.4
Matrices of the Generalized Two-Electron Operator $\hat{g}$ on the d^2 Triplets

The wisdom in expressions such as those exemplified in Eqs. (35) and (36) lies in the fact that the individual terms of the right-hand side, which are symmetry species, i.e., bases for irreducible representations, of R_3, are prevented by symmetry from mutually interacting under the influence of a spherically symmetrical operator. The effective two-electron operator $\hat{g}$ is such an operator whose domain – in the present use of it – is identical to that of the five-dimensional operator space of the PMT model on d^2. Here, where only its action upon the triplet subspace is under consideration, it is parameterized either by the energies H_P and H_F or by their average energy

$$H_{av.}\,[\mathrm{P, F}] = (1/10)(3H_P + 7H_F) \tag{38}$$

together with the parameter E^1 (Table 1 and Eq. 12). Within the triplet space the PMT model is equivalent to the SCS model.

The energy matrices of the operator $\hat{g}$ in the determinantal basis can be directly written down on the basis of the results of Tables 8–11 when it is remembered that the energies of all the component functions of a given L value are equal. We give an example taken from the B_3 overlap matrix

$$\langle|(\mathrm{d}\pi\mathrm{c})(\mathrm{d}\delta\mathrm{s})||\hat{g}||\mathrm{d}\pi\mathrm{s})(\mathrm{d}\delta\mathrm{c})|\rangle$$
$$= \langle {}^1\!/_{\sqrt{5}}\,\mathrm{P\Pi c} - {}^{\sqrt{3}}\!/_{\sqrt{10}}\,\mathrm{F\Pi c} + {}^1\!/_{\sqrt{2}}\,\mathrm{F\Phi c}|\hat{g}| - {}^1\!/_{\sqrt{5}}\,\mathrm{P\Pi c} + {}^{\sqrt{3}}\!/_{\sqrt{10}}\,\mathrm{F\Pi c} + {}^1\!/_{\sqrt{2}}\,\mathrm{F\Phi c}\rangle$$
$$= - {}^1\!/_5\,H_P - {}^3\!/_{10}\,H_F + {}^1\!/_2\,H_F = - {}^1\!/_5(H_P - H_F) = -2b^1 \tag{39}$$

where the following definition

$$b^1 \equiv (1/10)(H_P - H_F) = (6/21)E^1\ (b^1 > 0) \tag{40}$$

sees to it that b^1 is positive when referring to an experiment. The superscripts refer to S=1. If $\hat{g}$ is replaced by $\alpha_L^1\hat{L}^2$ in Eq. (39), one obtains the value $2\alpha_L^1$ for the matrix element in agreement with Eq. (12).

The coefficient to H_P and the two coefficients to H_F of Eq. (39) are the components of the scalar product of the two orthonormal rows corresponding to the two determinants. Accordingly, the sum of these components is vanishing. Similarly, if we had calculated a diagonal element, the analogous components of the self scalar product of the normalized row would add up to unity. These properties of the overlap matrix will prove useful in the next main section, where it will turn out that for reasons of symmetry the coefficients to b^1 are important for the whole d^2 configuration.

In Tables 12–15 we give all the triplet energy matrices in the same form as that of Eq. (39). All the functions possess gerade inversion symmetry and they fall in four symmetry blocks, which have been labeled as symmetry species of the point group D_2. The A(D_2) and B$_1$(D_2) blocks are fully symmetry adapted to the hierarchy $O_h \supset D_{4h} \supset D_{2h}$, a fact that results in A(D_2) being actually of the much higher symmetry FΔs(R_3) A$_2$(O) B$_1$(D_4), the unique B$_1$(D_2) function being FΔc(R_3) T$_2$(O) B$_2$(D_4), and the other B$_1$(D_2) functions T$_1$(O) A$_2$(D_4). The last two statements explain the block form of the B$_1$(D_2) matrix. The first function of each of the two blocks, B$_2$(D_2) and B$_3$(D_2), span together $\Pi(D_\infty)$.

The matrix A(D_2) represents the pure FΔs function with trace of -3 (Tables 8 and 12). The traces of each of the three 3×3 matrices is $+1$, thus confirming that the total trace over the 10-dimensional function space is zero, also in the determinantal basis. The trace of unity for each of the three B matrices is in agreement with the fact that each of these embodies one P component and two F components, (7–3–3=1), according to Tables 8–11. The area of the operator $\hat{Q}[b^1]$ is $3 \times 7^2 + 7 \times (-3)^2 = 210$, calculated from the weak-field matrix. Using the symmetry basis of Tables 8–11 together with the strong-field energy matrix B$_1$(D_2) of Tables 12–15, we calculate the energy of ^{3}P explicitly (in units of b^1)

$$\langle(^1/_{\sqrt{5}}|(d\pi c)(d\pi s)| + {}^2/_{\sqrt{5}}|(d\delta c)(d\delta s)|)|\hat{g}|(^1/_{\sqrt{5}}|(d\pi c)(d\pi s)|$$

$$+ {}^2/_{\sqrt{5}}|(d\delta c)(d\delta s)|)\rangle = {}^1/_5(-1) + {}^4/_5(5) + 2(^1/_{\sqrt{5}})(^2/_{\sqrt{5}})(4) = 7 \qquad (41)$$

It should be noted that a non-diagonal term occurred here. The result can alternatively be obtained by diagonalizing the two by two submatrix of B$_1$(D_2) of Tables 12–15 to obtain the eigenvalues 7 and -3, where the reader may notice that the area of the matrix stays invariant on diagonalization. The example shows that the orthogonal matrices of pure numbers of Tables 8–11 are the matrices connecting the weak-field and strong-field energy matrices. For fully symmetry-adapted function bases, which are not in general neat Slater determinants, these transformation matrices have for d^2 been shown to be the permutationally symmetry-adapted Racah lemma matrices so-called [17].

At this stage it is useful to relate also the area of the coefficient matrix of b^1 to that of E^1 which was discussed above, for example by comparing their energy expressions for ^{3}P, which are 7 b^1=2 E^1. This relationship may be rewritten as

$$b^1 = (2S + 1)(2/21)E^1 \qquad (42)$$

where the first coefficient to E^1 refers to the spin degeneracy. Using the relation $E^1\hat{Q}[E^1] = b^1\hat{Q}[b^1]$ and remembering the spin weighting, we obtain for the area: $\langle\hat{Q}[E^1]|\hat{Q}[E^1]\rangle = 210 \times 3 \times (4/49) = 360/7$ in agreement with Table 1.

4.5
Focus on the Spatial Symmetry

There are some general features that have been illustrated but not emphasized in Tables 12–15. We called them spatial earlier in order to avoid the word orbital, which sometimes is not only ambiguous, but in the context of operators also includes the seniority separator $\hat{Q}[D^v]$.

In the last two main sections we shall use the diagonal elements of Tables 12–15 to compute the parameters $(1/10)(3H_P+7H_F)$ and $(1/10)(H_P-H_F)$ using the ADF package. The first one of these is a sum of $H_{av.}[d^2]$ and a spin and seniority parameter, the second one is spatial. Once these parameters have been computed, the whole energy matrix is available through Tables 12–15. The diagonal elements thus obtain an unusual importance, especially in view of the fact that the degree of diagonality of the total triplet matrix is calculated to be only 11/35 in this determinantal basis.

Table 12 Expectation value of the totally symmetrical two-electron operator $\hat{g}$ with respect to the d^2 triplet state of symmetry A(D_2). This state also has the higher symmetry ^{3}FΔs(R_3) ^{3}A$_2$(O,T_d) ^{3}B$_1$(D_4,D_{2d}), which is the ground state according to Hund's rules. The upper entrance is the energy, written in the notation of the PMT set of Table 2; the lower entrance is the coefficient to the parameter b^1=(6/21)E^1=(1/10)(H_P−H_F), where b^1 and E^1 refer to the barycentered PMT model. The zeropoint of energy is arbitrary for the upper entrance and equal to H_{av}.[S=1]=(1/10)(3H_P+7H_F)=H_{av}.[d^2]−(2/3)D^S for the lower entrance (cf. Table 1). The parameter set {H_{av}.[d^2], D^S, E^1} is used in the text as the Hund's-rules computation. In all our computations, H_{av}.[d^2] is defined relative to the energy obtained by the ADF as the *average-of-configuration* computations. H_{av}.[d^2] cannot be compared with experimental data but its value is found computationally to be close to that of the parameter D^S when the PW91 set of functionals is used

A(D_2)	$|(\sigma)(\delta c)|$
$|(\sigma)(\delta c)|$	H_F −3

Table 13 Energy matrix of $\hat{g}$ with respect to the d^2 triplet states of symmetry B$_1$(D_2). Entrances are as described in the legend to Table 12. The Slater determinant $|(\sigma)(\delta s)|$ has the higher symmetry FΔc(R_3) T$_2$(O, T_d) B$_2$(D_4, D_{2d}). The other B$_1$(D_2) functions transform as T$_1$(O, T_d) A$_2$(D_4, D_{2d}). These statements explain the block form of the B$_1$(D_2) matrix. The first function of each of the two blocks, B$_2$(D_2) and B$_3$(D_2), span together Π($D_{\infty h}$) (Tables 14 and 15). One may observe that each of the three matrices of B(D_2) type involves one P and two F components

B$_1$(D_2)	$|(\delta c)(\delta s)|$	$|(\pi c)(\pi s)|$	$|(\sigma)(\delta s)|$
$|(\delta c)(\delta s)|$	$^4/_5\,H_P + {}^1/_5\,H_F$ 5	$^2/_5\,(H_P - H_F)$ 4	0 0
$|(\pi c)(\pi s)|$	$^2/_5\,(H_P - H_F)$ 4	$^1/_5\,H_P + {}^4/_5\,H_F$ −1	0 0
$|(\sigma)(\delta s)|$	0 0	0 0	H_F −3

Table 14 Energy matrix of $\hat{g}$ with respect to the d^2 triplet states of symmetry B$_2$(D_2). See legends of Tables 12 and 13

B$_2$(D_2)	$|(\sigma)(\pi c)|$	$|(\pi c)(\delta c)|$	$|(\pi s)(\delta s)|$
$|(\sigma)(\pi c)|$	$^3/_5\,H_P + {}^2/_5\,H_F$ 3	$^{\sqrt{3}}/_5\,(H_P - H_F)$ $2\sqrt{3}$	$^{\sqrt{3}}/_5\,(H_P - H_F)$ $2\sqrt{3}$
$|(\pi c)(\delta c)|$	$^{\sqrt{3}}/_5\,(H_P - H_F)$ $2\sqrt{3}$	$^1/_5\,H_P + {}^4/_5\,H_F$ −1	$^1/_5\,(H_P - H_F)$ 2
$|(\pi s)(\delta s)|$	$^{\sqrt{3}}/_5\,(H_P - H_F)$ $2\sqrt{3}$	$^1/_5\,(H_P - H_F)$ 2	$^1/_5\,H_P + {}^4/_5\,H_F$ −1

Table 15 Energy matrix of $\hat{g}$ with respect to the d^2 triplet states of symmetry $B_3(D_2)$. See legends of Tables 12, 13 and 14

$B_3(D_2)$	$\|(\sigma)(\pi s)\|$	$\|(\pi c)(\delta s)\|$	$\|(\pi s)(\delta c)\|$
$\|(\sigma)(\pi s)\|$	${}^3/_5\,H_P + {}^2/_5\,H_F$ 3	${}^{\sqrt{3}}/_5\,(H_P - H_F)$ $2\sqrt{3}$	$-{}^{\sqrt{3}}/_5\,(H_P - H_F)$ $-2\sqrt{3}$
$\|(\pi c)(\delta s)\|$	${}^{\sqrt{3}}/_5\,(H_P - H_F)$ $2\sqrt{3}$	${}^1/_5\,H_P + {}^4/_5\,H_F$ -1	$-{}^1/_5\,(H_P - H_F)$ -2
$\|(\pi s)(\delta c)\|$	$-{}^{\sqrt{3}}/_5\,(H_P - H_F)$ $-2\sqrt{3}$	$-{}^1/_5\,(H_P - H_F)$ -2	${}^1/_5\,H_P + {}^4/_5\,H_F$ -1

Table 16 Spatial symmetry coefficients to the energy parameters b^1 and b^0 of the pair inter-action model when this is applied to two-electron functions of real, linear-harmonics orbitals. The four energy classes of this table are named sub-classes because the main energy classes are those separated by spin and seniority parameters. These sub-classes may be symmetry labeled as $\delta\delta$, $\sigma\pi$, $\pi\pi$, and $\sigma\delta$ when it is noted that the $\pi\pi$ sub-class also contains the four $\pi\delta$ interaction terms. This degeneracy is not a symmetry restriction from linear symmetry. It has its origin in the spherical symmetry that lies behind the concept of d orbitals. The energies occur monotonically in the table but a common sign is not symmetry determined. The coefficients can be found in Tables 12–15, 18–22 and their association with the pair-interaction model has been depicted in Fig. 3

Sub-class number	Energy-coefficients	Weights	
1	5	1	$(d\delta c)\otimes(d\delta s)$
2	3	2	$(d\sigma)\otimes(\delta\pi c)$,$(d\sigma)\otimes(d\pi s)$
3	–1	5	$(d\pi c)\otimes(d\pi s)$, $(d\pi c)\otimes(d\delta c)$, $(d\pi c)\otimes(d\delta s)$, $(d\pi s)\otimes(d\delta c)$, $(d\pi s)\otimes(d\delta s)$
4	–3	2	$(d\sigma)\otimes(d\delta c)$, $(d\sigma)\otimes(d\delta s)$

Let us therefore focus on the diagonal elements of Tables 12–15. We note that this energy matrix contains only four different diagonal elements, associated with pairs of d orbitals. These elements give rise to energy subclasses, which, using decreasing numerical values for their ordering, are 5, 3, –1, and –3. These numbers, which serve as the symmetry factors of the coefficients to both spatial energy operators, $E^1\hat{Q}[E^1]$ and $E^0\hat{Q}[E^0]$, turn out to comprise all the spatial energetics of the linear-harmonics one-electron basis. A general diagonal element then has the form of a linear function consisting of $H_{av.}[d^2]$, a constant class term belonging to the spin and seniority space of operators, parameterized by D-type parameters, and a linearly varying subclass term belonging to the spatial operators, parameterized by E-type parameters. The numbers are associated with four energy subclasses of unordered products of harmonics, which are the energy
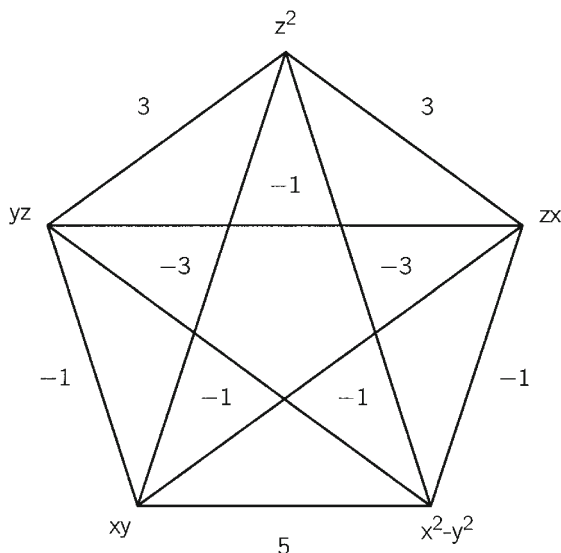
Fig. 3 Symmetry-determined weights for generalized interelectronic interactions (the totally symmetric operator $\hat{g}$) between pairs of real linear harmonics d orbitals. The figure is a geometrical illustration of the results of Table 16. The *sides* and *diagonals* represent pair interaction coefficients to energy parameters, these being b^1 for the (S=1)-states and b^0 for the (S=0)-states

coefficients of Table 16 and Fig. 3. Combined with the weights, the coefficients have the consequence that the barycenter rule is invariably fulfilled.

These symmetry-determined energy coefficients will prove important in the rest of this chapter. With an example from Table 17, we express the expectation value of the spherically symmetrical two-electron operator $\hat{g}$:

$$\langle {}^1\!/_{\sqrt{2}}\,[(\mathrm{d}\sigma)\otimes(\mathrm{d}\delta c) - (\mathrm{d}\delta c)\otimes(\mathrm{d}\sigma)]|\hat{g}|{}^1\!/_{\sqrt{2}}\,[(\mathrm{d}\sigma)\otimes(\mathrm{d}\delta c) - (\mathrm{d}\delta c)\otimes(\mathrm{d}\sigma)]\rangle$$

$$= \langle(\mathrm{d}\sigma)\otimes(\mathrm{d}\delta c)|\hat{g}|(\mathrm{d}\sigma)\otimes(\mathrm{d}\delta c)\rangle - \langle(\mathrm{d}\sigma)\otimes(\mathrm{d}\delta c)|\hat{g}|(\mathrm{d}\delta c)\otimes(\mathrm{d}\sigma)\rangle$$

$$= J^{\text{eff.}}_{(\sigma)(\delta c)} - K^{\text{eff.}}_{(\sigma)(\delta c)} = J^{\text{eff.}}_4 - K^{\text{eff.}}_4 \tag{43}$$

where $J^{\text{eff.}}_{(\sigma)(\delta c)}$ and $K^{\text{eff.}}_{(\sigma)(\delta c)}$ are effective Coulomb and exchange integrals, which degenerate into the corresponding genuine integrals when the operator $\hat{g}$ becomes the conventional interelectronic repulsion operator acting on tensor products of genuine d orbitals:

$$\hat{g} = (\mathrm{r}_{12})^{-1} \tag{44}$$

The integrals of Eq. (43) both belong to the subclass 4 of Table 16 and may accordingly be alternatively denoted by J_4 and K_4. Their symmetry evaluation is easy to illustrate by Table 17. The scalar product of any row or column with itself is of course equal to unity since we are concerned with an orthogonal matrix. If one conceives the components of this product as products of bras and kets, that is, overlaps, the sum of these overlaps is equal to unity. However, if the totally symmetrical operator $\hat{g}$ is included, the sum of the components is equal to the

Table 17 Wigner coefficients transformed into a linear harmonics basis

	SΣ	DΣ	GΣ	FΔs	DΔc	GΔc	GΓc
$(\sigma)\otimes(\sigma)$	$\sqrt{1/5}$	$\sqrt{2/7}$	$\sqrt{18/35}$	0	0	0	0
$(\pi c)\otimes(\pi c)$	$\sqrt{1/5}$	$\sqrt{1/14}$	$-\sqrt{8/35}$	0	$\sqrt{3/14}$	$\sqrt{2/7}$	0
$(\pi s)\otimes(\pi s)$	$\sqrt{1/5}$	$\sqrt{1/14}$	$-\sqrt{8/35}$	0	$-\sqrt{3/14}$	$-\sqrt{2/7}$	0
$(\delta c)\otimes(\delta c)$	$\sqrt{1/5}$	$-\sqrt{2/7}$	$\sqrt{1/70}$	0	0	0	$\sqrt{1/2}$
$(\delta s)\otimes(\delta s)$	$\sqrt{1/5}$	$-\sqrt{2/7}$	$\sqrt{1/70}$	0	0	0	$-\sqrt{1/2}$
$(\delta c)\otimes(\sigma)$	0	0	0	$\sqrt{1/2}$	$-\sqrt{2/7}$	$\sqrt{3/14}$	0
$(\sigma)\otimes(\delta c)$	0	0	0	$-\sqrt{1/2}$	$-\sqrt{2/7}$	$\sqrt{3/14}$	0

J_4 integral. Analogously, if the $\langle|\hat{g}|\rangle$ product of row six and row seven is formed, the result is K_4. These integrals have the explicit expressions

$$J_4^{\text{eff.}} = J_{(\sigma)(\delta c)}^{\text{eff.}} = \langle(\mathrm{d}\sigma)\otimes(\mathrm{d}\delta c)|\hat{g}|(\mathrm{d}\sigma)\otimes(\mathrm{d}\delta c)\rangle \tag{45}$$

and

$$K_4^{\text{eff.}} = K_{(\sigma)(\delta c)}^{\text{eff.}} = \langle(\mathrm{d}\sigma)\otimes(\mathrm{d}\delta c)|\hat{g}|(\mathrm{d}\delta c)\otimes(\mathrm{d}\sigma)\rangle \tag{46}$$

Both integrals degenerate into genuine Coulomb and exchange integrals when Eq. (44) is fulfilled.

J integrals represent non-observable quantities whereas K integrals and differences between J integrals represent quantities that are in principle observable since they correspond to non-diagonal elements or energy differences, which do not depend on the zero point of energy. The subindex 4 of our Eqs. (45) and (46) refers to that particular energy subclass of Table 16 and the specific spatial integrals of J and K type have the specific common subindex $(\sigma)(\delta c)$. The minus sign between the two inherently positive energy quantities J and K is the basis of the conventional explanation for Hund's first rule and allows us to name the triplet class alternatively the $[J–K]$-class.

5
The Spin Singlet States, their Orbital Factors and Energy Matrices

In this section we shall find that the spin singlets of d^2 comprise two classes of expectation values for the Hamiltonian, separated by D-type operators.

We first study the symmetry properties of the symmetrical combinations of the tensor product functions of two different linear harmonics of d type, the $[J+K]$-class. Their associated spin functions will then – because of the Pauli principle – have to be antisymmetrical and thereby eigenfunctions of the $\hat{S}^2$ operator with eigenvalues equal to zero; in other words, they will be neat spin singlet functions (cf. Eq. 36). The spatial situation is analogous to that of the antisymmetrical combinations except for the fact that five functions of a new

Table 18 Energy matrix of the totally symmetrical two-electron operator $\hat{g}$ with respect to the d^2 spin singlet states of symmetry $A(D_2)$. The basis comprises five Slater determinants containing doubly occupied d orbitals plus the symmetrical combination $\mathrm{sym}(\sigma)(\delta c) \equiv \dfrac{1}{\sqrt{2}}\left((\sigma)\otimes(\delta c) + (\delta c)\otimes(\sigma)\right)$ combined with an anti-symmetrical spin function. When diagonalized, the new basis consists of the S, the two D and the three G singlet states given in Table 17. Note that the sum of the coefficients to the energy parameters is unity for the diagonal elements and zero for the non-diagonal ones. This table should be compared with Table 12 for conceptual as well as practical reasons. In using this matrix in connection with the interpretation of the PMT computations of the present paper, it should be united with all the Tables 12–15 plus Tables 19–21

$A(D_2)$	$(\sigma)\otimes(\sigma)$	$(\pi s)\otimes(\pi s)$	$(\pi c)\otimes(\pi c)$	$(\delta s)\otimes(\delta s)$	$(\delta c)\otimes(\delta c)$	$\mathrm{sym}\,(\sigma)(\delta c)$
$(\sigma)\otimes(\sigma)$	$^1/_5 H_S + ^2/_7 H_D + ^{18}/_{35} H_G$	$^1/_5 H_S + ^1/_7 H_D - ^{12}/_{35} H_G$	$^1/_5 H_S + ^1/_7 H_D - ^{12}/_{35} H_G$	$^1/_5 H_S - ^2/_7 H_D + ^3/_{35} H_G$	$^1/_5 H_S - ^2/_7 H_D + ^3/_{35} H_G$	0
$(\pi s)\otimes(\pi s)$	$^1/_5 H_S + ^1/_7 H_D - ^{12}/_{35} H_G$	$^1/_5 H_S + ^2/_7 H_D - ^{18}/_{35} H_G$	$^1/_5 H_S - ^1/_7 H_D - ^2/_{35} H_G$	$^1/_5 H_S - ^1/_7 H_D - ^2/_{35} H_G$	$^1/_5 H_S - ^1/_7 H_D - ^2/_{35} H_G$	$-^{\sqrt{6}}/_7 (H_G - H_D)$
$(\pi c)\otimes(\pi c)$	$^1/_5 H_S + ^1/_7 H_D - ^{12}/_{35} H_G$	$^1/_5 H_S - ^1/_7 H_D - ^2/_{35} H_G$	$^1/_5 H_S + ^2/_7 H_D + ^{18}/_{35} H_G$	$^1/_5 H_S - ^1/_7 H_D - ^2/_{35} H_G$	$^1/_5 H_S - ^1/_7 H_D - ^2/_{35} H_G$	$+^{\sqrt{6}}/_7 (H_G - H_D)$
$(\delta s)\otimes(\delta s)$	$^1/_5 H_S - ^2/_7 H_D + ^3/_{35} H_G$	$^1/_5 H_S - ^1/_7 H_D - ^2/_{35} H_G$	$^1/_5 H_S - ^1/_7 H_D - ^2/_{35} H_G$	$^1/_5 H_S + ^2/_7 H_D + ^{18}/_{35} H_G$	$^1/_5 H_S + ^2/_7 H_D - ^{17}/_{35} H_G$	0
$(\delta c)\otimes(\delta c)$	$^1/_5 H_S - ^2/_7 H_D + ^3/_{35} H_G$	$^1/_5 H_S - ^1/_7 H_D - ^2/_{35} H_G$	$^1/_5 H_S - ^1/_7 H_D - ^2/_{35} H_G$	$^1/_5 H_S + ^2/_7 H_D - ^{17}/_{35} H_G$	$^1/_5 H_S + ^2/_7 H_D + ^{18}/_{35} H_G$	0
$\mathrm{sym}\,(\sigma)(\delta c)$	0	$-^{\sqrt{6}}/_7 (H_G - H_D)$	$^{\sqrt{6}}/_7 (H_G - H_D)$	0	0	$^4/_7 H_D + ^3/_7 H_G$

type arise from the product functions of two identical d functions. These all belong to the symmetry species $A(D_2)$, which also includes the particular product functions $(d\sigma) \otimes (d\delta c)$ and $(d\delta c) \otimes (d\sigma)$. All these functions already appeared in Table 17, from where the whole $A(D_2)$ energy matrix of $\hat{g}$ can be derived. The $F\Delta$ function does not appear here because it is the antisymmetrical combination of $(\sigma) \otimes (\delta c)$ and $(\delta c) \otimes (\sigma)$.

We begin with an example analogous to that of Eq. (43):

$$\langle (^1/_2)^{1/2} [(d\sigma) \otimes (d\delta c) + (d\delta c) \otimes (d\sigma)] | \hat{g} | (^1/_2)^{1/2} [(d\sigma) \otimes (d\delta c) + (d\delta c) \otimes (d\sigma)] \rangle$$

$$= \langle (d\sigma) \otimes (d\delta c) | \hat{g} | (d\sigma) \otimes (d\delta c) \rangle + \langle (d\sigma) \otimes (d\delta c) | \hat{g} | (d\delta c) \otimes (d\sigma) \rangle$$

$$= J^{\text{eff.}}_{(\sigma)(\delta c)} + K^{\text{eff.}}_{(\sigma)(\delta c)} = J^{\text{eff.}}_4 + K^{\text{eff.}}_4. \tag{47}$$

The difference is in the plus sign rather than the minus sign between the J and the K integrals and thereby the higher energy by $2K_4$. We shall call this energy class within the spin singlets the $[J+K]$-class.

The matrices of the totally symmetrical two-electron operator $\hat{g}$ on the spatial spin singlet functions are given in Tables 18–21 in the parameters H_S, H_D, and H_G and in Table 22 in the parameters $H_{\text{av.}}$, D^S, D^v, and $b^0 = (2/21) E^0$, where we remember that $\hat{Q}[D^S]$ is global on d^2 but $\hat{Q}[D^v]$ and $\hat{Q}[E^0]$ act non-trivially only within singlet space. Thus the latter two operators are observable within singlet space but D^S is not an observable either within this subspace or within triplet space. D^S requires knowledge (Table 1) about the average energies, $H_{\text{av.}}[S=1]$ and $H_{\text{av.}}[S=0]$.

Table 19 Energy matrices of $\hat{g}$ with respect to the singlet states of symmetries $B_1(D_2)$. The upper entrances are energy quantities given in the notation of Table 2 which refers to the $^{2S+1}$L eigenenergies. The lower entrances are spatially symmetry-determined coefficients to the positive parameters $b^0 = (2/21)E^0 = (1/14)(H_G - H_D)$, where b^0 and E^0 refer specifically to the singlets (S=0) and to the PMT model, their positive signs being invariably in agreement with spectroscopic results. In the use of the energy matrices, the relationships $H_{\text{av.}}[G,D] = (1/14)(9H_G + 5H_D) = H_{\text{av.}}[d^2] + (4/3)D^S - (2/7)D^v$ (Table 1), which involve only spin and seniority observables, must be used. One may observe that each of these matrices involves one ^{1}D and two ^{1}G components, the remaining two D components and three G components having $A(D_2)$ symmetry and belonging to the matrix of Table 18 (cf. Table 17). See also legends to Tables 12–15 and 18

$B_1(D_2)$	sym$(\delta c)(\delta s)$	sym$(\pi c)(\pi s)$	sym$(\sigma)(\delta s)$
sym$(\delta c)(\delta s)$	H_G	0	0
	5	0	0
sym$(\pi c)(\pi s)$	0	$^4/_7 H_G + {}^3/_7 H_D$	$\frac{2\sqrt{3}}{7} (H_G - H_D)$
	0	-1	$4\sqrt{3}$
sym$(\sigma)(\delta s)$	0	$\frac{2\sqrt{3}}{7} (H_G - H_D)$	$^3/_7 H_G + {}^4/_7 H_D$
	0	$4\sqrt{3}$	-3

Table 20 Energy matrices of $\hat{g}$ with respect to the singlet states of symmetries $B_2(D_2)$. See also legend of Table 19.

$B_2(D_2)$	sym(σ)(πc)	sym(πc)(δc)	sym(πs)(δs)
sym(σ)(πc)	$^6/_7\,H_G + {}^1/_7\,H_D$ 3	$-^{\sqrt{3}}/_7\,(H_G - H_D)$ $-2\sqrt{3}$	$-^{\sqrt{3}}/_7\,(H_G - H_D)$ $-2\sqrt{3}$
sym(πc)(δc)	$-^{\sqrt{3}}/_7\,(H_G - H_D)$ $-2\sqrt{3}$	$^4/_7\,H_G + {}^3/_7\,H_D$ -1	$-^3/_7\,(H_G - H_D)$ -6
sym(πs)(δs)	$-^{\sqrt{3}}/_7\,(H_G - H_D)$ $-2\sqrt{3}$	$-^3/_7\,(H_G - H_D)$ -6	$^4/_7\,H_G + {}^3/_7\,H_D$ -1

Table 21 Energy matrices of $\hat{g}$ with respect to the singlet states of symmetries $B_3(D_2)$. See also legend of Table 19.

$B_3(D_2)$	sym(σ)(πs)	sym(πc)(δs)	sym(πs)(δc)
sym(σ)(πs)	$^6/_7\,H_G + {}^1/_7\,H_D$ 3	$-^{\sqrt{3}}/_7\,(H_G - H_D)$ $-2\sqrt{3}$	$^{\sqrt{3}}/_7\,(H_G - H_D)$ $2\sqrt{3}$
sym(πc)(δs)	$-^{\sqrt{3}}/_7\,(H_G - H_D)$ $-2\sqrt{3}$	$^4/_7\,H_G + {}^3/_7\,H_D$ -1	$^3/_7\,(H_G - H_D)$ 6
sym(πs)(δc)	$-^{\sqrt{3}}/_7\,(H_G - H_D)$ $2\sqrt{3}$	$^3/_7\,(H_G - H_D)$ 6	$^4/_7\,H_G + {}^3/_7\,H_D$ -1

The $B(D_2)$-type matrices have a one-to-one correspondence with those of the spin triplets. Worth noting are the following differences. The determinantal functions of the triplet situations have been replaced by the normalized, symmetrized combinations as, for example, the function

$$\text{sym}\,(d\sigma)(d\delta c) \equiv (^1/_2)^{1/2}\,[(d\sigma)\otimes(d\delta c) + (d\delta c)\otimes(d\sigma)] \qquad (48)$$

from Eq. (47). The average energy that has been subtracted from the diagonal elements in order to obtain the b^0 matrix is

$$H_{av.}\,[G, D] = (1/14)(9H_G + 5H_D) \qquad (49)$$

The sign in the definition of b^0:

$$b^0 \equiv (1/14)(H_G - H_D) = (2S + 1)(2/21)E^0 = (2/21)E^0 \qquad (50)$$

is chosen so that b^0 be invariantly positive for the atomic systems as opposed to the situation of Eq. (13) where the Trees operator determines the expression and sign of α_L^0.

Table 22 The $A(D_2)$ energy matrix of Table 18, here given in the parameters of the PMT model after substituting b^0 for $(2/21)E^0$. The symmetry coefficients of Table 16 can be found also in this table (with a change of sign). This sign change as well as the matrix elements of the sixth row and column can be found from Table 18 or by using the operator equivalent $\alpha \hat{L}^2$ mentioned in connection with Eq. (11). The same applies to the other coefficients to b^0, but because of the occurrence of the orbital constant term $(6/7)D^v$, only energy differences should be used here

$A(D_2)$	$(\sigma)\otimes(\sigma)$	$(\pi s)\otimes(\pi s)$	$(\pi c)\otimes(\pi c)$	$(\delta s)\otimes(\delta s)$	$(\delta c)\otimes(\delta c)$	sym $(\sigma)(\delta c)$
$(\sigma)\otimes(\sigma)$	$H_{av.} + {}^4/_3 D^S + {}^4/_7 D^v$	${}^6/_7 D^v - 3b^0$	${}^6/_7 D^v - 3b^0$	${}^6/_7 D^v + 3b^0$	${}^6/_7 D^v + 3b^0$	0
$(\pi s)\otimes(\pi s)$	${}^6/_7 D^v - 3b^0$	$H_{av.} + {}^4/_3 D^S + {}^4/_7 D^v$	${}^6/_7 D^v + b^0$	${}^6/_7 D^v + b^0$	${}^6/_7 D^v + b^0$	$-2\sqrt{6}b^0$
$(\pi c)\otimes(\pi c)$	${}^6/_7 D^v - 3b^0$	${}^6/_7 D^v + b^0$	$H_{av.} + {}^4/_3 D^S + {}^4/_7 D^v$	${}^6/_7 D^v + b^0$	${}^6/_7 D^v + b^0$	$2\sqrt{6}b^0$
$(\delta s)\otimes(\delta s)$	${}^6/_7 D^v + 3b^0$	${}^6/_7 D^v + b^0$	${}^6/_7 D^v + b^0$	$H_{av.} + {}^4/_3 D^S + {}^4/_7 D^v$	${}^6/_7 D^v - 5b^0$	0
$(\delta c)\otimes(\delta c)$	${}^6/_7 D^v + 3b^0$	${}^6/_7 D^v + b^0$	${}^6/_7 D^v + b^0$	${}^6/_7 D^v - 5b^0$	$H_{av.} + {}^4/_3 D^S + {}^4/_7 D^v$	0
sym $(\sigma)(\delta c)$	0	$-2\sqrt{6}b^0$	$2\sqrt{6}b^0$	0	0	$H_{av.} + {}^4/_3 D^S - {}^2/_7 D^v - 3b^0$

The gamma-sinus component of the G multiplet term, GΓs, is equal to the symmetrical combination of the two dδ orbitals, that is, GΓs=sym(dδs)(dδc). Therefore we obtain

$$H_G = J_1^{\text{eff.}} + K_1^{\text{eff.}} \tag{51}$$

so that the b^0 coefficient in the expression for H_G is 5 in units of $(2/21)E^0$ according to Table 16, and by the barycentration, it is –9 for H_D (cf. Table 1).

Each B(D_2) matrix embodies one D and two G components and has accordingly a trace of +1, rather parallel to the triplet case. The area of $\hat{Q}[b^0]$ is 131 over each B(D_2) matrix and 237 over the A(D_2) matrix adding up to 630, that is, the same as the area of $\hat{Q}[b^1]$ of the triplet case. However, there the parametrical spin weighting was three, whereas here it is unity, which means that the area of $\hat{Q}[E^0]$ is one ninth of that of $\hat{Q}[E^1]$ (cf. again Table 1).

6
The Connection Between the PMT Model and the SCS Model. LF and KS-DFT Aspects

6.1
Overview

The purpose of this section is to illuminate various aspects of the validity of the PMT and the SCS models. The observable part of the PMT model is the four-parameter model that may be expressed as

$$\begin{aligned}
\hat{\bar{H}}_{\text{PMT}} &= \hat{H}_{\text{PMT}} - H_{\text{av.}}\,\hat{Q}\,[H_{\text{av.}}] \\
&= D^S\,\hat{Q}[D^S] + D^v\,\hat{Q}[D^v] + E^1\,\hat{Q}[E^1] + E^0\,\hat{Q}[E^0] \\
&= D\,\hat{Q}[D] + D^\perp\,\hat{Q}[D^\perp] + E\,\hat{Q}[E] + E^\perp\,\hat{Q}[E^\perp]
\end{aligned} \tag{52}$$

where all the coefficient operators but $\hat{Q}\,[H_{\text{av.}}]$ are traceless and their associated parameters observables. Analogously, the SCS model is the two-parameter model

$$\hat{\bar{H}}_{\text{SCS}} = \hat{H}_{\text{SCS}} - H_{\text{av.}}\hat{Q}[H_{\text{av.}}] = D\,\hat{Q}[D] + E\,\hat{Q}[E] \tag{53}$$

All the operators were defined in Tables 1 and 3. It is seen that $\hat{H}_{\text{SCS}}$ is a contraction of $\hat{H}_{\text{PMT}}$ obtained by dropping the terms $D^\perp\,\hat{Q}\,[D^\perp]$ and $E^\perp\,\hat{Q}\,[E^\perp]$ and thereby dropping the flexibility of two parameters in a modeling process. The contraction can alternatively be expressed by the parametrical restrictions of Eq. (21).

We shall now see that the PMT model refers to the effective two-electron operator $\hat{g}$ and the SCS model to the usual interelectronic repulsion operator, which consists of a multiplication by r_{12}^{-1} (atomic units). Moreover, we shall find that the transition from the weak ligand-field scheme to the strong-field scheme, which is usually connected with the SCS model, can equally well be connected with the full PMT model. Finally, we shall find that our method of using KS-DFT to embrace the whole atomic d^2 configuration should restrict this model to the SCS rather than PMT model. However, the internal incompatibilities of the Coulomb and the exchange/correlation functionals of the ADF make the PMT

model a good intermediate stage in the averaging analysis of the results when taking all the 45 computed microstate energies into account in obtaining the parameters of the SCS model.

6.2
Connection Between the Space of Doubly Occupied Orbitals and the Remaining Spin Singlet Space

We need to discuss the energy class J_0, defined by consisting of determinants containing the two electrons in the same spatial orbital. By the Pauli principle these electrons must have opposite spin; thus, all these functions lie in spin singlet space and have accordingly antisymmetric spin functions. Their spatial functions must therefore be symmetrical. We have, for example,

$$\langle |(\sigma, \alpha)(\sigma, \beta)||\hat{g}||(\sigma, \alpha)(\sigma, \beta)|\rangle = \langle (\sigma) \otimes (\sigma)|\hat{g}|(\sigma) \otimes (\sigma)\rangle = J_0^{\text{eff.}} \qquad (54)$$

which is one of the unique J integrals, of which there are five, corresponding to each of the five d orbitals. These five integrals can be shown to take on the same values independent of the function basis provided that this is real. J_0 can be taken as an effective parameter analogously to the J and K parameters of Eqs. (45) and (46).

We need to discuss also the non-diagonal elements of $\hat{g}$, which connect these Slater determinants of energy J_0^{eff}. They have, for example, the form (Tables 17 and 23)

$$\langle (\sigma) \otimes (\sigma)|\hat{g}|(\pi c) \otimes (\pi c)\rangle = K'_{(\sigma) \otimes (\pi c)} = K'_2$$
$$= (1/5)H^S + (1/7)H^D - (12/35)H^G \qquad (55)$$

which we shall call a pseudo-exchange integral and use a prime notation to be explained in the next subsection. We note that the sum of the coefficients is equal to zero as a consequence of the fact that the rows of coefficients of Table 17 are mutually orthogonal. This is consistent with the requirement that the non-diagonal element must be independent of the zero point of energy. Table 18 reveals that its top left 5×5 submatrix can alternatively be written in the form of Table 23. The columns of Table 17 immediately reveals four such components, namely Sσ, Dσ, Gσ, and GΓc. The last function of this space embodies two different LΛç functions, namely DΔc and GΔc functions, which together are included in the matrix of Table 18. The submatrix describing the Δc strong-field matrix under $\hat{g}$ is

$\hat{g}$	$^1/_2\,[|(\pi c)(\pi c)| - |(\pi s)(\pi s)|]$	sym$(\sigma)(\delta c)$
$^1/_2\,[|(\pi c)(\pi c)| - |(\pi s)(\pi s)|]$	$(4/7)H_G + (3/7)H_D$	$(12^{1/2}/7)(H_G - H_D)$
sym$(\sigma)(\delta c)$	$(12^{1/2}/7)(H_G - H_D)$	$(3/7)H_G + (4/7)H_D$

(56)

which is the cosine analog of the $B_1(D_2)$ matrix of Table 19. This cosine matrix is the only energy matrix connecting the doubly occupied orbitals (class J_0 of Tables 24 and 25, Section 8.2 and 8.3) and the other spin singlet determinants (the $[J+K]$ class of Table 25). By diagonalization, the GΔc and DΔc functions arise as the eigenfunctions of $\hat{g}$.

Table 23 The pseudo exchange integrals associated with the matrix elements of the interelectronic repulsion operator $\hat{g}$ when using a real orbital basis for the doubly occupied orbitals are the non-diagonal elements of the 5×5 matrix of $A(D_2)$ symmetry. The sub-indices refer to the spatial energy sub-classes of Table 16 (cf. also Table 22). The only occurrence of the Coulomb parameter J_0 is in this matrix

$A(D_2)$	$(\sigma)\otimes(\sigma)$	$(\pi s)\otimes(\pi s)$	$(\pi c)\otimes(\pi c)$	$(\delta s)\otimes(\delta s)$	$(\delta c)\otimes(\delta c)$
$(\sigma)\otimes(\sigma)$	J_0	K_2'	K_2'	K_4'	K_4'
$(\pi s)\otimes(\pi s)$	K_2'	J_0	K_3'	K_3'	K_3'
$(\pi c)\otimes(\pi c)$	K_2'	K_3'	J_0	K_3'	K_3'
$(\delta s)\otimes(\delta s)$	K_4'	K_3'	K_3'	J_0	K_1'
$(\delta c)\otimes(\delta c)$	K_4'	K_3'	K_3'	K_1'	J_0

The connection between the doubly occupied orbitals and the other singlet functions is revealed by comparing the energies of GΓs and GΓc

$$H[G\Gamma s] = J_1 + K_1 = J_0 - K_1' = H[G\Gamma c] \qquad (57)$$

Here the left-hand side is obtained from Eq. (51) and the right-hand side from Tables 18 and 23 using the functional form of GΓc given in Table 17.

Equation (57) can be generalized to

$$J_0 = (J_n + K_n) + K_n' \quad (n = 1, 2, 3, 4) \qquad (58)$$

where the parentheses contain a parameter combination that has pure spin singlet character, a property it has in common with J_0 and K_n'. Equation (58) is the PMT expression, valid for the $\hat{g}$ operator.

The connection between the doubly occupied orbitals and the rest of the d^2 configuration including the triplets is an alternative way of revealing the PMT model in the light of the Slater determinants. Taking the first and fourth rows of Table 17 in combination with Table 1 and Eq. (50) we obtain

$$\begin{aligned} K_{(\sigma)(\delta c)}' = K_4' &= (1/5)H_S - (2/7)H_D + (3/35)H_G \\ &= (1/5)H_S - (1/14)(9H_G + 5H_D) + 3(1/14)(H_G - H_D) \qquad (59) \\ &= (6/7)D^v + (2/7)E^0 \end{aligned}$$

which is a matrix element of Table 22.

Then we take the sixth and the seventh row of Table 17 to obtain a quite different expression:

$$\begin{aligned} K_{(\sigma)(\delta c)} &= -(1/2)H_F + (2/7)H_D + (3/14)H_G \\ &= (1/2)(1/14)(9H_G + 5H_D) - (1/10)(3H_P + 7H_F) \\ &\quad - (3/2)(1/14)(H_G - H_D) + (3/2)(1/10)(H_P - H_F) \\ &= D^S - (1/7)D^v - (1/7)E^0 + (3/7)E^1 \qquad (60) \end{aligned}$$

Both of these expressions are matrix elements consisting of a difference-in-average-energy term, that is, a term associated with operators from the spin and

seniority space (D-type parameters), and a spatial splitting term associated with operators from among the spatial operators (E-type parameters). From this, it is clear that in the PMT model on d^2, the K parameters belong to all the states of the seniority 2 while the K' parameters belong to all the states of the spin singlets.

With these results we conclude the discussion of the PMT model's illumination in terms of the operator $\hat{g}$ about which we only assumed that it was a totally symmetrical two-electron operator. This operator's domain was per definition the five multiplet terms. We have now established that this domain can alternatively be defined by the 45 Slater determinants built up out of d orbitals. In other words, these determinants then lead to a five-parameter model. This is a noteworthy result because if we start out using these determinants as our function basis and use the interelectronic repulsion operator $(r_{12})^{-1}$ on the d^2 space, we obtain the two-parameter SCS model.

6.3
The Background for the Contraction of the PMT Model to the SCS Model

We shall now examine the conditions under which the PMT model degenerates into the SCS model. Looking at first at the expression at Eq. (58), the analogous SCS expression is

$$J_0 = J_n + 2K_n \quad (n = 1, 2, 3, 4) \tag{61}$$

which means that one requirement for the degeneration of the two models is that the condition $K_n = K'_n$ is valid for real linear harmonics orbitals.

For the expressions of Eqs. (59) and (60) to be compatible within the two mutually exclusive D-type and E-type operator spaces independently, it is required that $D^S = D^v$ and $E^1 = E^0$ leading to the SCS model (cf. Eq. 21).

We have now come to the reason for our choice of notation for the pseudo exchange integrals K': all cross product integrals K' involving two different doubly occupied orbitals take on the same values as certain exchange integrals involving the same orbitals provided the orbitals are real. The numerical connection can be seen as follows:

$$
\begin{aligned}
K'_{(\sigma)(\pi s)} &= \langle |(\sigma, \alpha)(\sigma, \beta)| \hat{g} |(\pi s, \alpha)(\pi s, \beta)| \rangle \\
&= {}^1/_2 \langle (\sigma, \alpha) \otimes (\sigma, \beta) - (\sigma, \beta) \otimes (\sigma, \alpha) | \hat{g} | (\pi s, \alpha) \otimes (\pi s, \beta) \\
&\quad - (\pi s, \beta) \otimes (\pi s, \alpha) \rangle = \langle (\sigma) \otimes (\sigma) | \hat{g} | (\pi s) \otimes (\pi s) \rangle \\
&= \iint \sigma(1) \, \sigma(2) \, \hat{g} \, (\pi s(1) \, \pi s(2)) \, d\tau(1) \, d\tau(2)
\end{aligned}
\tag{62}
$$

Now, if the $\hat{g}$ operator were a multiplication operator as is the interelectronic repulsion operator $(r_{12})^{-1}$, this equals

$$
\begin{aligned}
\iint \sigma(1) \, \pi s(2) \, \hat{g} \, (\pi s(1) \, \sigma(2)) \, d\tau(1) \, d\tau(2) \\
= \langle (\sigma) \otimes (\pi s) | \hat{g} | (\pi s) \otimes (\sigma) \rangle = K^{\text{eff.}}_{(\sigma)(\pi s)}
\end{aligned}
\tag{63}
$$

since the orbitals involved are real. The key difference between the PMT model and the SCS model can accordingly be pinpointed to the difference between $\hat{g}$ and $(r_{12})^{-1}$.

7
Constrained Use of the ADF and Discarding of Errors

Let us now address the subject of how to constrain KS-DFT appropriately in order to allow it to mimic the LFR. For atomic ions we used a computation called the average-of-configuration (AOC) suggested by Baerends for calculating atomic ion ground state reference energies [74]. We shall here discuss how to extend the AOC to complexes of tetrahedral symmetry and emphasize the differences in treating atoms and complexes. In the last two main sections, computational results for the atomic d^2 and d^8 systems as well as for all of the complexes, VX_4^- and CrX_4 (X=F, Cl, Br, and I) will be given[7].

We modify the method we used for computations on atomic d^q ions [30] in such a way that the concepts of ligand-field theory are conserved. We refer to it as KS-DFT modeling and we want to emphasize that we aim at a generalization in the use of DFT so as to make it operate within a fixed frame comprising the complete set of the ligand-field states. In other words, we refrain from making an optimal use of the DFT for the description of any particular state.

We now proceed by describing a number of steps, most of which are individually well known and rather standard[8]. Characteristic of the method when applied to molecular systems is that it involves two and only two converged SCF computations. The first one is an unrestricted computation whose primary purpose is an optimization of the geometry to be used for all the following ligand-field mimicking. Its secondary purpose is an identification of the unrestricted eigenorbitals of the system in question. The second SCF computation is a restricted one, whose main purpose is to constrain KS-DFT by defining the Kohn-Sham restricted eigenorbitals that are to be fixed from then on and used for all the following computations and analyses.

7.1
Geometry Optimization by Unrestricted SCF Computation

This computation is only needed for molecular systems. All the complexes of VX_4^- and CrX_4 type are optimized in T_d symmetry, in agreement with the $^3A_2$ ground state expected from ligand-field theory in the form of LFR.

The metal to ligand distances are obtained as a first result and these computed distances have been used for all the subsequent molecular computations. Thereby we aim at the vertical transition energies, which probably are close to what is represented by ligand-field theory.

---

[7] The computations presented in this and the following sections are made with the Kohn-Sham DFT package ADF [44–47] version 2002.03 using the Perdew-Wang 91 gradient corrected exchange-correlation functional [75]. Triple zeta basis sets were used for all the atoms involved. The basis sets of the halide ligands included only one polarization function and in the case of iodine, orbitals were frozen up to and including 4p. For the 3d transition metals two polarization functions were used with no frozen core. Only basis sets with one polarization function are present for the heavier transition metals and here the core is frozen up to and including 3d, or 4f in the few cases of 5d metals.

[8] Similar procedures used by Atanasov et al. may be found in [39].

Orbital identification is made by symmetry, plotting, and Mulliken population analysis. The energy order found for the Kohn-Sham α spin orbitals containing an electron agrees in all the complexes with that predicted by simple qualitative molecular orbital considerations. The same order is found for the filled spin orbitals with β spin.

The α spin orbitals have two electrons in the HOMO $e(T_d)$ set of orbitals whereas the corresponding β orbitals are empty. The first empty orbital level is of $t_2(T_d)$ type. We associate these subsets of $e(T_d)$ and $t_2(T_d)$ symmetries with the partially filled shell and observe for all the present complexes that both orbitals contain in excess of 60% 3d of the metal.

Below, quantitative results based upon Mulliken population analysis of spin polarization support the concept of oxidation states without the use of ligand-field theory.

7.2
An "AOC"-SCF Computation Generating the "d" Molecular Orbitals

In this step a restricted SCF computation is made in which the ten "d" spin orbitals are occupied by $q/10$ electrons [31, 39]. The purpose of the average-of-configuration ("AOC") computation is to impose the full spinless symmetry on the system and to define the subsets of orbitals transforming as do d orbitals in the appropriate symmetry. In the present complexes the symmetry is T_d, *i.e.*, the orbitals transform as Griffith's standard components [62] of $e(T_d)$ and $t_2(T_d)$. These subsets of orbitals define the partially filled "d" shell and have a 1:1 relationship with our real d orbitals. Moreover, the d parts of these LCAO-MOs are mutually orthogonal by symmetry and thereby the correspondence between KS-DFT and LFR is established for our Slater determinants as well. The "d" orbitals remain fixed during our imaging of ligand-field energies, and the molecular core orbitals are fixed as well.

This computation matches the AOC of the central ion atomic system, but the "d" orbitals of $e(T_d)$ and $t_2(T_d)$ symmetries will now be LCAO-MOs containing different amounts of atomic orbitals as do the perturbed orbitals of LFR. The "AOC" computation may thus be seen as an approximate spherification, but the overall density distribution has T_d symmetry and the adaptation of the orbitals is to this point group. However, spherification is a crucial restriction for the parameterization of interelectronic repulsion by PMT as well as by SCS.

The SCS model and Jørgensen's symmetry-restricted covalency can be quantified simplistically by using the percentages of central ion d character in the "d" orbitals. The square of the weighted average percentages in the "de" and "dt₂" orbitals corresponds to the nephelauxetic ratio of this covalency. These nephelauxetic ratios $\beta["AOC"]$ were found from the Mulliken population analysis of the "AOC" computations as

$\beta["AOC"]$	F	Cl	Br	I	
CrX_4	0.553	0.423	0.409		(64)
VX_4^-	0.685	0.597	0.583	0.578	

These non-empirical computational ratios clearly follow the nephelauxetic series of ligands. By introducing the corresponding degrees of d covalency defined by Jørgensen [3]

$$\gamma_{\text{complex}} = (\beta_{\text{central ion}} - \beta_{\text{complex}})/\beta_{\text{central ion}} = 1 - \beta_{\text{complex}} \tag{65}$$

it is possible to test Jørgensen's semi-empirical factorization of these degrees of covalency by the gammas:

γ["AOC"]	F	Cl	Br	I	
CrX_4	0.447	0.577	0.591		(66)
VX_4^-	0.315	0.403	0.417	0.422	

Jørgensen's gamma factorizations are illustrated in Eq. (67), and in the columns of Eq. (68), which also demonstrate the expected results that Cr(IV) gives more covalent complexes than do V(III) and the heavy halides more covalent complexes than fluoride:

γ["AOC"]	F	Cl	Br	
CrX_4/VX_4^-	1.42	1.43	1.42	(67)

γ["AOC"]	Cl	Br	
CrX_4/CrF_4	1.29	1.32	(68)
VX_4^-/VF_4^-	1.28	1.33	

For the ligand-free central ion γ is, of course, equal to zero and the most disturbing computational result is the high d covalency of even the fluoride complexes. As we shall see in section 10, the computational difference between F^- and the heavy halides lies mainly in the s and p covalencies. Solomon has previously pointed out that KS-DFT has a tendency to exaggerate covalency [76].

An essential ligand-field parameter of the LFR model for our tetrahedral complexes is the spectrochemical parameter, which in the LFR model at the same time is an orbital energy difference and a one-electron energy difference:

$$\Delta = h[t_2] - h[e] \tag{69}$$

For our complexes this quantity and its ratios are obtained from the appropriate KS-DFT orbital energy difference of the "AOC":

Δ["AOC"]	F	Cl	Br	I	
CrX_4	0.968	0.678	0.584		
VX_4^-	0.672	0.491	0.426	0.372	
CrX_4/VX_4^-	1.44	1.38	1.37		(70)
CrF_4/CrX_4		1.43	1.66		
VF_4^-/VX_4^-		1.37	1.58	1.81	

They follow the spectrochemical series and again support Jørgensen's semi-empirical Δ factorizations computationally [3]. It is noteworthy that

the γ and Δ values give so similar schemes (in the last two rows reciprocal though).

In Section 10.1 the difference between the metal ion's oxidation state and charge is demonstrated.

7.3
ADF Energies of the Individual Slater Determinantal Microstates

The individual 45 determinantal microstates of the d^2 configuration above the closed shells are identified by allotting occupation numbers of unity to all possible pairs of "d" spin orbitals. The associated 45 ADF energies, previously [30] called unity-occupation-number energies, are then computed by using the fixed "AOC" orbitals. This is not an SCF computation, but it is identified by the ADF as the first cycle of an SCF computation (unconverged) as opposed to a genuine SCF computation, which is a multistep converged one. We denote these 45 energies our *direct* ADF energies and take them to represent expectation values of the KS-DFT Hamiltonian with respect to the determinants. The "d" parts of the determinants employ real space orbitals.

7.4
One-to-One Relationship Between ADF Energies and Ligand-Field Parameterized Energies

The comparison with the parametrical d^q model consists in identifying the 45 ADF energies of the individual "d" determinants with the ligand-field parameterized energies of their associated d determinants. Ligand-field parameterization is here used in the general form, LFR, where both the ligand field and the effective interelectronic interaction are included.

The comparison with ligand-field theory now consists of two steps, both involving all the states of the d^q configuration. The first step takes place within the LFR model in which the expectation values for the energies of the individual determinants are expressed in terms of its parameters. The second step is a comparative one, in which the $\binom{4l+2}{q}$ parametrical d^q energy expressions are put equal to their corresponding *direct* ADF energies. These equations are solved by the least squares method to obtain the parametrical KS-DFT results[9].

We use the ADF in an engineering kind of manner. We conceive it as a source of data that provides energies with a very high precision but with an inaccurate reproduction of the LFR parameterized energies. We thus take our LFR modeling as being the higher truth. Therefore, our method implies that we conceive the standard deviations of the computations based upon the least squares treatment of the "data" as the deficiency of our constrained ADF. Moreover, the fact [30] that the values of the SCS parameters based upon the Coulomb functional are in-

---

[9] Our method has the advantage that it allows the formalism of mutually orthogonal operators to work under the constraints of the AOC. Thus, the new molecular operators, which are of one-electron operator type, are automatically orthogonal to all the spherically symmeterized two-electron operators, which are used also for the molecular systems.

variably higher than the ones of the exchange/correlation, we consider an incommensurability of the two functionals. We therefore need to mention that not only is our LFR formalism a model concept, in particular that of a "d^q" configuration, but we actually do not know how good our assumption about the identification of the KS-DFT states with Slater determinants may be. For the atomic systems and even more so for the molecular ones, we even do not know for certain if the energies of these states are to be interpreted within the PMT or the SCS models, since the identification with Slater determinants symmetry-wise allows both.

In the Sections 9 and 10 we shall use the PMT model, which involves five parameters, as the transition step between the ADF energies and the repulsion part of the LFR parameterizations. For this use, we shall need all the 45 computed energies explicitly. From the four repulsion parameters of the PMT model, the two SCS parameters D and E are calculated using Eq. (27). These SCS parameter values together with Δ should be optimal for the comparison with empirical parameter values.

8
Two KS-DFT Function Bases, the Single Slater Determinantal Basis and the $\hat{S}^2$ Eigenbasis Leading from KS-DFT to LFR

8.1
Two Sets of KS-DFT Energy Classes and Subclasses: Two KS-DFT Function Bases

In a previous paper on KS-DFT [30], we discovered that real orbitals were necessary if the single determinantal KS-DFT states should follow the symmetry implications of the pair-interaction model on d^q. Moreover, in spite of the flexibility of KS-DFT to use fractional occupation numbers of its spin orbitals, only such computations that restrict these occupation numbers to be either zero or unity provide a simply interpretable link between KS-DFT and more conventional quantum mechanical approaches.

In the previous analysis, classes and sub-classes of energy emerged. The differences between the average energies of the classes were found to be of spin and seniority type, that is D-type, while the energy splitting of classes into sub-classes were of spatial operator type, that is E-type. Therefore, from a conceptual point of view, it was useful to think about our approach as involving an intermediate step, which was illustrated previously. This step consists in a data reduction transforming the $\binom{10}{q}$ pieces of ADF data into nine, referring to these energy subclasses (Tables 24 and 25), thus giving a nine-parameter model (NPM). This model averages out the intra-subclass symmetry deficiency of the ADF results making them compatible with a symmetry compliant parameterization model. From a conceptual point of view, this step shows that we are left with nine pieces of information from which to calculate for instance the three parameters, $H_{av.}[d^2]$, D and E, of the SCS model. For atomic V^{3+}, an explicit example of the intermediate data reduction to the NPM, and also to the SCS parameterization following from that, was given previously [30].

In this previous work we called the raw ADF results – for the d^2 and d^8 configurations either 45 or 9 – our primary ADF results, which we used for our SCS parameterization. Here we shall call these energies, which are associated with the energies of Slater determinants, our *direct* results. In the following subsection, the PMT parameterization will be discussed in this determinantal basis (db).

The determinantal basis was found by symmetry to fall in three energy classes. The high-energy J_0 class involves the five doubly occupied d orbitals, that is, five degenerate determinants. The middle-energy class, the J class, involves the 20 determinants with two different orbitals associated with opposite spin, and the low-energy, the $[J–K]$-class, the 20 determinants with two different orbitals with alike spin. Each of these two latter classes embodies four subclasses that can be labeled according to Table 16, however, with two independent spatial splitting parameters (Table 24).

The five determinants of the J_0 class, which all have doubly occupied orbitals and were chosen as basis functions for Tables 18, 22, and 23 have thus already been discussed above.

The J class embodies the 20 ordered pairs of standard d functions, exemplified by the two functions $|(\sigma,\alpha)(\pi s,\beta)|$ and $|(\pi s,\alpha)(\sigma,\beta)|$ belonging to subclass 2 of Table 16. The matrix of $\hat{g}$ is non-diagonal because these spin-mixed functions cannot be eigenfunctions of a spinless operator:

$\hat{g}$	$|(\sigma, \alpha)(\pi s, \beta)|$	$|(\pi s, \alpha)(\sigma, \beta)|$
$|(\sigma, \alpha)(\pi s, \beta)|$	J_2	K_2
$|(\pi s, \alpha)(\sigma, \beta)|$	K_2	J_2

$$(71)$$

The upper eigenvalue of this matrix is J_2+K_2 with the $[S=0]$-eigenfunction, $(^1/_2)^{1/2}[|(\sigma,\alpha)(\pi s,\beta)|+|(\pi s,\alpha)(\sigma,\beta)|]$, having the spatial factor $\mathrm{sym}(\sigma)(\pi s)$. The lower eigenvalue is $J_2–K_2$ with the $[S=1]$-eigenfunction, $(^1/_2)^{1/2}[|(\sigma,\alpha)(\pi s,\beta)|–|(\pi s,\alpha)(\sigma,\beta)|]$, having the spatial factor $|(\sigma)(\pi s)|$.

What we can expect to compute *directly* are the two diagonal elements of the matrix of $\hat{g}$ (Eq. 71) and of the 9 other analogous matrices covering the 20 dimensional space of the J-class functions corresponding to the orbital products of Table 16.

In a previous work [30] the final SCS-parametrical results were roughly compared with the *direct* ADF computations involving the individual determinants, which are all microstates but of which only a few are eigenstates. It was found that the energies of the individual determinants showed considerable deviations from the SCS model.

In Section 8.3, we shall replace the J class by the $[J+K]$-class whose energies can be obtained from the *direct* ADF results by using the energy formula

$$H[J_n + K_n] = 2H[J_n] – H[J_n – K_n] \tag{72}$$

applicable for each of the four subclasses of Table 16 ($n=1, 2, 3,$ and 4). We shall call the collection of energy classes: the J_0-class, the $[J+K]$-class, and the $[J–K]$-class the *indirect* KS-DFT classification. The functions underlying this classification are of course no longer single determinants, but now they are all

eigenfunctions of $\hat{S}^2$. These functions constitute what we shall call the spin basis (sb).

In the following subsections we shall focus in much more detail upon the deviations from the SCS model. We shall do this by first removing the part of the spatial information that is redundant from a symmetry point of view from the computed energies of the nine-parameter models of Tables 24 and 25. By removing this inter-subclass deficiency, that is, the spatial errors of the ADF, we arrive at the PMT model, which was discussed in detail earlier.

8.2
The *Direct* Link from Kohn-Sham-DFT to the Two-Electron Models on the d^2 Configuration: the Single-Determinant Energies. The First Nine-Parameter Model

The *direct* connection between the Kohn-Sham-DFT energies and the energies of the single Slater determinants in real d orbitals falls in the classes J_0, J and $J{-}K$, where the first two classes have $M_S=0$ and the $[J{-}K]$-class has $|M_S|=1$ and where the J_0 class has doubly occupied orbitals whereas the other two classes have two different orbitals occupied. We shall denote the function basis of this situation, the single-determinant basis, db.

Using the methods discussed earlier for the other classes, the elements of the J class can also be parameterized. For example, the Coulomb integral J_4 of $|(\sigma,\alpha)(\delta s,\beta)|$ is a diagonal element analogous to those discussed in connection with Eq. (71). It can be found as half the sum of the diagonal elements of the spatial functions, $(^1/_2)^{1/2}[(\sigma){\otimes}(\delta c)+(\delta c){\otimes}(\sigma)]$ and $(^1/_2)^{1/2}[(\sigma){\otimes}(\delta c)-(\delta c){\otimes}(\sigma)]$ as given in Tables 18, 22, or 23. All these diagonal elements are given in Table 24 together with the SCS parameterization and its extension to PMT. The table allows a systematic reduction from the nine-parameter model of the third column comprising the coefficients to J_0, and to the J and $[J{-}K]$-parameters, over the PMT model, to the SCS model containing only two parameters and the average energy.

Table 24 is adapted to all our use of KS-DFT, also for d^q configurations comprising $2<q<8$. It was designed primarily for the pair-interaction model. Thus, the SCS part of the table was used previously to obtain the SCS parameters for all d^q configurations [30]. The subclasses and the role of the different PMT parameters are further illustrated on the left-hand part of Fig. 4.

8.3
The *Indirect* Link from Kohn-Sham-DFT to the Two-Electron Operator Models on the d^2 Configuration: the Energies of Eigenspaces of $\hat{S}^2$. The Second Nine-Parameter Model

The most symmetry-adapted parametrical path from KS-DFT via the PMT model to the SCS model is outlined in Table 25. The particular sets of operators of these two models are not only mutually orthogonal but also diagonally orthogonal in the $\hat{S}^2$ eigenfunction basis of Table 25. This *spin basis* refers to the partial diagonalization of the $\hat{g}$ matrix in the determinant basis. All ten matrices exemplified in Eq. (71) have been diagonalized.

The classes differ somewhat between the determinantal basis of Table 24 and the spin basis of Table 25. The $[J{-}K]$-class acquires new members, which have

Table 24 The single-determinant basis(determinant basis, db). Overview and parameterization of the *direct* KS-DFT classes and subclasses corresponding to single Slater determinants. The subclass designations consist of J and K integrals whose parametrical energy expressions from the table should be read as in the following example $J_3 - K_3 = H_{av.}[d^2] - (14/21)D^S - (6/21)E^1 = H_{av.}[d^2] - (14/21)D - (6/21)E$, where the sub-class numbering is that of Table 16, whose relative coefficients can be seen here as the coefficients to all E-type parameters. The denominator 21 has not been included in the table. One may note that in every energy expression, the sum of the coefficients within D-space is the same in SCS and in PMT parameterization, as in Table 1. The same applies to E-space. Note also that the coefficient columns to the E parameters are linear-harmonics symmetry determined and therefore proportional to those of Table 16. For the J class, we have $b^J = (3/21)E^1 + (1/21)E^0$, that is, the average of the Eqs. (40) and (50) in agreement with the 50% mixing of S=1 and S=0 in this class. The coefficient columns of the SCS parameters are orthogonal, but that is not generally the case for the PMT model. Thus, while the columns of D-type are orthogonal to those of E-type, neither D-type nor E-type operators maintain this property within their own spaces. The reason for these facts, which might seem odd, is that we are concerned with the diagonal part of the matrices of all these operators. In the lower part of the table the areas of the coefficient columns are given together with two non-vanishing coefficient column overlaps

Class	Weight	Diagonal element and subclass	PMT	SCS
J_0	5	J_0	$28\ D^S + 12\ D^v$	$40\ D$
J	2	J_1	$7\ D^S - 3\ D^v + 15\ E^1 + 5\ E^0$	$4\ D + 20\ E$
	4	J_2	$7\ D^S - 3\ D^v + 9\ E^1 + 3\ E^0$	$4\ D + 12\ E$
	10	J_3	$7\ D^S - 3\ D^v - 3\ E^1 - E^0$	$4\ D - 4\ E$
	4	J_4	$7\ D^S - 3\ D^v - 9\ E^1 - 3\ E^0$	$4\ D - 12\ E$
$J-K$	2	$J_1 - K_1$	$-14\ D^S + 30\ E^1$	$-14\ D + 30\ E$
	4	$J_2 - K_2$	$-14\ D^S + 18\ E^1$	$-14\ D + 18\ E$
	10	$J_3 - K_3$	$-14\ D^S - 6\ E^1$	$-14\ D - 6\ E$
	4	$J_4 - K_4$	$-14\ D^S - 18\ E^1$	$-14\ D - 18\ E$

$\langle \hat{Q}[D] | \hat{Q}[D] \rangle_{\text{diag.}}^{\text{db}} = 1360/49$ $\langle \hat{Q}[E] | \hat{Q}[E] \rangle_{\text{diag.}}^{\text{db}} = 2288/147$

$\langle \hat{Q}[D^S] | \hat{Q}[D^S] \rangle_{\text{diag.}}^{\text{db}} = 20$ $\langle \hat{Q}[E^1] | \hat{Q}[E^1] \rangle_{\text{diag.}}^{\text{db}} = 660/49$

$\langle \hat{Q}[D^v] | \hat{Q}[D^v] \rangle_{\text{diag.}}^{\text{db}} = 100/49$ $\langle \hat{Q}[E^0] | \hat{Q}[E^0] \rangle_{\text{diag.}}^{\text{db}} = 44/147$

$\langle \hat{Q}[D^S] | \hat{Q}[D^v] \rangle_{\text{diag.}}^{\text{db}} = 20/7$ $\langle \hat{Q}[E^0] | \hat{Q}[E^1] \rangle_{\text{diag.}}^{\text{db}} = 44/49$

$M_S=0$ and S=1 and the new $[J+K]$-class consists of members with $M_S=0$ and S=0. Only the J_0 class is identical in the two function bases. The subclasses allow a new nine-parameter model to be made, consisting of J_0, four $[J+K]$-subclass parameters and four $[J-K]$-subclass parameters. This model may again be contracted to the PMT model, and progressively to the SCS model. The subclasses and the influence of the PMT model in the spin basis, is illustrated on the right-hand side of Fig. 4.

Table 25 The $\hat{S}^2$ eigenbasis (spin basis, sb). Overview and parameterization of the *indirect* KS-DFT classes corresponding to eigenstates of the $\hat{S}^2$ operator. This table has subclasses whose members have energies that correspond to eigenstates of the $\hat{S}^2$ operator but in the $[J+K]$-class not to single determinants. However, the energies are simple linear combinations of single-determinant energies and are thereby *indirectly* obtainable from the KS-DFT computations (cf. Eq. 72). The subclass designations also represent J and K integrals whose parametrical energy expressions from the table should be read by including a factor of 21 as with Table 24. The following example illustrates this: $J_1+K_1 = H_{av.}[d^2] + (28/21)D^S - (6/21)D^v+(10/21)E^0=H_{av.}[d^2]+(22/21)D+(10/21)E$. Note that the weight factors are different from those of Table 24. With the new weight factors, all the columns of coefficients to the parameters of the PMT model in the $\{D^S, E^1, D^v, E^0\}$ parameterization are mutually orthogonal. The trace – and thereby the average energy – remains invariant on going from Table 24 to Table 25. However, this is not true of the areas, which increase on going from db to sb. The reason for this increase is that going from db to sb means a partial diagonalization (cf.Eq. 71), which becomes complete when the ^{2S+1}L basis is reached. At this stage the diagonal area is equal to total area because the ^{2S+1}L basis is the eigenbasis of $\hat{g}$, thus making its matrix diagonal. The degrees of diagonality of the coefficient operators are 1, 11/35, 1/7, and 11/105, respectively. The determinant basis of Table 24 and the spin basis of Table 25 are both KS-DFT bases

Class	Weight	Subclass	PMT subclass	SCS
J_0	5	J_0	$28\,D^S + 12\,D^v$	$40\,D$
$J+K$	1	$J_1 + K_1$	$28\,D^S - 6\,D^v + 10\,E^0$	$22\,D + 10\,E$
	2	$J_2 + K_2$	$28\,D^S - 6\,D^v + 6\,E^0$	$22\,D + 6\,E$
	5	$J_3 + K_3$	$28\,D^S - 6\,D^v - 2\,E^0$	$22\,D - 2\,E$
	2	$J_4 + K_4$	$28\,D^S - 6\,D^v - 6\,E^0$	$22\,D - 6\,E$
$J-K$	3	$J_1 - K_1$	$-14\,D^S + 30\,E^1$	$-14\,D + 30\,E$
	6	$J_2 - K_2$	$-14\,D^S + 18\,E^1$	$-14\,D + 18\,E$
	15	$J_3 - K_3$	$-14\,D^S - 6\,E^1$	$-14\,D - 6\,E$
	6	$J_4 - K_4$	$-14\,D^S - 18\,E^1$	$-14\,D - 18\,E$

$\langle \hat{Q}[D] | \hat{Q}[D] \rangle^{sb}_{diag.} = 2080/49$ $\qquad$ $\langle \hat{Q}[E] | \hat{Q}[E] \rangle^{sb}_{diag.} = 2464/147$

$\langle \hat{Q}[D^S] | \hat{Q}[D^S] \rangle^{sb}_{diag.} = 40$ $\qquad$ $\langle \hat{Q}[E^1] | \hat{Q}[E^1] \rangle^{sb}_{diag.} = 792/49$

$\langle \hat{Q}[D^v] | \hat{Q}[D^v] \rangle^{sb}_{diag.} = 120/49$ $\qquad$ $\langle \hat{Q}[E^0] | \hat{Q}[E^0] \rangle^{sb}_{diag.} = 88/147$

8.4
The Diagonal Part of the Coefficient Operators in the Two KS-DFT-Adapted Function Bases. The PMT Model as an Ideal Bridging Model from KS-DFT to LFR

In our analysis of the DFT results, we begin with the 45 determinantal energies, which can be obtained by *direct* computation. This collection of 45 *direct* energies is – at least conceptually – first reduced to the nine-parameter model of Table 24, or by using Eq. (72) the *direct* energies may be translated to the *indirect* spin basis ones from which the nine-parameter results of this basis can be obtained (Table 25). We use the ADF as a tool that allows the determination of determinantal energies. In this spirit, the reduction of the number of "data" from 45 to 9 may be considered to be a removal of intra-subclass deviations or "random errors".
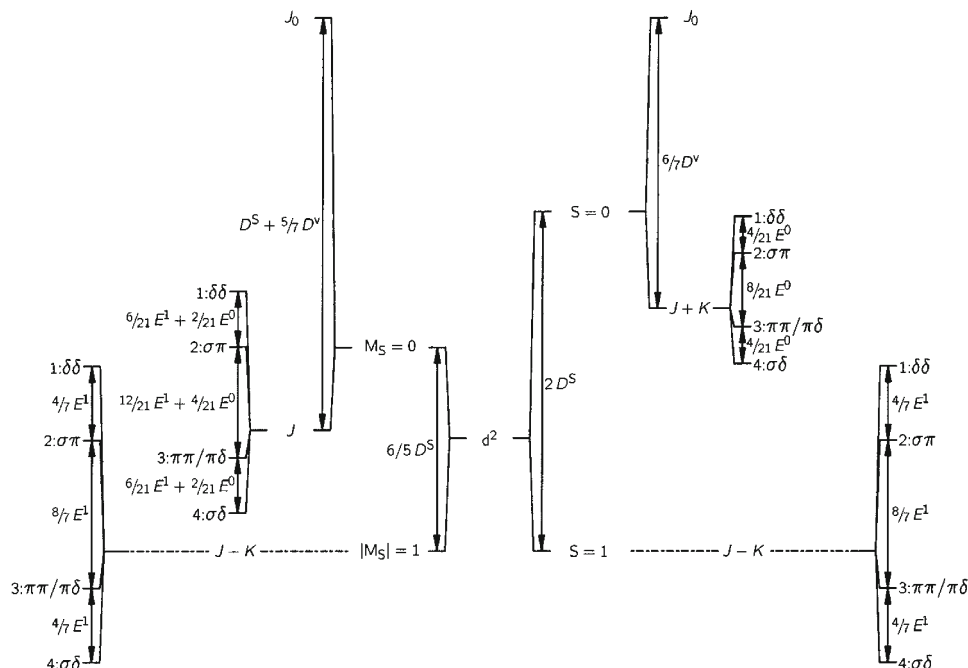
Fig. 4 *Left-hand side of figure*: effective repulsion splitting of the d² configuration as far as its single-determinant representation is concerned, that is, diagonal elements of the operator $\hat{g}$ in the single-determinant basis. This state-function basis (Table 24) is the *direct* connection between the ligand-field plus repulsion model, LFR, and KS-DFT. It begins with a classification of the determinants according to $|M_S|$, $|M_S|=1$ already belonging to the [$J–K$]-class and $M_S=0$ splitting into the J_0- and the J-class. At this stage the spin and seniority splittings have been taken care of. The spatial splitting of the ($J–K$)-class depends on the single parameter E^1 while that of the J-class, which has 50% singlet and 50% triplet character, depends on a spin-weighted sum of E^1 and E^0. For both splittings the interval ratios 1:2:1 follow the symmetry results of Table 16 and Fig. 3. *Right-hand side of figure*: here the Slater determinants containing two different spatial orbitals have been combined pair-wise so as to obtain eigenfunctions of $\hat{S}^2$ (first splitting step). In the next step the (S=0)-states have been separated by the seniority operator into the J_0-class and the [$J+K$]-classes. The interval ratios 1:2:1 of the spatial splittings follow symmetry (Table 16 and Fig. 3), the small intervals being $2b^1$ and $2b^0$ for the [$J–K$]- and [$J+K$]-class, respectively (cf. Eqs. 42 and 50). This state-function basis has the advantage that it makes the PMT operator set {$\hat{Q}$ [D^S], $\hat{Q}$ [D^v], $\hat{Q}$ [E^1], $\hat{Q}$ [E^0]} form a set of mutually diagonally orthogonal operators (Table 25). This means that the values of the parameters can be determined by a scalar product procedure (cf. Eq. 20)

   We note that the function bases of Tables 24 and 25, which are both adapted to KS-DFT, are close to being adapted to the PMT model. Both of them have three class average energies that may be parameterized by $H_{av.}$ plus two parameters of spin and seniority type, D-type. In addition, both have two sets of energy sub-classes whose splittings depend on two spatial parameters, when the symmetry restrictions of Table 16 are used. Thus, if a "data" reduction removing the spatial symmetry deviations of the ADF is performed, a form of the KS-DFT computa-

tional results, which is completely adapted to the PMT model is obtained, that is, a reduction bringing us from the nine-parameter model to the five-parameter PMT model. One might call this process the removal of the inter-subclass deviations or the "spatial errors".

It is therefore gratifying but not surprising that both function bases (Tables 24 and 25) when used with the same set of ADF computations, even without pre-removal of errors, give the same values for the parameters of the PMT model. However, we shall find that the values for the SCS parameters do not come out the same by using the db and sb bases. The difference is not large but clearly discernible. This illustrates the important point that the way from the diagonal representations of KS-DFT to the complete d^2 space representations of the SCS model is not uniquely determined.

Just as the diagonals of the coefficient matrices depend on the function bases, the relationship between the PMT parameters and the SCS parameters will also vary with the function bases. For the spin basis the coefficient matrices of the SCS operators are

$$
\begin{aligned}
\mathbf{Q}^{sb}[D^{sb}] &= \mathbf{Q}^{sb}[D^{S}] + \mathbf{Q}^{sb}[D^{v}] \\
\mathbf{Q}^{sb}[E^{sb}] &= \mathbf{Q}^{sb}[E^{1}] + \mathbf{Q}^{sb}[E^{0}]
\end{aligned}
\tag{73}
$$

where the indices on the SCS parameters indicate their basis dependence. However, ADF combined with Eq. (72) provides us with diagonal energies only and therefore we need to examine the diagonals of these coefficient matrices. In order to complete the PMT model, we need the SCS complementaries. These are defined by being the linear combinations of D- and E type coefficient matrices that are orthogonal to, and have the same areas as, $\mathbf{Q}^{sb}[D^{sb}]$ and $\mathbf{Q}^{sb}[E^{sb}]$ on the diagonal alone

$$
\begin{aligned}
\mathbf{Q}^{sb}[D^{sb\perp}] &= (3/49)^{1/2}\ \mathbf{Q}^{sb}[D^{S}] - (49/3)^{1/2}\ \mathbf{Q}^{sb}[D^{v}] \\
\mathbf{Q}^{sb}[E^{sb\perp}] &= (1/27)^{1/2}\ \mathbf{Q}^{sb}[E^{1}] - (27)^{1/2}\ \mathbf{Q}^{sb}[E^{0}]
\end{aligned}
\tag{74}
$$

where $\mathbf{Q}^{sb}[D^{sb\perp}]$ has the same diagonal area as $\mathbf{Q}^{sb}[D^{sb}]$ (cf. Table 25). This property makes the absolute values of D^{sb} and $D^{sb\perp}$ directly comparable (referring to sb). Since the SCS model is good for all the systems investigated, $D^{sb\perp}$ is expected to be small. Analogous statements apply to the E^{sb} and $E^{sb\perp}$ parameters.

The diagonal areas of these matrices are equal to the diagonal areas of the corresponding coefficient operators in spin basis. For example,

$$
\langle \mathbf{Q}^{sb}[D^{sb}]\,|\,\mathbf{Q}^{sb}[D^{sb}]\rangle_{\text{diag.}} = \langle \hat{Q}[D]\,|\,\hat{Q}[D]\rangle^{sb}_{\text{diag.}}
\tag{75}
$$

Fitting of the diagonal of the coefficient operators only results in parameters that are related to the standard parameters of the PMT model:

$$
\begin{aligned}
D^{sb} &= (49/52)D^{S} + (3/52)D^{v} \\
D^{sb\perp} &= (147^{1/2}/52)(D^{S} - D^{v}) \\
E^{sb} &= (27/28)E^{1} + (1/28)E^{0} \\
E^{sb\perp} &= (27^{1/2}/28)(E^{1} - E^{0})
\end{aligned}
\tag{76}
$$

to be compared with Eq. (27). The coefficients to the SCS parameters D^{sb} and E^{sb} are the relative areas of the PMT and SCS models found in Table 25. As indicated

by the super indices, these relations are basis dependent, whereas the parameters of the PMT model are not.

Thus we have obtained a diagonally orthogonal formulation of the PMT model containing the SCS parameters, thereby providing an *operator contraction* of the PMT model in the spin basis: Discarding the parameters $D^{sb\perp}$ and $E^{sb\perp}$, one obtains the SCS modeling of the ADF results in the spin basis.

In a previous paper [30] we used the *direct* connection with KS-DFT, in other words the determinantal basis, and obtained excellent values for D and E associated with our atomic systems by using a linear least squares adaptation to the SCS model over the complete d^q configuration. In the present chapter, we find that the D and E parameters are function basis dependent, and we therefore devise an alternative and more general method for obtaining the parameter values. This method involves the PMT parameterization as an intermediate step.

The standard parameter scheme $\{D^S, D^v, E^1, E^0\}$ of the PMT model is particularly beautiful in the spin basis where the coefficient matrices are all mutually diagonally orthogonal. It is the intertwining of the total spins in the J class of Table 24, which makes the single-determinant function basis less beautifully, but still completely adaptable to KS-DFT. Nevertheless, the single-determinant function basis is the one to be used in the pair-interaction model required for an immediate extension to applications to other d^q systems ($2<q<8$).

We have on the one hand described an ambiguity in the translation of ADF energies to the parameters of the SCS model whereas those of the PMT model remain uniquely defined. On the other hand, we shall find that the SCS model is clearly superior to the PMT model when it comes to comparing the computational results with experimental data from atomic spectroscopy. This is a good reason for searching for an unambiguous transformation of ADF "data" into SCS parameters.

A method for obtaining the same result for both function bases is to determine a set of PMT parameters from the KS-DFT energies. These parameters obtain the same values with the db and sb function bases. A convenient set of PMT parameters for describing the four independent multiplet term energy differences is the set $\{D, D^\perp, E, E^\perp\}$, defined on the ^{2S+1}L eigenfunction basis of the PMT model (Tables 1 and 3) and determined in either of the function bases db or sb. The SCS parameters D and E contained in this set have values that are basis independent.

As we have seen, the enforcement of SCS modeling on to KS-DFT results in basis-dependent values of the parameters. In practice this dependence is rather small, however, but our computational results can be summed up by noting the systematics that the db values are higher than the sb ones and the basis independent D and E values obtained from a PMT fitting of $\{D, D^\perp, E, E^\perp\}$ highest of all. As a typical example, take atomic V^{3+} for which we determined the following values:

$$
\begin{aligned}
D^{db} &= 0.668 \ \mu m^{-1} & E^{db} &= 0.485 \ \mu m^{-1} \\
D^{sb} &= 0.613 \ \mu m^{-1} & E^{sb} &= 0.475 \ \mu m^{-1} \\
D &= 0.725 \ \mu m^{-1} & E &= 0.490 \ \mu m^{-1}
\end{aligned}
\tag{77}
$$

where the last result is the unambiguous set recommended for the comparison with the experimental values of $D=0.650 \ \mu m^{-1}$ and $E=0.462 \ \mu m^{-1}$.

Typical variances for the two bases are:

$$\text{NPM:} \quad \text{var}^{\text{db}}_{\text{diag.}} = 0.0031 \ \mu\text{m}^{-2} \qquad \text{var}^{\text{sb}}_{\text{diag.}} = 0.0049 \ \mu\text{m}^{-2} \qquad (78)$$

$$\text{PMT:} \quad \text{var}^{\text{db}}_{\text{diag.}} = 0.0083 \ \mu\text{m}^{-2} \qquad \text{var}^{\text{sb}}_{\text{diag.}} = 0.0108 \ \mu\text{m}^{-2}$$

$$\text{SCS:} \quad \text{var}^{\text{db}}_{\text{diag.}} = 0.2684 \ \mu\text{m}^{-2} \qquad \text{var}^{\text{sb}}_{\text{diag.}} = 0.5297 \ \mu\text{m}^{-2}$$

$$\text{H}_{\text{av.}}: \quad \text{SSS}^{\text{db}}_{\text{comp.}} = \text{var}^{\text{db}}_{\text{diag.}} = 16.3133 \ \mu\text{m}^{-2} \quad \text{SSS}^{\text{db}}_{\text{comp.}} = \text{var}^{\text{sb}}_{\text{diag.}} = 20.2889 \ \mu\text{m}^{-2}$$

valid for the computations on gaseous V^{3+}. The last line contains the sum square splitting ($\text{SSS}_{\text{comp.}}$) of the ADF "data", that is, the sum of the squares of the barycentered diagonal elements. This SSS equals the variance obtained by fitting only the non-observable parameter $H_{\text{av.}}$. The transformation from db to sb amounts to a diagonalization of the exchange interactions (K_1, K_2, K_3, K_4) and results in consistently larger variances than in the db calculations irrespective of the number of parameters (9, 5, 3, or 1).

The variance of the nine-parameter model, NPM, corresponds to the information lost in the random errors while the variance of the PMT model corresponds to that lost in spatial symmetry errors plus random errors. Even though the (small) spatial errors are not unsystematic [30], we are not able to account for them by our symmetry-based considerations. The five different parameters of the PMT model are those left after imposing the symmetry restrictions that we must require the ADF to fulfill. The variance of the PMT model thus corresponds to the information lost in repairing the imperfection of the ADF, which is left after its restriction by the use of AOC orbitals.

It is seen that the variance of the PMT model, which we cannot account for, is very minor compared to the systematic variance, which is the difference between the variances of the SCS and PMT models. In other words, the PMT model is extremely good for reproducing our ADF results. This fact will prove useful for us in the forthcoming analyses. The variance of the PMT model reflects that of the exchange/correlation fitting

$$\text{Coulomb} \quad \text{var}^{\text{db}}_{\text{diag.}} = 0 \qquad \text{var}^{\text{sb}}_{\text{diag.}} = 0$$

$$\text{XC} \quad \text{var}^{\text{db}}_{\text{diag.}} = 0.0164 \quad \text{var}^{\text{sb}}_{\text{diag.}} = 0.0228 \qquad (79)$$

reached when the exchange correlation energies are fitted to the exchange expressions of the SCS parameterizations. However, the variances of the PMT model are somewhat smaller since the Coulomb and exchange SCS coefficient operators are non-orthogonal, even when barycentered.

Finally, we should not forget that our previous excellent results on atomic ions [30] were based upon fitting the *direct* computational results, i.e., using the determinantal basis, to the SCS model without introducing the PMT model as an intermediate step. These results are exemplified by the first set of values given in Eq. (77).

Nor should we forget that our previous *Hund's-second-rule* computations [31] only used the energies of the ten states having $M_S=1$. These computations provide the easiest way of getting a very good determination of the ligand-field parameter Δ and the PMT parameter E^1, which is close to the SCS parameter E.

Moreover, they are the most obvious ones to mimic the majority of experimental values found for these parameters. The 10 computations may be supplemented by the average energy of the entire configuration, to give a value for the *Hund's-first-rule* parameter

$$D^S = \frac{3}{2} \left(H_{av.} - H_{av.}[M_S = 1] \right) \tag{80}$$

(cf. Eq. 9b).

Since the operators $\hat{Q}[D^S]$ and $\hat{Q}[E^1]$ do not discriminate between the singlet states, by Eq. (20) their parameters will obtain the same values in the Hund's-rules computations as in the PMT parameterization of the entire configuration by D^S, D^v, E^1 and E^0. However, this statement does not apply to $\hat{Q}[\Delta]$ and the calculations may therefore give values that depend on which part of the states that are used. The fact that Δ does obtain different values in the two computations is another manifestation of the incommensurability of the Coulomb and exchange-correlation functionals. On the other hand, the difference is minor [31] and this fact is satisfactory for our mimicking process.

8.5
Complete Consanguinity of the Orthogonal-Operators Description and the Linear Least Squares Adaptation. A Variation Principle for Sets of Mutually Orthogonal Operators

The considerations of the previous section make it useful to analyze the coefficient operators more closely. These operators were used in connection with the non-linear regression analysis described earlier. In using KS-DFT for our parametrical purposes, we have a different regression analysis, which is linear because the function basis stays the same during the process, either as the determinantal basis db (Table 24) or the spin basis sb (Table 25).

We remind the reader about our separation of sum square splittings into diagonal and non-diagonal parts and about our distinction between orthogonality of operators and diagonal orthogonality of the same operators. Here we focus on these diagonal properties with respect to the two specified diagonals of the db and sb function bases.

The linear analysis using sets of mutually orthogonal coefficient operators is conceptually revealing. Thus each parameter can be generated by renormalizing its coefficient operator and calculating its overlap with the diagonal DFT "data" matrix in the spin basis. For example, the parameter value of D^S is found as the overlap between $\mathbf{H}^{sb}_{comp.}$ and the matrix of the parameter generating operator corresponding to D^S:

$$D^S = \left\langle \mathbf{H}^{sb}_{comp.} \left| \frac{\mathbf{Q}^{sb}[D^S]}{\langle \hat{Q}[D^S] | \hat{Q}[D^S] \rangle^{sb}_{diag.}} \right. \right\rangle \tag{81}$$

Here $\mathbf{H}^{sb}_{comp.}$ is the computed diagonal matrix of 45 ADF energies corresponding to the expectation values of our parametrical Hamiltonian in a strong-field basis of the hierarchies of Eq. (34). Equation (81) is the analog of Eq. (20).

The parameter value for D^S can alternatively be found by fitting the parameter D^S to the matrix $\mathbf{H}^{sb}_{comp,}$ thereby finding the D^S contribution to the SSS. In this case the variance is that associated with the SSS of the remaining PMT parameters plus the variance that remains when the complete set has been fitted. This is the variation principle mentioned earlier, where the consanguinity between the orthogonal-operators description and the least-squares description was discussed. Let us finish this discussion by giving a numerical example using the standard PMT set of parameters, whose operators are simultaneously mutually orthogonal and diagonally orthogonal in the spin basis.

For V^{3+} whose complete parameter set is $\{H_{av,}, D^S, D^v, E^1, E^0\}=\{-0.612, 0.587, 1.047, 0.467, 0.697\}$, the computed SSS consists of the following terms (Table 25):

$$\begin{aligned}
SSS^{sb}_{diag.} &= (D^S)^2 \langle \hat{Q}\,[D^S]\,|\hat{Q}\,[D^S]\rangle^{sb}_{diag.} + (D^v)^2 \langle \hat{Q}\,[D^v]\,|\hat{Q}\,[D^v]\rangle^{sb}_{diag.} \\
&\quad + (E^1)^2 \langle \hat{Q}\,[E^1]\,|\hat{Q}\,[E^1]\rangle^{sb}_{diag.} + (E^0)^2 \langle \hat{Q}\,[E^0]\,|\hat{Q}\,[E^0]\rangle^{sb}_{diag.} + (\chi^{sb}_{diag.})^2 \\
&= 0.587^2 \times (40) + 1.047^2 \times (120/49) + 0.467^2 \times (792/49) \\
&\quad + 0.697^2 \times (88/147) + 0.011 \\
&= 13.777 + 2.685 + 3.525 + 0.291 + 0.011 = 20.288 \;\mu m^{-2} \qquad (82)
\end{aligned}$$

where the last term in the sum is the variance when all the four parameters are fitted and where the $H_{av.}$ term has no contribution to the SSS. $H_{av.}$ is the difference between the computed average energy of d^2 and the energy of the AOC. It may be removed before the parametrical analysis is performed, just by subtracting $H_{av.}$ from all the individual computed energies (prebarycentration). This subtraction has no influence upon the numerical values of all the other quantities including the variance. If the least squares calculation is made by fitting only the parameter $H_{av.}$, then the variance of this regression is $SSS^{sb}_{diag.}$ (cf. Eq. 78). If then D^v say, is fitted, then its parameter value would still be the same as above. Moreover, in this case the variance would be the sum of the SSS terms of all the remaining terms plus the variance of the complete PMT model, fitted in sb, while the associated diagonal matrix would be orthogonal to those of $\mathbf{1}^{sb}$ and $\mathbf{Q}^{sb}_{diag.}\,[D^v]$.

An alternative way of looking at this orthogonal operators' analysis is by focusing on the analogy with the variation principle. One may think of the complete analysis as taking place in steps. The zeroth step then is barycentration and the variance before and after this step is equal to the value of $SSS^{sb}_{diag.}$. In the first step the parameter D^S reduces this variance by its own contribution, $(D^S)^2 \langle \hat{Q}[D^S]\,|\hat{Q}[D^S]\rangle^{sb}$. In the second step D^v reduces the new variance by its contribution and so on until the final variance of the complete model is reached. This final variance is a measure of the numerical validity of the PMT model and it can be obtained in the orthogonal operators' formulation by subtracting all the parametrical terms from $SSS^{sb}_{diag.}$.

8.6
Completion of the KS-DFT Computational Results via the Parameterization Method

One of the deficiencies of the KS-DFT method in dealing with excited states of open shell systems is that the quantities that correspond to the non-diagonal elements of the single Slater determinant bases cannot be computed. By the transformation of Eq. (71), we saw a simple and effective example of how the use of Coulomb and exchange integrals as energy parameters allowed a partial diagonalization of an energy matrix image of KS-DFT. The details of this image were expressed in PMT and SCS parameters in Tables 24 and 25.

   One aspect of this parametrical completion of KS-DFT can be illustrated by focusing upon Eq. (82) and dropping the spin basis and diagonality restrictions so as to embrace the full effective d^2 function space. Since the parameters are globally valid within this space, one only has to replace the areas of the associated coefficient operators by the global areas given in Table 1. By doing this, one obtains for the four terms making up the model part of the configurational area:

$$\text{SSS}_{\text{PMT}} = 0.587^2 \times (280/7) + 1.047^2 \times (120/7) + 0.467^2 \times (360/7)$$
$$+ 0.697^2 \times (40/7)$$
$$= 13.78 + 18.79 + 11.22 + 2.78 = 46.57 \ \mu\text{m}^{-2} \tag{83}$$

to be compared with the 20.277 μm^{-2}, which is the value of the corresponding diagonal part of the spin basis excluding the variance found in Eq. (82). We see that even in this case where a partial "diagonalization" has taken place on going from the basis of Table 24 to that of Table 25, the full description of the effective d^2 configuration by the present parametrical method is in this example based upon only about half the area of the configuration. The area most heavily affected by the diagonalization is that of E^1, which is only about 28% diagonal in spin basis, while the area of D^S is unchanged since the spin basis implies that $\hat{Q}\,[D^S]$ is diagonal. But the four parameters may be determined, since we are in possession of enough computationally independent diagonal elements linearly expressed in the same parameters. However, it is obvious that if the degree of diagonality in any parameter were zero in the determinantal basis, it would be impossible to get anywhere at all with this parameter unless KS-DFT made it possible to change the orbital basis and thereby change the determinantal basis sufficiently and still obtain energies that could be interpreted as expectation values of a Hamiltonian of the old system in the spin basis.

   The energy matrices of Tables 12–15, 17, 18, 22, and 23 are set up in the spin basis. By inserting the computed PMT parameter values of the set $\{D^S, D^v, E^1, E^0\}$ into these energy matrices, one obtains the full energy matrices of the $\hat{g}$ operator. Being strong-field matrices of the special hierarchies of Eq. (34), they are diagonal in all ligand-field operators of these hierarchies, whose matrices therefore are easy to add before the computed eigenstates and eigenenergies can be obtained by diagonalization of the sum of the R and LF matrices.

   In conclusion, if computed values of the complete set of parameters of an LFR model can be obtained by KS-DFT computations, then, in addition to the diagonal elements of the Hamiltonian, all the non-diagonal elements will also have become available, and thereby the complete computed LFR model.

9
ADF-Computations for Atomic d² and d⁸ Ions. Comparison of PMT Parametric and SCS Parametric Results with those Based on Atomic Spectroscopy

9.1
The Relationship Between the ADF Coulomb and Exchange Results and the PMT Parameterization

Our KS-DFT computations give a much better agreement with experimental results by using the restrictions of the SCS model rather than the less severe restrictions of the PMT model. This is perhaps understandable in view of the symmetry analysis discussed earlier. However, the detailed connection between this chapter's treatment based upon the symmetries of orbitals and operators and KS-DFT needs further comments.

Our restrictive way of applying KS-DFT fixes the entirety of orbitals in the first place while imposing the restrictions of the d^q configuration and of the spherically symmetrical Hamiltonian. Thereby our approach suggests using the SCS model for the KS-DFT states. However, we found previously [30] that both the Coulomb and exchange functionals act in SCS-faithful ways, but in such a fashion that the two functionals become associated with different SCS energy parameters. When these two incompatible SCS functionals are added, their sum will obey the PMT model rather than the SCS model. In this way the ADF produces two D-type parameters and two E-type parameters, one Coulomb parameter and one exchange parameter of each type[10].

For gaseous V^{3+} the PW91 results are:

$$D^{\text{Coul.}} = 0.779 \ \mu m^{-1} \quad E^{\text{Coul.}} = 0.524 \ \mu m^{-1}$$
$$D^{\text{exch.}} = 0.510 \ \mu m^{-1} \quad E^{\text{exch.}} = 0.352 \ \mu m^{-1} \tag{84}$$

These parameter values can be translated into the following PMT values:

$$D^{\text{S}} = 0.587 \ \mu m^{-1} \quad E^0 = 0.697 \ \mu m^{-1}$$
$$D^{\text{v}} = 1.047 \ \mu m^{-1} \quad E^1 = 0.467 \ \mu m^{-1} \tag{85}$$

by using the relationships

$$D^{\text{S}} = (1/7)(2D^{\text{Coul.}} + 5D^{\text{exch.}}) \quad E^0 = 2E^{\text{Coul.}} - E^{\text{exch.}}$$
$$D^{\text{v}} = 2D^{\text{Coul.}} - D^{\text{exch.}} \quad \quad \quad E^1 = (1/3)(2E^{\text{Coul.}} + E^{\text{exch.}}) \tag{86}$$

obtained by realizing that the coefficients defining $\hat{Q}\,[D^{\text{Coul.}}]$ are those of the expressions of classes J_0 and J_i (i=1,2,3,4) and those defining $\hat{Q}\,[D^{\text{exch.}}]$ are obtained

---

[10] In our previous paper [30], we found, in addition, that all the exchange functionals of the LDA sets gave parameter values of zero for $E^{\text{exch.}}$ and thus were unable to distinguish between the energies of states characterized by the same value for the quantum number M_S. This means that this approximation is only able to distinguish between the different spatial situations through their Coulomb energies (cf. above and the appendix of the previous paper).

by subtraction of the class J coefficients from corresponding ones of the $[J–K]$-class.

The Eqs. (86) apply to two independent computations (Eqs. 84 and 85) using the PMT model on the ADF energies computed from the sum of the Coulomb and the exchange-correlation functionals. If the Coulomb parameters are computed from the Coulomb functional and the exchange parameters from the exchange functional, a set of parameter values, which are much the same but not identical, are obtained from these equations except for that of the parameter E^0, which comes out rather different. In view of the fact that even the barycentered coefficient operators of the right-hand side pairs of parameters of Eq. (86) are non-orthogonal, it is not surprising that the parameter values obtained in the two different ways are non-identical. Conversely, it is a surprising regularity that they are identical to the last figure when a pure exchange functional is used (local density functional exchange, Becke-exchange [77] or PW91-exchange [75]). The reason is that the exchange functionals only include interactions of electrons of like spins, whereas the correlation functionals include interactions of electrons of different spins and therefore induce noise into the exchange results, a noise which is partially fitted by the Coulomb parameters in the PMT fitting of the total energy. Therefore, this fitting cannot end up with the same parameter set as that of the independent fitting of the Coulomb and exchange-correlation functionals.

Remembering that the ADF invariably gave the Coulomb parameters higher values than the corresponding exchange parameters, we obtain a connection between this fact and the persistent observation of the inequalities illustrated in Table 26, Section 9.4:

$$D^v > D^S \quad \text{and} \quad E^0 > E^1 \tag{87}$$

The coefficient operators $\hat{Q}\,[D^{Coul.}]$ and $\hat{Q}\,[D^{exch.}]$ have traces of 8/21 and –8/21, respectively, and even after barycentration, they remain non-orthogonal.

9.2
Strong-Field Comparisons Between Two Sets of Parametrical ADF Results. Systematic Deviations Between PMT and SCS Energies

In the discussion associated with Tables 24 and 25, it was pointed out that our PMT model was ideally suited for removing the "random noise" as well as the "spatial noise" from the ADF data. We shall apply this insight here to make an intermediate data reduction of the data into PMT parameters. In this way we shall be able to describe and quantify the systematic deviations between the PMT parameterized expectation values for the microstate energies, and the corresponding energies calculated from the final SCS parameters.

There is a choice to be made between the two equivalent ways of giving a strong-field description of the ADF "data". We found above that in the single-determinantal function basis (db), our preferred orthogonal operator basis for the PMT model lost their diagonal orthogonality. When we used the spin basis (sb), which inherently has a higher symmetry because it makes up an eigenbasis of the $\hat{S}^2$ operator, we accomplished our goal of diagonal orthogonality. It should, however, be stressed that the two function bases give the same inherent infor-

mation although the spin basis provides this information in a form, which simplifies the conceptual interpretation of the deviations between the expectation values of the PMT and SCS Hamiltonians. We shall therefore mostly use the spin basis of Table 25 here.

We begin by recalling that the PMT parameters D^S and D^v would take on equal values if the restrictions of the SCS model were valid. In this case we would also have $E^1 = E^0$ (cf. Eq. 21). It turns out that the inequalities in Eq. (87) are valid for the computed parameters of all the d^2 and d^8 systems (cf. Table 26). This means that the parameters of the PMT model exhibit systematic deviations from those of the SCS model. These deviations are easy to remember because the smaller PMT parameters correspond to Hund's first and second rules, respectively (Fig. 1). Thus as a consequence of Eqs. (27) and (76), the PMT model does not stabilize the ground states as much as do the SCS parameters.

By using the D part of Eq. (76), the parametrical SCS energies of Table 25 can be expressed in the PMT parameters D^S and D^v. Once this has been done, it is possible to express the differences in PMT and SCS spin and seniority energies in terms of the same two class parameters. The results are the following:

$$J_0^{PMT} - J_0^{SCS} = (12/26)(D^v - D^S)$$

$$[J + K]_{av.}^{PMT} - [J + K]_{av.}^{SCS} = -(9/26)(D^v - D^S) \qquad (88)$$

$$[J - K]_{av.}^{PMT} - [J - K]_{av.}^{SCS} = +(1/26)(D^v - D^S)$$

These expressions are purely theoretical and purely symmetry based. They obey the barycenter rule when the class weights of Table 25 are used. The PMT class energies have a one-to-one correspondence with the ADF computed energies, adjusted by removal of the random errors and the spatial errors. Denoting these adjusted energies "ADF" energies, then it is a question of a linear transformation to go from the "ADF" to the PMT parameterization. Thereby Eq. (88) quantifies the relative over- and underestimations [30] of the class energies by the ADF. Including now the qualitative result of all the computations made, namely that $(D^v - D^S) > 0$ (cf. Table 26), we can conclude that the energies of the J_0 and $[J-K]_{av.}$-classes are overestimated and that of the $[J+K]_{av.}$-class underestimated by the ADF. Moreover, it may be noted that the J^0 class has an overestimation, which is twelve times that of the $[J-K]$-class. Finally, the ADF has problems, which are an order of magnitude greater with the spin singlet space than with the spin triplet space. However, when both spaces are added – as we do here – the standard deviations of the parametrical values remain reasonable.

In a similar fashion an analysis of the E-type of operators can tell about the energy splitting of the $[J+K]_{av.}$ and $[J-K]_{av.}$-classes, the spatial splittings. The results are as follows:

$$[J + K]_1^{PMT} - [J + K]_1^{SCS} = 5(9/98)(E^0 - E^1)$$

$$[J + K]_2^{PMT} - [J + K]_2^{SCS} = 3(9/98)(E^0 - E^1)$$

$$[J + K]_3^{PMT} - [J + K]_3^{SCS} = -1(9/98)(E^0 - E^1)$$

$$[J + K]_4^{PMT} - [J + K]_4^{SCS} = -3(9/98)(E^0 - E^1) \qquad (89)$$

$$[J - K]_1^{\mathrm{PMT}} - [J - K]_1^{\mathrm{SCS}} = -5(1/98)(E^0 - E^1) \qquad \text{(89 con.)}$$

$$[J - K]_2^{\mathrm{PMT}} - [J - K]_2^{\mathrm{SCS}} = -3(1/98)(E^0 - E^1)$$

$$[J - K]_3^{\mathrm{PMT}} - [J - K]_3^{\mathrm{SCS}} = 1(1/98)(E^0 - E^1)$$

$$[J - K]_4^{\mathrm{PMT}} - [J - K]_4^{\mathrm{SCS}} = 3(1/98)(E^0 - E^1)$$

All the quantitative remarks made for the ADF class energies have analogs for the sub-class energy differences (cf. Table 26), but the signs are changed. The ADF splittings of the $[J+K]$-class are overestimated and those of the $[J–K]$-class (very slightly) underestimated relative to the SCS-averaged spatial energies. This is not surprising since it can be directly concluded from the inequality of the E parameters and the energy expressions of Table 25. Again the deviations between PMT and SCS are more pronounced for the singlets than for the triplets and again we meet a factor of 9. The spatial symmetry collected together in Table 16 can again be observed in Eq. (89).

Because of the requirement of a five-parameter model to obtain the full advantage of the ADF computations (Table 1), at least five Slater determinants have to be included. They will then provide five ADF energies and four independent energy differences corresponding to four physically significant parameters that are independent of the zero point of energy and may be expressed in the form of the standard PMT parameters. However, five arbitrary determinants would not suffice. They must be chosen with the following restrictions with reference to Table 24: one determinant from the J_0 class, two from the J class and two from the $[J–K]$-class. Otherwise, the information-content is not high enough. All the rest of the determinants are then redundant if you want a quick answer. However, the ADF behaves in a certain sense as a tool measuring its results. Certain results that ought to be identical by symmetry are only approximately so. Therefore, in order to remove the two kinds of errors, which we have named the random errors and the spatial errors, it is useful to include at least 25 out of the 45 microstates of d^2: all determinants of the J_0 class and – in an obvious, systematic way – half the determinants of the two other classes. However, it is useful to include the complete set of 45 microstates in order to take advantage of the orthogonal operator's description of the present LFR approach. The final data reduction has in discarding the non-SCS faithful part of the ADF results the function of removing the "systematic errors". An interpretation of what one has actually computed by taking a given Slater determinant can be read out of the combination of Tables 16 and Table 24.

It should be mentioned in the present context that in earlier papers [41, 43] addressing in some detail the question about computing the multiplet term energies by KS-DFT, only three determinants were chosen to represent the whole d^2 configuration. Moreover, these so-called non-redundant determinants were chosen as one from the J_0 class and two from the $[J–K]$-class. From Table 24 one may now observe that this means that the computed SCS parameters will, except for random and spatial errors, be $\frac{42}{54} D^{\mathrm{S}} + \frac{12}{54} D^{\mathrm{v}}$ and E^1, both values lower than our SCS values according to Eqs. (27) and (87).

9.3
Weak-Field Comparisons Between Two Sets of Parametrical ADF Results. Systematic Deviations Between PMT and SCS Energies

Our first aim of these atomic computations was to obtain the relative energies of the gaseous multiplet terms ^{2S+1}L. We have computed two sets of multiplet term energies for all the d^2 and d^8 systems for which we have complete, spectroscopically determined values to compare with (Tables 4–7). One set of computed values for these energies is based upon the PMT model, which is complete in the same sense as the spectroscopic data and corresponds to the five pieces of "ADF" data. The other computed set is obtained via the enforcement of the SCS model where we have discarded the $SCS^\perp$ part of the computational results by using the operator contraction to discard the $D^\perp$ and $E^\perp$ parts of the PMT model (cf. above).

Table 1 contains the parametrical expressions for all the multiplet term energies in the PMT model, which still corresponds in a one-to-one fashion to the ADF energies deprived of their noises as in the previous subsection. It also contains the SCS coefficient operators. By combining these latter quantities with the expressions of Eq. (27), we obtain the following results, which are analogous to those of Eqs. (88) and (89).

The spin and seniority classes have the following purely symmetry-based expressions:

$$
\begin{aligned}
H_S^{PMT} - H_S^{SCS} &= (12/5)(D^v - D^S) \\
H_G^{PMT} - H_G^{SCS} = H_D^{PMT} - H_D^{SCS} &= -(3/5)(D^v - D^S) \\
H_P^{PMT} - H_P^{SCS} = H_F^{PMT} - H_F^{SCS} &= (1/5)(D^v - D^S)
\end{aligned}
\tag{90}
$$

which when including the inequalities that are found so consistently (cf. Eq. 87 and Table 26) show that ^1S is overestimated systematically by the ADF by an amount four times as large as the amount by which the other singlets are underestimated. The triplets are overestimated slightly meaning that Hund's first rule is not defended so well by the noise-corrected ADF results as by those enforced by the SCS model.

The spatial symmetry results are

$$
\begin{aligned}
H_G^{PMT} - H_G^{SCS} &= (15/35)(E^0 - E^1) \\
H_D^{PMT} - H_D^{SCS} &= -(27/35)(E^0 - E^1) \\
H_P^{PMT} - H_P^{SCS} &= -(7/35)(E^0 - E^1) \\
H_F^{PMT} - H_F^{SCS} &= (3/35)(E^0 - E^1)
\end{aligned}
\tag{91}
$$

which, when the inequalities at Eq. (87) are included, show that the ADF results overestimate the energy of the ^3F term, also with respect to the operator that we associated with Hund's second rule. Because of the symmetry-based barycentration, which is valid for the singlets and the triplets independently, another way of expressing this is to say that the triplets are computed to split too little and the singlets too much.

In order to illustrate the meaning of Eqs. (90) and (91), we give just one example.

For V^{3+} the barycentered ADF value for the energy of ^3F is

$$\bar{H}_F^{PMT} = -0.791 \ \mu m^{-1} \tag{92}$$

with the associated PMT parameters already given in Eq. (85) from which the following SCS parameters can be obtained by using Eq. (27): $D=0.724$; $E=0.489$; giving the SCS multiplet term energy

$$\bar{H}_F^{SCS} = -0.903 \ \mu m^{-1} \tag{93}$$

It is seen that using the PMT rather than SCS parameterization overestimates the energy of the ground term ^3F term by 0.11 μm^{-1}. By adding the corrections of Eqs. (90) and (91) to $\bar{H}_F^{SCS}$, one obtains $-0.903+(1/5)(D^v-D^S)+(3/35)(E^0-E^1)=$ $-0.791 \ \mu m^{-1}$, which is the value of $\bar{H}_F^{PMT}$.

9.4
Deviations Between ADF Values for the Multiplet Term Energies of Atomic Ions and the Spectroscopically-based Energies

We have chosen to use the experimental term values (Tables 4–7) as our standard and, in order to make all the sets comparable, we have first of all removed the effect of their different zero points of energy by barycentration. In this way we are left with a vector of five energy components which, when properly weighted, add up to zero and thus in fact contain only four pieces of number information.

A qualitative way of making a comparison between the relative computed and observed multiplet energies is to remove one piece of information by transforming (normalizing) the computed vectors so as to give them the same length as the observed ones. This provides the normalized computed energy values for the individual multiplet terms, which are directly comparable with the corresponding quantities based on observation. There is, of course, still a quantitative difference in the uniform splitting of the whole configuration, measured by the renormalization constant.

We collect together five rows of barycentered term values (μm^{-1}) for $^1S, ^1G, ^3P, ^1D, ^3F$ illustrating first of all their decreasing energy order. The example is again V^{3+}, which is typical. In the two top rows the computed, barycentered PMT values and those normalized to have the same length as the experimental vector are given. The third and fourth rows are the analogous SCS quantities

	^1S	^1G	^3P	^1D	^3F
PMT:	4.970	0.815	0.542	−0.113	−0.791
PMT (normalized):	4.394	0.720	0.479	−0.100	−0.699
SCS:	3.866	0.992	0.496	0.339	−0.903
SCS (normalized):	3.526	0.905	0.453	0.309	−0.823
EXP:	3.374	0.968	0.462	0.228	−0.828

It is seen that except for the ^1S and ^3P terms, which are calculated high (^1S invariably considerably so), the experimental energies lie in between the PMT values and the SCS values. However, it is also seen that the SCS values are closer to experiment.

Table 26 Two sets of PMT results of the complete d^2 and d^8 computations. Two different parameterization schemes have been given for the same ions for which experimental multiplet term values were given in tables of Section 3. The first row of parameters belongs to our standard set of orthogonal coefficient operators (Table 1), which are diagonally orthogonal in the spin basis of Table 25. The parametrical inequalities of Eq. (87) can be seen to be quite general. The four parameters can be used to calculate the computed barycentered multiplet term energies and SSS_{PMT} for the d^2 and d^8 configurations. The comparable experimental quantity $SSS_{exp.}$ was obtained from the data of Tables 4–7. The square root of the ratio between these two sum square splittings, $(SSS_{PMT}/SSS_{exp.})^{(1/2)}$ (denoted by PMT-ratio in the table and given together with the first row of parameters), is a global measure of the relative root mean square splittings, computed relative to observed. The second row of parameters contains among them the SCS parameters D and E, and in addition the parameters, $D^\perp$ and $E^\perp$, which supplement the SCS model to make it become the PMT model. The relationship between the two sets is given in Eq. (27). The inequalities of Eq. (87) immediately give the signs of the two supplementary parameters whose signs could have been chosen to be both positive, had the computational "data" been known before the coefficient operators were defined. If the parameters $D^\perp$ and $E^\perp$ are discarded, we have the SCS model, whose root mean square splitting $(400/7)^{\frac{1}{2}}\rho$ is given in the form of the parameter ρ, defined in Eq. (23). The SCS-ratios appear in the second row for each metal ion. It is seen that these ratios represent a clearly improved description of observation. The ratio $\eta = D/E$ is seen to be remarkably constant. The comparison of the splittings by length has been supplemented by one comparing the relative positions of the multiplet terms in a global way, that is, using only a single parameter, which serves as a measure of the distortion of the structure of the configuration. This comparison has been made by way of the scalar product (using the weights of Table 2) of the computed, barycentered parametrical multiplet term vector (normalized to unity) and the corresponding observed vector. This scalar product was interpreted as the cosine to an angle, where the angle, which is zero for no distortion, is a sensitive measure of the distortion. These angles have been entered in the table as PMT-angles and SCS-angles. It is seen that the SCS-angles are clearly smaller than the PMT-angles. Our single example of an LDA computation illustrates the general feature that LDA gives a distortion that is larger for the D-type parameters and smaller for the E-type, when compared to PW91. This trade-off leaves the PMT angle and ratio rather unchanged. The quality of the SCS parameters are equally good for VWN and PW91, and only the fact that VWN gives an exchange E parameter of zero makes us prefer PW91

| | $H_{av.}$ | D^S | D^v | E^1 | E^0 | PMT-ratio | PMT-angle | | |
	$H_{av.}$	D	E	$D^\perp$	$E^\perp$	SCS-ratio	SCS-angle	ρ	η
Ti/d2	−0.542	0.483	0.807	0.381	0.559	1.16	14.0		
	−0.542	0.580	0.399	−0.148	0.053	1.13	3.5	0.70	1.45
V/d2	−0.611	0.586	1.047	0.467	0.696	1.13	15.0		
	−0.611	0.724	0.489	−0.210	0.068	1.10	2.9	0.87	1.48
Cr/d2	−0.679	0.671	1.228	0.536	0.804	1.10	15.4		
	−0.679	0.838	0.563	−0.255	0.080	1.06	2.7	1.01	1.49
Mn/d2	−0.748	0.751	1.393	0.601	0.905	1.08	15.6		
	−0.748	0.944	0.632	−0.294	0.090	1.04	2.7	1.14	1.49
Fe/d2	−0.818	0.826	1.535	0.661	0.998	1.05	15.6		
	−0.818	1.038	0.695	−0.325	0.101	1.02	2.6	1.25	1.49
Co/d2	−0.895	0.909	1.697	0.727	1.100	1.05	15.9		
	−0.895	1.145	0.764	−0.361	0.112	1.01	2.6	1.38	1.50
Zr/d2	−0.471	0.384	0.519	0.277	0.453	1.17	8.2		
	−0.471	0.424	0.294	−0.061	0.052	1.16	6.3	0.52	1.44
Nb/d2	−0.457	0.439	0.648	0.316	0.545	1.10	9.8		
	−0.457	0.501	0.339	−0.095	0.068	1.08	2.5	0.60	1.48
Mo/d2	−0.454	0.492	0.770	0.353	0.630	1.09	11.4		
	−0.454	0.575	0.381	−0.127	0.083	1.06	1.7	0.69	1.51

Table 26 (continued)

	$H_{av.}$	D^S	D^v	E^1	E^0	PMT-ratio	PMT-angle		
	$H_{av.}$	D	E	$D^\perp$	$E^\perp$	SCS-ratio	SCS-angle	ρ	η
Ta/d2	−0.392	**0.433**	**0.627**	**0.304**	**0.582**	**0.98**	**9.5**		
	−0.392	**0.491**	**0.332**	**−0.089**	**0.083**	**0.96**	**3.5**	**0.59**	**1.48**
W/d2	−0.387	0.478	0.728	0.332	0.656	1.10	10.8		
	−0.387	0.553	0.365	−0.114	0.097	1.08	3.9	0.66	1.52
Ni/d8	−0.479	0.706	1.261	0.565	0.894	1.12	15.5		
	−0.479	0.873	0.598	−0.254	0.098	1.08	2.6	1.06	1.46
Cu/d8	−0.524	0.805	1.446	0.640	1.024	1.10	15.3		
	−0.524	0.997	0.679	−0.293	0.115	1.07	2.2	1.21	1.47
Zn/d8	−0.555	0.902	1.640	0.715	1.160	1.10	15.5		
	−0.555	1.123	0.760	−0.338	0.133	1.06	2.4	1.36	1.48
Pd/d8	−0.255	0.523	0.919	0.389	0.721	1.14	14.5		
	−0.255	0.642	0.422	−0.181	0.099	1.10	2.5	0.77	1.52
Ag/d8	−0.250	0.579	1.040	0.427	0.809	1.13	15.3		
	−0.250	0.718	0.465	−0.211	0.114	1.09	1.7	0.86	1.54
Cd/d8	−0.247	0.631	1.152	0.463	0.888	1.13	15.6		
	−0.247	0.788	0.505	−0.238	0.127	1.08	1.4	0.94	1.56
V/d2	−0.279	**0.650**	**0.773**	**0.377**	**1.130**	**1.07**	**14.2**		
(VWN)	−0.279	**0.687**	**0.452**	**−0.056**	**0.226**	**1.03**	**3.3**	**0.82**	**1.52**

After the normalization, the comparisons illustrate the internal structure of the configuration and the superiority of the SCS model becomes even clearer. The ground term ^3F is more stabilized by the SCS than by the PMT modeling.

A quantitative way of making the comparison between the computed vector and the observed one is by focusing on their relative lengths and the angle between them. These comparisons have been collected together in Table 26. This table contains the results for all the gaseous ions of d^2 and d^8 configurations. The computed values of the standard PMT sets of parameters as well as those of an additional set have been given.

We may talk about the experimental sum square splitting $SSS_{exp.}$ in just one way: the weighted sum of the squares of the barycentered experimental multiplet term energies. However, for the ADF-computed values the sum square splitting SSS_{ADF} has two different parametrical values, one based upon the fitting to the PMT model (SSS_{PMT}) and one to the enforced model (SSS_{SCS}). The square root of the two ratios describing the computed sum square splittings relative to the experimental values have been collected together in Table 26 with the PMT ratios in the top line and the SCS ratio in the bottom line associated with each metal ion (based upon the parameters and parameter values printed in bold). These ratios make up a summaric way of comparing, by length, the root mean square splittings.

It is seen from the table that the SCS modeling is always the better one. It is also seen that the computed total splitting is invariably larger than the experimental one but the excess is almost always less than 10%. This is a satisfactory result because it is more than two times better than that of the open-shell Hartree-Fock

method, which up until now has been the basis that we have been forced to accept when using orbitals in chemistry without configuration interaction [48, 49].

Table 26 also contains the angles between the computed and the experimental vectors whose components are the barycentered multiplet term energies. The scalar product of the computed and experimental vectors makes a good way of obtaining a measure of the resemblance of the two vectors, and the associated angle is a very sensitive measure. Again the SCS-based multiplet term energies resemble the spectroscopic ones much more than do the PMT-based energies.

We have made the angular comparisons by using alternative sets of SCS parameters (cf. Eq. 77). They vary some by length, but not enough to justify further comments here except for referring to a previous paper [30] where we obtained even better SCS parameter values by fitting of the determinant basis of Table 24. However, it is worth noting that by angle all our SCS fitted parameters exhibit a marked improvement relative to those fitted with PMT. This conclusion was also the symmetry-based theoretical one arrived at above. In spite of this, the PMT model is still the more useful one for the analysis of the "ADF data".

The external zero point of energy in all the present ADF computations is that provided by the AOC computation. Even though the AOC energy is thought impossible to interpret, we used this energy in the previous paper [30] together with that of other computations on which spherical symmetry, and thereby fractional occupation numbers, was imposed. It turned out that by interpreting these energies as average energies of appropriate states and combining this interpretation with the SCS model, the energy differences depended on Jørgensen's spin-pairing energy parameter D. It is, however, well known [40, 74] that the energy of the AOC is not equal to the average energy of the configuration calculated from the energies of the determinantal states. Since this latter concept is well defined in our present fixed-d-orbital computations and has the energy $H_{av.}$ relative to that of the AOC and since our computed values of $H_{av.}$ have turned out to be close to those of D^S, we have included them in Table 26 as "empirical" results from the ADF.

10
KS-DFT-Results for VX_4^- (X=F, Cl, Br, I) and CrY_4 (Y=F, Cl, Br).
Evidence Against the Philosophy of the Cellular Ligand-Field Model (CLF)

10.1
KS-DFT Computational Corroboration of the Molecular Orbital Background of Qualitative LFT and Thereby Evidence for the Philosophy the AOM and Against that of the CLF

After the classical electrostatic models (EM) of the ligand field, the additive [12] and the non-additive [21] ones, were given up as physical models, the angular overlap model (AOM) took over [7]. About 20 years later the cellular ligand field model (CLF) was proposed [78–80]. This model has a "master equation" (p 232 in [79]), which is identical to that of the AOM. Nevertheless, the inventors claim that the CLF has a fundamentally different philosophy than the AOM (p 231 in [79]): "In higher oxidation states of Werner complexes,…, the d electrons are little involved in the valence shell. Bonding with ligands takes place between ligand

functions and metal s and/or p orbitals,…. In this way, ligand-field theory is excused the tasks of bond theory." Moreover, the authors forwarding the CLF ideas deliver a rather formal derivation of the "master equation", which they claim can be used to compute the empirical parameters from first principles. Mainly for practical reasons (p 230 in [79]), however, they do not pursue this task. The speculative and formal character of the arguments in favor of the CLF and the large number of papers advocating the CLF made it almost irrefutable and the schism between the CLF and the AOM philosophies has not been resolved.

In this context there is however one point that requires comments. The CLF authors add an idea to the CLF model, which is foreign to the AOM, namely that coordinatively sparse complexes must be treated with additional cells representing lacking ligands, so-called void regions in space. This type of cell should – according to the philosophy – be associated with negative empirical energy parameters of e_σ type, and this was found to be in agreement with experiments on square planar four-coordinate complexes. Nevertheless, the idea of void regions has been criticized [81, 82] and by using the AOM on square complexes, it was shown that d-s mixing [83–87] was able to account for the existence of an effective σ operator acting on d space and associated with a negative e_σ parameter. Thereby, the idea of void regions became superfluous. This idea was nice to avoid because it was only symmetry defined in a square planar complex in which case it was obviously defined as the regions above and below the molecular unit. Otherwise the position of the void was not well-defined and, for this reason alone, not scientifically sound. In this subsection we shall show that our KS-DFT modeling provides qualitative as well as quantitative counterevidence against the other main arguments associated with the CLF.

Earlier the method of using the ADF was described. After the initial unrestricted self-consistent-field computation has determined the geometry and allowed us to identify the KS-orbitals, the restricted SCF computation on the d^2 configuration with occupation numbers of (2/10) for all the ten "d" spin orbitals, that is, the four $e(T_d)$ and the six $t_2(T_d)$ spin orbitals, gives us the analog of the average-of-configuration (AOC) computation of the atomic case. We have already denoted this computation, by which the molecular symmetry (here T_d) becomes imposed upon our problem, by the "AOC" computation. "C" here refers to the ligand-field configuration or the partially filled shell configuration, "d^2", consisting of the three subconfigurations, e^2, et_2, and t_2^2. Thus, the KS-DFT description – through parameterization – goes beyond Hartree-Fock by including subconfiguration interaction, just as does the LFR description.

There are some immediate results of the "AOC" computations, which we shall comment on here by specifically focusing on the system VCl_4^- (and, for comparison, VF_4^-). First of all, we want to point to some qualitative results where the KS-DFT shows its potential for reviving ligand-field theory. This theory can be conceived of as having three parts:

1. A very strong qualitative part that provides symmetry-species assignments to the ground states and lower excited states of metal complexes containing a partially filled shell of d electrons. These assignments imply physical contents of the concept of oxidation states.

2. A quantitative part employing empirical energy parameters whose values come from comparison of model and experiment.

3. A qualitative philosophy that attempts to bridge between ligand-field theory and LCAO-MO theory. This part, which inspired the invention of the Angular Overlap Model, will here be discussed without the assumption of any kind of additivity of single ligand contributions.

Referring first to 1 – with our chemical examples – the qualitative arguments of the past ran as follows: semi-empirical LFR shows that VCl_4^- has a partially filled d shell containing two electrons in a spin triplet state of the e^2 (T_d) subconfiguration, that is, VCl_4^- has a "d^2" configuration and accordingly is physically – in addition to formally – a V^{III} complex [64].

   Referring to 3, all the electrons that we want to associate mainly with the ligands of the complex, that is, the bound ligands, must have lower energy than the partially filled shell or the LFR description of the excited states would be invalid. The bonding process mainly involves a transfer of charge from the ligands that were originally Cl^- to the metal ion that was V^{3+}. In the complex we have valence electrons in filled bonding and non-bonding molecular orbitals, mainly of ligand character, and empty or partially filled antibonding orbitals, mainly of central ion character.

   If these arguments have an essence of reality, they can be strengthened by symmetry arguments. The bonding can be looked at in the very chemical way of focusing upon the individual bonds when the concepts of σ and π bonding come up, probably written here in order of decreasing importance for the large majority of chemical systems. Symmetry tells that the σ orbitals, which span four dimensions in the four-coordinated complex, belong to the T_d symmetry species a_1 and t_2. These orbitals are filled and bonding and have mainly ligand character. The a_1 orbital has no angular nodes and interacts with the vanadium atomic LUMO 4s. This "interaction with" is described in MO-AOM language as "perturbation by". The t_2 orbitals have one angular node and interact with (are perturbed by) the vanadium 3d(t_2) and 4p orbitals. Actually, in our "AOC" computations on VCl_4^- and VF_4^-, these (mainly) σ-bonding t_2 orbitals turn out to have the Vd participations of 16% and 13.5%, respectively, when analyzed in terms of Mulliken percentages. As to the Vp participations, the analogous numbers are 2% and <1%, respectively. The filled and bonding σ-orbitals are expected to lie below those of π symmetry, the σ-orbitals being the stronger-bonding ones. Actually, this is found to be generally true in "AOC". Moreover, the two kinds of bonding σ orbitals turn out to have similar energies in spite of the fact that they contain mutually exclusive central ion orbitals.

   The π orbitals span the eight dimensions of the e, t_2 and t_1 symmetry species, which should be found in this order of increasing energy for the following reason. The e orbitals cannot by symmetry be involved in σ bonding and therefore according to Kimball [88] should form the most bonding π orbitals. The t_2 orbitals form weaker π bonds and the t_1 orbitals must remain non-bonding. In the AOM [89] the relative π bonding propensity of the ligand e and t_2 orbitals is determined by symmetry to first order, in which case the ratio between their squared angular overlaps, which is equal to three should match their relative percentages

of d character. These are found to be 17% and 5%, respectively, for VCl_4^-. In addition, these t_2 orbitals have a small content of Cl p-σ (2%) and V p orbital (2%) character. However, for VF_4^- the situation is more complicated because there is a 10% σ-π mixing of the t_2 orbitals. Nevertheless, the energetic order of all the bonding orbitals remains the same. Also the bonding e orbitals are qualitatively similar for VCl_4^- and VF_4^- having a content of d character of 16% and 13% respectively.

Going further up the energy scale, we find the partially filled shell, which transforms as the d orbital set in T_d, that is, as e and t_2 in order of increasing energy. The energy ordering comes from the fact that the t_2 orbitals become σ anti-bonding (as well as π anti-bonding) while the e orbitals only become π anti-bonding.

The next sets of orbitals are a_1 and t_2 deriving symmetry-wise from the 4s and 4p orbitals of V^{3+}. These two sets of orbitals have vastly different energies in the atoms and (moderately charged) cations and are therefore expected to be found in their anti-bonding version in this same order of increasing energy. These results, based upon an "AOC" computation, have been depicted in Fig. 5.

We find it impressive that all these qualitative ideas about the electronic structure of VX_4^- (and especially about its bonding orbitals) have been corroborated without exception by the "AOC" computations. Moreover, these computations show that mixing of σ and π interactions is of minor significance for VCl_4^-, but at least of some importance for VF_4^-. This result simplifies the conventional views on orbital energies in this part of chemistry, provides some support to the idea of treating σ and π bonding independently, and adds qualitative confidence to an additive model such as the angular overlap model (AOM).

Even though the qualitative discussion given above is somewhat ad hoc and would seem to have limited scientific value, similar discussions have not only been in the textbooks for decades, but they have also been part of the chemical vocabulary in the discussion section of scientific papers. Since the philosophy of chemistry embraces intelligent ways of generalizing chemistry's diversity, and since computational chemistry has had a tendency to produce numbers referring to specific systems rather than results that have a general aspect to them, we have found it worth emphasizing that our qualitative ADF-"AOC" results with the single exception of the ordering of the bonding σ orbitals can be all depicted by using the quantitative results for VCl_4^- to exemplify them (Fig. 5). Moreover, it is significant that the ADF program package delivers these qualitative results – in a quantitative form – with very little computational effort.

Also the quantitative side of these computations (point 2 above) have chemical ramifications of interest. Thus, a quantitative result of the unrestricted computation adds new qualitative support for the chemical idea of oxidation states. The total Mulliken charges on V^{III}, which is found to be 0.63 for VCl_4^- and 1.5 for VF_4^-, shows the huge difference in covalency (charge transfer from X^- to V^{3+} in the bonding process) between the two ions and demonstrates that the oxidation state has little to do with the actual Mulliken charge. On the other hand, from the difference between the densities of electronic charges associated with α and β spins on V^{III}, one obtains a rough measure of the number of unpaired electrons on the metal ion through the net number of electrons corresponding to the uncompensated spins. This quantified number of unpaired electrons is 1.99 for VCl_4^- and 1.95 for VF_4^-. In both cases, this number is close to two, corresponding to the

$(t_2)^0$ ⎯ ⎯ ⎯

$(a_1)^0$ ⎯

σ and π antibonding $(t_2)^{1.2}$ ⎯ ⎯ ⎯
π antibonding $(e)^{0.8}$ ⎯ Δ ⎯

nonbonding $(t_1)^6$ ⎯ ⎯ ⎯
π bonding $(t_2)^6$ and $(e)^4$ ⎯ ⎯ ⎯
σ bonding $(t_2)^6$ ⎯ ⎯ ⎯
σ bonding $(a_1)^2$ ⎯

Fig. 5 Eigenorbitals of VCl_4^- in the "AOC" computation. One observes from below the filled ligand σ orbitals, a_1 and t_2, which are the most bonding ones; then the filled π set of orbitals e, t_2, and t_1; then the "d" orbitals, which are fractionally occupied in the "AOC", and finally the empty antibonding orbitals of symmetries a_1 and t_2 corresponding to the vanadium 4s and 4p orbitals. Even the relative order of π orbitals follows the rules of the qualitative ligand-field molecular orbital model, the t_1 orbitals being non-bonding and the e orbitals being the most bonding ones having a squared angular overlap with the d orbitals, which is three times as large as that of the t_2 orbitals. This qualitative picture is exactly that used in the teaching of the connection between ligand-field theory and molecular orbital theory. Mulliken analysis of the molecular orbitals' contents of atomic orbitals reveals little mixing of σ and π characters in support of the Angular Overlap Model. Figure 5 applies qualitatively to all the complexes of Table 27. There is, however, one exception: CrF_4. Here the bonding σ orbitals are permuted and a_1 is even moved above the bonding π set of e symmetry in the unrestricted computation. In the remaining complexes the order of the orbitals of the "AOC" and of the surplus spin orbitals of the unrestricted computation is the same

number of unpaired electrons in the d^2 system of V^{III}. These results are satisfactory for the inorganic chemist's conceptual world, a nice supplement to the strong qualitative results of ligand field theory, mentioned above.

Perhaps the fact that the surplus spin on the metal ion is smaller than two for the fluoride complex and larger than two for the complexes of the three heavy halides has to do with the lack of back bonding in the former case and the existence of it in the case of the heavy halides. Here one might think in particular of π back bonding to empty d orbitals on the halides, but also of σ back bonding to these orbitals. Anyway, both of these back-bonding phenomena are distinguishable in the percentage analysis of the eigenorbitals. π interaction between halides and central ions has in the literature been discussed mainly in terms of π donation from the halides and all the spectroscopic evidence pointed in this direction, because this evidence was based upon the net charge transfer. The dominance of this is also quantitatively strongly supported by the "AOC" computations. However, the back bonding aspect of the interaction is, as mentioned, discernible by the "AOC". This aspect was in focus early on in trying to understand the *a* character (hardness) of F and the *b* character (softness) of the other halogens.

The results of this subsection conflict with the philosophy of the cellular ligand-field model (CLF) of Gerloch and Woolley (G. and W.) even though this model is operationally identical to the angular overlap model (AOM) when this is used as a ligand-field model. Their philosophy (p 231 in [79]) is that the d electrons are little involved in the valence shell and we found here that they provide the dominating contribution to the covalency. In the case of VF_4^- the s and p charge transfers, which G. and W. consider the dominating ones, are found here to be very small indeed compared with the d contributions, which for all our complexes dominate those of s and p. A summation of our "AOC" results can be expressed in terms of the Mulliken net charge transfer from the X^- ions to the V^{3+} ion (integrated per l value):

$$
\begin{array}{cccc}
 & s & p & d \\
VCl_4^- & 0.2 & 0.6 & 1.6 \\
VF_4^- & 0 & 0.2 & 1.2
\end{array}
\qquad (94)
$$

G. and W. were so convinced by their bonding considerations that they felt obliged to emancipate themselves from the molecular orbital orientation of the AOM by introducing a whole new concept, "the cell", in chemistry and by renaming the ligand-field version of the AOM so as to call it the CLF model.

The fact that the heavy halides have a much higher degree of central ion s and p participation in their covalencies than fluoride is not surprising. What is surprising is the computational result that the d covalencies are so pronounced for the fluoride binding, almost as pronounced as for binding to the heavy halides. The fluoride ion has given surprises before in a comparative ligand-field (AOM) context by exhibiting higher e_σ as well as e_π parameters than the heavy halides [57].

The present results also show that while the integrated d covalencies increase gradually down the halide series, this is not the case for the s and p covalencies. Here chloride and bromide change places with the result that the total Mulliken charge on the central ions is lower in the chloride complexes than in the bromide

complexes. The two large gaps to the wing halides are noticeable in these charges found in the "AOC"-SCF computations. From tetrafluorido vanadate(III) to the corresponding iodido complex, they are, 1.46, 0.63, 0.78 and –0.15 respectively, and for chromium(IV) halides, 1.76, 0.37, 0.54, (–0.49). The last number, written in parentheses, refers to the corresponding unrestricted computation on CrI_4. This number can be considered to be an upper limit since it is a general feature of all our computations that this total charge is slightly lower in the restricted than in the corresponding unrestricted computation. Again the reversal of chloride and bromide in these series of numbers is not too surprising: An occasional small break in the monotonicity on going from period 3 to period 4 (row 2 to row 3) in the Periodic Table is well established. Furthermore, it is at least noteworthy that the metal ion has a lower charge in the chromium complexes with the three heavier halide ligands, than in the corresponding vanadium complexes.

However, possibly because the spin polarization is more pronounced for the d electrons, the uncompensated spin on the central ion, counted as number of electrons, nevertheless changes monotonically down the halide series. Down the vanadium(III) series the unrestricted SCF ground state computations give these numbers of electrons as 1.95, 1.99, 2.06 and 2.19 and down the chromium(IV) series they are found to be 1.84, 1.89, 2.04 and 2.28, respectively. All these numbers approximate the number of electrons in the partially filled shell and thereby provide a computational support to the concept of the oxidation state.

10.2
Addition of the Ligand-Field to the Repulsion. The Quantitative KS-DFT/LFR Model

Earlier we outlined our constrained use of the KS-DFT. In the other previous sections, we built up a unified picture of how the generalized two-electron operator $\hat{g}$ of the PMT model could be defined in its eigenbasis, which is a weak-field basis from an LFR point of view. We also produced the matrix of the same operator in a strong-field basis of the group hierarchies of Eq. (34). The single-determinant function basis (Table 24), which provides the *direct* link to KS-DFT, was transformed into the same strong-field basis (Table 25) by using Eq. (72). After discarding the small amount of information that we cannot parameterize from the set of ADF-computed energies, a numerically exact 1:1 relationship between these and the parametrical energy expressions of the PMT model was established. Then, by discarding a theoretically well-defined part of the PMT model, the interelectronic repulsion results of the ADF could be expressed in terms of parameters of the SCS model. For atomic systems, the Coulomb functional obeys the SCS model exactly and the exchange/correlation functional obeys it almost as well as the sum of the two functionals obeys the PMT model.

We now add a ligand field of tetrahedral symmetry by considering the complexes VX_4^- (X=F, Cl, Br, I). We include the complexes CrX_4 previously considered by Atanasov et al. in [39]. The spectrochemical parameter Δ is defined in the usual way (Eq. 69). By attributing an orbital energy $h_t=(2/5)\,\Delta$ to the "d"t_2 orbitals and $h_e=-(3/5)\,\Delta$ to the "d" e orbitals, the coefficient operators $\hat{Q}[\Delta]$ are immediately defined in all "d^q" cubic strong-field bases. As a one-electron operator $\hat{Q}[\Delta]$ is orthogonal to all the two-electron operators. Moreover, since the two function

bases that bridge between KS-DFT and LFR are both strong-field bases, $\hat{Q}[\Delta]$ is diagonal in these bases, and $\hat{Q}[\Delta]$ is therefore also diagonally orthogonal to all the PMT operators. This means that all the previous statements that are based upon the mutual orthogonality and diagonal orthogonality of the PMT operators can be extended so as to include $\Delta\hat{Q}[\Delta]$ and thus become valid for LFR with R representing either SCS or PMT.

$\hat{Q}[\Delta]$ exhibits both kinds of orthogonality with all sets of PMT operators, and the barycentered two-electron part of an ADF energy matrix can be obtained as the residual matrix after a least-squares removal of the $H_{av.}\hat{1}$ and the $\Delta\hat{Q}[\Delta]$ terms. This residual matrix can then – as in the case of the atomic ion – be analyzed using the PMT and the SCS models and either the determinant basis (db, Table 24) or the spin basis (sb, Table 25). Alternatively, in the spin basis all the PMT parameters can be removed at first and the matrix thus obtained as the residual matrix can then be used to find Δ. It is also possible to find Δ and all the two-electron parameters in a single least squares operation (either using the db or the sb). If the spin basis of Table 25 and the standard set of PMT parameters are used, it is possible to use the overlap method of Eq. (81) to find any one of the six parameters, whose coefficient operators are then all mutually diagonally orthogonal in addition to being orthogonal.

10.3
The LFR-ADF Molecular Problem as Compared with the Atomic One

Our 45 ADF energies are obtained as a sum of three diagonal matrices corresponding to three functionals: the kinetic energy functional, a one-electron property, the Coulomb functional, which contains a nuclear-nuclear term, an electron-nuclear term and an electron-electron term contributing collectively to the LFR, and the exchange/correlation functional, which in our parametric description also behaves as an LFR property.

When the problem was that of a d^q ion, we saw that our constrained ADF Coulomb functional handled the interelectronic repulsion exactly. Two parameters $D^{Coul.}$ and $E^{Coul.}$ were computable, thus following the SCS model. The exchange/correlation model also followed the SCS model delivering values for the parameters $D^{exch.}$ and $E^{exch.}$. However, in the fitting of XC "data", the variance was largely the same as that obtained by using the sum of the two functionals to fit the PMT model, that is, a lot smaller than when fitting the SCS model (cf. Eq. 78).

In the molecular case, the PMT and SCS models are insufficient for symmetry reasons because they contain too few R parameters to match the number required by the T_d symmetry [62]. However, in order to mimic LFR, we nevertheless impose these models upon the ADF computational "data". An analysis using each functional individually yields three sets of LFR parameters, valid for VCl_4^-:

$$
\begin{array}{lccc}
 & \Delta & D & E \\
\text{Kinetic} & -1.956 & & \\
\text{Coulomb} & +1.906 & 0.428 & 0.288 \\
\text{XC} & +0.553 & 0.291 & 0.179
\end{array}
\qquad (95)
$$

where the fit is exact only for the kinetic energy functional since the Coulomb and exchange/correlation functionals both deviate from the LF-SCS model. The combined LF-SCS description sorts the one-electron LF from the two-electron SCS parameters, but even in the case of the Coulomb "data", does so only approximately because of the symmetry insufficiency of the SCS part of the model. Enforcing either the SCS or the PMT restrictions on the ADF "data" nevertheless give unexpectedly satisfactory results from a chemical point of view and one may say that the LFR and the ADF fertilize each other. In the molecular case, the Coulomb functional carries the variance of the PMT model. This is qualitatively understandable: The Coulomb functional has a larger SSS than does the exchange/correlation one and because of the lower symmetry, it contains unfitted two-electron terms. The exchange functional alone – in spite of its symmetry difficulties – describes its "data" better than in the atomic case.

In the mimicking of LFR by KS-DFT, the energies of the individual Slater determinants computed by the three functionals of Eq. (95) have to be added. The same applies to the three Δ values of this equation. One may observe then that the sum of these Δ values is equal to the PMT value of Table 27, which again is equal to the one that would have been obtained by a fitting to the LFR with R=SCS (one may use Eq. 81) instead of going through a fitting procedure). Equation (95) shows clearly the modeling character of our present approach by the fact that the exchange/correlation functional gives a non-vanishing Δ value. It is curious that the Δ values obtained from the kinetic energy functional and the Coulomb functional largely cancel in the DFT results, which means that the value provided by the exchange correlation functional actually is close to that of the sum of the three functionals.

For the VX_4^- and CrY_4 systems the parameters of the LF-PMT and LF-SCS models have been collected together in Table 27. We found in Eq. (78) that for the atomic case a considerable systematic change in variance was associated with going from the PMT model to the SCS model. In the molecular case, this change is relatively smaller. For VCl_4^- the variances in μm^{-2} are collected together with those of the nine-parameter models:

$$
\begin{array}{lll}
\text{LF-NPM:} & \text{var}_{\text{diag.}}^{db} = 0.0374 & \text{var}_{\text{diag.}}^{sb} = 0.0391 \\[4pt]
\text{LF-PMT:} & \text{var}_{\text{diag.}}^{db} = 0.0450 & \text{var}_{\text{diag.}}^{sb} = 0.0469 \\[4pt]
\text{LF-SCS:} & \text{var}_{\text{diag.}}^{db} = 0.1150 & \text{var}_{\text{diag.}}^{sb} = 0.1847 \\[4pt]
H_{\text{av.}}: & (\text{SSS}_{\text{comp.}}^{db}) = \text{var}_{\text{diag.}}^{db} = 9.8359 & (\text{SSS}_{\text{comp.}}^{sb}) = \text{var}_{\text{diag.}}^{sb} = 11.1297
\end{array}
\tag{96}
$$

In the molecular case already the nine-parameter models obtain rather large variances as expected from the lower symmetry.

These variances may be compared with those of the Coulomb and the exchange/correlation ones when the two sets are fitted to their respective LF-SCS parameterizations:

$$
\begin{array}{lll}
\text{Coulomb} & \text{var}_{\text{diag.}}^{db} = 0.0471 & \text{var}_{\text{diag.}}^{sb} = 0.0471 \\[4pt]
\text{XC} & \text{var}_{\text{diag.}}^{db} = 0.0056 & \text{var}_{\text{diag.}}^{sb} = 0.0088
\end{array}
\tag{97}
$$

Table 27 Computational results for the tetrahalido complexes (μm^{-1}). The nephelauxetic series is reproduced for the interelectronic repulsion parameters of the PMT model of Table 1 and for the accumulative parameter ρ. β_ρ is in every case found to be somewhat smaller than β["AOC"] (see text). The order of the absolute values of the PMT parameters is consistently F≫Cl>Br>I. The nephelauxetic ratios are calculated from a given parameter and its corresponding free ion value found in Table 26. The SCS parameters D and E are supplemented by the SCS$^\perp$ parameters (Table 3). The nephelauxetic ratios here follow the same trends as those of the other PMT set and the order $D^v>D^s>E^0>E^1$ found in all the atomic calculations is repeated. Added to the table is also the average energy of the configuration, and as may be seen it is nephelauxetically reduced as well, clearly placing this quantity in the two-electron regime. The D/E ratio η increases from the atomic ion over fluoride to iodide. The PMT parameters are supplemented by determinations of the ligand field parameter Δ. A few of the calculated values may be compared to the empirical ones reported in [55]. These were determined from transitions within the spin triplets: VCl$_4^-$ have $(\Delta, E^1)=(0.553, 0.259)$ μm^{-1} and VBr$_4^-$ have $(\Delta, E^1)=(0.520, 0.228)$ μm^{-1}, following the same nephelauxetic and spectrochemical trends as the computations, but having a reversed internal field strength series ($\Sigma=2.14$ and 2.28 respectively). For comparison an LDA computation of VCl$_4^-$ is added to the table. The LDA computation gives a larger Δ parameter and smaller SCS parameters in accordance with the shorter metal-ligand distances obtained with LDA. In addition the distortion of the D and E parameters are similar to that of the atomic computations of Table 26. The main point that one may raise against the LDA computation is the large ratios D/E and $\Delta/\rho=\Sigma$

	$H_{av.}$	D^S	D^v	E^1	E^0	D	E	$D^\perp$	$E^\perp$	ρ	η	$\Delta[d^2]$	Σ
VF$_4^-$	−0.381	0.394	0.671	0.302	0.373	**0.477**	**0.309**	−0.126	0.021	**0.57**	1.54	**0.675**	1.19
β		0.624	0.672	0.641	0.647	0.536	**0.659**	**0.632**	0.600	0.309	**0.65**		
VCl$_4^-$	−0.316	0.329	0.572	0.252	0.305	**0.402**	**0.257**	−0.111	0.015	**0.48**	1.56	**0.502**	1.05
β		0.517	0.561	0.546	0.540	0.438	**0.555**	**0.526**	0.529	0.221	**0.55**		
VBr$_4^-$	−0.304	0.317	0.559	0.243	0.297	**0.390**	**0.249**	−0.110	0.016	**0.46**	1.57	**0.449**	0.97
β		0.498	0.541	0.534	0.520	0.427	**0.539**	**0.509**	0.524	0.235	**0.53**		
VI$_4^-$	−0.286	0.302	0.539	0.232	0.278	**0.373**	**0.236**	−0.108	0.013	**0.44**	1.58	**0.377**	0.85
β		0.468	0.515	0.515	0.497	0.399	**0.515**	**0.483**	0.514	0.191	**0.51**		
CrF$_4$	−0.323	0.372	0.652	0.281	0.358	**0.456**	**0.289**	−0.128	0.023	**0.54**	1.58	**0.967**	1.79
β		0.476	0.554	0.531	0.524	0.445	**0.544**	**0.513**	0.502	0.288	**0.53**		
CrCl$_4$	−0.236	0.284	0.506	0.209	0.253	**0.350**	**0.213**	−0.101	0.013	**0.41**	1.64	**0.682**	1.66
β		0.348	0.423	0.412	0.390	0.315	**0.418**	**0.378**	0.396	0.163	**0.41**		
CrBr$_4$	−0.220	0.270	0.489	0.199	0.243	**0.335**	**0.203**	−0.100	0.013	**0.39**	1.65	**0.601**	1.53
β		0.324	0.402	0.398	0.371	0.302	**0.400**	**0.361**	0.392	0.163	**0.39**		
VCl$_4^-$ VWN	−0.103	0.334	0.416	0.186	0.527	**0.359**	**0.221**	−0.037	0.102	**0.42**	1.62	**0.531**	1.26
β		0.369	0.514	0.538	0.493	0.466	**0.496**	**0.489**	0.661	0.451	**0.51**		

10.4
Molecular Hund's-Rules Computations

Earlier we gave reasons for putting an emphasis on energy states with the highest spin multiplicity and in a previous paper [37] we went into details only with this case. This means that we restricted ourselves to the ten "d²" states that are associated with S=1 and M$_S$=1. In this situation, we are concerned with the Hund's-second-rule computation, which quantifies this rule by computing the value of the parameter E^1 of the PMT model as defined in Table 1. This parameter will take on the same value if the PMT model is applied to the complete "d²" configuration

because $\hat{Q}\,[E^1]$ acts only trivially on the [S=0]-states, which thus may or may not be included in the "data" set (cf. Tables 1 and 25). The ligand-field problem of the VX_4^- complexes also has only one ligand-field parameter, the usual spectrochemical parameter Δ. Previously, it was pointed out that over M_S=1, the diagonal area of $E^1\hat{Q}\,[E^1]$ in the spin basis was smaller than that of $\Delta\hat{Q}[\Delta]$ whereas the two analogous quantities over "d^2", were of almost equal magnitude. The relevant coefficient operator areas are

$$\langle \hat{Q}[\Delta]|\hat{Q}[\Delta]\rangle_{\text{diag.}}^{\text{sb}} = \langle \hat{Q}[\Delta]|\hat{Q}[\Delta]\rangle = 18/5$$

$$\langle \hat{Q}[E^1]|\hat{Q}[E^1]\rangle_{\text{diag.}}^{\text{sb}} = 264/49; \qquad\qquad\qquad (98)$$

$$\langle \hat{Q}[E^1]|\hat{Q}[E^1]\rangle = 120/7 = 840/49$$

as can be read from Tables 1 and 25.

The degrees of diagonality of the coefficient operators are 1 for $\hat{Q}[\Delta]$, but only 11/35 for $\hat{Q}\,[E^1]$. In the atomic case, Δ=0, the degree of diagonality of the repulsion may be interpreted by the statement that only the ratio 11/35 of the total [M_S=1]-LFR information is accessible by our KS-DFT method. However, there is more than enough information left, and there are – at least in principle – only two consequences of the partial non-diagonality. One is that the parameter's formal statistical standard deviation, which is inversely proportional to the component of the length of the coefficient operator in the function basis used for the computation, will be the higher the more non-diagonal. The other consequence is that the parameter's contribution to the diagonal sum square splitting decreases, being proportional to the degree of diagonality. In the molecular case, this contribution will of course be further decreased by the dilution of the diagonal by the ligand field.

Equation (98) immediately reveals the increased competitiveness of $E^1\hat{Q}\,[E^1]$ on inclusion of the non-diagonal terms. With VCl_4^- as our example, we have Δ=0.523 µm^{-1} and E^1=0.252 µm^{-1}, and the conglomerate operator quantities are in µm^{-2} for M_S=1

$$\text{SSS}_\Delta = \Delta^2\langle \hat{Q}[\Delta]|\hat{Q}[\Delta]\rangle = \Delta^2\langle \hat{Q}[\Delta]|\hat{Q}[\Delta]\rangle_{\text{diag.}}^{\text{sb}} = 0.985$$

$$\text{SSS}_{E^1,\,\text{diag.}}^{\text{sb}} = (E^1)^2\,\langle \hat{Q}[E^1]|\hat{Q}[E^1]\rangle_{\text{diag.}}^{\text{sb}} = 0.342 \qquad\qquad (99)$$

$$\text{SSS}_{E^1} = (E^1)^2\,\langle \hat{Q}[E^1]|\hat{Q}[E^1]\rangle = 1.089$$

In addition to SSS_Δ, $\text{SSS}_{E^1,\,\text{diag.}}^{\text{sb}}$ is the quantity that can be computed by the ADF and the LFR allows the comparison with SSS_{E^1}. The example illustrates how the KS-DFT model as an electron density model favors the computation of the one-electron quantity Δ relative to the two-electron quantity E^1. The situation is particularly simple here because of the fact that there is just one two-electron parameter and one one-electron parameter. The prediction was [31] that the order of the ADF-computed energies, expressed as the diagonal energies in the spin basis should be governed by the Δ terms of their parametrical expressions and this prediction was confirmed.

If the complete "d^2" set of ADF energies is used for the parameterization but only the average energy of the [S=0]-states taken into account, the PMT param-

eter D^S, which is that associated with Hund's first rule, is the only D parameter that can be determined. The computation determining D^S and E^1 is conveniently made in two steps (Eq. 9), which we shall call the Hund's-rules computations. They are particularly important because by far the majority of experimental data available are based upon the spin-allowed transitions of d^3 and d^8 systems and they do not, therefore, involve the standard PMT parameters D^v and E^0.

10.5
Additional Results

Inspired by Atanasov et al. [39] we added the chromium(IV) halides to our vanadium series and, in addition, repeated all the chromium computations using LDA [90]. These turned out to give somewhat lower standard deviations than GGA on being used to transform the "AOC" Slater determinantal energies into LFR parameters. In Table 26 we have added the LDA computation on vanadium in order to illustrate the very different distortion of the SCS model obtained in general by LDA: LDA distorts the $D\hat{Q}[D]$ space less and the $E\hat{Q}[E]$ space more than does GGA, but with the same sign of the distortion following Eq. (87). Thus, in addition to all the formulae made in the previous section, all the qualitative statements made there are also valid for both approximations. Of course, the discussions involving actual parameter values are specific for our GGA computations. The parameter H_{av}, which cannot have any spatial character, is quite different in the two approximations but must still be of D^S- or D-type. Therefore, it is sort of understandable that its nephelauxetic variation resembles that of the other repulsion parameters.

10.5.1
Using the Local Density Approximation, LDA, for Complexes

LDA has often been used with Werner-type complexes. In our previous work [30], which focused on the interelectronic repulsion parameters, we discovered that the exchange correlation functional of LDA was unable to distinguish between the energies of the different pair interactions of Fig. 3. Therefore, we decided to use a GGA set of functionals and we chose the set denoted by PW91. We also found that the Coulomb functional was able to compensate for the deficiency of the exchange functional. Therefore, and also in order to be able to make a comparison with previous work easier [39], we have compared the results of the present work using PW91 with those, which came out of using the LDA in the form of VWN.

The main difference is that all metal to ligand distances are decreased by about 1%. This results in an increase in Δ values by 6% and a decrease in ρ values by about 10%, and thereby an increase in Σ values by as much as 18%. However, all our qualitative results and conclusions are independent of a choice of LDA or GGA. This applies to statements based upon the "AOC" alone (see above) as well as those based on the KS-DFT/LFR (earlier this section). In particular, the spectrochemical and the nephelauxetic series are imaged nicely. In other words, relative chemical differences are largely invariant to the choice of KS-DFT approximation whereas the numerical values of all quantities vary on going from GGA to LDA.

10.5.2
$[V(NH_3)_4]^{3+}$ Containing a Molecular Ligand, which is a Pure σ-Donor in Both AOM and KS-DFT

Common to all the chemical systems treated here is the monoatomic nature of the ligands and the fact that their site symmetries are C_{3v}. Ammonia is a molecular C_{3v}-ligand so that four ammonia molecules can form the tetrahedral $[V(NH_3)_4]^{3+}$ ion with the nitrogen ligators in C_{3v} sites. This ligand is not only the most important ligand-field ligand of all, having been used as a reference ligand (cf. above), but it also has the interesting AOM property of being a pure σ donor, apart from hyperconjugation effects that have always been assumed to be small. Therefore, we could not resist trying our double-approach on $[V(NH_3)_4]^{3+}$ in which the molecular fragment NH_3 exhibits its σ donation as $a_1(C_{3v})$ and its π donation as $e(C_{3v})$ [57].

The computations were most encouraging, placing ammonia correctly in the respective ligand series. The "AOC" gives $\Delta[\text{"AOC"}]=0.929\,\mu m^{-1}$ and $\beta[\text{"AOC"}]=0.695\,\mu m^{-1}$ and the KS-DFT/LFR based results are $\Delta[d^2]=0.944\,\mu m^{-1}$ and $\beta[d^2]=0.545\,\mu m^{-1}$. Moreover, while the Mulliken analysis of the σ donation from ammonia leaves the "dt_2" orbitals with 17% ligand character, the π donation from ammonia contributes to the "dt_2" and "de" orbitals only ligand characters that are rather small, 2% and 4%, respectively. When these three numbers are compared with those of VCl_4^-, which are 14, 7, and 16%, respectively, a convincing support to the conceptual background of the AOM is exhibited [57].

11
Conclusion

KS-DFT was used in a constrained form. At first the partially filled shell was identified. Then the "average-of-configuration" ("AOC") computation was used to define this partially filled shell in terms of its Kohn-Sham molecular orbitals. This computation also defined the core orbitals. All orbitals were fixed during the following computations. Thereby, the computations take place within the framework of a "d^q" configuration. The d^q is meant to remind about the fact that the pair-interaction operator $\hat{g}$, which is used for the PMT modeling of the interelectronic repulsion, is spherically symmetrical, and the quotation marks about the fact that the d orbitals are no longer pure d in character, but the LCAO molecular orbitals that carry the partially filled shell.

The computed energies correspond to the diagonal elements of a function basis, which is a strong-field basis of the ligand-field plus repulsion model, LFR. This statement also applies to atomic ions in which case we have the well-defined, but curious concept of the zero-field strong-field situation. This situation is far from being diagonal in the interelectronic repulsion, but it is by definition diagonal in the ligand field. The computed diagonal elements, 45 in the case of a "d^2" configuration, can be expressed in LFR parameters, which can be determined by solution of the linear equations.

We have found that the KS-DFT in the form of the ADF fits the Parametrical Multiplet Term (PMT) model extremely well, the standard deviations being of the

order of 0.01 μm^{-1} for atomic systems for which those of the SCS model are about six times as large. For the molecular systems, VX_4^- (X=F, Cl, Br, I), the PMT standard deviations increase in all cases by only a factor of about 2.5 relative to that of the V^{3+} ion, while the SCS standard deviations consistently *decrease* to about two thirds. This is remarkable in view of the fact that our "data" analyses impose spherical symmetry upon the systems as far as the two-electron interactions are concerned.

Moreover, we have found that two different strong-field bases provide the same PMT parameter values, but different values for the SCS parameters by direct fitting. Our recommendation, therefore, is to find the "proper" SCS parameters by a contraction of the PMT model that corresponds to projecting out the SCS part of this model in the multiplet term function basis. Thereby, the "systematic errors" of the ADF are removed and a much better comparison with the spectroscopically known values for the multiplet term energies is obtained. The whole procedure is completely well-defined and has allowed us to track down the systematic errors to the Coulomb and exchange functionals being both SCS faithful but giving energy splittings that are not commensurable, those associated with the Coulomb functional being high and those with the exchange functional low.

For molecular systems, that is, ligand-field systems, the procedure has been tested for the systems VX_4^- and CrX_4 (X=F, Cl, Br, I) to provide the spectrochemical and the nephelauxetic series computationally. Qualitatively, there is agreement with experiment and the jump from F$^-$ to the heavy halides is clearly borne out. Moreover, the spectrochemical parameter Δ as well as the nephelauxetic ratio β are reproduced remarkably well computationally in two rather different ways (se above). It should be noted that by symmetry the d parts of LCAO-MOs are mutually orthogonal for our chosen examples.

In addition to the good agreement with experiment, the relevant Kohn-Sham "AOC" orbital energy difference obtained by using the ADF agrees remarkably well with the value for the empirical ligand-field parameter computed by the LFR imaging. This fact adds to the chemical value of the ADF program package as does also its symmetry faithfulness and its built-in symmetry facilities and possibilities of performing Mulliken analyses. These analyses allow quantification of the nephelauxetic phenomenon directly from the "AOC" computations, that is, without an LFR parameterization.

The quantitative outcome of our fixed-orbital ADF computations and their associated parametrical "data" treatment is not only a transformation of the strong-field expectation values of the KS-DFT Hamiltonian to its eigenvalues, but also a parameterization that corresponds to knowing strong-field, weak-field, and all intermediate-field representations of ligand-field theory.

Our method of mimicking ligand-field theory by KS-DFT using the ADF must have similar limitations to ligand-field theory itself. On the other hand, experimental chemistry has different limitations, and we have by our treatment of VX_4^-, CrX_4, and $[V(NH_3)_4]^{3+}$ demonstrated that the ADF program package has the potential of being able to act as a supplement to experimental ligand-field studies.

We have presented a KS-DFT method by which we are able to compute the empirical parameters of certain ligand-field systems consistently, and in two almost

independent ways. It is remarkable that this KS-DFT-based method, which at least in principle is non-empirical, allows the ADF program package to be used to compute parameters, which have up until now only been obtainable semi-empirically. It is even more remarkable that in spite of the fact that our constrained use of KS-DFT invalidates the virial theorem in just the same way as do the Slater-Condon-Shortley model and the Ligand Field Repulsion model, we have at hand a model, which is in principle an all-electron model and which yet allows the computation of the eigenvalues of effective operators acting on either a fixed atomic orbital d^q configuration or a fixed molecular orbital "d^q" configuration: in either case the configuration of the partially filled shell.

The KS-DFT orbitals of the whole valence shell obtain an energy order which is predictable by the symmetry and energy arguments that are an established part of the chemical reasoning used in molecular orbital oriented ligand-field theory and therefore also in the angular overlap model.

The systems chosen for the present study are atoms and molecular entities whose point group T_d belongs to the cubic class. Thereby we obtained at least two simplifications as compared with more general chemical systems:

1. The d part of our "d" molecular eigenorbitals, which make up the partially filled shell, have a 1:1 relationship with our standard d orbitals and are therefore mutually orthogonal.
2. The local metal to ligand symmetry is C_{3v} so that the π orbitals remain degenerate by symmetry.

In a recent paper on square planar d^8 systems, the lack of π degeneracy was shown to complicate KS-DFT/LFR mimicking [91].

When the name of the semi-empirical series of decreasing repulsion parameters was chosen as the nephelauxetic series, the basis for this naming was the model fact that analogous parameters existed for a transition metal complex and the central ion contained in it. Since in LFT the repulsion was parameterized by the SCS model just as in atomic theory, the parameters of the molecular and atomic systems were directly comparable. The fact that the repulsion parameters of complexes invariably had lower values than those of their naked central ions was an imaging of a situation where these ions had had their charges reduced and concomitantly their radial functions expanded. Thus it was obvious to explain the phenomenon by invasion of charge from the ligands to the central ion in the bonding process. This could happen by s and p covalency, and with or without a contribution from d covalency. Thereby the concepts of *central-field covalency* and the expanded radial function model arose. Jørgensen considered an alternative mechanism for explaining the observed nephelauxetic phenomenon, which he named *symmetry-restricted covalency*. This concept was based upon the dilution of the d contents of the partially filled shell by delocalization as it can be formulated by using an LCAO-MO description of the d covalency. Jørgensen expected this mechanism to provide only a minor part of the nephelauxetism and the genuine nephelauxetism of the central field covalency became accepted largely by the whole chemical community as the explanation of the phenomenon.

However, we found earlier that the nephelauxetic series could be explained computationally by delocalization using the "AOC" computation exclusively, that

is, without introducing the LFR and thus without the use of energy parameters. In Table 27 the β_ρ values based upon the KS-DFT/LFR model and the accumulative repulsion splitting parameter $\rho=(D^2+E^2)^{1/2}$ exhibit values that are only slightly smaller than those discussed above. The conclusion therefore is that the phenomenological nephelauxetism is not mainly caused by a genuine expansion of the d electron cloud, but rather by the fact that the partially filled shell can only very partially be described as a d electron shell. In other words, the nephelauxetic phenomenon, which images a cloud expansion, is actually mainly caused by a dilution of the d electron contents of the partially filled shell. Therefore, the parametrical d^q model is a more appropriate name for LFR than is the expanded radial function model.

12
References

1. Schäffer CE, Jørgensen CK (1958) J Inorg Nucl Chem 8:143
2. Schäffer CE (1958) J Inorg Nucl Chem 8:149
3. Jørgensen CK (1962) In: Cotton FA (ed) Interscience. Prog Inorg Chem 4:73
4. Yamatera H (1958) Bull Chem Soc Jpn 31:95
5. Jørgensen CK, Pappalardo R, Schmidtke HH (1963) J Chem Phys 39:1422
6. Jørgensen CK, Schmidtke HH (1963) Z Phys Chem 38:119
7. Schäffer CE, Jørgensen CK (1965) Mol Phys 9:401
8. Schäffer CE (1967) Proc R S London Series A Math Phys Eng Sci 297:96
9. Schäffer CE (1968) Struct Bond 5:68
10. Schäffer CE (1971) Int J Quant Chem 5:379–390
11. Schäffer CE (1973) In: Price WC, Chissick SS, Ravensdale T (eds) Wave mechanics – the first 50 years. Butterworths, London, chap 12, p 174
12. Schäffer CE (1973) Struct Bond 14:69
13. Schäffer CE (1970) Pure Appl Chem 24:361
14. Harnung SE, Schäffer CE (1972) Struct Bond 12:257
15. Harnung SE, Schäffer CE (1972) Struct Bond 12:201
16. Damhus T, Harnung SE, Schäffer CE (1984) Theor Chim Acta 65:317, 365, 389, 405, 419, 433
17. Schäffer CE (1982) Physica A 114A:28
18. Bendix J, Schäffer CE, Brorson M (1989) Coord Chem Rev 94:181
19. Brorson M, Damhus T, Schäffer CE (1983) Comm Inorg Chem 3:1
20. Brorson M, Jensen GS, Schäffer CE (1986) J Chem Ed 63:387
21. Schäffer CE (1974) Theor Chim Acta 34:237
22. Bendix J, Brorson M, Schäffer CE (1994) ACS Symp Ser 565:213
23. Judd BR, Leavitt RC (1986) J Phys B Atomic Mol Phys 19:485
24. Brorson M, Schäffer CE (1988) Inorg Chem 27:2522
25. Condon EU, Shortley GH (1935) The theory of atomic spectra. Cambridge University Press, Cambridge, UK
26. Uylings PHM (1984) J Phys B Atomic Molec Phys 17:2375
27. Judd BR, Leavitt RC (1986) J Phys B Atomic Mol Phys 19:485
28. Hansen JE, Judd BR (1985) J Phys B Atomic Mol Phys 18:2327
29. Parr RG, Yang W (1989) Density functional theory of atoms and molecules. Oxford University Press, New York
30. Anthon C, Schäffer CE (2002) Coord Chem Rev 226:17
31. Anthon C, Bendix J, Schäffer CE (2003) Inorg Chem 42:4088

32. Deeth RJ (1995) Struct Bond 82:1
33. Chermette H (1998) Coord Chem Rev 178:699
34. Te Velde G, Bickelhaupt FM, Baerends EJ, Fonseca Guerra C, van Gisbergen SJA, Snijders JG, Ziegler T (2001) J Comp Chem 22:931
35. Bendix J, Deeth RJ, Weyhermueller T, Bill E, Wieghardt K (2000) Inorg Chem 39:930
36. Deeth RJ (1990) J Chem Soc Dalton Trans 365
37. Deeth RJ (1991) J Chem Soc Dalton Trans 1467
38. Deeth RJ (2001) J Chem Soc Dalton Trans 664
39. Atanasov M, Daul CA, Rauzy C (2003) Chem Phys Lett 367:737
40. Ziegler T, Rauk A, Baerends EJ (1977) Theor Chim Acta 43:261
41. Mineva T, Goursot A, Daul CA (2001) Chem Phys Lett 350:147
42. Daul CA, Guedel HU, Weber J (1993) J Chem Phys 98:4023
43. Daul CA (1994) Int J Quant Chem 52:867
44. Versluis L, Ziegler T (1988) J Chem Phys 88:322
45. Baerends EJ, Ellis DE, Ros P (1973) Chem Phys 2:41
46. Te Velde G, Baerends EJ (1992) J Comp Phys 99:84
47. Vrije Universiteit, De Boelelaan 1083, 1081 HV Amsterdam, The Netherlands, ADF version 2002.03
48. Watson RE (1959) Technical Report No 12. Cambridge, MA, MIT
49. Watson RE (1960) Phys Rev 118:1036
50. Bendix J, Brorson M, Schäffer CE (1993) Inorg Chem 32:2838
51. Ferguson J, Wood DL (1970) Aust J Chem 23:861
52. Scaife DE (1959) Chem Soc Spec Publ No 13, p 152
53. Gruen DM, Gut R (1961) Nature 190:713
54. Scaife DE (1970) Aust J Chem 23:2205
55. Clark RJH, Nyholm RS, Scaife DE (1966) J Chem Soc A 1296
56. Casey AT, Clark RJH (1968) Inorg Chem 7:1598
57. Glerup J, Mønsted O, Schäffer CE (1976) Inorg Chem 15:1399
58. Glerup J, Mønsted O, Schäffer CE (1980) Inorg Chem 19:2855
59. Löwdin PO (1959) J Mol Spectrosc 3:46
60. Katriel J, Pauncz R (1977) Adv Quant Chem 10:143
61. Vanquickenborne LG, Hoet P, Pierloot K (1986) Inorg Chem 25:4228
62. Griffith JS (1961) The theory of transition-metal ions. Cambridge University Press, Cambridge UK
63. Hund F (1925) Z Phys 33:345
64. Jørgensen CK (1969) Oxidation numbers and oxidation states. Springer, Berlin Heidelberg New York
65. Jørgensen CK (1971) Modern aspects of ligand field theory. North-Holland, Amsterdam
66. Trees RE (1951) Phys Rev 83:756
67. Jørgensen CK (1962) Absorption spectra and chemical bonding in complexes. Pergamon Press, Oxford
68. Jørgensen CK (1962) Orbitals in atoms and molecules. Academic Press, London
69. Slater JC (1968) Phys Rev 165:655
70. Ballhausen CJ, Moffitt W (1956) J Inorg Nucl Chem 3:178
71. Yamatera H (1957) Naturwissenschaften 44:375
72. Soliverez, CE (1973) Int J Quant Chem 7:1139
73. Hempel JC, Donini JC, Hollebone BR, Lever ABP (1974) J Am Chem Soc 96:1693
74. Baerends EJ, Branchadell V, Sodupe M (1997) Chem Phys Lett 265:481
75. Perdew JP, Chevary JA, Vosko SH, Jackson KA, Pederson MR, Singh DJ, Fiolhais C (1992) Phys Rev B Condens Matter Mater Phys 46:6671
76. Szilagyi RK, Metz M, Solomon EI (2002) J Phys Chem A 106:2994
77. Becke AD (1988) Phys Rev A 38:3098
78. Gerloch M (1987) In: Avery JS, Dahl JP, Hansen A (eds) Understanding molecular poperties, vol 111. Dordrecht, Reidel
79. Duer MJ, Fenton ND, Gerloch M (1990) Int Rev Phys Chem 9:227 and references therein

80. Gerloch M (1990) Coord Chem Rev 99:117
81. Schäffer CE (1995) Inorg Chim Acta 240:581
82. Riley MJ (1998) Inorg Chim Acta 268:55
83. Schäffer CE (1966) Theor Chim Acta 4:166
84. Smith DW (1977) Inorg Chim Acta 22:107
85. Hitchman MA, Cassidy PJ (1979) Inorg Chem 18:1745
86. Ceulemans A, Beyens D, Vanquickenborne LG (1982) Inorg Chim Acta 61:199
87. Schäffer CE (1995) Inorg Chim Acta 240:581
88. Kimball GE (1940) J Chem Phys 8:188
89. Schäffer CE (2000) Inorg Chim Acta 300/302:1035
90. Vosko SH, Wilk L, Nusair L (1980) Can J Phys 58:1200
91. Deeth RJ (2003) Faraday Discuss 124:379

Author Index Volumes 101–107

Subject Index